



**HAL**  
open science

## Wetting, nucleation and growth in soldering

Oleksii Liashenko

► **To cite this version:**

Oleksii Liashenko. Wetting, nucleation and growth in soldering. Other. Université Grenoble Alpes; Université Nationale Bogdan Khmelnytsky de Cherkasy, 2015. English. NNT: 2015GREAI076 . tel-01266355

**HAL Id: tel-01266355**

**<https://theses.hal.science/tel-01266355>**

Submitted on 2 Feb 2016

**HAL** is a multi-disciplinary open access archive for the deposit and dissemination of scientific research documents, whether they are published or not. The documents may come from teaching and research institutions in France or abroad, or from public or private research centers.

L'archive ouverte pluridisciplinaire **HAL**, est destinée au dépôt et à la diffusion de documents scientifiques de niveau recherche, publiés ou non, émanant des établissements d'enseignement et de recherche français ou étrangers, des laboratoires publics ou privés.



UNIVERSITÉ  
GRENOBLE  
ALPES

## THÈSE

Pour obtenir le grade de

**DOCTEUR DE L'UNIVERSITÉ GRENOBLE  
ALPES**

**préparée dans le cadre d'une cotutelle entre  
l'Université Grenoble Alpes et l'Université de  
Cherkasy**

Spécialité : **Matériaux, Mécanique, Génie Civil, Electrochimie**

Arrêté ministériel : le 6 janvier 2005 - 7 août 2006

Présentée par

**Oleksii LIASHENKO**

Thèse dirigée par **Fiqiri HODAJ** et  
codirigée par **Andriy GUSAK**

préparée au sein des **Laboratoires SIMaP et SSM**

dans l'École Doctorale **I-MEP2**

# **Mouillage, germination et croissance lors du brasage en électronique**

Thèse soutenue publiquement le **23 Octobre 2015**,  
devant le jury composé de :

**Mme. Marie-Laurence GIORGI**

Professeur à l'Ecole Centrale de Paris, Rapporteur

**M. Dominique MANGELINCK**

Directeur de Recherches IM2NP, Université d'Aix-Marseille, Rapporteur

**M. Alain HAZOTTE**

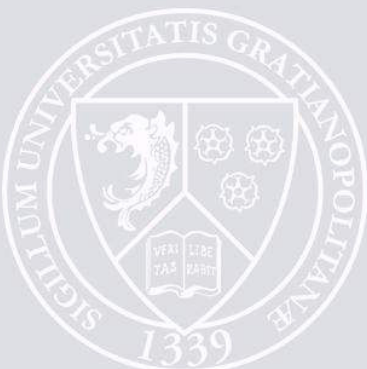
Professeur à l'Université de Lorraine, Président

**M. Andriy GUSAK**

Professeur à l'Université de Cherkasy, Co-directeur

**M. Fiqiri HODAJ**

Professeur à Grenoble INP, Directeur





## Acknowledgements

First and foremost I would like to thank my supervisors Prof. Fiqiri Hodaj and Prof. Andriy M. Gusak for the strong support, inspiration and guidance they provided during all these years. Their devotion to science, research and teaching was the basis that made this project complete.

This thesis was performed at Grenoble Alpes University and Cherkasy National University and was partially supported by the Ministry of Education and Science of Ukraine.

I would like to thank Prof. Michel Pons, director of SIMaP laboratory and Prof. Anatolii Kuzminskii and lately Prof. Oleksandr Cherevko, rectors of Cherkasy National University, for having hosted me during my studies.

I am grateful to Prof. Alain Hazotte for accepting to preside over the jury of the thesis.

I am sincerely grateful to Prof. Marie-Laurence Giorgi and Prof. Dominique Mangelinck for the expert evaluation and valuable comments given as "rapporteurs" in the jury.

I would like to thank Dr. Rayisa Voytovich for teaching me the main experimental techniques and mainly the wetting test equipment as well as providing the valuable hints when needed.

I am also grateful to SIMaP and CMTc teams for all the support. These gratitudes are especially sent to Prof. Sabine Lay, Mr. Frédéric Charlot, Mr. Hérve Collas, Mrs. Fabienne Fonseca, Mr. Laurent Artaud, Mrs. Jacqueline Cuoq, Mrs. Sylvie Champavier, Dr. Iona Nuta, Mrs. Christèle Poggi, Mr. Stéphane Coindeau, Mrs. Florence Robaut, Mrs. Joelle Calabro.

I would like also to thank staff from Cherkasy National University for strong administrative support during performing this thesis. My thanks are especially sent to Mr. Volodymyr Vlasenko, Mrs. Tetiana Platoshkina, Mrs. Valentyna Danilova, Prof. Nina Tarasenkova, Prof. Serhii Kornovenko, Prof. Vasyl Moysienko, Prof. Tetiana Zaporozhets, Dr. Yuriy Andriyako, Dr. Grigoriy Lucenko, Mrs. Ludmila Kiba, Mrs. Tamara Terentieva, Dr. Yaroslav Korol, Dr. Mykola Pasichniy, Dr. Semen Kornienko, Dr. Nadiya Storozhuk, Mr. Serhiy Nikitin, Mrs. Yana Ivashchenko, Mrs. Marina Vozhova.

I would like to thank my friend Dr. Jean-Pierre Avon for the strong help, support and attention. My special thanks are also sent to my friends Nikolay, Mohammed, Yaofeng, Qingquan and Maxim.

My deepest gratitude is sent to my wife Tania for staying by my side all these years. Her strong support and presence made my life much more colourful and meaningful. I am also grateful to our small dog Lilou for making the last year of performing thesis less stressful.

I am grateful to my big family for all the love, support and attention. I hope to keep deserving all this.

I want to dedicate this work to my father Yuriy. His passionate approach to science, teaching enthusiasm and love were the prerequisites for my professional choice.

## Table of content

<b>General introduction.....</b>	<b>1</b>
<b>Chapter 1 Bibliographic literature review.....</b>	<b>4</b>
1. Introduction.....	4
2. Soldering in microelectronics.....	4
2.1. Introduction .....	4
2.2. The Cu-Sn system in soldering technology.....	4
2.3. Packaging in the microelectronics .....	5
2.3.1. Wire Bonding method .....	5
2.3.2. Flip Chip method .....	5
2.3.3. Advanced packaging methods for Integrated Circuits (IC).....	6
2.3.4. Reliability in microelectronics .....	7
2.3.4.1. Mechanical strength of the solder bumps and microbumps.....	7
2.3.4.2. Voiding in the solder joint.....	8
2.4. Conclusions.....	9
3. Wettability of Cu and Cu/Sn intermetallic surfaces by liquid Sn or Sn alloys.....	10
3.1. Introduction.....	10
3.2. General aspects of wetting: thermodynamics.....	10
3.2.1. The fundamental equations of wetting and adhesion .....	10
3.2.2. Wetting of real solid surfaces.....	11
3.2.3. Effect of the surface asperities.....	11
3.2.4. Effect of the chemical deterioration of the surface.....	13
3.3. Wetting dynamics.....	13
3.3.1. Non reactive wetting.....	13
3.3.2. Reactive wetting.....	15
3.3.2.1. Dissolutive wetting.....	15
3.3.2.2. Formation of the reaction layer at the interface.....	16
3.4. Wetting of Cu and Cu-Sn intermetallics by liquid Sn or Sn based alloys.....	18
3.4.1. Wetting of Cu.....	18
3.4.2. Wetting of Cu-Sn intermetallics.....	22
3.5. Conclusions.....	22
4. Interfacial reaction between Cu substrate and Sn or Sn-based alloys.....	23
4.1. Introduction.....	23
4.2. Very early stages of reaction at Cu/Sn interface.....	23
4.3. Interfacial reactions at Cu/solid Sn interface.....	28
4.3.1. Experimental results on Cu/solid Sn reactions.....	28
4.3.1.1. From -2°C to 80°C.....	28
4.3.1.2. From 70°C to 220°C.....	29
4.3.2. Kirkendall voids during solid-state reactions.....	32
4.3.3. Modeling of the phase growth and competition during solid-state reactions.....	34
4.4. Interfacial reactions at Cu/liquid Sn interface.....	36
4.4.1. Experimental results on Cu/liquid Sn reactions.....	36
4.4.2. Modeling of the phase growth and competition during reflow (Cu/liquid Sn reaction).....	40
4.5. Conclusions.....	41
5. Heterogeneous nucleation in crystallization of liquid Sn or liquid Sn-Ag-Cu alloys: solder balls and solder joints solidification.....	42
6. Conclusions.....	45

<b>Chapter 2 Experimental methods and materials.....</b>	<b>47</b>
1. Introduction.....	47
2. Sessile drop method.....	47
3. Experimental equipment.....	50
3.1. Alumina furnace.....	50
3.2. Metallic furnace.....	50
3.3. Calibration of alumina and metallic furnaces.....	51
3.4. Acquisition system of the droplet shape.....	52
3.5. Muffle furnace.....	53
3.6. Fast dipping experimental setup.....	53
3.7. DSC setup.....	54
4. Characterization equipment.....	54
5. Materials.....	54
5.1. Materials received from the suppliers.....	54
5.2. Alloys processed in laboratory.....	54
5.3. Intermetallics processed in laboratory ( $\eta$ -Cu <sub>6</sub> Sn <sub>5</sub> , $\epsilon$ -Cu <sub>3</sub> Sn and Ag <sub>3</sub> Sn).....	55
5.3.1. Bulk $\eta$ -Cu <sub>6</sub> Sn <sub>5</sub> and Ag <sub>3</sub> Sn.....	55
5.3.2. Scalloped $\eta$ -Cu <sub>6</sub> Sn <sub>5</sub> .....	57
5.3.3. Bulk $\epsilon$ -Cu <sub>3</sub> Sn.....	57
6. Metallographic preparation of materials.....	58
6.1. Mounting and cutting.....	58
6.2. Polishing of the substrates.....	58
6.3. Etching.....	59
7. Conclusions.....	59
<b>Chapter 3 Wetting of Cu, Ag and Cu-Sn and Ag-Sn intermetallic compounds by liquid Sn or Sn-Cu alloys.....</b>	<b>60</b>
1. Introduction.....	60
2. Wetting of Cu substrate by liquid Sn or Sn-Cu alloys.....	60
2.1. Introduction.....	60
2.2. Experiments without preheating of Cu substrate.....	61
2.3. Experiments with preheating of the Cu substrate.....	62
2.3.1. Introduction.....	62
2.3.2. Investigation of wetting using conventional camera.....	62
2.3.3. Investigation of wetting using the rapid camera.....	64
2.3.3.1. Wetting of Cu by the liquid Sn-7.8wt.%Cu alloy.....	64
2.3.3.2. Wetting of Cu by liquid Sn.....	67
2.3.4. Characterization of some Cu/Sn samples.....	69
2.4. Conclusions.....	73
3. Wetting of Cu <sub>3</sub> Sn by liquid Sn.....	73
3.1. Introduction.....	73
3.2. Investigation of wetting of Cu <sub>3</sub> Sn by using a conventional camera.....	73
3.2.1. Experiments without preheating of the Cu <sub>3</sub> Sn substrate.....	73
3.2.2. Experiments with preheating of the Cu <sub>3</sub> Sn substrate.....	75
3.3. Investigation of wetting by using a rapid camera.....	75
3.4. Characterization of some selected samples.....	76
3.5. Conclusions.....	80
4. Wetting of Cu <sub>6</sub> Sn <sub>5</sub> substrates.....	81
4.1. Introduction.....	81
4.2. Wetting of Cu <sub>6</sub> Sn <sub>5</sub> substrate by a presaturated Sn-7.8wt.%Cu alloy at 390°C.....	81

4.3. Wetting of bulk $\text{Cu}_6\text{Sn}_5$ by pure Sn.....	84
4.4 Conclusions.....	85
5. Wetting of scalloped $\text{Cu}_6\text{Sn}_5$ surfaces.....	86
5.1. Introduction.....	86
5.2. Experimental results.....	86
5.3. Conclusions.....	88
6. Wetting of Ag and $\text{Ag}_3\text{Sn}$ by liquid Sn.....	88
6.1. Introduction.....	88
6.2. Wetting of Ag substrate by liquid Sn.....	89
6.3. Wetting of $\text{Ag}_3\text{Sn}$ substrate by liquid Sn.....	91
6.4. Discussion.....	92
6.5. Conclusions.....	93
7. Conclusions.....	93

## **Chapter 4 Nucleation in soldering.....95**

1. Introduction.....	95
2. Experimental investigation of initial stage formation of reaction product at Cu/liquid Sn interface.....	96
2.1. Introduction.....	96
2.2. Description of the experiment.....	96
2.3. SEM-FEG study of the reaction spots after the FIB preparation.....	98
2.4. The TEM study of the reaction samples.....	101
2.5. Conclusions.....	108
3. Modeling of $\text{Cu}_3\text{Sn}$ nucleation and growth at Cu/ $\text{Cu}_6\text{Sn}_5$ interface in Cu/ $\text{Cu}_6\text{Sn}_5$ /liquid Sn system.....	109
3.1. Introduction.....	109
3.2. $\text{Cu}_3\text{Sn}$ suppression criterion for solid Cu/liquid Sn reaction.....	109
3.2.1. Introduction.....	109
3.2.2. Model of $\text{Cu}_3\text{Sn}$ suppression criterion at Cu/Sn interface.....	109
3.2.3. Conclusions.....	112
3.3. Criteria of kinetic suppression of lateral growth of intermediate phases, application to $\text{Cu}_3\text{Sn}$ .....	113
3.3.1. Introduction.....	113
3.3.2. Problem formulation and general solution.....	113
3.3.3. Application to Cu-Sn system.....	118
3.3.4. Summary.....	118
3.4. Conclusions.....	118
4. Spectrum of nucleation modes in crystallization of Sn-Cu solder: experimental results versus theoretical model calculations.....	119
4.1. Introduction.....	119
4.2. Experimental procedure.....	119
4.3. Experimental results.....	120
4.4. Discussion.....	123
4.4.1. Homogeneous nucleation.....	124
4.4.2. Heterogeneous nucleation at the flat interface molten Sn / $\text{Cu}_6\text{Sn}_5$ .....	125
4.4.3. Nucleation of a spherical cap on a spherical particle.....	126
4.4.4. Nucleation of a nanolayer on a spherical nanoparticle.....	127
4.4.5. Nucleation of a spherical cap on a spherical cavity.....	129
4.4.6. Nucleation on the microgrooves.....	131
4.4.6.1. The small solid particles of the $\eta$ -phase have microgrooves on their surface.....	131
4.4.6.2. Nucleation on a step with various misorientation angles.....	132

4.5. Conclusions.....	135
5. Conclusions.....	135
<b>Chapter 5 Growth kinetics of intermetallic layers in the Cu /Sn system.....</b>	<b>137</b>
1. Introduction.....	137
2. Phase growth competition in solid-liquid reactions between Cu or Cu <sub>3</sub> Sn compound and liquid Sn-based solder.....	138
2.1. Experimental procedure.....	138
2.2. Experimental results.....	138
2.3. Theoretical analysis.....	140
2.3.1. Growth kinetics limited by solid state diffusion - parabolic regime.....	141
2.3.2. Reaction of Cu with liquid Sn occurs by Cu penetration through the liquid intergranular channels of η-phase.....	142
2.4. Comparison of theory and experiment.....	145
2.5. Conclusions.....	146
3. Differences between Cu/solid Sn and Cu/metastable liquid Sn interfacial reactions at identical temperature: role of the liquid state on the kinetics of interfacial reactions and the morphology of the reaction product.....	146
3.1. Introduction .....	146
3.2. Experimental procedure.....	146
3.3. Results and discussion.....	147
3.3.1. Comparison of the growth kinetics between Cu/metastable liquid alloy and Cu/solid alloy at identical temperature, role of the driving force of Cu <sub>6</sub> Sn <sub>5</sub> formation.....	147
3.3.2. Modelling of growth kinetics of η-Cu <sub>6</sub> Sn <sub>5</sub> layer at Cu/liquid Sn-based alloy interface.....	156
3.3.3. Application.....	159
3.4. Conclusions.....	160
4. Theoretical prediction of the liquid channel width in Cu/liquid solder reactions.....	161
5. Conclusions.....	163
<b>General conclusions.....</b>	<b>164</b>
<b>Appendices.....</b>	<b>167</b>
<b>References.....</b>	<b>174</b>

## General introduction

It is hard to imagine the sphere of life that was not influenced or at least slightly touched on by microelectronics. Being one of the gems of the general scientific breakthrough in the last century, its capacity as a science opens borders for emerging technologies and stimulates comprehensive and profound research of new horizons. As an industry microelectronics spreads to new challenges from economic reliability and quality to design. In a moment, which lasted several decades but that is comparatively small to age of our civilization, microelectronics became a revelation and wizardry that makes our everyday life more comfortable, effective and accessible.

The rate of development of microelectronics brings us to well-known Moore law, which has proved its verity in the last half of the century: the number of the components in the Integrated Circuits was doubling every two years. In the words of numbers the world science and industry managed to increase the number of transistors per chip by a factor of  $5 \times 10^5$  with relevant decrease in the smallest feature size on a chip by a factor of 700, being about 14 nm up to date. The trend of miniaturization is still there, but obviously its limit lies somewhere in the atomic scale. This natural limitation should be bypassed by some technological breakthrough in order to keep the tendency defined by the Moore's law. However, economical reasons can suppress the lowering of the size of the chip features even earlier - it might be not reasonable to miniaturize the chip parts anymore due to *high costs of the technology implementation*. While the cost of one transistor decreased significantly during last decades, the general price of the whole manufacturing process (starting from research and development of the new technology, reliability tests and manufacturing) increases exponentially with time. This second law (called Rock's law or Moore's second law) may not limit the general scientific development but it may stop the application of the existing approaches to fulfill the basic Moore's law.

Therefore, to keep the trend of complexity growth of the integrated-circuit technology some new approaches should emerge. *One of them is the transition from two-dimensional paradigm to three-dimensional one in **packaging** of the integrated circuits, which should provide few more generations to go. One of the principal limitations in the packaging is the ability to join different parts of the integrated circuit.* The process used for this is **soldering**, meaning the joining of metallic parts by use of a filler metallic alloy or pure metal (solder alloy) placed between the parts to be joined. The whole system is heated at a temperature, higher than the melting point of the filler alloy and lower than the melting points of both parts to be joined. A good adhesion should be attained not only between the liquid alloy and the solid parts but also between the solidified alloy and the solid parts after cooling at room temperature.

There are numerous phenomena that intervene in the soldering process such as: wetting of the solids parts by the liquid alloy and solid/liquid interfacial interactions (dissolution, diffusion, nucleation and growth of interfacial products) when the solder is in the liquid state (*reflow process*) as well as undercooling, nucleation and solidification of the bulk solder alloy during cooling of the whole system to room temperature.

Soldering is the one mostly used techniques in microelectronic industry to join the under-bump metallization layers (UBM), namely the Cu thin films on the printed boards, Cu wires, etc. The Cu-Sn system is the most in demand system in the soldering technology and the Sn-based solders, often used in the form of a solder ball, are serving almost all the packaging techniques. The size of the solder balls in the packaging technology is less than 100  $\mu\text{m}$  and decreases following the trend of miniaturization.

The size of the solder bumps used during that process dictates the ability to miniaturize the whole chip assembly. The various technological difficulties emerge with this miniaturization. One of them is the anisotropy of the joint properties due to the development of very limited number of the grains formed at the interface between solder and metallic substrate or inside the solder bulk. It becomes crucial to control the interfacial interactions

between the solder bulk and the substrate but also the microstructure of both solder and metallic substrates before and after soldering in order to limit the reliability issues, which emerge during in-service operation of the device. For example, the use of the nanostructured copper substrate full of nano-twins can be beneficial for control of the microstructure of the microbumps.

By using nanosized constituents (or nanostructured components) the modern science came to another field called nanoelectronics. Its degree of success in mass production of devices is very limited at the moment. One of the main reasons of that is the implementation of the bottom-up approach in building of the devices from molecular level. This approach is very challenging and requires the understanding of key processes that control evolution of the nano-sized structural parts.

When the size of a solder bump decreases significantly (for example up to about some micrometers), the interfacial interactions should be controlled at the nanometer scale in order to control the interfacial microstructure. Moreover, during cooling of the system down to the room temperature, very high degree of undercooling can be attained in such micrometric systems leading to the appearance of metastable equilibria and/or metastable phases that can deeply influence the microstructure of the solder ball and thus the mechanical properties of the joint. Thus, the fundamental study of such phenomena in the most used solid Cu/liquid Sn system in joining technologies for electronic industry becomes crucial nowadays.

The mentioned above scientific challenges in micro- and nano- electronics concerning *soldering process* define the scope of this thesis. We aim to answer key scientific questions in the field of soldering, which are important for resolving the problems that emerge with required miniaturization of the Integrated Circuits.

Firstly, we describe in *Chapter 1* the problematic of the modern soldering technology in more details. It includes an overview of the packaging technology, in-service mechanical reliability, wettability of metallic substrates by liquid solders and reaction between them (dissolution, nucleation at interfaces and growth kinetics of the reactive layers) as well as the nucleation phenomena on the solder bulk that intervene during cooling.

The *Chapter 2* summarizes all the experimental methods and materials used in this study. In particular, it gives detailed description of the processing of bulk intermetallic phases used for wetting experiments as well as description of the specific equipment used for the study of the initial stage of interaction between the liquid solder and Cu substrate.

As our purpose is to provide a deep insight into the initial stages of interaction between metallic substrates and liquid alloys (such as nucleation and growth), the knowledge of the basic parameters of this process is crucial. The contact angle of the liquid solders over the copper substrate, that in principle allows evaluation of the interfacial energies, is one of these parameters. For this purpose, in *Chapter 3* we study in particular the wettability of the Cu substrate by the liquid Sn-based solders. At the reactive Cu/liquid Sn based alloys (often Sn-Ag-Cu alloys) interface, two intermetallic layers are formed,  $\text{Cu}_3\text{Sn}$  at the Cu side and  $\text{Cu}_6\text{Sn}_5$  phase at the solder side. Thus, for the study of the reactive wetting, but also of the nucleation phenomena at reactive interface, it is very useful to know the wetting properties of these intermetallic phases. Moreover, as during cooling of Sn-Ag-Cu solders, the  $\text{Ag}_3\text{Sn}$  phase can nucleate first inside the solder bulk, the wetting properties of this phase by the liquid solder are very useful for the study of nucleation in the supercooled liquid solders. For these reasons, in Chapter 3 we have studied also wetting of  $\text{Cu}_3\text{Sn}$ ,  $\text{Cu}_6\text{Sn}_5$  and  $\text{Ag}_3\text{Sn}$  intermetallics by liquid Sn.

In *Chapter 4*, the question of the nucleation at the solid Cu/liquid alloy interface during the soldering process as well as that of nucleation inside the solder bulk during cooling of the system down to room temperature are treated from both experimentally and theoretically points of view:

- In order to answer the important question of the phase formation sequence at reactive Cu/liquid Sn interface we have performed specific experiments of very fast dipping of Cu foils in liquid Sn (reaction time from 1 ms to 1 s). Moreover, we have developed the

theoretical approach on the suppression criteria of the second phase formation ( $\text{Cu}_3\text{Sn}$  in this case) at  $\text{Cu}_6\text{Sn}_5/\text{Sn}$  interface of the  $\text{Cu}/\text{Cu}_6\text{Sn}_5/\text{Sn}$  system.

- The nucleation of Sn in the supercooled liquid Sn-Cu alloy is studied by specific Differential Scanning Calorimetry experiments performed by using cyclic temperature change of the solder with total melting or with partial melting of the solder in two configurations (a) solder over  $\text{Cu}_6\text{Sn}_5$  phase and (b) solder without any specially prepared interfaces. Moreover, in this Chapter, a theoretical approach of heterogeneous nucleation is proposed in order to determine the sites of the favorable nucleation.

The morphology and the thickness of the intermetallic layers formed at solid Cu/liquid Sn interface play a crucial role on the physical properties of the interfaces as well as on the mechanical properties of the joint. In literature a lot of controversy exists concerning the exponent of the growth law of the  $\text{Cu}_6\text{Sn}_5$  layer and above all concerning the mechanisms governing the growth and the morphology of this layer. In order to give a deeper insight into this field, we performed two kinds of specific experiments on the Cu/Sn system that are presented in **Chapter 5**:

- We compare the kinetics of  $\text{Cu}_6\text{Sn}_5$  phase growth for normal couple Cu/liquid Sn and for the incremental couple  $\text{Cu}_3\text{Sn}/\text{liquid Sn}$ . The change in the growth rate may give us a link with the mechanism of the IMC growth.

- We compare, for the first time, the reaction of copper with metastable liquid solder and with stable solid solder at the same temperature. This is achieved by performing specific DSC experiments in order to monitor and control the physical state of the alloy as well as to set the accurate reaction temperature. By this way, we reveal the factors that affect morphology of the reaction products and mechanisms of the growth of phases, thus a modeling of growth kinetics is proposed.

Finally, in this Chapter, a theoretical evaluation (for the first time) of the liquid channel width inside the  $\text{Cu}_6\text{Sn}_5$  phase, responsible for the fast diffusion paths through this phase, in the  $\text{Cu}/\text{Cu}_3\text{Sn}/\text{Cu}_6\text{Sn}_5/\text{Sn}$  system, is performed.

A synthesis of the main conclusions of this study will be given at the end of this manuscript as well as a certain number of perspectives concerning some of the fundamental questions about soldering process that are not yet elucidated.

## Chapter 1: Bibliographic literature review

### 1) Introduction

In this bibliographic review we firstly tend to describe in section 2 the knowledge base of the soldering technology starting from essential topics concerning the physical aspects of the process itself. We will also mention various applications of soldering to different joining technologies in microelectronics.

A certain number of phenomena take place during the soldering process: wetting of the substrate by the liquid alloy, nucleation and growth of reaction compounds at the liquid solder alloy/interface and nucleation of the tin (and  $\text{Cu}_6\text{Sn}_5$  compound) in the solder bulk alloy during cooling.

Section 3 gives a literature review on the wettability of Cu substrate and Cu-Sn intermetallics by pure liquid Sn or Sn-based alloys. The section 4 describes the state of the art of the nucleation and growth kinetics of intermetallic layers at liquid solder alloy/Cu interface and, finally, section 5 concerns the nucleation of solid tin in the liquid alloy during solidification.

### 2) Soldering in microelectronics

#### 2-1) Introduction

Soldering is the key technological way to join the separate metallic parts with use of the filler metallic alloy or pure metal placed between the parts to be joined. Known for thousands of years, this technique is the one mostly used in microelectronic industry to join the under-bump metallization layers (UBM), namely the Cu thin films on the printed boards, Cu wires, etc. The Cu-Sn system is the most in demand system in the soldering technology and the Sn-based solders are used in almost all the packaging techniques. The solders (soldering alloys) are basically the pure tin or tin-based eutectic alloys often used in the form of a solder ball. The most used solder alloys nowadays are the Sn-based Sn-Ag-Cu alloys called SAC alloys. The size of the modern solder balls used in the packaging technology is less than 100  $\mu\text{m}$  and decreases following the trend of miniaturization.

The conventional solder reaction that develops during the so-called reflow process incorporates reactive wetting of the copper substrate with instantaneous reaction growth of common intermetallic compounds (IMC) at the solid substrate/liquid solder interface [Tu\_2007]. Reflow operation is the heating cycle, during which the temperature exceeds the melting eutectic temperature of solder by two-three tens of degrees and the allotted time of reaction is fixed to be couple of minutes (typically 2-3 minutes).

The permanent trend of miniaturization produces the new challenges. The most crucial are the reliability issues. The significant decrease of the solder size obeys the following tendency [Tu\_2013]: (i) the modern flip-chip technology operates with solder balls with diameter of 100  $\mu\text{m}$ ; (ii) the transition to 3D-integrated circuits lowers the size to 20  $\mu\text{m}$ ; (iii) the forecast is that the solder joint diameter could be reduced down to 1  $\mu\text{m}$ .

#### 2-2) The Cu-Sn system in soldering technology

There are two common IMCs in soldering,  $\text{Cu}_6\text{Sn}_5$  and  $\text{Cu}_3\text{Sn}$ . The IMCs appear in the form of submicron embryos which grow rapidly and merge to continuous layers. The nucleation rate of the IMCs, the sequence of their nucleation and place of nucleation are the topics of great scientific interest and discussion. As operation temperatures of the microelectronic devices are significantly lower than the melting temperature of the solder, the rapid growth of IMCs during the short reflow process plays a crucial role in the establishing of the strong mechanical bond between the substrate and the solder.

### 2-3) Packaging in the microelectronics

There are different methods of joining in packaging technology, see for example Ref. [Tu\_2007]. Here below we will develop three of them: (i) the wire bonding and (ii) the flip chip method and (iii) the advanced packaging methods for Integrated Circuits (IC). Finally, some reliability issues in microelectronics in relation with the mechanical strength of the joint will be presented.

#### 2-3-1) Wire Bonding method

This method is considered to be one of the cheapest and effective ways to make interconnect between IC or its components and the package terminal or the printed board. The modern industry uses the copper wires with a diameter as small as 20  $\mu\text{m}$  [Amkor 2012] and the roadmap is that the wire diameter should achieve submicron size in the close future. The expensive gold wires were also used for a while but industry almost succeeded in the replacement of them by the cost-effective Cu wires.

To make a good soldering of the Cu wire to the Board Pad the wire is coated by the lead-free tin-based layer. The bond between Cu wire or leg and the Board Pad is made by reflow of the solder bump (see Figure 1-1).

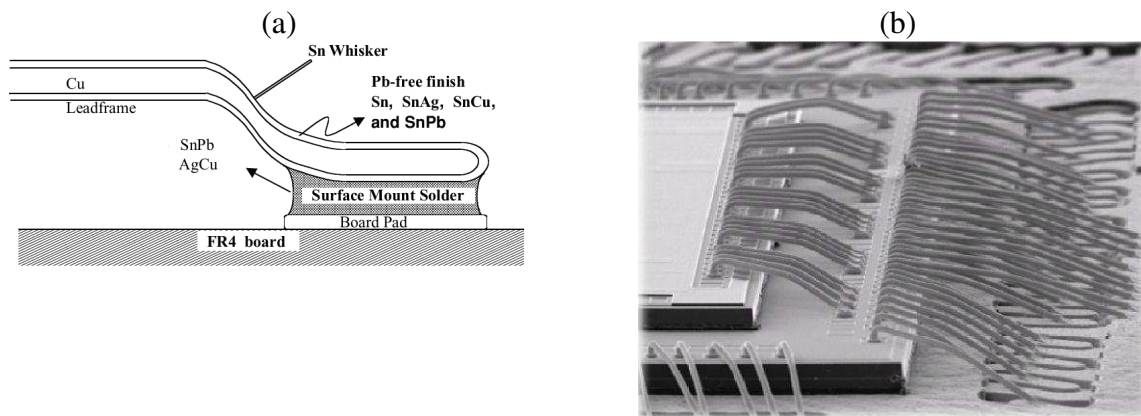


Figure 1-1. (a) Schematic diagram of the solder joint between a leg and a substrate board [Tu\_2007] (b) Stacked die with stand-off-stitch bond with 20  $\mu\text{m}$  Pd coated Cu wires [Amkor 2012].

The insufficient amount of the I/O (Input/Output) pads could be the serious obstacle for the bonding of the single die by the wire bonding technique. The problem emerges due to the limited place on the perimeter of the die where the wires could be bonded. Nevertheless, the wire bonding is widely used nowadays when the number of the needed I/O pads is small. It is also used to stack multiple chips on each other.

#### 2-3-2) Flip Chip method

In the packaging technology we can distinguish different approaches and techniques which are used on the basis of the desired device portability, manufacturing costs and in-service conditions. The good example could be the conventional flip-chip method firstly introduced by IBM for the half a century ago. This method is used normally for the single die attachment on the printed board and it was a technological breakthrough at the time of its introduction. As it can be seen from the Figure 1-2 the key benefit of the technology is a high density of the I/O conductive solder bumps placed directly on a chip surface. Once the bonding (normally after the first reflow) is made between die and the Ball-Grid Array (BGA) on its surface the complete assembly is “flipped” and bonded with a printed board by the second reflow process. After that the complete medium between chip-die and the printed board is filled by the special underfill (normally an epoxy) to achieve the mechanical strength and thermal stress resistance.

A typical temperature-time profile of the reflow process is given in Figure 1-3. During the reflow the soldering alloy melts, wets the substrate, reacts with it and finally solidifies during cooling.

The modern technology operates with fine-pitch interconnects as small as 10  $\mu\text{m}$  in diameter and uses lead-free tin-based solders [Tung\_2014].

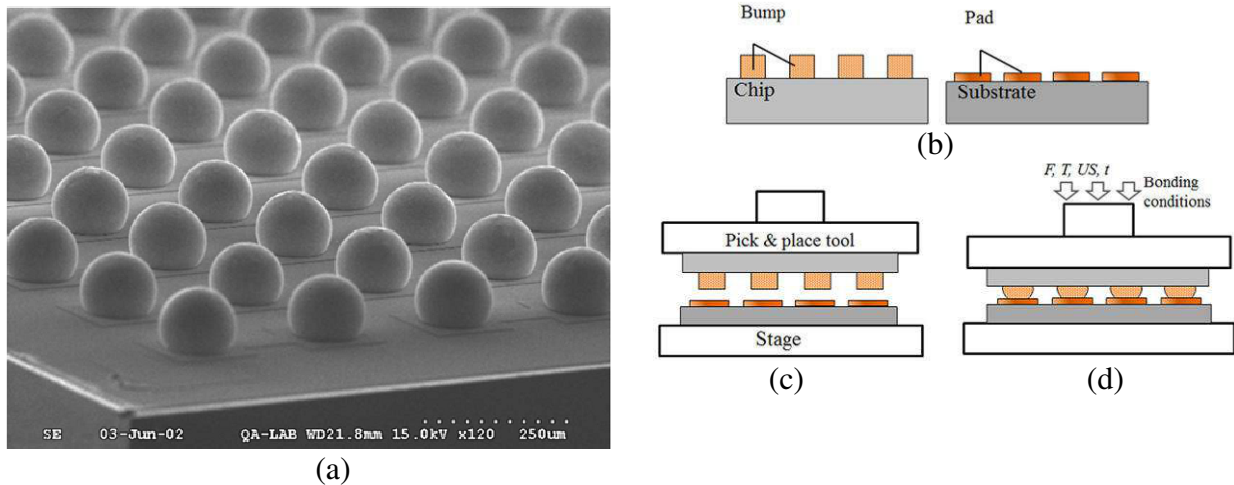


Figure 1-2. a) Ball Grid Array (BGA) of solder balls on a chip surface [Tu\_2007]; Schematic of flip chip packaging technology process [Tung\_2014] for joining of prepared chip with bumps on it and a substrate with Cu pads (b) with alignment pick and place tool (c) and final reflow (d).

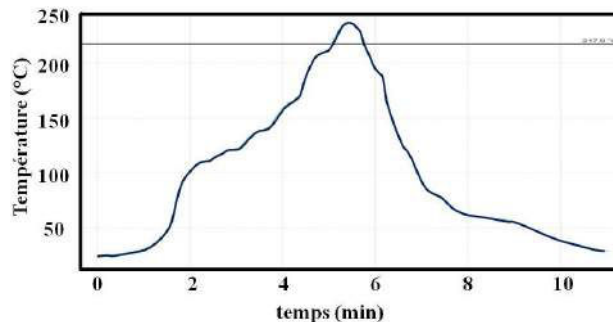


Figure 1-3. Temperature-time profile of the reflow measured by thermocouples placed on a sample plate.

### 2-3-3) Advanced packaging methods for Integrated Circuits (IC)

To fulfill the demand of miniaturization and power efficiency the industry is seeking for the advanced methods of packaging. The general classification distinguishes the spatial classification in terms of the number of the planes at which the IC dice are placed (this classification incorporates 2D, 2.5D and 3D stacking) and grouping classification in terms of the approaches to group different dice, chips, packages on/next each other [Tu\_2007]. The second classification includes system-in-packaging (SiP), system-on-packaging (SoP), system-on-chip (SoC), package-on-package (PoP) etc.

The good example of the 3D IC could be the 3D SiP that incorporates the discussed above methods of joining as flip chip and wire bonding with multiple dice stacking and use of the through-silicon-vias (TSVs) to connect directly the dice for the “communication”.

The example of simultaneous use of the wire bonding and double flip-chip methods is shown schematically on the Figure 1-4a. This is a simplified case as the TSVs are not used here. The wire-bonding is used to link the upper die with a SiP substrate. The Figure 1-4b shows the cross-section of the real SiP package that was consolidated with use of the TSVs

and microbumps with a size of  $20\ \mu\text{m}$  [Amkor\_2011]. The solders used for the microbumps are lead-free pure tin or tin-based alloys, such as Sn [Yu\_2009, Panchenko\_2014] or Sn-Ag-Cu alloys [Bertheau\_2014].

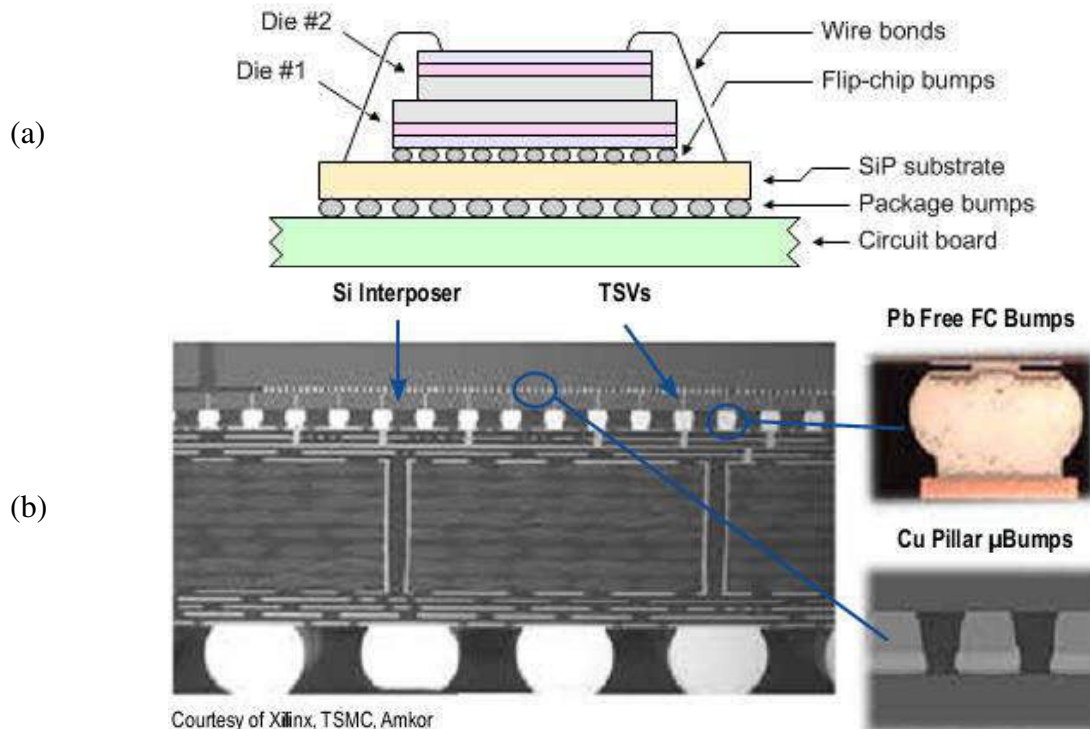


Figure 1-4. a) The SiP package with two dice b) Through-Silicon-Vias (TSV's), microbumps and Cu Pillar microbumps [Amkor\_2011]

#### 2-3-4) Reliability in microelectronics

Regardless the size of the solder joint, its prolonged heating during operation of the device results in the solid-state aging of the joint with slow but constant growth of the IMC layers. The reliability issues connected with voiding and subsequent mechanical weakening of the solder joint due to the thickening of the IMC's are emerging during long-term solid-state annealing.

##### 2-3-4-1) Mechanical strength of the solder bumps and microbumps

###### a) Solder bumps

The small size of the solder balls and an unaltered thickness of the under-bump metallization can lead to complete transformation of the solder bulk to the IMCs. It is under discussion whereas the IMC are brittle and can cause the failure of the solder joint [Keller\_2011] but numerous shear stress experiments point to  $\text{Cu}_6\text{Sn}_5$  phase as the most brittle one.

Figure 1-5 shows the principal scheme of the shear test applied on the solder bump. Generally two parameters that are varied in such type of the test are the shear height and the shear speed [Bertheau\_2014\_II].

###### b) Solder microbumps

The shear test proposed by Bertheau et al [Bertheau\_2014\_II] was applied to the SAC microbumps placed over the copper pillars with diameter of  $25\ \mu\text{m}$  and overall height ( $h$ ) of  $16\ \mu\text{m}$  (see Figure 1-5). The solder joints were isothermally annealed for different times before the test. The time of the annealing varied from 0 (as reflowed) to 30 min and the temperature was set to be  $240^\circ\text{C}$ . Due to the liquid state reaction the  $\text{Cu}_6\text{Sn}_5$  IMC layer was significantly thicker than  $\text{Cu}_3\text{Sn}$  layer but the later contained the Kirkendall voids as early as

just after reflow (see Figure 1-6a). The longer annealing time resulted in the transformation of the almost 60% of the solder bulk to the IMC (see Figure 1-6b). The shear rate varied from 70  $\mu\text{m/s}$  to 500  $\mu\text{m/s}$ . The load was applied on the different heights and namely on the different regions: to the copper pillar (the height between 11 and 12  $\mu\text{m}$ ), the interface region between two IMC's –  $\text{Cu}_3\text{Sn}$  and  $\text{Cu}_6\text{Sn}_5$  phases (the height between 13 and 14  $\mu\text{m}$ ) and the last tested region was a pure  $\text{Cu}_6\text{Sn}_5$  bulk (the height between 15 and 16  $\mu\text{m}$ ). Whatever the rate of the shear test the results indicate that the shear force decreased with increase of the shear height (see Figure 1-6c).

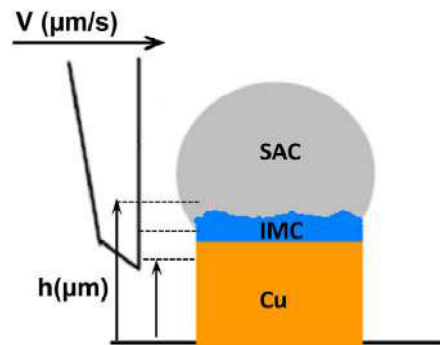


Figure 1-5. Schematic drawing of shear testing on solder microbump joint. [Bertheau\_2014\_II]

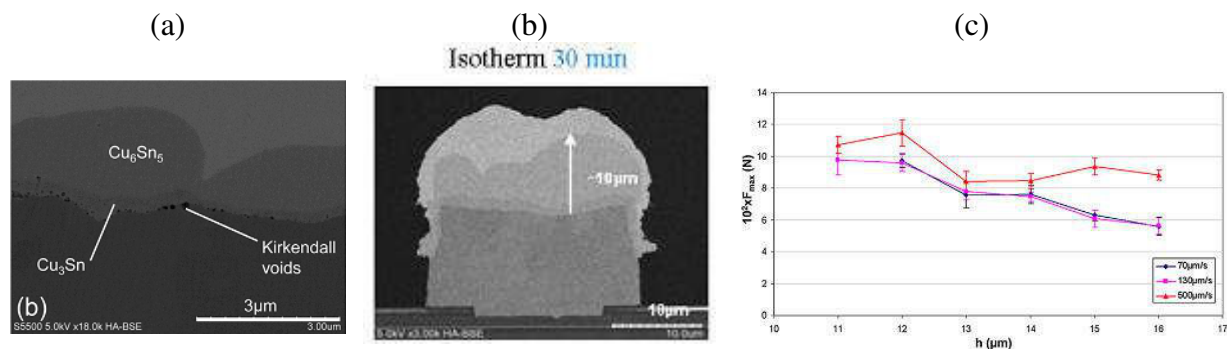


Figure 1-6. SEM cross-sections micrograms showing the formation of  $\text{Cu}_6\text{Sn}_5$  and  $\text{Cu}_3\text{Sn}$  intermetallics and Kirkendall voids at the interface between Cu micropillars and SAC microbumps (a, b) and variation of the shear force  $F$  with shear height  $h$  for reflowed Cu pillars at different shearing rates: 70, 130 and 500  $\mu\text{m}\cdot\text{s}^{-1}$  (c) [Bertheau\_2014\_II].

The main conclusions of this study include the fact that the Cu/ $\text{Cu}_3\text{Sn}$  interface was found to be as strong as the  $\text{Cu}_3\text{Sn}/\text{Cu}_6\text{Sn}_5$  interface despite the absence of the Kirkendall voids on the later. When the shear test was conducted on the area of the single  $\text{Cu}_6\text{Sn}_5$  layer, the combination of the ductile and brittle profiles was observed supporting the claim of the brittleness of this IMC.

#### 2-3-4-2) Voiding in the solder joint

The voiding in the solder joints is due to two reasons: Kirkendall voids and voids induced by electromigration. A short description of formation of both types of voids in solder joints is given in the following.

##### a) Kirkendall voids

The first reason of voiding is due to the difference of diffusion fluxes of Cu and Sn atoms during solid-state aging or operation heating [Tu\_2007]. The formation of voids is strongly connected with formation of the  $\text{Cu}_3\text{Sn}$  (and  $\text{Cu}_6\text{Sn}_5$ ) IMC layer during reaction between Cu and Sn. As the  $\text{Cu}_3\text{Sn}$  forms the flux of vacancies emerges in the direction of the Cu substrate and the lack of the sinks results in the voids formation.

It is still under discussion the choice of the proper substrate or electrolyte for the electroplating of the Cu pads to eliminate the formation of the Kirkendall voids. For example, in the literature there is a discussion whether the Kirkendall voids are formed on the bulky polycrystalline Cu substrates or electroplated foils [Yin\_2011, Yu\_2014].

### b) Electromigration induced voids formation

The second reason of voiding process is the electromigration induced void formation [Tu\_2003] which appears due to current crowding. Tian et al [Tian\_2011] have studied the rapid electromigration induced void nucleation and growth in flip chip solder joint, using synchrotron radiation. The formation of the numerous voids was revealed instead of the formation of a single void (see Figure 1-7a). A model of the void nucleation, similar to the Johnson-Mehl-Avrami (JMA) or Kolmogorov-Mehl-Avrami (KMA) models, was proposed and the good fit of the experimental results by Weibull distribution was achieved for the life-time prediction of the joints under electromigration tests (see Figure 1-7b).

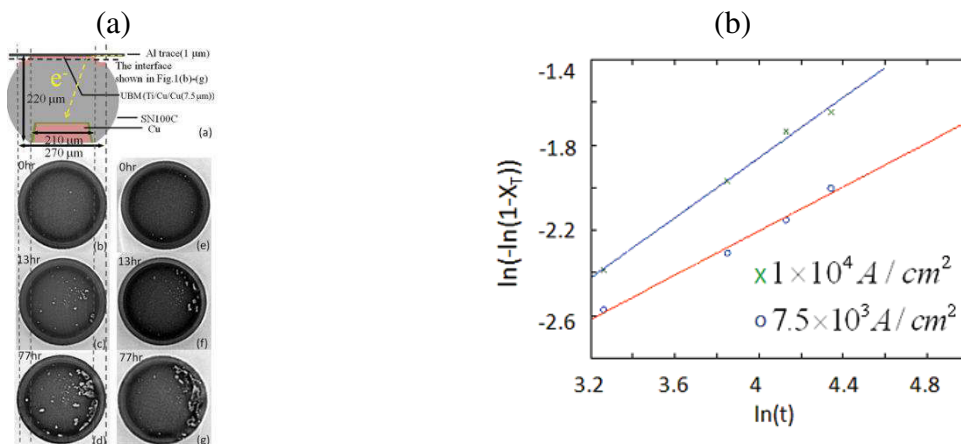


Figure 1-7. a) Formation of the voids due to the high current electromigration test; b) experimental points and model fit.  $X_T$  is the fraction of the transformed phase (evidentially, the pores fraction) [Tian\_2011].

### 2-4) Conclusions

It was shown in this paragraph that Cu-Sn reaction is of key interest regardless the exact technique used in packaging (wire bonding, flip-chip or sophisticated combinations of techniques). The reliability of the joints depends on the production quality and ability to control emerging phenomena during in-service operation of the devices. The reliability issues include initial quality of the interface between solder and substrate, mechanical strength of the joint due to their mechanical properties and voiding. That is the reason why wetting of the under-bump metallization and its reaction with solder is of peculiar interest for the microelectronics.

### 3) Wettability of Cu and Cu/Sn intermetallic surfaces by liquid Sn or Sn alloys

#### 3-1) Introduction

The wettability of the common surfaces in the microelectronic industry is of primary interest as it strongly affects the geometry and mechanical reliability of the substrate/solder joint as well as the initial reactivity at the interface between origin substrate and solder. In general, the wetting can be distinguished as non-reactive and reactive [Eustathopoulos\_1999]. The soldering technology incorporates the latter as far as common solders with high Sn content are highly reactive with Cu, which means that the wetting is followed by rapid formation of intermetallic compounds at interface [Tu\_2007] (often both processes proceed simultaneously - reactive wetting). The wetting process is governed by the set of conditions including surface finish, solder viscosity, ambient atmosphere, reactivity and oxidation of the substrate or solder surface.

We focus our attention on the wetting of pure metallic Cu and Ni substrates as well as on the wetting of the prepared IMCs surface by liquid lead-free solders with high tin content.

#### 3-2) General aspects of wetting : thermodynamics

##### 3-2-1) The fundamental equations of wetting and adhesion

The wettability of a planar solid surface (S) by a non-reactive liquid (L) in the case of presence of a third vapor phase (V) can be characterized by the equilibrium contact angle  $\theta$  formed at the triple line, where all the phases come into contact. The case, when  $\theta = 0^\circ$  corresponds to the perfect wetting with formation of a very thin film on the surface of the solid (see Figure 1-8). The partial wetting is characterized by the contact angle in the range  $0^\circ < \theta < 180^\circ$ . In this case a spherical liquid droplet is formed on the solid surface. Again, two sub-cases can be distinguished in this case: the so-called non-wetting liquid when the contact angle is higher than  $90^\circ$  (see Figure 1-9a) and wetting liquid with contact angle less than  $90^\circ$  (see Figure 1-9b).

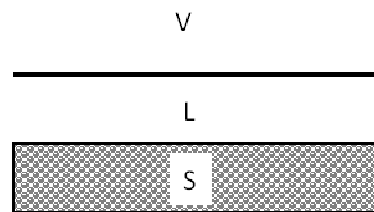


Figure 1-8. Perfect wetting.

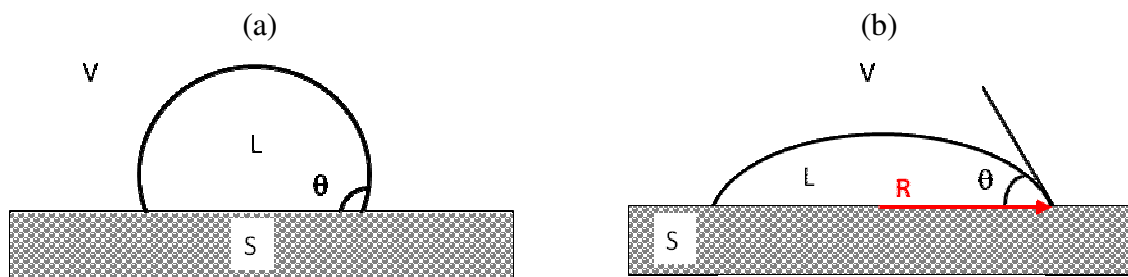


Figure 1-9. Two cases of the partial wetting showing the equilibrium contact angle  $\theta$  in the case of a non-wetting (a) and wetting liquid (b)

In the “ideal” case, when the solid is flat, smooth, not mechanically deformed and chemically homogenous, the equilibrium contact angle can be expressed by the classical Young’s equation [Young\_1805]:

$$\cos \theta_Y = \frac{\gamma_{SV} - \gamma_{SL}}{\gamma_{LV}}, \quad (1-1)$$

where  $\gamma_{SV}$ ,  $\gamma_{SL}$  and  $\gamma_{LV}$  are the interfacial energies at solid-vapor, solid-liquid and liquid-vapor interfaces respectively.

Equation (1-1) can be presented in another form by considering the work of adhesion  $W_a$  defined by Dupré [Dupré\_1869]. This quantity represents the energy needed to separate reversibly a unit area of the solid/liquid interface and to transform it to two free surfaces: solid/vapor and liquid/vapor.

$$W_a = \gamma_{LV} + \gamma_{SV} - \gamma_{SL} \quad (1-2)$$

Combination of the Eqs. (1-1) and (1-2) leads to the Young- Dupré equation:

$$\cos \theta_Y = \frac{W_a}{\gamma_{LV}} - 1 \quad (1-3)$$

If we take into account the physical meaning of quantities  $W_a$  and  $\gamma_{LV}$  in the Eq. (1-3) then we'll find that the wetting phenomena is the competition between forces of adhesion at solid/liquid interface (which promote wetting) and the forces of cohesion (which tend to minimize the surface area between liquid and vapor).

### 3-2-2) Wetting of real solid surfaces

The real surface cannot satisfy all the conditions needed for the proper application of the Young equation. In fact, when the real surfaces are involved in the wetting the contact angle  $\theta$  can vary in the interval defined by the advancing contact angle  $\theta_a$  measured after the spreading of the droplet and the receding contact angle  $\theta_r$  achieved when removing the liquid. It is always valid that [Eustathopoulos\_1999]:

$$\theta_r < \theta_Y < \theta_a \quad (1-4)$$

There are two reasons for that: (i) the surface roughness and (ii) the chemical heterogeneity of the surface, which can lead to the pinning of the triple line in the certain point of the given interval (see Eq. (1-4)). The first one includes the appearance of obstacles for the spreading or shrinkage of the droplet, whereas the second one deals with the deterioration of the surface. The mentioned variation of the wetting angle on the real surfaces is called the wetting hysteresis.

### 3-2-3) Effect of the surface asperities

The effect of roughness of the surface on the contact angle was firstly considered by R.N. Wenzel [Wenzel\_1936]. He supposed that the only effect of the roughness is the increase of the actual interface area by a factor  $k$  (Wenzel factor). This factor is equal to the ratio between the actual solid-liquid interface area and the ideally planar interface area limited by the triple line. Wenzel minimized the free energy of the system and obtained the simple dependence of the contact angle on the rough surface  $\theta_w$  on the Young's contact angle  $\theta_Y$ :

$$\cos \theta_w = k \cos \theta_Y \quad (1-5)$$

and showed that  $k > 1$ .

In the model of Wenzel it is supposed that the size of the surface defects is negligible in comparison with the size of the droplet. Therefore, the geometry of the defects is not influencing the wetting. Eq. (1-5) predicts the increase of the contact angle for intrinsically non-wetting systems (with  $\theta_Y > 90^\circ$ ) and decrease of the contact angle in the wetting systems. Nevertheless, the experimentally proved variation of the contact angle between the advancing and receding contact angles cannot be described by this model.

R. Shuttleworth and G.L.J. Bailey [Shuttleworth\_1948] proposed a model valid for interpretation of the wetting hysteresis. In their model they consider the possible pinning of the triple line in the positions, which could not be predicted by the Wenzel model. In fact, the

concept of the local microscopic contact angle, which is equal to the Young contact angle, was used to explain the pinning (see Figure 1-10).

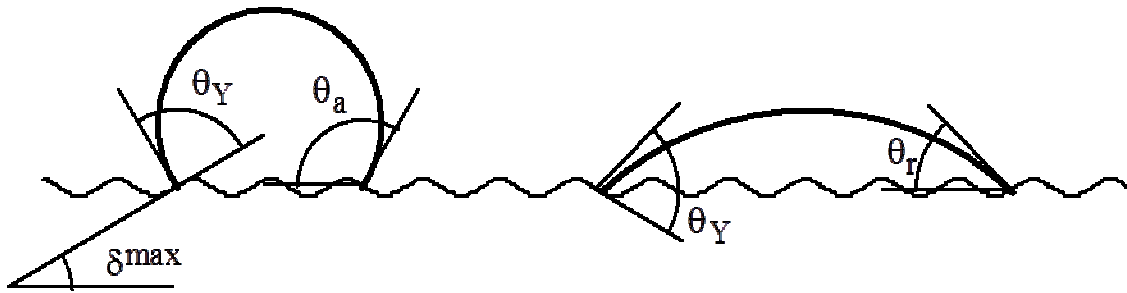


Figure 1-10. Schematic representation of the roughness impact on the contact angle according to the model of Shuttleworth et Bailey [Shuttleworth\_1948].

As it can be seen from Figure 1-10, the advancing contact angle is higher than the Young's contact angle because it is measured relatively to the general plane of the solid surface, whereas the "real" microscopic contact angle is equal to intrinsic Young's contact angle. For the same reason the receding contact angle is underestimated. In case of the two-dimensional roughness which is due to the appearance of the asperities, which are parallel to the triple line, the value of the contact angle can vary in the range:

$$\theta = \theta_Y \pm \theta^{max} \quad (1-6)$$

where  $\theta^{max}$  is a maximum slope of the asperities relatively to the general plane of the solid surface. Thereafter, the model of Shuttleworth et Bailey [Shuttleworth\_1948] considers contact angle hysteresis with amplitude of  $2\theta^{max}$ .

Practically, the experimentally observed advancing (or receding) contact angle depends not only on the value  $\theta_Y$  and roughness of the substrate, but also on the vibration energy, which can be used to overcome the surface asperities. S.J. Hitchcock et al. [Hitchcock\_1981] experimentally studied the wetting of the substrates with different roughness. They found that the difference  $\theta_a - \theta_Y$  rises linearly with  $R_a/\lambda_a$ , where  $R_a$  is the mean height and  $\lambda_a$  is the "wavelength" of asperities (see Figure 1-11). If we tend to measure the real contact angles, which differ from the Young's contact angle by just few degrees (say 2 or 3°) then we need to have the relation  $R_a/\lambda_a \sim 10^{-2}$ . Such values correspond to the substrates with  $R_a \leq 100$  nm [Eustathopoulos\_2005]. Therefore, in wetting experiments we need to consider that value while preparing the substrates.

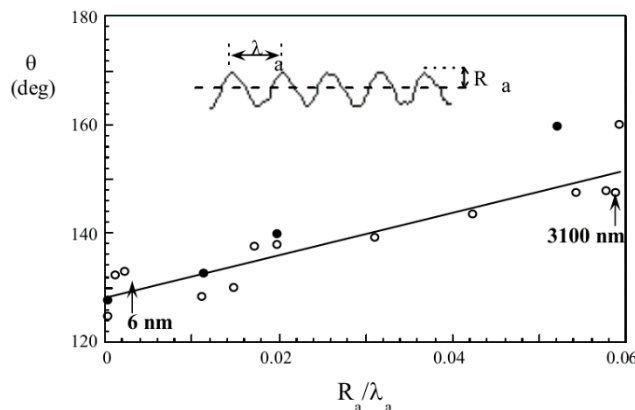


Figure 1-11. Variation of the advancing contact angle as a function of the relation  $R_a/\lambda_a$ , formed by the mercury droplet on the polished substrate of silica (with random roughness) [Hitchcock\_1981].

### 3-2-4) Effect of the chemical deterioration of the surface

The presence of two phases with different chemical composition on the solid surface leads to a phenomena similar to the one that appear due to the surface asperities. Let us consider the simple case of the surface composed with two phases  $\alpha$  and  $\beta$  with surface fraction  $f_\alpha$  and  $f_\beta$  respectively. Let it be that the phase  $\beta$ , which is wettable, is characterized by the equilibrium contact angle  $\theta_\beta < 90^\circ$  and the non-wettable phase  $\alpha$  is characterized by the equilibrium contact angle  $\theta_\alpha > 90^\circ$ .

The macroscopic contact angle in such system can be expressed by the Cassie equation [Cassie\_1948]:

$$\cos \theta_c = f_\alpha \cos \theta_\alpha + (1 - f_\alpha) \cos \theta_\beta \quad (1-7)$$

This equation is similar to the Wenzel equation (1-5) and it gives the equilibrium contact angle on the heterogeneous surface.

In real systems the observed contact angle depends on the distribution of phases on the solid surface and vibration energy of the system. Horsthemke and Schröder [Horsthemke\_1981] took into consideration the texture of the heterogeneous surface and derived the equations for advancing and receding contact angles (that will not be developed here):

$$\cos \theta_a = z_{\max} \cos \theta_\alpha + (1 - z_{\max}) \cos \theta_\beta \quad (1-8)$$

$$\cos \theta_r = z_{\min} \cos \theta_\alpha + (1 - z_{\min}) \cos \theta_\beta \quad (1-9)$$

where  $z_{\max}$  and  $z_{\min}$  are the maximum and minimum fraction of the triple line length that traverse the non-wettable phase (phase  $\alpha$ ).

### 3-3) Wetting dynamics

Having discussed the static wetting and the fundamental equations of wetting we can now turn to the wetting dynamics, the process that covers the spreading of the spherical droplet from the moment of the first contact with the substrate and till relaxation to the equilibrium form. We should distinguish two cases:

(i) Non-reactive systems: In such systems the interfacial energies are staying constant during all the experiment.

(ii) Reactive systems: In this case the interfacial energies can change during the process due to formation of the intermediate phase(s) at the liquid/solid interface.

It should be noted that in the following study the case of the deposition of the “massive” droplets (with mass exceeding 100 mg) is excluded for the reason that the gravitation forces can deform the shape of the spherical droplet. The Laplace tension and wetting phenomena should be the only processes influencing the shape of the droplet.

#### 3-3-1) Non reactive wetting

The driving force of wetting per unit length of the triple is equal to  $\gamma_{LV} \cdot (\cos \theta_F - \cos \theta)$ , where  $\theta_F$  and  $\theta$  are the equilibrium and instantaneous contact angles respectively.

If the wetting is limited by viscosity of the liquid then according to Tanner [Tanner\_1979] and de Gennes [de Gennes\_1985] the spreading rate of wettable liquid (with  $\theta < 90^\circ$ ),  $U = dR/dt$  ( $R$  is the drop base radius), is given by the expression:

$$U = \frac{\gamma_{LV}}{3 \cdot \eta \cdot K} \tan \theta \cdot (\cos \theta_F - \cos \theta) \quad (1-10)$$

where  $\eta$  is a dynamic viscosity of the liquid and  $K$  is a constant.

The liquid metals are fluids with low viscosity ( $\eta$  is some  $\text{mPa} \cdot \text{s}^{-1}$ ). It explains the very rapid spreading of the metallic droplets (in about  $10^{-2}$  s) with velocity of several  $\text{m} \cdot \text{s}^{-1}$  [Eustathopoulos\_1999]

In their experiments with water over glass surface A.L. Bianco et al [Bianco\_2004] have reported that non-reactive wetting starts with inertia regime with square-root law of growth of the droplet base radius ( $r \sim t^{1/2}$ , see Figure 1-12a) and lasts approximately from 1 to 10 ms

depending on the drop size (Figure 1-12b) and finish with the capillary regime ( $r \sim t^{1/10}$ ). A.L. Biance showed also that the duration ( $\tau$ ) of the inertial regime depends on the viscosity of the liquid as well (see Figure 1-12c). In log-log scale the dependence is almost linear with slope 1/4.

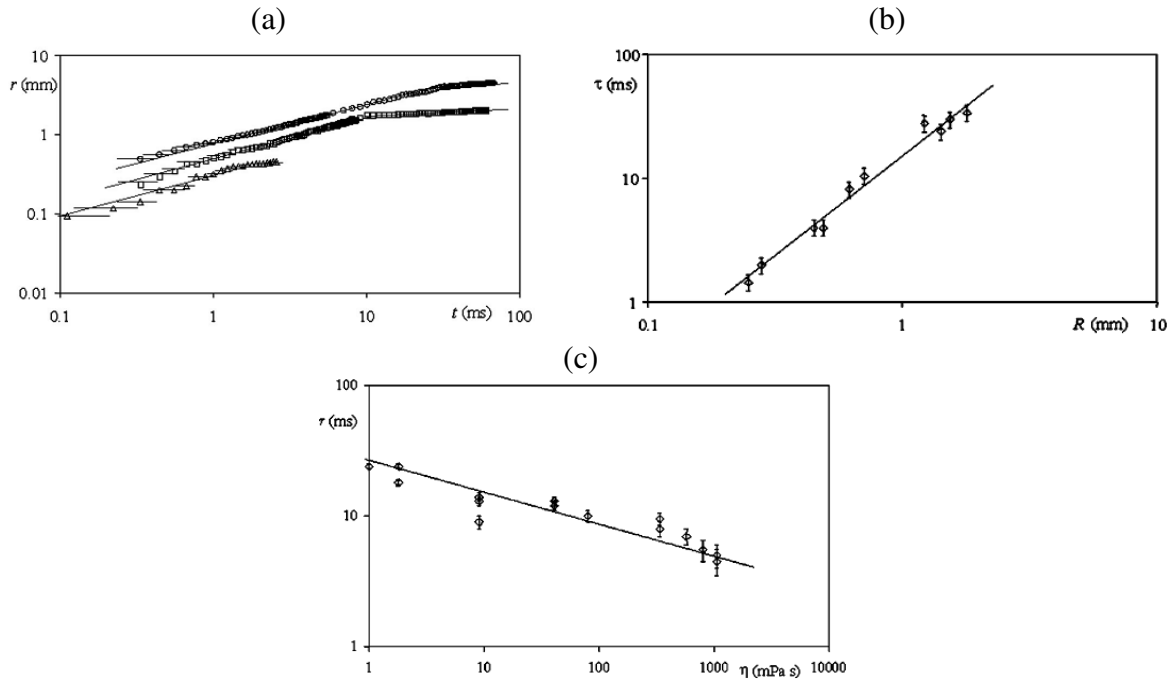


Figure 1-12. The log-log scale dependence of the base radius  $r$  of the water drop, brought into contact with a glass surface versus time, plotted for three different initial droplet radii  $R = 1.2$  mm ( $\circ$ ),  $R = 0.7$  mm ( $\square$ ) and  $R = 0.27$  mm ( $\Delta$ ) (a). The inertial regime with slope 1/2 switches to the capillary regime with slope 1/10. The duration ( $\tau$ ) of the inertial regime depends on the initial drop radii (b) according to [Biance\_2004] as well as on the viscosity (c) of the liquid ( $\eta$ ).

E. Saiz et al [Saiz\_2007] have studied the non-reactive wetting of the Mo substrate by various liquid metals (Cu, Ag, Au) under controlled atmosphere in a vacuum furnace. The partial pressure of the oxygen was kept below  $10^{-20}$  atm. The liquid droplets were transferred from above by the sapphire substrate to the Mo substrate. Whatever the droplet size (from 1 to 3 mm), the experimental temperature and the type of liquid metal (see Figure 1-13a), the continuous spreading of the droplet was observed in the first 8 - 12 ms whereas the total spreading of the droplets took 10-20 ms. This continuous regime of droplet spreading corresponds to the inertial regime of spreading with time exponent of the droplet base radius dependence as  $R \sim t^{1/2}$  and geometrical configuration, at which the liquid bridge exists between the sapphire and the molybdenum substrate (Figure 1-13b). When the liquid link between two substrates collapses the droplets begins to oscillate and contact angle varies also (Figure 1-13c). Moreover, the linear dependence between the spreading velocity  $v$  and the dynamic contact angle  $\theta_D$  was detected in some cases, as for example during spreading of liquid Cu at 1150°C (see Figure 1-13d).

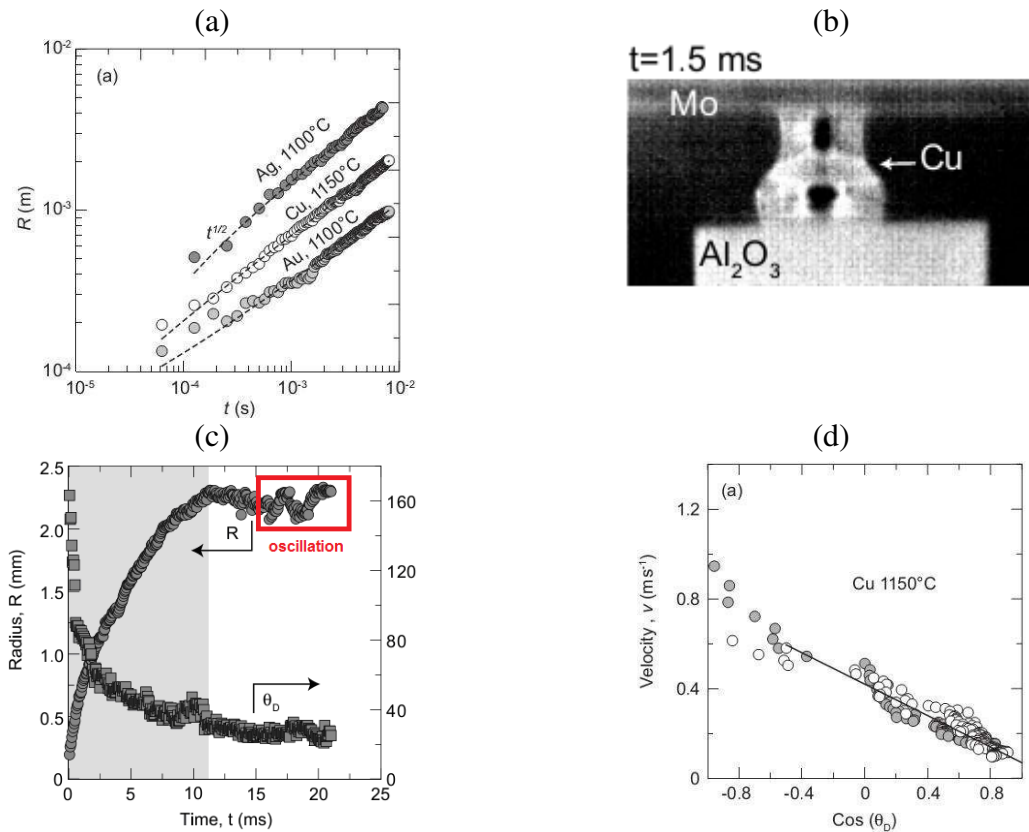


Figure 1-13. The inertial regime with time exponent dependence  $R \sim t^{1/2}$  detected during the non-reactive spreading of the Ag, Cu and Au droplets on Mo substrate (a); the system geometry with formation of the liquid bridge during inertial regime (b); the inertial regime ends with collapse of the liquid link between substrates and subsequent oscillations of the droplet (c); the linear dependence between the spreading velocity  $v$  and the dynamic contact angle  $\theta_D$  obtained during spreading of liquid Cu over Mo at 1150°C [Saiz\_2007].

### 3-3-2) Reactive wetting

Two general types of reactivity between solid materials (metal, ceramic or composite) and liquid metals can be distinguished: (a) the dissolution of the solid in the liquid and (b) the formation of a three-dimensional reactive product as a result of the chemical reaction between liquid and solid. Consequently, two type of reactive wetting exist: (i) dissolutive wetting and (ii) reactive wetting, with formation of a reactive product at the interface (see Figure 1-14).

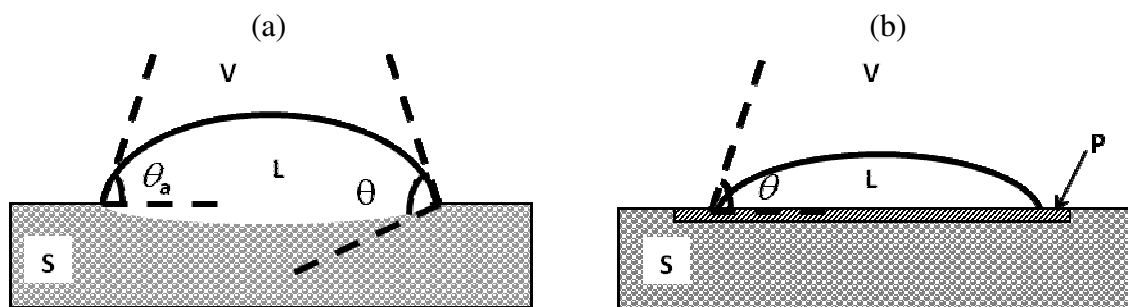


Figure 1-14. Types of reactive wetting: (a) dissolutive wetting, (b) formation of a reaction product (P) by chemical reaction between liquid (L) and solid (S).

#### 3-3-2-1) Dissolutive wetting

In the simple case when the constituents of the solid phase are not modifying the  $\gamma_{LV}$  the principal consequence of the dissolution of the solid in the liquid is the change of the triple line geometry (Figure 1-14a). The contact angle measured during such kind of wetting experiments is the apparent contact angle ( $\theta_a$ ) as far as it doesn't correspond to the angle at

the planar solid surface. This effect is purely geometrical and doesn't play an important role except the case when the dissolution is really intensive [Warren\_1998].

In the wetting experiments recorded with a rapid camera (recording rate  $3.2 \cdot 10^4$  frames/s) E. Saiz et al. [Saiz\_2010] have studied the initial stages of wetting in dissolutive model systems: Cu/Ni, Au/Ni and Au-18wt.%Ni/Ni at  $1100^\circ\text{C}$ . The initial spreading kinetics was found to be completely similar to the case of non-reactive spreading as was shown in the previous section [Saiz\_2007]. The total spreading time was less than 20 ms with maximum recorded velocity of  $1 \text{ m}\cdot\text{s}^{-1}$ . In the case of the Cu drop on Ni substrate at  $1150^\circ\text{C}$  the inertial regime with  $R \sim t^{1/2}$  took approximately 5ms with subsequent oscillation of the droplet after the liquid neck breakup (see Figure 1-15).

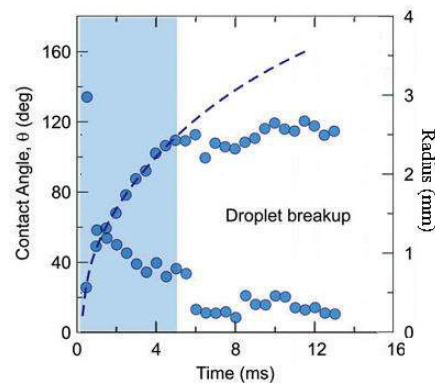


Figure 1-15. Evolution of the contact angle  $\theta$  (descending) and drop base radius  $R$  (ascending) during very initial stage of the dissolutive wetting in the model Cu/Ni system at  $1150^\circ\text{C}$  [Saiz\_2010]. The continuous spreading (i.e. inertial stage) took 5 ms, the radius changed by  $R \sim t^{1/2}$  law during this stage.

### 3-3-2-2) Formation of the reaction layer at the interface

In this paragraph we will review the role of the interfacial reaction in wetting, by the formation of a new three-dimensional phase in the form of a continuous layer at solid/liquid interface. Even if the thickness of the reaction layer is negligible in comparison with macroscopic dimensions of the droplet, the contact angle can be drastically influenced by the presence of the reaction product. The multiple studies (see for example Refs. [Kritsalis\_1994, Espie\_1994, Landry\_1996]) have shown that the final contact angle in reactive systems ( $\theta_F$ ) corresponds to the equilibrium contact angle of the liquid on the reaction product ( $\theta_F \approx \theta_P$ ). In these systems, the reaction product (P) is formed by reaction between substrate and a reactive species contained in the liquid alloy.

The kinetics of wetting in reactive systems depends on the kinetics of the lateral growth of the reaction product at the triple line that is controlled itself by one of the following mechanisms [Landry\_1996]: (a) reaction controlled by kinetics of reaction at the triple line (b) reaction controlled by the diffusion of the reactive species from the centre of the droplet to the reaction front.

#### a) Reactive wetting limited by the chemical reaction at the triple line

In this case the supply by diffusion of the reactive specie to the triple line is not the limiting process. Typical examples of such type of wetting process are the liquid Al/C [Landry\_1996] and Cu-Si/C couples (Figure 1-16). In the latter case the wetting is limited by the formation of the SiC compound at the interface. In their works, O. Dezellus et al [Dezellus\_2000, Dezellus\_2002] give an example of the spreading  $R(t)$  curve and explain its evolution [Dezellus\_2002, Dezellus\_2003]. Dezellus et al. based their description on the initial approach of K. Landry et al. [Landry\_1996], but a lot of modifications allowed them to describe the experimental results better.

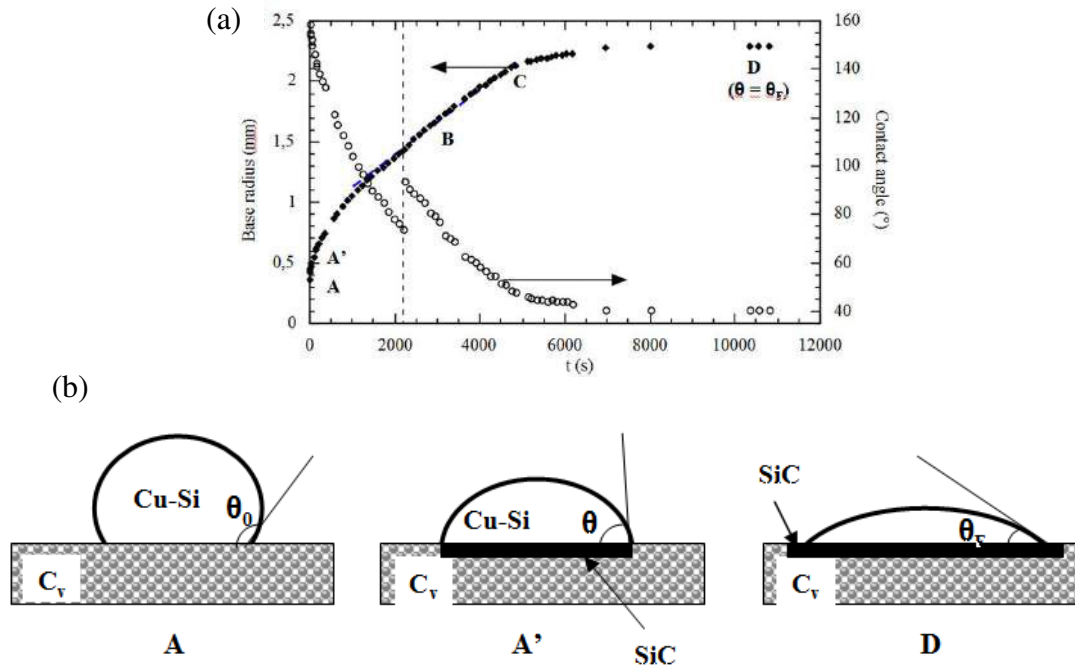


Figure 1-16. (a) Kinetics of the wetting of vitreous carbon by liquid droplet of Cu-30at%Si alloy at  $T=1150^{\circ}\text{C}$  [Dezellus\_2000], (b) interfacial configuration in the beginning of the wetting (left), during the A'C regime (centre), at final equilibrium state (right).

The segments of the  $R(t)$  curve could be described as follows: the contact angle  $\theta_0$ , that corresponds to point A is a contact angle of the Cu-Si alloy on the surface of non reacted vitreous carbon ( $C_v$ ). This angle is achieved very rapidly ( $< 10^{-2}\text{s}$ , see section on non-reactive wetting). Dezellus et al [Dezellus\_2000] have shown that configuration A changes to configuration A' rapidly in some seconds, during which a part of solid-liquid interface is covered by the reaction product (P) within the so-called "mixed zone". This zone can "touch" the triple line but the liquid still can contact a fresh surface of the solid. At point C, the whole interface is covered by the reaction product. Dezellus et al [Dezellus\_2002] modeled the quasi-linear spreading stage A'C that is the main stage of this type of reactive wetting. The modeling of the A'C stage, resulted in the following equations for the wetting velocity  $U = dR/dt$  and the instantaneous contact angle  $\theta$ :

$$\frac{U}{F(\theta)} = k \cdot \left( \frac{3 \cdot V}{\pi} \right)^{1/3} (\cos \theta_F - \cos \theta) \quad (1-11)$$

where  $V$  is the droplet volume.

$$F(\theta) = - \frac{\cos \theta \cdot (2 - 3 \cos \theta + \cos^3 \theta) - \sin^4 \theta}{\sin \theta \cdot (2 - 3 \cos \theta + \cos^3 \theta)^{4/3}} \quad (1-12)$$

$$\cos \theta_F - \cos \theta = (\cos \theta_F - \cos \theta_0) \cdot e^{-k \cdot t} \quad (1-13)$$

### b) Reactive wetting limited by diffusion

In the case when the kinetics of reaction at the triple line is fast, the radial growth of the reaction product can be limited by the diffusion of the diffusing specie from the volume of the liquid droplet to the triple line. With decrease of the contact angle during the wetting process (see Figure 1-17) the diffusion field decreases as well. Consequently, the wetting velocity decreases also [Landry\_1996, Eustathopoulos\_1999].

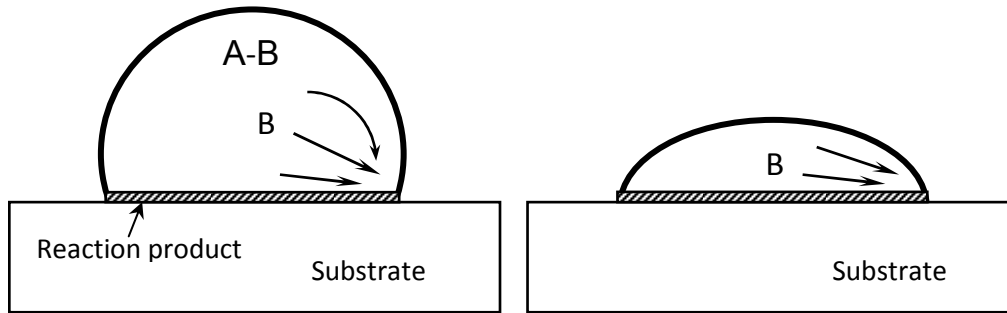


Figure 1-17. The wetting process controlled by diffusion of the reactive element B from the centre of the droplet to the triple line. The decrease of the wetting velocity is linked with decrease of the diffusion field during spreading.

Mortensen et al. [Mortensen\_1997] developed a simple analytical model that derives the expression for the wetting velocity  $v = dR/dt$  controlled by the diffusion with spreading kinetics proportional to the instantaneous contact angle  $\theta$ :

$$\frac{dR}{dt} = \frac{2 \cdot D \cdot F(t)}{e \cdot n_v} \cdot (C_0 - C_e) \cdot \theta \quad (1-14)$$

$D$  is the diffusion coefficient of the reactive specie in the liquid phase,  $e$  is the thickness of the reaction product at the triple line,  $n_v$  is the number of moles of the reactive specie per unit of volume of the reaction product and  $F(t)$  is a function of time, which for the experimental condition of the sessile drop is practically a constant ( $\sim 0.04$ ).  $C_0$  is the initial concentration of the reactive specie and  $C_e$  is its equilibrium concentration at the triple line.

Contrary to the case (a), the reactive wetting limited by diffusion is not appearing to have the linear part on the  $R(t)$  curve (see A'C stage in Figure 1-16a). Otherwise, the wetting velocity is independent from the substrate structure, that is confirmed by experiment [Drevet\_1996].

### 3-4) Wetting of Cu and Cu-Sn intermetallics by liquid Sn or Sn based alloys

The soldering reaction (or reflow) is a wetting process during which the Cu substrate is wetted by the tin-based solder. As far as Cu is highly reactive with Sn, the wetting in this case is a reactive wetting with formation of the common intermetallics ( $\text{Cu}_3\text{Sn}$  and  $\text{Cu}_6\text{Sn}_5$ ) at the interface.

In this section we will present a review of the literature results on the wetting of Cu and Cu-Sn intermetallics by liquid Sn or liquid Sn-based alloys.

#### 3-4-1) Wetting of Cu

Matsumoto et al. [Matsumoto\_2005] reviewed the experimental data on wetting of Cu by lead-free solder alloys (Sn based alloys). Accordingly to their review, the final contact angle of Sn and lead-free Sn-based solders on Cu substrate at  $T = 240\text{-}300^\circ\text{C}$  lies in the range  $26\text{-}43^\circ$ .

In their investigation Arenas et al. [Arenas\_2004] report that the final contact angle of Sn-Ag-Cu alloys on Cu substrate measured by using the sessile drop method have been found to be lower than  $26^\circ$ . Low contact angles were obtained by wetting of polished substrates by lead-free solder by using RMA flux under air. The reflow time was set to be 2 min, the contact angle measurement were made from side-view images in situ, the temperature varied in the range  $240\text{-}280^\circ\text{C}$  and the values were measured three times. The lowest values of the final contact angle  $\theta$  were obtained at  $240^\circ\text{C}$  and  $\theta$  increased with the temperature for all solders except Sn-0.7wt.%Cu. Authors reported  $\theta = 17^\circ$  for Sn-3.5wt.%Ag,  $12^\circ$  for Sn-3.5wt.%Ag-4.8wt.%Bi,  $14^\circ$  for Sn-3.8wt.%Ag-0.7wt.%Cu and  $19^\circ$  for Sn-0.7wt.%Cu at  $240^\circ\text{C}$ . The lowest value of contact angle for Sn-0.7wt.%Cu was  $17^\circ$  at  $280^\circ\text{C}$ . Note however that such contact angles are obtained after 2 min of interaction between liquid alloys and solid Cu.

Amore et al. [Amore\_2008] investigated wetting of binary lead-free Sn-based alloys with high Cu content (5-30 at.%) on Cu and Ni substrates under controlled atmosphere (under Ar with a partial pressure of oxygen between  $10^{-4}$  to  $10^{-2}$  Pa) without flux using sessile drop technique. The mass of the solder material was 0.1 g. The heating rate was 12 K/min and isothermal conditions for 600s were maintained at each temperature step (400, 500 and 600K). Very low contact angles  $<5^\circ$  were obtained for Sn-Cu alloys with high Cu content on Cu substrates. The contact angle and temperature versus time for Sn-5at.%Cu alloy on Cu are given on the Figure 1-18. Due to very long reaction time and small mass of the solder the formation of very thick ( $>200\mu\text{m}$ ) reaction product, namely  $\text{Cu}_3\text{Sn}$  phase (due to the high final reaction temperature) was observed. Thus the reported values of contact angles lower than about  $25^\circ$  (see the rapid slope change of the ( $\theta$ ) curve in Figure 1-18 at about  $25^\circ$ ) are difficult to interpret and maybe have no any physical meaning in these cases.

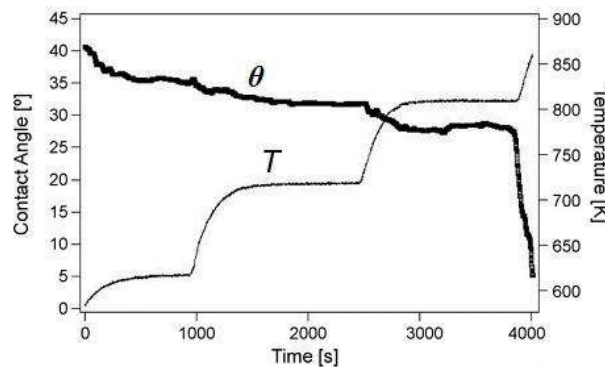


Figure 1-18. Variation with time of the contact angle  $\theta$  of a Sn-5wt.%Cu alloy on Cu substrate during heating and isothermal holdings at 623, 723 and 823K [Amore\_2008]

Zang et al. [Zang\_2011, Zang\_2012] investigated wetting of Cu and Ni substrates by SAC and Sn-3.5wt.%Ag solders by sessile drop technique in controlled atmosphere (in Ar-5vol.% $\text{H}_2$  flow) without using of flux. The heating rate was 20-30K/min and dwell time was 30 min for isothermal conditions. For Cu substrate and Sn-Ag-Cu solder alloy authors obtained final contact at different temperatures:  $32^\circ$  at  $230^\circ\text{C}$ ,  $29^\circ$  at  $250^\circ\text{C}$ ,  $27^\circ$  at  $300^\circ\text{C}$  and  $26^\circ$  at  $400^\circ\text{C}$ . For Cu substrate and Sn-3.5wt.%Ag solder alloy authors obtained about  $36^\circ$  at  $250^\circ\text{C}$ ,  $33^\circ$  at  $300^\circ\text{C}$ ,  $25^\circ$  at  $350^\circ\text{C}$  and  $32^\circ$  at  $400^\circ\text{C}$ . Note once again that the final contact angles are obtained after long time of interactions between liquid alloys and Cu substrate.

Kang et al [Kang\_2005] designed the equipment to deliver melted solder balls with flux coverage to the substrate (see Figure 1-19a). The environment of the experiment was air or pure nitrogen. Authors made the set of experiments with eutectic Sn-Pb and SAC (Sn-4.0wt.%Ag-0.5 wt.%Cu) solder over polished Cu and Cu/Ni/Au. For the eutectic Sn-Pb solder over Cu at  $195^\circ\text{C}$  and  $230^\circ\text{C}$  the obtained values of final contact angle were  $10^\circ$  with spreading time in 0.8 s (see Figure 1-19b), spreading to  $30^\circ$  took 0.02 s at  $230^\circ\text{C}$  and 0.08 s at  $195^\circ\text{C}$ . For the SAC alloy over Cu substrate at  $230^\circ\text{C}$  the final contact angle of  $30^\circ$  was attained in 0.02 s (see Figure 1-19c). In all cases the first measured contact angle is about  $160^\circ$ .

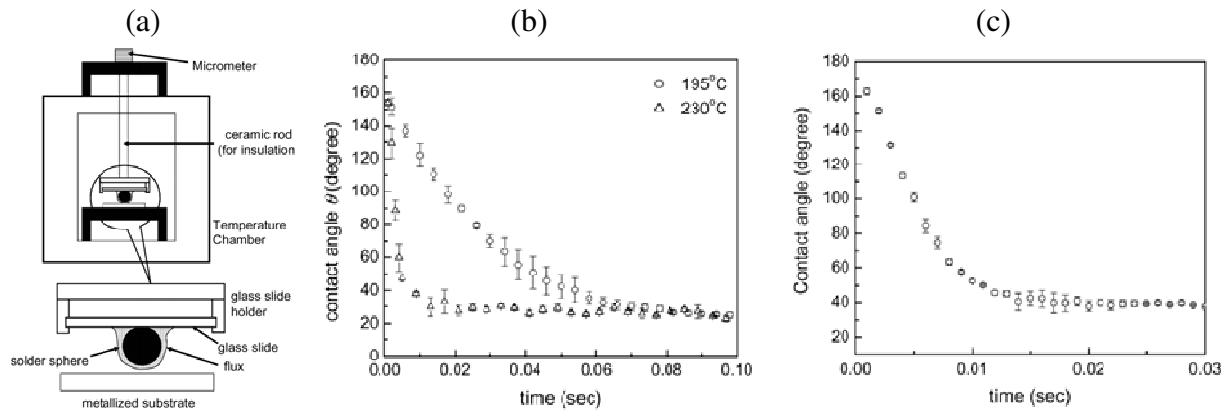


Figure 1-19. a) Schematic presentation of the specific equipment. b) Variation of contact angle  $\theta$  over time for a eutectic Sn-Pb solder on a Cu substrate at different temperatures. c) Variation of contact angle  $\theta$  over time for a lead-free Sn-4.0wt.%Ag-0.5 wt.%Cu solder on Cu substrate at 230°C.

Shen et al. [Shen\_2010] performed wetting experiments of Cu substrates with different grain size by liquid SAC alloy (Sn-3.5wt.%Ag-0.7 wt.%Cu). The Cu substrates have two types of grain structure: coarse grains ( $30 \pm 10 \mu\text{m}$ ) and fine grains ( $25 \pm 5 \text{nm}$ ) and were polished up to  $0.5 \mu\text{m}$ . The experiments were performed under high vacuum ( $2 \times 10^{-6}$  mbar) and solder was melted separately. The experimental temperatures were: 228, 238 and 248°C. For the coarse-grained substrates the first measured contact angle was  $55^\circ$ , the final contact angle was  $27-30^\circ$  almost independent on temperature and the spreading process took about 10 s (see Figure 1-20a). For the nanocrystalline substrates the first measured contact angle was  $90^\circ$  and the final contact angles were about  $50^\circ$ , the spreading process took more than 500s (Figure 1-20b). The coarse-grained and fine-grained substrates were kept at different temperatures in contact with liquid solder for 10 and 20 min respectively and the resulting interfacial microstructures are shown on the Figure 1-21. Two main differences can be noted: (i) a bit thinner IMC layer and (ii) a presence of large number of Kirkendall voids in the case of fine-grained substrate. Authors discuss possible reasons of these differences and connect them with surface contamination or more pronounced oxidation of the nano-grained Cu.

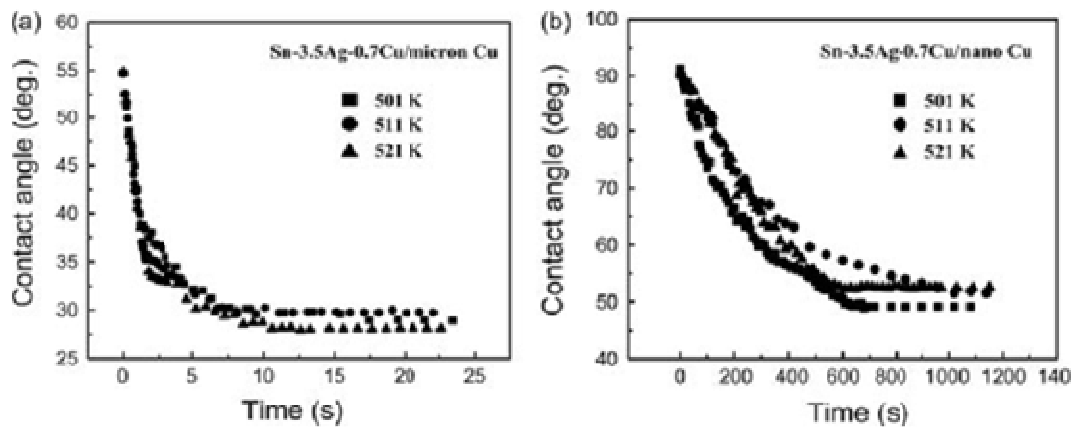


Figure 1-20. Variation in contact angle for molten Sn-3.5wt.%Ag-0.7 wt.%Cu alloy on the (a) micromete-grained and (b) nanometer-grained Cu substrates during isothermal dwells [Shen\_2010].

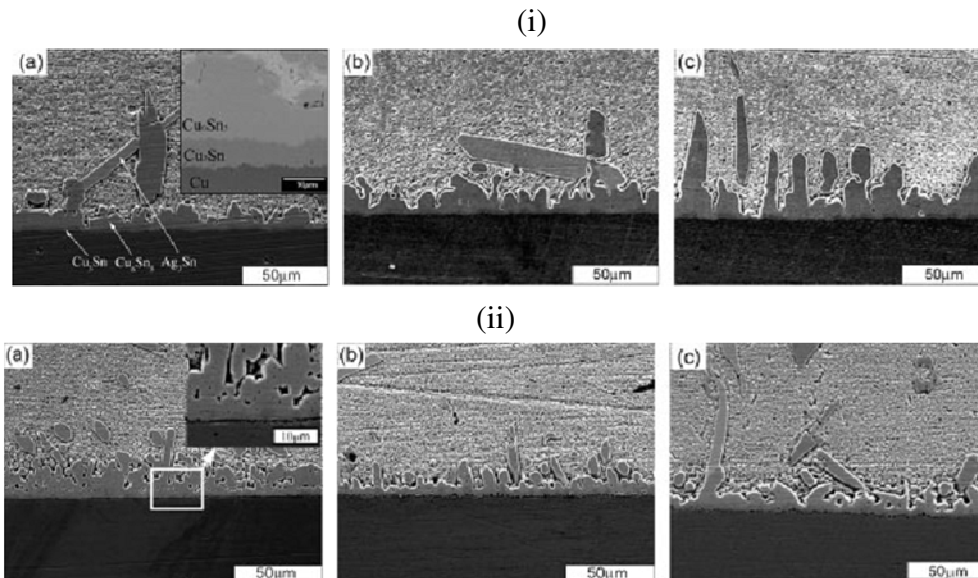


Figure 1-21 Interfacial microstructures for the Sn-3.5wt.%Ag-0.7wt.%Cu alloy on the micrometer-grained (i) and nanometer-grained (ii) Cu substrates after wetting at (a) 501K, (b) 511K and (c) 521 K after 10 min (i) and 20 min (ii) respectively [Shen\_2010].

Sobczak et al. [Sobczak\_2007] discussed factors affecting wettability and bond strength of solder joint couples. The authors call their method of transferring liquid solder as “Capillary purification” (CP). In this method the droplet is squeezed from a graphite syringe. Authors claim that during squeezing the surface of droplet is becoming oxide free (experiments are held in the vacuum chamber). Authors performed experiments for wetting of cleaned and polished Cu substrate by Sn and Sn-based lead-free solders (see Table 1-1). In experiments incorporating the transferred drop technique (or CP technique) the vacuum level is within the interval  $2.6-3 \times 10^{-6}$  mbar [Sobczak\_2007], the contact angle in the range of  $10-23^\circ$  and spreading time was 5 min (the exact time of achieving final contact angle is not indicated). It should be noted that during contact melting (conventional sessile drop, called CH technique - see Table 1-1) even at better vacuum of  $2 \times 10^{-6}$  mbar the measured contact angle is more than 2 times higher than for the case of transferred droplet. The values of contact angles at the sessile drop experiment under vacuum are almost the same as for the sessile drop experiments with use of flux under the air.

Solder	Conditions of sessile drop tests				$\theta, ^\circ$
	Method	Atmosphere	$T_{exp}, ^\circ\text{C}$	Time, min	
Sn	CH	air	230	5	136
	CH	vac. $4 \times 10^{-6}$ hPa	230	5	99
	CH	vac. $3 \times 10^{-6}$ hPa	230	5	60
	CH	vac. $2 \times 10^{-6}$ hPa	230	5	52
	CH	air + flux	230	5	47
	CP	vac. $3 \times 10^{-6}$ hPa	230	5	23
SnAg4	CH	vac. $2 \times 10^{-6}$ hPa	230	5	49
	CH	air + flux	230	5	40
	CP	vac. $2.6 \times 10^{-6}$ hPa	230	5	18
SnAg3.5Cu0.9	CH	vac. $2 \times 10^{-6}$ hPa	220	5	42
	CH	air + flux	220	5	40
	CP	vac. $3 \times 10^{-6}$ hPa	220	5	10

Table 1-1. Effect of testing conditions on contact angle of solder/Cu couples. CH = sessile drop technique, CP = Capillary Purification (transferred drop) technique [Sobczak\_2007].

### 3-4-2) Wetting of Cu-Sn intermetallics

In literature, there are only few data on the wettability of Cu-Sn intermetallics by liquid Sn or Sn-based alloys.

Boettinger et al. [Boettinger\_1992] performed series of experiments on the wetting of the polished Cu-Sn IMC substrates by eutectic Sn-Pb solder with use of sessile drop method under the air with use of two types of flux: rosin non-activated flux (R) and activated flux (RMA). The experimental temperature was 235°C. The final contact angles  $\theta_F$  were obtained in 20 s. The values of  $\theta_F$  were either obtained from metallographic cross-sections or were calculated from known area of spread, mass of droplet and solder density. For RMA flux the values of  $\theta_F$  were in the range 2.5-3° for Cu, 6.5-15° for Cu<sub>3</sub>Sn and 6-17° for Cu<sub>6</sub>Sn<sub>5</sub> substrates. For R flux the  $\theta_F$  values were in the range 16-23° for Cu, 44-101° for Cu<sub>3</sub>Sn and 35-180° for Cu<sub>6</sub>Sn<sub>5</sub> substrates. The conclusion was that there is a strong influence of oxidation of substrate surface on the wettability.

Zhao et al. [Zhao\_2009, Zhao\_2009\_II] performed wetting experiments using hot stage equipment for the Cu substrate covered by continuous layers of the reaction product with Sn (Cu/Cu<sub>3</sub>Sn/Cu<sub>6</sub>Sn<sub>5</sub> configuration) and polished Cu substrate. The wetting liquids were eutectic Sn-Pb and lead-free solders. The initial Sn/Cu/Sn sandwiches were obtained by dipping of the Cu sheets in the Sn melt for 10 s at 260°C. Afterwards the Cu/Sn couples were annealed in different way, resulting in different thickness and morphology of the intermetallics at the interface. The final surfaces (Cu/Cu<sub>3</sub>Sn/Cu<sub>6</sub>Sn<sub>5</sub> configuration) were obtained after etching the Sn layer in order to reveal the surface of the Cu<sub>6</sub>Sn<sub>5</sub> phase. The contact angles were not measured in this study. The authors have only calculated the spreading rate by measurements of the drop base radius during spreading. They report that in general the spreading velocity is faster over the IMC than over polished Cu substrate.

### 3-5) Conclusions

All studies reported in literature on the wetting of metallic substrates by liquid Sn-based alloys show that only few wetting experiments with implementation of the dispensed (or transferred) drop technique are performed up to now. The majority of wetting experiments in these systems are performed by using the classic sessile drop technique where the melting and homogenization of the metallic alloy interfere with the spreading process and spreading is not performed in isothermal conditions. Moreover, the combination of the dispensed drop technique with an atmosphere control is reported only by a very limited number of studies. The majority of studies report measured final contact angles of liquid Sn or Sn-based alloys over Cu substrate in the range 26-43°. It should be noted that addition of Ag, Cu or Bi in the solder leads to decrease of the contact angle down to 13°. Note however that, in general, these final contact angles are obtained after interaction of liquid solder with solid Cu for at least some minutes without specifying their physical meaning.

Only few studies focused their interest on the wetting of the Cu-Sn intermetallic phases (Cu<sub>6</sub>Sn<sub>5</sub> and Cu<sub>3</sub>Sn) by liquid Sn-based solders. Up to date these studies include implementation of the only sessile drop technique with use of fluxes. Thus, it is hard to conclude whereas the contact angle of liquid tin over IMC phases is lower or higher than the contact angle over the unreacted Cu substrate. Nevertheless, the strong effect of surface oxidation was detected for the wetting of the IMC phases.

Recent studies on the very early stages (up to 10 ms) of non-reactive spreading in metallic systems (liquid Ag, Cu and Au droplets on Mo substrate) is a kind of guide for detection of non-reactive spreading stage in the Cu/liquid Sn and Ag/ liquid Sn systems. The detection of this stage (and corresponding contact angles) would be essential for the determination of the equilibrium contact angle of liquid Sn on the unreacted solid Cu or solid Ag before formation of a reaction product at corresponding liquid/solid interfaces.

#### 4) Interfacial reaction between Cu substrate and Sn or Sn-based alloys

##### 4-1) Introduction

In solder joints, the copper is commonly used as the UBM (under bump metallization) and interacts with tin. Usually the soldering reactions proceed at the temperatures below 350°C. As it can be seen from the binary Cu-Sn phase diagram given in Figure 1-22, at such temperature, the reaction at the Cu/Sn interface leads to formation of  $\epsilon$ -Cu<sub>3</sub>Sn and  $\eta$ -Cu<sub>6</sub>Sn<sub>5</sub> compounds [Furtauer\_2013]. There are two allotropic forms of the Cu<sub>6</sub>Sn<sub>5</sub> phase:  $\eta'$  with monoclinic structure, which is stable for the temperatures less than 187.5°C and  $\eta$  with hexagonal structure, which is stable for the temperatures above 187.5°C.

In this paragraph, the interactions between Sn or Sn-based alloys (in the solid and liquid state) with the Cu substrate are described (Note that, as already mentioned before, the most used Sn-based alloys are Sn-Ag-Cu (SAC) alloys - see Appendix 1 for phase diagrams).

We will distinguish the works that discuss:

- (i) the very early stage of reactions, where the IMC phase nucleation and suppression are studied,
- (ii) the reaction between solid Cu and solid tin or tin-based solder, where the reaction time is normally very long and the reliability issues due to voiding are emerging and,
- (iii) the reaction between solid Cu and liquid tin or tin-based solder, where the reaction time vary from few minutes (as in the case of a reflow process) and up to several hours.

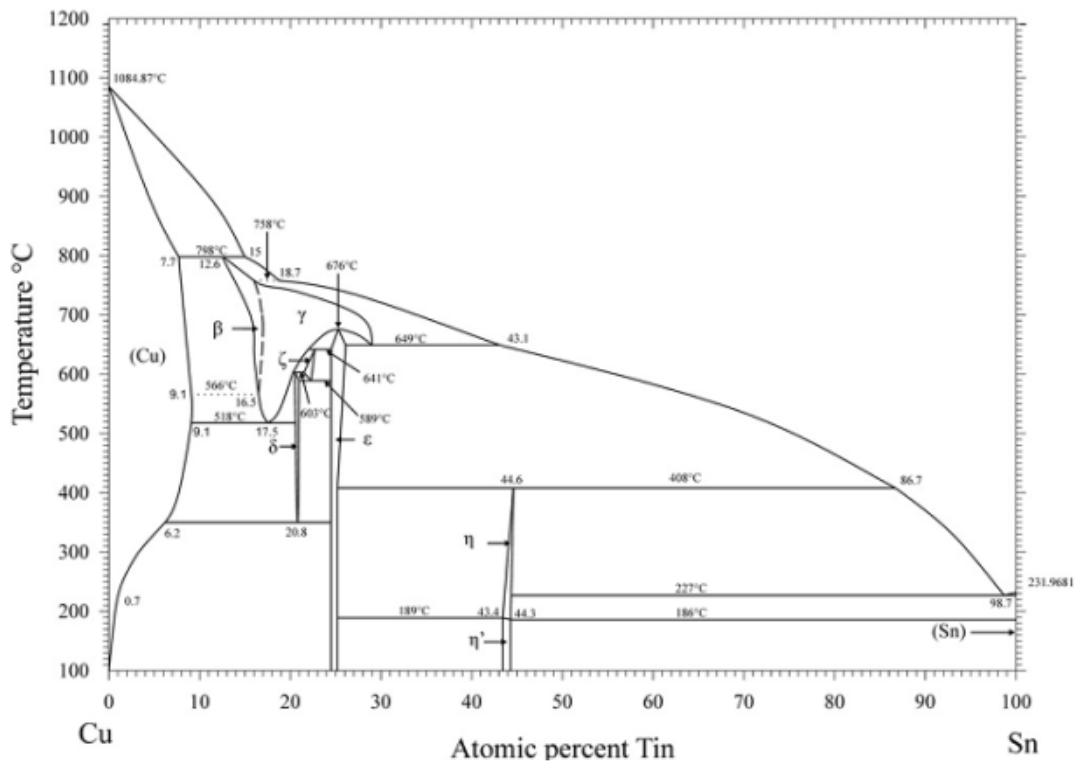


Figure 1-22. Phase diagram of the binary Cu-Sn system [Furtauer\_2013].

##### 4-2) Very early stages of reaction at Cu/Sn interface

R.A. Gagliano et al. [Gagliano\_2002] investigated the nucleation of the Cu<sub>6</sub>Sn<sub>5</sub> compound at Cu/liquid Sn interface. For this purpose they dipped the pre-fluxed polished Cu coupons in the pure Sn melt heated up to 240-300°C for 1 and 2 seconds. After dipping the foils were quenched subsequently in the icy water. The Cu substrates were polished with 1 $\mu$ m finish and with 6 $\mu$ m finish. The observations were made from above after etching the remained tin. It was shown that the copper substrate is completely covered by  $\eta$ -Cu<sub>6</sub>Sn<sub>5</sub> crystallites even after such short time of reaction whatever the temperature of the tin bath (see Figure 1-23).

In this work, authors consider that the first phase that nucleates and grows at the liquid Sn/Cu interface is the  $\text{Cu}_6\text{Sn}_5$  phase but no experimental proof for this claim exists in literature.

It was demonstrated that the higher nucleation rate per unit area was for the copper surface with 6  $\mu\text{m}$  finish. Authors explained this by: (i) nucleation of the  $\eta$ -phase on the copper surface and (ii) larger actual surface area for 6  $\mu\text{m}$  finish. Authors demonstrated that the highest number of particles per unit area was reached at the temperature between 260-270°C for all cases (inverse C-shape curve “number of crystallites-temperature”). Also it was shown that the minimum radius of crystallites was reached at 260°C. It is considered that each crystallite corresponds to the initially formed nucleus, which rapidly grew up. With use of classical nucleation theory, authors fitted their experimental results and obtained empirically kinetic parameters for heterogeneous nucleation of  $\eta$  assuming that: (i) the nucleation rate is constant over the time interval and (ii) the liquid/ $\eta$  interfacial energy is equal to  $\gamma_{\eta} = 0.055 \text{ J/m}^2$ . Authors obtained nucleation rate constants equal to  $K_{1\mu\text{m}} = 1.08 \times 10^{17} \mu\text{m}^{-2}\text{s}^{-1}$  and  $K_{6\mu\text{m}} = 2.11 \times 10^{17} \mu\text{m}^{-2}\text{s}^{-1}$ , with contact angles 22.7° and 23.1°. For all temperature ranges and surface finishes the calculated radius of the critical nucleus was in the range of 4-5.7 nm. From estimated values of  $K$  the possible nucleation sites were analyzed and it was concluded that the heterogeneous nucleation is predominant process.

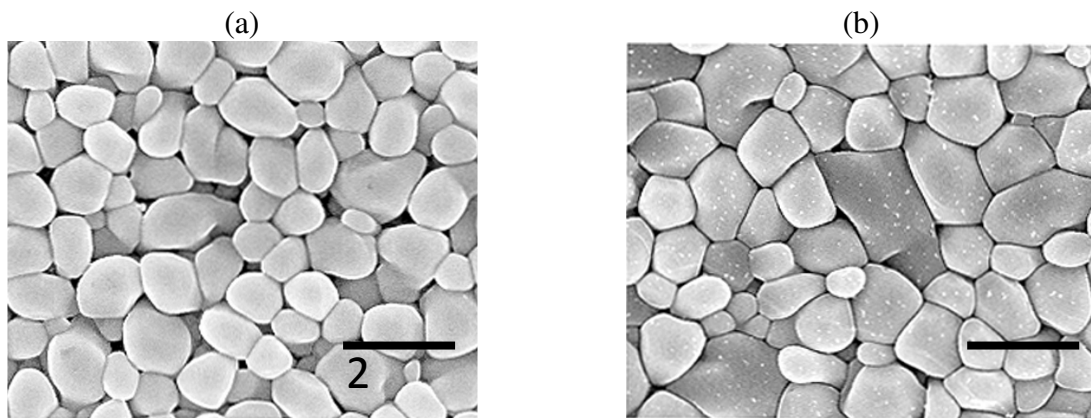


Figure 1-23. Top-view SEM images showing the microstructure of the  $\text{Cu}_6\text{Sn}_5$  layer formed at Cu/liquid Sn interface after dipping of Cu in the molten Sn for 1 s at (a) 240°C and (b) 300°C [Gagliano\_2002].

J. Gong et al. [Gong\_2008] have investigated the evolution of the IMC during reflow process in an arbitrary moment. For this purpose they designed the equipment which allowed to heat the patterned Cu pad with the deposited SAC paste and the flux to the desired temperature and to interrupt the process by the removal of the liquid solder by the rapid rotation of the specimen (the solder flew away due to the centrifugal force). The variation of the temperature with time is given on the Figure 1-24a along with the points (A-I), which indicate the principal moments of the experiment. Authors present the micrographs at the temperature range starting from 505K, whereas the solder started to melt at 483K. The heating rate was 10 K/min, so the time of reaction with liquid alloy is approximately 2 min for point A, which corresponds to the shortest reaction time (Figure 1-24a). The TEM (Figure 1-24b) and the SEM (Figure 1-24c) micrographs reveal the formation of the  $\text{Cu}_3\text{Sn}$  fine-grained layer with the thickness of approximately 300 nm and the  $\text{Cu}_6\text{Sn}_5$  layer with the thickness approximately 1  $\mu\text{m}$ . It is reported [Gong\_2008] that the growth of the IMC is slow during the heating stage, whereas the dissolution is the dominant process. If the dwelling time is long enough the liquid solder is becoming saturated and growth accelerates. A pronounced growth of the IMC is observed also during the cooling stage. The EBSD analysis demonstrates the preferred [0001] orientation of the  $\text{Cu}_6\text{Sn}_5$  grains after solidification.

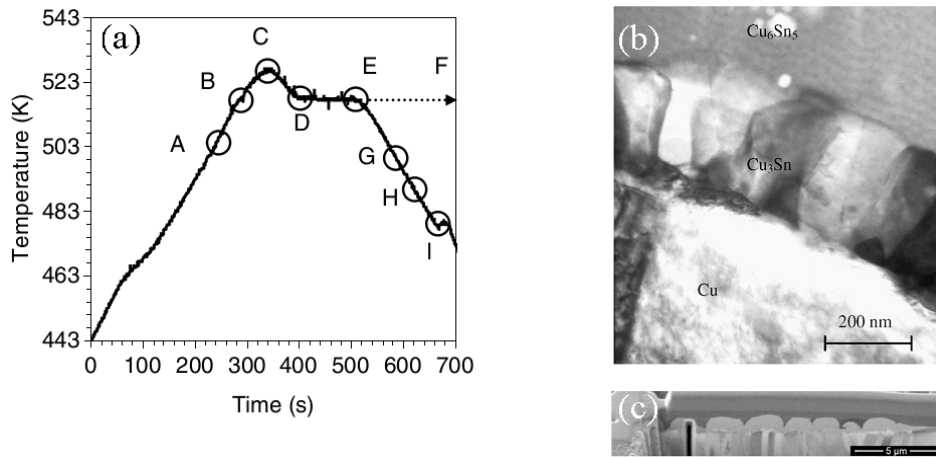


Figure 1-24. Variation of the temperature with time during a reflow process (a); The TEM micrograph (b) and SEM micrograph (c) showing the Cu/Sn interfacial zone corresponding to the A point, namely after 2 min of reaction with liquid alloy with heating from 483K to 505K. The formation of the planar layer of the  $\text{Cu}_3\text{Sn}$  phase with thickness 300 nm and scallop-like  $\text{Cu}_6\text{Sn}_5$  with thickness 1  $\mu\text{m}$  is revealed [Gong\_2008].

The same equipment was used to investigate the very early stage of the soldering reaction [Gong\_2009]. Having the SAC solder melted at 490K the first domains of IMC are observed only at 505K. After spindle test, when the solder is removed by the centrifugal force, authors distinguish the large main domain and the several secondary domains (see Figure 1-25a). In the middle of all domains the coarse  $\text{Cu}_6\text{Sn}_5$  crystals are observed. But authors detect the large number of fine particles on the edges. Naturally, authors link the edges of the domains to the nucleation sites of the IMC and name this zone as the “transition zone”. The entire interfacial zone inside “transition zone” was analyzed by TEM (see Figure 1-25b). It reveals that the fine particles are  $\text{Cu}_3\text{Sn}$  and authors claim that they are initially formed. The  $\text{Cu}_6\text{Sn}_5$  is formed at later stages of reaction and always “stands” on the  $\text{Cu}_3\text{Sn}$  layer. In another experiment, the solder is not removed by the spindle rotation but is rapidly quenched at 505K, the authors observe the solder that “sits” on the layer of the coarse  $\text{Cu}_6\text{Sn}_5$  grains and the formation of the  $\text{Cu}_3\text{Sn}$  IMC prior to the solder. The similar interfacial structure was observed for the Sn-3.8wt.%Ag (see Figure 1-25c), proving the fact of supplying of Cu atoms from the substrate. The TEM EDX analysis detected approx 4% of Sn in the flux, thereby, the supply of Sn is considered to be from the flux. The initial formation of the  $\text{Cu}_3\text{Sn}$  is explained in the frames of the concept of local nominal composition approach [Rönkä\_2008].

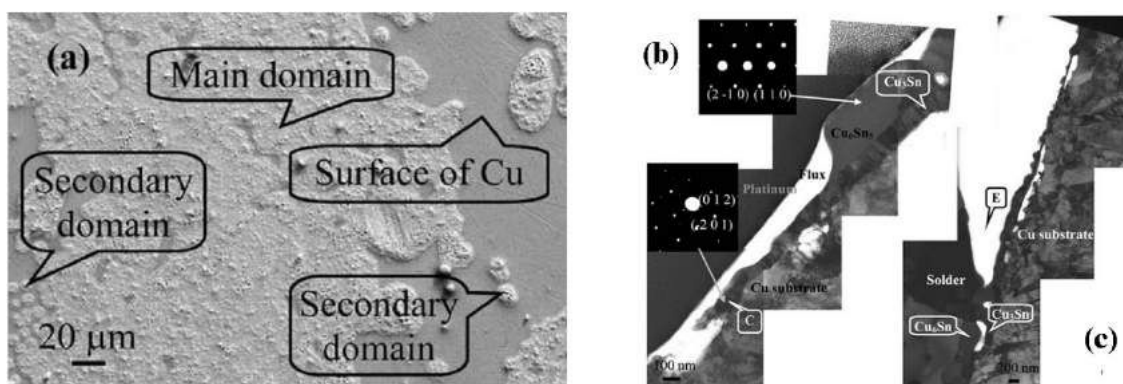


Figure 1-25. Top-view SEM image of the IMC domains formed on the Cu substrate after the spindle test (a); The TEM micrographs showing the interfacial zone after spindle test (b) and after the rapid quenching of the joint at 505K (c). The formation of the  $\text{Cu}_3\text{Sn}$  phase in advance of the solder bulk is detected [Gong\_2009].

In their work P.J. Shang et al. [Shang\_2009] were investigating the formation and growth of  $\text{Cu}_3\text{Sn}$  compound with use of SEM and TEM techniques. The polished polycrystalline Cu was put in contact with Sn-Bi solder, the reflow process took 3-5 s at 443K (melting point of eutectic Sn-Bi alloy is 412K). Then the sample was air cooled to the room temperature, the total reaction time (i.e. the time during which the solder was in the liquid state) is not specified. For such reflow process TEM investigation revealed the formation of both  $\text{Cu}_6\text{Sn}_5$  and  $\text{Cu}_3\text{Sn}$  IMCs. The thickness of the  $\text{Cu}_3\text{Sn}$  layer was approximately 100 nm and that of  $\text{Cu}_6\text{Sn}_5$  layer about 0.5-1  $\mu\text{m}$ .

C. Key Chung et al. [Key Chung\_2010] were investigating the initial stage of the reaction between Sn-4wt.%Ag-0.5wt.%Cu BGA array and the Cu substrate by using DSC and high-resolution TEM. The melting temperature of such solder alloy is close to 217°C. After the joint temperature reached 217.4°C the samples were quenched in the icy water. The heating rate as well as the use of the fluxes for deoxidation are not discussed in this work [Key Chung\_2010]. TEM analysis revealed formation of both IMC's:  $\text{Cu}_6\text{Sn}_5$  with scalloped morphology with unspecified thickness and 80-90 nm thick  $\text{Cu}_3\text{Sn}$  layer (see Figure 1-26). Also author performed DSC analysis of the cooling process and detected two isothermal peaks at 173.2 and 186.2°C. They linked these peaks with transformation from  $\eta'$ - $\text{Cu}_6\text{Sn}_5$  to  $\eta$ - $\text{Cu}_6\text{Sn}_5$ . Authors concluded that  $\eta'$ - $\text{Cu}_6\text{Sn}_5$  nucleates heterogeneously prior to the melting of the solder. Authors also investigated the interface between  $\text{Cu}_3\text{Sn}$  and  $\text{Cu}_6\text{Sn}_5$  by TEM. They detected the Cu enriched region with the concentration 80.3 - 84.5 at.%Cu and the thickness 4-6 nm. They have linked the existence of this thick interface with the large lattice mismatch between the two IMC. Almost of the same thickness (3-5 nm), the Cu-enriched interface was found in between solder and  $\text{Cu}_6\text{Sn}_5$ . Authors claim that the Cu diffusion through the intermetallics phases (obviously being volume diffusion) and along grain boundaries of intermetallics are the dominant mechanism for the growth of intermetallics in the early stage of reflow, what is granted by existence of detected Cu-enriched regions.

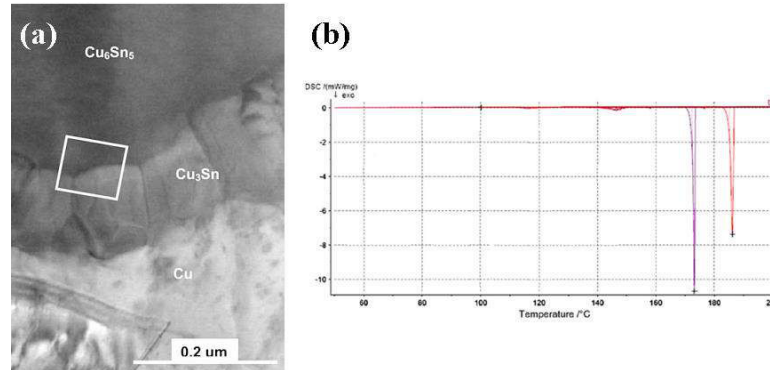


Figure 1-26. TEM image of the interfacial zone of the Cu/Sn-4wt.%Ag-0.5wt.%Cu couple after partial melting at 217.4°C showing the formation of the 80-90 nm thick  $\text{Cu}_3\text{Sn}$  layer below scalloped  $\text{Cu}_6\text{Sn}_5$  layer (a). The DSC cooling curve showing two exothermic peaks, which are linked by authors in [Key Chung\_2010] with transformation from  $\eta'$ - $\text{Cu}_6\text{Sn}_5$  to  $\eta$ - $\text{Cu}_6\text{Sn}_5$ .

In their recent work the same team [Key Chung\_2013] investigated the contact points between the not completely melted solder and the solid substrate (so-called premelting reaction). They have detected the formation of both IMCs on these contact points before melting. The thickness of the  $\eta$ - $\text{Cu}_6\text{Sn}_5$  wasn't specified, whereas the thickness of the  $\text{Cu}_3\text{Sn}$  layer (80-100 nm) was the same as one measured in their previous work [Key Chung\_2010].

K.L Lin et al. [Lin\_2012] prepared a series of experiments of short time reactions (5-15 s) between Cu and pre-fluxed liquid lead-free solder balls. Authors distinguish the different stages of soldering: heating stage in solid state, dissolution stage with melting, counterdiffusion, nucleation, growth and ripening. The substrates were polished and then preheated to the desired temperature, the solder balls (0.76 mm in diameter) were first dipped

in the flux and then put on the preheated substrates, the samples were rapidly quenched (in 1 s) in nitrogen after a short reaction time (5-15 s). The TEM investigation revealed the existence of the “broken lattice zone” with thickness 1 nm (see Figure 1-27a), the “atomic cluster zone” of less than 5 nm and realization of the zigzag dissolution mechanism (see Figure 1-27b). The amorphous layer that serves as the diffusion zone with width that does not exceed 50 nm is formed between the substrate and the atomic cluster zone (see Figure 1-27a). The sequence of the regions is as follows: broken lattice zone 1 nm (see Figure 1-27a) → atomic cluster zone 5 nm → amorphous diffusion zone 50 nm and the IMC (for couples: Cu/Sn [Yu\_2006], Cu/Sn-3wt.%Ag-0.5wt.%Cu [Pan\_2008] and Cu/Sn-9wt.%Zn-1wt.%Ag [Pan\_2011]).

The main conclusion of these research investigations is that in very early stage of the soldering the homogeneous nucleation of the  $\text{Cu}_3\text{Sn}$  compound proceeds in the amorphous region B (see Figure 1-28a,b,d), which is 50 nm far from the substrate. Authors distinguish the amorphous layer without presence of any nucleus (region B) and the amorphous layer with nuclei (see Figure 1-28c). The size of the formed crystallites is approximately 10 nm. Their crystallographic orientation has no connection with crystallographic orientation of the substrate [Yu\_2006]. The amorphous layer B (50 nm thick) is considered as a region insufficiently saturated by tin in order to prohibit the nucleation of the IMC.

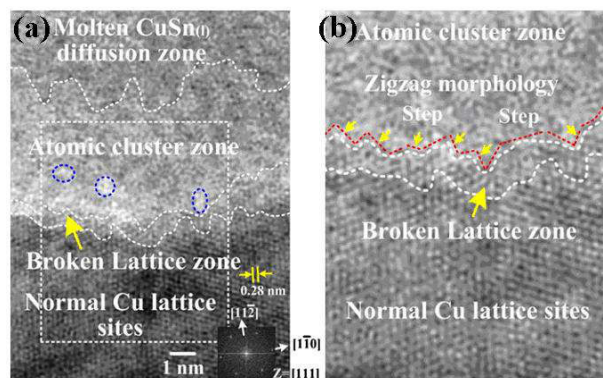


Figure 1-27. The dissolution of Cu in liquid solder proceeds by zigzag mechanism. The broken lattice zone, the atomic cluster zone and molten CuSn diffusion zone are emerging between Cu substrate and tin-based solder according to [Lin\_2012]. The right is a zoom of the region in a dotted box.

The initial stage of the soldering reaction was studied also by M.A.A. Mohd Salleh et al. [Salleh\_2015]. The growth of the IMC was tracked from the very beginning of the reaction between Cu and Sn-0.7wt.%Cu solder at the melting temperature of the solder ( $\sim 227^\circ\text{C}$ ) and subsequent cooling using a synchrotron X-ray imaging. Authors detected the formation of the planar (within resolution of the imaging) layer of the IMC. The IMC layer develops to the scallop-like morphology subsequently. The voids were also detected in the vicinity of the IMC. The reaction kinetics was also studied at higher temperature of  $244^\circ\text{C}$  after placing the liquid droplet of solder on the substrate at this temperature. Authors measured the IMC thickness versus time (see Figure 1-29a) and plotted the logarithmic dependence of the layer thickness with time (see Figure 1-29b) in order to identify the growth constants. The planar IMC layer precipitates at the very beginning ( $\sim 1$  s) of the wetting reaction. As it can be seen from Figure 1-29b, the growth of the IMC is not monotonic, three different regimes were distinguished: (i) the initial slow growth with time exponent 0.07 within first 10 s of reaction at  $244^\circ\text{C}$ ; (ii) the rapid growth with time exponent 0.31 at 10-50 s of reaction time; (iii) slow growth during cooling to  $213^\circ\text{C}$  (unfortunately, the cooling rate is not specified) the growth exponent decreased significantly to 0.03. Cooling stage took approximately 110 s.

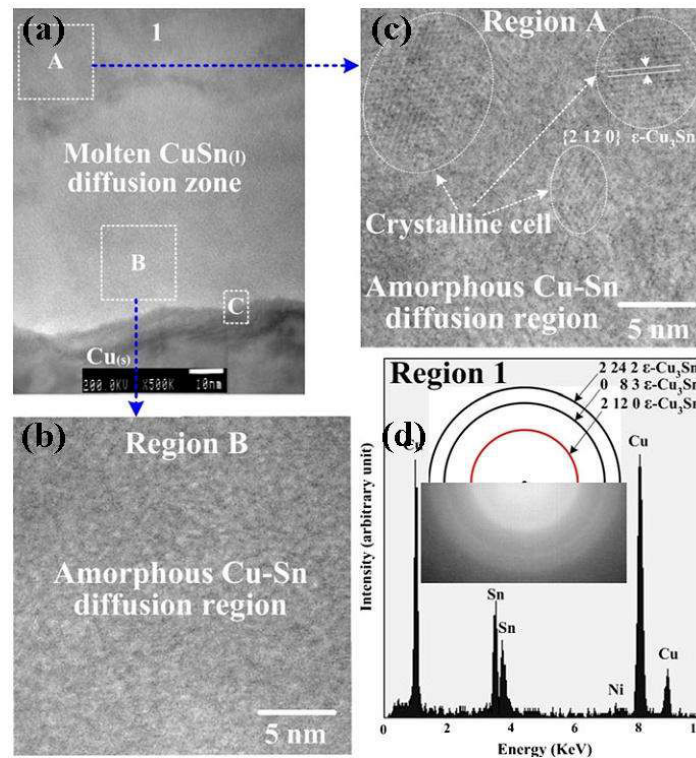


Figure 1-28. The interfacial zone after 15s reaction between Cu and Sn at 250°C after quenching in the liquid nitrogen (a) with zoom on amorphous Cu-Sn diffusion region, i.e. Region B (b), the amorphous Cu-Sn diffusion region, i.e. Region A (c) and the diffraction pattern indicating the formation of the  $Cu_3Sn$  phase inside the amorphous region (d). [Lin\_2012]

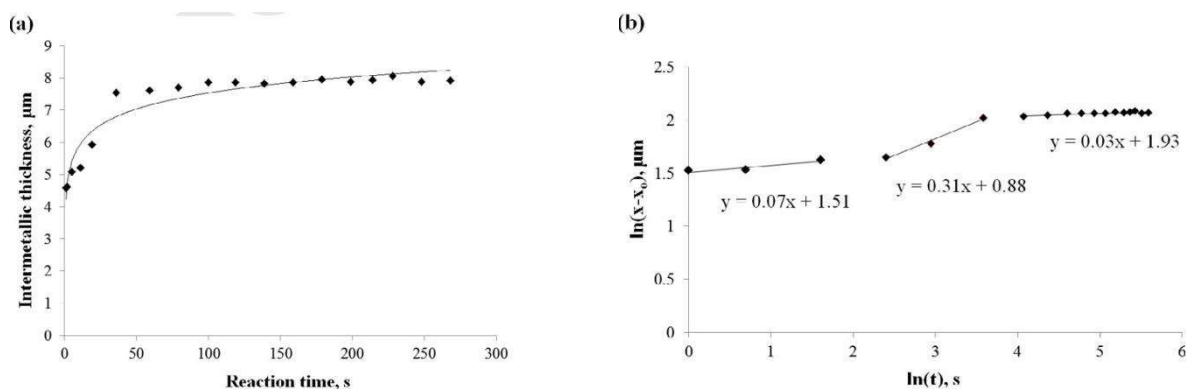


Figure 1-29. a) The mean IMC thickness versus time; b)  $\ln$ - $\ln$  dependence between IMC thickness and time indicating three stages of the IMC growth during reflow process (temperature range 213-244°C) [Salleh\_2015].

#### 4-3) Interfacial reactions at Cu/solid Sn interface

##### 4-3-1) Experimental results on Cu/solid Sn reactions

###### 4-3-1-1) From -2°C to 80°C:

K.N. Tu [Tu\_1973, Tu\_1996] and K. N. Tu and R. D. Thompson [Tu\_1982] performed series of the annealing experiments with Cu/Sn thin films at temperatures lower than melting temperature of tin. The thicknesses of films were: Sn 350nm/Cu 180 nm; Sn 350 nm/Cu 600 nm and Sn 2500 nm/Cu 600 nm. Thin films were annealed at -2°C and 20°C for the time up to 1 year under air as well as at 60°C and 100°C under the vacuum for the time up to 60

hours. The XRD and TEM study revealed the formation of the only  $\text{Cu}_6\text{Sn}_5$  phase at the interface while  $\text{Cu}_3\text{Sn}$  phase is detected only for temperature higher than  $60^\circ\text{C}$ .

In their turn, R. Chopra et al. [Chopra\_1982] had studied the kinetic of interaction between tin and copper thin films (with thickness 4nm and 2-3nm respectively) deposited by thermal evaporation under vacuum while keeping isotherm at  $80^\circ\text{C}$  and  $86^\circ\text{C}$  for 160 and 320 minutes respectively. The methods of characterization were TEM and Auger electronic spectroscopy (AES). It was reported that for reaction times less than 160 minutes at  $80^\circ\text{C}$  the only  $\text{Cu}_6\text{Sn}_5$  phase was formed at the interface. After 360 minutes of reaction the  $\text{Cu}_3\text{Sn}$  was detected also. The qualitative analysis by AES showed that the growth kinetics of the reaction layer at  $86^\circ\text{C}$  for the time less than 360 minutes obeys the linear law and that the growth is limited by the interfacial reaction kinetics [Chopra\_1982].

The Cu/Sn interactions at ambient temperatures were also studied by R. Halimi et al. [Halimi\_1987]. The experiments were held with copper and tin thin films with thickness changing from 2nm to 5nm deposited by thermal evaporation under vacuum with deposition rate of  $20 \text{ \AA/s}$ . The X-ray diffraction (XRD) analysis revealed the formation of  $\eta'$  phase at the interface even during deposition and during room temperature holding only  $\eta'$  phase was detected. C.N. Liao and C.T. Wei [Liao\_2004] reported similar results on the basis of the experiments with Cu/Sn thin films, in which they measures *in situ* the resistivity and performed XRD analysis during heating of the system. The thickness of the films deposited by cathodic pulverization was  $\sim 200 \text{ nm}$ .

Recently W.M. Tang et al. [Tang\_2010] studied the interaction between electroplated copper and tin films with thickness of few micrometers. The current densities of tin and copper deposition were  $10 \text{ mA/cm}^2$  and  $25 \text{ mA/cm}^2$  respectively and the deposition rate  $0.5 \text{ }\mu\text{m/min}$  and  $0.3 \text{ }\mu\text{m/min}$ . By using the DRX technique the formation of  $\text{Cu}_6\text{Sn}_5$  phase was detected at the Cu/Sn interface even during deposition. Besides, the electronic microscope analysis with energy-dispersive X-ray spectroscopy (EDX) of the specimen aged for 76 days at ambient temperature revealed very clearly the  $\text{Cu}_6\text{Sn}_5$  layer with thickness less than  $1\mu\text{m}$ .

#### 4-3-1-2) From $70^\circ\text{C}$ to $220^\circ\text{C}$ :

The reactions at the Cu/Sn interfaces in the solid state at the range of temperatures  $70\text{-}220^\circ\text{C}$  were studied in literature in details. Two types of experiments could be distinguished: the one based on the diffusion couple Cu/Sn or Cu/Sn-based alloys. Such kind of experiments need: (i) to incorporate accurate metallographic preparation of the surface of two solids and (ii) to be performed either under secondary vacuum, or under air but with use of the acidic flux in order to exclude the oxidation of the surfaces. The initial contact can be also performed by fast dipping of a copper substrate into the flux and then into the bath of melted tin and subsequent cooling to room temperature. Afterwards the Cu/Sn-based alloy couple is isothermally aged for a certain time (as long as 170 days [Laurila\_2005]). The main number of the studies reports the presence of two phases, namely  $\text{Cu}_6\text{Sn}_5$  and  $\text{Cu}_3\text{Sn}$  at the interface.

Figure 1-30 shows a scanning electron microscopy (SEM) image of the interfacial zone of the Cu/Sn diffusion couple after aging at  $215^\circ\text{C}$  for 225 h under the vacuum [Paul\_2004]. The micrometric inert  $\text{ThO}_2$  particles were placed as markers at the initial interface. Two phases  $\eta\text{-Cu}_6\text{Sn}_5$  and  $\varepsilon\text{-Cu}_3\text{Sn}$  with thickness  $10\text{-}15 \text{ }\mu\text{m}$  and  $7\text{-}10 \text{ }\mu\text{m}$  respectively are seen. As it can be seen, the Cu/ $\varepsilon$  interface is relatively plane in comparison with the irregular  $\varepsilon/\eta$  and  $\eta/\text{Sn}$  interfaces. The inert  $\text{ThO}_2$  particles are situated in the middle of the  $\text{Cu}_6\text{Sn}_5$  layer.

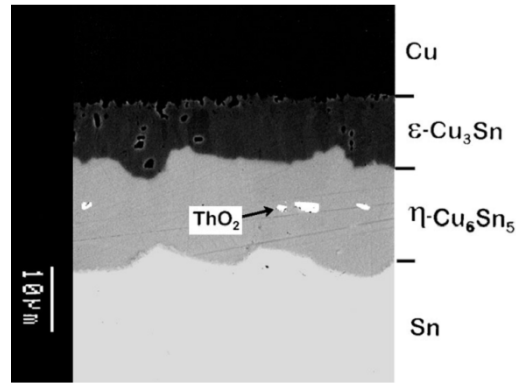


Figure 1-30. SEM image of the Cu/Sn interfacial zone developed after reaction at 215°C in vacuum for 225 hours [Paul\_2004].

In their study M. Onishi et al [Onishi\_1975] measured the average thickness of each phase ( $\epsilon$  and  $\eta$ ), formed at Cu/Sn interface, as a function of reaction time up to 900 h in the range of temperatures between 190°C and 220°C. The growth kinetics of both phases obeys parabolic law ( $e^2=k't$  or  $e=kt^{1/2}$ ), which means that the growth of reaction layers is limited by diffusion. The layer thickness  $e_i$  ( $i = \eta$  or  $\epsilon$ ) could be described by the following relations:

$$e_i = k_i t^{1/2} \text{ and } k_i = k_i^0 \exp\left(\frac{-Q_i}{RT}\right), \quad (1-15)$$

where  $k_\eta$  and  $k_\epsilon$  are the growth constants and  $Q_\epsilon = 61 \text{ kJ}\cdot\text{mol}^{-1}$  and  $Q_\eta = 55 \text{ kJ}\cdot\text{mol}^{-1}$  are the diffusion activation energies of the  $\epsilon$  and  $\eta$  phases respectively. Authors report that the growth rate of the  $\eta$  phase was higher than the one of the  $\epsilon$  phase whatever the annealing time in the range of temperatures between 190°C and 220°C (Figure 1-31).

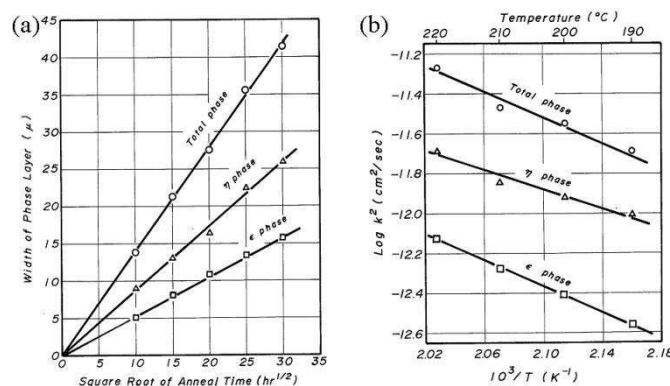


Figure 1-31. Variation of the intermetallic layer thickness ( $e$ ) with reaction time for Cu/Sn couple at 220°C (a); variation of the growth constant  $k$  ( $e = kt^{1/2}$ ) with temperature (b) [Onishi\_1975].

The same trend in the phase competition is supported by T.Y. Lee et al. [Lee\_2002] who performed experiments with electroplated Cu UBM with thickness of 15  $\mu\text{m}$ . The solder balls used in this study with diameter of about 100  $\mu\text{m}$  were reflowed for 1 min above the melting temperature with a peak temperature of 240°C. Solders used in the study were eutectic SnPb, Sn-3.5wt.%Ag, Sn-3.8wt.%Ag-0.7wt.%Cu and Sn-0.7wt.%Cu. The annealing time varied from 0 (just reflow) to 1500 hours and the annealing temperatures were 125, 150 and 170°C. In all cases the growth rate of the  $\eta$ -Cu<sub>6</sub>Sn<sub>5</sub> phase was higher than that of the  $\epsilon$ -Cu<sub>3</sub>Sn phase.

Nevertheless, R. Labie et al. [Labie\_2007] report faster growth of the Cu<sub>3</sub>Sn phase at late stage of reaction (annealing time more than 70 hours) at 125°C (see Figure 1-32). The principal differences, compared to the experiments performed by Onishi et al. [Onishi\_1975], are the use of the thin electroplated Cu UBM (5  $\mu\text{m}$ ) as well as thin layer of the Sn-bump (40  $\mu\text{m}$  height). It should be noticed that in order to obtain an initial bonding at Cu/Sn interface before to perform the solid state treatments at 125°C [Labie\_2007], the Cu/Sn couple was first

reflowed for 40s at 260°C which leads to the formation of a thick initial  $\eta$ -Cu<sub>6</sub>Sn<sub>5</sub> layer (experiment corresponding to  $t = 0$  in Figure 1-32). Basically, the total thickness of the reaction layer increases due to the increase of the  $\epsilon$ -Cu<sub>3</sub>Sn phase thickness that obeys square root law and, evidentially, grows by the diffusion controlled mechanism.

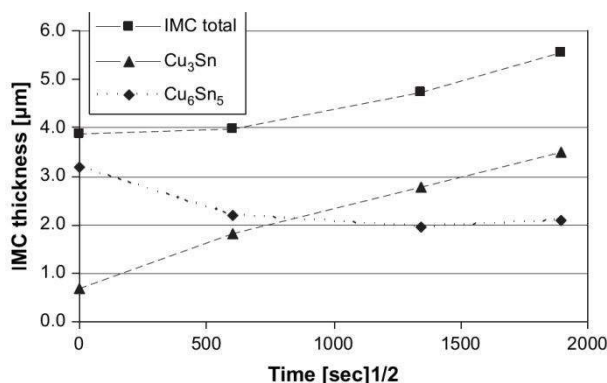


Figure 1-32. Variation of the thickness for each individual IMC phase and total IMC change with time in Cu-Sn couple annealed at 125°C [Labie\_2007].

In their experiments with electroplated Cu and Sn films, W.M. Tang et al. [Tang\_2010] measured the thickening kinetics of the individual IMCs. Annealing was held at 150, 200 and 225°C. Authors report that the  $\eta$ -Cu<sub>6</sub>Sn<sub>5</sub> phase grows faster only at 150°C. The reported growth constants are higher for the Cu<sub>3</sub>Sn phase at 200 and 225°C (see Figure 1-33).

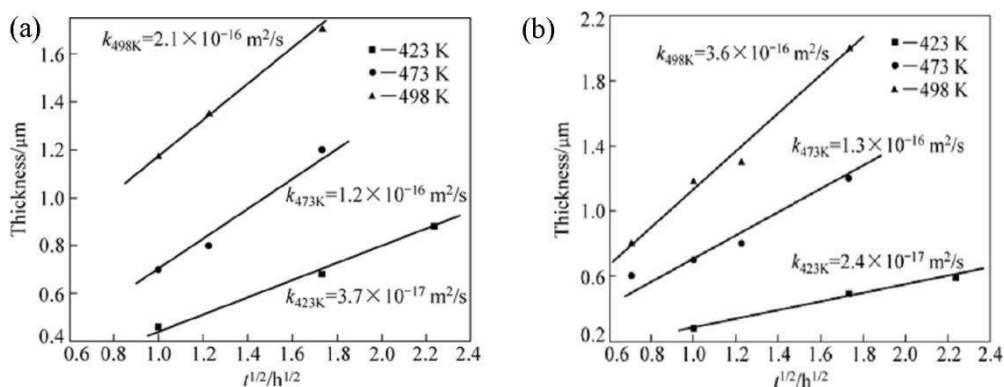


Figure 1-33. Average thickness of the  $\eta$ -Cu<sub>6</sub>Sn<sub>5</sub> phase (a) and  $\epsilon$ -Cu<sub>3</sub>Sn phase (b) versus square root of time for Cu-Sn couple annealed at 150, 200 and 225°C [Tang\_2010].

P. T. Vianco et al [Vianco\_2004] also measured the total mean thickness of the reaction layers formed between Cu and Sn or between Cu and a Sn-3.5wt.%Ag alloy as a function of the temperature of the solid state aging. The experiments were performed at various temperatures from 70°C to 250°C with aging time up to 400 days (Figure 1-34). It should be noticed that the case of Cu/Sn couple the growth is slightly higher than in the case of Cu/Sn-Ag couple. As in previous cases, the growth kinetics obeys parabolic law. The activation energy of the reaction layer growth ( $\epsilon + \eta$ ) was determined:  $Q_{\epsilon+\eta}(\text{Cu/Sn}) = 43 \text{ kJ}\cdot\text{mole}^{-1}$ ;  $Q_{\epsilon+\eta}(\text{Cu/Sn-Ag}) = 50 \text{ kJ}\cdot\text{mole}^{-1}$ .

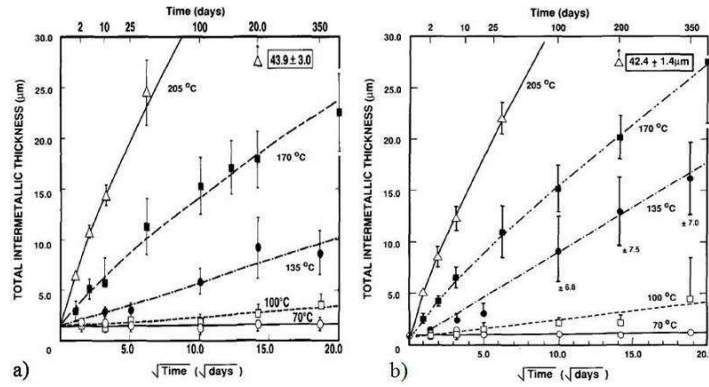


Figure 1-34. Variation of the total IMC thickness with square root of time in Cu/Sn-Ag couple (a) and Cu/Sn couple annealed at different temperature [Vianco\_2004].

In their experiments C. Yu et al. [Yu\_2013] investigated the solid state reaction between Cu foils (thickness 0.1 mm) with three types of the solders: pure Sn, Sn-0.7wt.%Cu and Sn-3.5wt.%Ag. The isothermal ageing was held at 150°C and 180°C. The initial contact was performed by reflow at 260°C for 60s. Such relatively high reflow temperature resulted in thick  $\eta$ -Cu<sub>6</sub>Sn<sub>5</sub> layer (2-3 μm). Only in the case of Cu/Sn-3.5wt.%Ag and Cu/Sn-0.7wt.%Cu couples the  $\eta$ -Cu<sub>6</sub>Sn<sub>5</sub> continues to grow during isothermal annealing at 150°C and 180°C up to 700 hours surpassing the growth of the  $\epsilon$ -Cu<sub>3</sub>Sn layer. In the case of Cu/pure Sn couple the growth of the  $\eta$ -Cu<sub>6</sub>Sn<sub>5</sub> layer was frozen, only the initial scallop-like interface was flattened. The parabolic growth of the  $\epsilon$ -Cu<sub>3</sub>Sn layer proceeds up to a thickness comparable with one of the  $\eta$ -Cu<sub>6</sub>Sn<sub>5</sub> layer (see Figure 1-35).

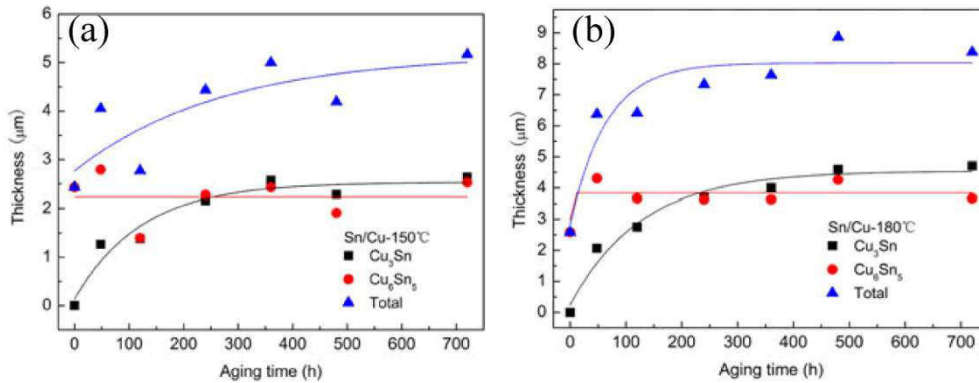


Figure 1-35. Variation of the average thickness of  $\eta$ -Cu<sub>6</sub>Sn<sub>5</sub> phase,  $\epsilon$ -Cu<sub>3</sub>Sn phase and total IMC versus time for Cu-Sn couple annealed at 150°C (a) and 180°C (b) [Yu\_2013].

#### 4-3-2) Kirkendall voids during solid-state reactions

The reason of voiding during reactive interdiffusion in Cu/Sn couple is the difference of diffusion fluxes of Cu and Sn atoms during solid-state aging or heating operations [Tu\_2007]. The formation of voids is strongly connected with formation of the  $\epsilon$ -Cu<sub>3</sub>Sn layer during reaction between Cu and Sn. As the Cu<sub>3</sub>Sn forms the flux of vacancies emerges in the direction of the Cu substrate and the lack of the sinks results in the voids formation. It should be emphasized that in common soldering reaction the formation of voids is strongly linked with formation or later stages of growth of the  $\epsilon$ -Cu<sub>3</sub>Sn layer [Zeng\_2005]. Therefore, the factors that can influence the formation, suppression or growth of the  $\epsilon$ -Cu<sub>3</sub>Sn layer are of great interest.

It is still under discussion how to choose correctly the proper substrate or electrolyte for the electroplating of the Cu pads in order to eliminate the formation of the Kirkendall voids. For example, in literature there is a discussion whether the Kirkendall voids are formed on the bulky polycrystalline Cu substrates or electroplated foils.

W. Yang et al [Yang\_1994] report the formation of the Kirkendall voids in the  $\text{Cu}_3\text{Sn}$  layer during reaction in the electrodeposited Cu/Sn-Ag solder couple for 3 days at  $190^\circ\text{C}$  (Figure 1-36a). It is important to notice that when the Cu pad was rolled no voids were detected even after 12 days of annealing at the same temperature (Figure 1-36b). It means that mechanical treatment of the UBM can influence the important reliability issue.

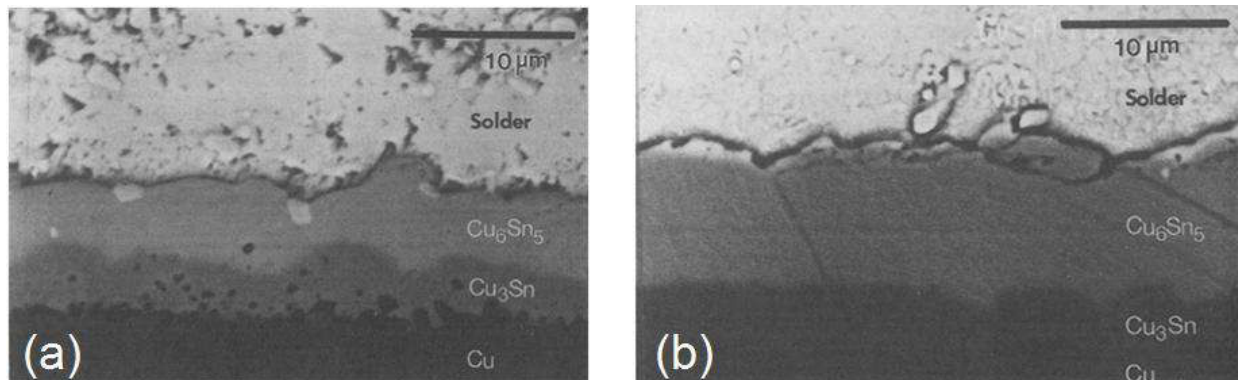


Figure 1-36. SEM images of electrodeposited Cu/Sn-Ag couple after 3 days annealing at  $190^\circ\text{C}$  (a) and rolled Cu/Sn-Ag after 12 days annealing at  $190^\circ\text{C}$  (b) [Yang\_1994].

A. Paul [Paul\_2004] reports the formation of the Kirkendall voids after reaction in the polycrystalline Cu/Sn couple at relatively high temperature of  $215^\circ\text{C}$  for 225 hours (see Figure 1-30).

K. Zeng et al. [Zeng\_2005] report the formation of the Kirkendall voids just after reflow between electrodeposited Cu and Sn-Pb solder (see Figure 1-37a). The reflow peak temperature was given to be  $220^\circ\text{C}$  but the reflow time wasn't specified. The density of voids increases drastically after 3 days of annealing at  $150^\circ\text{C}$  (see Figure 1-37b).

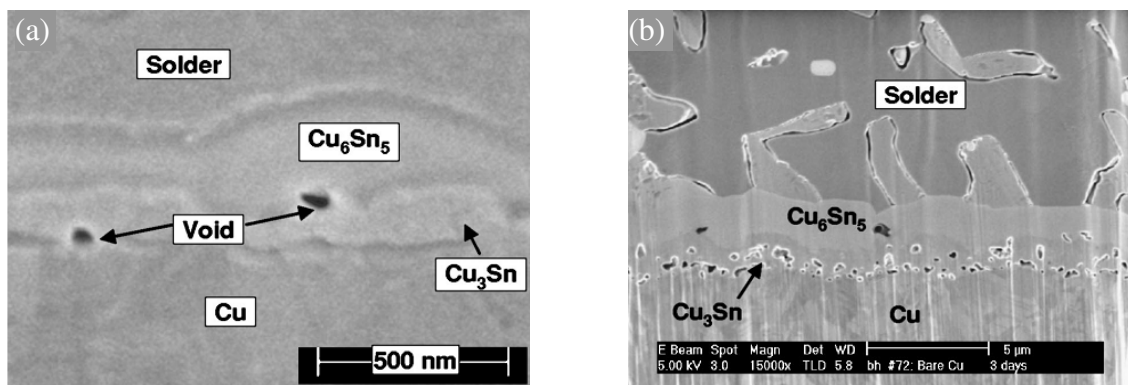


Figure 1-37. FIB images of the: a) just reflowed electrodeposited Cu/SnPb joint; b) annealed at  $150^\circ\text{C}$  for 3 days [Zeng\_2005].

V. Vuorinen et al. have studied the influence of the Cu purity on the voiding [Vuorinen\_2007]. They demonstrated the absence of voids for the case when the very pure polycrystalline Cu was used (99.99%) for reaction with Sn (99.95%) at  $125^\circ\text{C}$  for 3500 hours (Figure 1-38a). The excessive voiding appeared when the Cu was substituted by Cu(Ni) alloy with a composition Cu1.0at.%Ni and annealed under the same conditions (Figure 1-38b). Good result were obtained when the composition of the Ni in the Cu(Ni) alloy was increased to 10at.% and no voids were detected (Figure 1-38c).

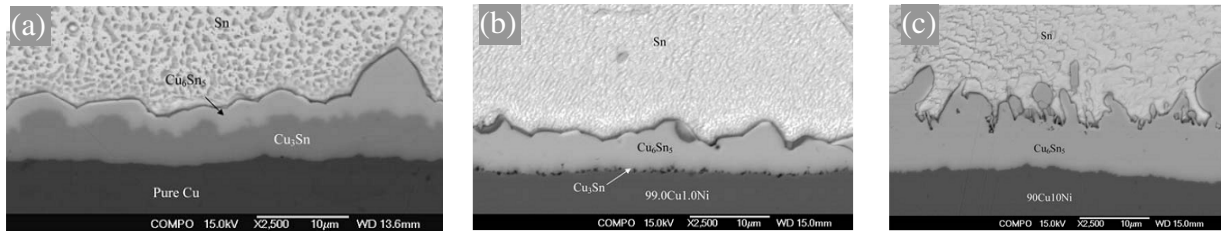


Figure 1-38. SEM images of the samples annealed for 3500 hours at 125°C. a) Pure Cu/Sn couple; b) Cu1.0at.%Ni/Sn couple; c) Cu10.0at.%Ni/Sn couple [Vuorinen\_2007].

The use of the nano-twinned Cu as UBM is believed to eliminate the formation of the Kirkendall voids. The H.Y. Hsiao et al. [Hsiao\_2012] have tested the densely packed [111] nanotwinned Cu for UBM. The thickness of the Cu layer was 20 µm and it was annealed in the sandwich structure with Sn-3.5wt.%Ag alloy at 150°C for 1000 hours. Kirkendall voids were not detected (see Figure 1-39a), what is believed to happen because of the existence of the numerous vacancy sinks between nano-twinned Cu grains. The same type of substrate material was tested by W.L. Chiu et al. [Chiu\_2014] in the reaction with pure molten Sn at 260°C. The authors also investigated the sandwich structure and achieved the complete transformation of the solder bulk to the Cu<sub>3</sub>Sn IMC in 24 hours (Figure 1-39b). No voids were detected as well.

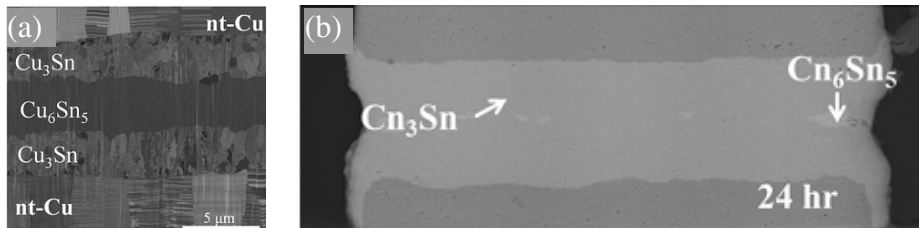


Figure 1-39. a) nt-Cu/Sn-3.5wt.%Ag couple annealed for 1000 hours at 150°C [Hsiao\_2012]; b) nt-Cu/Sn couple annealed for 24 hours at 260°C [Chiu\_2014].

#### 4-3-3) Modeling of the phase growth and competition during solid-state reactions

Nowadays, the standard model of the phase growth kinetics is well established [Gusak\_2010]. For the late stages of the solid state reaction, when the sufficient amount of reagents is present, the phase layer growth obeys the well-known parabolic law. Nevertheless, from 1970's the microelectronic industry provided new problems by operating with thin films. It was found that the intermediate phases could be suppressed partially or completely. Most successful theories of this type belong to U.Gösele and K.N.Tu [Gösele\_1982] and A. M. Gusak and K.P. Gurov [Gusak\_1982]. Nucleation issues, in terms of standard nucleation approach, but in application to solid state reactions, have been discussed by F. d'Heurle in 1986 [d'Heurle\_1986].

Let's review the general case of the growth of two phases (1 and 2) between two insoluble components (A and B). It can be done by considering the flux balance at three emerging interfaces (see Figure 1-40a). The concentration profile of such system is given on Figure 1-40b.

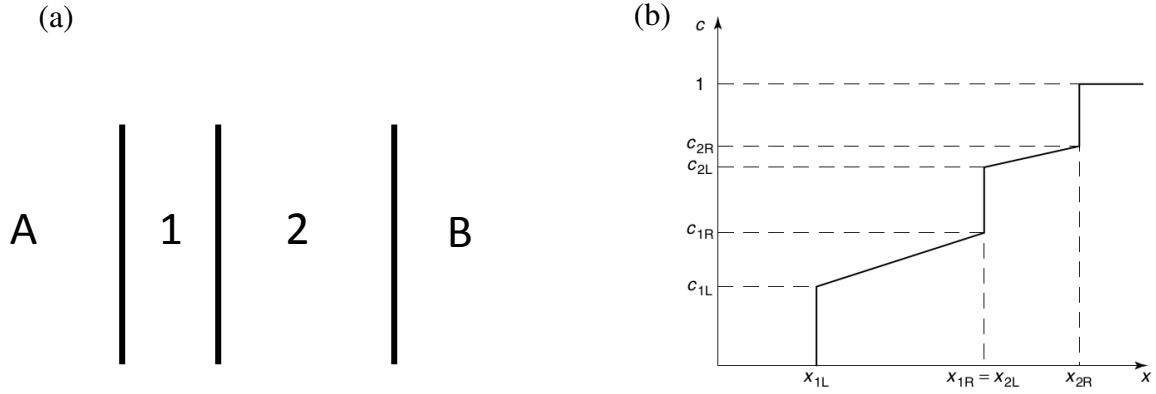


Figure 1-40. The principal scheme of the reaction couple A/B with formation of two intermediate phases 1 and 2 (a) and the concentration profile of component B through the system (b).

Let us consider the case when the growth of the phases is controlled by the bulk diffusion through the growing intermediate phases. The equations of flux balance at the interfaces can be written as:

$$\begin{aligned}
 (1 - c_{2R}) \frac{dx_{2R}}{dt} &= \frac{D_2 \Delta c_2}{\Delta x_2}, \\
 (c_{2L} - c_{2R}) \frac{dx_{2L}}{dt} &= -\frac{D_2 \Delta c_2}{\Delta x_2} + \frac{D_1 \Delta c_1}{\Delta x_1}, \\
 (c_{1L} - 0) \frac{dx_{1L}}{dt} &= -\frac{D_1 \Delta c_1}{\Delta x_1},
 \end{aligned} \tag{1-16}$$

where  $c_{1L}$ ,  $c_{2L}$ ,  $c_{1R}$  and  $c_{2R}$  are equilibrium concentration at different interfaces;  $x_{1L}$ ,  $x_{2L} = x_{1R}$  and  $x_{2R}$  are the A/1, 1/2 and 2/B (L and R mean Left and Right) interface positions;  $D_1 \Delta c_1$  and  $D_2 \Delta c_2$  are Wagner's integrated coefficient [Wagner\_1969] in intermediate phases.

The system of differential equations for phase thicknesses could be obtained easily as:

$$\begin{aligned}
 \frac{d\Delta x_1}{dt} &= a_{11} \frac{D_1 \Delta c_1}{\Delta x_1} + a_{12} \frac{D_2 \Delta c_2}{\Delta x_2}, \\
 \frac{d\Delta x_2}{dt} &= a_{21} \frac{D_1 \Delta c_1}{\Delta x_1} + a_{22} \frac{D_2 \Delta c_2}{\Delta x_2}.
 \end{aligned} \tag{1-17}$$

Here

$$a_{ik} = \begin{pmatrix} \frac{c_2}{c_1} & -1 \\ -1 & \frac{1-c_1}{1-c_2} \end{pmatrix} \frac{1}{c_2 - c_1}.$$

It can be found by direct substitution that that system has parabolic solutions

$$\Delta x_1 = k_1 t^{1/2} \text{ and } \Delta x_2 = k_2 t^{1/2}, \tag{1-18}$$

where  $k_1$  and  $k_2$  are growth constants.

In fact, there are a lot of real systems in which one phase can have much lower diffusion permeability than another one. Mathematical condition reads as  $D_2 \Delta c_2 \ll D_1 \Delta c_1$  in this case. The system controls the necessary flux of atoms to build the fast growing phase 1 by keeping the thickness of the phase 2 very small. It means that  $\frac{d\Delta x_2}{dt} \approx 0$  and that the thickness of that thin phase can be derived from (1-17) as:

$$\Delta x_2 \approx \Delta x_1 \frac{1 - c_1}{1 - c_2} \frac{D_2 \Delta c_2}{D_1 \Delta c_1} \tag{1-19}$$

Hence, the growth of the fast growing phase can be derived as:

$$\frac{d\Delta x_1}{dt} = \frac{1}{c_1(1-c_1)} \frac{D_1\Delta c_1}{\Delta x_1} \quad (1-20)$$

Surprisingly, Eq.(1-20) says that the growth rate of the dominant phase 1 is not depending on the thickness of the suppressed phase 2.

#### 4-4) Interfacial reactions at Cu/liquid Sn interface

##### 4-4-1) Experimental results on Cu/liquid Sn reactions

The interaction between solid copper and liquid tin or tin-based solder starts with rapid dissolution of copper till the metastable solubility of tin by copper is reached [Laurila\_2005]. The metastable solubility is always higher than the “stable” one (corresponding to the equilibrium between the liquid Sn-Cu alloy and  $\text{Cu}_6\text{Sn}_5$  or  $\text{Cu}_3\text{Sn}$  phase), so even during reaction of copper with pre-saturated tin-based solder the dissolution should happen. The copper diffusion in liquid tin is a very rapid process, as it is well known that the magnitude of the diffusion coefficient in liquids can be as high as  $10^{-9} \text{ m}^2/\text{s}$ . As a result, the copper concentration profile of the “diffusion profile” type emerges rapidly in the liquid tin or tin-based solder. The conventional solder balls of size of  $100 \mu\text{m}$  can be saturated in Cu at time less than 10 s [Gusak\_2010].

As it was emphasized before, the formation of the reaction layers proceeds in the metastable state. It is generally accepted that the growth of the  $\eta\text{-Cu}_6\text{Sn}_5$  crystallites is dominant for the initial stages of the reaction [Laurila\_2005, Gagliano\_2002, Park\_2012]. As it will be shown below the thickness of  $\eta\text{-Cu}_6\text{Sn}_5$  layer exceeds drastically the thickness of the  $\varepsilon\text{-Cu}_3\text{Sn}$  phase at any moment of the reaction between liquid tin and solid copper. Nevertheless, the nucleation sequence of phases is still under discussion as it was described in the section 4.2.

The morphology of the  $\eta$  grains can be very different, depending on the temperature [Yang\_2012], Cu crystallographic orientation [Zou\_2008, Suh\_2007, Suh\_2007\_II, Chen\_2011] and solder composition [Suh\_2008]. The variety of the  $\eta$  grains growing during reaction between Cu and liquid tin includes: scallop-like [Yang\_2012], faceted [Suh\_2008] or longitudinal [Gagliano\_2003].

One example of the morphology evolution can be given on the basis of the work of R.A. Gagliano et al. [Gagliano\_2003]. The study of the reaction layers of the Sn/Cu couple revealed the formation of the longitudinal  $\eta$  phase grains (see Figures 1-41 and 1-42). It was found that the aspect ratio (namely the ratio between grain height  $H$  and width  $D$ ) is growing with annealing time (Figures 1-41) as well as with annealing temperature (Figures 1-42).

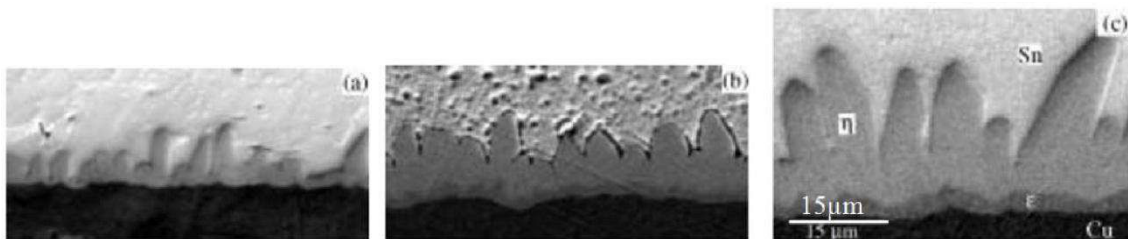


Figure 1-41. Morphology evolution of the  $\eta$ -phase grains during solid Cu/liquid tin reaction at  $275^\circ\text{C}$  for 3 min (a), 45 min (b) and 180 min (c) (the same magnification is given for three images) [Gagliano\_2003].

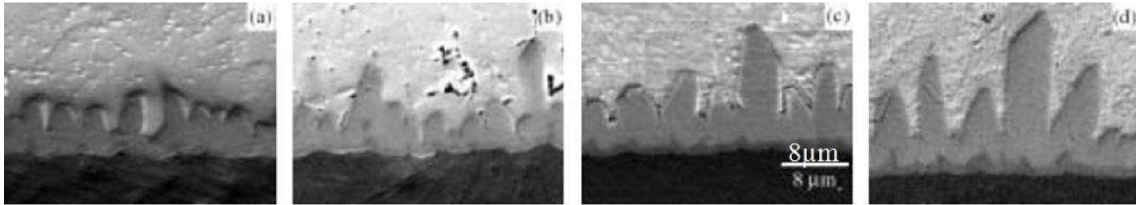


Figure 1-42. Morphology evolution of the  $\eta$ -phase grains during solid Cu/liquid tin reaction for 20 minutes at different temperature. 250°C (a), 275°C (b), 300°C (c) and 325°C (the same magnification is given for three images) [Gagliano\_2003].

In their work J.O. Suh et al. [Suh\_2008] have shown that faceted dendrites of the  $\eta$ -phase are formed at the interface between Cu and pure Sn at 250°C after 2 min of reaction (see Figure 1-43a). The clearly different morphology, namely round scallop-like  $\eta$ -phase scallops, was observed by M. Yang et al. [Yang\_2012] after 2 min of reaction at almost identical temperature of 240°C (see Figure 1-43b). In both studies it was found that the mean size of dendrites grows with time and temperature following the Ostwald ripening mechanism.

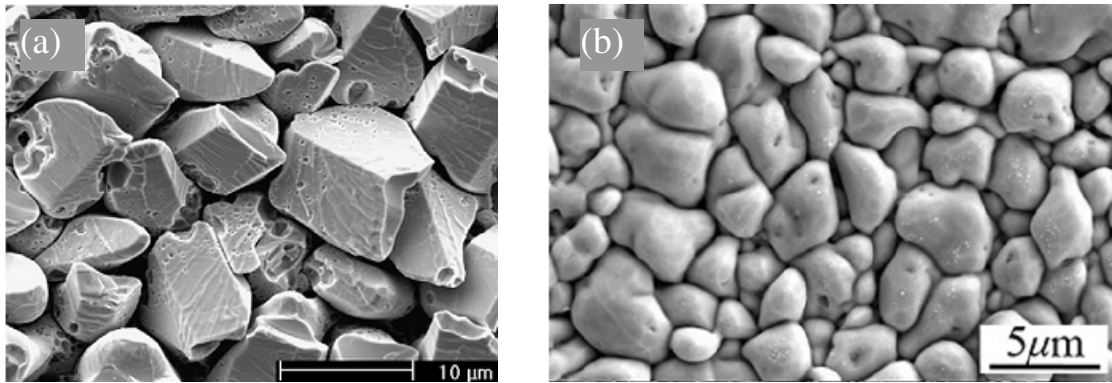


Figure 1-43. Top view SEM image on the  $\eta$ -phase after 2 min of reaction between solid Cu and pure liquid Sn: formation of the faceted dendrites at 250°C [Suh\_2008] (a) and formation of round the scallop-like dendrites at 240°C [Yang\_2012] (b).

Recently, a couple of studies implemented synchrotron radiation to track the different stages of the  $\eta$ -phase growth *in situ* [Huang\_2014, Salleh\_2014]. M.L. Huang et al. [Huang\_2014] implemented synchrotron radiation *in situ* observation technique for pre-annealed Cu/pure Sn couple at 260°C for 2 h. The heating cycle during observation was as following: start from the room temperature  $\rightarrow$  heating up to 280°C with a heating rate 15°C/min  $\rightarrow$  dwelling for 226s at 280°C  $\rightarrow$  cooling down with a cooling rate 10°C/min. Authors succeed to detect the decrease of the single grain aspect ratio  $H/D$  (see Figure 1-44a) as well as the average IMC thickness (see Figure 1-44b) during heating stage. The change in aspect ratio values indicates the transition from the longitudinal to the scallop-like shape during the heating stage. During dwelling stage both aspect ratio and average thickness stayed almost constant. During cooling stage the  $\text{Cu}_6\text{Sn}_5$  compound re-precipitated on the existing  $\text{Cu}_6\text{Sn}_5$  grains resulting in the significant increase of the aspect ratio of individual scallops as well as the average thickness of the IMC. The proposed model fitted well the experimental data on the basis of the suggested parameters (see Figure 1-44b).

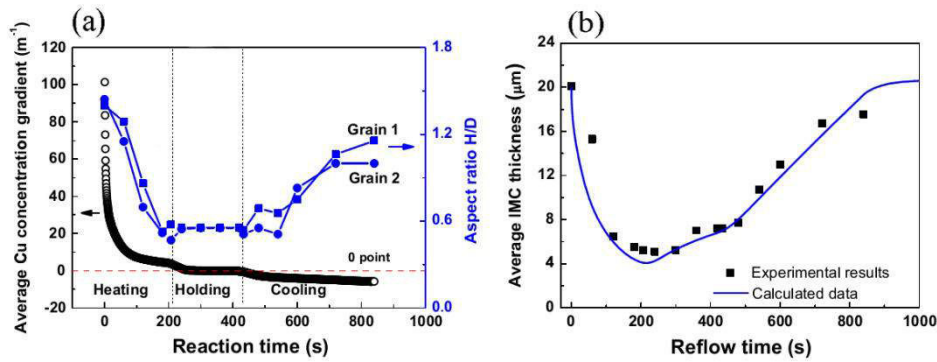


Figure 1-44. The aspect ratio between grain height  $H$  and width  $D$  ( $H/D$ ) of two individual grains and the average Cu concentration gradient (a); the average IMC thickness as a function of the reaction (reflow) time (b) [Huang\_2014].

It is believed in majority of studies that the formation of the  $\epsilon$ -phase is suppressed initially for some period time ranging from 8-10 s [Park\_2012, Bader\_1995, Görlich\_2005] to 80 s [Gagliano\_2003]. Normally, after the reflow process that lasts few minutes the  $\epsilon$ -phase is formed in the form of the continuous and relatively uniform layer. Therefore, during reaction between solid copper and liquid tin the interfacial system consists of two intermetallic layers  $\eta$ -Cu<sub>6</sub>Sn<sub>5</sub> and  $\epsilon$ -Cu<sub>3</sub>Sn organized in the following way: Cu/ $\epsilon$ / $\eta$ /Sn. Two examples of the interfacial layers formed after prolonged reaction of copper with liquid tin are given on the Figure 1-45 that shows cross-sections of the Cu/Sn interface after 64 minutes of reaction at 250°C (Figure 1-45a) and after 25 hours of reaction at 300°C (Figure 1-45b). In the latter case the thickness of the  $\epsilon$ -phase is comparable to the thickness of the  $\eta$ -phase. Normally, during soldering reaction, when the peak temperature exceeds the melting temperature of the solder by some tens of degrees the  $\epsilon$ -phase is much thinner than  $\eta$ -phase.

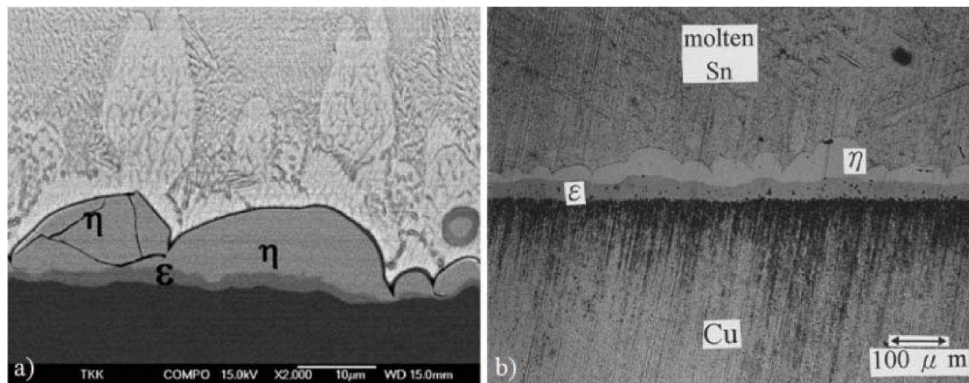


Figure 1-45. SEM micrographs showing the interfacial zone after Cu-Sn reaction for 64 minutes at 250°C (a) [Laurila\_2005] and for 25 hours at 300°C [Su\_1997].

The growth kinetics of the IMC layers has been studied extensively in the literature (see for example [Gagliano\_2003, Yang\_2012, Su\_1997, Bader\_1995]). A systematic study of the reaction between solid Cu and liquid Sn is presented by S. Bader et al [Bader\_1995] who studied the reaction at the initial stage starting from 5 s to 2.5 minutes. Such duration of reaction corresponds to the reaction time during conventional soldering procedure. In their work [Bader\_1995] authors studied the reaction between micrometric layers of copper and tin deposited by physical vapor deposition (or PVD). The reaction temperature was 240°C and 300°C and, whatever the temperature, the authors found that growth kinetics of IMC obeys to law  $e \sim kt^n$ , where  $n = 0.2 \div 0.3$  for Cu<sub>6</sub>Sn<sub>5</sub> phase and  $n = 0.45 \div 0.49$  for Cu<sub>3</sub>Sn phase.

In the study of R.A.Gagliano and M.E.Fine [Gagliano\_2003], numerous measurements of intermetallic layer thicknesses were performed at the range of temperature from 250°C to 325°C and time of reaction up to 100 minutes (Figure 1-46). It was found that the  $\eta$  phase

growth is governed by cubic power law of time, whereas the evolution of the  $\varepsilon$  phase is diffusion controlled following the parabolic growth regime. The layer thickness  $e_i$  ( $i = \eta$  or  $\varepsilon$ ) could be described by the following relations:

$$e_i = k_i t^n \quad \text{and} \quad k_i = k_i^0 \exp\left(\frac{-Q_i}{RT}\right), \quad (1-21)$$

where  $k_\varepsilon^0 = 2.26 \mu\text{m}\cdot\text{s}^{0.57}$ ;  $k_\eta^0 = 2.52 \mu\text{m}\cdot\text{s}^{0.3}$  and  $Q_\varepsilon = 29.2 \text{ kJ}\cdot\text{mole}^{-1}$ ;  $Q_\eta = 13.4 \text{ kJ}\cdot\text{mole}^{-1}$ .

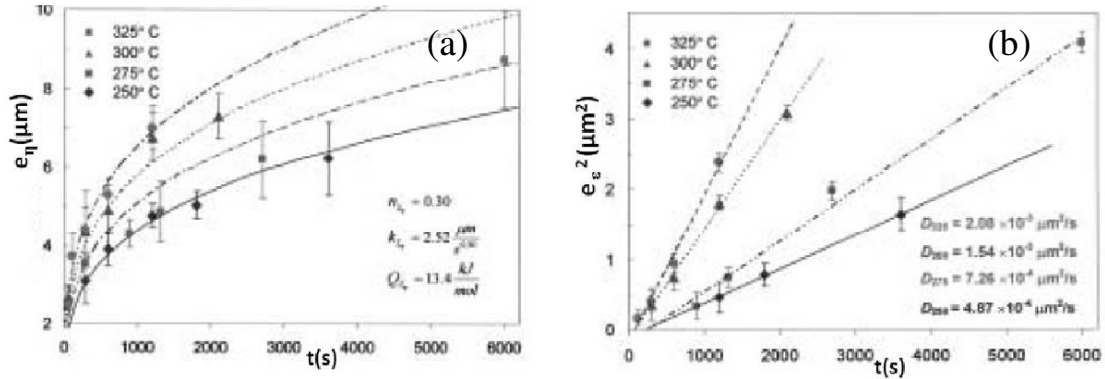


Figure 1-46. Growth kinetic of the  $\eta$ - $\text{Cu}_6\text{Sn}_5$  phase (a) and  $\varepsilon$ - $\text{Cu}_3\text{Sn}$  phase (b) in the temperature range 250-325 °C [Gagliano\_2003].

The parabolic growth of the  $\varepsilon$ - $\text{Cu}_3\text{Sn}$  phase and cubic law of growth of the  $\eta$ - $\text{Cu}_6\text{Sn}_5$  phase were also found by M. Yang [Yang\_2012] at  $T = 240^\circ\text{C}$  and  $T = 280^\circ\text{C}$ . Nevertheless, the transition from cubic with  $n \approx 1/3$  to parabolic regime  $n \approx 1/2$  of growth was detected for  $\eta$ - $\text{Cu}_6\text{Sn}_5$  phase at later stages of reaction, namely after reaching 30 min of reaction at both experimental temperatures. The  $\varepsilon$ - $\text{Cu}_3\text{Sn}$  phase was growing following the parabolic regime with  $n \approx 1/2$  whatever the time and temperature (see Figure 1-47). The growth constants of the  $\eta$ - $\text{Cu}_6\text{Sn}_5$  phase at the initial stages of reaction ( $t < 30$  min) could be determined as  $k_\eta = 0.139$  and  $0.179 \mu\text{m}\cdot\text{s}^{1/3}$  for  $T = 240$  and  $280^\circ\text{C}$  respectively. The growth constants of the  $\varepsilon$ - $\text{Cu}_3\text{Sn}$  phase at the initial stages of reaction ( $t < 30$  min) were determined to be  $k_\varepsilon = 0.021$  and  $0.032 \mu\text{m}\cdot\text{s}^{1/2}$  for  $T = 240$  and  $280^\circ\text{C}$  respectively.

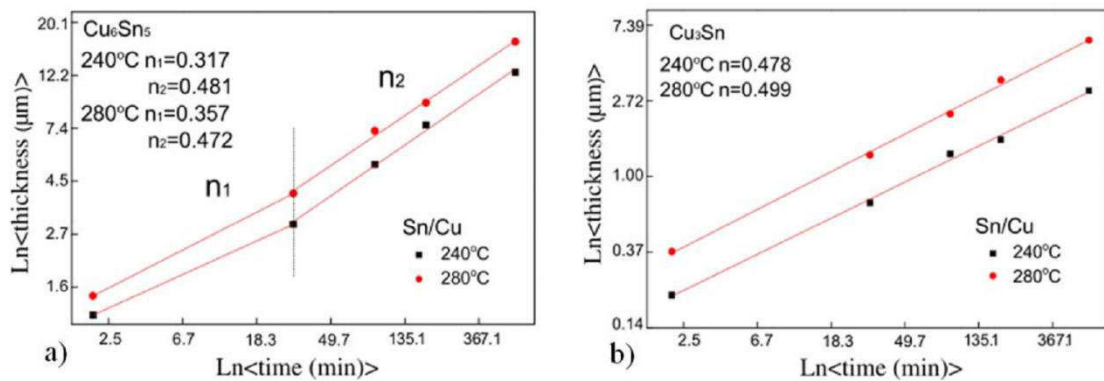


Figure 1-47. Growth kinetic of the  $\eta$ - $\text{Cu}_6\text{Sn}_5$  phase (a) and  $\varepsilon$ - $\text{Cu}_3\text{Sn}$  phase (b) at  $T = 240$  and  $T = 280^\circ\text{C}$  [Yang\_2012].

M.L. Huang and F. Yang [Huang\_2014] have conducted experiments with Sn-Ag-Cu solder balls of different size varying from 200 to 500  $\mu\text{m}$  and demonstrated that the growth kinetics depends on the size of the solder balls. Figure 1-48 gives the variation of the IMC layer thickness with time during reaction between Cu and Sn-3.0wt.%Ag-0.5wt.%Cu solder alloy (Figure 1-48a) and Cu and Sn-3.5wt.%Ag solder (Figure 1-48b). Authors have also proposed a model of growth called the concentration gradient controlled (CGC) model but as it can be seen from Figure 1-48 in some cases it overestimates or underestimates the IMC growth rates in comparison with experimentally measured values.

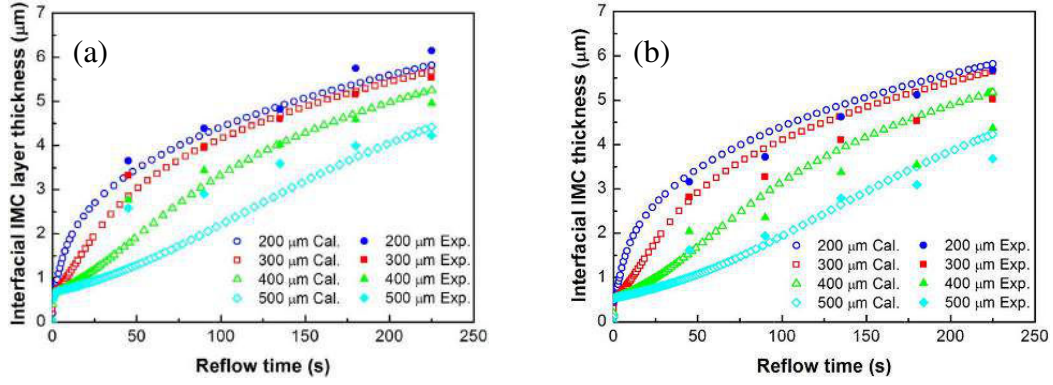


Figure 1-48. Variation of the IMC thickness with time during Cu/Sn-3.0wt.%Ag-0.5wt.%Cu reaction (a) Cu/Sn-3.5wt.%Ag reaction (b) at  $T = 250^{\circ}\text{C}$  [Huang\_2014].

#### 4-4-2) Modeling of the phase growth and competition during reflow (Cu/liquid Sn reaction)

In their work A.M. Gusak and K.N.Tu [Gusak\_2002] established a theory called Flux-Driven Ripening (FDR) theory that was called to model the growth of the IMC layer during the soldering reaction. Two important constraints were used in modeling the system:

(i) The first one is the *geometrical* constraint meaning that the interface of the reaction stays constant. By assuming that the scallops have hemispherical shape (Figure 1-49a), it means that the total surface of the growing scallops is equal to the double surface between scallops and copper substrate (in their model [Gusak\_2002] neglected the formation of the  $\epsilon$ - $\text{Cu}_3\text{Sn}$  phase). In fact, authors were considering the ripening process at which the growth of one scallop is happening at expense of other. As it can be seen from Figure 1-49a the existence of the nanometric liquid channels (with width  $\delta$ ) between scallops was suggested, but the fracture of the channels total cross-section was considered to be negligible, so the total interface area between scallops and melt can be expressed as:

$$S^{\text{scallops/melt}} = \sum_{i=1}^N 2\pi R_i^2 = 2 \times \sum \pi R_i^2 = 2S^{\text{total}} = \text{const} \quad (1-22)$$

(ii) The second constraint is the *conservation of mass* which determines that all the in-flux of Cu atoms is used for the scallop construction. In algebraic representation it means that:

$$n_i C_i \frac{dV_i}{dt} = J^{\text{in}} S^{\text{free}}, \quad (1-23)$$

where  $n_i$  and  $C_i$  are atomic density and mole fraction of copper in the intermetallic respectively. The in-flux is found by applying Fick's law and knowing the average gradient equal to the ratio between equilibrium supersaturation  $\Delta C = C^b - C^e$  and mean size of the scallops  $\langle R \rangle$ :

$$J^{\text{in}} \cong -nD \frac{C^e - C^b}{\langle R \rangle}, \quad (1-24)$$

where  $D$  is the diffusion coefficient of Cu in the melt and the supersaturation corresponds to the difference between equilibrium concentration of Cu in the liquid alloy near the substrate  $C^b$  and equilibrium concentration of Cu in the liquid alloy near the top of the IMC,  $C^e$ . Both equilibrium concentrations can be found by constructing the common tangents if the thermodynamic assessment of the system is known (see Figure 1-49b).

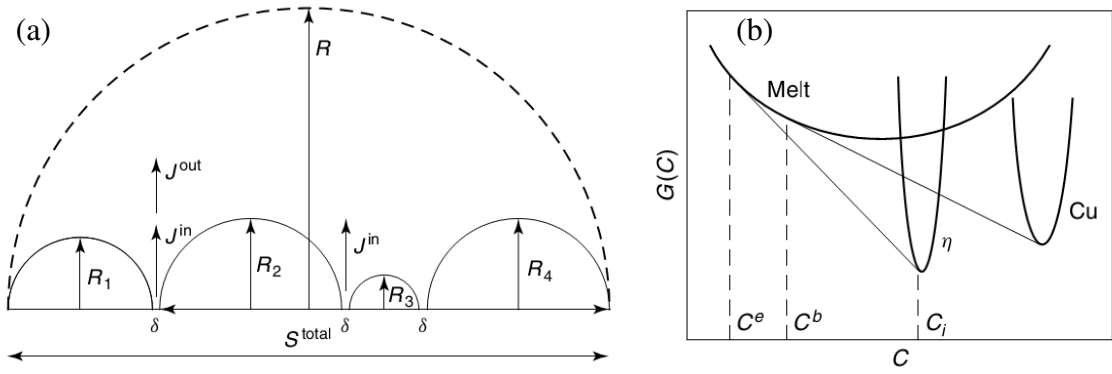


Figure 1-49. (a) Schematic diagram of the cross section of an array of scallops on Cu substrate [Gusak\_2002]. Here  $J_{in}$  is an input flux of Cu from substrate, which is supplied by liquid channels of width  $\delta$ ,  $J_{out}$  is a flux of “unused” Cu atoms which haven’t been incorporated in building IMC phase; (b) Schematic dependence of Gibbs free energy on composition for Sn-Cu system where only the formation of  $\eta$ -Cu<sub>6</sub>Sn<sub>5</sub> intermediate phase is considered.

The final result of the model is derivation of the well-known interface controlled regime of the growth with power 1/3 dependence:

$$\langle R^3 \rangle = kt, \quad (1-25)$$

where the growth rate  $k$  is determined as:

$$k = \frac{9}{2} \frac{n}{n_i} \frac{D(C^b - C^e)\delta}{C_i}. \quad (1-26)$$

The FDR theory was tested in various studies and proved its efficiency. For example, J.O. Suh et al. [Suh\_2008] compared the experimentally measured distributions of scallop sizes obtained by reaction of Cu with Sn-45wt.%Pb solder with theoretical curves from the FDR theory and obtained good correspondence for reaction times varying from 30 s to 8 min (see Figure 1-50). After fixing  $D \approx 10^{-5} \text{ cm}^2\text{s}^{-1}$  and  $C^b - C^e \approx 0.001$  the width of the liquid channels was determined to be  $\delta = 2.54 \text{ nm}$ .

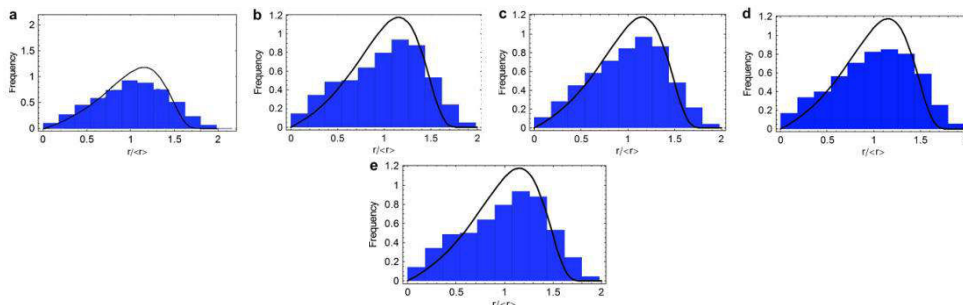


Figure 1-50. Size distribution of Cu<sub>6</sub>Sn<sub>5</sub> scallops after (a) 30s, (b) 1 min, (c) 2 min, (d) 4 min and (e) 8 min reflow at  $T = 200^\circ\text{C}$ . The solid curve corresponds to theoretical calculations from FDR theory [Suh\_2008]. The curves are normalized by the average radius of the scallops  $\langle r \rangle$ .

#### 4-5) Conclusions

The growth of the intermetallic phases is well studied experimentally during the late stages of reaction between solid copper and liquid tin-based solder. The FDR model can be used for the description of the growth during conventional reflow process when the time of reaction with liquid solder is not exceeding couple of minutes. Nevertheless, the recent results show that the growth kinetics models should be reviewed for the initial stage of reaction (time of reaction is less than 10 s) as well as during the late stages of reaction (time > 30 min). The

IMC nucleation sequence is still under discussion and should be reviewed; the suppression criterion of the  $\varepsilon$ -phase growth (if it exists) should be defined.

During solid-state reaction the intermetallic phases grow following parabolic law of growth. The growth process can be described well by existing models of phase during solid state reactions. However, the ambiguity of the experimental results in the growth competition during the late stages of the solid state ageing, when the dominant phase is not clearly identified, should be studied in details. The special effort should be made to reveal factors leading to voiding at the interface as far as this problem affects significantly the reliability of the solder joints.

## **5) Heterogeneous nucleation in crystallization of liquid Sn or liquid Sn-Ag-Cu alloys: solder balls and solder joints solidification**

For micro-scale solder interconnects, the microstructure of the solder joint and the soldering defects are directly related to the solidification behavior of the undercooled solder. Moreover, Sn is a well known example of a high degree of supercooling in the bulk.

It has been reported in literature that both the cooling rate as well as the solder size have an effect on:

(i) The growth of the intermetallic compounds (see for example [Jeong\_2004, Park\_2010]). Indeed, the contact time between the metastable liquid and the substrate is extended as long as the nucleation in the liquid solder does not occur, leading thus to a significant growth of intermetallic layer(s) formed at the liquid/substrate interface. This effect is especially pronounced for very low cooling rates ( $<1^\circ\text{C}/\text{min}$ , see Ref. [Jeong\_2004]).

(ii) The solder joint microstructure (see for example Refs. [Kim\_2002, Maveety\_2004, Tsao\_2011, Satyanarayan\_2011, Li\_2012]). The nucleation and growth processes during cooling from the melt, in standard processing reflow, can strongly affect the morphology in Sn-Ag-Cu solder joints especially in the case of small solder balls and high cooling rates as used in practice (some hundreds of  $^\circ\text{C}$  per minute) for which very high undercooling degree are observed.

Thus, the undercooling degree of solder alloys is of a high importance in industrial practice processes.

Previous studies [Kang\_2007, Hodaj\_2013, Arfaei\_2012, Zhou\_2012] mainly focused on the effect of the solder size and the effect of the presence of a metallic solid in contact with the liquid solder on the undercooling behavior of the solder. Kang et al. [Kang\_2007] and Hodaj et al. [Hodaj\_2013] showed that the undercooling ( $\Delta T$ ) is significantly decreased in the presence of solid Cu in contact with the solder alloy. Kang *et al.* [Kang\_2007] showed by Differential Scanning Calorimetry (DSC) measurements that, for a cooling rate of  $6^\circ\text{C}/\text{min}$ , the solidification temperature of a large number (165) of Sn-0.7wt.%Cu solders balls of about  $100\ \mu\text{m}$  in diameter, sitting in cavities of a glass mold, varies from about  $140$  to  $180^\circ\text{C}$  (undercooling  $\Delta T$  varying from  $50$  to  $90^\circ\text{C}$ , see Figure 1-51). In the case of 114 flip-chip Sn-1wt.%Ag-0.7wt.%Cu solder bumps (chips deposited with Cu/Ni UBM,  $100\ \mu\text{m}$  pad size on  $200\ \mu\text{m}$  pitch) with the same cooling rate, they found that the undercooling degree decreases significantly ( $\Delta T$  varying from about  $37$  to  $55^\circ\text{C}$ , see Figure 1-52). These results clearly show that the undercooling is significantly decreased in presence of solid Cu in contact with the solder alloy.

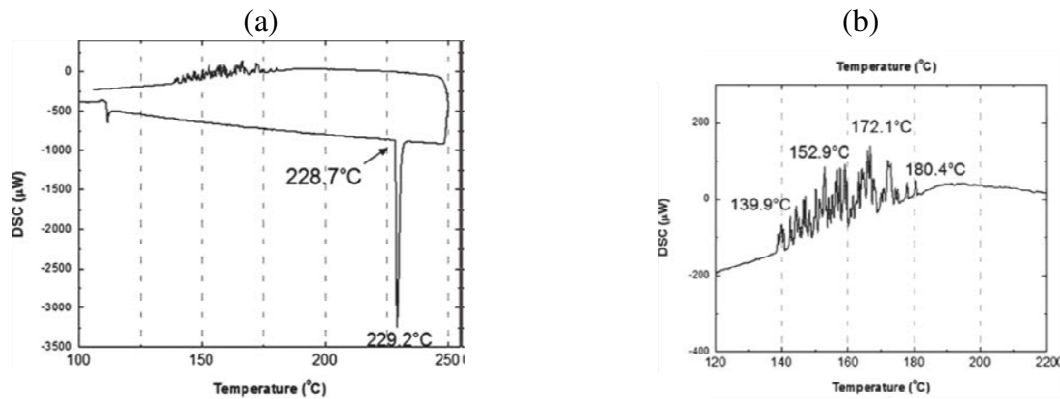


Figure 1-51. Typical DSC profiles obtained from Sn-0.7wt.%Cu solder balls of about 100  $\mu\text{m}$  in diameter sitting in cavities of a glass mold: (a) heating and cooling curve at 6  $^{\circ}\text{C}/\text{min}$  and holding for 10 min at 250 $^{\circ}\text{C}$  and (b) enlarged portion of the cooling curve between 120 and 220  $^{\circ}\text{C}$  [Kang\_2007].

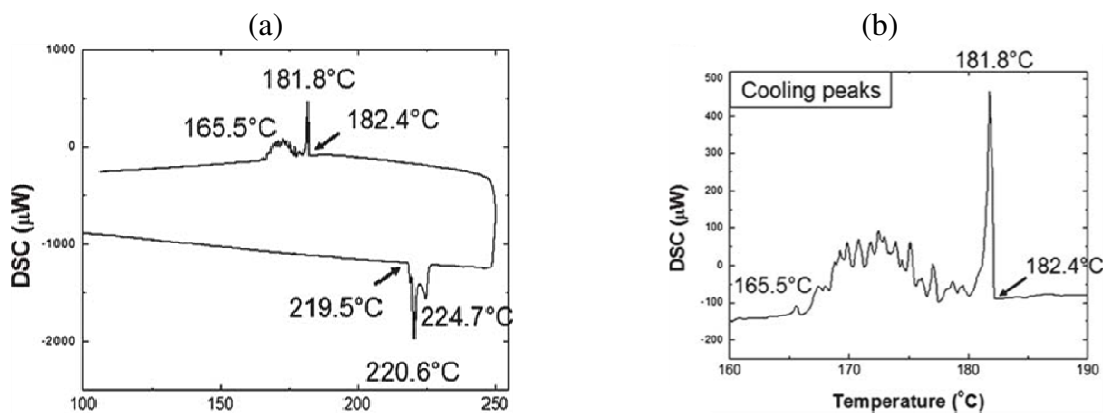


Figure 1-52. Typical DSC profiles obtained from a thinned Si chip with more than 100 solder bumps of Sn-1.0wt.%Ag-0.9wt.%Cu with the UBM of Cu/Ni: (a) heating curve from room temperature to 250 $^{\circ}\text{C}$ , holding for 10 min at 250 $^{\circ}\text{C}$ , and cooled down to room temperature, and (b) enlarged view of cooling curve between 150 and 190 $^{\circ}\text{C}$  [Kang\_2007].

Recently, Arfaei et al. [Arfaei\_2012] studied the dependence of Sn grain morphology of Sn-Ag-Cu solder on solidification temperature. Figure 1-53 gives the heat flow versus time during an isothermal hold at a temperature of 200 $^{\circ}\text{C}$  of 88 flip chip solder balls of SAC 3510 (Sn-3.5wt.%Ag-1.0wt.%Cu) on Ni(V)/Al substrate. This Figure clearly shows that the time at which the nucleation of supercooled solder balls (undercooling of about 20K) occurs is very different from one ball to the other and it varies from about 113 to 136 minutes of maintaining at 200 $^{\circ}\text{C}$ . For a cooling rate of 60 $^{\circ}\text{C}/\text{min}$ , they reported that undercooling for Sn-3wt.%Ag-0.5wt.%Cu balls, of diameter varying from 100 to 760  $\mu\text{m}$ , varies from about 55 to 18 $^{\circ}\text{C}$  for commercial samples and from 85 to 40 $^{\circ}\text{C}$  for lab made samples respectively (see Figure 1-54). These results indicate that undercooling depends not only on the solder ball size but also on the impurities contained in the solder alloy.

Note that the *discrepancy in results on undercooling degrees* among different solder pieces reported in literature by different authors is due not only to the probabilistic nature of heterogeneous nucleation but also to the variation in the impurity content and the form and surface defects of inclusions in the solder alloy which can be potential sites for heterogeneous nucleation, can influence the heterogeneous nucleation process and thus the degree of undercooling.

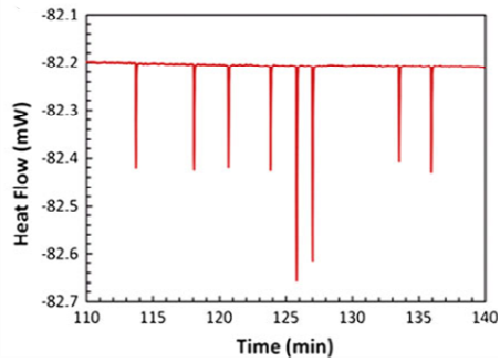


Figure 1-53. Heat flow versus time during an isothermal hold at a temperature of 200°C, 88 flip chip solder balls of SAC 3510 on Ni(V)/Al substrate [Arfaei\_2012].

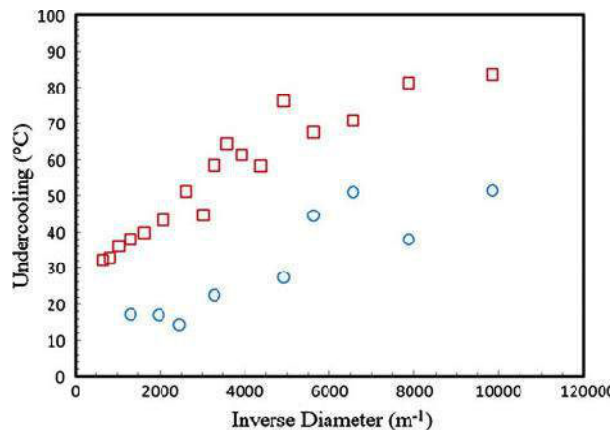


Figure 1-54. Plot of undercooling versus inverse diameter of free standing samples. Each data point represents the average undercooling for twelve runs. The lab made SAC305 samples (squares) were prepared in the vacuum tube furnace using high purity elements. The circles show the samples obtained from commercial supplier [Arfaei\_2012].

Zhou et al. [Zhou\_2011] studied the undercooling and solidification behavior of Sn-3wt.%Ag-0.5wt.%Cu solder balls (of diameters 300, 500 and 760  $\mu\text{m}$ ) and of solder joints (Sn-3wt.%Ag-0.5wt.%Cu balls of 320 and 480  $\mu\text{m}$  on copper pads) using DSC incorporated into the reflow soldering process. For a cooling rate of 10°C/min, they found that the average values of the undercooling of 500 and 760  $\mu\text{m}$  diameter solder balls are 12 and 7.8°C respectively while for the solder joints samples they found higher undercooling values, i.e., 21.6°C and 10.9°C. These results are not in agreement with results reported by Kang et al. [Kang\_2007]. Moreover, Zhou et al. reported that the average value of the undercooling of 300  $\mu\text{m}$  diameter solder balls is as high as 50.6°C.

Huang et al. [Huang\_2004] studied by DSC the effects of size, composition and substrate (Al, Cu, Ni, Ag) in contact with the solder alloy upon the degrees of undercooling of various Pb-free solders (Sn-Cu, Sn-Ag and Sn-Ag-Cu) of three different sizes, large ( $5 \pm 1$  mg, noted L), small ( $2.5 \pm 0.5$  mg, noted S) and very small ( $0.5 \pm 0.3$  mg, noted VS) samples corresponding to solder balls of about 500, 850 and 1000  $\mu\text{m}$  in diameter respectively. For a cooling rate of 10°C/min, they found that undercooling increases with the decreasing solder ball diameter (see Figure 1-55). For example, for ten samples of Sn-3.8wt.%Ag-0.7wt.%Cu alloys, they found average undercooling values ( $\overline{\Delta T}$ ) of 20; 22.6 and 27.6°C for L, S and VS samples respectively. Moreover, these authors note in particular that the degrees of undercooling are not necessarily reduced when solders are placed on wetting substrates. For example, in the case of large samples (L), it was found that undercooling values vary from 15.8 to 24.9°C ( $\overline{\Delta T}=20^\circ\text{C}$ ) for solder alloys and from 19 to 24°C ( $\overline{\Delta T}=22^\circ\text{C}$ ) for solder

joints with copper substrate. These results are in agreement with results obtained by Zhou et al. [Zhou\_2011] and in disagreement with those obtained by Kang et al. [Kang\_2007].

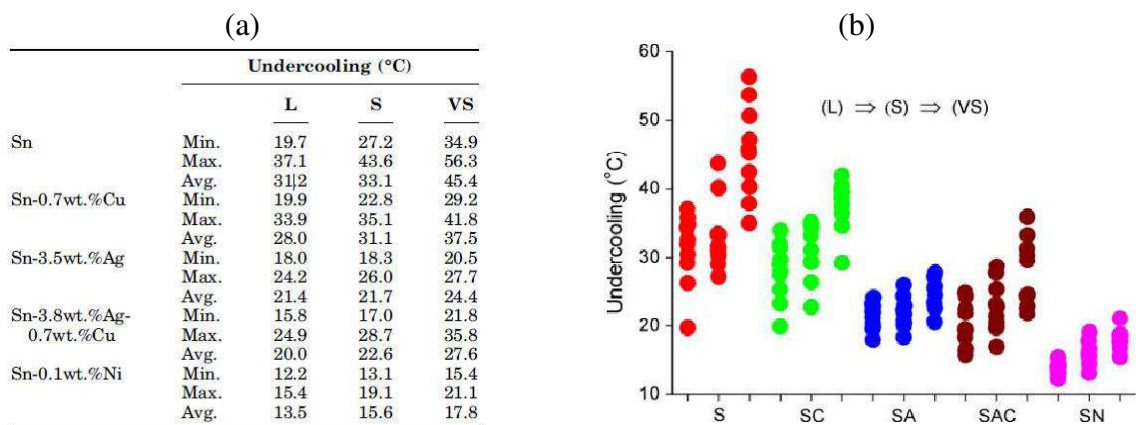


Figure 1-55. Degrees of undercooling of solders of various sizes. Large ( $m = 5 \pm 1$  mg, L), small ( $m = 2.5 \pm 0.5$  mg, S) and very small ( $0.5 \pm 0.3$  mg, VS) samples [Huang\_2004].

The fact that the liquid solder alloys wet the copper substrate very well (reactive wetting) and other metallic substrates (Ni, Ag,... see for example Refs. [Chang\_2003, Wang\_2006, Sobczak\_2007, Matsumoto\_2008, Kim\_2009]), can lead to a preliminary conclusion that nucleation during cooling of a liquid solder becomes easier by a heterogeneous nucleation on the metallic substrate (in fact on the intermetallic reaction layer formed at substrate/solder interface). However, the degree of undercooling during soldering of pure Sn or Sn based alloys on Ag or Cu substrates is still high ( $> 15$ K), so it was concluded in a recent work of Belyakov and Gourlay [Belyakov\_2014] that the common intermetallic compounds (IMCs) in soldering,  $Ag_3Sn$  and  $Cu_6Sn_5$  are ineffective at catalyzing Sn nucleation. These authors [Belyakov\_2014] have shown that other intermetallics  $NiSn_4$ ,  $PdSn_4$  and  $PtSn_4$  crystals are nucleation sites for  $\beta$ -Sn, reducing its nucleation undercooling from about 35K for commercially pure Sn to 3-4K.

Note that despite the fact that several works were recently dedicated to the nucleation of tin in the solder bulk, the role of different potential sites of heterogeneous sites on the nucleation of tin inside the solder ball is not yet elucidated. Moreover, that there are no specific studies in literature treating the comparison of undercooling degrees obtained after a partial melting of the solder and after a reflow in configurations of (i) solder balls and (ii) solder joint samples prepared by reflowing solder alloy on copper substrate.

## 6) Conclusions

The aim of this chapter was to demonstrate the importance of wetting, nucleation and growth problems in Cu/Sn and Ag/Sn systems for the modern microelectronic industry and to review the state of the art of these scientific topics. It was demonstrated that regardless the technique used in packaging it is the Cu-Sn reaction that produce the bonding between different components.

The wetting in Cu/Sn system was reviewed and it was shown that amount of experiments implementing dispensed drop is very limited. This technique in combination with high-temperature preheating of the substrates could be beneficial for determination of intrinsic contact angles in reactive Cu/Sn couple. To complete the picture the accurate studies of wettability of intermetallic phases by liquid Sn or Sn-based alloys should be also performed. Implementation of the rapid camera in order to study the very early stages of wetting should make possible distinguish different stages of wetting and fix the relation

between contact angle of tin over unreacted solid Cu and intermetallics that are formed at the interface during reactive wetting.

The current understanding of the phase nucleation sequence and growth competition is well established for the reaction between Cu and Sn in solid stage. It was shown that  $\text{Cu}_6\text{Sn}_5$  appears first and  $\text{Cu}_3\text{Sn}$  phase emerges after certain time or after reaching some critical temperature. The growth of intermetallics in solid state is well defined and classical models describe well their growth behaviour. Nevertheless reaction between solid Cu and solid Sn at very late stages with emerging phenomena as excessive voiding inside intermetallic layer is of a great interest due to reliability issues.

In its turn the early stage of reaction between solid Cu and liquid Sn is still the topic of a basic research. Up to now the nucleation sequence of the intermetallic phases during reaction between solid Cu and liquid Sn is an open question as far as there is no direct experimental evidence of nucleation sequence. Therefore, detailed study of this reaction at the very early stages (say in few milliseconds) is a challenging and interesting problem.

The undercooling of the solder bulk can have a strong influence on the microstructure evolution of the intermetallics in its bulk or at interface between liquid solder and Cu substrate. The extent of undercooling is changing with change of the solder cooling rate, size of the solder bulk and presence of the substrate below the solder or intermetallic particles in solder bulk. Nevertheless, the peculiar places of the Sn nucleation with indication of the corresponding undercooling extent are not revealed completely. The effect of presence of small intermetallic dendrites or impurities in the solder bulk should be studied in more details.

## Chapter 2: Experimental methods and materials

### 1) Introduction

As is it was shown in the Chapter 1, the modern soldering technology still has an ensemble of challenging problems in the field of wetting, nucleation and reactivity in Cu-Sn and Ag-Sn systems. The aim of Chapter 2 is to give details of the main experimental approaches and to describe the experimental set-ups used in this study.

In the wetting problematic the key experimental approach is to implement the dispensed drop method as it allows measuring the intrinsic contact angle between different metals even in reactive systems. It was successfully done with combination of the dispensed drop technique performed in a high vacuum metallic furnace and a rapid camera. The beneficial procedure of de-oxidation of metallic surface by high-temperature annealing at high vacuum allows to understand the influence of the surface condition on the measured contact angle. The implementation of the rapid camera opens the door for investigation of the first instance of wetting before the formation of the equilibrium spherical shape of the drop over the substrate.

The abundance of studies over the reactivity in Cu-Sn system still lacks the proper study of the very initial (in time less than few tens of milliseconds) stage of reaction between solid copper and liquid tin. The construction of the fast dipping set-up used in this study made possible to fill this gap. Combination of this technique with accurate FIB and TEM characterization should clarify the question of the first intermetallic phase formation and evolution in time less than 1 s at temperature corresponding to the reflow process (around 250°C) presented in Chapter 4.

Given the fact that only a very few studies of wetting of Cu<sub>6</sub>Sn<sub>5</sub> and Cu<sub>3</sub>Sn and no study on the wetting of Ag<sub>3</sub>Sn intermetallics by liquid Sn or Sn based alloys exist in literature, it is very useful to evaluate the contact angles on these intermetallics that emerge during soldering. Thus, this chapter describes the experimental methods of processing and characterization of Cu<sub>6</sub>Sn<sub>5</sub>, Cu<sub>3</sub>Sn and Ag<sub>3</sub>Sn intermetallics that are used for wetting experiments presented in Chapter 3. Moreover, having bulk samples such as Cu<sub>3</sub>Sn, the incremental diffusional couple Cu/Cu<sub>3</sub>Sn could be also prepared in order to study the growth kinetics of intermetallics and main mechanisms of this process presented in Chapter 5.

### 2) Sessile drop method

The sessile drop method consists in observation of the shape of a metallic liquid droplet formed over a flat planar substrate at temperature higher than the melting temperature of the involved metal or alloy. Normally, the sessile drop has a low mass (from 20 to 100 mg) in order to practically cancel the influence of the gravitation on its shape and thus allowing consideration of the drop as a spherical one.

This method allows to measure the main characteristic parameters of the drop: the base radius  $R$  of the drop, its height  $h$ , left ( $\theta_l$ ) and right ( $\theta_r$ ) contact angles (Figure 2-1).

After the measurement we can deduce the mean value of the contact angle:

$$\theta = (\theta_l + \theta_r)/2 \quad (2-1)$$

We can also calculate this value from the linear dimensions accepting the spherical shape of the droplet:

$$\theta = 2\arctan\left(\frac{h}{R}\right) \quad (2-2)$$

We can check if the droplet keeps a circular shape by comparing values of  $\theta$  derived by Eqs. (2-1) and (2-2).

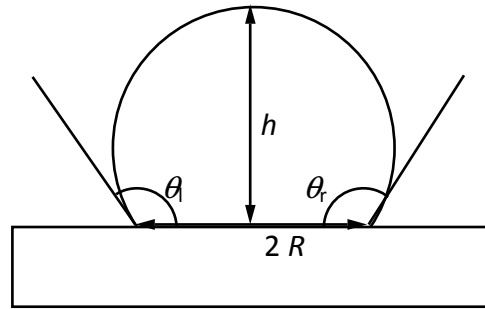


Figure 2-1. Characteristic parameters of the sessile droplet.

The volume of the droplet can be calculated as:

$$V = \frac{\pi \cdot R^3}{3} \cdot \frac{2 - 3 \cdot \cos \theta + \cos^3 \theta}{\sin^3 \theta} \quad (2-3)$$

If the liquid metal involved in the experiment is volatile then it should be verified by weighting that the variation of the droplet volume during experiment is less than 3%. Thus, during isothermal wetting experiments the droplet volume should stay almost constant with time.

The classical sessile drop method consists in the placement of a small solid metallic piece (or some small pieces) over the solid substrate and heating up all the system at a temperature higher than the melting temperature of the solid piece. The melting temperature of the substrate should be higher than the experimental temperature. The metallic droplet can be a pure metal, an alloy (A,B) elaborated before wetting experiment (see Figure 2-2a) or even an alloy (A,B) that is produced *in-situ* during the sessile drop experiment (see Figure 2-2b).

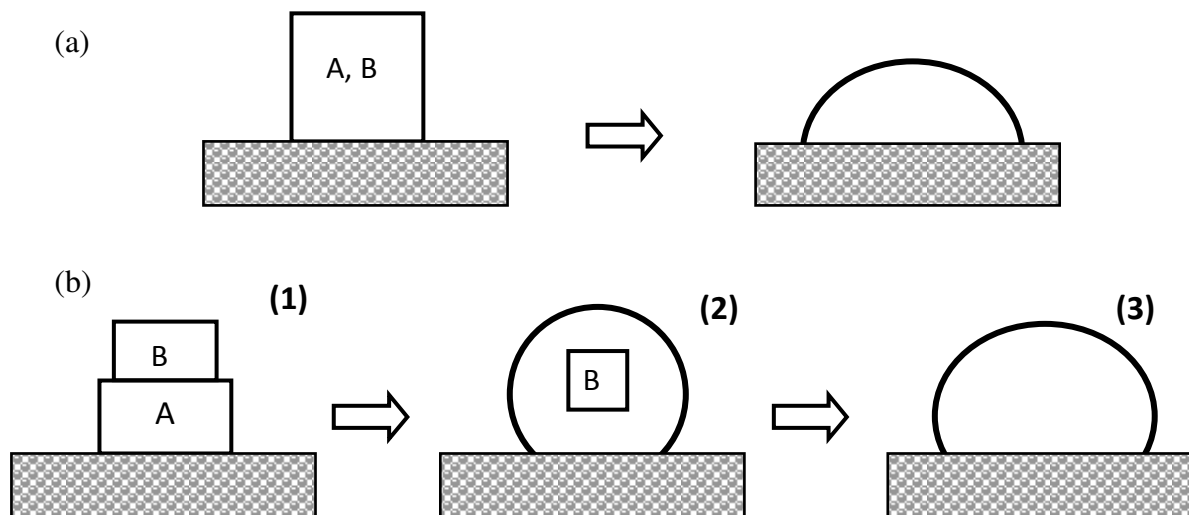


Figure 2-2. Classic sessile drop method: (a) an alloy prepared before wetting experiment; (b) *in situ* elaboration of an alloy (1) - initial configuration, (2) - dissolution of B in liquid A ( $T_m^B > T_m^A$ ), (3) - formation of the homogenous droplet over the substrate.

The classical version of the sessile drop method has some shortcomings because the melting and homogenization of the metallic alloy interfere with the spreading process. For this reason, we implement the modified version of the sessile drop technique - the dispensed drop method. This method allows separation of the melting and spreading of an alloy or a metal over a substrate. For this purpose a special setup is implemented with a principal scheme given on Figure 2-3. As it can be seen in this figure, the substrate is placed on a turning “table”, whereas the liquid metal or alloy is formed in a ceramic crucible situated over the substrate. The crucible has an opening in its bottom through a thin capillary with 1 mm outer diameter and 0.6 mm inner diameter. Once the alloy is completely melted, a liquid

droplet is extruded through the capillary and then the whole crucible (with a formed droplet below the capillary) is displaced towards the substrate. Once the bottom of the droplet touches the substrate a spontaneous spreading of the drop over the substrate occurs.

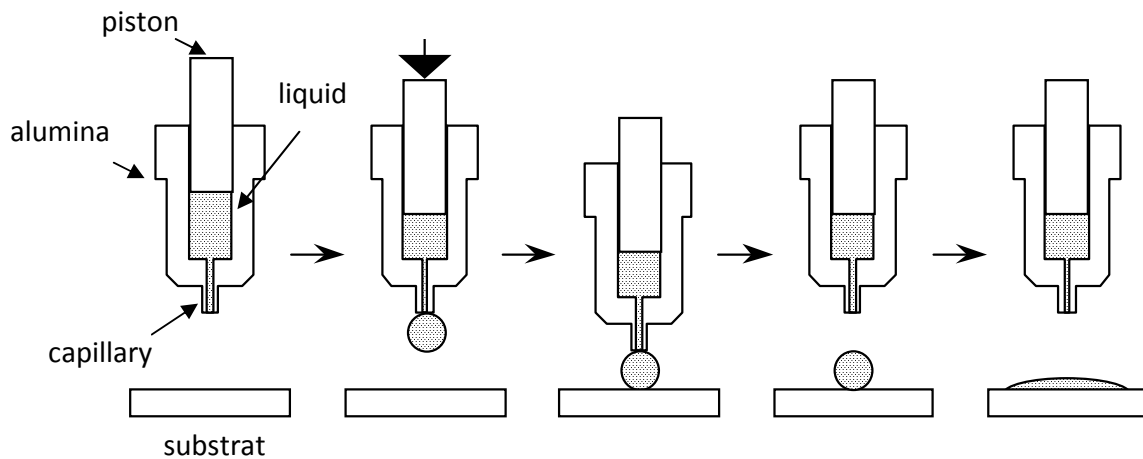


Figure 2-3. Different stages of the droplet deposition by the dispensed drop technique. Once the liquid is formed inside the ceramic crucible the droplet is extruded through the thin capillary and then transferred to the substrate.

The advantage of this method is that it allows separation of the processes of melting and spreading, so fully isothermal experiments can be performed. Another advantage is that during extrusion any oxide layer on the liquid surface alloy is broken.

The whole process of deposition could be recorded either by a conventional VGA camera with recording speed of 25 images/s (40 ms time-step) or by a high speed camera with recording speed up to 5000 images/s. It allows us to visualize all the important stages of the droplet deposition and spreading (see Figure 2-4). As can be seen from this figure these stages are: extraction of the liquid droplet through the capillary (Figure 2-4a); transferring of the drop to the substrate (Figure 2-4b); the very initial stages of wetting with formation of the liquid bridge with capillary (Figure 2-4c) and detachment of the droplet from the capillary (Figure 2-4d).

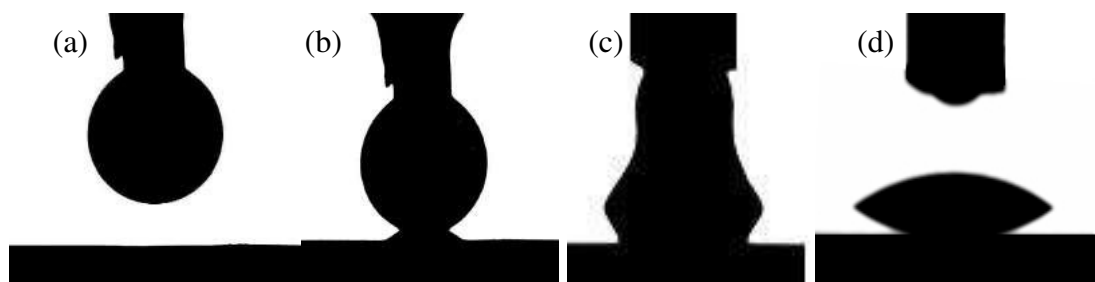


Figure 2-4. Different stages of the droplet deposition by the dispensed drop technique: a) extrusion of the droplet; b) droplet transfer; c) initial stage of spreading with formation of the liquid bridge; d) detachment of the droplet.

### 3) Experimental equipment

The wetting experiments were performed in two apparatus: an alumina furnace (for the classic sessile drop experiments) and a metallic furnace (for the dispensed drop technique).

#### 3-1) Alumina furnace

A scheme of the alumina furnace is shown on Figure 2-5. Its principal parts are an alumina tube, which is externally heated by silicon carbide resistors. The tube is kept under vacuum or gas atmosphere. The maximum operation temperature of the furnace is 1450°C. The accuracy of the temperature measurements is  $\pm 3^\circ\text{C}$  and it is verified by a Pt- Pt10%Rh thermocouple. For this study, the calibration of the furnace was performed for the temperature range from 227 to 660°C.

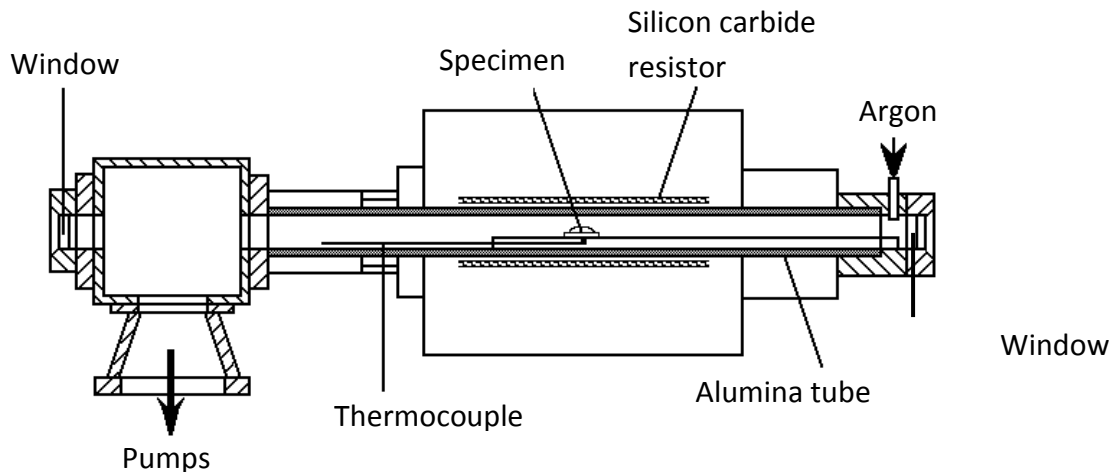


Figure 2-5. Scheme of the alumina furnace.

The pumping system of this setup consists of a primary mechanical pump and a secondary oil diffusion pump. The pumps are equipped with cold traps filled with liquid nitrogen in order to limit the oil vapor income inside the furnace chamber and to make the pumping process more efficient. Such pumping system permits to operate under a vacuum of  $1 \times 10^{-4}$  Pa even at temperatures as high as 1250°C.

The inert gas could be introduced in the very extreme point of the pumping system. It permits us to purge a whole system with a gas in order to ameliorate the vacuum or to hold the experiment under the gas atmosphere. The gas used in this study is Ar (with a purity of 99.999%).

Two opposite windows allow to illuminate the internal chamber and to record the experimental process.

#### 3-2) Metallic furnace

The principle of operation of the metallic furnace is similar to that of the alumina furnace. The apparatus consists essentially of a molybdenum heater surrounded by molybdenum radiation shields, located in a water-cooled stainless-steel chamber. The chamber is fitted with two windows enabling the illumination of the sessile drop on the substrate (see Figure 2-6).

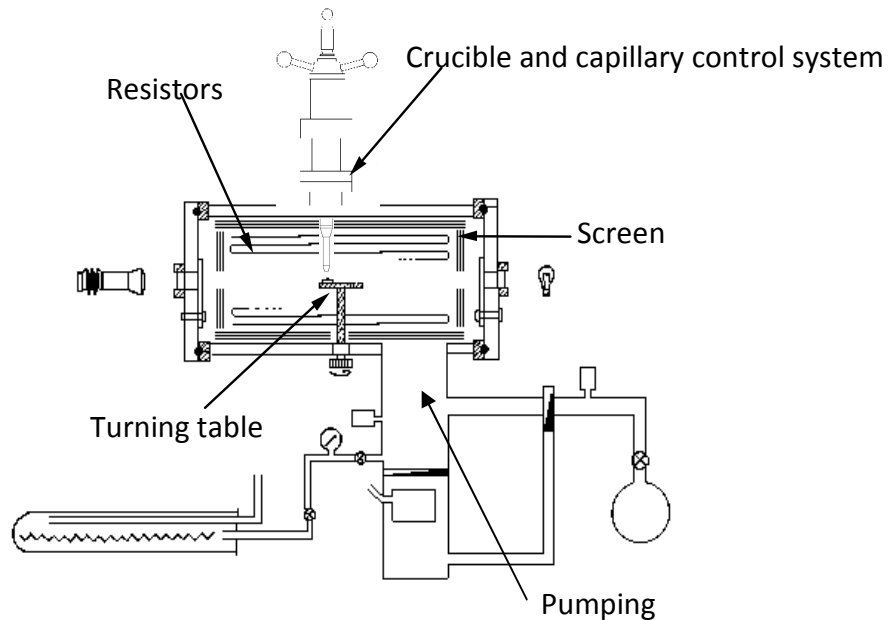


Figure 2-6. Scheme of the metallic furnace.

The sample is placed in the centre of the furnace on a rotating alumina table. The rotation mechanism as well as the system of positioning of the ceramic crucible and capillary can be controlled externally. The crucible containing the liquid alloy is placed above the rotating table and the droplets can be dispensed precisely on the different substrates or different places of one large substrate. Two windows allow observation and recording of the whole system (substrate/drop/capillary).

The maximum operation temperature of this furnace is 1500°C. The heating is controlled by the proportion-integral-derivative (PID) controller. The temperature is controlled with 3°C accuracy by two Pt-Pt10%Rh thermocouples, one is used by the temperature control system and another to measure the temperature in the vicinity of the sample (5 mm in distance).

The pumping system of the metallic furnace is similar to the one of the alumina furnace. Normally the quality of the vacuum during the isothermal experiments up to 800°C is around  $2 \times 10^{-5}$  Pa. It is possible to keep the vacuum around  $5 \times 10^{-5}$  Pa up to 1300°C if the heating rate is slow. In this furnace the quality of vacuum at 400°C is about  $2.5 \times 10^{-5}$  Pa.

### 3-3) Calibration of alumina and metallic furnaces

The temperature calibration of alumina furnace was performed by checking the melting temperature of the Sn and Pb under vacuum. The melting of both pure metals was checked twice and thus the temperature control was recorded. Given the fact that alumina furnace was in principle designed for the high-temperature application ( $T > 400^\circ\text{C}$ ) it was found that a difference between the temperature indicated by the thermocouple situated just under the substrate (real temperature  $T_{\text{true}}$ ) and the set temperature (from temperature control system -  $T_{\text{set}}$ ) is in the range  $\Delta T = T_{\text{true}} - T_{\text{set}} = 36 \div 44^\circ\text{C}$  (see Figure 2-7a).

In the same way we have calibrated the temperature of metallic furnace by checking melting of Sn, Pb and Al (see Figure 2-7b). The vacuum quality was  $2 \times 10^{-5}$  Pa during melting of all metals. The melting was made twice and averaged set temperature  $T_{\text{set}}$  and the real temperature  $T_{\text{true}}$  were compared. It was found that only at relatively low temperature of 232°C (melting of Sn) the  $\Delta T$  was about 15°C (Figure 2-7b). At higher temperatures, namely 327°C (melting of Pb) and 660°C (melting of Al) the  $\Delta T$  decreased to about 4 and 2°C respectively (Figure 2-7b).

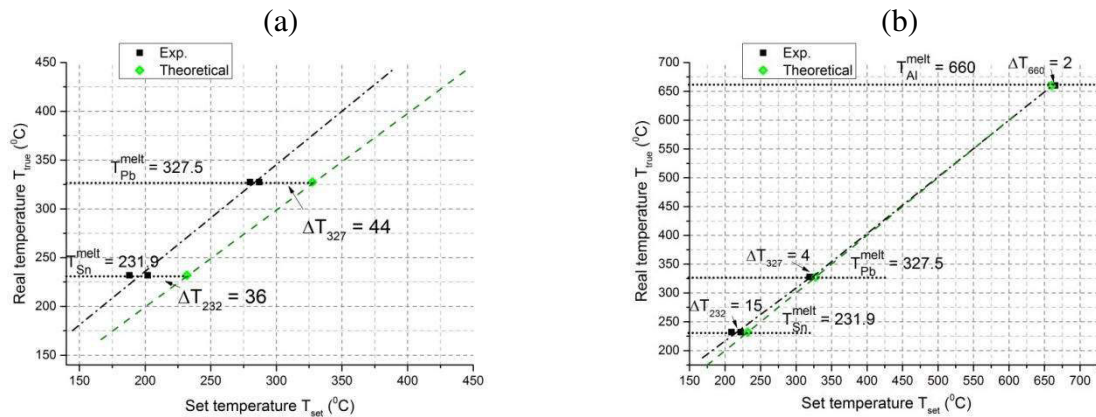


Figure 2-7. Temperature calibration of (a) alumina furnace and (b) metallic furnace.

### 3-4) Acquisition system of the droplet shape

The principle of the wettability studies partially consists in the droplet shape visualization and recording. The additional illumination by the external light source is needed if the experimental temperature is low ( $< 800^{\circ}\text{C}$ ). Normally, the light source is placed next to the end of the furnace. The quality of the light source (namely luminosity) should be adjusted for the type of the recording camera installed in the optical system. The CCD camera used in this study is capable to record 25 images per s and it is coupled with an ordinary electric lamp. When the high-speed camera is installed, it is coupled with a tungsten halogen lamp. To record the deposition of small droplets, the photographic objective with zoom 70-210 mm was employed.

Both CCD and high-speed camera were operating in the black and white mode. The high-speed camera involved in this study is Phantom Miro M310 capable to make up to 5000 images per s with resolution  $768 \times 576$  pixels (see Figure 2.8).



Figure 2-8. High-speed camera Phantom Miro M310 involved in the study.

The recordings of the droplet shape evolution and spreading kinetics were analyzed by the DSA-1 software (Drop Shape Analysis) delivered by KRÜSS. In the case of the implementation of the normal CCD camera the *avi* file was digitalized from the VHS video recording made by the VCR (Video Cassette Recorder). One *bmp* slide of the video file corresponds to the single recording time-step: 40 ms for the CCD camera. The recordings made by the high-speed camera were stored directly to the *avi* files on the hard drive. Once having an *avi* file the image sequence can be analyzed by DSA-1 software. It allows determination of the contact angles of the droplet and its linear dimensions. The method used for the determination of these parameters is called “tangent method” in the software. The “left” and “right” contact angles could be measured separately. In fact, the software approximates the small part of the droplet profile (few hundreds of microns from the triple line) by the polynomial function of type  $y = a + bx + cx^{0.5} + d/\ln x + e/x^2$ . The contact angle is calculated from the tangent in the point of intersection of the droplet profile and basis line. To

apply this method the quality of an image should be perfect, and the part of the droplet close to the triple line should be of circular form. The error on the contact angle value was estimated to be about  $1^\circ$ . It is not always the case when the very initial stages of wetting are filmed by the rapid camera. Sometimes, for the moments when the liquid neck is formed between the major part of the droplet and the capillary (see Figure 2-4b,c) the software can approximate the droplet profile, so the contact angle should be measured manually. For such measurement the image analyze software ImageJ was used. The error on the contact angle value of semi-manual measurements was estimated to be about  $5^\circ$ . This error is acceptable as far as for the very initial stages of wetting the contact angle is higher than  $90^\circ$  (see Figure 2-4b).

### 3-5) Muffle furnace

Some of the alloys involved in the experimental part of this study were prepared inside the muffle furnaces Nabertherm LE1/11 (with inner dimensions  $90 \times 115 \times 110$  mm) and Nabertherm LE5/11 (with inner dimensions  $200 \times 170 \times 130$  mm). The maximum operation temperature of these furnaces is  $1100^\circ\text{C}$ . The temperature control was verified by an additional K-type (chromel-alumel) thermocouple always placed close to the samples (1 cm far). It was found that the Nabertherm LE5/11 keeps good isotherm even at the low temperature of  $200^\circ\text{C}$  (the oscillations of the temperature were around  $3^\circ\text{C}$ ) whereas the Nabertherm LE1/11 couldn't fulfill ideal isothermal conditions for the heat treatment at  $200^\circ\text{C}$  (the oscillations of the temperature were around  $10^\circ\text{C}$ ). Both muffle furnaces could keep good isotherm (temperature oscillations less than  $1^\circ\text{C}$ ) at temperatures higher than  $500^\circ\text{C}$ .

### 3-6) Fast dipping experimental setup

In order to study the very initial stages of the solid-liquid reaction between metals we have designed the experimental setup shown on the Figure 2-9 that is used for performing fast dipping experiments. These experiments consist in dipping of a substrate in a liquid bath for a given time.

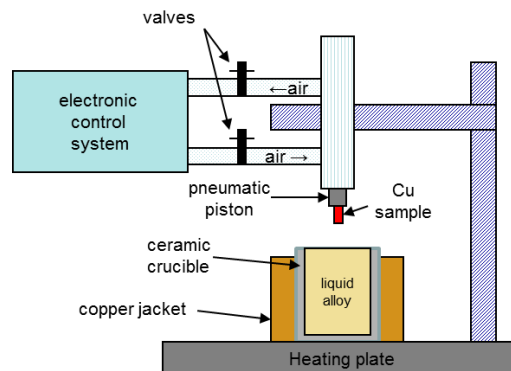


Figure 2-9. Experimental setup for the fast dipping experiments.

The ceramic crucible containing the alloy is placed over a heating plate capable to heat up to  $350^\circ\text{C}$ . The crucible is surrounded by a Cu jacket with a wall thickness of 1 cm in order to ensure good heat conductance and to ensure the thermal homogeneity around the crucible. A pneumatic piston was employed to transfer the Cu substrate into the liquid melt for a time of about 100-150 ms. A special electronic control system was built in our laboratory during the thesis in order to control the switch of the high pressurized air flow direction for blowing and retracting of the pneumatic piston. The pressure of the incoming and outgoing air flux could be also adjusted manually by two valves. This permits to control the dipping speed of the sample that was measured by recording the sample movements by a CCD camera. All details concerning the calibration of the dipping speed will be given in Chapter 4.

### 3-7) DSC setup

Differential scanning calorimetry (DSC) is a tool for detecting heat exchange. The DSC usually uses a reference sample (called reference) for which it is known that no phase transition occurs and it remains inert from a thermodynamic viewpoint during the execution of the thermal profile. The second sample is the object of the study. Both samples are placed in two different cells obeying the same thermal profile, the whole system being located in the same calorific room. The temperature of these two cells should remain the same during the execution of the thermal profile. Thus, it is possible to measure with good accuracy the heat exchange between the two cells. When a phase transition occurs in the sample, a power generator provides the energy required to maintain the temperature equivalent to the reference sample. This energy (or heat flow) is stored as a function of time. Thus, the DSC allows determining the temperature of phase transitions as well as the enthalpies associated with these phase transitions. The DSC equipment used in this study is a TA Instruments 2920.

## 4) **Characterization equipment**

During this study a certain number of characterization equipment was used such as:

- Olympus BX60M optical microscope;
- Leo - S440 scanning-electron microscope (SEM) operating in (SE) or backscatter-electron (BSE) mode coupled energy-dispersive X-ray spectroscopy (EDX);
- SEM – FEG Zeiss Ultra 55;
- Focused ion-beam (FIB) ZEISS-Cross Beam NVision 40;
- Transmission-electron microscopes TEM JEOL 3010 and JEOL 2010;
- Diffractometer X'Pert PRO MPD PANalytical;
- Optical Profilometer ZYGO NEWVIEW 600.

## 5) **Materials**

### 5-1) Materials received from the suppliers

Materials used in this study were:

- OFHC (oxygen-free high thermal conductivity) Cu sheets 99.99% from Goodfellow SARL France with a thickness of 1.5 mm and 99.99% purity;
- Sn rod 12.7 mm in diameter with 99.98% from Alfa Aesar France;
- Ag rod 7.0 mm in diameter with 99.99% from Goodfellow SARL France;
- Pb rod 12.7 mm diameter with 99.95% from Goodfellow SARL France;

### 5-2) Alloys processed in laboratory

Two Sn-Cu alloys were used in this study: eutectic one with nominal composition Sn-0.7wt.%Cu and hypo-eutectic Sn-7.8wt.%Cu alloy. Both of them were prepared in the alumina furnace under vacuum by putting suitable ratios of pure pieces of Sn and Cu in an alumina crucible and performing a thermal cycle that was different for each alloy:

1) *Sn-0.7wt.%Cu alloy* was prepared by heating up to 200°C with a rate 5°C/min and then with a rate 20°C/min up to 400°C followed by an isothermal holding for 1 hour at 400°C under high vacuum of  $1.6 \times 10^{-4}$  Pa and natural cooling with a rate 2°C/min to 200°C under high vacuum of  $1.2 \times 10^{-4}$  Pa. Then the diffusion pump was turned off and system cooled down to the room temperature with the same cooling rate under a primary vacuum (0.1 Pa).

In order to characterize the as-prepared bulk Sn-0.7wt.%Cu alloy, a piece of this alloy was first cold mounted and cut. Then it was grinded by SiC paper and finally polished with a 0.25 µm diamond suspension and cleaned by ethanol in ultrasonic bath. Figure 2-10 gives a

typical Scanning Electron Microscopy (SEM) image obtained with back-scattered electrons (BSE) mode operating at 20 kV. It shows a homogeneous microstructure containing  $\text{Cu}_6\text{Sn}_5$  particles some tens of micrometers long and some micrometers large. The microstructure shown in Figure 2-10 is very similar to that obtained by Nogita et al. [Nogita\_2005] who studied the microstructure control of Sn-0.7wt.%Cu alloys.

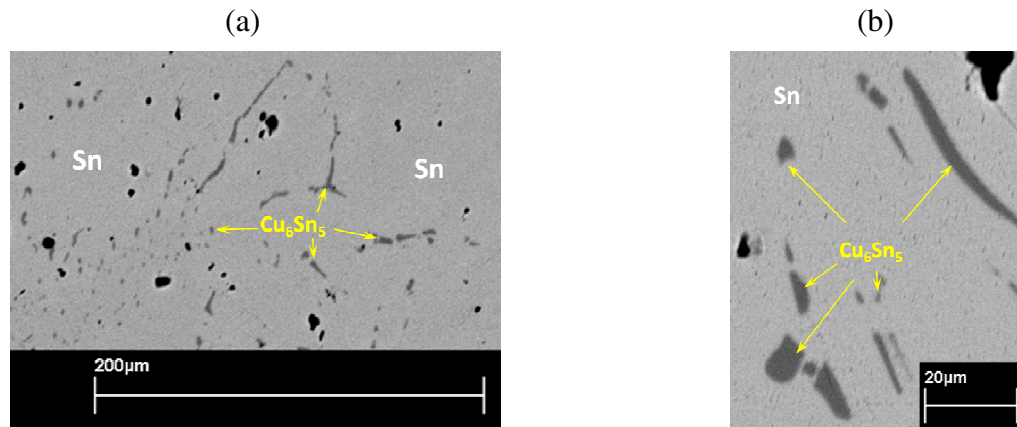


Figure 2-10. Scanning Electron Micrographs of Sn-0.7wt.%Cu alloy after processing at 400°C under high vacuum.

2) Sn-7.8wt.%Cu alloy was prepared by heating up to 200°C with a rate of 5°C/min and then with a rate 20°C/min up to 600°C under high vacuum of  $2 \times 10^{-4}$  Pa. At 600°C the Ar gas was introduced in the chamber (Ar pressure of about 0.1 bar) in order to avoid evaporation process, and the system was heated up to 800°C with the same heating rate 20°C/min. An isothermal holding for 1 hour at 800°C (under Ar) was made and then the system was naturally cooled with a rate 2°C/min to 200°C. The same description as for the Sn-0.7wt.%Cu alloy is valid here.

### 5-3) Intermetallics processed in laboratory ( $\eta\text{-Cu}_6\text{Sn}_5$ , $\varepsilon\text{-Cu}_3\text{Sn}$ and $\text{Ag}_3\text{Sn}$ )

Three intermetallics were prepared for the further studies of reactivity and wettability in Cu-Sn and Ag-Sn binary systems:  $\eta\text{-Cu}_6\text{Sn}_5$  (40.0wt.%Cu),  $\varepsilon\text{-Cu}_3\text{Sn}$  (62.0wt.%Cu) and  $\text{Ag}_3\text{Sn}$  (3.7wt.%Ag). One more type of the IMC substrate was used in this study: the scalloped  $\text{Cu}_6\text{Sn}_5$  grown by reaction between solid Cu and liquid Sn at Cu/Sn interface and “opened” by the selective chemical etching of Sn. The detailed description of the processing procedure of these intermetallics is given in the following.

#### 5-3-1) Bulk $\eta\text{-Cu}_6\text{Sn}_5$ and $\text{Ag}_3\text{Sn}$

These intermetallics (IMCs) were prepared from the pure Cu, Ag and Sn by sealing the small pieces of these metals in suitable ratio in the quartz ( $\text{SiO}_2$ ) tube under Ar atmosphere. (The total mass of the samples is about 5 g). Then tubes were annealed in the muffle furnace at 1000°C for 24 hours. Afterwards, samples were rapidly quenched in cold ( $\sim 18^\circ\text{C}$ ) water. The final preparation step was an isothermal annealing of samples in the muffle furnace for 20 days at 350°C. XRD analysis of the cross-sectioned surface of both IMCs was performed (see Figure 2-11). This XRD analysis shows that only peaks of expected phases appear: monoclinic  $\eta\text{-Cu}_6\text{Sn}_5$  and orthorhombic  $\text{Ag}_3\text{Sn}$ , without any other peak of other IMC's or pure metals.

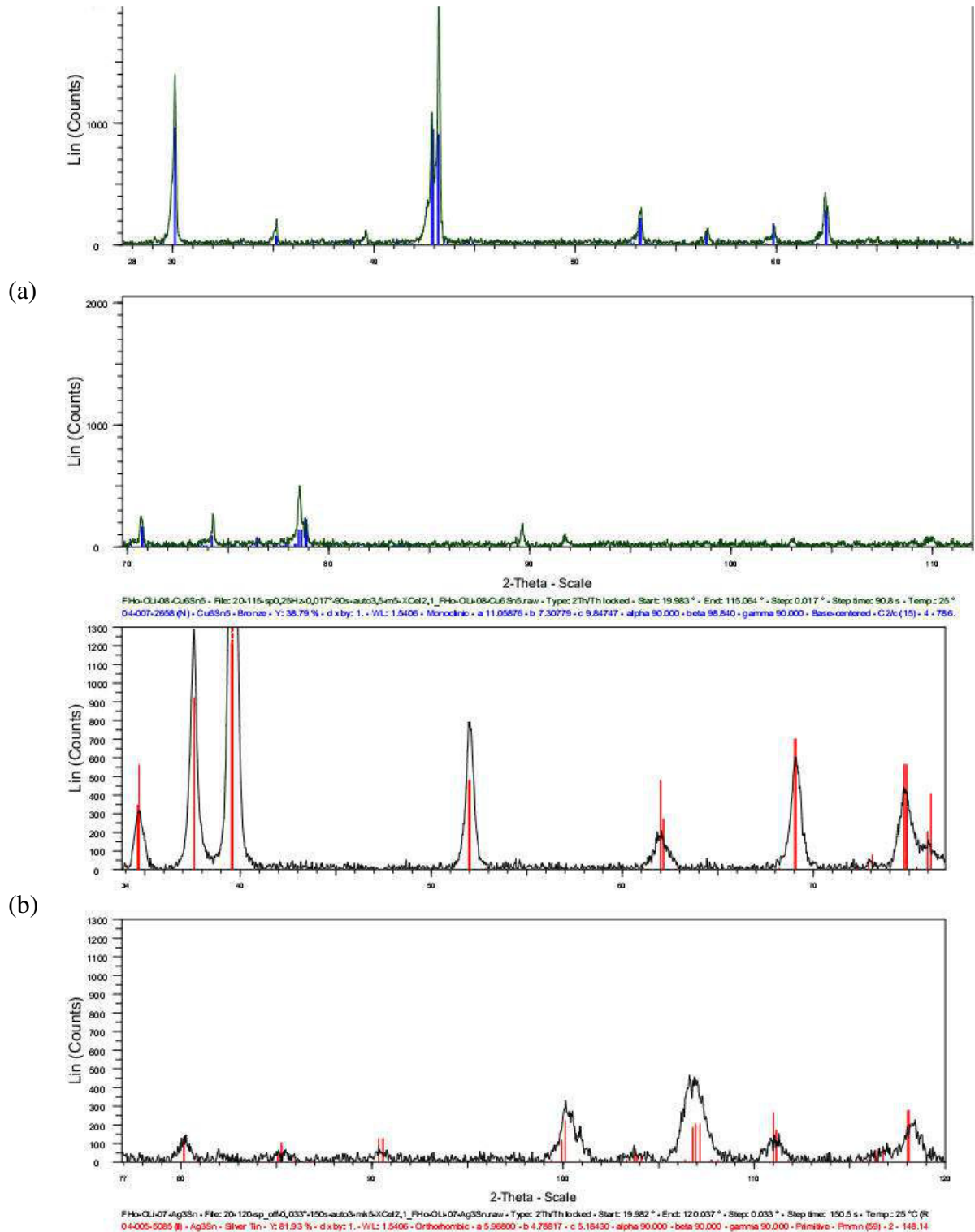


Figure 2-11. XRD scan of the bulk samples: (a) monoclinic  $\text{Cu}_6\text{Sn}_5$  and (b) orthorhombic  $\text{Ag}_3\text{Sn}$ .

Figure 2-12 gives the SEM micrographs in BSE mode of the cross-sections of as-prepared  $\text{Cu}_6\text{Sn}_5$  (Figure 2-12a) and  $\text{Ag}_3\text{Sn}$  (Figure 2-12b) alloys. It is seen that the bulk of  $\text{Cu}_6\text{Sn}_5$  alloy contains a lot of micrometric pores as well as some small elongated inclusions of another phase with maximum size of about  $100\ \mu\text{m}$ . These inclusions were not detected by XRD analysis which could be due to their small quantity. They could be either Cu or  $\text{Cu}_3\text{Sn}$  phase. In its turn the  $\text{Ag}_3\text{Sn}$  phase is homogenous and free of pores as can be seen from Figure 2-12b.

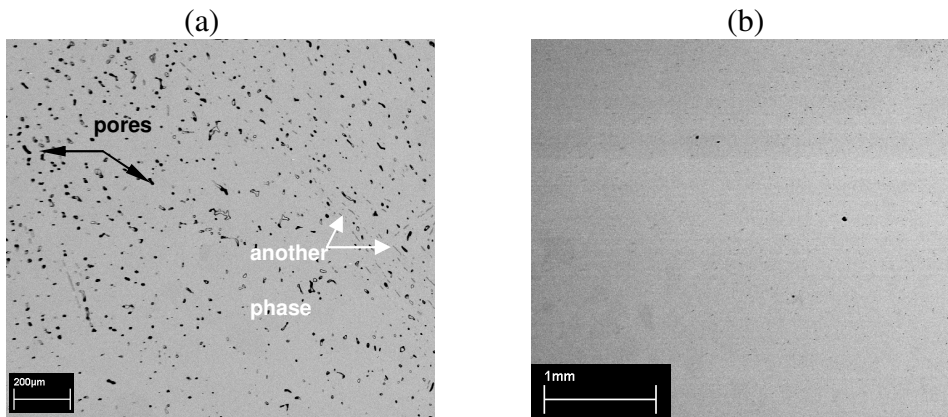


Figure 2-12. BSE-SEM cross-sections of elaborated  $\text{Cu}_6\text{Sn}_5$  (a) and  $\text{Ag}_3\text{Sn}$  (b) alloys.

### 5-3-2) Scalloped $\eta\text{-Cu}_6\text{Sn}_5$

A scalloped  $\text{Cu}_6\text{Sn}_5$  sample was prepared by reaction between Cu and liquid Sn at  $350^\circ\text{C}$  for 2 hours in an alumina furnace under the high vacuum of  $1.6 \times 10^{-4}$  Pa.

After the reaction the tin was etched away by an acidic solution (HCl 10%,  $\text{C}_2\text{H}_5\text{OH}$  90%) heated up to  $70^\circ\text{C}$ . The etching process was held for some hours till the tin was etched completely.

Figure 2-13 gives the SEM micrographs of as prepared scalloped surfaces of the  $\text{Cu}_6\text{Sn}_5$  IMC after the etching in acidic solution. As it can be seen the average grain size of  $\text{Cu}_6\text{Sn}_5$  grains varies from 5 to 25  $\mu\text{m}$ .

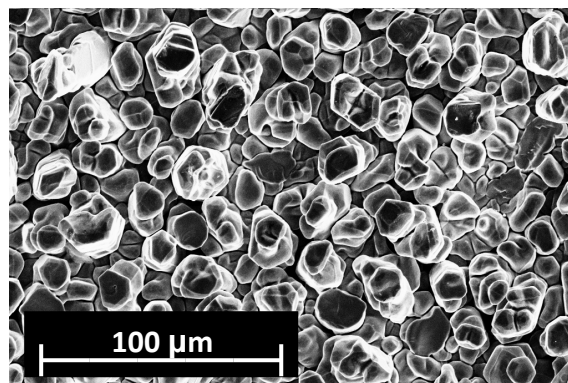


Figure 2-13. SEM micrographs of the scalloped surface obtained after etching of tin in aged Cu-Sn sandwich sample for 2h at  $350^\circ\text{C}$  (SE mode).

### 5-3-3) Bulk $\varepsilon\text{-Cu}_3\text{Sn}$

This intermetallic was prepared in the alumina furnace from pure Cu and Sn pieces placed in an alumina crucible. The chosen composition of the alloy was 62.0wt.%Cu. The alloying cycle comprised pumping the whole system to  $1.6 \times 10^{-4}$  Pa, heating with a rate  $5^\circ\text{C}/\text{min}$  up to  $200^\circ\text{C}$ , then heating with a rate  $20^\circ\text{C}/\text{min}$  up to  $600^\circ\text{C}$ . After reaching this temperature the Ar was introduced into the chamber and the whole system was heated up to  $800^\circ\text{C}$  with the same heating rate  $20^\circ\text{C}/\text{min}$  and held at this temperature for 30 min. Then the system was cooled down to  $750^\circ\text{C}$  with a cooling rate  $10^\circ\text{C}/\text{min}$  and very slowly to  $630^\circ\text{C}$  with a cooling rate  $1^\circ\text{C}/\text{min}$ . The whole system was held at  $630^\circ\text{C}$  for 4 hours in order to “stabilize” the  $\text{Cu}_3\text{Sn}$  phase (see Cu-Sn phase diagram - Figure 1-22, Chapter 1) and then naturally cooled down to the room temperature with a cooling rate  $2^\circ\text{C}/\text{min}$ . The piece of the obtained alloy was crushed into powder in order to enhance the XRD signal. The XRD analysis of the powders is given on the Figure 2-14. It revealed the presence of the only phase – orthorhombic  $\text{Cu}_3\text{Sn}$  phase.

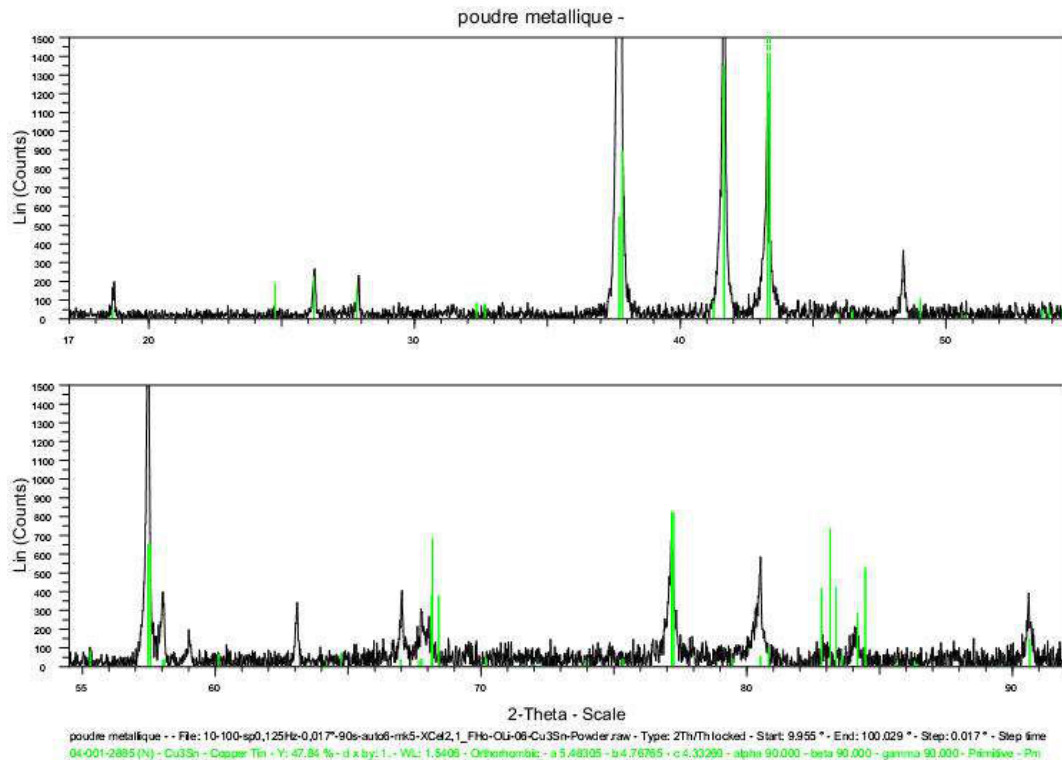


Figure 2-14. XRD scan of the powder obtained after braking of the  $\text{Cu}_3\text{Sn}$  sample into powder.

Figure 2-15 shows a SEM micrograph of the cross section of the prepared  $\text{Cu}_3\text{Sn}$  alloy in BSE mode. It is seen that the sample contains large millimetric grains and does not contain inclusions of another phase. Nevertheless the cracks abundance observed in this sample points out the brittle character of the  $\text{Cu}_3\text{Sn}$  intermetallic.

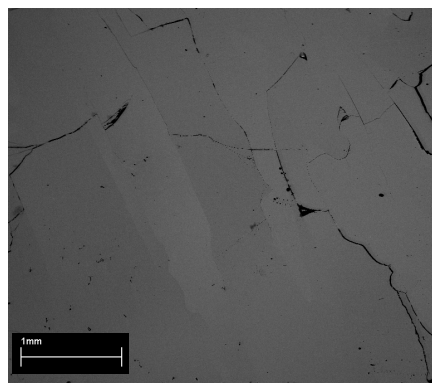


Figure 2-15. BSE-SEM cross-sections of elaborated  $\text{Cu}_3\text{Sn}$  sample.

## 6) Metallographic preparation of materials

### 6-1) Mounting and cutting

The samples were mounted with Presi KM-U cold-mounting resin. The cutting of the samples was made by the Buehler IsoMet low-speed saw.

### 6-2) Polishing of the substrates

The metallographic preparation of the substrates included grinding of them by SiC papers P800, P1000, P1200 and P2400 with subsequent ultrasonic cleaning in ethanol for 5 min. The grinded substrates were then polished by diamond suspension (Buehler MetaDi and LamPlan BioDiamant) with different steps from 15 to 0.25  $\mu\text{m}$  (in diamond particle size). Afterwards, samples were ultrasonically cleaned in ethanol for 5 min and rinsed in water after

each polishing step. The polishing procedure was adjusted for each type of sample and polishing quality was checked after each polishing step by optical microscope.

Finally, polishing quality was checked by the optical profilometer. The average and total roughness of the polished samples were measured. The average roughness  $R_a$  is defined as arithmetic mean of the absolute deviations of the surface profile from its total median. The total roughness  $R_t$  is the vertical distance between the highest and the lowest distance of the inspected surface. Normally, the total roughness is around 10 times higher than the average roughness. The measured  $R_a$  and  $R_t$  roughness values for the polished Cu, Cu<sub>3</sub>Sn, Cu<sub>6</sub>Sn<sub>5</sub> and Ag<sub>3</sub>Sn substrates are given in the Table 2-1. The measurements were made for a region of 259  $\mu\text{m} \times 349 \mu\text{m}$ .

	Cu	Cu <sub>3</sub> Sn	Cu <sub>6</sub> Sn <sub>5</sub>	Ag <sub>3</sub> Sn
$R_a$ , nm	0.5	0.9	1-3	1.4
$R_t$ , nm	8	10	46-77	20

Table 2-1. Mean  $R_a$  and total  $R_t$  roughness of Cu, Cu<sub>3</sub>Sn, Cu<sub>6</sub>Sn<sub>5</sub> and Ag<sub>3</sub>Sn polished substrates.

### 6-3) Etching

To clean the sample surface after the metallographic preparation a 10% solution of the HCl acid with ethanol was used. The samples were dipped into this solution for 10 s just after polishing. Afterwards, they were ultrasonically cleaned in ethanol before SEM observation.

## 7) Conclusions

In this chapter we had firstly presented the principle of "sessile drop" as well as that of the modified version of this technique, the dispensed drop method. The last method was used for determination of the spreading kinetics of liquid Sn and Sn alloys on different substrates such as Cu, Cu<sub>3</sub>Sn, Cu<sub>6</sub>Sn<sub>5</sub>, Ag and Ag<sub>3</sub>Sn as well as for determination of the stationary contact angles of these liquid alloys on these substrates. The apparatus used for performing wetting experiments, presented in *Chapter 3*, are the metallic furnace for the dispensed drop experiments and the alumina furnace for the classical sessile drop experiments. In both furnaces, a high vacuum of about  $2 \times 10^{-5}$  Pa is attained at temperatures between 300 and 400°C. The images of the drop during the spreading process can be recorded either by a classical CCD camera (25 images/s) or by a high-speed camera (up to 5000 images/s). The linear dimensions of the drops and the contact angles can be determined by an automatic analysis of the obtained profiles. The accuracy for the linear values (base radius  $R$  and height  $h$  of the drop) is  $\pm 2\%$  and for the contact angle  $\theta$  is  $\pm 1^\circ$ .

We have also presented a specific fast dipping experimental set-up that we have constructed in our laboratory in order to study the very initial interactions between Cu substrate and liquid Sn-based alloys. As it will be presented in *Chapter 4*, the combination of this specific technique with accurate FIB and TEM characterization should clarify the question of the first intermetallic phase formation and evolution in time for contact time less than 1 s at temperature corresponding to the reflow process (around 250°C).

Afterwards, we have presented the techniques of processing and characterization of Cu<sub>6</sub>Sn<sub>5</sub>, Cu<sub>3</sub>Sn and Ag<sub>3</sub>Sn intermetallics that are used for wetting experiments presented in *Chapter 3* as well as for performing the incremental Cu/Cu<sub>3</sub>Sn diffusional couple that are used for the study of the growth kinetics of intermetallics and main mechanisms of this process presented in *Chapter 5*.

Finally, the different techniques applied for characterization of materials used in this study as well as the metallographic preparation of these materials are briefly presented.

## **Chapter 3: Wetting of Cu, Ag and Cu-Sn and Ag-Sn intermetallic compounds by liquid Sn or Sn-Cu alloys**

### **1) Introduction**

This chapter deals with the study of wetting by liquid solders of metallic substrates such as Cu and Ag or the intermetallic compounds formed between these elements and Sn such as  $\text{Cu}_6\text{Sn}_5$ ,  $\text{Cu}_3\text{Sn}$  and  $\text{Ag}_3\text{Sn}$ . The main part of this chapter is dedicated to the wetting of Cu,  $\text{Cu}_6\text{Sn}_5$  and  $\text{Cu}_3\text{Sn}$ .

Moreover, as the ternary Sn-based Sn-Cu-Ag alloys are widely used in electronic industry and, as it is already mentioned in Chapter 1, the solidification of these alloys under metastable conditions (undercooling) can start by the formation of large  $\text{Ag}_3\text{Sn}$  precipitates, therefore it is interesting to study the wetting of  $\text{Ag}_3\text{Sn}$  compound by liquid Sn. Indeed, under these conditions, the heterogeneous nucleation sites for the Sn can be "intrinsic" micrometric solid particles contained in the liquid alloy or  $\text{Cu}_6\text{Sn}_5$  compound formed at the liquid side of the liquid Sn/Cu interface or even  $\text{Ag}_3\text{Sn}$  primary precipitates firstly formed in the liquid bulk during solidification. Thus, we studied the wetting of  $\text{Ag}_3\text{Sn}$  but also the wetting of pure Ag by liquid Sn in order to deduce the better analysis of the wetting behaviour.

Almost all solids used for wetting experiments are bulk substrates either furnished by Goodfellow SARL France either by Alfa Aesar or processed in our laboratory under vacuum ( $\text{Cu}_6\text{Sn}_5$ ,  $\text{Cu}_3\text{Sn}$  and  $\text{Ag}_3\text{Sn}$ ) - see Chapter 2 for the preparation details. For  $\text{Cu}_3\text{Sn}$  and  $\text{Ag}_3\text{Sn}$  substrates, the average roughness is around 10 and 20 nm respectively (see Chapter 2), whereas the bulk  $\text{Cu}_6\text{Sn}_5$  substrate has an average roughness of around 60 nm. Only one specific  $\text{Cu}_6\text{Sn}_5$  scalloped surface substrate is used for the wetting experiments (the processing technique is given in the Chapter 2).

During wetting experiments, the measurement of the contact angle  $\theta$  and the drop base radius  $R$  are performed either with a conventional CCD camera (25 frames/s) or with a rapid camera (up to 5000 frames/s) - see Chapter 2.

Note that only initial stages of wetting (some seconds for example) can be followed with a rapid camera, while some tens of minutes or even hours can be recorded by the conventional camera. Note moreover that in SIMaP laboratory we have our own conventional camera whereas the rapid camera, belonging to Grenoble University, should be booked in advance and for a limited period of time. For this reason, some of wetting experiments are followed by the conventional camera and some others by the rapid camera.

In the following we will present and discuss successively the results of wetting experiments on (i) Cu, (ii)  $\text{Cu}_3\text{Sn}$ , (iii)  $\text{Cu}_6\text{Sn}_5$  bulk substrate, (iv)  $\text{Cu}_6\text{Sn}_5$  scalloped surface substrate and (v)  $\text{Ag}_3\text{Sn}$  and Ag substrates.

### **2) Wetting of Cu substrate by liquid Sn or Sn-Cu alloys**

#### **2-1) Introduction**

In this section the results concerning the wetting of Cu by liquid Sn or Sn-Cu alloys at temperatures between 250°C and 800°C are presented.

In order to study the influence of the surface oxidation of the substrates on the wetting process we had performed two types of wetting experiments:

(i) The deposition of the liquid droplet is performed once the experimental temperature is attained. These experiments are called "without preheating of substrate".

(ii) The substrate is firstly heated to high temperature and maintained at this temperature for a given time under vacuum before cooling down to the experimental temperature and performing the wetting experiment. These experiments are called "with preheating of substrate".

## 2-2) Experiments without preheating of Cu substrate

The very first experiments of wetting on Cu substrate were performed without preheating of the substrate and followed by the conventional camera. We recall that, the Cu surface is polished and cleaned (till 0.25  $\mu\text{m}$  diamond suspension with ultrasonic cleaning in ethanol and acetone after each polishing step) just before placing of Cu substrate in the experimental set-up and starting performing the vacuum in the furnace chamber.

The experimental temperature varies from 250 to 600°C and the wetting experiments were performed under the high vacuum in the range  $(2-4)\times 10^{-5}$  Pa.

Figure 3-1 gives the temperature-time profile of different samples before the wetting experiment. An isothermal holding for 10 min was made after the deposition of each droplet. All the droplets were transferred by the dispensed drop techniques. Moreover, another experiment performed at 300°C (not shown in Figure 3-1) was performed by using the classical sessile drop technique.

As it is shown in Figure 3-2, for wetting experiments performed at temperatures from 250 to 500°C, we noted that the measured contact angle remains constant for 10 min and is equal to the initially measured contact angle (40 ms after the drop deposition). The drop base diameter also remains constant for these experiments. On the contrary, for  $T = 600^\circ\text{C}$ , the apparent contact angle decreases from 27 to 0° in about 15 min (see Figure 3-2).

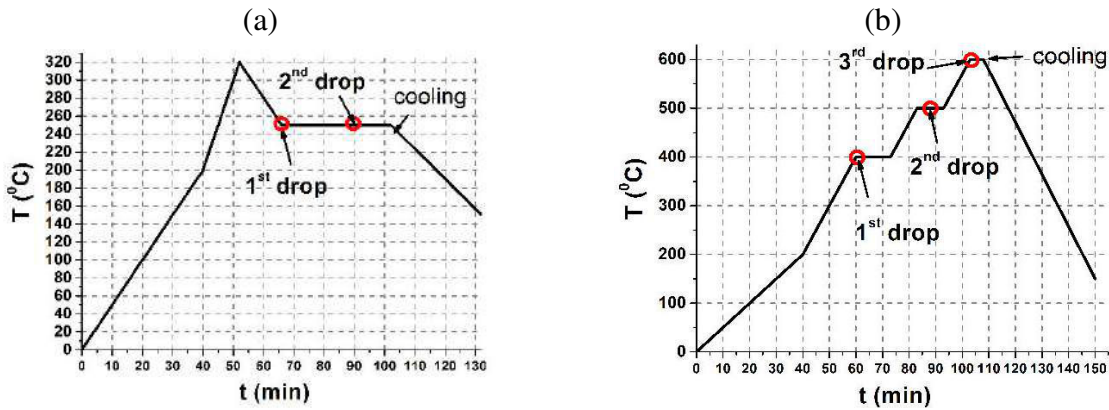
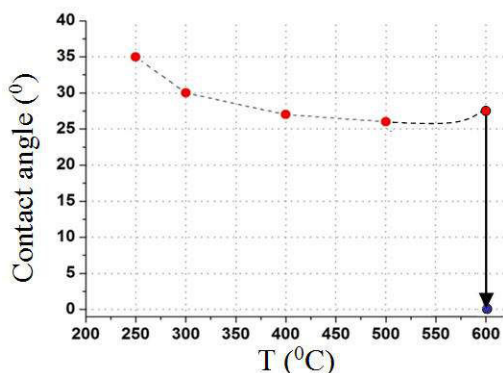


Figure 3-1. Temperature-time profile during wetting of Cu substrate by liquid Sn (experiments without preheating of the substrate). (a)  $T = 250^\circ\text{C}$  (2 drops); (b)  $T = 400, 500$  and  $600^\circ\text{C}$ .



$T(^{\circ}\text{C})$	250	300	400	500	600	
$\theta(^{\circ})$	35	35	30	27	26	27→0

Figure 3-2. Measured contact angle of liquid Sn on Cu substrate at different temperatures. Experiments performed without preheating of substrate. The contact angle remains constant during 10 minutes for  $T = 250$  to  $500^\circ\text{C}$  and for  $T = 600^\circ\text{C}$  it decreases from 27 to 0° in about 15 min.

These experiments show that the initial measure contact angle (in 40 ms) is lower than 35° and it decreases with the temperature.

In fact, when a droplet of Sn is put in contact with a Cu substrate, the dissolution of Cu in liquid Sn will be followed by the intermetallics formation at the interface:  $\text{Cu}_6\text{Sn}_5$  (on the Sn side) and  $\text{Cu}_3\text{Sn}$  (on the Cu side). The reaction between Cu and liquid will continue with the growth of intermetallic layer and the diffusion of Cu in liquid (the reactivity between solid Cu and liquid Sn is developed in details in Chapter 5).

Without going into details of the interfacial reactivity it appears astonishing that no spreading is observed for  $T < 500^\circ\text{C}$  despite the fact that the solubility of Cu in liquid Sn is significant (about 13 at.% at  $400^\circ\text{C}$  and 25at.% at  $500^\circ\text{C}$ ). Note however that observation of droplets deposited at  $T \leq 500^\circ\text{C}$  showed that during their subsequent heating and isothermal holding at  $600^\circ\text{C}$  (see Figure 3-1b) all droplets started to spread after about 10 min of maintaining at  $600^\circ\text{C}$ . Once the spreading process starts at  $600^\circ\text{C}$  it is very rapid and the contact angle becomes lower than  $10^\circ$  in less than 4 min. This spreading process at  $600^\circ\text{C}$  is undoubtedly linked with the interfacial interaction (dissolution + reaction) between Cu and liquid alloy.

In order to verify if the oxidation of Cu surface (native oxide) has any effect on the wetting process we have performed wetting experiments with preheating of Cu substrate.

### 2-3) Experiments with preheating of the Cu substrate

#### 2-3-1) Introduction

Some of wetting experiments on the preheated Cu substrate are followed with the conventional camera in order to have a rapid and general idea of wetting behavior during the first seconds and minutes of contact as it is the case during the reflow process. Afterwards, we have used the rapid camera in order to study the very first stage of wetting (contact time less than 1 s).

#### 2-3-2) Investigation of wetting using conventional camera

This series of experiments was performed by annealing of the copper substrate at  $800^\circ\text{C}$  for one hour prior to the deposition of the liquid tin droplets. The principal time-temperature profiles of these experiments are given on Figure 3-3. The droplets were deposited during the cooling stage. The duration of the observation of each deposited droplet was only 3 min because, in all cases, no evolution of the contact angle was observed after 3 min of contact. Note that for low temperature ( $300^\circ\text{C}$ ) and high temperature ( $700$  and  $800^\circ\text{C}$ ) experiments the spreading of the drop was not observed (i.e. the initial and final measured contact angles are the same).

Figure 3-4 gives the variation of the contact angle and droplet base diameter ( $d$ ) with spreading time for experimental temperatures 400, 500 and  $600^\circ\text{C}$ . This figure shows that spreading from the initial measured contact angle (in 40 ms) to the final measured contact angle is very rapid.

For example at  $400^\circ\text{C}$  the initial measured contact angle of  $28^\circ$  decreases to  $23^\circ$  in 4s and at  $500^\circ\text{C}$  the contact angle decreased drastically from  $33^\circ$  to  $9^\circ$  in 1 s. It should be emphasized that in experiments without deoxidation procedure we haven't observed any variation of the contact angle at 400 and  $500^\circ\text{C}$ . These observations point out the strong correlation between contact angle measurements and oxidation extent of both copper substrate and liquid tin surfaces even under high vacuum of  $2 \times 10^{-5}$  Pa.

Figure 3-5 and Table 3-1 summarize the values of the initial measured contact angles and final contact angles at different temperature. As it can be seen from the Table 3-1 the switch to the longer deoxidation duration at  $800^\circ\text{C}$  (experiments at  $500^\circ\text{C}$  marked by \*) does not lead to much lower initially measured contact angle. This result suggests that 1 hour of deoxidation at  $800^\circ\text{C}$  is sufficient to overcome the oxidation of the copper substrate surface.

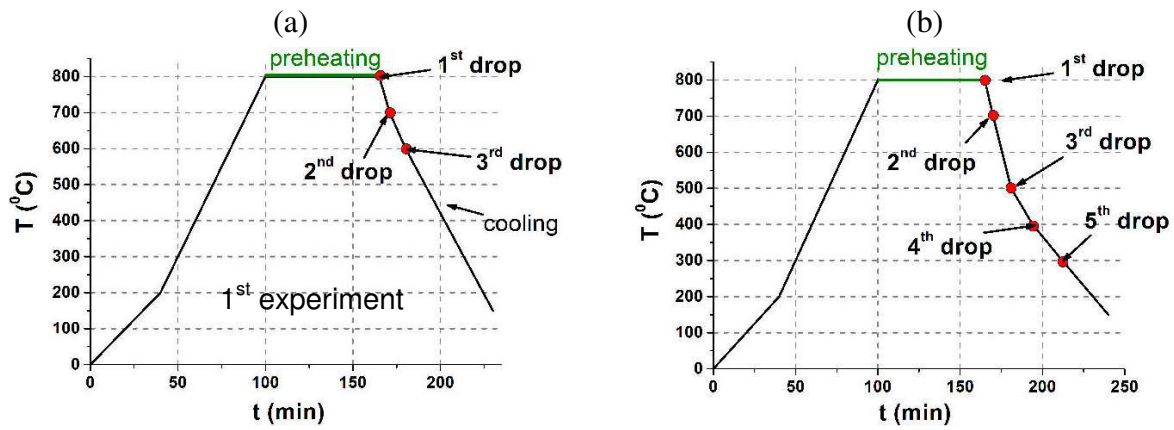


Figure 3-3. Temperature-time profile of experiments performed with preheating at 800°C for 1 hour. The deposition of Sn droplets on Cu substrate was made while cooling from 800°C and performing an isothermal holding of about 3 min at experimental temperature. Droplet deposition marked by  $\circ$ .

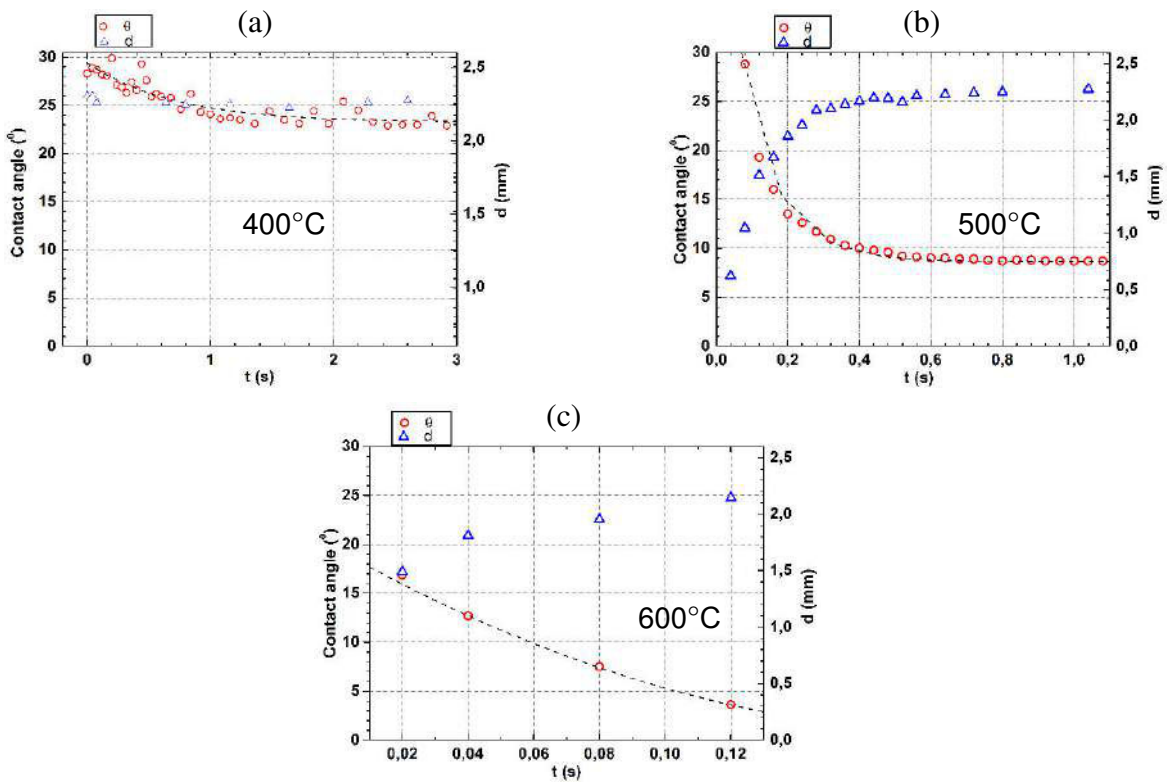


Figure 3-4. Variation with time of the contact angle ( $\circ$ ) and drop base diameter ( $\Delta$ ) of the droplet at 400°C (a), 500°C (b) and 600°C (c) in Cu/Sn couple.

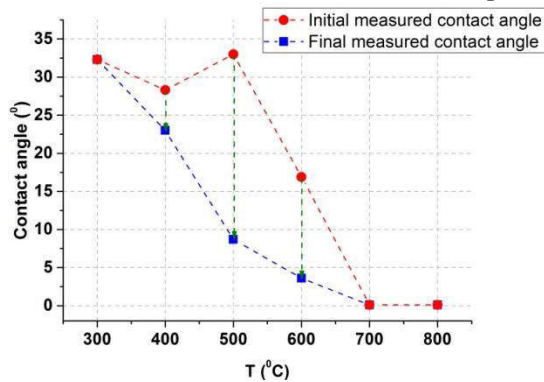


Figure 3-5. Wetting of Cu by liquid Sn with preheating of the Cu substrate at 800°C for 1 hour. Variation of the initial measured contact angle  $\theta_i$  (in 40 ms) and final measured contact angle  $\theta_f$  with temperature (for the spreading time see Table 3-1).

T, °C	300	400	500	500*	500*	600	700	800
$\theta_i$ , °	32	28	33	20	32	17	0	0
$\theta_f$ , °	32	23	9	12	14	4	0	0
$t_{\text{spread}}$ , S	#	4	1	1	3	0.1	#	#

Table 3-1. Wetting data in Cu/Sn couple at different temperature:  $\theta_i$  = initial measured contact angle (in 40 ms);  $\theta_f$  = final measured contact angle. Preheating of the substrate for 1 h at 800°C except for experiments marked by (\*) for which the preheating time was 2 h at 800°C. (#) – not measured.

The comparison of the wetting experiments of liquid Sn on Cu substrate without preheating and with preheating, followed by the conventional camera (see Figures 3-2 and 3-5) shows that:

(i) If the wetting experiments are performed at low temperature range 250-400°C, the preheating process at 800°C has no influence on the initial measured contact angle or even on the final contact angle. This suggests that even if deoxidation process occurs at  $T = 800^\circ\text{C}$ , during cooling at low  $T$  (with a cooling rate around  $5^\circ\text{C}/\text{min}$  - see Figure 3-3) an oxidation of the Cu substrate is possible at low  $T$ .

(ii) For experiments performed at 500°C, even if the initial measured contact angle seems to be almost the same as in the case of the Cu substrate preheated at 800°C a rapid spreading occurs from  $\theta_i = 20 - 33^\circ$  to  $\theta_f = 9 - 14^\circ$  whereas no spreading is observed with substrate not preheated at 800°C.

Moreover, the initial measured contact angles (in 40 ms) for experiments performed at high temperatures (700 and 800°C - see Figure 3-4) are close to  $0^\circ$ .

However, knowing that the stage of non reactive spreading of liquid metals is very rapid (about 10 ms), we performed other experiments of wetting of Cu substrate by liquid Sn or Sn-Cu alloys investigated by using rapid camera (up to 5000 frames/s) in order to study the first stage of wetting.

### 2-3-3) Investigation of wetting using the rapid camera

The principal aim of this section is to investigate the initial stage of wetting of Sn or Sn-Cu alloys on a Cu substrate by using a rapid camera (up to 5000 frames/s).

In order to avoid the very first stage of reactive wetting of solid Cu by liquid Sn, that is the dissolution of Cu substrate (that precedes the nucleation and growth of reactive products  $\text{Cu}_6\text{Sn}_5$  and  $\text{Cu}_3\text{Sn}$  formed at the interface), we firstly study the wetting of Cu by a Sn-7.8wt.%Cu alloy saturated at 430°C. The wetting experiments with this alloy were performed at 390°C in order to obtain the formation of the  $\text{Cu}_6\text{Sn}_5$  intermetallic at the Cu/Sn interface which is possible only for  $T < 415^\circ\text{C}$  as it is shown par the binary Cu-Sn phase diagram (see Figure 1-22).

For experiments with Sn-7.8wt.%Cu alloy we did not preheat the Cu substrate, the aim of these experiments was to obtain some “reference experiments” investigated by rapid camera in order to validate the method and to verify the reproducibility of wetting kinetics.

Once the method was validated, we performed wetting experiments of Cu substrate preheated at 800°C for 1h by liquid Sn at different temperatures (from 390 to 600°C).

#### 2-3-3-1) Wetting of Cu by the liquid Sn-7.8wt.%Cu alloy

Figure 3-6 that gives the temperature - time profile for this wetting experiment, shows that two droplets were deposited at 390°C after 2 hours of preheating at this temperature.

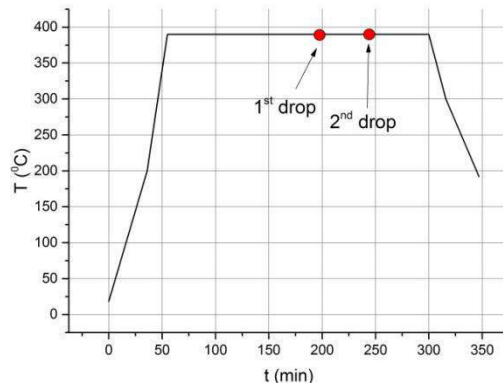


Figure 3-6. Temperature-time profile of wetting experiment in Cu/Sn-7.8wt.%Cu alloy system at 390°C.

Figures 3-7a,c give the time dependence of the mean value of the contact angle (averaged out two values: “left side” and “right side” contact angle) in linear and logarithmic scale respectively for the 1<sup>st</sup> drop (see Figure 3-6). The dependence of the droplet diameter on time is given on the Figures 3-7b,d in linear and logarithmic scale respectively. As it can be seen from this figure the very rapid spreading of the drop, with contact angle decreasing from 120 to about 30°, happened at the first  $10^{-2}$  s of spreading.

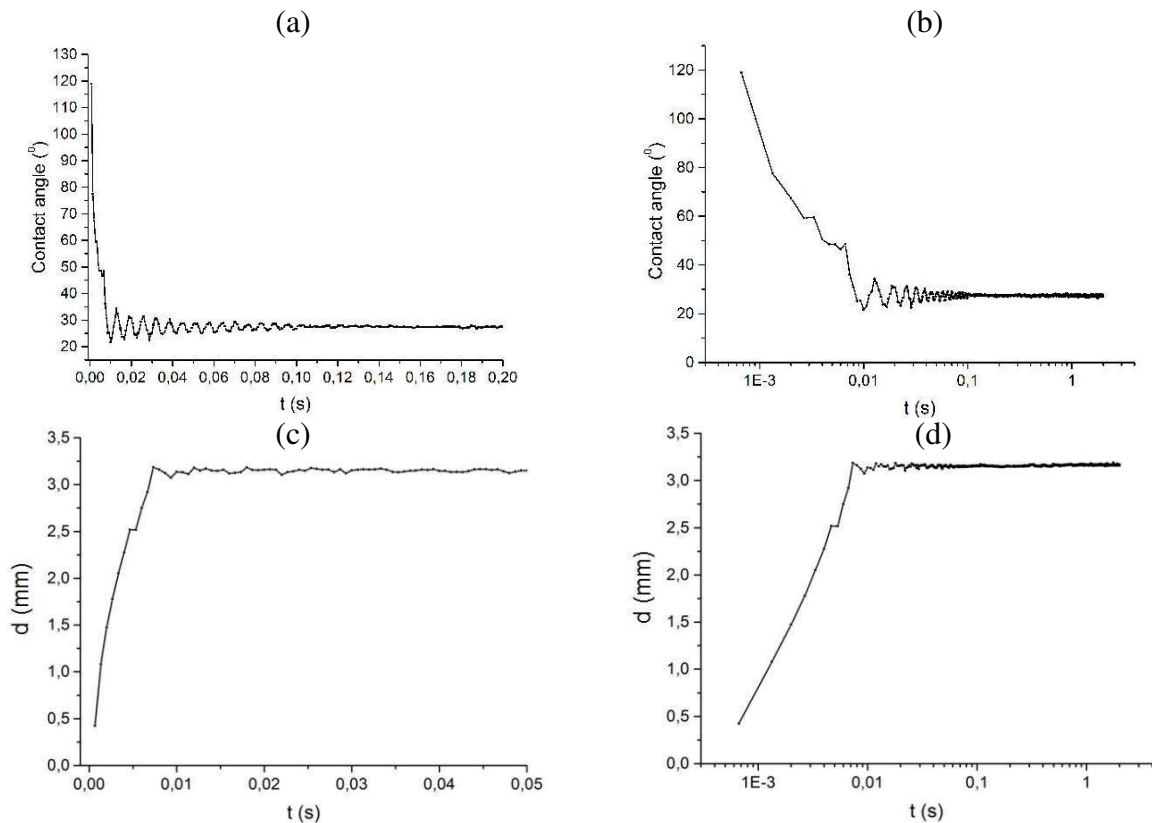


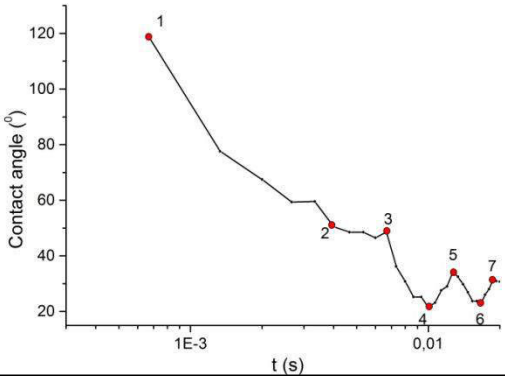
Figure 3-7. Variation of the mean values of contact angle  $\theta$  and drop base diameter  $d$  with time: in normal scale (a,c) and log-scale (b,d). Cu/Sn-7.8wt.%Cu alloy system at 390°C.

Figure 3-8 connects some peculiar experimental points with real time images taken during the wetting experiment. It can be seen that up to about  $(6-7) \times 10^{-3}$  s the liquid neck exists between the drop and the capillary. Afterwards this neck breaks and the droplet spreads rapidly down to around 20° but then oscillates. Oscillation was not damped up to about 0.1s. An important point was verified in this case: the oscillations are linked to the variation in the contact angle and diameter of the deposited droplet (see Figure 3-9). The maximum amplitude of the drop base diameter oscillation was around 1.5% of its equilibrium value measured at

0.1 s ( $d = 3.15$  mm) while the initial amplitude of the contact angle variation was about 30% of its final values ( $\theta_f = 27^\circ$ ). The frequency of these oscillations is about  $150\text{ s}^{-1}$ .

The reproducibility of the observed phenomena was checked by comparison of the spreading characteristics for two droplets (see Figure 3-10). As it can be seen from this figure the behavior of the second droplet (variation with time of the contact angle and drop base diameter) is completely similar to the one described above.

We can thus conclude that the spreading of the liquid droplet on the Cu substrate occurs in about 10 ms. This statement does not take into account the oscillation of the drop and the triple line around the final measured contact angle (for experiment times lower than 2 s) that is about  $27^\circ$ .



Point	1	2	3	4
Time (ms)	0.7	3.9	6.6	10.0
Point	5	6	7	
Time (ms)	12.7	16.6	18.7	

Figure 3-8. Oscillations of the deposition droplet of solder alloy Sn-7.8wt.%Cu on Cu substrate at  $390^\circ\text{C}$ .

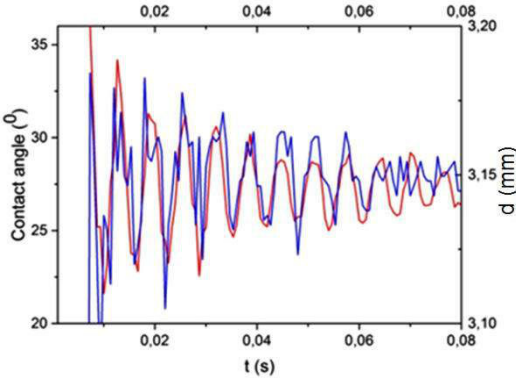


Figure 3-9. Oscillations resulting in the variation of the contact angle (blue line) and drop base diameter (red line) of the deposited droplet of solder alloy Sn-7.8wt.%Cu on Cu substrate at  $390^\circ\text{C}$ .

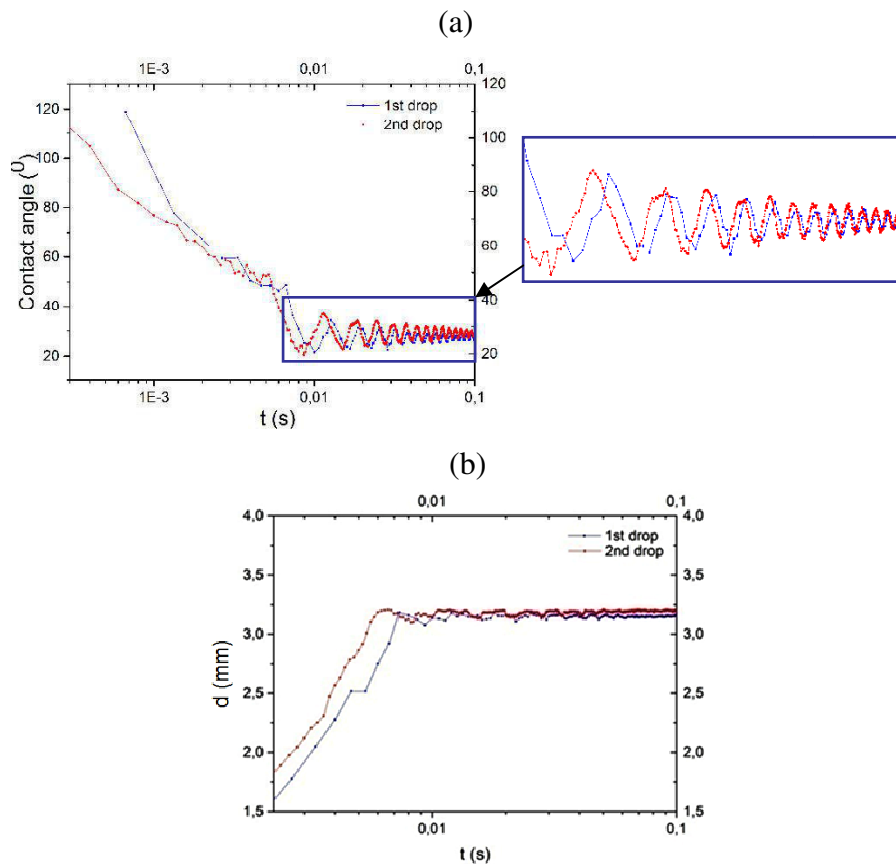


Figure 3-10. Variation of the contact angle (a) and drop base diameter of two deposited solder alloy Sn-7.8wt.%Cu droplets on Cu substrate.

### 2-3-3-2) Wetting of Cu by liquid Sn

The substrate preheating procedure consists in an initial annealing at 800°C for 1 hour with subsequent deposition of the droplet at 600°C (see Figure 3-11). Afterwards we performed additional annealing at 800°C for 15 minutes before deposition of the droplets at 500 and 390°C. Finally, we deposited a last droplet at 300°C (just after deposition of the droplet at 390°C) without additional preheating at 800°C (due to the long cooling time from 800 to 300°C that is about 40 minutes).

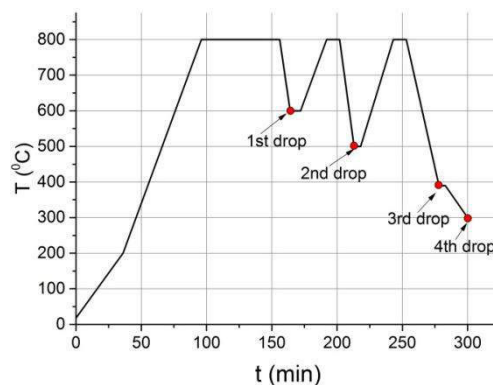


Figure 3-11. Temperature-time profile of wetting of Cu substrate by liquid Sn at different temperatures after 1 hour preheating at 800°C

Figure 3-12 gives the variations of the contact angle and normalized droplet base diameter with time during wetting experiments. For the droplets deposited at lower temperature (390 and 300°C) the contact angle measured, after liquid neck collapse, at about  $(6-7) \times 10^{-3}$  s is practically equal to the final contact angle measured at some seconds after the deposition. On the contrary, for droplets deposited at higher temperatures (600 and 500°C) the

measured contact angle continues to decrease continuously and attains about  $5^\circ$  in 0.1 s at  $600^\circ\text{C}$  and  $15^\circ$  in 0.2 s at  $T = 500^\circ\text{C}$ .

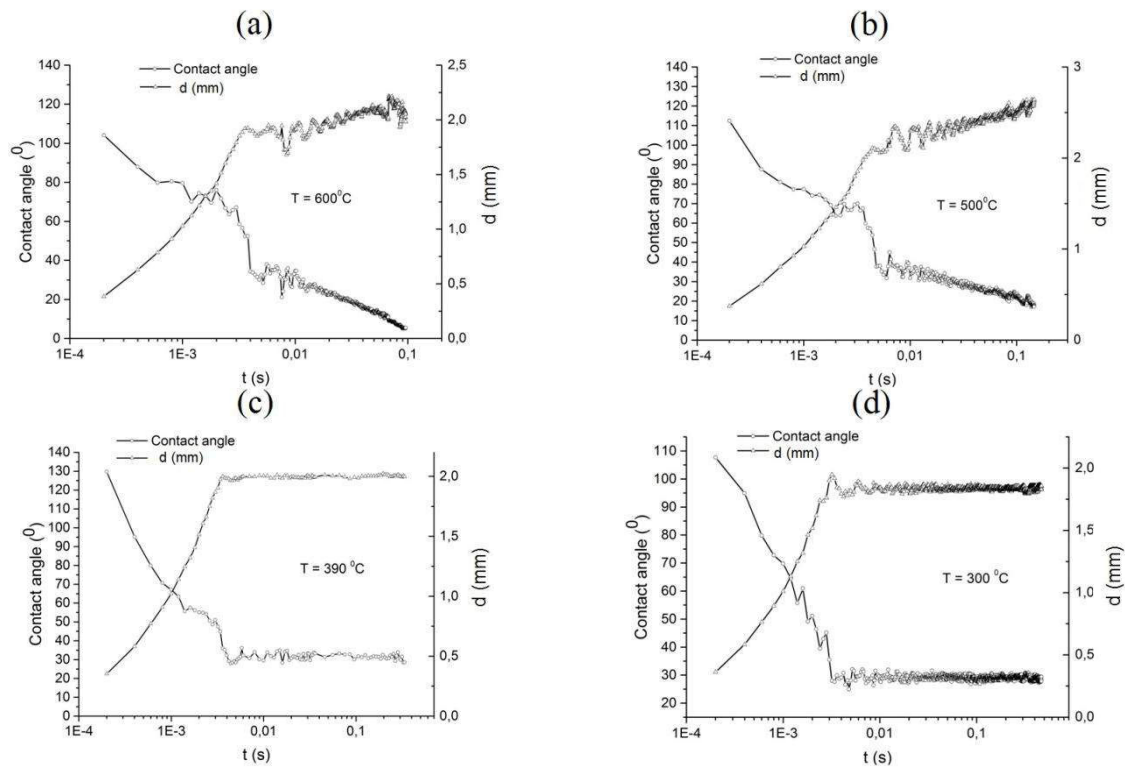


Figure 3-12. Variation with time of the contact and drop base diameter during wetting by liquid Sn of Cu substrate preheated at  $800^\circ\text{C}$  under high vacuum at different temperatures: a)  $600^\circ\text{C}$ ; b)  $500^\circ\text{C}$ ; c)  $390^\circ\text{C}$ ; d)  $300^\circ\text{C}$ .

Note that the mean value of the drop base diameter increases also continuously with time up to the end of experiment (0.1 or 0.2 s). However, it can be easily seen from Figure 3-12a,b that a clear decrease in the spreading rate  $V = dR/dt (= 0.5dd/dt) \approx 0.25 \text{ m/s}$  of the drop occurs at time of about  $(3-4) \times 10^{-3} \text{ s}$  for  $T = 600^\circ\text{C}$  and at time of about  $(7-8) \times 10^{-3} \text{ s}$  for  $T = 500^\circ\text{C}$ . In both cases, the corresponding contact angle is about  $30^\circ$ .

These observations are in agreement with those reported by investigations of wetting followed by a conventional camera of wetting by liquid Sn of preheated Cu substrate at  $600^\circ\text{C}$  and  $500^\circ\text{C}$  (see Figure 3-4). The only (but very important) difference is that the very fast spreading for contact angles higher than about  $30^\circ$  (occurring in less than 10 ms) cannot be detected by the conventional camera.

The first stage of spreading of liquid droplets down to a contact angle of about  $30^\circ$  in less than 10 ms can be attributed to the non reactive wetting of liquid Sn on the Cu surface. Indeed, the non reactive spreading time of liquid metallic droplets occurs in few milliseconds as it was demonstrated by [Protsenko\_2001, Saiz\_2010]. Afterwards, for a reactive system, spreading can continue with a lower spreading rate that depends on the kinetics of interfacial interactions between liquid alloy and substrate (dissolution, growth kinetics of interfacial reaction layer).

In order to verify this statement we performed a specific wetting experiment of liquid Pb on Cu substrate at  $400^\circ\text{C}$ . No intermediate phase exists in the binary Pb-Cu system and the solubility of Cu in liquid Pb at  $400^\circ\text{C}$  is less than 1% [Chakrabarti\_1984]. Thus the wetting of Cu substrate by liquid Pb can be considered as practically non reactive wetting. Before this wetting experiment, the Cu substrate was preheated at  $800^\circ\text{C}$  for 1.5 h.

Figure 3-13 presents the variation with time of the contact angle  $\theta$  and the drop base diameter  $d$  during wetting of Cu by liquid Pb at  $400^\circ\text{C}$ . For comparison purpose, in the same figure the variation of  $\theta$  and  $d$  during wetting of Cu by liquid Sn at  $390^\circ\text{C}$  are reported. This

figure clearly shows that the spreading kinetics of liquid Sn and liquid Pb on Cu substrate are very similar. This fact strongly suggests that the spreading kinetics of liquid Sn on Cu surface from  $\theta = 180^\circ$  to  $\theta = 30^\circ$  in less than 10 ms corresponds to the rapid stage of non reactive wetting of Sn on the Cu surface.

Note however that the Cu surface could be not exempted completely of oxide nanoparticles and thus the contact angle of about  $30^\circ$  corresponds to the equilibrium contact angle of liquid Pb or Sn on the composite surface (Cu + oxide nanoparticles).

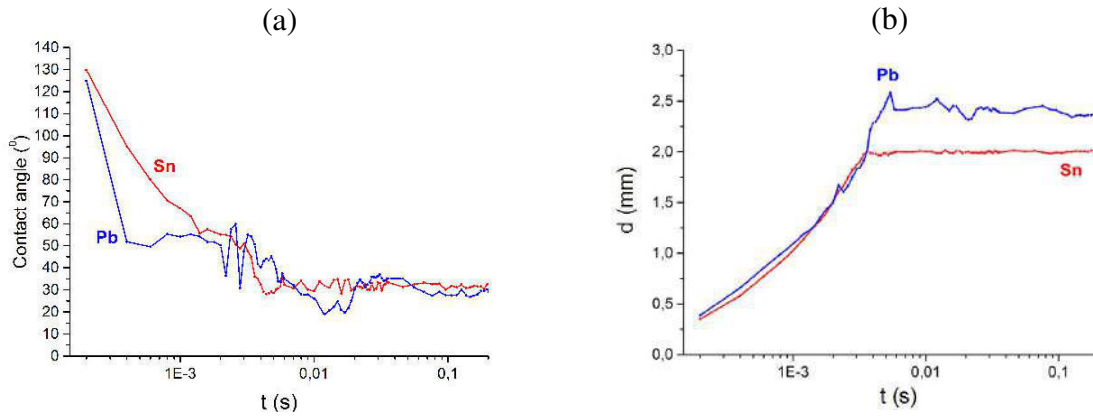


Figure 3-13. Variation with time of contact angle (a) and drop base diameter (b) during wetting of Cu by liquid Pb at  $400^\circ\text{C}$  and by liquid Sn at  $390^\circ\text{C}$ .

Given the fact that in the case of Sn droplets, the very rapid stage of spreading occurs in about 10 ms whatever the experimental temperature from  $300$  to  $600^\circ\text{C}$  (see Figure 3-12), we have reported on the same figure the spreading kinetics of Sn on Cu at different temperatures as well as that of liquid Pb at  $400^\circ\text{C}$  (see Figure 3-14).

Figure 3-14 indicates that for the very initial stage of wetting the spreading kinetics of Sn droplets on Cu is almost temperature independent. Moreover the spreading kinetics of non reactive Pb in this stage is very similar to that of Sn.

Note moreover that the almost linear dependence of the variation of the base drop diameter  $d$  with square root of time ( $d \sim t^{1/2}$ ) is in good agreement with works of Saiz et al. [Saiz\_2010] who studied the non reactive spreading of liquid metals on metallic substrates.

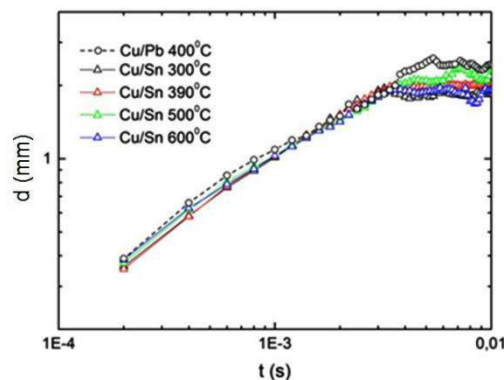


Figure 3-14. Comparison of the drop base diameter change with time for Sn droplets deposited on Cu substrate at  $T = 300$  to  $600^\circ\text{C}$  and Pb droplet deposited on Cu substrate at  $400^\circ\text{C}$ .

#### 2-3-4) Characterization of some Cu/Sn samples

In this section, interfacial characterization of some selected Cu/Sn samples that have undergone the wetting experiments at different temperatures will be presented.

Note however that the aim of this section is not necessarily to present evidence of a relationship between spreading kinetics and interfacial microstructure observed only after

cooling of samples from experimental to room temperature. Indeed, during cooling of samples from experimental to room temperature, spreading and reactivity phenomena continue as long as the drop is in the liquid state which can lead to a change in the composition and morphology of the interfacial system. Note moreover that, from differential scanning calorimetric experiments presented in Chapter 4 we know that in the Cu/liquid drop configuration the Sn or Sn-Cu alloys solidify at about 200-210°C. This means that undercooling can attain from 20 to 30°C. Under these conditions, during cooling of a liquid droplet from 250°C (or 300 or 400°C) to the room  $T$ , the alloy will stay in liquid state during about 10 (or 20 or 35) minutes respectively. This interaction time between Cu and liquid alloy during cooling is much higher than the studied spreading time in all wetting experiments presented here. For this reason, the configuration of the Cu/alloy interface can be modified significantly during cooling.

For characterization, we have selected three Cu/Sn samples corresponding to the following experiments:

- (i)  $T = 250^\circ\text{C}$  without Cu preheating (marked as 2<sup>nd</sup> droplet in Figure 3-1a)
- (ii)  $T = 300^\circ\text{C}$  with Cu preheating (marked as 5<sup>th</sup> droplet in Figure 3-3b)
- (iii)  $T = 400^\circ\text{C}$  with Cu preheating (marked as 4<sup>th</sup> droplet in Figure 3-3b)

The deposited droplets were inspected by SEM from the top view and on their cross-section as well. Figure 3-15 gives the top-view of the droplet deposited at 250°C (marked as 2<sup>nd</sup> droplet on the Figure 3-1a) isothermally annealed for 11 minutes at that temperature under a vacuum of  $2 \times 10^{-5}$  Pa. Knowing that undercooling extent can be as far as 20-30°C, the cooling prior to the solidification of the droplet could have taken 10 min. The solidified droplet has a practically circular form (see Figure 3-15a) and formation of the intermetallic halo around the drop is detected (see Figure 3-15b). The EDX analysis revealed the existence of the distinct  $\epsilon$ -Cu<sub>3</sub>Sn and  $\eta$ -Cu<sub>6</sub>Sn<sub>5</sub> phase layers of the same width of about 10  $\mu\text{m}$  ahead the solidified tin bulk.

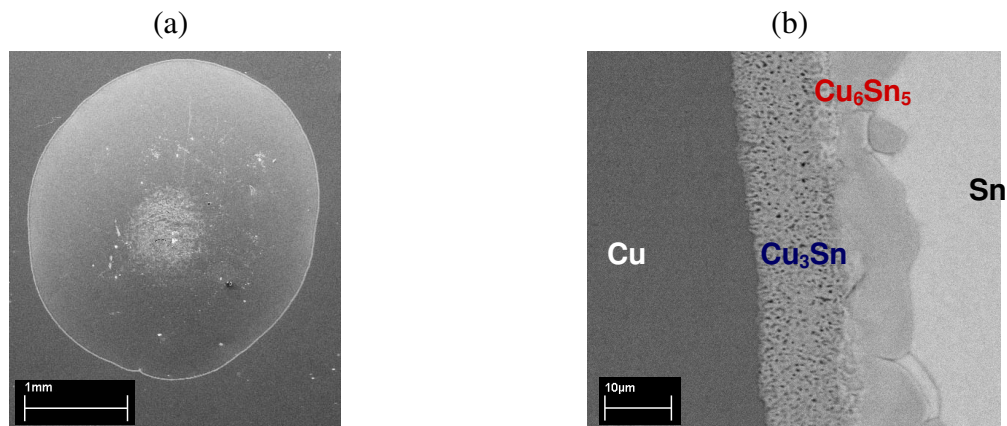


Figure 3-15. SEM micrographs of the top-view on the droplet deposited by transferred drop technique at 250°C and subsequent isothermal holding for 11 min under  $2 \times 10^{-5}$  Pa vacuum. General view (a) and triple line configuration (b).

The cross-section analysis of the same droplet (see Figure 3-16) shows the formation of a thin planar layer close to the Cu substrate that is the  $\epsilon$ -Cu<sub>3</sub>Sn compound (see Figure 1-22) and a thick scallop-like layer on the Sn side that is identified as  $\eta$ -Cu<sub>6</sub>Sn<sub>5</sub> phase. As it can be seen from this figure, no evidence of a significant dissolutive wetting is seen at that temperature as far as the  $\epsilon$ -Cu<sub>3</sub>Sn/Cu boundary seems to be relatively planar and the bulk of the solidified Sn is free from large Cu<sub>6</sub>Sn<sub>5</sub> precipitates. This is due to the low experimental  $T$  as well as to the low solubility limit of Cu in liquid Sn at 250°C (less than about 5at.% [Saunders\_1997]).

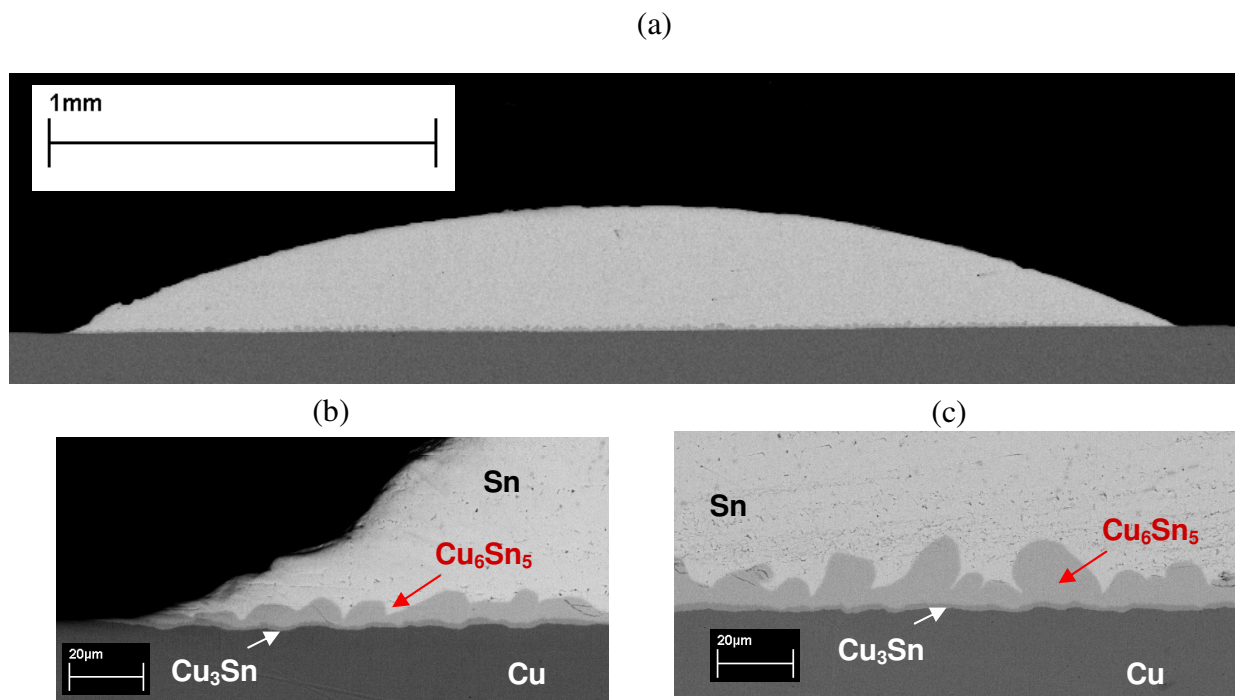


Figure 3-16. SEM micrographs of the droplet deposited by dispensed drop technique at 250°C and subsequent isothermal holding for 11 min under  $2 \times 10^{-7}$  mbar vacuum. General view (a), triple line configuration (b) and magnification of the section of the droplet at its central zone (c).

In its turn the cross-section of the droplet deposited at 400°C after preheating procedure - referred as 4<sup>th</sup> droplet on the Figure 3-3b (see Figure 3-17) revealed a strong dissolution process that happened during the stage of spreading (that lasts about 5 s - see Figure 3-4a), but also and above all during the interaction for times longer than 5 s where no significant spreading occurs. Indeed, for this experiment, during 35 minutes down to the solidification temperature the triple line advances only about 150  $\mu\text{m}$ .

The important dissolution of Cu in liquid Sn is testified by the existence of numerous large  $\text{Cu}_6\text{Sn}_5$  precipitates inside the drop bulk, which are formed during cooling of Sn-Cu liquid alloy. It is interesting to note that the Cu/droplet interface in the region of about 200  $\mu\text{m}$  close to the triple line is not planar (see Figure 3-17c) and has a profile similar to the dissolutive wetting profile described in [Eustathopoulos\_1999].

It is noted also the formation of two intermetallic layers at the interface:  $\epsilon$ - $\text{Cu}_3\text{Sn}$  layer of average thickness of about 6  $\mu\text{m}$  and a scalloped  $\eta$ - $\text{Cu}_6\text{Sn}_5$  layer of average thickness of about 12  $\mu\text{m}$  (see Figure 3-17b).

The same comments done for the droplet deposited at 400°C are valid for the droplet deposited at 300°C (see Figure 3-18). The only difference between two samples is that the dissolution process is much lower at 300°C compared to 400°C (the thickness of intermetallic layers formed at the interface at 300°C is also lower (factor  $\sim 1.2$ )).

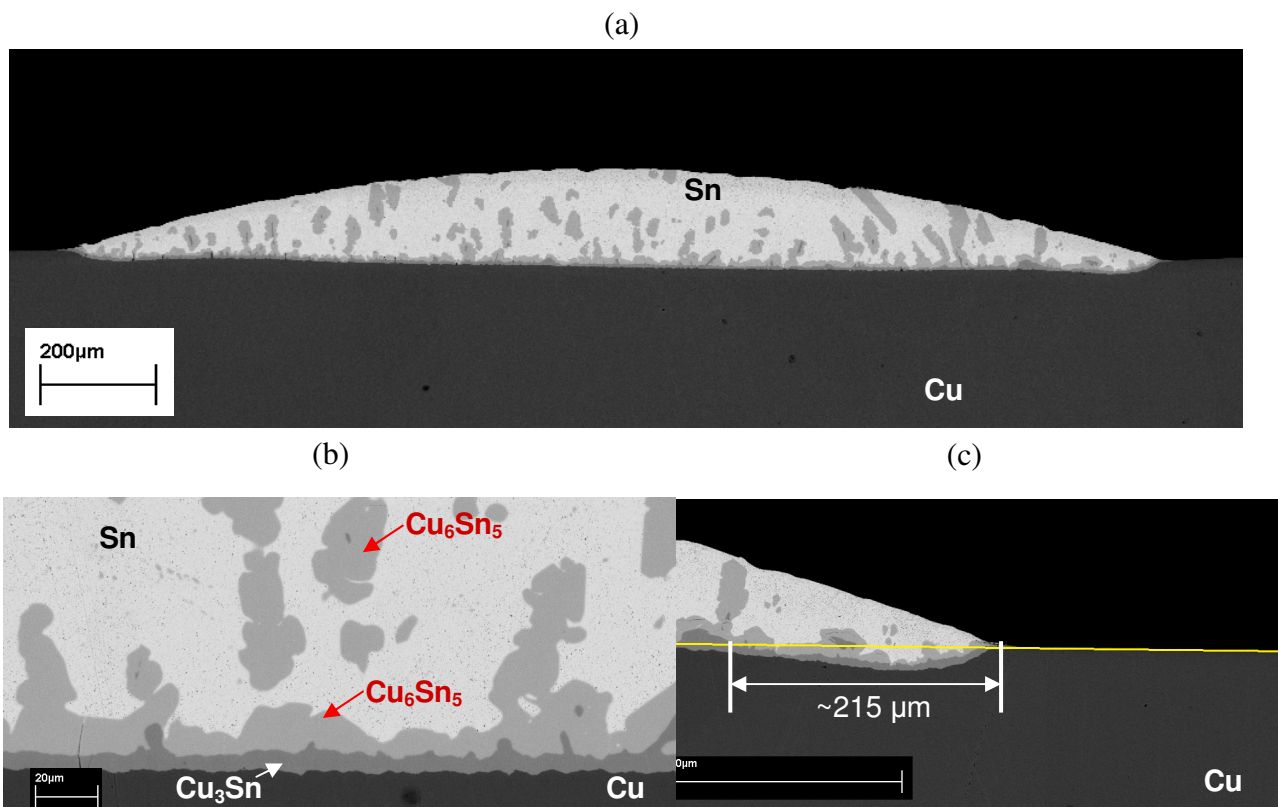


Figure 3-17. Cross-section of the interface between tin droplet and copper substrate at 400°C after wetting experiment with preheating. The first measured contact angle is 28° and the final contact angle of 23° was reached after 1.5 s of spreading (see Figure 3-4a). The drop was maintained for 3 min at 400°C and then cooled (see Figure 3-3b).

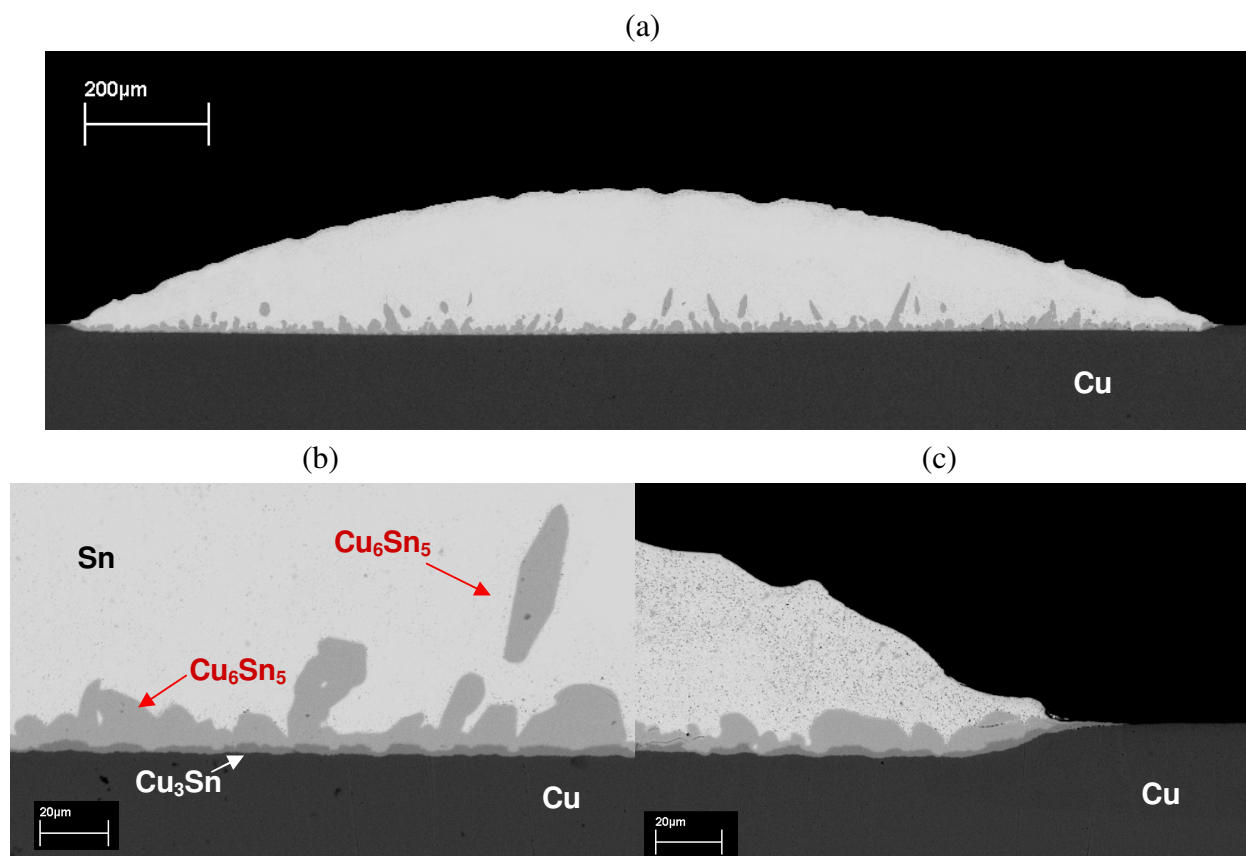


Figure 3-18. Cross-section of the interface between tin droplet and copper substrate at 300°C after wetting experiment with preheating.

## 2-4) Conclusions

Wetting experiments of a preheated Cu substrate by a pre-saturated Sn-7.8wt.%Cu liquid alloy at 390°C show that the spreading of the liquid droplet occurs in less 10 ms. Afterwards the liquid droplet oscillates during about 0.1 s around the final position that corresponds to a measured contact angle of about 27°. The frequency of these oscillations is about 150 s<sup>-1</sup>. The reproducibility of experimental results was checked by comparison of the spreading characteristics for two droplets deposited under the same experimental conditions.

Wetting experiments of preheated Cu substrates by liquid Sn at temperatures from 300 to 600°C show that the first stage of spreading down to a contact angle of about 30° in less than 10 ms can be attributed to the non reactive wetting of liquid Sn on the Cu surface. During this first stage, the spreading kinetics is practically temperature independent and it is similar to the spreading kinetics of non reactive Pb liquid droplets on Cu substrate at 400°C. Given the fact that these wetting experiments are performed with Cu surface that could be not exempted completely of oxide nanoparticles it can be concluded that the value of the equilibrium contact angle of liquid Sn on a non reacted and clean Cu surface is less than 30°.

The very rapid and non reactive spreading stage can be followed by the reactive spreading stage that can correspond to the dissolution of Cu substrate on the liquid drop and/or to the formation of reactive Cu<sub>3</sub>Sn and Cu<sub>6</sub>Sn<sub>5</sub> layers at Cu/Sn interface. Indeed, for the contact time longer than 10 ms and experimental temperature higher than 390°C a second spreading stage is observed. Especially at  $T = 400^\circ\text{C}$  a final contact angle of about 23° is attained in about 3 s.

The possible role of the interfacial reactive layers on the wetting process will be studied in the next sections.

## 3) **Wetting of Cu<sub>3</sub>Sn by liquid Sn**

### 3-1) Introduction

As in the case of Cu substrate, the wetting of Cu<sub>3</sub>Sn was studied on the non preheated or preheated substrate. The temperature of preheating process under high vacuum was chosen to be equal to 600°C in order to be lower than the decomposition temperature of Cu<sub>3</sub>Sn compound (640°C - see Figure 1-22 for the Cu-Sn phase diagram).

The investigation of wetting experiments is performed by using either a conventional camera either a rapid camera for the same reasons as in the case of Cu substrate.

### 3-2) Investigation of wetting of Cu<sub>3</sub>Sn by using a conventional camera

#### 3-2-1) Experiments without preheating of the Cu<sub>3</sub>Sn substrate

Figure 3-19 gives the temperature-time profile for two sets of experiments during which 7 wetting experiments were performed at temperatures from 250 to 600°C.

For  $T = 250^\circ\text{C}$  and  $300^\circ\text{C}$  two wetting experiments were performed (1<sup>st</sup> and 2<sup>nd</sup> drop on Figure 3-19a and 3<sup>rd</sup>, 4<sup>th</sup> drops on Figure 3-19b).

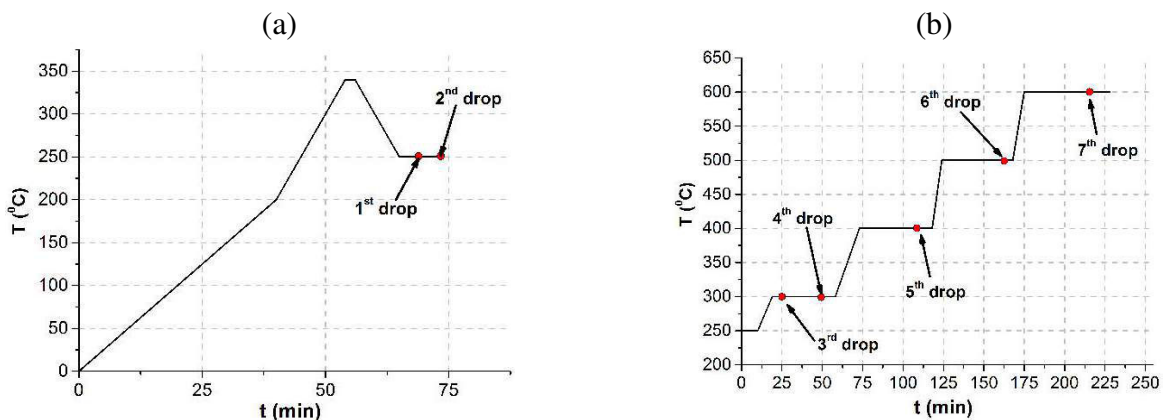


Figure 3-19. Temperature-time profile during two sets of experiments. Wetting of Cu<sub>3</sub>Sn substrate. by liquid Sn at different temperature.

Figure 3-20 gives the spreading curves corresponding to the experiments performed at 250, 300 and 350°C. These curves show that the first measured contact angle values (in 40 ms) are very high for low temperatures:  $\theta_0 = 125$  and  $76^\circ$  at 250 and 300°C respectively. Afterwards, the contact angle decreases rapidly to about  $40^\circ$  in about 10s. Finally a slow spreading stage is observed at 300°C down to  $\theta = 30^\circ$  in some minutes.

The very high values of the first measured contact angle at 250°C ( $\theta_0 = 125^\circ$ ) corresponds undoubtedly to the equilibrium contact angle of liquid tin on an oxide surface. Indeed, it is well known that the equilibrium contact angle of non reactive liquid metals on oxide surfaces such as  $\text{Al}_2\text{O}_3$ ,  $\text{Cu}_2\text{O}$ ,  $\text{SnO}_2$ ,  $\text{MgO}$ ,  $\text{SiO}_2$ ... are as high as  $120$ - $140^\circ$  [Eustathopoulos\_1999].

The rapid decrease of the contact angle with time corresponds to the destruction of the native oxide layer by interaction with the liquid phase.

The same comments are valid for the experiment performed at 300°C.

At  $T = 400^\circ\text{C}$ , the first measured contact angle in 40 ms is  $37^\circ$ , this value is close to those obtained at 250 and 300°C after some seconds of interaction between liquid Sn and substrate. We will discuss in the next section the physical meaning of this contact angle value (about  $40^\circ$ ). Afterwards, the contact angle decreases from  $37^\circ$  to about  $25^\circ$  in about 5 minutes.

Note that at  $T = 250$  to  $400^\circ\text{C}$ , liquid Sn can react with  $\text{Cu}_3\text{Sn}$  substrate and forms the interfacial reaction compound  $\text{Cu}_6\text{Sn}_5$ . While for  $T > 415^\circ\text{C}$ , no reactive compound is formed between liquid Sn and  $\text{Cu}_3\text{Sn}$  (see Figure 1-22), only dissolution of  $\text{Cu}_3\text{Sn}$  in liquid Sn occurs.

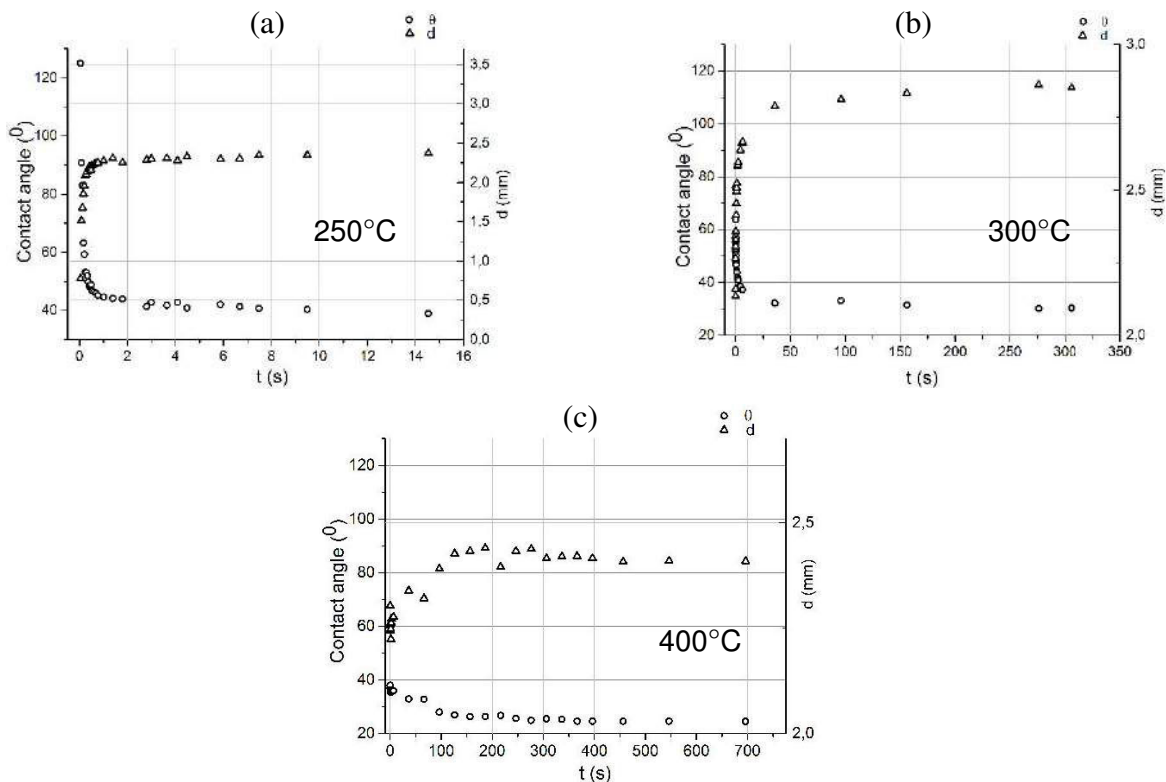
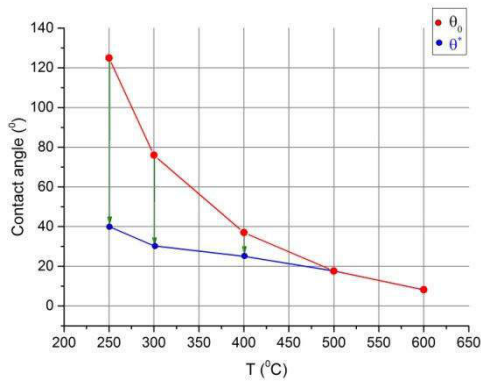


Figure 3-20. Variation of the contact angle and drop base diameter with time during wetting of  $\text{Cu}_3\text{Sn}$  by liquid Sn at  $T = 250, 300$  and  $400^\circ\text{C}$  without preheating.

Contrary to the experiments performed at temperature lower than  $400^\circ\text{C}$ , the high temperature experiments show very low values of the first measured contact angle in 40 ms ( $\theta_0 = 18^\circ$  at  $500^\circ\text{C}$  and  $\theta_0 = 8^\circ$  at  $600^\circ\text{C}$ ) and no spreading kinetics was observed in about 5 minutes.

Figure 3-21 summarizes the first measured contact angle in 40 ms ( $\theta_0$ ) and the “final” measured contact angle (noted  $\theta^*$ ) after 5 minutes of contact between liquid Sn and Cu<sub>3</sub>Sn substrate.



T(°C)	250	300	400	500	600
$\theta_0$ (°)	120	125	76	45	37
$\theta^*$ (°)	40	40	30	33	25

Figure 3-21. Wetting of Cu<sub>3</sub>Sn by Sn without preheating of the substrate. Variation with temperature of the first measured contact angle in 40 ms ( $\theta_0$ ) and final measured contact angle  $\theta^*$  measured after 5 minutes of contact.

### 3-2-2) Experiments with preheating of the Cu<sub>3</sub>Sn substrate

Figure 3-22 gives the temperature-time profile for wetting experiments with Cu<sub>3</sub>Sn substrate preheated at 600°C under vacuum for 1 h.

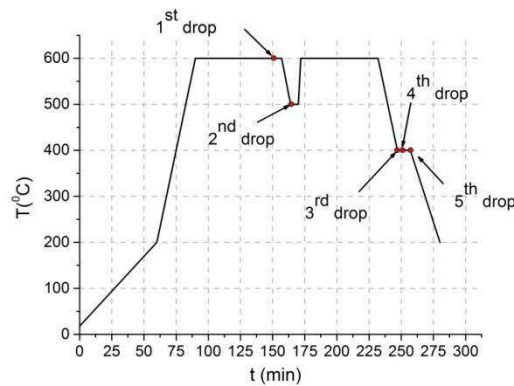


Figure 3-22. Temperature-time profile of wetting experiments with the Cu<sub>3</sub>Sn substrate.

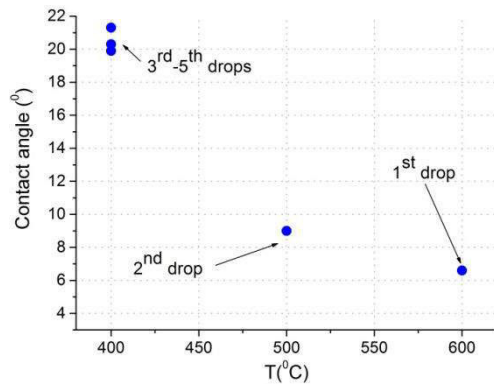
For all wetting experiments performed at 400, 500 and 600°C the spreading was instantaneous (in 40 ms) and no evolution of the contact angle was observed during 5 minutes. These first measured values of contact angles (in 40 ms) at different temperatures are summarized in Figure 3-23.

Comparison of Figure 3-23 with Figure 3-21 clearly indicate the role of the preheating of the Cu<sub>3</sub>Sn substrate on the wetting kinetics as well as on the values of the final contact angles and thus the role of the surface deoxidation. For this reason, in the next section, wetting experiments followed by the rapid camera will be performed only on preheated Cu<sub>3</sub>Sn substrates.

### 3-3) Investigation of wetting by using a rapid camera

These wetting experiments were performed on Cu<sub>3</sub>Sn substrates initially preheated at 600°C. The temperature-time profile of wetting experiments is given in Figure 3-24.

Figure 3-25 gives the spreading kinetics of Sn droplets at different temperatures. As in the case of liquid Sn/Cu substrate experiments (see Figure 3-12) it is interesting to note that, whatever the experimental temperature, the contact angle decreases very rapidly from the first measured value (about 55 to 70°) at 0.2 ms down to a “limit” value (about 10 to 20°) in a time less than 10 ms and afterwards it oscillates around this “limit” value noted  $\theta^*$ . This limit value is about 10° at 500° and 600°C, about 15° at 390°C and 20° at 300°C.



$T(^{\circ}\text{C})$	400			500	600
$\theta_0(^{\circ})$	20	20	21	9	7

Figure 3-23. First measured contact angles in 40 ms ( $\theta_0$ ) versus temperature for the Sn droplets deposited on  $\text{Cu}_3\text{Sn}$  substrate preheated at  $600^{\circ}\text{C}$  under vacuum (see Figure 3-22). The wetting is instantaneous (in 40 ms) and no evolution of the contact angle was observed during 5 minutes of isothermal holding.

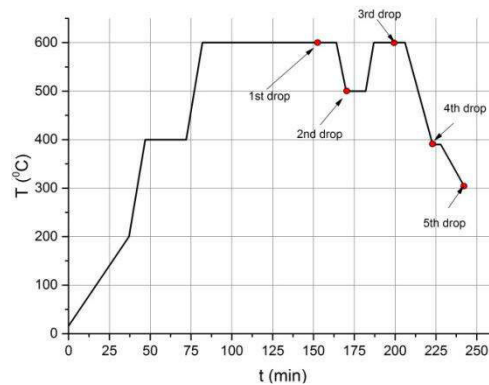


Figure 3-24. Temperature-time profile of wetting experiment with  $\text{Cu}_3\text{Sn}$  substrate and liquid Sn at different temperatures after preheating at  $600^{\circ}\text{C}$ .

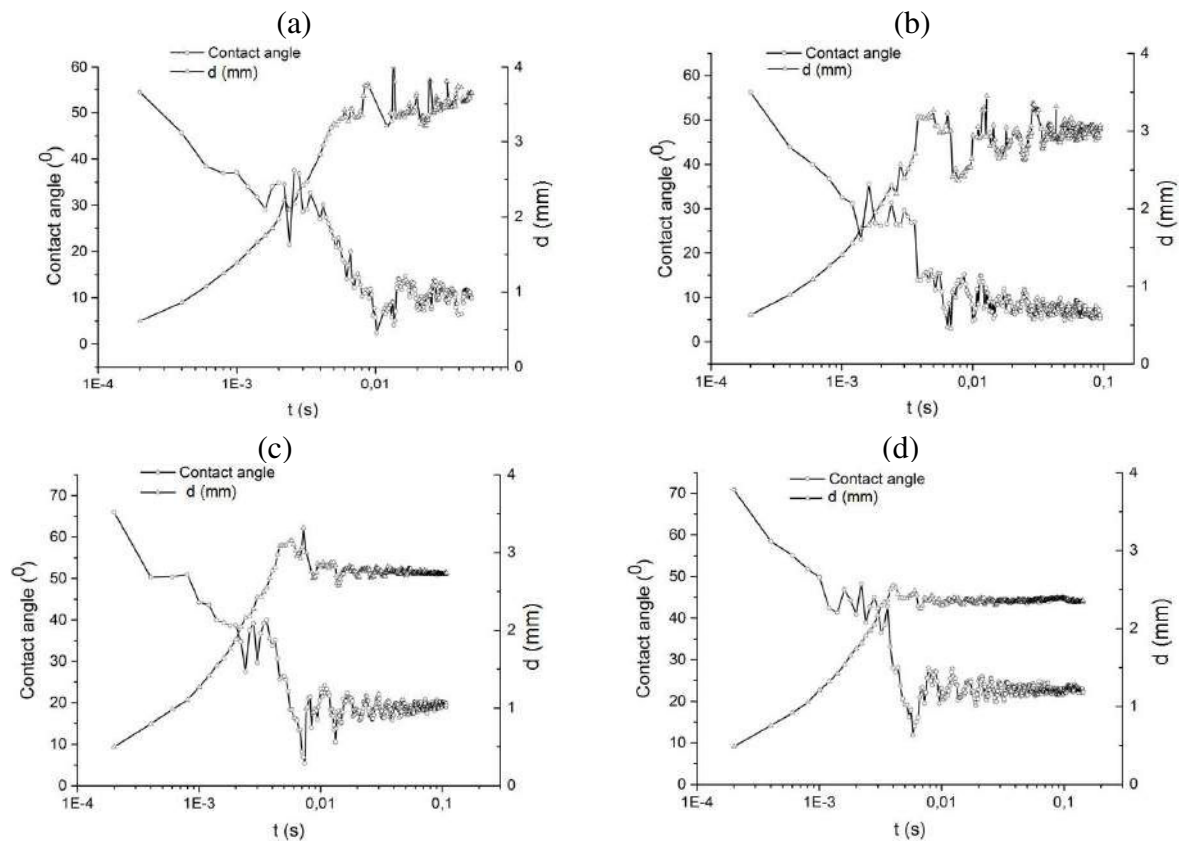
Note that these values are in agreement with those obtained from experiments followed by the conventional camera (see Figure 3-23) showing that the contact angle of liquid Sn on  $\text{Cu}_3\text{Sn}$  surface decreases with temperature. As it was already discussed in section 2-3-3-2, this “limit” value corresponds to the equilibrium contact angle of liquid Sn on the  $\text{Cu}_3\text{Sn}$  surface at the considered temperature. The question about the  $\text{Cu}_3\text{Sn}$  surface exempt of oxide particles will be discussed at the end of this Chapter.

#### 3-4) Characterization of some selected samples

Figure 3-26 gives some micrographs of the sample corresponding to the wetting experiment on  $\text{Cu}_3\text{Sn}$  substrate performed at  $250^{\circ}\text{C}$  without preheating of the substrate (2<sup>nd</sup> Sn drop in Figure 3-19). The contact time at  $250^{\circ}\text{C}$  was 5 minutes and the cooling time from  $250$  to  $200^{\circ}\text{C}$  was about 15 minutes.

A top view of the sample, given in Figure 3-26a, shows that the deposited droplet had a perfectly circular form. Halos with fine-grained  $\text{Cu}_6\text{Sn}_5$  phase are detected on the very edge of the droplet (see Figures 3-26b,c). Single large grains of the  $\text{Cu}_6\text{Sn}_5$  are detected as well by EDX analysis. These large grains can be attributed to the single scallop-type  $\text{Cu}_6\text{Sn}_5$  crystals, formed at the interface by reaction between  $\text{Cu}_3\text{Sn}$  and Sn, that are not covered totally by the solidified tin bulk (see Figures 3-26b,c).

Figures 3-26d,e,f give SEM micrographs of cross-section of the droplet/ $\text{Cu}_3\text{Sn}$  sample at different magnification. These figures clearly show the continuous and not homogenous in thickness reaction layer of  $\text{Cu}_6\text{Sn}_5$  phase formed by reaction between Sn and  $\text{Cu}_3\text{Sn}$ . The average thickness of the reaction layer was about  $10\ \mu\text{m}$ .



$T(^{\circ}\text{C})$	300	390	500	600
$\theta^*(^{\circ})$	23	19	7	10

Figure 3-25. Spreading kinetics of Sn droplets on  $\text{Cu}_3\text{Sn}$  substrates: variation with time of the contact angle and the drop base diameter at different temperatures: (a)  $600^{\circ}\text{C}$ , (b)  $500^{\circ}\text{C}$ , (c)  $390^{\circ}\text{C}$ , (d)  $300^{\circ}\text{C}$ .

Note that the quantity and the size of  $\text{Cu}_6\text{Sn}_5$  precipitates in the drop bulk was very low which is due to the low limit solubility of Cu in Sn at  $250^{\circ}\text{C}$  (about 1.4wt.%Cu) but also to the low dissolution kinetics of  $\text{Cu}_3\text{Sn}$  in liquid Sn which in this case is limited by the diffusion of Cu through the continuous  $\text{Cu}_6\text{Sn}_5$  layer.

Figure 3-27 gives SEM micrograph of the sample corresponding to the wetting experiment performed at  $300^{\circ}\text{C}$ . This sample corresponds to the 5<sup>th</sup> drop of Figure 3-24, the time of reaction at  $300^{\circ}\text{C}$  is 5 minutes and the time during cooling from  $300$  to  $200^{\circ}\text{C}$  is evaluated to be about 20 minutes. As in the case of  $T = 250^{\circ}\text{C}$ , the deposited droplet had a circular form (see Figure 3-27a) and a  $\text{Cu}_6\text{Sn}_5$  reaction layer of thickness about  $20\ \mu\text{m}$  was formed at the interface.

From Figure 3-27b it can be seen that  $\text{Cu}_3\text{Sn}$  substrate was dissolved in liquid Sn which is testified by the presence of large particles of  $\text{Cu}_6\text{Sn}_5$  phase inside the drop bulk (see Figures 27c,d). Even if the contact time at  $300^{\circ}\text{C}$  is lower than that at  $250^{\circ}\text{C}$ , the quantity of diluted Cu in liquid Sn is higher at  $300^{\circ}\text{C}$ , which is due to a higher Cu solubility limit (2 wt.% at  $300^{\circ}\text{C}$  against 1.4wt.% at  $250^{\circ}\text{C}$ ) as well as to a higher dissolution kinetics.

Cross-sections of the droplet deposited at  $400^{\circ}\text{C}$  (corresponding to the 4<sup>th</sup> droplet of Figure 3-24) reveal the formation of a “scalped”  $\text{Cu}_6\text{Sn}_5$  reaction layer and a large quantity of  $\text{Cu}_6\text{Sn}_5$  precipitates inside the drop bulk (Figure 3-28). The reaction time at  $400^{\circ}\text{C}$  was about 8 min and the time during cooling from  $400^{\circ}\text{C}$  to  $200^{\circ}\text{C}$  was about 35 min.

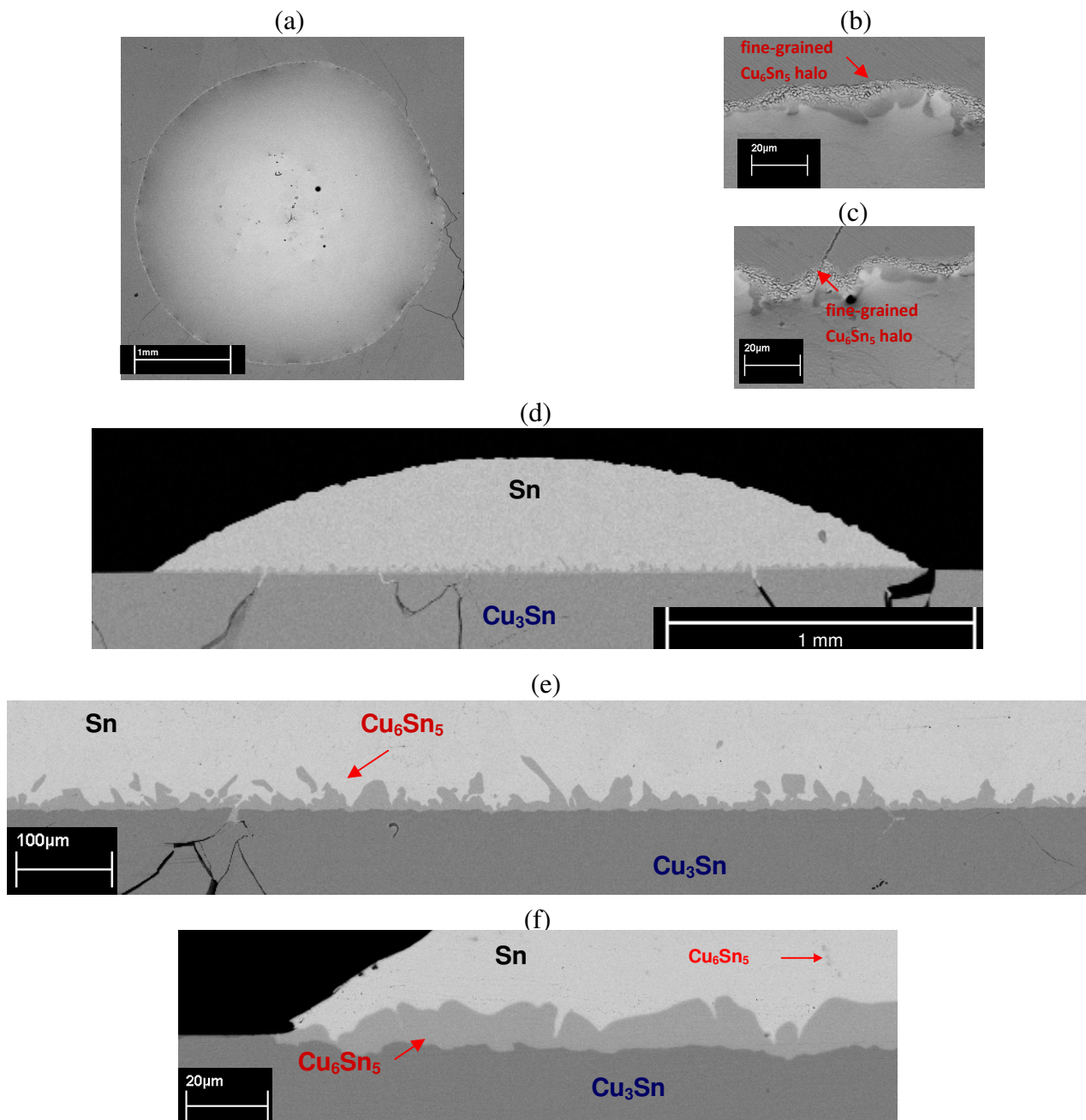


Figure 3-26. Top-view SEM images of Sn droplet on  $\text{Cu}_3\text{Sn}$  substrate deposited at  $250^\circ\text{C}$  (a,b,c). Cross-section of the interface between tin droplet and  $\text{Cu}_3\text{Sn}$  substrate at  $250^\circ\text{C}$  (d,e,f).

Figure 3-29 gives cross sections of the droplet deposited at  $600^\circ\text{C}$  (corresponding to the 3<sup>rd</sup> droplet of Figure 3-24). The reaction time at  $600^\circ\text{C}$  was about 8 min and the time during cooling from  $600^\circ\text{C}$  to  $200^\circ\text{C}$  is evaluated to be about 55 min. This figure clearly shows a strong dissolution of  $\text{Cu}_3\text{Sn}$  substrate in liquid Sn (the limit solubility of Cu in liquid Sn at  $600^\circ\text{C}$  being very high - about 30wt.%).

The solidification of the droplet from  $600^\circ\text{C}$  firstly leads to the precipitation of primary  $\text{Cu}_3\text{Sn}$  particles (see Figure 1-22). Afterwards, at  $T = 415^\circ\text{C}$  the Cu-Sn system undergoes the peritectic transformation:  $\text{Cu}_3\text{Sn} + \text{liq} \rightarrow \text{Cu}_6\text{Sn}_5$  which leads to the formation of a  $\text{Cu}_6\text{Sn}_5$  layer around the primary  $\text{Cu}_3\text{Sn}$  particles (see Figure 3-29b)

Note that, small precipitates of the  $\eta$ - $\text{Cu}_6\text{Sn}_5$  phases were as well detected in the bulk of the  $\epsilon$ - $\text{Cu}_3\text{Sn}$  substrate (see Figure 3-29d). This can be due to the  $\text{Cu}_3\text{Sn}$  grain boundary wetting and penetration by the liquid Sn followed by the subsequent reaction between  $\epsilon$ - $\text{Cu}_3\text{Sn}$  and Sn during cooling leading to the formation of the  $\eta$  -  $\text{Cu}_6\text{Sn}_5$  phase (see above).

These micrographs clearly indicate once more the very good wetting of  $\text{Cu}_3\text{Sn}$  substrate by liquid Sn as it was observed by wetting experiments.

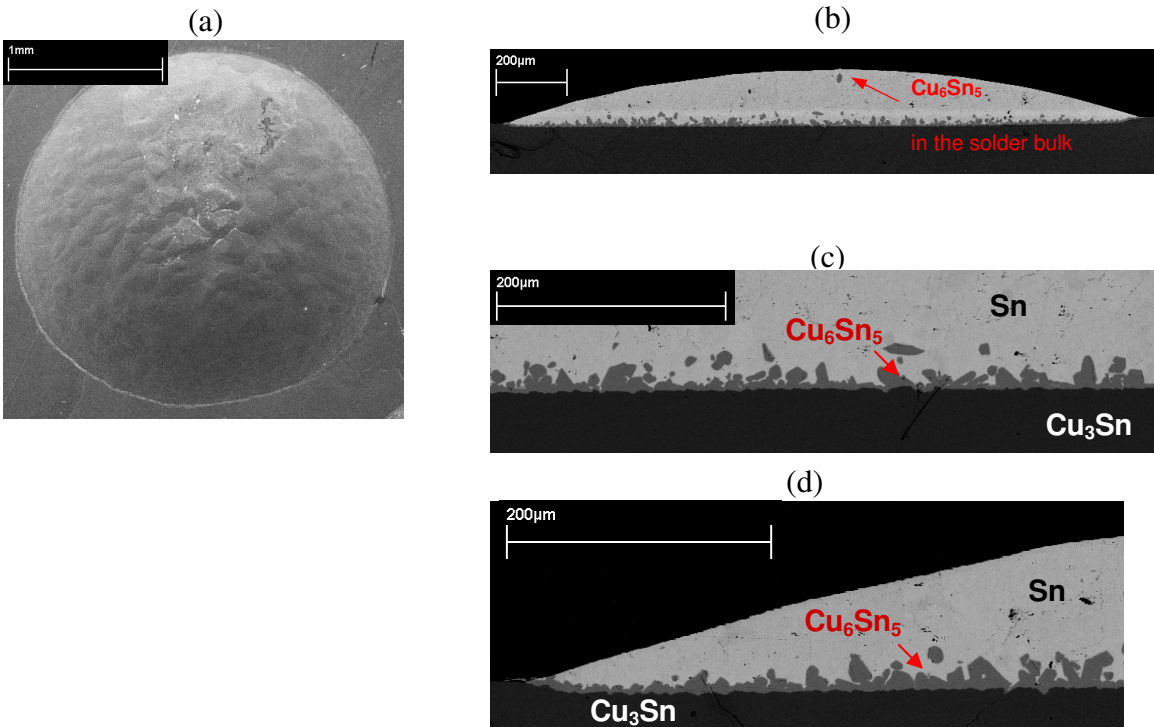


Figure 3-27. SEM micrographs of the Sn droplet deposited on the bulk  $\text{Cu}_3\text{Sn}$  surface at  $300^\circ\text{C}$ .

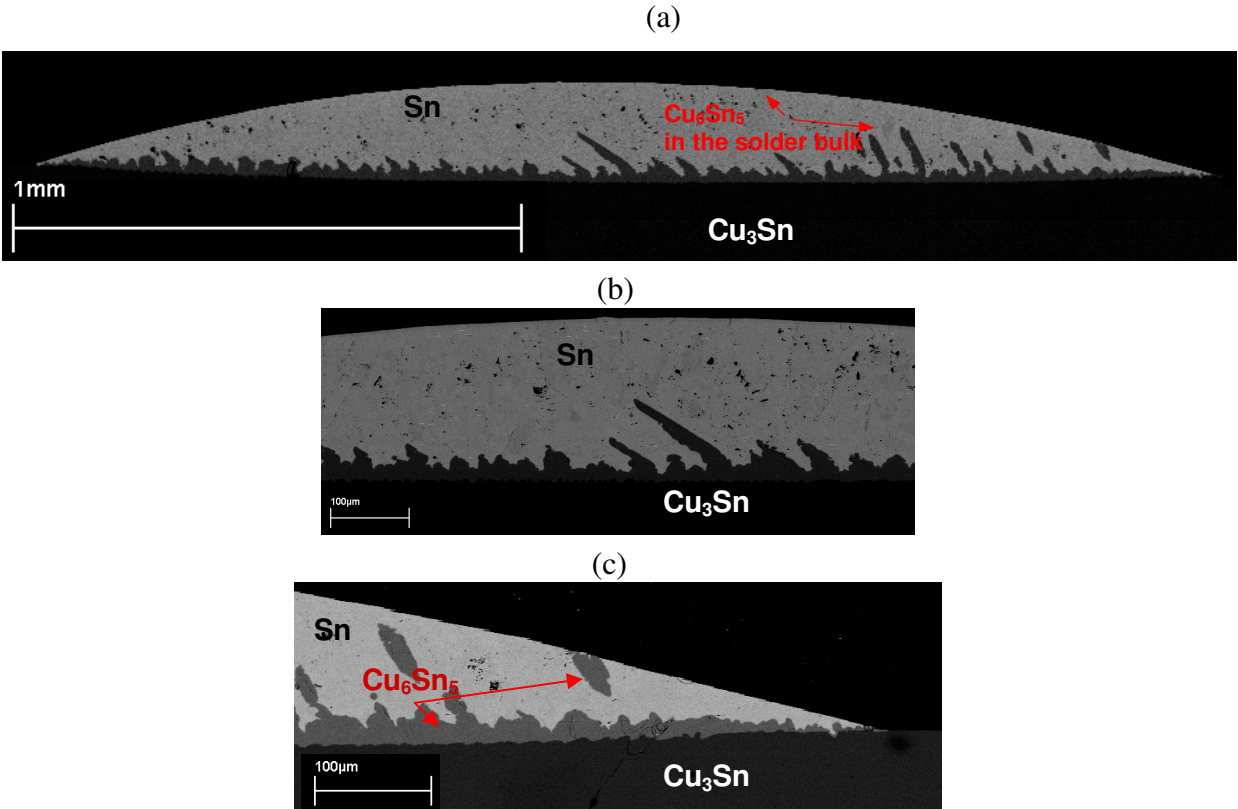


Figure 3-28. Cross-section of the interface between tin droplet and  $\text{Cu}_3\text{Sn}$  substrate at  $400^\circ\text{C}$  for wetting experiment with preheating. No dissolution is detected in the vicinity of the triple line as in case of Cu and Sn at  $400^\circ\text{C}$  with preheating.

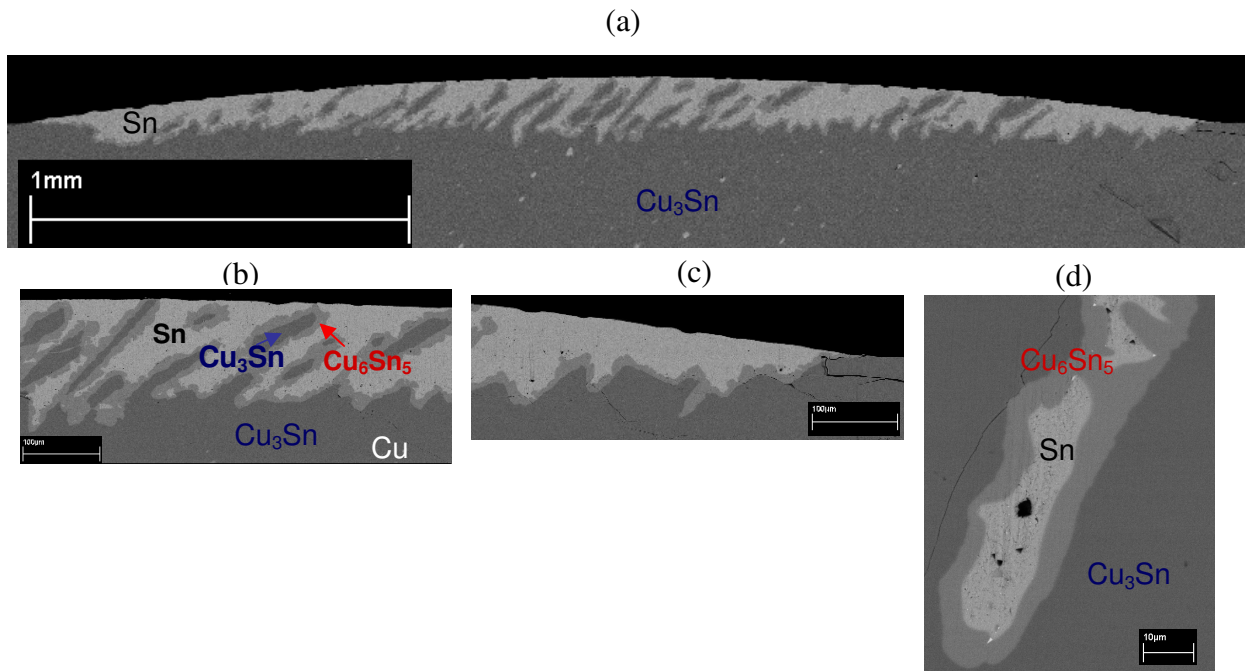


Figure 3-29. Cross-section of the interface between tin droplet and  $\text{Cu}_3\text{Sn}$  substrate at  $600^\circ\text{C}$  for wetting experiment without preheating. The infiltration of tin is detected in the bulk of  $\text{Cu}_3\text{Sn}$ .

### 3-5) Conclusions

Wetting experiments of liquid Sn on  $\text{Cu}_3\text{Sn}$  substrate at temperatures between  $250$  and  $600^\circ\text{C}$  had been performed for the first time by the dispensed drop technique.

Investigations of wetting by using a conventional camera showed that for not preheated substrate, the first measured contact angle values (in 40 ms) are very high for low temperatures:  $\theta_0 = 125^\circ$  at  $250^\circ\text{C}$  and  $\theta_0 = 76^\circ$  at  $300^\circ\text{C}$ .  $\theta = 125^\circ$  corresponds to the equilibrium contact angle of liquid Sn on an oxide surface whereas  $\theta = 76^\circ$  corresponds to the equilibrium contact angle of liquid Sn on a composite surface  $\text{Cu}_3\text{Sn} + \text{oxide}$ . Afterwards, in both cases the contact angle decreased rapidly to about  $40^\circ$  in about 10s. Finally a slow spreading stage is observed only at  $300^\circ\text{C}$  down to  $\theta = 30^\circ$  in some minutes. The decrease of the contact angle corresponds to the destruction of the oxide native layer by interaction with liquid phase that depends on the thickness of the native oxide layer and the experimental temperature. Thus the final contact angle of liquid Sn on  $\text{Cu}_3\text{Sn}$  at  $250$ ,  $300$  and  $400^\circ\text{C}$  is about  $40^\circ$ ,  $30^\circ$  and  $25^\circ$ , which reflects the fact that the surface deoxidation is more efficient with increasing experimental temperature.

For preheated  $\text{Cu}_3\text{Sn}$  substrate, the first contact angle at  $400^\circ\text{C}$  (in 40 ms) is  $20^\circ$  much lower than the first measured contact angle at the same temperature obtained in the case without heat treatment ( $37^\circ$ ) meaning that, starting from  $400^\circ\text{C}$ , the heat treatment under vacuum of  $\text{Cu}_3\text{Sn}$  at  $600^\circ\text{C}$  has an impact on its surface deoxidation.

Investigation of wetting by using a rapid camera clearly indicate that the non reactive contact angles of liquid Sn on a  $\text{Cu}_3\text{Sn}$  surface preheated at  $600^\circ\text{C}$ , obtained after less than 10 ms of spreading, strongly depend on the experimental temperature: about  $10^\circ$  at  $500$  and  $600^\circ\text{C}$ ,  $19^\circ$  at  $390^\circ\text{C}$  and  $23^\circ$  at  $300^\circ\text{C}$ . From our experiments, it is difficult to determine the exact role of temperature on the intrinsic equilibrium angle of liquid Sn on a clean  $\text{Cu}_3\text{Sn}$  surface and on a partially oxidized  $\text{Cu}_3\text{Sn}$  surface. However, the fact that the different interfacial energies do not strongly depend on temperature [Eustathopoulos\_1999] suggests that the observed effect of temperature could mainly be due to the  $\text{Cu}_3\text{Sn}$  surface deoxidation. In any case, the non reactive equilibrium contact angles of liquid Sn on  $\text{Cu}_3\text{Sn}$  surface are always lower than those on Cu surface (about  $30^\circ$  whatever the temperature between  $300$  and  $600^\circ\text{C}$ ).

#### 4) Wetting of $\text{Cu}_6\text{Sn}_5$ substrates

##### 4-1) Introduction

Given the fact that no reaction layer is formed between liquid Sn or Sn-Cu alloys and  $\text{Cu}_6\text{Sn}_5$  substrate (see Figure 1-22), we are interested here especially on the first stage of non reactive spreading of the liquid Sn on  $\text{Cu}_6\text{Sn}_5$  substrate. During and/or after this first spreading stage, dissolution of  $\text{Cu}_6\text{Sn}_5$  in the liquid Sn-Cu alloy may occur if this alloy is not saturated with Cu. Thus, in order to avoid the dissolution of Cu in liquid alloy, a presaturated Sn-Cu alloy should be used.

Note also that  $\text{Cu}_6\text{Sn}_5$  phase is not stable at  $T \geq 415^\circ\text{C}$  (see Figure 1-22) because at  $T = 415^\circ\text{C}$  it undergoes a peritectic decomposition:  $\text{Cu}_6\text{Sn}_5 \rightarrow \text{Cu}_3\text{Sn} + \text{liquid}$ . Thus the experimental  $T$  should be lower than  $415^\circ\text{C}$ . We choose to perform wetting experiments at relatively high temperature ( $390^\circ\text{C}$  but lower than  $415^\circ\text{C}$ ) in order to deoxidize under vacuum (if possible) the  $\text{Cu}_6\text{Sn}_5$  surface.

Moreover, we study the wetting of  $\text{Cu}_6\text{Sn}_5$  not only by pure Sn liquid but also by a presaturated Sn alloy at  $430^\circ\text{C}$  (Sn-7.8wt.%Cu) in order to avoid dissolution of  $\text{Cu}_6\text{Sn}_5$  in liquid alloy during wetting experiments.

Thus, in this section we will firstly present the wetting experiments performed at  $390^\circ\text{C}$  with a presaturated Sn-7.8wt.%Cu alloy and afterwards the wetting experiments performed at the same temperature by pure liquid Sn.

All wetting experiments on  $\text{Cu}_6\text{Sn}_5$  substrate were investigated by using a rapid camera.

##### 4-2) Wetting of $\text{Cu}_6\text{Sn}_5$ substrate by a presaturated Sn-7.8wt.%Cu alloy at $390^\circ\text{C}$

Figure 3-30 gives the temperature-time profile of the wetting experiments and shows that 3 successive droplets were deposited at  $390^\circ\text{C}$ , the first one being deposited after 4 h of isothermal holding at  $390^\circ\text{C}$ .

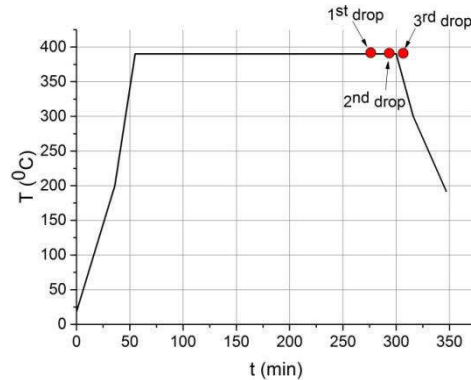


Figure 3-30. Temperature-time profile of the wetting experiment with Sn-7.8wt.%Cu droplet deposition over bulk  $\text{Cu}_6\text{Sn}_5$  substrate at  $390^\circ\text{C}$ .

Figures 3-31a,b give the variation with time of the contact angle  $\theta$  and drop base diameter  $d$  for droplets №1 and №3 respectively. Both figures show that the instantaneous contact angle decreases very rapidly to about  $20^\circ$  in less than 10 ms and afterwards it oscillates around this value. The same remark concerns the drop base radius (its maximum is attained in less than 10 ms, and then oscillates around this value).

Thus, based on three different experiments, we can deduce that the equilibrium contact angle of the liquid alloy on  $\text{Cu}_6\text{Sn}_5$  surface is about  $20^\circ$ . This value is lower than one obtained on Cu surface and close to that obtained on  $\text{Cu}_3\text{Sn}$  surface at the same temperature.

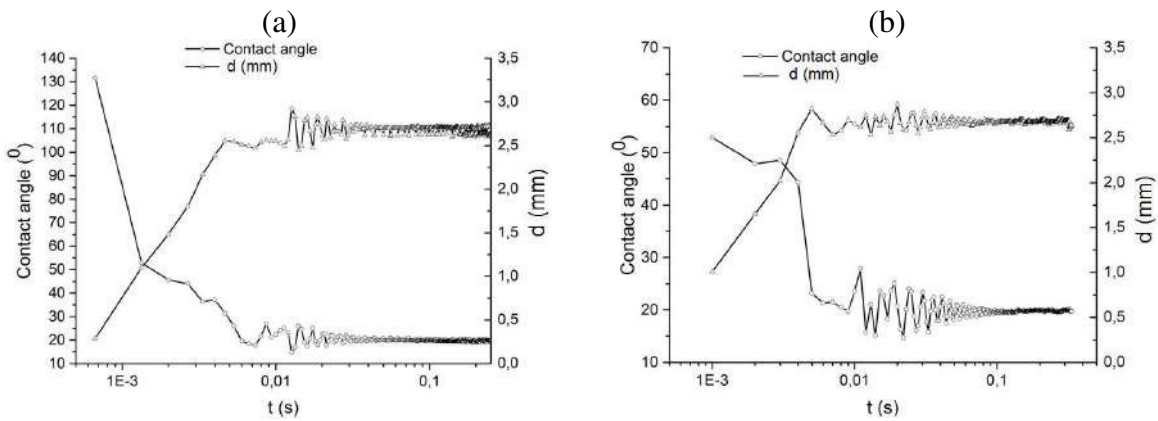


Figure 3-31. Change of the contact angle  $\theta$  and the drop base diameter with time for the Sn-7.8wt.%Cu droplets №1 (a) and №3 (b) deposited on  $Cu_6Sn_5$  substrate at  $390^\circ C$ .

Figure 3-32 gives some details over oscillations, i.e. of the variation of the contact angle (red circles, red line) and drop base diameter (blue triangles, blue lines) with time measured for the droplet №3. The peculiar moments of oscillation are pointed out and show that both contact angle and drop base diameter are varying during the oscillations. These oscillations practically disappear after about 1 s (see Figure 3-31).

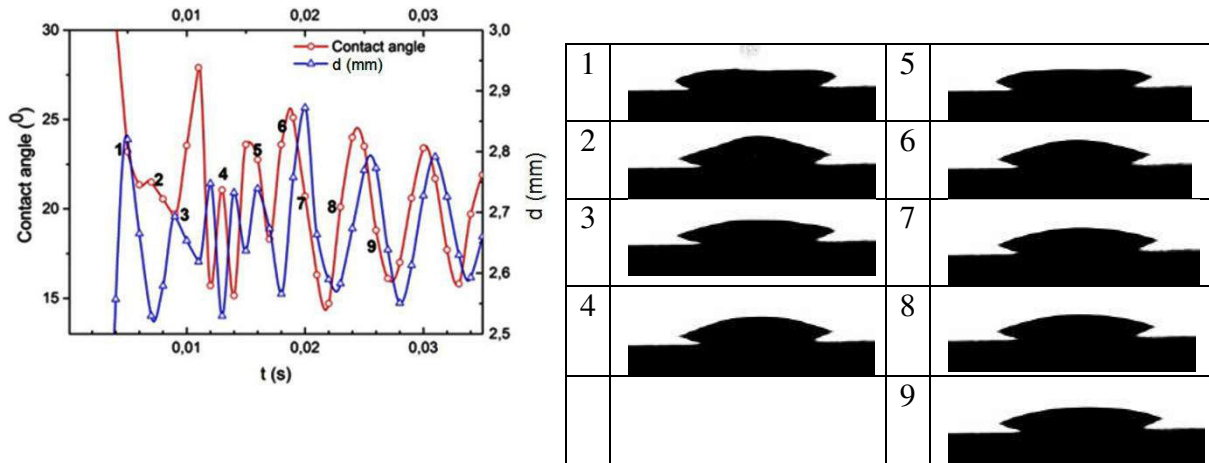


Figure 3-32. Oscillations of the deposited droplet №3 of the solder alloy Sn7.8wt.%Cu on  $Cu_6Sn_5$  at  $390^\circ C$ .

As it is shown in Figure 3-31a, the contact angle for the droplet №1 remains almost constant (about  $20^\circ$ ) for wetting time lower than 0.4 s but afterwards it starts to decrease. We continued to follow (with the rapid camera) this evolution of the contact angle with time up to about 10 s of spreading and observed a significant decrease in the drop height ( $h$ ) without any noticeable change in the base diameter of the droplet (see Figure 3-33). The last point on the graph was taken after 16 min as a snapshot. Indeed, as during these experiments we did not expect such sudden decrease of the contact angle with time we could not register other images of the drop between 10 s and 1000 s. Thus, the points in red (---) on the Figure 3-33 are just a hypothetic extrapolation of the variation of the drop height with time.

After about 16 min of contact with the  $Cu_6Sn_5$  substrate at  $390^\circ C$ , the height of the drop decreases from 0.2 mm to about 0.05 mm.

Similar behavior was obtained for the droplets №1 and №2 (significant decrease of the drop height ( $h$ ) without any noticeable change in the base diameter of the droplets) but the kinetics of the variation of  $h$  with time were not measured.

Note that the total contact time between the liquid droplets and  $Cu_6Sn_5$  substrate at  $390^\circ C$  was 35, 15 and 1 minute for droplets №1, №2 and №3 respectively. Moreover, the

additional contact time between the liquid droplets and  $\text{Cu}_6\text{Sn}_5$  substrate during cooling from  $390^\circ\text{C}$  to the Sn-Cu eutectic temperature ( $227^\circ\text{C}$ ) was about 35 minutes.

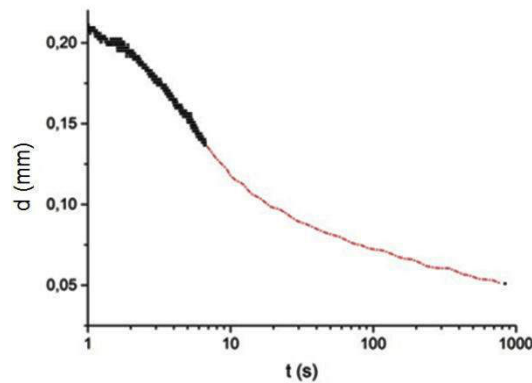


Figure 3-33. Variation of the droplet height due to the infiltration of Sn-7.8wt.%Cu liquid alloy into the  $\text{Cu}_6\text{Sn}_5$  bulk for the droplet №1 deposited at  $390^\circ\text{C}$ . The base drop diameter remains practically constant during all the time.

In order to understand the phenomenon of the drop height decreasing without variation of the drop base diameter we have performed SEM analysis of the droplets (top views - see Figure 3-34) as well as of the cross sections of the samples (see Figure 3-35).

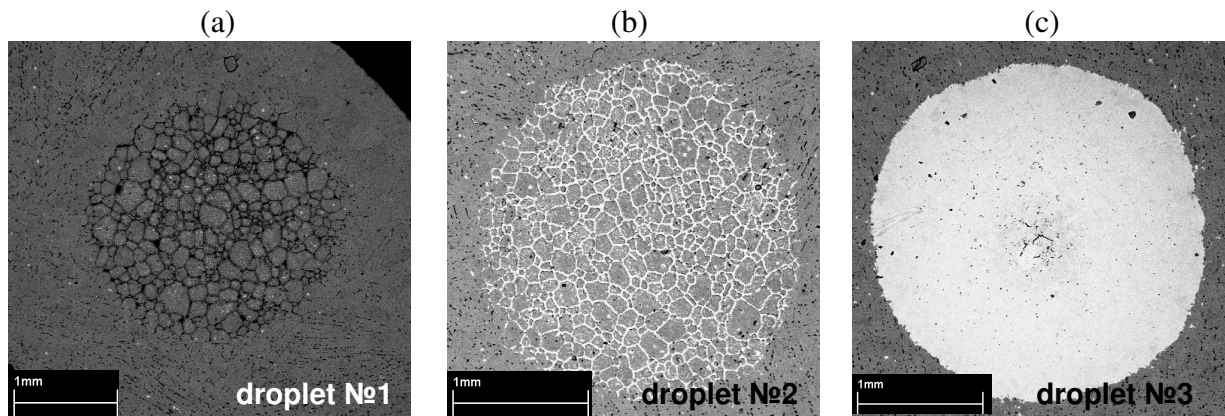


Figure 3-34. Top view on three Sn-7.8wt.%Cu droplets deposited on bulk  $\text{Cu}_6\text{Sn}_5$  substrate. The infiltration phenomena is detected with wetting of the grain boundaries. Droplets №1(a), 2(b) and 3(c). Droplet №1 was deposited on a separate substrate while droplets №2 and №3 were deposited on the same substrate.

The accurate SEM analysis of the samples has revealed that the liquid alloy is infiltrated inside the substrate to different extent (see Figures 3-34 and 3-35). Moreover, they show that the “infiltration paths” are the grain-boundaries of the  $\text{Cu}_6\text{Sn}_5$  substrate.

SEM investigations of the top-view and cross-section of the droplet №1 (see Figures 3-34 and 3-35a) show that no bulky solidified tin is observed over the  $\text{Cu}_6\text{Sn}_5$  substrate. Only small Sn precipitates are observed everywhere inside the  $\text{Cu}_6\text{Sn}_5$  substrate (not only beneath the droplet deposition place) - see Figure 3-36. The complete infiltration of the droplet №1 took approximately 30 min.

The cross-section study by SEM shown in Figure 3-35b clearly reveals a not planar solid/liquid interface indicating thus dissolution of the  $\text{Cu}_6\text{Sn}_5$  substrate (initially polished).

This rapid infiltration of the liquid alloy into the bulk  $\text{Cu}_6\text{Sn}_5$  substrate can take place by infiltration of open porosities of the  $\text{Cu}_6\text{Sn}_5$  substrate and/or by grain-boundary infiltration. As we have no data on the open porosity of  $\text{Cu}_6\text{Sn}_5$  substrate, we do not know for sure in which extent this porosity exists.

Note that infiltration can also take place by a combination of infiltration of closed porosity and wetting of grain boundaries in order to attain the next close porosity and so on.

However, the examination of Figures 34a,b strongly suggests that the infiltration takes place at least via the  $\text{Cu}_6\text{Sn}_5$  grain boundary wetting.

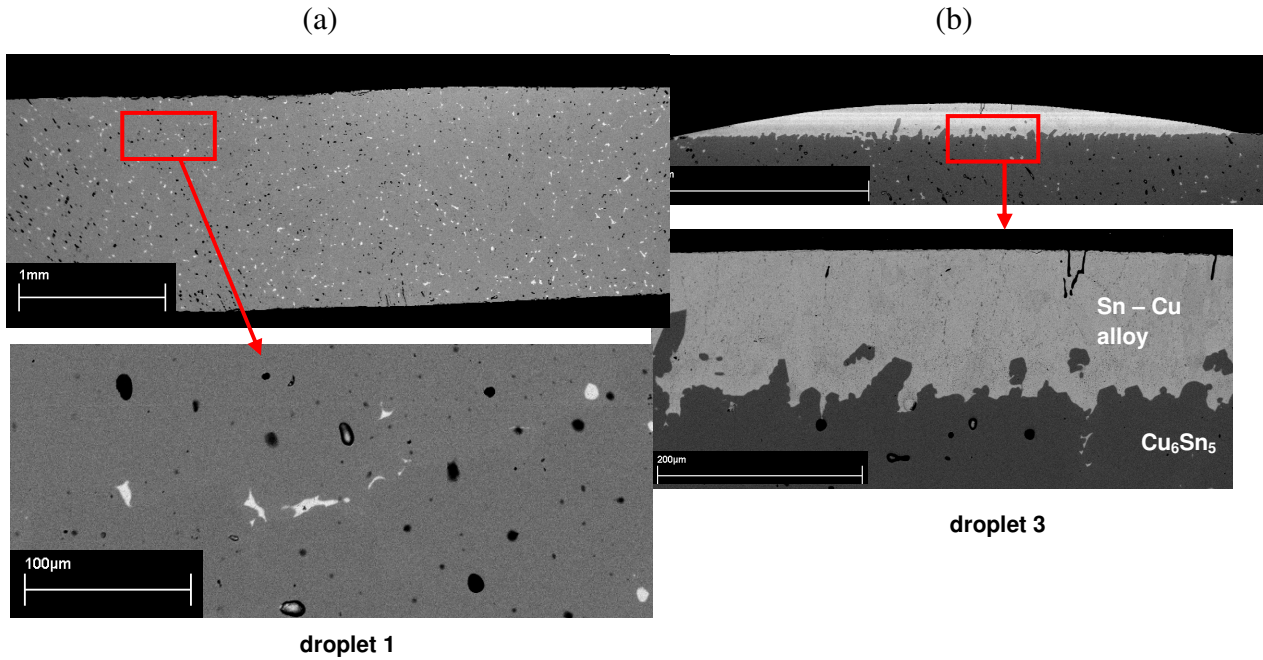


Figure 3-35. Cross-section of the droplets №1 (a) and №3 (b) of solder alloy Sn7.8wt%Cu deposited on bulk  $\text{Cu}_6\text{Sn}_5$  substrate. The contact time at 390°C is about 35 min for droplet №1 and about 1 min for droplet №3. The liquid alloy Sn7.8wt%Cu of the droplet №1 completely infiltrated into the substrate and large Sn particles are detected in the  $\text{Cu}_6\text{Sn}_5$  bulk.

These results are in good agreement with the observed low contact angle of Sn-Cu alloy on  $\text{Cu}_6\text{Sn}_5$  substrate (at least lower than 20°) as well as with the experimental results of growth kinetics of  $\text{Cu}_6\text{Sn}_5$  reaction layer between Cu substrate and liquid Sn-Cu alloys (see Chapter 5). Indeed, as it will be shown in Chapter 5 the very high growth kinetics of  $\text{Cu}_6\text{Sn}_5$  layer formed between Cu and liquid Sn-Cu alloys, can be explained only by fast diffusion through liquid channels formed between  $\text{Cu}_6\text{Sn}_5$  grain boundaries or/and at the triple  $\text{Cu}_6\text{Sn}_5$  joints.

#### 4-3) Wetting of bulk $\text{Cu}_6\text{Sn}_5$ by pure Sn

We also studied the wetting of the bulk  $\text{Cu}_6\text{Sn}_5$  substrate by pure liquid Sn at 390°C. In this case we implemented the preheating procedure for 2 hours at 390°C and droplet deposition at the same temperature (see Figure 3-36).

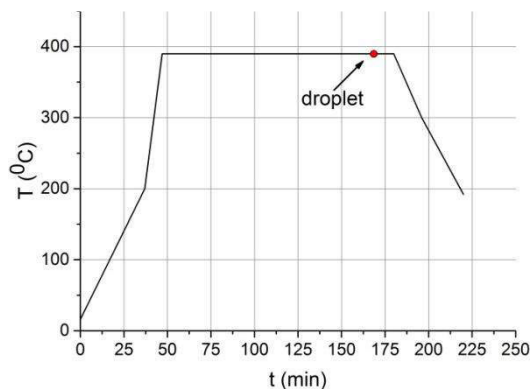


Figure 3-36. Temperature-time profile during wetting experiment with pure liquid Sn droplet deposition over the bulk  $\text{Cu}_6\text{Sn}_5$  substrate at 390°C.

The total contact time between liquid Sn and Cu<sub>6</sub>Sn<sub>5</sub> substrate at 390°C was about 20 minutes. Moreover the additional contact time between the liquid droplet and Cu<sub>6</sub>Sn<sub>5</sub> substrate during cooling from 390°C to the Cu-Sn eutectic temperature (227°C) was about 30 minutes.

Figure 3-37 gives the variation with time of the contact angle  $\theta$  and drop base diameter. This figure shows that during the first stage of spreading, the instantaneous contact angle decreased very rapidly to a value of about 20° in a time less than 10 ms and afterwards the droplet oscillates around this mean value of contact angle.

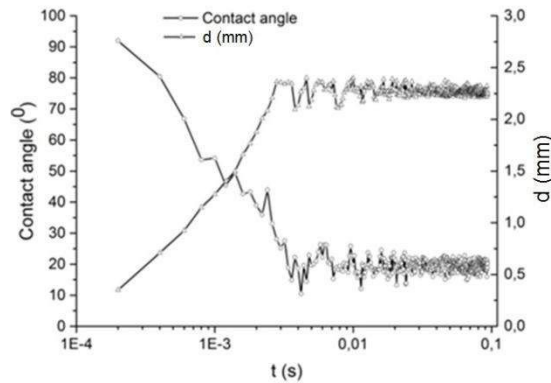


Figure 3-37. Change of the contact angle and the drop base diameter with time for pure liquid Sn droplet deposited on the bulk Cu<sub>6</sub>Sn<sub>5</sub> substrate at 390°C.

As in the previous case of wetting of Cu<sub>6</sub>Sn<sub>5</sub> by the liquid Sn-7.8wt.%Cu alloy, the equilibrium contact angle of pure liquid Sn on Cu<sub>6</sub>Sn<sub>5</sub> surface is about 20°.

The complete infiltration of the liquid Sn inside the Cu<sub>6</sub>Sn<sub>5</sub> bulk (see Figure 3-38) was also detected in this case (after 30 min of contact) as in the case of deposition of Sn-7.8wt.%Cu over the bulk Cu<sub>6</sub>Sn<sub>5</sub> substrate.

Indeed, the droplet is not detected on the cross-section of the sample and tin particles are detected inside the bulk Cu<sub>6</sub>Sn<sub>5</sub> substrate. As in the case of Sn-7.8wt.%Cu/Cu<sub>6</sub>Sn<sub>5</sub> couple, the Cu<sub>6</sub>Sn<sub>5</sub> grain-boundaries are wetted by liquid Sn only underneath the drop but also all over the substrate (see Figure 3-38b).

The same considerations as in the Sn-7.8wt.%Cu/Cu<sub>6</sub>Sn<sub>5</sub> system are valid here, moreover the substrate dissolution in liquid Sn should be higher than in the Sn-7.8wt.%Cu alloy.

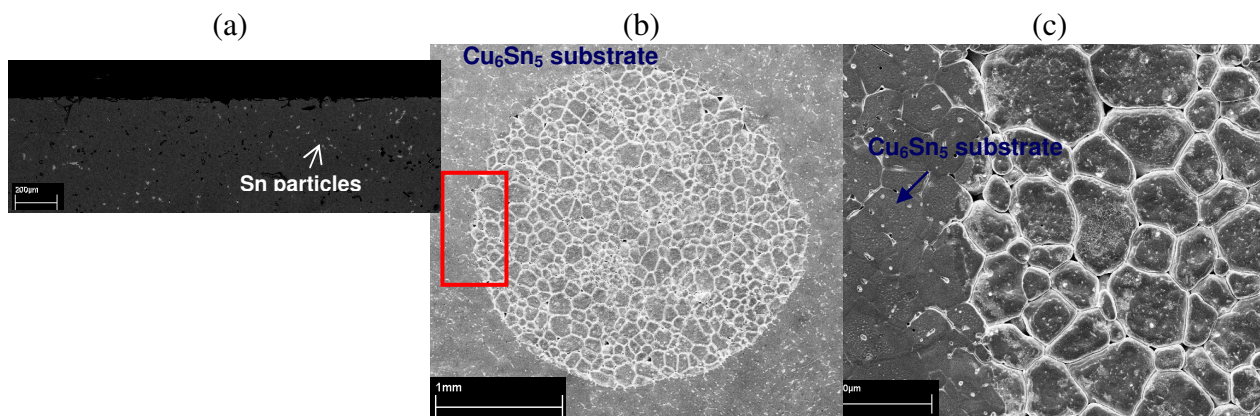


Figure 3-38. SEM micrographs of the sample liquid Sn/Cu<sub>6</sub>Sn<sub>5</sub> substrate held at 390°C for 20 minutes. (a) cross-section, (b) top-view, (c) enlargement of the zone indicated by a red rectangle in (b).

#### 4-4) Conclusions

Wetting experiments of liquid Sn and Sn-7.8wt.%Cu alloy on flat Cu<sub>6</sub>Sn<sub>5</sub> substrate at 390°C have been performed for the first time by the dispensed drop technique.

From experimental results, it is deduced that the equilibrium contact angle of the pure liquid Sn and liquid Sn-7.8wt.%Cu alloy on  $\text{Cu}_6\text{Sn}_5$  surface is about  $20^\circ$ . This value is lower than that obtained on Cu surface and close to that obtained on  $\text{Cu}_3\text{Sn}$  surface at the same temperature. This contact angle value ( $20^\circ$ ) is obtained after less than 10 ms of spreading and afterwards the contact angle remains constant in time.

During the contact between the liquid Sn or Sn-Cu alloy and  $\text{Cu}_6\text{Sn}_5$  substrate a significant decrease in the drop height without any noticeable change in the drop base diameter of the droplet is observed. SEM investigations of the top-view and cross-section of the droplet show that a complete infiltration of the liquid alloy occurs on the  $\text{Cu}_6\text{Sn}_5$  substrate in less than 30 min. This rapid infiltration takes place by infiltration of open porosities of the  $\text{Cu}_6\text{Sn}_5$  substrate and/or by grain-boundary infiltration.

The examination of infiltrated samples strongly suggests that the infiltration takes place at least via the  $\text{Cu}_6\text{Sn}_5$  grain boundary wetting. These results are in good agreement with the observed low contact angle of Sn-Cu alloy on  $\text{Cu}_6\text{Sn}_5$  substrate (at least lower than  $20^\circ$ ) as well as with the experimental results of growth kinetics of  $\text{Cu}_6\text{Sn}_5$  reaction layer between Cu substrate and liquid Sn-Cu alloys (see Chapter 5).

## 5) Wetting of scalloped $\text{Cu}_6\text{Sn}_5$ surfaces

### 5-1) Introduction

As it is already seen, the contact of liquid Sn or Sn-Cu alloys with Cu leads to the formation of two intermetallic layers: a thin and continuous  $\text{Cu}_3\text{Sn}$  layer on the Cu side and a scalloped-form  $\text{Cu}_6\text{Sn}_5$  layer on the liquid side. Thus, in this system, the liquid alloy is in contact with the scalloped-form  $\text{Cu}_6\text{Sn}_5$  phase and the wetting properties of this scalloped layer by liquid alloy are interesting not only for the adhesion properties at the interface but also for the heterogeneous nucleation of solid Sn on this scalloped-form interface (see Chapter 4).

### 5-2) Experimental results

In order to study the wetting of scalloped surface of  $\text{Cu}_6\text{Sn}_5$  we prepared specific samples by reaction between a Cu substrate and liquid Sn at  $350^\circ\text{C}$  for 2 hours. Then the scalloped surfaces of the  $\text{Cu}_6\text{Sn}_5$  intermetallic were obtained after etching of the Cu/Sn sandwiches in acidic solution (all details are given in the Chapter 2).

Figure 3-39 gives a SEM micrograph of the obtained scallop surface indicating that the grain size varies between 5 and 25  $\mu\text{m}$ .

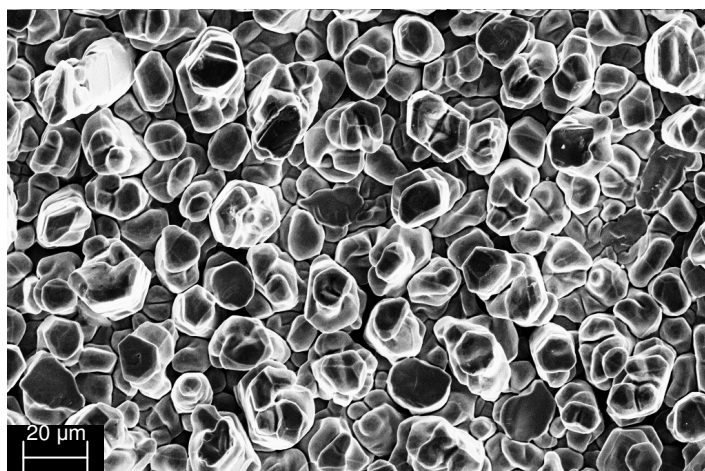


Figure 3-39. SEM micrograph of the scalloped surface produced after etching of tin after Cu/Sn reaction at  $350^\circ\text{C}$  for 2 hours (SE mode).

Wetting experiments of  $\text{Cu}_6\text{Sn}_5$  scalloped surface were performed at  $280^\circ\text{C}$  and  $390^\circ\text{C}$  and investigated only by using the conventional camera.

The temperature-time profile of experiments performed at  $280^\circ\text{C}$  is given on the Figure 3-40a and it can be seen that the chamber of the furnace was shortly heated up to  $350^\circ\text{C}$  in order to insure the melting of tin pieces in alumina crucible situated about 5 mm above the  $\text{Cu}_6\text{Sn}_5$  substrate. Two successive Sn droplets were deposited at  $280^\circ\text{C}$ .

The temperature-time profile for experiments performed at  $390^\circ\text{C}$  is given in Figure 3-40b. The first and the second droplets were deposited after a holding time (at  $390^\circ\text{C}$ ) of about 25 min and 85 min respectively.

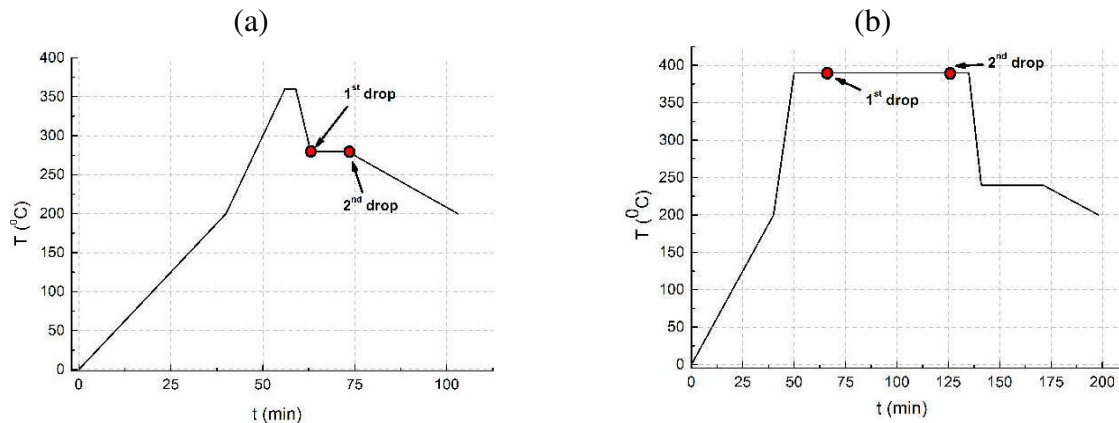


Figure 3-40. Temperature - time profile for wetting experiments in liquid Sn/ $\text{Cu}_6\text{Sn}_5$  scalloped surface system performed at  $280^\circ\text{C}$  (a) and  $390^\circ\text{C}$  (b).

No spreading kinetics was observed after deposition of droplets at  $280^\circ\text{C}$ . The initial measured contact angles (in 40 ms) are  $54^\circ$  and  $46^\circ$  for the first and the second drop respectively. As we have not performed wetting experiments on bulk flat surfaces of  $\text{Cu}_6\text{Sn}_5$  at  $280^\circ\text{C}$  we cannot compare this result with results of the previous section (wetting of the bulk flat  $\text{Cu}_6\text{Sn}_5$  surface at  $390^\circ\text{C}$ ). However, we can note that these values are larger than those measured for Cu/Sn system at  $250^\circ\text{C}$  ( $\theta = 35^\circ$ ). This difference can be partially explained by higher oxidation of the  $\text{Cu}_6\text{Sn}_5$  substrate compared to Cu substrate, which is due to the high content of the Sn atoms inside the  $\text{Cu}_6\text{Sn}_5$  intermetallic.

Figure 3-41a gives top-view micrograph of the first deposited droplet at  $280^\circ\text{C}$  (deposition without preheating of the substrate). As it can be seen from this figure, the Sn droplet deposited on the rough substrate had a perfect circular shape.

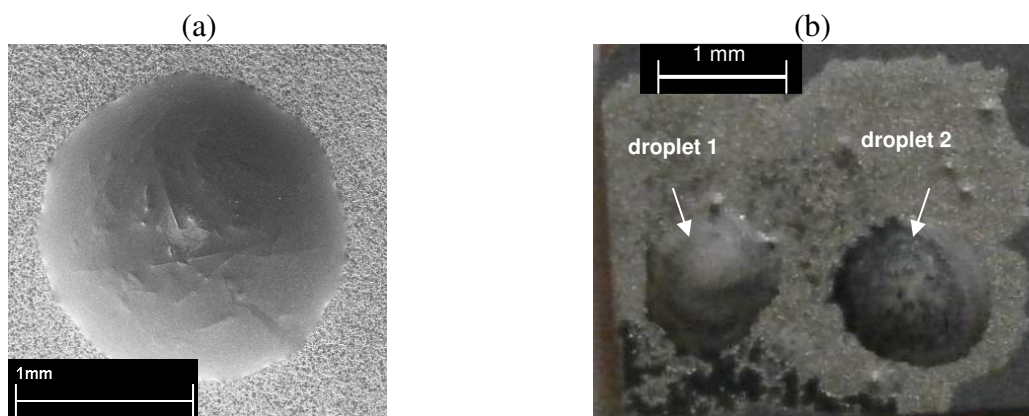


Figure 3-41. (a) Top-view SEM image taken after spreading of the liquid tin over rough scalloped  $\text{Cu}_6\text{Sn}_5$  surface at  $280^\circ\text{C}$  (droplet 1, Figure 3-40a); (b) Top-view optical image taken after spreading of two droplets of the liquid tin over rough scalloped  $\text{Cu}_6\text{Sn}_5$  surface at  $390^\circ\text{C}$ .

Figure 3-42 gives the wetting kinetics observed for the first drop deposited at 390°C. The first measured contact angle (in 40 ms) is 34°. Afterwards a very rapid spreading of the drop is observed and the contact angle decreases from 34 to 22° in about 20 s. Finally the drop spreads very slowly; the contact angle decrease by only 4° in 5 minutes. Note that the first measured contact angle (34°) is much lower than those measured at 280°C (54 and 46°). However, this angle is higher than that one measured on the bulk flat Cu<sub>6</sub>Sn<sub>5</sub> surface at the same temperature (about 20° - see section 4-3).

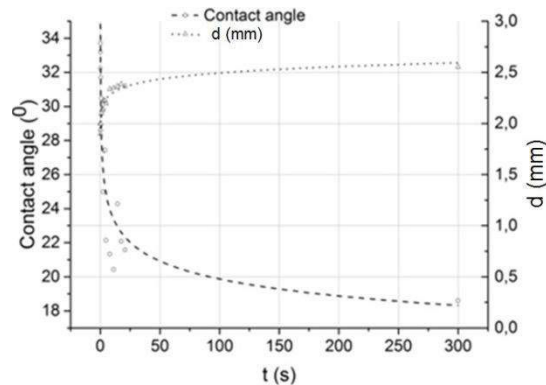


Figure 3-42. Variation with time of the contact angle and the drop base diameter of the 1<sup>st</sup> droplet deposited at 390°C over the scalloped Cu<sub>6</sub>Sn<sub>5</sub> surface (see Figure 3-40b).

This difference can be due partly to the fact that the bulk phase Cu<sub>6</sub>Sn<sub>5</sub> surface sample is annealed under high vacuum for 2 h at 390°C (see Figure 3-36) that can lead to at least a partial deoxidation of the Cu<sub>6</sub>Sn<sub>5</sub> surface. Indeed, the first measured contact angle of the second Sn droplet deposited at 390°C on scalloped surface (after 85 min of annealing at 390°C, see Figure 3-40b) is 20°, similar to that obtained with flat Cu<sub>6</sub>Sn<sub>5</sub> surface under the same experimental conditions. However, some doubt exists if this second droplet was deposited on a pre-wetted Cu<sub>6</sub>Sn<sub>5</sub> surface because both Sn drops were deposited on the same scalloped Cu<sub>6</sub>Sn<sub>5</sub> sample. This is shown in Figure 3-41b that gives a top view optical image taken after spreading of both droplets at 390°C. This figure clearly shows that the scallop surface all over the drops is infiltrated by liquid tin by capillary infiltration. This phenomenon is observed also by Zhao et al. [Zhao\_2009] who studied the spreading kinetics of liquid Sn-based solders on the scalloped Cu<sub>6</sub>Sn<sub>5</sub> surfaces by performing sessile drop experiments.

### 5-3) Conclusions

Even if the wetting kinetics of liquid Sn on scalloped Cu<sub>6</sub>Sn<sub>5</sub> surface is not studied in details by changing the average size of scallops we can conclude that the wetting of this scalloped surface at 390°C is similar to that of bulk planar Cu<sub>6</sub>Sn<sub>5</sub> surface (obtained in this study) and similar to the experimental results reported by Zhao et al. [Zhao\_2009] on wetting of scalloped Cu<sub>6</sub>Sn<sub>5</sub> surface by Sn based liquid alloys obtained by performing sessile drop experiments.

## 6) Wetting of Ag and Ag<sub>3</sub>Sn by liquid Sn

### 6-1) Introduction

In this section we are interested particularly on the wetting of Ag<sub>3</sub>Sn compound by liquid Sn because this is an important factor on the nucleation of Sn on the primary Ag<sub>3</sub>Sn plate that could form first during cooling of the Sn-Ag-Cu solder alloys. In order to better understand the wetting behavior of Ag<sub>3</sub>Sn we studied also the wetting of pure Ag by liquid Sn. For both substrates the wetting experiments were performed under high vacuum at 300°C and 400°C after 1h of preheating at 450°C. The temperature-time profile during these experiments is given in Figure 3-43. Wetting experiments were investigated by using a rapid camera.

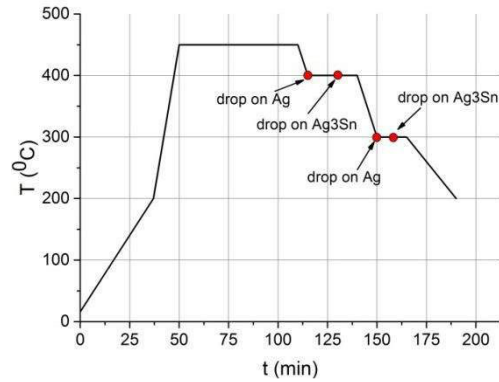


Figure 3-43. Temperature-time profile of wetting experiments of Ag and Ag<sub>3</sub>Sn substrates by liquid Sn at 400°C and 300°C after 1 hour preheating at 450°C.

### 6-2) Wetting of Ag substrate by liquid Sn

Figure 3-44 gives the spreading kinetics of liquid Sn droplets on Ag substrate at 300°C and 400°C.

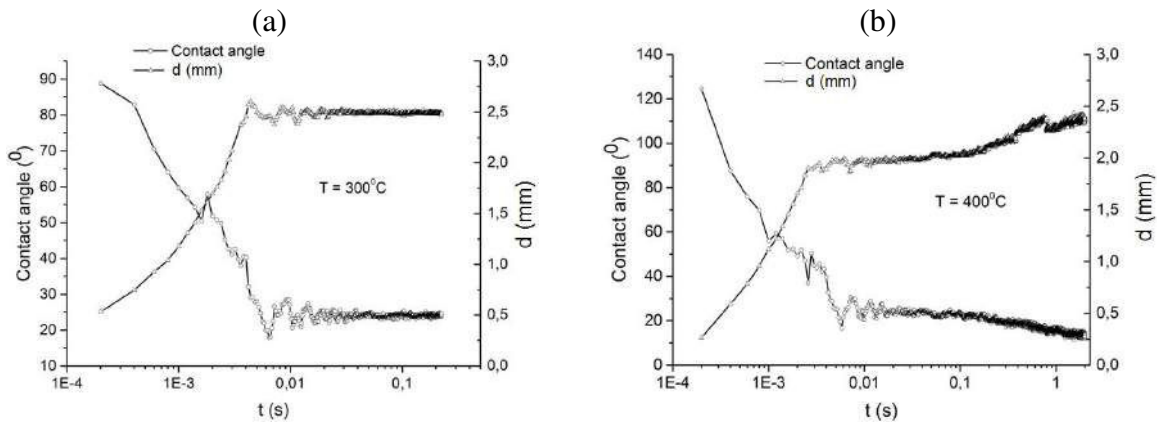


Figure 3-44. Variation with time of the contact angle  $\theta$  and the drop base diameter  $d$  of Sn droplets deposited on Ag substrate at 300°C (a) and 400°C (b).

Figures 3-44 shows that at 300°C the spreading of liquid Sn occurred very rapidly and the contact angle decreased down to about 25° in less than 10 ms. Afterwards the liquid drop oscillated around the final contact angle ( $\approx 20^\circ$ ) and these oscillations disappear practically after about 1 s. As in the previous sections, we can conclude here that the equilibrium contact angle of liquid Sn on Ag at 300°C substrate is about 25°.

In the case of wetting experiment performed at 400°C the same behavior of the variation with time of contact angle and drop base diameter as at 300°C was observed for spreading times lower than about 10 ms, and the contact angle of about 20° is attained in less than 10 ms. However, contrary to the experiment at 300°C, here the drop continued to spread even after 10 ms but with a much lower spreading rate than for time lower than 10 ms. The contact angle decreased from 20 to 10° in about 1 s. The average spreading rate for  $t < 10$  ms was  $V_1 = (dR/dt)_1 \approx 0.14$  m/s whereas for  $10 \text{ ms} < t < 2 \text{ s}$  the spreading rate was several orders of magnitude lower:  $V_2 = (dR/dt)_2 \approx 3.5 \times 10^{-4}$  m/s; here  $r = d/2$  is the drop base radius.

In section 6-4 we will discuss the differences between spreading kinetics at 300°C and 400°C as well as the large decrease in spreading kinetics at 400°C at time around 10 ms.

Figures 3-45 and 3-46 give SEM micrographs of Ag/Sn sample from wetting experiments performed at 300 and 400°C. It is seen that the tin droplet had a perfect circular form in both cases. These figures show that in both cases a continuous reaction layer, identified as Ag<sub>3</sub>Sn phase, was formed at the interface. It is clearly seen that the Sn droplet at the triple line is situated above the Ag<sub>3</sub>Sn reaction layer. Moreover, for experiment performed

at 300°C no strong dissolution of Ag substrate was observed while at  $T = 400^\circ\text{C}$  the dissolution was much more pronounced.

The Ag dissolution at 400°C is put in evidence by the large quantity of  $\text{Ag}_3\text{Sn}$  precipitated in the drop bulk during solidification but also by the non planar form of the liquid/solid interface. This rapid increase in the quantity of Ag substrate dissolved in liquid Sn is due to the rapid increase of the solubility limit of Ag in liquid Sn when  $T$  increases from 300°C to 400°C as well as to kinetic factors.

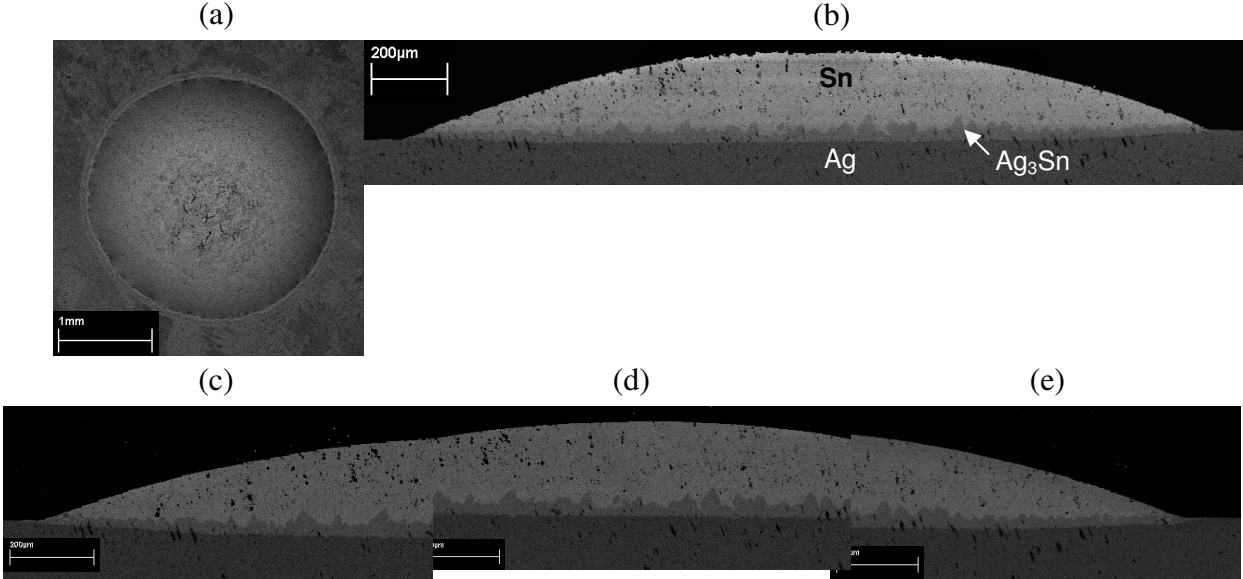


Figure 3-45. SEM micrographs of the tin droplet deposited over the Ag substrate at 300°C. Top view (a) and cross-sections (c,d,e).

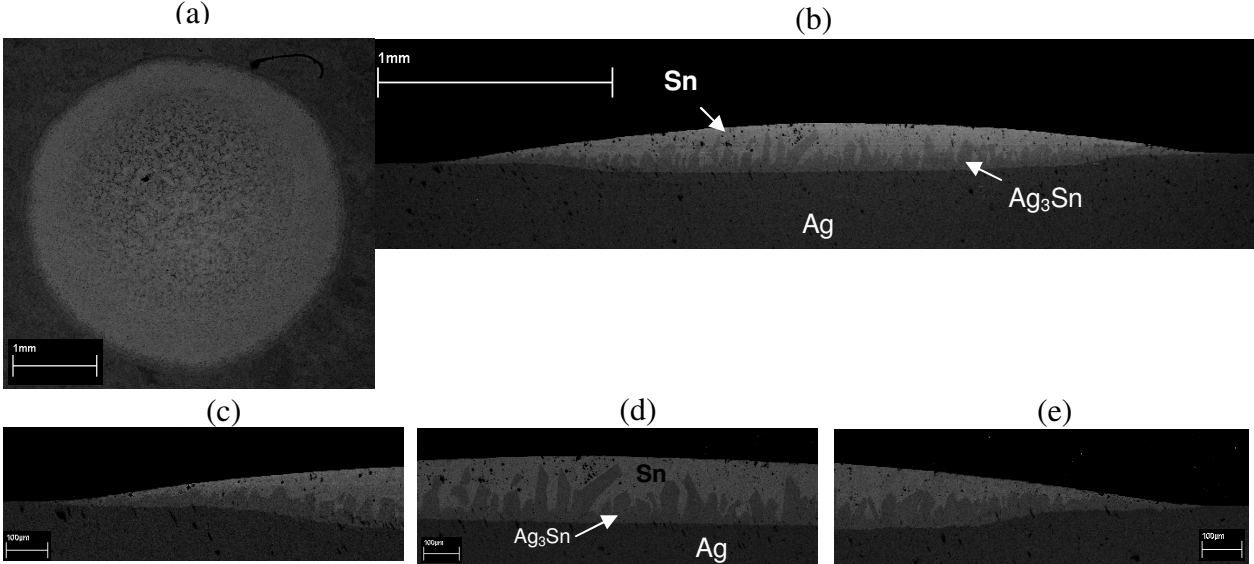


Figure 3-46. SEM micrographs of the tin droplet deposited over the Ag substrate at 400°C. Top view (a) and cross-sections (c,d,e).

### 6-3) Wetting of $\text{Ag}_3\text{Sn}$ substrate by liquid Sn.

Figure 3-47 gives spreading kinetics of liquid Sn droplets on  $\text{Ag}_3\text{Sn}$  substrate at  $300^\circ\text{C}$  and  $400^\circ\text{C}$ . This figure shows that spreading kinetics is similar for both temperatures. The instantaneous contact angle decreased very rapidly in less than 10 ms to  $15^\circ$  and  $10^\circ$  for temperature equal to  $300^\circ\text{C}$  and  $400^\circ\text{C}$  respectively.

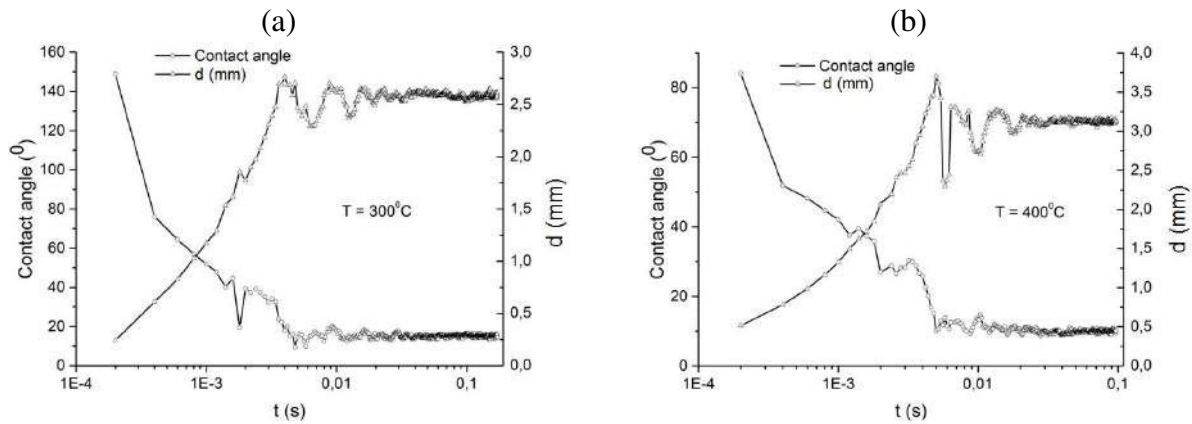


Figure 3-47. Variation with time of the contact angle  $\theta$  and drop base diameter of Sn droplets deposited on  $\text{Ag}_3\text{Sn}$  substrate at  $300^\circ\text{C}$  (a) and  $400^\circ\text{C}$  (b).

Afterwards, in both cases, the contact angle values oscillated around  $15^\circ$  or  $10^\circ$  until the total disappearance of the oscillation in less than 1s.

Figure 3-48a and Figure 3-49a show that the tin droplets deposited over the  $\text{Ag}_3\text{Sn}$  substrate at  $300^\circ\text{C}$  and  $400^\circ\text{C}$  had not perfect circular form. At  $300^\circ\text{C}$  the liquid/solid interface is almost planar (see Figures 3-48b,c) and there are no precipitates of  $\text{Ag}_3\text{Sn}$  phase inside the tin bulk. On the contrary, at  $400^\circ\text{C}$  the interface is not planar, the substrate is dissolved in liquid Sn and then, during solidification,  $\text{Ag}_3\text{Sn}$  precipitated from the oversaturated liquid (see Figures 3-49b,c).

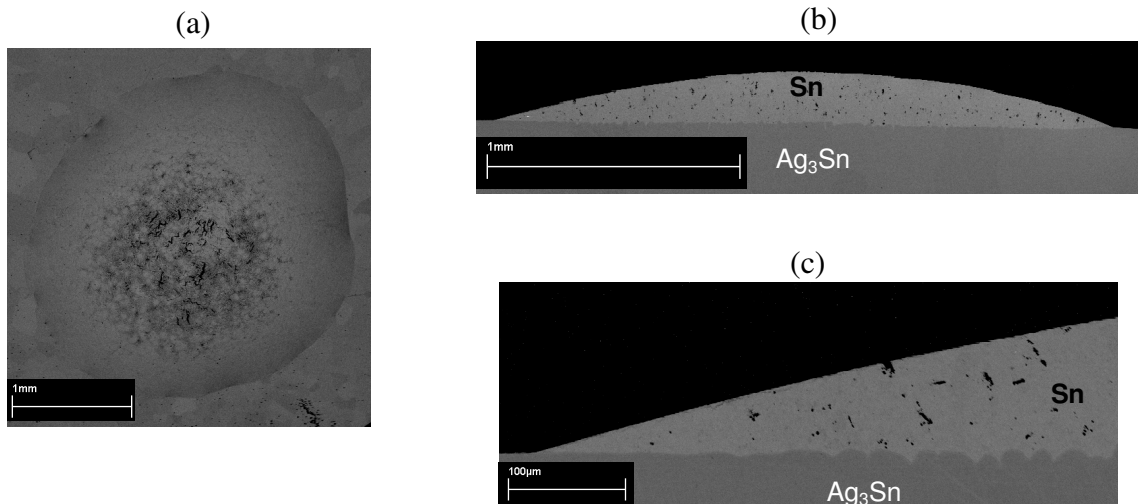


Figure 3-48. SEM micrographs of the tin droplet deposited over the  $\text{Ag}_3\text{Sn}$  substrate at  $300^\circ\text{C}$ . Top view (a), cross-section (b,c).

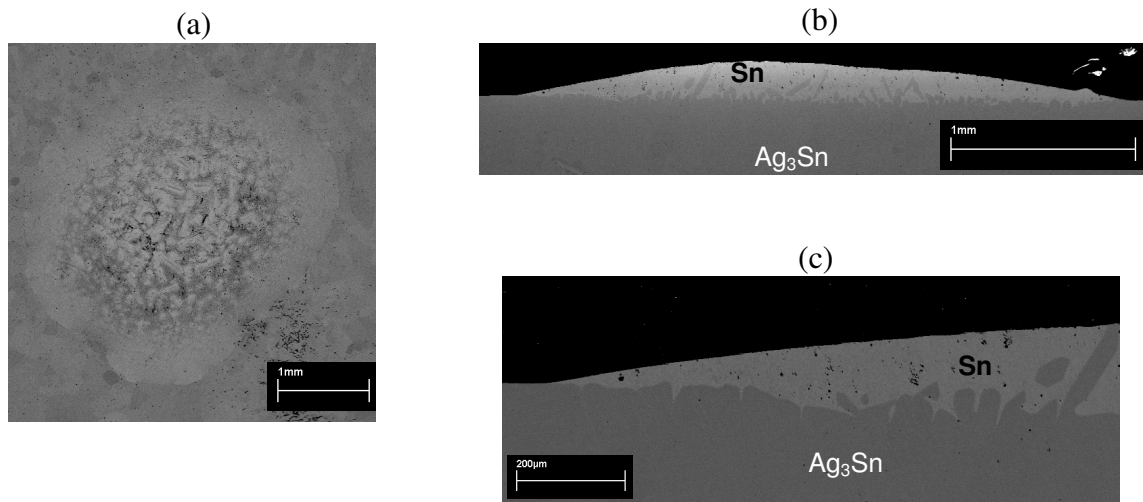


Figure 3-49. SEM micrographs of the tin droplet deposited over the  $\text{Ag}_3\text{Sn}$  substrate at  $400^\circ\text{C}$ . Top view (a), cross-section (b,c).

#### 6-4) Discussion

Comparison of Figures 3-47 and 3-44 shows two significant differences in spreading kinetics of Sn droplets on  $\text{Ag}_3\text{Sn}$  and Ag substrate:

- The contact angle attained in about 10 ms (noted  $\theta^0$ ) on  $\text{Ag}_3\text{Sn}$  substrate is lower than that on Ag:

at  $T = 300^\circ\text{C}$   $\theta_{\text{Ag}}^0 = 25^\circ$  and  $\theta_{\text{Ag}_3\text{Sn}}^0 = 15^\circ$ ;

at  $T = 400^\circ\text{C}$   $\theta_{\text{Ag}}^0 = 20^\circ$  and  $\theta_{\text{Ag}_3\text{Sn}}^0 = 10^\circ$ ;

- At  $T = 400^\circ\text{C}$ , after  $t = 10$  ms no spreading occurs on  $\text{Ag}_3\text{Sn}$  substrate, i.e. the final contact angle ( $\theta_{\text{Ag}_3\text{Sn}}^f$ ) remains equal to the initial contact angle ( $\theta_{\text{Ag}_3\text{Sn}}^0$ ). On the contrary, for Ag substrate at  $T = 400^\circ\text{C}$ , spreading of the drop continues even after  $t = 10$  ms with a spreading rate much lower than before and the contact angle varies from  $\theta_{\text{Ag}}^0$  ( $t \approx 10$  ms) =  $20^\circ$  to a final contact angle  $\theta_{\text{Ag}}^f$  ( $t \approx 1$  s) =  $10^\circ$ .

Thus, at  $T = 400^\circ\text{C}$ , the final contact angle observed on Ag substrate ( $10^\circ$ ) is equal to the final contact angle on  $\text{Ag}_3\text{Sn}$  substrate.

From these results we can propose the following scenario for the wetting of Ag substrate at  $400^\circ\text{C}$  (see Figure 3-50):

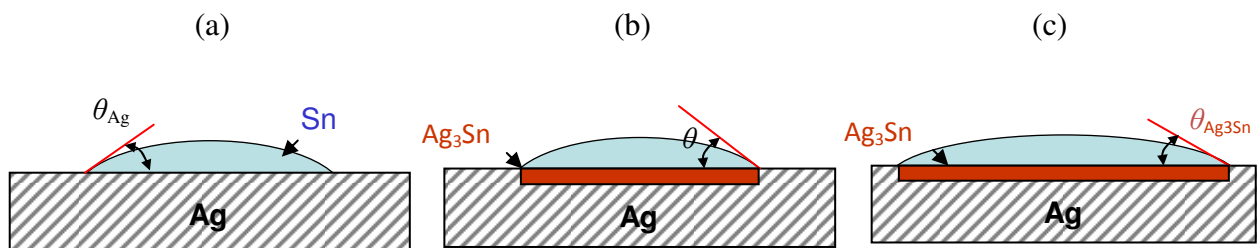


Figure 3-50. Schematic presentation of reactive wetting of Ag substrate by liquid Sn with formation, at the interface, of a  $\text{Ag}_3\text{Sn}$  reactive layer better wetted than the unreacted Ag substrate.

The equilibrium contact angle of liquid Sn on unreacted Ag substrate  $\theta_{\text{Ag}} (\approx 20^\circ)$  is higher than the equilibrium contact angle on  $\text{Ag}_3\text{Sn}$  substrate  $\theta_{\text{Ag}_3\text{Sn}} = 10^\circ$ . Thus, when a droplet of liquid Sn is put in contact with an Ag substrate, the droplets will first spread with an instantaneous contact angle which will decrease from  $180^\circ$  to the equilibrium contact angle on the unreacted Ag substrate  $\theta_{\text{Ag}} = 20^\circ$  is attained in less than 10 ms (non reactive wetting). Afterwards, the interfacial reaction between liquid Sn and Ag leads to the formation of a continuous layer of  $\text{Ag}_3\text{Sn}$  compound at the interface. Thus, the liquid Sn is situated over

Ag<sub>3</sub>Sn layer with a contact angle  $\theta_{Ag}$  that is higher than the equilibrium contact angle on Ag<sub>3</sub>Sn ( $\theta_{Ag_3Sn}$ ). This way the reaction between liquid Sn and Ag substrate will take place in the front of the triple line (TL) liquid-solid-vapor leading to the lateral growth of Ag<sub>3</sub>Sn compound. This coupling between wettability and reactivity leads to the spreading of the liquid until the instantaneous contact angle becomes equal to the equilibrium contact angle of liquid Sn on the reaction product, i.e. on Ag<sub>3</sub>Sn layer (reactive wetting, see for example [Eustathopoulos\_1999]). Thus, the liquid Sn droplets will spread by reactive wetting from  $\theta_{Ag} = 20^\circ$  to  $\theta_{Ag_3Sn} = 10^\circ$ .

#### 6-5) Conclusions

Wetting experiments of liquid Sn on Ag and Ag<sub>3</sub>Sn substrates at 300°C and 400°C have been performed for the first time by dispensed drop technique.

The equilibrium contact angle (attained in about 10 ms) on Ag substrate are 25° and 20° at 300°C and 400°C respectively.

The equilibrium contact angle (attained in about 10 ms) on Ag<sub>3</sub>Sn substrate are 20° and 10° at 300°C and 400°C respectively meaning that Ag<sub>3</sub>Sn is better wetted by liquid Sn than Ag substrate.

From experimental results obtained at 400°C a mechanism of reactive wetting of Ag is proposed: first the liquid drop spreads very rapidly with instantaneous contact angle decreasing from 180° to the equilibrium contact angle on the non reacted Ag surface  $\theta_{Ag}$  (**non reactive wetting**, with a spreading rate about 0.2 m/s) and afterwards it spreads with a spreading rate several orders of magnitude lower than the first one from  $\theta_{Ag}$  to a final contact angle that corresponds to the equilibrium contact angle of liquid Sn on the reaction product layer, i.e., on Ag<sub>3</sub>Sn substrate (**reactive wetting** with a spreading rate about  $3.5 \times 10^{-4}$  m/s).

### 7) **Conclusions**

The wettability of the metallic substrates such as Cu, Ag and their main intermetallics with Sn (Cu<sub>3</sub>Sn, Cu<sub>6</sub>Sn<sub>5</sub> and Ag<sub>3</sub>Sn) by liquid Sn, Sn-Cu solders and Pb was studied by implementing the dispensed drop technique in the high-vacuum furnace. Different approaches were used in order to reveal the intrinsic equilibrium contact angle of Sn or Sn-Cu alloy droplets on these substrates. It was found that the oxidation extent of the substrate can be altered by prolonged annealing at high temperature under the vacuum. Another beneficial experimental approach was the implementation of the rapid camera.

Preliminary wetting experiments of liquid Sn on Cu substrate followed by a CDD camera allow us to study, in a qualitative way, the influence of the annealing of the Cu substrate under high vacuum at 800°C on its wetting behavior: If the wetting experiments are performed at low temperature range 250-400°C, this annealing has practically no influence on the first and final measured contact angles. On the contrary, for higher temperature wetting experiments (500-600°C) this annealing leads to a small decrease in the first measured contact angles (in 40 ms) and a significant increase in the spreading kinetics.

In order to distinguish the non-reactive spreading of liquid Sn or liquid Sn-Cu alloys on the non reacted Cu substrate (annealed at high temperatures under vacuum) and the possible reactive spreading with formation of intermetallics, we implemented the high speed camera. It allowed us to reveal that, in temperature range 300-600°C, the first stage of wetting of Cu substrate by liquid Sn or Sn-Cu liquid alloy is very rapid (in less than 10 ms), the spreading rate being about  $1 \text{ m}\cdot\text{s}^{-1}$ . During this stage, corresponding to a non reactive spreading process, the instantaneous contact angle decreases very rapidly from 180° to about 30°, the spreading kinetics of Sn or Sn-Cu alloy droplet is temperature independent and similar to that of the non-reactive liquid Pb over Cu substrate at 400°C. It allows us to conclude that the equilibrium contact angle of liquid Sn on a non-reacted and clean surface is lower than 30°.

In order to better understand the reactive wetting of Cu by liquid Sn we performed for the first time the wetting experiments with  $\text{Cu}_3\text{Sn}$  and  $\text{Cu}_6\text{Sn}_5$  intermetallic compounds by the dispensed drop technique. We have found that the non-reactive contact angles of liquid Sn on a  $\text{Cu}_3\text{Sn}$  surface preheated at  $600^\circ\text{C}$  are attained in less than 10 ms and depend on the experimental temperature: they decrease from  $23^\circ$  to  $10^\circ$  in the temperature range  $300\text{-}500^\circ\text{C}$ , which should be mainly due to the oxidation extent of the surface of the substrate. During wetting experiments of the bulk and scalloped  $\text{Cu}_6\text{Sn}_5$  compound at  $390^\circ\text{C}$  by liquid Sn and Sn-Cu liquid alloy we have found low values of non reactive contact angle of about  $20^\circ$  attained in less than 10 ms. It allows us to conclude that the non-reactive equilibrium contact angles of liquid Sn on two main Cu-Sn intermetallics is very low and could be lower than that on Cu. The pronounced infiltration of Sn or Sn-Cu alloy into the  $\text{Cu}_6\text{Sn}_5$  bulk is another feature observed during our experiments. It was found that complete infiltration of millimetric metallic droplet take about 30 minutes and proceeds through the wetted grain-boundaries of the  $\text{Cu}_6\text{Sn}_5$  and/or open porosities of the intermetallic bulk.

From experimental results of wetting of Cu and  $\text{Cu}_6\text{Sn}_5$  substrates it can be concluded that wetting of Cu proceeds in two stages: (i) a rapid *non-reactive stage* during which the contact angle decreases down to  $30^\circ$  in less than 10 ms and (ii) a slow *reactive stage* during which the contact angle decreases from  $30^\circ$  to  $23^\circ$  in about 3 s at  $400^\circ\text{C}$ .

The study of wetting of Ag and  $\text{Ag}_3\text{Sn}$  substrates at  $300$  and  $400^\circ\text{C}$  was performed by the dispensed drop technique for the first time. The measurements of the equilibrium contact angles of the non reacted Ag and  $\text{Ag}_3\text{Sn}$  substrates by liquid Sn allow us to propose a mechanism of spreading kinetics of liquid Sn on Ag substrate. First the liquid drop spreads very rapidly with instantaneous contact angle decreasing from  $180^\circ$  to the equilibrium contact angle on the non reacted Ag surface  $\theta_{\text{Ag}}$  (*non reactive wetting*, with a spreading rate about 1 m/s) and afterwards it spreads with a spreading rate several orders of magnitude lower than the first one from  $\theta_{\text{Ag}}$  to a final contact angle that corresponds to the equilibrium contact angle of liquid Sn on the reaction product layer, i.e., on  $\text{Ag}_3\text{Sn}$  substrate (*reactive wetting*).

## Chapter 4: Nucleation in soldering

### 1) Introduction

As it is already mentioned in Chapter 1, formation and growth of  $\eta$ -Cu<sub>6</sub>Sn<sub>5</sub> and  $\epsilon$ -Cu<sub>3</sub>Sn IMCs greatly affects the physical properties and especially the mechanical properties of the joints formed during soldering process. A schematic presentation of the evolution of the Cu/Sn system during soldering is shown in Figure 4-1. This figure gives also a schematic presentation of the variation of temperature with time during soldering.

Among the main phenomena occurring during this soldering process, we can distinguish:

- (i) nucleation and growth of intermetallic phases at Cu/liquid Sn interface, and
- (ii) nucleation of solid Sn during cooling and solidification.

Despite the fact that the number of studies focused on the interfacial reactions between Cu substrate and liquid Sn or Sn-based alloys is quite impressive, the question about the initial stage of phase formation in this system is open. This is the reason why in this thesis we have performed specific experiments of very fast dipping of Cu foils in liquid Sn (reaction time from 1 ms to 1 s) in order to investigate by Transmission Electron Microscopy the order of phase formation in this system. This dedicated experimental study is presented in *section 2*.

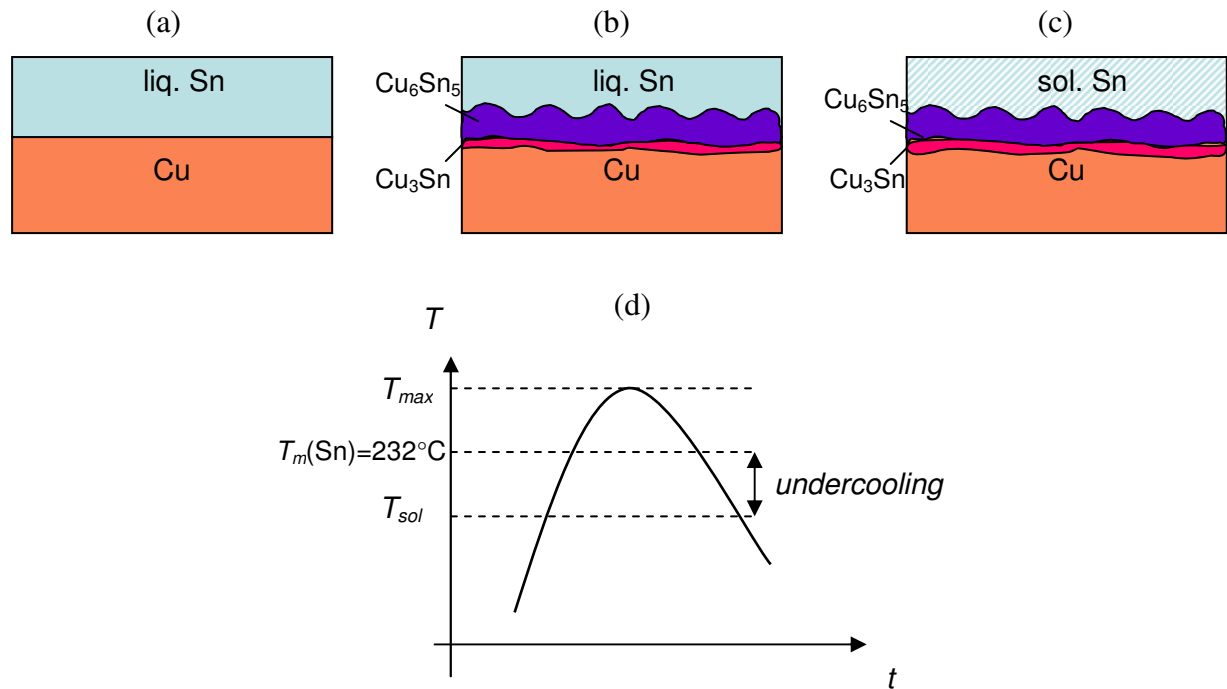


Figure 4-1. Schematic presentation of a solid Cu/liquid Sn diffusion couple in the initial configuration just after dipping of a Cu plate in the liquid Sn (a) nucleation and growth of Cu<sub>3</sub>Sn and Cu<sub>6</sub>Sn<sub>5</sub> layers at the interface during reflowing process - Sn being in the liquid state (b) and after solidification of Sn (c). Time-temperature profile of the simplified reflow process showing the undercooling extent of the liquid Sn (d).

Moreover, in this Chapter we have developed a theoretical approach on the suppression criteria of the second phase formation (phase 2) at A/1 interface of the A/1/B system, where the phase 1 is the first phase formed at A/B interface. This approach has been applied to the Cu/Sn system (Cu=A and Sn=B) with Cu<sub>6</sub>Sn<sub>5</sub> as the first formed phase and Cu<sub>3</sub>Sn the second phase to be formed (see *section 3*). The aim of this section is to establish a critical thickness of phase 1 under which the phase 2 cannot grow.

Another nucleation phenomenon appears during cooling of liquid Sn: nucleation of solid Sn followed by solidification. As it has been mentioned in the Chapter 1, different degrees of undercooling of the solder bulk are observed depending on the experimental conditions and they can have a strong influence on the microstructure evolution of the intermetallics in its bulk or even at the interface between liquid solder and Cu substrate. Despite the fact that several recent works are dedicated to the nucleation of tin in the solder bulk, the role of different potential sites or heterogeneous sites on the nucleation of tin inside the solder ball is not yet elucidated. Moreover, there are no specific studies in literature treating the comparison of undercooling degrees obtained after a partial melting of the solder and after a reflow in configurations of (i) solder balls and (ii) solder joint samples prepared by reflowing solder alloy on copper substrate. This problem is treated from an experimental and theoretical point of view in *section 4*.

## 2) Experimental investigation of initial stage formation of reaction product at Cu/liquid Sn interface

### 2-1) Introduction

In this section we present an experimental study of the interfacial reaction between solid Cu and liquid Sn-Cu alloy for the very short duration of contact (from 1 ms to 1 s ) at 250°C.

This study is performed by implementing a fast dipping experimental set-up (made in our laboratory), SEM-FEG and TEM techniques in order to reveal the sequence of formation of intermetallic compounds at the interface between Cu and liquid Sn-Cu alloy as well as the evolution of their morphology and the average thickness during the reaction products at the very beginning of reaction. Thus, the aim of this section is to give a deeper insight into the sequence of phase formation at Cu/liquid Sn interface that is still a very important and opened question.

### 2-2) Description of the experiment

The experiments were held using high-speed dipping equipment described in the Chapter 2. The crucible with a height 4 cm and an internal diameter of 3 cm was completely filled with melt of a Sn-0.7wt.%Cu alloy prepared in alumina furnace under the vacuum (see Figure 4-2). The control of the alloy temperature in the crucible was realized by two K-type thermocouples. One of them was put inside the Cu cylinder around the crucible and another was placed in a thin ceramic tube dipped in the alloy melt to control precisely its temperature. The temperature control error was about 2°C.

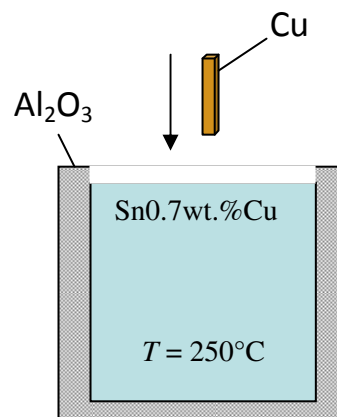


Figure 4-2. Scheme of the dipping experiment.

The maximum total dipping time, corresponding to the tip of the Cu sheet, was about 30-38 ms while using the fast dipping set-up (see below). We also performed the manually dipping, resulting in a total dipping duration estimated to be about 1 s.

In the case of the fast dipping experiment the thickness of the dipped Cu sheet (in the following Substrate 1) was about 115-500  $\mu\text{m}$ , its length was 10 mm and its width was 2 mm. Its surface was polished up to 0.25  $\mu\text{m}$  particle size and cleaned ultrasonically in ethanol. The immersion depth of the Cu sheet was 6 mm. Just before dipping in the liquid bath, the Cu sheet was dipped for 10 s in the conventional liquid RMA flux. The dipping process was controlled by the conventional CCD camera capable to make 25 images/s and was repeated 5 times in order to measure the dipping duration. The full piston motion cycle took 130-170 ms (see Figure 4-3), thus the dipping speed was measured to be in the range 0.32 - 0.4 m/s. Accordingly, having the dipping depth of the sample about 6 mm, the time of the immersion of the Cu sheet takes from  $\sim 1$  ms (for the point of the shortest contact with liquid) to 30-38 ms for the top of the Cu sheet.

In the case of the manual dipping, the Cu sheet had thickness around 0.5 mm with same linear dimensions as Substrate 1 and the dipping depth was about 2 mm. The dipping time was verified by a timekeeper. The interface between Cu and Sn was analyzed in the distance 1.5 mm from the tip of the sample, resulting in the reaction time about 1 s.

Table 4-1 gives the list of the samples dipped for the time  $t$  varying from  $\sim 1$  ms to 1 s. The samples A-F were extracted from the same Cu substrate dipped in liquid Sn by the fast dipping equipment (Substrate 1) - see Figure 4-4, whereas the sample Z was extracted from the manually dipped Cu sheet (in the following Substrate 2) - see Figure 4-5.

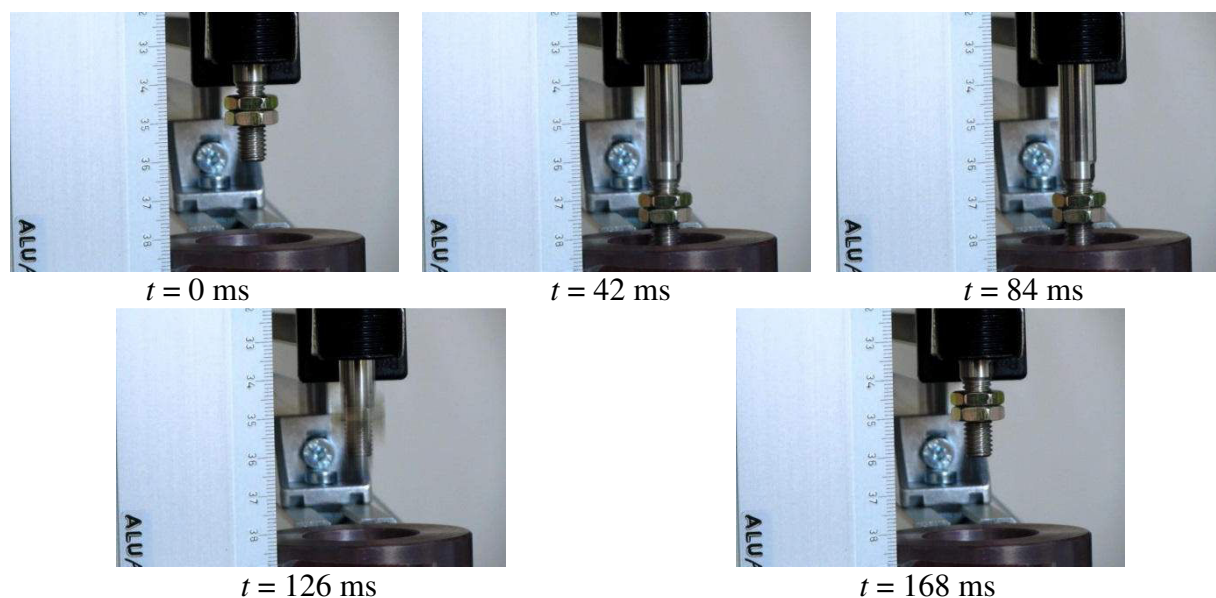


Figure 4-3. Control of the dipping speed. The piston makes its motion cycle with a period of 130-170 ms, resulting in the dipping speed of 0.32-0.4 m/s.

Sample	A	B	C	D	E	F	Z
$t$ (ms), range	0-1	1-1.5	2-2.5	10-13	15-19	30-38	$\sim 1000$

Table 4-1. List of the characterized samples that undergone dipping experiments and the respective reaction time between solid Cu and liquid Sn at 250°C.

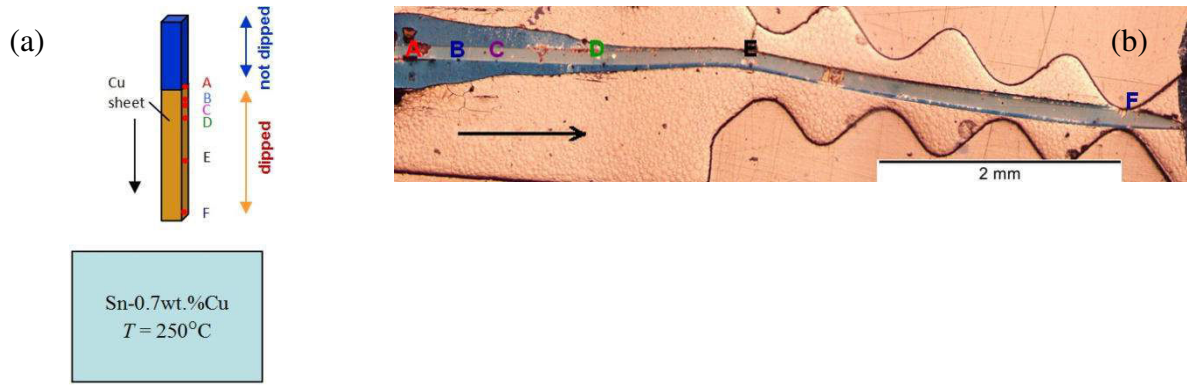


Figure 4-4. a) Schematic indication of the reaction spots over the Substrate 1; b) optical image of the Substrate 1 with indication of the sample spots A-F and dipping direction.

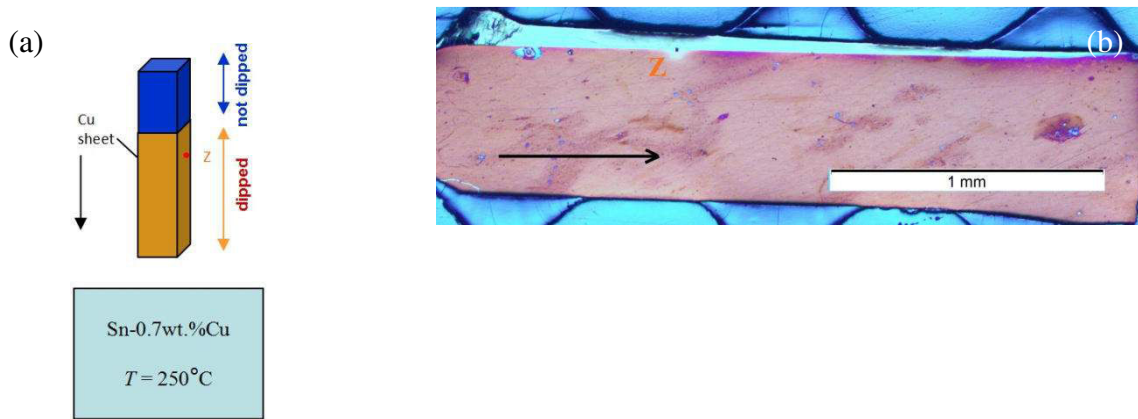


Figure 4-5. a) Schematic indication of the reaction spot over the Substrate 2; b) optical image of the Substrate 2 with indication of the spot Z and dipping direction.

The spots were analyzed by SEM-FEG after the FIB etching and by TEM. The SEM-FEG analysis was made by two kinds of detectors: by the BSE detector and In-Lens SE detector both located in the column. In order to reveal and discuss in details both chemical and surface details we give the SEM micrographs on the spots obtained by both detectors.

### 2-3) SEM-FEG study on the reaction spots after the FIB preparation

On the SEM-FEG micrograph on the reaction spot A (reaction time less than 1 ms), analyzed after the FIB etching, one single layer is seen above the Cu substrate in the BSE mode at 1.5kV (see Figure 4-6). This layer is not homogeneous: the discontinuous cracks are present above or inside the layer as it can be better seen on the SE image (see Figure 4-6b). The average thickness of the layer is around 50 nm. The polycrystalline Cu substrate has fine-grained structure as it is revealed by the FIB etching with grain size varying from 200 to 400 nm.

Figure 4-7a gives the SEM-FEG micrograph in the BSE mode after a reaction time between 1 and 1.5 ms (spot B). The single reaction layer becomes thicker than that on the spot A and gets scalloped shape. No voids or cracks are seen between reaction layer and tin. The average thickness of the layer is about 200 nm. The micrograph in BSE mode on the spot C is shown on the Figure 4-7b. It is seen that the thickness of the reaction layer is the same as in Figure 4-7a and it appears again in the scalloped form. The interface between reaction layer and tin is continuous, there are no voids detected.

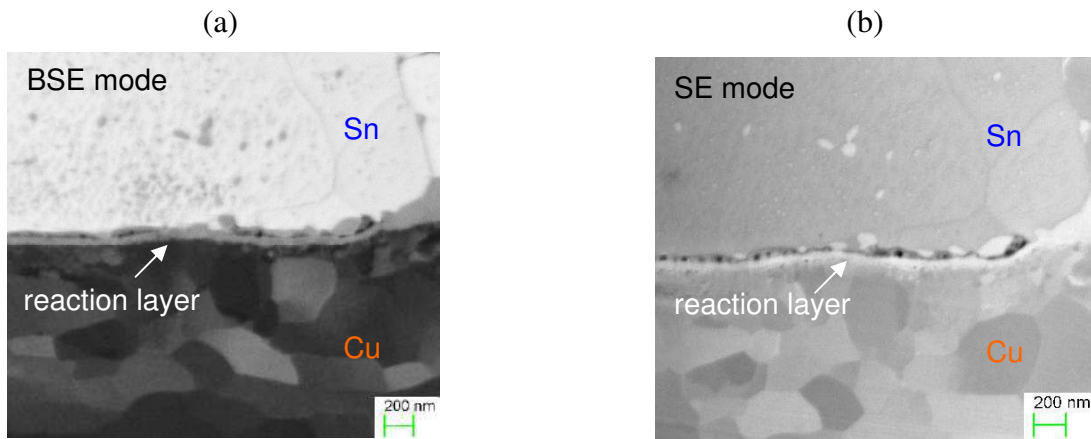


Figure 4-6. The SEM-FEG micrographs in the BSE (a) and SE (b) modes showing the cross-section on the reaction spot A corresponding to the shortest reaction time (less than 1 ms). The single layer is seen above the Cu.

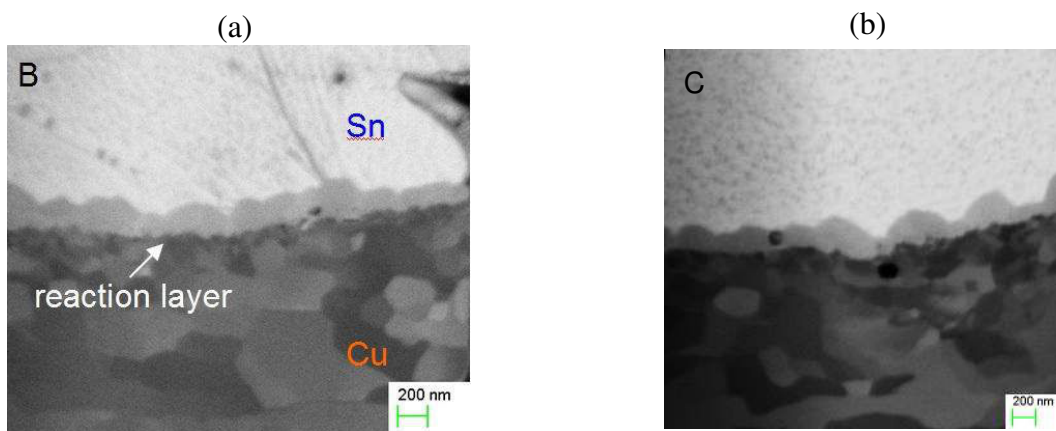


Figure 4-7. The SEM-FEG micrograph in the BSE mode showing the cross-section on the reaction spot B (reaction time between 1 and 1.5 ms) and reaction spot C (reaction time between 2 and 2.5 ms). The layer becomes thicker and no voids are seen between reaction layer and tin.

Figure 4-8 gives the micrographs of the reaction zone on the spot D. As the time of the reaction was more than 10 ms the reaction layer became clearly scallop-shaped. The SE mode study reveals the presence of voids between the reaction layer and the Cu substrate (see Figure 4-8b).

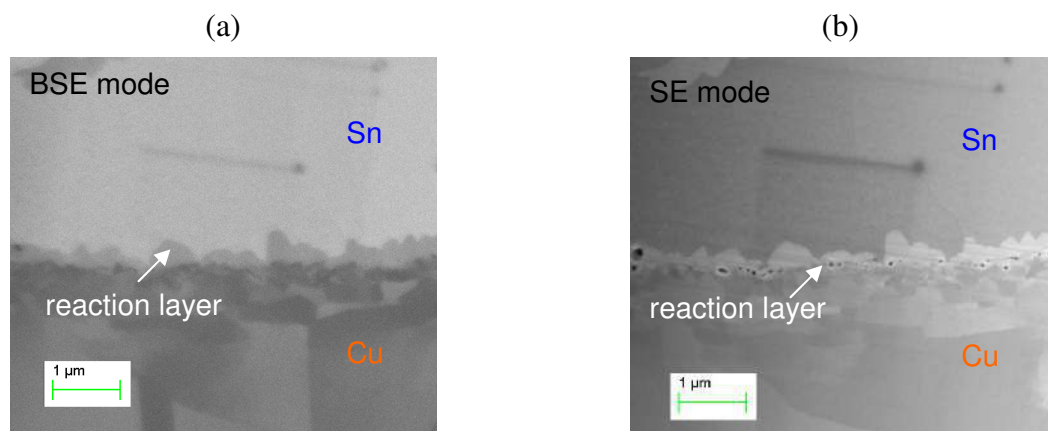


Figure 4-8. The SEM-FEG micrograph in BSE (a) and SE (b) mode showing the cross-section on the reaction spot D (reaction time between 10 and 13 ms). Two important features emerge at this reaction duration: the morphology of the reaction layer becomes scallop-like and voiding is detected to appear at the interface between reaction layer and Cu.

The scalloped-like morphology is clearly seen (see Figure 4-9) on the spot E (reaction time between 15 and 19 ms). It is seen that some scallops are free-standing with tin “channels” between them coming down to the Cu substrate. The voids are clearly seen at the interface between scallops of the reaction layer and Cu substrate in the SE mode. The height of the scallops is almost equal and comprises 500 nm.

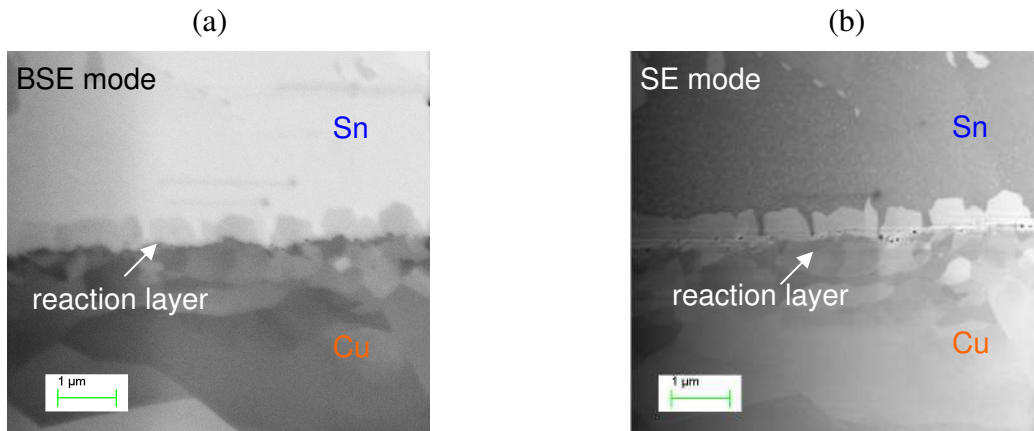


Figure 4-9. The SEM-FEG micrograph in BSE (a) and SE (b) mode showing the cross-section on the reaction spot E (reaction time between 15 and 19 ms).

The micrographs of the longest reaction time (between 30 and 38 ms) spot F on the Substrate 1 are given on Figure 4-10. The single reaction layer is seen between Sn and Cu as well as the voids between the reaction layer and the Cu substrate. The average thickness of the layer is about 1 μm, while the layer appears to be not planar.

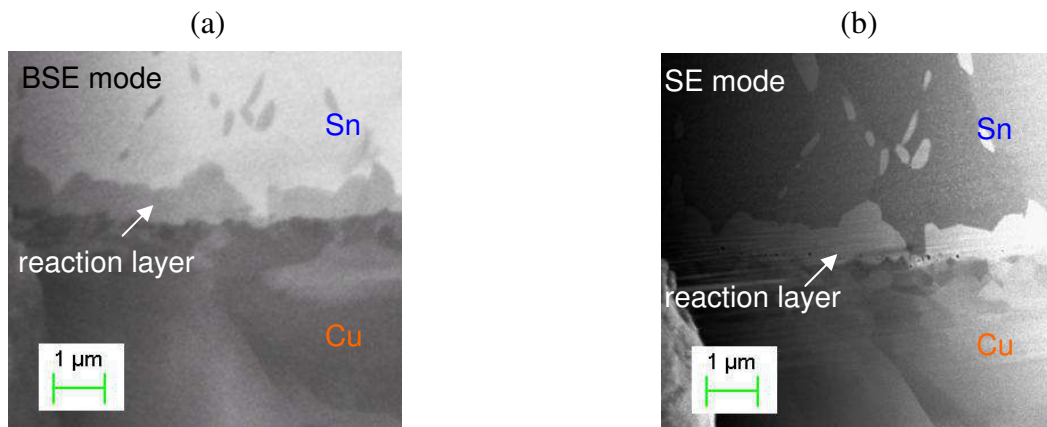


Figure 4-10. The SEM-FEG micrograph in BSE (a) and SE (b) mode showing the cross-section on the reaction spot F (reaction time between 30 and 38 ms).

The Substrate 2 (and respective spot Z) was analyzed in the BSE mode (see Figure 4-11). As it can be seen, after about 1 s of reaction between solid Cu and liquid Sn, the reaction product contains two layers. It should be noticed that the total thickness of the reaction layers is less than 1 μm, which is less than the total thickness of the reaction layer on the spot F.

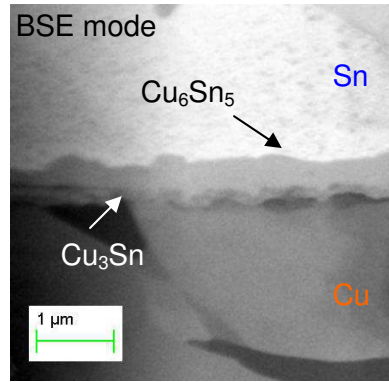


Figure 4-11. The SEM-FEG micrograph in BSE mode showing the cross-section on the reaction spot Z (reaction time around 1 s).

#### Summary of the SEM-FEG results

The reaction between solid Cu and liquid Sn-0.7wt.%Cu alloy was studied after the very short reaction time varying from 1 ms to 1 s by the SEM-FEG microscope working in the SE and BSE mode by implementing FIB preparation of the samples. It was found that the reaction product consists in one single layer for the reaction time between 1 ms and 40 ms. Its morphology changes from the planar layer with a thickness 40 nm to the scallop-like morphology with an average thickness 1  $\mu\text{m}$ . When the reaction time between solid Cu and liquid alloy increases up to 1 s, two layers are detected on the initial interface with a total thickness about 600 nm. In order to reveal the reaction layer(s) phase identity the TEM study was performed.

#### 2-4) The TEM study of the reaction samples

The TEM study was performed on the three spots A, B and E of the Substrate 1 (see Figure 4-4) and on the single spot Z of the Substrate 2 (see Figure 4-5). The possible matches between measured diffraction patterns and crystallographic unit cells were found using the Carine Crystallography 3.1 software with use of the Pearson's crystal structure database [Pearson's database\_2014]. The list of the phases and their crystal structures is given in the Table 4-2. For the  $\text{Cu}_6\text{Sn}_5$  phase three different crystalline structures were verified: the NiAs hexagonal structure that will be called  $\eta^*$  in the following, the  $\text{Cu}_6\text{Sn}_5$  high temperature superstructure (called  $\eta$ ) and the  $\text{Cu}_6\text{Sn}_5$  low temperature or room temperature superstructure called  $\eta'$ . The  $\eta^*$  hexagonal structure is the basic structure for both  $\eta$  and  $\eta'$  superstructures.

Phase	Notation	Crystal structure parameters
Cu	Cu	Face-centered cubic, Fm-3m, $a = b = c = 0.3615 \text{ nm}$ .
$\beta$ -Sn	Sn	Body-centered cubic, I41/amd, $a = b = 0.5829 \text{ nm}$ , $c = 0.3180 \text{ nm}$ .
$\text{Cu}_3\text{Sn}$	$\epsilon$	Orthorhombic, Pmmn O2, $a = 0.4320 \text{ nm}$ , $b = 0.5490 \text{ nm}$ , $c = 0.4740 \text{ nm}$ .
$\text{Cu}_6\text{Sn}_5$ , base	$\eta^*$	NiAs hexagonal structure type, P6 <sub>3</sub> /mmc, $a = b = 0.4218 \text{ nm}$ , $c = 0.5106 \text{ nm}$ .
$\text{Cu}_6\text{Sn}_5$ , ht	$\eta$	Hexagonal, P121/c1, $a = 0.9840 \text{ nm}$ , $b = 0.7070 \text{ nm}$ , $c = 0.9840 \text{ nm}$ .
$\text{Cu}_6\text{Sn}_5$ , rt	$\eta'$	Monoclinic, C12/c1, $a = 1.1020 \text{ nm}$ , $b = 0.7282 \text{ nm}$ , $c = 0.9840 \text{ nm}$ , $\alpha = \gamma = 90^\circ$ , $\beta = 117.4^\circ$ .

Table 4-2. List of the crystal structures checked while identifying the phase identity [Pearson's database\_2014].

### a) Spot A

On the spot A a thin reaction layer on the Cu side comprised by a row of the tiny rectangular grains with equal aspect ratio and height of about 40 nm is detected (see Figure 4-12). In the following this layer will be called “the thin reaction layer”. Above the thin layer on the Sn side the individual free standing scallop-like grains are also detected with height varying from 50 to 200 nm. Small holes are seen between the thin continuous reaction layer and individual scallops and/or Sn. They are filled by an amorphous phase, which probably arises from the deposition in the holes of the matter removed by FIB.

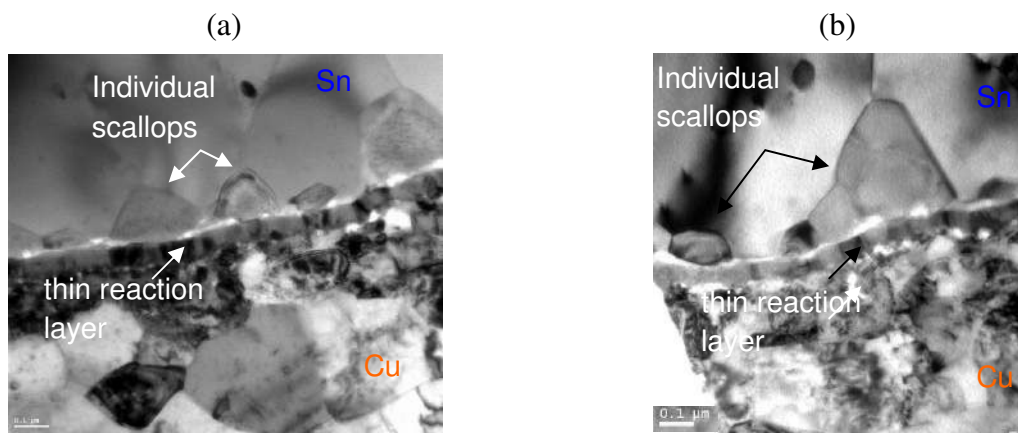


Figure 4-12. The Cu/liquid Sn interface (spot A, reaction time around 1 ms) by TEM.

The TEM analysis (see Figure 4-13) of the thin reaction layer shows that it corresponds perfectly to the  $\eta^*$  structure type (see Figure 4-13c). It was attentively checked that diffraction patterns do not correspond at all to the  $\text{Cu}_3\text{Sn}$  basic structure or Cu. The number of the grains checked individually was equal to 10. As far as  $\eta$  and  $\eta'$  are superstructures of  $\eta^*$ , the calculated diffraction patterns differ by the presence of superlattice spots between the fundamental reflections of  $\eta^*$  [Larsson\_1995]. As the analyzed grains of the thin layer are very small, the diffraction patterns were obtained by converging electron beam in the grains. The obtained experimental patterns consist of large spots, whereas no superlattice spots were detected. Therefore, no superstructure could be pointed out although some ordering could exist.

Note that when the grains are smaller than 100 nm a selection area aperture cannot be used and the nano-beam diffraction is carried out. This method gives a rather uniform intensity for the diffraction patterns that makes difficult the distinction between different compounds. Moreover, in the diffraction patterns, some spots that are forbidden (structure factor = 0) are present due to the dynamic scattering effects. Thus, the comparison is still more difficult.

The crystal structure of the free-standing individual scallops above the thin reaction layer has also a perfect match with the basic  $\eta^*$  structure type and this was verified on three individual scallops (see Figure 4-14 for the representative case). No superlattice spots were detected for the scallops.

To check the chemical composition of these reaction layers and scalloped grains the EDX analysis with a beam size 2-3 nm (which is smaller than the size of the crystals in the thin reaction layer and free-standing scallop-like crystals) was held. As it can be seen on the Table 4-3, four individual scalloped grains and 5 spots in the reaction layer were probed by the electron beam. Note that no standard samples were used to get quantitative analyses. The composition of the scalloped grains was assumed to be the theoretical  $\text{Cu}_6\text{Sn}_5$  composition. A mean Cliff Lorimer factor was deduced and used to determine the composition of the thin

layer. A slightly higher amount of Cu is found in the thin layer. It could be due to the proximity of the Cu phase.

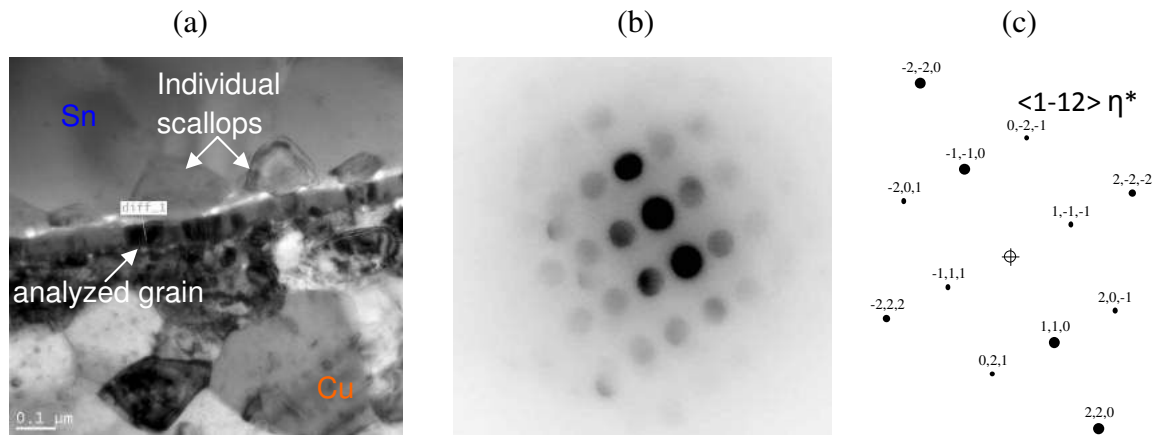


Figure 4-13. TEM image (a) and diffraction pattern (b) of the individual grain in the thin reaction layer. The crystal belongs to the  $\eta^*$  basic phase (c). (Spot A, reaction time around 1 ms).

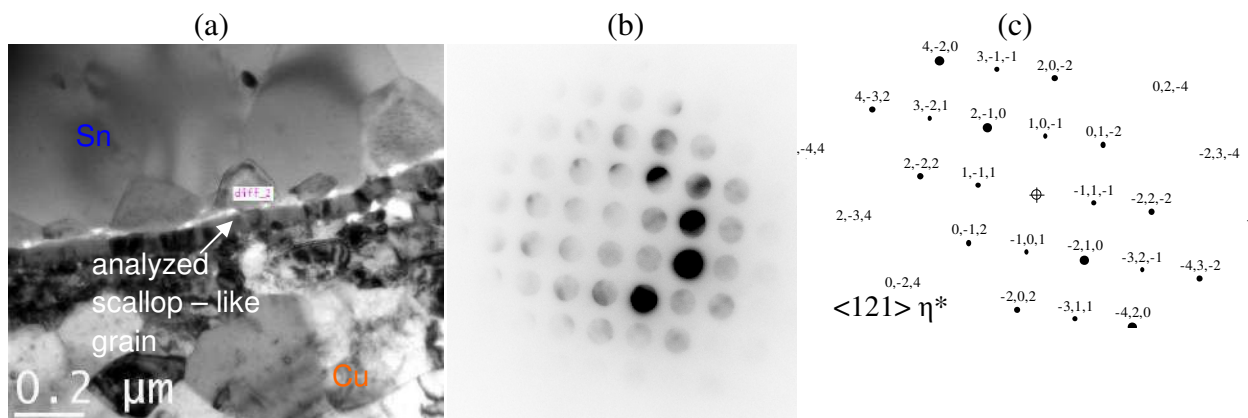


Figure 4-14. TEM image (a) and diffraction pattern (b) of the individual scallops above the thin reaction layer. The crystal belongs to the basic  $Cu_6Sn_5$  phase  $\eta^*$  (c). (Spot A, reaction time around 1 ms).

Phase	Cu (at.%)	Sn (at.%)
Reaction layer	60.7	39.3
Reaction layer	66.0	34.0
Reaction layer	59.1	40.9
Reaction layer	57.4	42.6
Reaction layer	57.1	42.9
Scalloped grain	55.3	44.7
Scalloped grain	58.8	41.2
Scalloped grain	55.5	44.5
Scalloped grain	54.3	45.7

Table 4-3. EDX analysis of the reaction layers on the Cu/Sn-0.7wt.%Cu interface. (Spot A, reaction time around 1 ms).

**b) Spot B**

Figure 4-15 gives a general view on the Cu/Sn interface on the reaction spot B that was studied by TEM. Due to the difficulties with the lamella preparation in this case only three individually scalloped crystals were analyzed. Still all of the scalloped crystals have a crystalline structure corresponding to the  $\eta^*$  basic  $\text{Cu}_6\text{Sn}_5$  phase (see Figure 4-16). No superlattice spots were observed.

For this sample the thin reaction layer was studied in only one place (see Figure 4-17). Similarly to the analysis of the scalloped individual grains it was found that the crystal structure of the grain corresponds to the  $\eta^*$  basic  $\text{Cu}_6\text{Sn}_5$ .

The EDX analysis of both thin reaction layer and scallops has shown the same results as given in Table 4-3

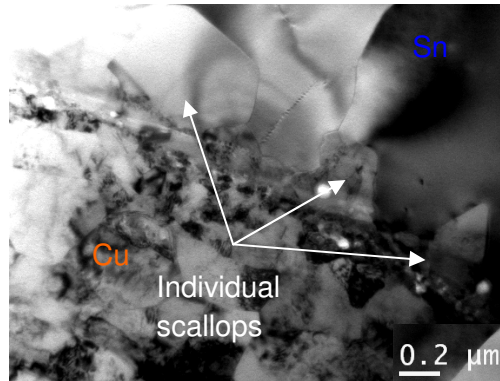


Figure 4-15. General view at the interface on the reaction spot B (reaction time 1-1.5 ms). The scallops are seen above the Cu layer while the thin reaction layer is could not be easily distinguished.

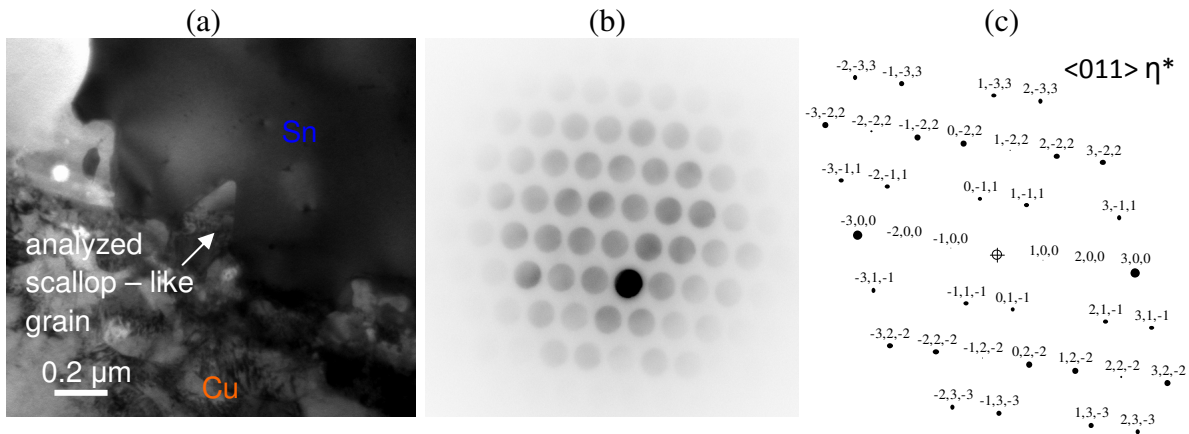


Figure 4-16. TEM image (a) and diffraction pattern (b) of the individual scallops above the thin reaction layer. The crystal belongs to the  $\eta^*$  basic  $\text{Cu}_6\text{Sn}_5$  phase (c). (Spot B (reaction time 1-1.5 ms).

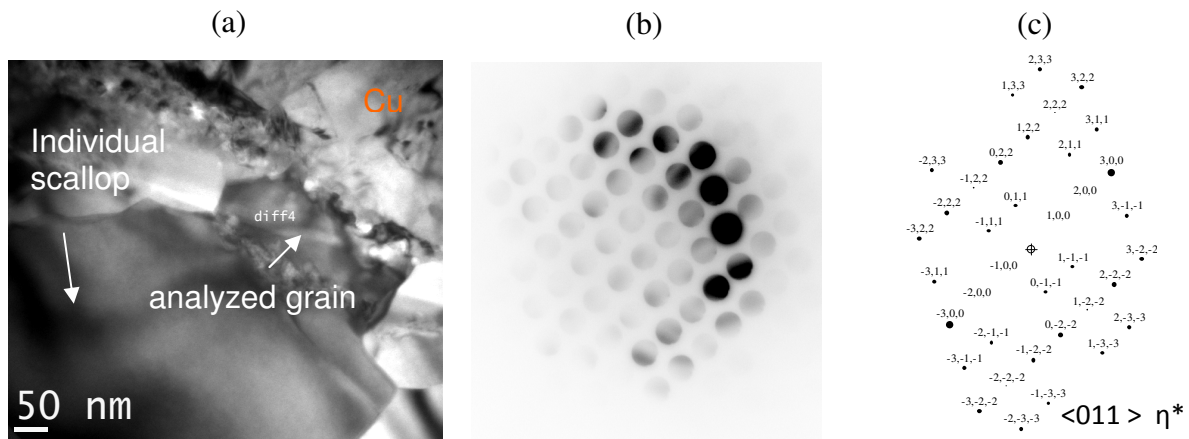


Figure 4-17. TEM image (a) and diffraction pattern (b) of a grain in the thin reaction layer. The crystal belongs to the  $\eta^*$  basic  $\text{Cu}_6\text{Sn}_5$  phase (c). (Spot B (reaction time 1-1.5 ms).

### c) Spot E

The TEM analysis of the reaction spot E (with reaction time around 15-19 ms) revealed two layers on the interface between Cu and tin alloy (see Figure 4-18).

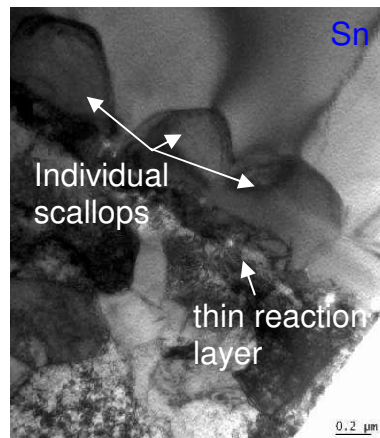


Figure 4-18. General TEM image of the interface on the reaction spot E (reaction time 15-19 ms). The scallops are seen above the thin reaction layer. A chain of pores is also seen between the scallops and the thin reaction layer.

The emerging peculiarity of this reaction spot is that it was found that some scalloped-like grains are adjusted (and have even the same structure  $\eta^*$  and orientation) to the "tiny grains" in the thin reaction layer situated below them (see Figure 4-19). The large scalloped grained (diff 4) is adjacent to the "tiny grain" (df 7) below it (see Figure 4-19a). They have the same crystal structure (basic  $\eta^*$   $\text{Cu}_6\text{Sn}_5$ ) and the same orientation  $\langle 011 \rangle$  (see Figures 4-19c,d,e), most obviously being the same crystal. But it was found that another grain below the scallop (diff 3 on the Figure 4-19b) is in fact a Cu grain with orientation  $\langle 011 \rangle$  (see Figures 4-19f,g). These results suggest that the thin homogenous layer of the tiny  $\text{Cu}_6\text{Sn}_5$  grains (as on the Figure 4-12) had transformed to the mixture of the tiny  $\text{Cu}_6\text{Sn}_5$  grains and Cu grains.

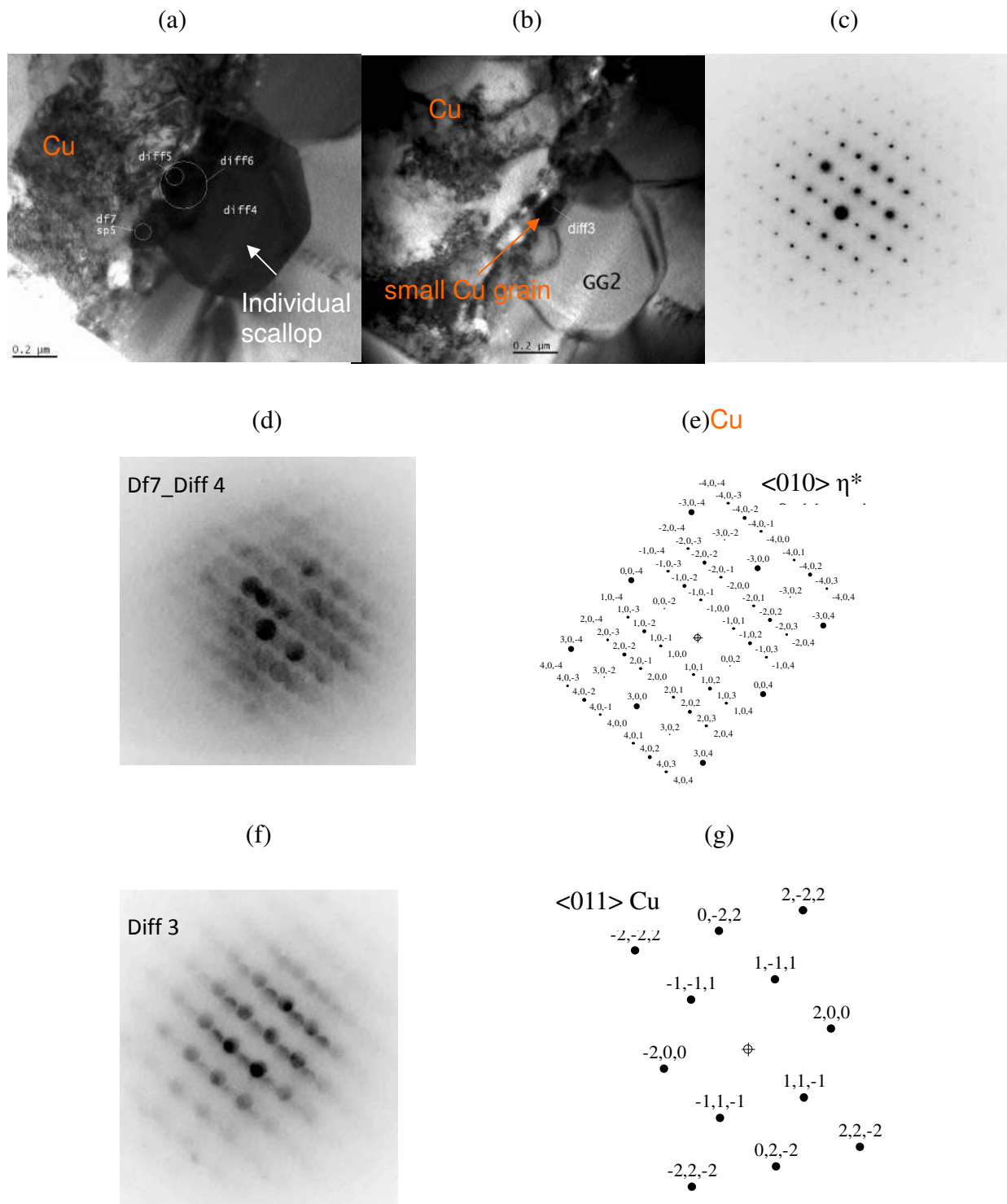


Figure 4-19. TEM image of the interface on the reaction spot E (reaction time 15-19 ms). The scallop-like grain is adjusted to the "tiny grain" in the thin reaction layer (a). Both of them (c,d,e) have the same crystal structure of the  $\eta^*$  basic  $\text{Cu}_6\text{Sn}_5$  phase and the same orientation  $\langle 011 \rangle$ , most obviously being the same crystal. Another small grain (b) just below the large scallop-like grain is a Cu grain (f,g).

#### d) Spot Z

When the reaction time was increased to about 1 s, the classical reaction products formed during soldering process were detected at the interface between Cu and Sn based alloy: (i) the scalloped  $\text{Cu}_6\text{Sn}_5$  phase (with a grain height up to 500 nm) on the Sn side and (ii) a thin and continuous layer about 100 nm thick composed of small rectangular grains (of almost the same size of 100 nm), with a crystal structure that corresponds perfectly to the basic orthorhombic  $\text{Cu}_3\text{Sn}$  crystal structure. This statement was verified for 6 large scalloped-grains and 5 tiny grains in the thin layer. The scalloped grains demonstrate the basic  $\eta^*$   $\text{Cu}_6\text{Sn}_5$  structure except one grain, in which superlattice spots were observed (Figure 4-20).

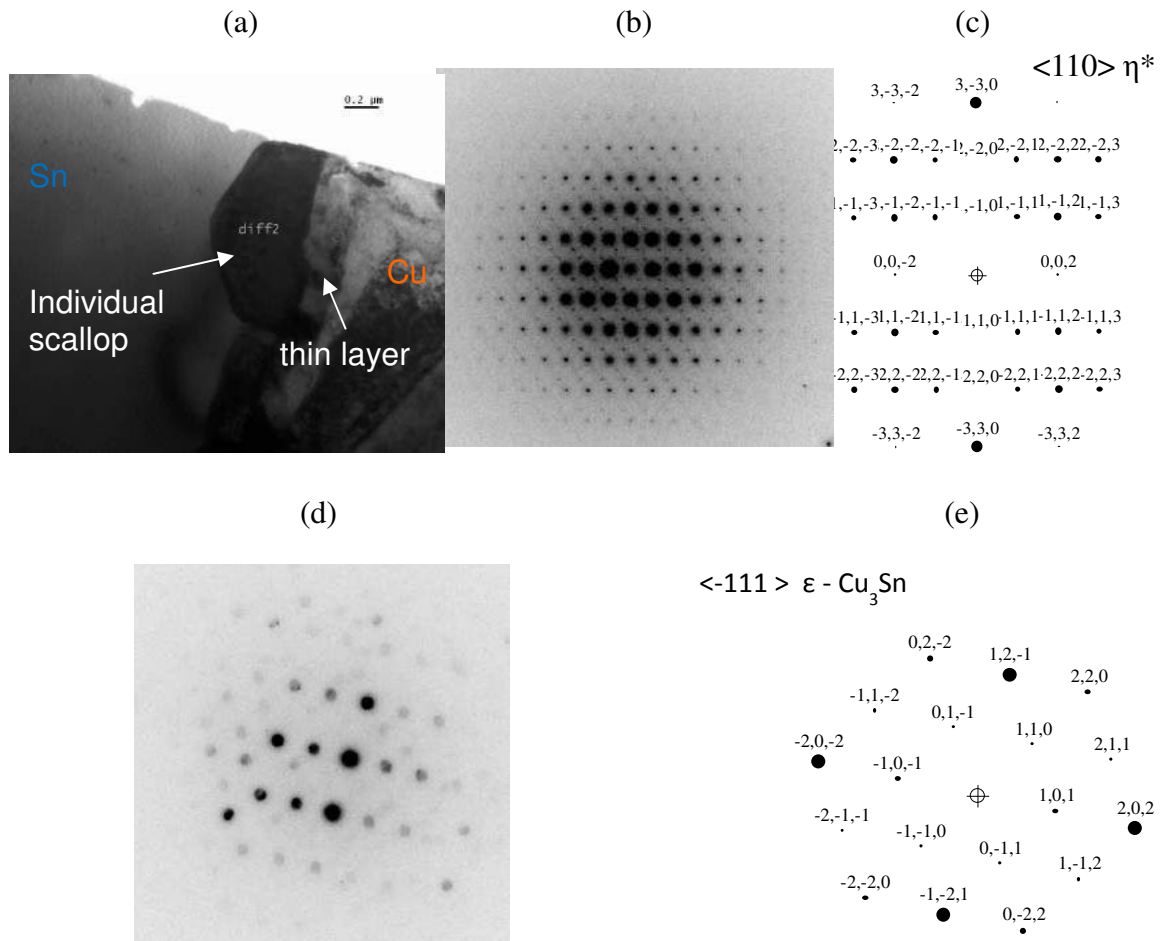


Figure 4-20. TEM image of the Cu/Sn interface after about 1 s reaction at 240°C (spot Z) showing the  $\eta$  – phase scalloped-grain on the Sn side and the  $\epsilon$  phase on the Cu side (a). The scallop-like grain above the thin layer is a  $\text{Cu}_6\text{Sn}_5$  phase, whereas (diff2) is a superstructure of  $\eta^*$  (b,c) and all the grains in the thin layer correspond to the basic  $\text{Cu}_3\text{Sn}$  structure (d,e).

#### Summary the TEM results

The TEM analysis on the reaction spots A, B and E on the Substrate 1 (with reaction time varying from about 1 to about 19 ms) has shown for the first time that the reaction layer at the interface between Cu and Sn-based alloy is actually comprised two layers:

- (i) free-standing scallops (with size varying from 50 to 500 nm) with the crystal structure corresponding to the basic  $\eta^*$   $\text{Cu}_6\text{Sn}_5$  structure;
- (ii) a thin and homogeneous layer of tiny grains (with size varying from 40 to 100 nm) having the same  $\eta^*$  structure as the scallops above it. At the longest reaction time spot it was

found that this homogenous layer of the  $\eta^*$  grains breaks to the layer of the  $\eta^*$  and tiny Cu grains. The interesting peculiarity is that some "tiny  $\eta^*$  grains" are adjusted to the large scalloped grain and have the same crystalline orientation, obviously being the same crystal.

The analysis of the reaction spot Z (with reaction time around 1 s) revealed the classical as-reflowed assembly microstructure: scalloped grains on the Sn side and a thin and homogenous layer of the  $\varepsilon$ -Cu<sub>3</sub>Sn grains. Some scalloped grains demonstrate an ordering of their crystal lattice.

## 2-5) Conclusions

In this section we presented an experimental study of the interfacial reaction between solid Cu and liquid Sn-Cu alloy for the very short duration of contact (from 1 ms to 1 s) at 250°C.

By implementing a fast dipping experimental set-up (made in our laboratory), SEM-FEG and TEM techniques, we succeed to study *for the first time* the sequence of formation of intermetallic compounds at the interface between Cu and liquid Sn-Cu alloy at the very beginning of reaction. Important information about the morphology of the reaction products at the very beginning of reaction is also found.

These experiments give the answer to one of the most interesting questions in soldering: the initial nucleation and growth of the dominant  $\eta$ -Cu<sub>6</sub>Sn<sub>5</sub> phase is proved to happen first. It is also found what thickness (and at what time) this dominant phase should reach before formation of another, initially suppressed,  $\varepsilon$ -Cu<sub>3</sub>Sn phase.

### 3) Modeling of Cu<sub>3</sub>Sn nucleation and growth at Cu/Cu<sub>6</sub>Sn<sub>5</sub> interface in Cu/Cu<sub>6</sub>Sn<sub>5</sub>/liquid Sn system

#### 3-1) Introduction

Given the fact that Kirkendall voids, formed during soldering process, are reported as a damaging factor leading to the weakening of the joint [Zeng\_2005, Mei\_2005, Xu\_2006], initiating failures notably during thermal aging [Yang\_1994], it would be advisable to avoid their formation. It is very important to underline that in almost all studies, the Kirkendall voids formed in Sn based solders/Cu substrate system is related to the formation of the  $\epsilon$ -Cu<sub>3</sub>Sn compound.

In the case of solid state interactions between Sn-based solders and Cu substrate, the thickness of  $\epsilon$ -Cu<sub>3</sub>Sn layer is comparable to that of  $\eta$ -Cu<sub>6</sub>Sn<sub>5</sub> phase [Yang\_1994, Paul\_2011, Kumar\_2011]. On the contrary, in liquid Sn-based solder/Cu systems the thickness of Cu<sub>3</sub>Sn phase is much lower than that of Cu<sub>6</sub>Sn<sub>5</sub> phase [Chan\_1998, Chen\_1999, Gagliano\_2003]. Note that, most of these studies are not concentrated on the early stages of nucleation and growth of intermetallics in liquid Sn/solid Cu system, thus for reactions times of some minutes the size of Cu<sub>6</sub>Sn<sub>5</sub> scallops reaches at least some micrometer, then Cu<sub>3</sub>Sn grows (see for example [Gagliano\_2003]). Moreover, it is generally accepted that the first phase that forms and grows at the liquid solder/Cu interface is  $\eta$ -Cu<sub>6</sub>Sn<sub>5</sub> phase and it is only afterwards that the growth of the  $\epsilon$ -Cu<sub>3</sub>Sn phase occurs at Cu/Cu<sub>6</sub>Sn<sub>5</sub> interface. However, at the best of our knowledge, the conditions under which the  $\epsilon$ -Cu<sub>3</sub>Sn phase starts to grow are not well known. We think that the growth conditions of the  $\epsilon$ -Cu<sub>3</sub>Sn are strongly related to the mass flux balance at Cu/Cu<sub>6</sub>Sn<sub>5</sub> interface and so to the thickness of the first  $\eta$ -Cu<sub>6</sub>Sn<sub>5</sub> phase growing at this interface. Thus, the aim of this section is to evaluate, from thermodynamic and kinetic considerations, the average thickness of the  $\eta$ -Cu<sub>6</sub>Sn<sub>5</sub> phase above which  $\epsilon$ -Cu<sub>3</sub>Sn starts to grow at Cu/Cu<sub>6</sub>Sn<sub>5</sub> interface during liquid Sn/solid Cu interaction. For that, we will consider two cases:

- (i) Nucleation and growth of Cu<sub>3</sub>Sn phase as a thin continuous layer at Cu/Cu<sub>6</sub>Sn<sub>5</sub> interface (*section 3-2*).
- (ii) Nucleation and lateral growth of Cu<sub>3</sub>Sn phase islands at Cu/Cu<sub>6</sub>Sn<sub>5</sub> interface (*section 3-3*).

#### 3-2) Cu<sub>3</sub>Sn suppression criterion for solid Cu/liquid Sn reaction

##### 3-2-1) Introduction

The fact that the  $\eta$ -Cu<sub>6</sub>Sn<sub>5</sub> phase grows faster than  $\epsilon$ -Cu<sub>3</sub>Sn phase is due to the fact that during the reaction between molten solder and copper, the growth of Cu<sub>6</sub>Sn<sub>5</sub> scallops takes place at the solder/metal interface by rapid liquid state diffusion through nanometric liquid channels between Cu<sub>6</sub>Sn<sub>5</sub> scallops, leading thus to a rapid growth rate of this phase [Kim\_1996, Suh\_2008]. This important assumption will be verified experimentally in the Chapter 5. Thus, the aim of this section is to evaluate, from thermodynamic and kinetic considerations, the average thickness of the  $\eta$ -Cu<sub>6</sub>Sn<sub>5</sub> phase above which  $\epsilon$ -Cu<sub>3</sub>Sn starts to grow as a continuous layer at Cu/Cu<sub>6</sub>Sn<sub>5</sub> interface during liquid Sn/solid Cu interaction.

##### 3-2-2) Model of Cu<sub>3</sub>Sn suppression criterion at Cu/Sn interface

In our case diffusion through the Cu/Cu<sub>3</sub>Sn interface is not a growth rate controlling process [Gusak\_2002]. As a first approximation, we assume that liquid channels with average thickness  $\delta$  exist between the mono-sized hemispherical scallops (with radius  $R$ ) of growing  $\eta$ -Cu<sub>6</sub>Sn<sub>5</sub> phase (see Figure 4-21a). Also we assume that  $\epsilon$ -phase layer of some minimal constant thickness  $l_{cr}$  (say  $l_{cr} \sim 2$  nm) has just formed by nucleation and lateral growth and now is trying to grow normally between  $\eta$ -phase and Cu. It seems physically evident that  $\epsilon$ -phase (as any other phase) cannot be thinner than, say, nanometer (due to nucleation issues or/and due to existence of minimal size of elementary cell with the structure of Cu<sub>3</sub>Sn).

In this section we shall not discuss the details of nucleation and lateral growth of  $\varepsilon$ -phase since the voiding in this phase seems to become a problem only after formation of a continuous layer. All what we need now is: at what conditions the minimally possible layer of this phase is stopped to be kinetically suppressed by the fast-growing  $\eta$ -phase?

We want to evaluate the crossover scallop size  $R = R^*$  of  $\eta$ -phase at which  $\varepsilon$ -phase layer will start to grow.

We assume that the liquid is homogeneous in concentration and already saturated by copper for  $x > R$  and a constant concentration gradient exists in the liquid phase (channels) from the top of the liquid/ $\eta$  interface ( $x = x^{\eta}$ ) where the copper concentration corresponds to the liquid/ $\eta$  equilibrium concentration ( $c^{\eta}$ ) to the  $\varepsilon$ / $\eta$  interface at the bottom of the channels ( $x = x^{\varepsilon\eta}$ ) where the copper concentration in the liquid channels corresponds to the liquid/ $\varepsilon$  metastable equilibrium ( $c^{\varepsilon}$ ) - see Figure 4-21b.

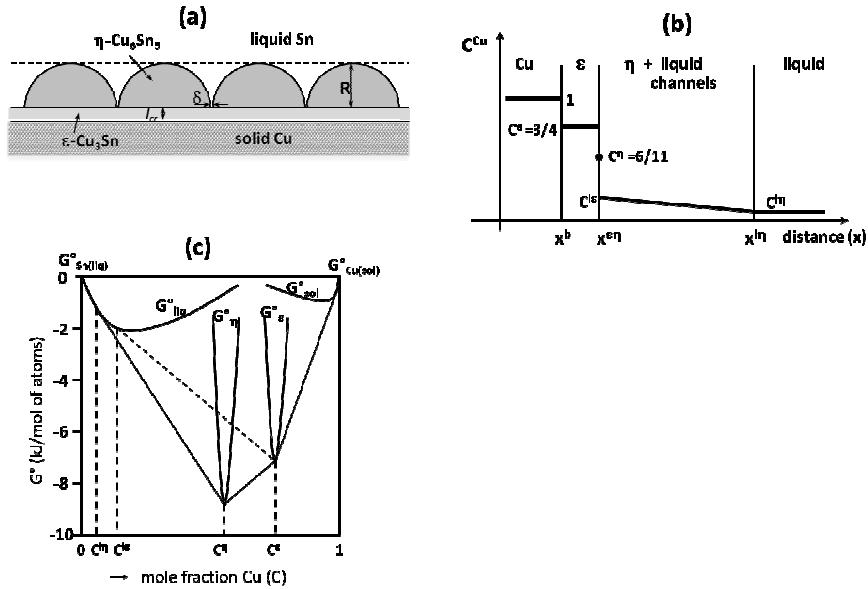


Figure 4-21. Model system : (a) schematic morphology of  $\eta$ - $\text{Cu}_6\text{Sn}_5$  phase formed at solid Cu/liquid Sn interface and (b) schematic presentation of variation of Cu concentration through the solid Cu/liquid Sn system. (c) Schematic presentation of variation of the Gibbs free energy formation of (Sn,Cu) liquid phase, (Cu,Sn) solid phase and  $\eta$ - $\text{Cu}_6\text{Sn}_5$  and  $\varepsilon$ - $\text{Cu}_3\text{Sn}$  compounds at  $T = 523\text{K}$  indicating the stable equilibria (—) and the metastable liquid/ $\varepsilon$  equilibrium (---). References states: stable states at 523K (pure liquid Sn and pure solid Cu) [Dinsdale\_1991, Shim\_1996].

For the fluxes of Cu atoms (number of atoms per unit area per unit time) through both intermetallic phases (evidently, through  $\varepsilon$ -phase layer and liquid channels) we can use the following expressions [Gusak\_2002]:

$$\Omega J^{(\varepsilon)} = \frac{\tilde{D}^{(\varepsilon)} \Delta c_{\varepsilon}^{eq}}{l_{cr}}, \quad (4-1)$$

$$\Omega J^{(\eta)} = D_{Cu}^{melt} \frac{c^{l/\varepsilon} - c^{l/\eta}}{R} \frac{S^{free}}{S^{total}} = \frac{\delta}{R^2} D_{Cu}^{melt} (c^{l/\varepsilon} - c^{l/\eta}), \quad (4-2)$$

where  $\Omega$  is an atomic volume,  $\tilde{D}^{(\varepsilon)} \Delta c_{\varepsilon}^{eq}$  is the integrated diffusion coefficient in  $\varepsilon$  - phase,  $D_{Cu}^{melt}$  is the diffusion coefficient of Cu in liquid Sn-Cu solution,  $c^{l/\varepsilon}$  and  $c^{l/\eta}$  are the equilibrium concentration of Cu at the liquid/ $\varepsilon$  - phase and liquid/ $\eta$  - phase interface correspondingly (see Figure 4-21c). According to the constraint that the interface between the scallops and Cu is occupied completely by scallops except the thin channels, we have:  $N\pi R^2 \approx S^{total} = \text{constant}$ , where  $N$  is the number of scallops. The free surface (the cross-sectional area

of channels at the bottom) for the supply of Cu from the substrate is:  $S^{\text{free}} = 2\pi RN(\delta/2) = (\delta R)S^{\text{total}}$  where  $\delta$  is the channel width. Note that the number of liquid channels per unit area of reaction interface (proportional to  $S^{\text{free}}/S^{\text{total}} = \delta/R$ ) is higher for a scallop-form  $\eta$ -phase compared to a semispherical-form  $\eta$ -phase. The error on  $\delta R$  value can be estimated to be given by the  $a/h$  ratio (about 20-30%) where  $a$  and  $h$  are the average values of base radius and height of a  $\eta$ -scallop respectively ( $a = h = R$  in the case of a semispherical-form).

At that, both planar solid interfaces Cu/ $\varepsilon$ ,  $\varepsilon/\eta$  and averaged nonplanar (scallop-like) interface  $\eta/\text{melt}$  will shift accordingly to the following growth laws:

$$\begin{aligned} (1-c^\varepsilon) \frac{dx^{\text{Cu}/\varepsilon}}{dt} &= 0 - \frac{\tilde{D}^{(\varepsilon)} \Delta c_\varepsilon^{\text{eq}}}{l_{\text{cr}}^\varepsilon}, \\ (c^\varepsilon - c^\eta) \frac{dx^{\varepsilon/\eta}}{dt} &= \frac{\tilde{D}^{(\varepsilon)} \Delta c_\varepsilon^{\text{eq}}}{l_{\text{cr}}^\varepsilon} - \frac{\delta D_{\text{Cu}}^{\text{melt}}}{R^2} (c^{l/\varepsilon} - c^{l/\eta}), \\ (c^\eta - 0) \frac{dx^{\eta/\text{Sn}}}{dt} &= \frac{\delta D_{\text{Cu}}^{\text{melt}}}{R^2} (c^{l/\varepsilon} - c^{l/\eta}) \end{aligned} \quad (4-3)$$

Eventually, the growth rate of  $\varepsilon$ -phase layer could be found as the difference in the velocities of two interfaces ( $\frac{d\Delta x^\varepsilon}{dt} = \frac{dx^{\varepsilon/\eta}}{dt} - \frac{dx^{\text{Cu}/\varepsilon}}{dt}$ ):

$$\frac{d\Delta x^\varepsilon}{dt} \Big|_{l_{\text{cr}}} = \left( \frac{1}{c^\varepsilon - c^\eta} + \frac{1}{1 - c^\varepsilon} \right) \frac{\tilde{D}^{(\varepsilon)} \Delta c_\varepsilon^{\text{eq}}}{l_{\text{cr}}^\varepsilon} - \frac{1}{c^\varepsilon - c^\eta} \frac{\delta D_{\text{Cu}}^{\text{melt}}}{R^2} (c^{l/\varepsilon} - c^{l/\eta}), \quad (4-4)$$

Finally, the growth condition of the  $\varepsilon$ -phase layer becomes:

$$\frac{1}{R^2} \frac{1}{c^\varepsilon - c^\eta} \delta D_{\text{Cu}}^{\text{melt}} (c^{l/\varepsilon} - c^{l/\eta}) < \frac{1 - c^\eta}{(c^\varepsilon - c^\eta)(1 - c^\varepsilon)} \frac{\tilde{D}^{(\varepsilon)} \Delta c_\varepsilon^{\text{eq}}}{l_{\text{cr}}^\varepsilon}, \quad (4-5)$$

$$R > R^* = \sqrt{\frac{(c^{l/\varepsilon} - c^{l/\eta})(1 - c^\varepsilon)}{1 - c^\eta} \frac{D_{\text{Cu}}^{\text{melt}}}{\tilde{D}^{(\varepsilon)} \Delta c_\varepsilon^{\text{eq}}} \delta \cdot l_{\text{cr}}^\varepsilon}. \quad (4-6)$$

For the estimation of exact values of  $R^*$  we need to find values of  $c^{l/\varepsilon}$ ,  $c^{l/\eta}$ ,  $D_{\text{Cu}}^{\text{melt}}$  and  $\tilde{D}^{(\varepsilon)} \Delta c_\varepsilon^{\text{eq}}$ . It is generally accepted that  $D_{\text{Cu}}^{\text{melt}} = 10^{-9} \text{ m}^2 / \text{s}$ .

In their recent work Paul et al. [Paul\_2011] measured experimentally the value of integrated diffusion coefficients for  $\varepsilon$ -phase (the product  $\tilde{D}^{(\varepsilon)} \Delta c_\varepsilon^{\text{eq}}$ ) in the range 498 – 623K. At 523K:  $\tilde{D}^{(\varepsilon)} \Delta c_\varepsilon^{\text{eq}} = 0.87 \times 10^{-16} \text{ m}^2 \text{ s}^{-1}$ .

To find equilibrium concentration of Cu at the liquid/ $\varepsilon$  – phase and liquid/ $\eta$  – phase interface we used CALPHAD data to build the  $G_l(c)$  dependence (in J/mole) on the Figure 4-22 in the form of  $G$ - $H$ SER [Dinsdale\_1991].

All details concerning calculations of  $G_l(c)$  dependence as well as calculations of  $G^\eta$  and  $G^\varepsilon$  are given in Appendix 2. From Appendix 2 we obtain at  $T = 523\text{K}$ :

$$G^\eta = -30412.3 \text{ J / mole},$$

$$G^\varepsilon = -29784.2 \text{ J / mole}.$$

Figure 4-23 gives the calculated variation of the Gibbs free energy of formation ( $G^0$ ) of (Cu,Sn) liquid phase as a function of molar fraction of Cu as well as the Gibbs free energy of formation  $\varepsilon$ -Cu<sub>3</sub>Sn and  $\eta$ -Cu<sub>6</sub>Sn<sub>5</sub> compounds and pure solid Cu.

By simple calculation using common tangent rule (see Figure 4-22) we found the values  $c^{l/\varepsilon} = 0.03152$  and  $c^{l/\eta} = 0.02277$ .

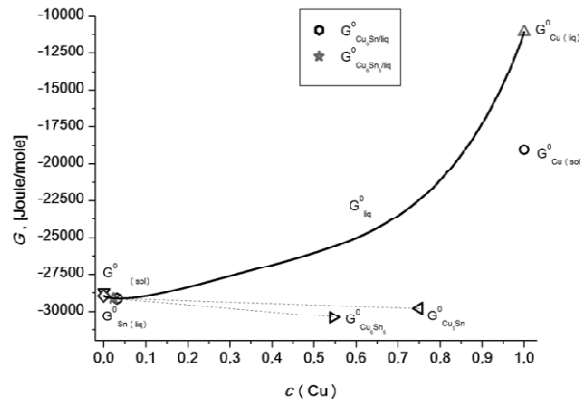


Figure 4-22. Thermodynamics of Cu-Sn system. Calculated variation of the Gibbs free energy of formation ( $G^0$ ) of (Cu,Sn) liquid phase as a function of molar fraction of Cu ( $c^{Cu}$ ). Gibbs free energy of formation  $\epsilon$ -Cu<sub>3</sub>Sn and  $\eta$ -Cu<sub>3</sub>Sn<sub>5</sub> compounds and pure solid Cu. Reference states G-HSER: FCC\_A1(Cu) and BCT\_A5(Sn) at 298.15 K [Dinsdale\_1991, Shim\_1996].

After substitution of all parameters into equation (4-6) we can build the dependence  $R^*(\delta)$  (see Figure 4-23). According to Jong-Ook Suh et al. [Suh\_2008] the width of the channel was estimated to be about 2.5 nm which gives the value  $R^* \approx 0.6 \mu\text{m}$ .

In principle, details of the channel parameters should be found from the conditions of optimal non-equilibrium steady-state wetting in open system under competition between tendency to complete wetting and tendency to transform the liquid channel into intermetallic phase by reaction.

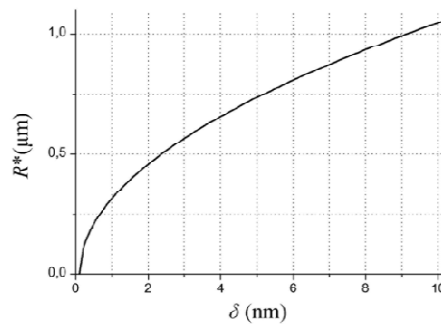


Figure 4-23. Variation of the crossover  $\eta$ -scallop size ( $R^*$ ) as a function of liquid channels size ( $\delta$ ) inside  $\eta$  phase - see equation (4-6).

### 3-2-3) Conclusions

So, our crude evaluations predict that  $\epsilon$ -Cu<sub>3</sub>Sn phase layer can overcome suppression by  $\eta$ -Cu<sub>6</sub>Sn<sub>5</sub> phase after mean size of scallops exceeds about 1 micron. Immediately after this we can expect beginning of voiding due to the difference of mobilities in  $\epsilon$ -phase. This result could be supported by experimental findings given in the section 2. The formation of the  $\epsilon$ -Cu<sub>3</sub>Sn phase was detected only after some incubation time less than 1 s when the thickness of the  $\eta$ -Cu<sub>6</sub>Sn<sub>5</sub> phase had reached about 0.5  $\mu\text{m}$  (see sections 2-3 and 2-4d for the Z sample - Cu plate dipped for 1 s).

### 3-3) Criteria of kinetic suppression of lateral growth of intermediate phases, application to $\text{Cu}_3\text{Sn}$

#### 3-3-1) Introduction

In many cases the formation of intermediate phases in solid state reaction starts from nucleation, proceeds at first by lateral spreading along interface in the form of narrow layer, and after that continues slow growth in normal direction. So far the lateral growth stage was considered as something almost instant. Yet, if the emerging phase is not the first one, and the already growing phase layer has high diffusivity, the lateral growth can be also kinetically suppressed due to “sucking out” of atoms from the moving interface into the growing first phase layer.

In 1990s during the investigation of reaction in multilayers by methods of Differential Scanning Calorimetry (DSC) it was shown that the variety of phases are demonstrating two peaks on thermogram, which correspond to two growth stages [Emeric\_2006, Coffey\_1989, Barmak\_1990, Lucadamo\_2001]. The first stage is the nucleation and lateral growth of the new phase islands with the thickness of few nanometers up to formation of a continuous phase layer. The second stage is the slow normal growth of the phase layer. At least three models were suggested to describe the lateral growth and all of them assumed the diffusion along the interface under frozen bulk diffusion. These models differ in the way of description of the driving force (capillary or/and chemical one) and growth geometry [Klinger\_1998, Lucenko\_2003, Pasichnyy\_2005].

However, to the best of our knowledge, synergy of lateral growth and nucleation (nucleation via lateral growth) was not considered so far. Moreover, the possibility of suppression of lateral phase growth by diffusion fluxes, which pass through the bulk of neighboring fast growing phase layers wasn't considered anywhere. This will be done in this section. It should be considered because typically, the second phase to form has higher melting point, so that bulk diffusion through this phase nuclei during the continuing growth of the first phase (typically, low melting or amorphous one) is practically frozen. So, one should take into account the formation of second phase nuclei by “side diffusion” along its interfaces.

From a general point of view, this problem will be formulated in section 3-3-2 where the reactive diffusion between A and B components leads first to the formation of a continuous layer of the reactive phase 1 at A/B interface. We do not treat here the conditions of nucleation and growth of the first phase to be formed at the interface. The condition of the growth of a second reactive phase (2) at the 1/B interface of the A/1/B system will be formulated and a general solution of this problem will be given. In this case, the second phase has higher melting point whereas first phase is a low melting point compound.

In section 3-3-3, this general solution will be applied to the case of reactive diffusion during growth of  $\text{Cu}_3\text{Sn}$  phase at  $\text{Cu}_6\text{Sn}_5/\text{Cu}$  interface of the  $\text{Sn}/\text{Cu}_6\text{Sn}_5/\text{Cu}$  system at  $250^\circ\text{C}$ .

#### 3-3-2) Problem formulation and general solution

Consider the reactive diffusion between almost pure materials A and B. Let the first phase to grow be the phase 1, with the average concentration  $c_1$  of component B, in the form of continuous planar phase layer. Let's consider the attempts of formation and growth of the phase 2 at the interface 1/B. In most cases the nucleation is heterogeneous. Natural sites of heterogeneous nucleation are the junctions of boundaries of B grains or boundaries of phase 1 grains with the interface 1/B (lines) or junctions of triple joint of grains boundaries with the same interface (points). It may be assumed that even if the nucleus appears at the intersection of triple junction of grain boundaries with the interface, the phase grows, firstly, along the intersection of grains boundaries with interface, and only after, from the boundaries.

That is why during this particular stage the growth of an island could be considered to be one-dimensional, and the island is considered to be a stripe. In this case the cross-section of the system on the site of island nucleation is represented on the Figure 4-24.

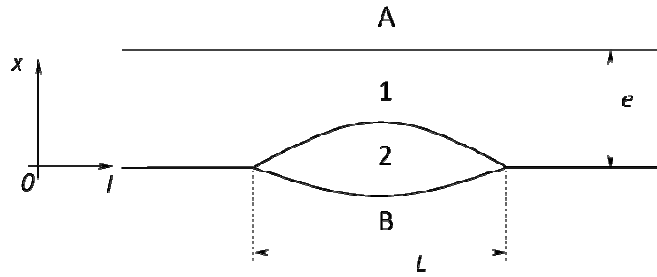


Figure 4-24. Schematic presentation of the interfacial A/B system showing the formation of the first compound 1 as a continuous layer of thickness  $\Delta x_1$  and of phase 2 at the B/1 interface with a rather cylindrical lens-type form.

Let consider the kinetics of the phase 2 island growth in the form of a stripe along the interface 1/B, realized due to lateral diffusion along interfaces 1/B, 1/2 and 2/B. The main model assumptions are the following:

- 1) Diffusion in the volume of the phase 2 is considered to be frozen.
- 2) Diffusion of components occurs along moving interfaces of the island: atoms B are moving along 1/2 interface and atoms A are moving along 2/B interface. For the sake of simplicity the diffusion coefficients of atoms A and B along corresponding interfaces will be considered identical and equal  $D_{int}$ .
- 3) Diffusion along interface leads to a local supersaturation  $\Delta c(l)$  along the phase boundary; excess of B component on the boundary 1/2 and excess of component A on the boundary 2/B lead to the growth of phase 2 and accordingly to the motion of both interfaces along the normal direction.
- 4) Local interface displacement velocity  $U$  is taken to be proportional to local supersaturation on the boundary:

$$U = k\Delta c \quad (4-7)$$

Note that here we make the assumption of small deviation from equilibrium which makes valid the linear approximation of the driving force in terms of composition supersaturation.

The coefficient of proportionality  $k$  (in m/s) is called coefficient of reaction rate. Supersaturation  $\Delta c$  on the boundary 1/2 is the difference between the concentration  $c(l)$  on the interface and the concentration  $c_{1/2}^{eq}$  ( $c$  is the molar fraction of the component B), that corresponds to the equilibrium between phases 1 and 2. Supersaturations on the opposite boundary 2/B should be naturally calculated by the component A. In our simplified model, we consider the processes on two boundaries to be symmetrical (otherwise the grain boundary 1/B near the junction 1/2/B should move and deviate from planar shape). Modeling of such picture is not simple and was described for the first time in Ref. [Pasichnyy\_2008]. That is why we will consider only the motion of interface 1/2 in explicit form, assuming that interface 2/B moves in opposite direction symmetrically. For now we consider the value  $k$  to be the same for both boundaries.

- 5) Opposite to model [Pasichnyy\_2005], excessive material may not only react on particular interface, but also may diffuse through phase layer 1 and react with A on the boundary A/1. Therefore the phase competition for material needed for construction of these phases is realized.

6) Density of diffusion outflow to the boundary through the phase 1 approximately equals to  $\frac{1}{\Omega} \frac{D_1 \Delta c_1}{\Delta x_1}$ .  $D_1$  is the diffusion coefficient in the phase 1,  $\Delta x_1$  is the thickness of the phase 1 and  $\Omega$  is the atomic volume. The coordinate  $x$  is taken  $x = 0$  at 1/B interface (Figure 4-24).

- 7) Let us mark our elementary area of the boundary with coordinate of borders  $l, l + dl$ . Balance of incoming and outgoing flows (in the frame of reference connected with given

elementary area) on this area (see Figure 4-25) with taking into account the law of conservation of matter could be written as:

$$j_{\parallel}(l)\delta W - j_{\parallel}(l+d)W + c_1 U d l W - c_2 U d l W - \frac{D_1 \Delta c_1}{\Delta x_1} d l W = 0, \quad (4-8)$$

where  $l$  is curvilinear coordinate of the point on the interface,  $j_{\parallel}(l)$  and  $j_{\parallel}(l+d)$  are the densities of lateral fluxes along the boundary,  $W$ ,  $\delta$  and  $d l$  are the linear sizes of elementary area of the boundary,  $c_1$  and  $c_2$  are the stoichiometric concentration of phases 1 and 2. The first two terms in equation (4-8) are the fluxes incoming into elementary volume and outgoing from it along the interface. The third term is the convection flux into the elementary volume from the side of the phase 1, “covering” this volume by normal displacement of the boundary with the velocity  $U$ . The fourth term is the convection flux outgoing from given area with the same velocity through the low boundary with the concentration  $c_2$ . The fifth term is bulk diffusion withdrawal of substance through phase layer 1 from interphase boundary 2/1. It provides the supply of atoms B to interphase boundary A/1 and subsequent reaction with atoms A, which leads to the growth of phase layer 1 at extent of A. Just this term is new in comparison with the works [Klinger\_1998, Lucenko\_2003, Pasichnyy\_2005]. Below we will see that just this term can make the growth of nucleus kinetically impossible, even if the process is advantageous thermodynamically.

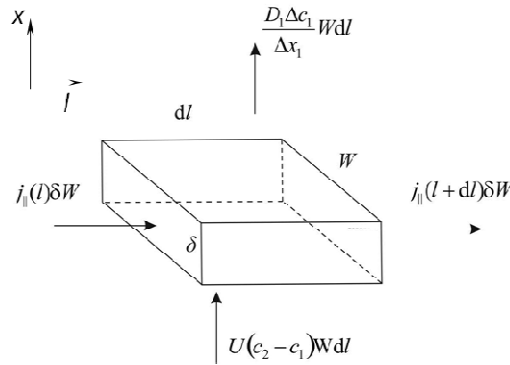


Figure 4-25. Schematic presentation of an elementary volume  $\delta W dl$  of the island of the phase 2 (thickness  $\delta$ , width  $W$ ) situated at B/1 interface indicating the incoming and outgoing fluxes.

In continuous form the equation (4-8) transforms into:

$$D_{\text{int}} \frac{\partial^2 c}{\partial l^2} - (c_2 - c_1) \frac{k \Delta c}{\delta} - \frac{D_1 \Delta c_1}{\delta \Delta x_1} = 0, \quad (4-9)$$

Simple algebraic transformations lead to second order differential equation:

$$\frac{\partial^2 (\Delta c)}{\partial l^2} = \frac{k(c_2 - c_1)}{D_{\text{int}} \delta} (\Delta c + I), \quad (4-10)$$

where  $I = \frac{D_1 \Delta c_1}{k \Delta x_1 (c_2 - c_1)}$  is an additional term which corresponds to the phase competition. Namely, “excess” atom B on the interface 1/2 has three possible ways to decrease the supersaturation:

- It can diffuse further along the interface towards the decreasing chemical potential;
- It can react with atoms A in the phase 1 and, as a result, to increment the phase 2, shifting the interface in perpendicular direction;
- It can diffuse through the volume of the phase 1 to the interface 1/A, to react with atoms A and to promote the growth of phase 1 instead of growth of the phase 2. In above

mentioned works [Gusak\_1982, Gusak\_2010, Geguzin\_1979] only the first two possibilities had been taken into consideration.

The solution of equation (4-10) can be represented in the following form:

$$\Delta c(l) = A_1 e^{\frac{l-L/2}{\lambda}} + A_2 e^{-\frac{l-L/2}{\lambda}} - I, \quad (4-11)$$

where  $\lambda = \sqrt{\frac{D_{\text{int}} \delta}{k(c_2 - c_1)}}$ .

We use the following boundary conditions:

$$\begin{cases} \Delta c|_{l=0} = \frac{\Delta c_2}{2}, \\ \frac{\partial \Delta c}{\partial l}|_{l=L/2} = 0 \end{cases}, \quad (4-12)$$

The first of these equations is related to the maximal supersaturation of the component B on the boundary of interface 1/2, in the point of joint 1/B/2. In this work we consider only symmetrical situations. In this case, the concentration in the middle of the phase 2 ( $x = 0$ ,  $x$  is a coordinate along the global diffusion direction from B to A, see Figure 4-24) should correspond to the middle of the concentration range of this phase  $\Delta c_2$ . Here  $\Delta c_2 = c_{2/B} - c_{2/1}$  is a difference between the concentrations in phase 2 corresponding to the equilibrium with neighboring phases on the opposite boundaries *i.e.*, phase B ( $c_{2/B}$ ) and phase 1 ( $c_{1/B}$ ) respectively, that can be found using common tangent rule (Figure 4-26). That is why the supersaturation of B on the edge of the interface (triple junction 1-2-B contact) is considered to be equal to half of the concentration range of phase 2. The second equation is related also with the symmetry of the problem, for a given time the minimum of supersaturation of B is realized in the center of interface ( $l = L/2$ ). For wide enough islands this minimum of supersaturation tends to zero. After substitution (4-11) into (4-12) we have:

$$A_1 = A_2, A_1 = \frac{\frac{\Delta c_2}{2} + I}{2 \text{ch}\left(\frac{L}{2\lambda}\right)}. \quad (4-13)$$

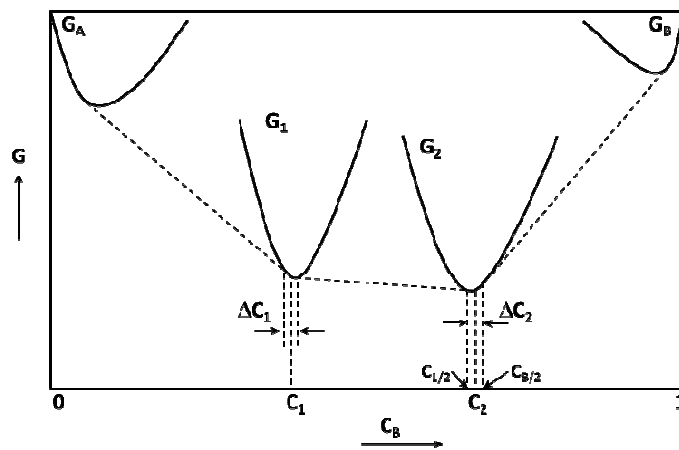


Figure 4-26. Schematic presentation of variation of the Gibbs free-energy formation of A, B solid solutions and compounds 1 and 2, indicating the indicating the stable equilibria ( - - ) and equilibrium concentrations.

In Eq. (4-13), **ch** designates the cosine hyperbolic function:  $\text{ch}x = (e^{+x} + e^{-x})/2$ . Full solution of equation (4-10) leads to:

$$\Delta c(l) = -I + \frac{\Delta c_2 + I}{\operatorname{ch}\left(\frac{L}{2\lambda}\right)} \operatorname{ch}\left(\frac{l-L/2}{\lambda}\right). \quad (4-14)$$

Now we can obtain the condition of phase 2 growth:

$$\Delta c\left(\frac{L}{2}\right) > 0. \quad (4-15)$$

Indeed, if the supersaturation in the center of the island appears to be zero or negative, then the growth of the island becomes impossible. In other words, for the growth of nucleus it is necessary that sucking out of component B through phase 1 layer is slow enough characterized by critical value of  $I$ :

$$I < I_{\text{cr}} = \frac{\Delta c_2}{2\left(\operatorname{ch}\left(\frac{L}{2\lambda}\right) - 1\right)}.$$

Taking into consideration the evident form of expression for  $I$  we obtain the following condition of lateral growth of nucleus of the phase 2:

$$\frac{D_1 \Delta c_1}{\Delta x_1 k (c_2 - c_1)} < \frac{\Delta c_2}{2\left(\operatorname{ch}\left(\frac{L}{2\lambda}\right) - 1\right)}.$$

This condition may be interpreted as condition of the start of the phase 2 growth - it becomes possible when phase layer 1 becomes wide enough:

$$\Delta x_1 > \frac{2D_1 \Delta c_1}{k \Delta c_2 \cdot (c_2 - c_1)} \left(\operatorname{ch}\left(\frac{L}{2\lambda}\right) - 1\right). \quad (4-16)$$

We should take into account that in the condition (4-16) the length of the boundary  $L$  changes with the time and has a minimal value  $L = \delta$ .

$$\text{In the case, when } \lambda \gg L : \left(\operatorname{ch}\left(\frac{L}{2\lambda}\right) - 1\right) \approx \frac{1}{2} \left(\frac{L}{2\lambda}\right)^2,$$

This leads to a simplified condition of growth:

$$\Delta x_1 > \frac{L}{4} \frac{D_1 \Delta c_1}{\frac{\delta}{L} D_{\text{int}} \Delta c_2}. \quad (4-17)$$

$$\text{At } t = 0, L = \delta: \quad \Delta x_1 > \frac{\delta}{4} \frac{D_1 \Delta c_1}{D_{\text{int}} \Delta c_2}. \quad (4-18a)$$

Yet, from thermodynamic point of view, lateral size  $L = \delta$  is, most probably, undercritical. Critical lateral size  $L_{\text{cr}}$  of the lens-type nucleus can be easily found from classical nucleation theory and is typically a few nanometers (depending on exact values of surface tensions and of bulk driving force of phase formation). Therefore, more correct equation would be:

$$\Delta x_1 > \frac{L_{\text{cr}}^2}{4\delta} \frac{D_1 \Delta c_1}{D_{\text{int}} \Delta c_2}. \quad (4-18b)$$

On the other hand, on the basis of these results we can make another interesting prediction: the size of the phase 2 islands could be controlled by the thickness of the phase 1:

$$L < \sqrt{\frac{4\Delta x_1 \delta D_{\text{int}} \Delta c_2}{D_1 \Delta c_1}}. \quad (4-19)$$

This conclusion seems to be new and can be checked experimentally. Current understanding is the following: it is believed that some phase at first is not nucleated due to various reasons of suppression, but after its nucleation it grows fast by lateral diffusion till the

formation of a continuous layer. Now we see that this lateral growth may well be controlled by the thickness of neighboring phase layer.

### 3-3-3) Application to Cu-Sn system

Let A = Sn, B = Cu, phase 1 =  $\eta$ -Cu<sub>6</sub>Sn<sub>5</sub> ( $T_{\text{melt}} = 415^\circ\text{C}$ ),  $\Delta x_I = e_\eta$  and phase 2 =  $\epsilon$ -Cu<sub>3</sub>Sn ( $T_{\text{melt}} = 676^\circ\text{C}$ ), *i.e.*,  $\Delta C_1 = \Delta C_\epsilon$ .

With the following data  $D_1\Delta C_1 = D_\eta\Delta C_\eta = 2 \times 10^{-16} \text{ m}^2 \cdot \text{s}^{-1}$  [Paul\_2011, Kumar\_2011] and  $\Delta C_2 = \Delta C_\epsilon = 2 \times 10^{-3}$  [Park\_2012] Eq. (4-19) becomes:

$$\frac{L_\epsilon^2}{e_\eta} < 4 \times 10^{13} \delta D_{\text{int}} \quad (4-20)$$

Almost all data on grain boundary diffusion or interphase boundary diffusion given in Ref. [Mehrer\_1990] for temperatures around to  $250^\circ\text{C}$  indicate values of ( $\delta D_{\text{int}}$ ) which lie in the interval  $10^{-21}$  to  $10^{-24} \text{ m}^2 \text{ s}^{-1}$  (except the case when Zn is implied). Table 4-4 gives the corresponding values of  $L_\epsilon$  and  $e_\eta$  deduced from Eq. (4-20) for different values of the parameter  $\delta D_{\text{int}}$ . This table shows that for high values of  $\delta D_{\text{int}}$  the nucleation of  $\epsilon$  phase is not suppressed by the growth of the "vampire"  $\eta$  phase while for low values of  $\delta D_{\text{int}}$  the nucleation of  $\epsilon$  phase can be suppressed by the growth of the "vampire"  $\eta$  phase.

$\delta D_{\text{int}} (\text{m}^2 \text{s}^{-1})$	$10^{-21}$	$10^{-22}$	$10^{-23}$	$10^{-24}$	$10^{-25}$
$L_\epsilon$ (in nm) for $e_\eta = 1 \mu\text{m}$	200	60	20	6	2
$e_\eta$ (in $\mu\text{m}$ ) for $L_\epsilon = 1 \text{nm}$	0.025	0.25	2.5	25	250

Table 4-4. Corresponding values of  $L_\epsilon$  and  $e_\eta$  deduced from Eq. (4-20) for different values of the parameter  $\delta D_{\text{int}}$ .

So, deviation of some part of the interface flux to the bulk diffusion flux across the first growing phase layer may lead to full or to partial suppression of the second phase to grow. As a result, one might observe isolated islands of the second phase instead the continuous layer of this phase. Lateral sizes of such islands should grow parabolically and depends on the thickness of suppressing phase.

### 3-3-4) Summary

As known after series of Barmak et al. investigations [Barmak\_1990], rather often the intermediate phase formation during reactive diffusion consists in two stages - first - nucleation and lateral growth, and second (at higher temperatures or/and longer times) - normal growth. In this section, the possibility of kinetic suppression of the lateral growth is discussed for the first time. The criteria of suppression are formulated and applied to Cu-Sn system.

### 3-4) Conclusions

In this section we have developed a theoretical approach on the suppression criteria of the second phase formation ( $\epsilon$ -Cu<sub>3</sub>Sn) at Cu/Cu<sub>6</sub>Sn<sub>5</sub> interface in the Cu/Cu<sub>6</sub>Sn<sub>5</sub>/Sn system by assuming that Cu<sub>6</sub>Sn<sub>5</sub> is the first phase that grow at Cu/Sn interface in form of a continuous layer before the nucleation and growth of the second phase. This assumption is based on the experimental results obtained in section 2 of this Chapter. This theoretical model of the Cu<sub>3</sub>Sn suppression criterion at Cu/Sn interface matches well with the experimental findings presented in section 2. The theoretical criterion gives an estimate for the thickness of the initially formed  $\eta$ -Cu<sub>6</sub>Sn<sub>5</sub> phase to be about  $0.6 \mu\text{m}$  before the nucleation and growth of the second phase  $\epsilon$ -Cu<sub>3</sub>Sn occurs, which is in agreement with the experimental results.

Moreover, a theoretical modeling of even earlier stages of the  $\epsilon$ -Cu<sub>3</sub>Sn phase nucleation is developed. In this second approach, the possibility of kinetic suppression of the lateral

growth (from initially formed isolated nucleus) was discussed for the first time. The criterion of the lateral growth suppression was applied for Cu-Sn system on the basis of the available data of diffusivity in this system.

#### **4) Spectrum of nucleation modes in crystallization of Sn-Cu solder: experimental results versus theoretical model calculations**

##### 4-1) Introduction

In this section we analyze both experimentally and theoretically the various possibilities of Sn-0.7wt.%Cu solder crystallization and in particular we report, for the first time, low undercooling degrees (1-7 K) for this alloy. The supercooling of Sn-0.7wt.%Cu alloy is measured by Differential Scanning Calorimetry experiments performed by using cyclic temperature change of the solder with total melting or with partial melting of the solder. Two different conditions for the solder alloy are used: (i) solder over  $\text{Cu}_6\text{Sn}_5$  phase prepared by dipping a Cu sheet into a bath of Sn-0.7wt.%Cu liquid alloy at 250°C for 1 s providing natural interface for the heterogeneous nucleation of Sn crystals and (ii) solder alloy without any specially prepared interfaces. At least three categories of undercooling degrees of Sn-Cu alloy are observed according to the experimental conditions. For each undercooling category we try to find the type of the heterogeneous nucleation site responsible for the start of the crystallization. Possible nucleation sites and nucleation modes of the crystallization are explored: (i) in the bulk (homogeneous), (ii) at the planar interface liquid alloy/solid  $\text{Cu}_6\text{Sn}_5$  surface, (iii) as a cap over a spherical particle (a), or as a spherical shell covering a  $\text{Cu}_6\text{Sn}_5$  phase sphere (b), (iv) in a spherical cavity and (v) in a groove - at the step of the surface. Theoretical and experimental values of undercooling degrees are compared and the sites of the favorable nucleation are proposed for each case.

##### 4-2) Experimental procedure

Two types of samples are used in this study for DSC experiments: (i) Laboratory made Sn-0.7wt.%Cu alloy, and (ii) one sided solder joints performed by dipping small coupons of copper into the Sn-0.7wt.%Cu liquid alloy. The sample preparation procedures were as follows:

The eutectic Sn-0.7wt.%Cu alloy was prepared from pure base materials following a procedure described in Chapter 2.

Small pieces of the alloy with approximate mass of about 0.5 mg were cut from the bulk alloy sample (about 0.07 mm<sup>3</sup>).

Cu coupons with dimensions 10×6×1.5 mm<sup>3</sup> were successively cut, ground and fine polished from one side with a 0.25 μm particle size diamond suspension and ultrasonically cleaned. Afterwards, the Cu coupons were manually dipped into conventional liquid RMA flux and then into a bath of Sn-0.7wt.%Cu liquid alloy at 250°C for 1 s. After the dipping process, the thickness of the Sn alloy layer over the Cu coupon varied from 20 to 50 μm. The obtained sandwich structures (Sn-0.7wt.%Cu / Cu substrate / Sn-0.7wt.%Cu) were ground from the unpolished side of Cu substrate until the Sn alloy layer is completely eliminated from this side and then cut in small pieces of approximately 2×2 mm<sup>2</sup>. Thus the total mass of Sn alloy over a small piece of the copper substrate is about 0.6 to 1.5 mg (volume 0.08 to 0.2 mm<sup>3</sup>). In the following, this structure is called "sandwich structure".

The dipping conditions (flux, temperature, time) were determined in order to obtain good wetting and thus an intimate contact between the solder and the copper substrate. This important point is verified after dipping experiments as well as after the reflow experiment by scanning electron microscopy (SEM) examination of the copper/solder interface (see section 4-3).

The melting and solidification temperatures of the alloy in the obtained pieces or in the sandwich structures were determined by using a Differential Scanning Calorimeter (DSC). In

the center of an aluminum pan were placed either ten pieces of Sn-0.7wt.%Cu alloy (total mass of about 5 mg) sealed by aluminum cap or a piece of the Cu/Sn-0.7wt.%Cu joint (containing about 0.6 to 1.5 mg of Sn alloy). Two thermal cycles were applied to the samples (see Figure 4-27):

(a) The samples were heated at a constant heating rate of  $10 \text{ K}\cdot\text{min}^{-1}$  up to  $235^\circ\text{C}$ , held isothermally for 5 minutes and then cooled down to room temperature at a constant cooling rate of  $1 \text{ K}\cdot\text{min}^{-1}$ . (**regime A** - called "reflow").

(b) Heating up to  $200^\circ\text{C}$  with a heating rate of  $10 \text{ K}\cdot\text{min}^{-1}$  then with a heating rate of  $2 \text{ K}\cdot\text{min}^{-1}$  followed by an instantaneous stop of the heating after reaching approximately the bottom of the melting peak and cooling with a cooling rate of  $10 \text{ K}\cdot\text{min}^{-1}$  (**regime B** - called "interrupted melting peak").

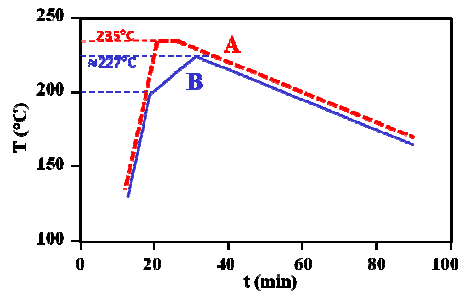


Figure 4-27. Heating and cooling profiles of DSC experiments.

#### 4-3) Experimental results

Figure 4-28 presents Scanning Electron Micrographs of the Cu substrate/solder alloy interfaces after the dipping experiments, i.e., after 1 s of contact at  $250^\circ\text{C}$  between liquid alloy and Cu substrate (Figure 4-28a) and after 5 minutes at  $235^\circ\text{C}$  (Figure 4-28b cycle A). In both cases, the interfacial reaction between copper substrate and the solder alloy led to the formation of a scallop-like interfacial layer about  $1 \mu\text{m}$  and  $5 \mu\text{m}$  thick respectively. The formation of intermetallic compounds between liquid Sn-Cu alloys and Cu substrate has been widely studied in literature (see for example Ref. [Tu\_2007]) and it is well established that the reaction layer is composed of  $\text{Cu}_3\text{Sn}$  compound on the copper side and of  $\text{Cu}_6\text{Sn}_5$  compound on the solder side (see also results presented in section 2 of this chapter concerning the characterization of intermetallic phases formed at Cu/liquid Sn interface).

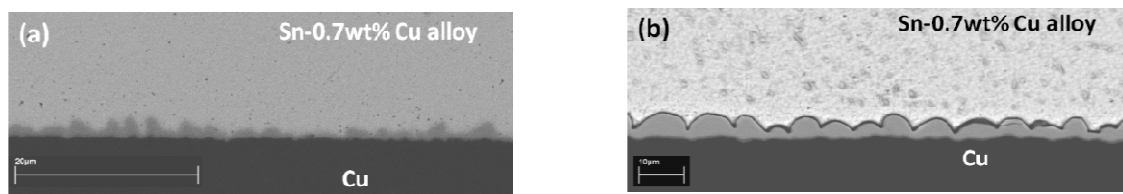


Figure 4-28. Scanning Electron Micrographs of copper substrate/solder balls interface, after dipping of Cu substrate in a Sn-0.7wt.%Cu alloy at  $250^\circ\text{C}$  for 1 s (a) and after a contact for 5 min at  $235^\circ\text{C}$  obtained with back-scattered electrons (BSE) mode operating at 20 kV.

In the DSC measurements where solder balls were placed directly on the aluminum pan, no reaction occurs between solder ball and aluminum pan. Indeed, it is well known that (i) the aluminum surface is covered by an alumina thin layer, (ii) liquid metals such as copper, silver, nickel or tin do not wet alumina (the contact angle being higher than  $90^\circ$  [Eustathopoulos\_1999]) and moreover (iii) these metals do not reduce alumina [Kubaschewski\_1993]. These points are well verified after the DSC experiments, since there were no noticeable interfacial reactions between solder pieces and aluminum pan, thus the Al pans can be considered as inert and non-wetting by the molten solder alloys and the compositions of the solders remain unchanged after the DSC measurements. Note moreover

that, as the solder alloy is oxidized on the surface, even if ten pieces of solder alloy are sealed in one aluminum pan, during melting and holding of solder pieces in liquid state they stay separated from one another. This last point was well verified after numerous experiments.

Figures 4-29 shows the heating and cooling curves of ten Sn-0.7wt.%Cu pieces in the aluminum pan when the *thermal cycle A* is applied. The onset temperatures of the heating curve indicate that the average melting temperature of Sn-0.7wt.%Cu alloy is  $227 \pm 1$  K which is very close to the melting temperature of the binary Cu-Sn eutectic alloy given by the literature [Fürtauer\_2013]. In the cooling curves of Figure 4-29, nine solidification peaks can be seen (the larger first peak corresponds to the simultaneous solidification of two solder pieces). These results clearly indicate that the solidification of each solder piece occurs independently of the other pieces, consistent with each solder piece having different supercooling, and thus undergoes solidification at different temperatures. The uncertainty of solidification temperature for each solder piece is evaluated to be about  $\pm 1$  K. The minimum and maximum observed values of supercooling are between about 45 and 60 K. These undercooling values that we obtain are slightly greater than those obtained, by Huang et al. [Huang\_2009] for Sn-3.8wt.%Ag-0.7wt.%Cu alloy (from 16 to 36 K) and Hodaj et al. [Hodaj\_2013] for Sn- $x$  wt.%Ag-0.5wt.%Cu ( $x = 2.5, 4$  and  $4.5$ ) alloys (from 22 to 49 K) for the same cooling rate but larger solder ball diameter (750  $\mu\text{m}$ ). These undercooling values indicate that the heterogeneous nucleation process occurs because the homogeneous process requires much greater undercooling values, up to 190 K (see Refs. [Perepezko\_1984, Wei\_2012]). Moreover, such a large degree of variation of undercooling among different solder pieces (about 15 K) is due to the probabilistic nature of heterogeneous nucleation of the solidification. Note also that the variation in the impurity content and the form and surface defects of inclusions in the solder alloy, of the tin oxide that covers solder balls, which can be potential sites for heterogeneous nucleation, can influence the heterogeneous nucleation process and thus the undercooling degree. This can be one of the reasons of the discrepancy in results on undercooling degrees reported in literature by different authors.

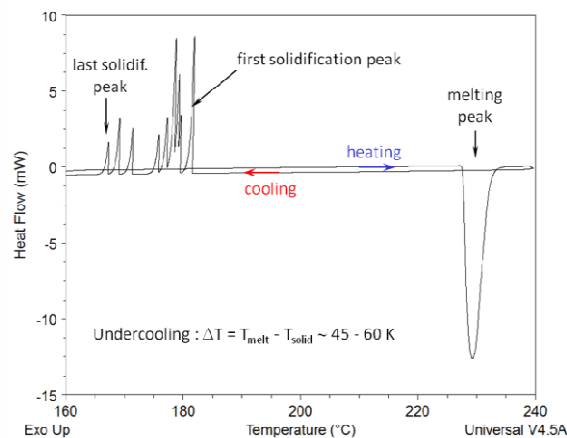


Figure 4-29. DSC curves of 10 pieces of the Sn-0.7wt.%Cu alloy showing the melting and solidification peaks when the heating and cooling regime A is applied.

Figure 4-30 shows the heating and cooling curves of one piece of the sandwich Cu/Sn-0.7wt.%Cu alloy structure when the *thermal cycle A* is repeated 10 times. The onset temperatures of the heating curves indicate that the average melting temperature of Sn-0.7wt.%Cu alloy is the same as in the case of solder alloy pieces, i.e.,  $227 \pm 1$  K and this temperature does not practically evolve with the number of the thermal cycles. The cooling curve of Figure 4-30 shows that undercooling degrees are situated in the range 17-20 K. These undercooling degrees are significantly lower than those observed in the case of solder pieces (about 45-60 K). These results clearly show that the presence of copper substrate in contact with the solder alloy decreases the undercooling degree by about 35 K. These results strongly suggest that in the case of sandwich samples the heterogeneous nucleation at liquid

solder/intermetallic layer interface is favored in comparison with the heterogeneous nucleation on the inclusions contained in the solder balls or on tin oxide layer liquid solder interface. Note, however, that heterogeneous nucleation on the external tin oxide layer or on surface oxidized aluminum is not favored due to the fact that neither tin oxide nor alumina are wetted by liquid metals, the contact angle being higher than  $90^\circ$  [Eustathopoulos\_1999].

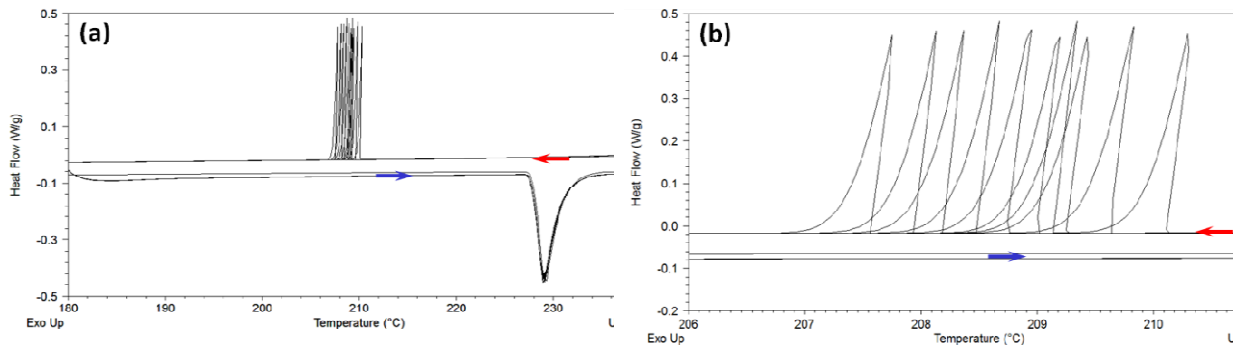


Figure 4-30. DSC curves of 1 sample of the Sn-0.7wt.%Cu alloy/Cu sandwich structure showing the melting and solidification peaks when the heating and cooling regime A is applied 10 times.

Figure 4-31 shows the heating and cooling curves of ten Sn-0.7wt.%Cu pieces when **thermal cycle B** is applied. The heating is stopped at about 229.5 K, i.e. very close the end of the melting peak. This figure shows that there is a drastic decrease in the undercooling values observed here (about 2 to 7 K) compared with those obtained when the **thermal cycle A** is applied to the same samples (45 to 60 K - Figure 4-29).

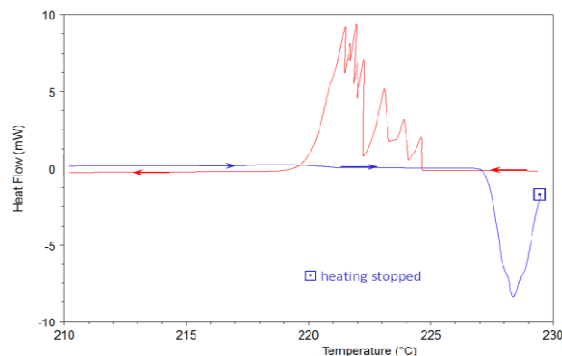


Figure 4-31. DSC curves of 10 pieces of the Sn-0.7wt.%Cu alloy showing the melting and solidification peaks when the heating and cooling regime B is applied.

Figures 4-32 gives the heating and cooling curves of one piece of the sandwich Cu/Sn-0.7wt.%Cu alloy structure when the **thermal cycle B** is repeated ten times. The heating process is stopped at indicated temperatures between 227.6 K and 227.8 K. As shown in this Figure, the undercooling is about 1 to 2 K for 4 cycles, 5 to 7 K for 3 cycles and 14 to 17 K for 3 cycles. It must be emphasized that most of these values (7 of 10) are very similar to the undercooling values obtained when the same thermal cycle is applied to Sn-0.7wt.%Cu alloy pieces (2 to 7 K).

Table 4-5 summarizes all DSC results concerning undercooling values obtained for both configurations (alloy pieces alone or sandwich configuration - Cu/Sn-Cu alloy) when thermal cycles A (reflow) and B (interrupted peak) are applied. According to this table, one can classify the undercooling degrees of Sn-0.7wt.%Cu alloy in at least three categories: (a) low (1-7 K); (b) intermediate (14-20 K) and (c) high undercooling degrees ( $\Delta T = 45-60$  K).

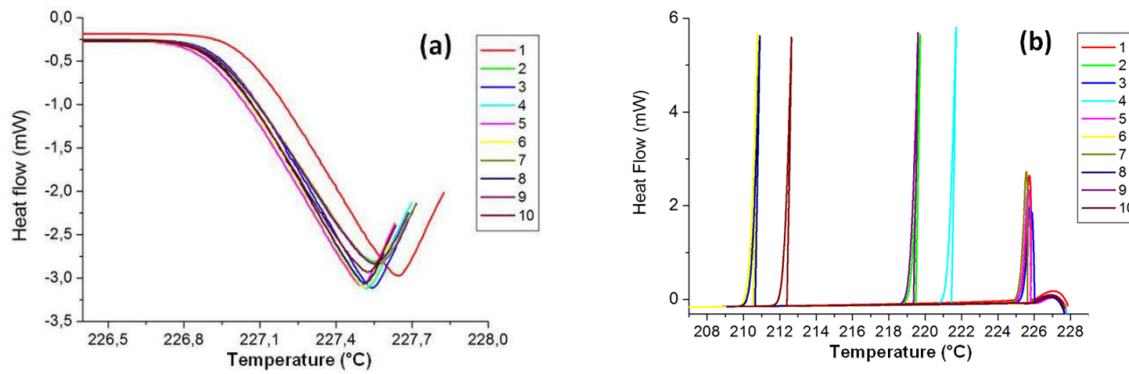


Figure 4-32. DSC curves of 1 sample of the Sn-0.7wt.%Cu alloy/Cu sandwich structure showing the melting and solidification peaks when the heating and cooling regime B is applied 10 times.

Configuration	Thermal cycle A (reflow)		Thermal cycle B (interrupted)	
	Sn-Cu	Cu/Sn-Cu	Sn-Cu	Cu/Sn-Cu
Undercooling (K)	45-60	17-20	2-7	1-7 (7 times); 14-17 (3 times)

Table 4-5. Experimental undercooling values, obtained for both configurations (alloy pieces alone or sandwich configuration - Cu/Sn-0.7wt.%Cu alloy), when thermal cycles A (reflow) and B (interrupted peak) are applied.

#### 4-4) Discussion

The significant reduction in undercooling of the liquid alloy after the thermal cycle A (reflow process), from 45-60 K (case of solder pieces) to 17-20 K (case of solder joint) is most likely due to the presence of  $\text{Cu}_6\text{Sn}_5$  compound at liquid solder/copper interface which promotes the heterogeneous nucleation of solder on due to its very good wetting on  $\text{Cu}_6\text{Sn}_5$ . This significant reduction in undercooling strongly suggests that maintaining of Sn-0.7wt.%Cu alloy pieces for 5 minutes at 235°C leads to the complete dissolution of  $\text{Cu}_6\text{Sn}_5$  precipitates in this alloy. These results are in very good agreement with other experimental results reported in the literature on the undercooling of solder alloys in solder ball and solder joint configurations (see for example Refs. [Kang\_2007, Hodaj\_2013, Chang\_2003, Wang\_2006, Sobczak\_2007, Matsumoto\_2005, Kim\_2009]). The discrepancy in results on undercooling degrees among different solder pieces, found in this study (from 47 to 60 K - see Table 4-5) and reported in literature by different authors (50 to 90 K in Ref. [Park\_YS\_2010] for example), is due not only to the probabilistic nature of heterogeneous nucleation but also to the variation in the impurity content and the form and surface defects of inclusions in the solder alloy which can be potential sites for heterogeneous nucleation, can influence the heterogeneous nucleation process and thus the degree of undercooling.

In the following we will mainly focus on the factors that lead to the low undercooling values (1-7 K) when using the thermal cycle B (interrupted heating) for both configurations: solder pieces only as well as solder joint (sandwich) configuration. In particular, we will discuss the role of the pre-existing  $\eta\text{-Cu}_6\text{Sn}_5$  particles, either in the solder bulk or at the solder/Cu interface, in contact with the liquid solder.

From a general point of view, in order to explain the variety of the undercooling values we must relate each undercooling extent to the corresponding type of the heterogeneous nucleation site. For this we must make a list (as full as possible) of possible nucleation sites and find the interrelations between geometrical characteristics of these sites (curvature, angles) and most probable supercooling values. The most rigorous approach is a calculation

of nucleation rate from classical nucleation theory as was made for example by Turnbull [Turnbull\_1950]. Yet, there is still a lot of discussion on the applicability of the classical nucleation theory to the various nucleation modes. Thus a less rigorous but more practical empirical criteria consists in taking the nucleation barrier energy  $\Delta G^* = 60kT$  as a condition of successful nucleation [Johnson\_1975].

We use this rule as an equation for determining of the undercooling provided by a particular nucleation mode. Namely, for each nucleation mode we find the nucleation barrier as a function of undercooling  $\Delta T$ , solid/liquid interfacial tension  $\gamma_{sl}$ , wetting angle  $\theta$ , interface curvature radius (in the case of heterogeneous nucleation at a curved interface) and geometrical angle if any (for the case of the nucleation on a step or a groove). We approximate the surface tension as temperature independent and take the bulk driving force  $\Delta g$  as a linear function of undercooling (actually, the linear dependence is valid only for small undercooling).

To make our scheme self-consistent, we try to determine all necessary parameters only from undercooling experiments. Namely, we evaluate the liquid/solid interfacial tension  $\gamma_{sl}$  from experimental supercooling values for homogeneous nucleation of tin found in literature (see section 4-4-1). Simultaneously we check if this evaluation is consistent with more rigorous approach of Turnbull [Turnbull\_1950]. Further applying the same criterion for nucleation at the flat interface liquid/ $\eta$ -phase, we evaluate the probable contact angle  $\theta$  (see section 4-4-2). Afterwards, knowing  $\gamma_{sl}$  and  $\theta$  we can proceed to more complex nucleation modes, namely, we consider nucleation of a spherical cap at the surface of a spherical particle (see section 4-4-3), nucleation of a spherical shell over a spherical nano-particle (see section 4-4-4), nucleation on a surface cavity (see section 4-4-5) and finally nucleation at a surface step or groove (see section 4-4-6).

#### 4-4-1) Homogeneous nucleation

Homogeneous nucleation is well described and gives the change in Gibbs free energy during formation of a spherical nucleus of **radius**  $r_1$  and containing  $n$  atoms:

$$\Delta G_{\text{homo}} = -\Delta g n + \gamma_{sl} 4\pi r_1^2 = -\Delta g n + \gamma_{sl} 4\pi r_0^2 n^{2/3}, \quad (4-21)$$

$$\Omega_{\text{at}} \text{ is the atomic volume : } \Omega_{\text{at}} n = \frac{4}{3} \pi r_1^3 \Rightarrow r_1 = (3\Omega_{\text{at}} / 4\pi)^{1/3} n^{1/3} = r_0 n^{1/3},$$

$$\text{where } r_0 = \left( \frac{3\Omega_{\text{at}}}{4\pi} \right)^{1/3}.$$

The critical size is  $r_1^{\text{cr}} = \frac{2\gamma_{sl}\Omega}{\Delta g}$  and the nucleation barrier is given by:

$$\Delta G_{\text{homo}}^* = \frac{16\pi}{3} \Omega_{\text{at}}^2 \frac{\gamma_{sl}^3}{\Delta g^2}, \quad (4-22)$$

where  $\gamma_{sl}$  is a solid/liquid interfacial tension and  $\Omega_{\text{at}}$  the atomic volume.

The driving force  $\Delta g$  depends on undercooling ( $\Delta T = T_m - T$ ):

$$\Delta g(\Delta T) = \frac{q}{T_m} \Delta T \quad (q - \text{fusion heat per atom, } T_m - \text{the equilibrium melting temperature}).$$

Nucleation criterion  $\Delta G^* = 60kT$  [Johnson\_1975] and equation (4-22) give:

$$\frac{16\pi}{3} \Omega_{\text{at}}^2 \frac{\gamma_{sl}^3}{q^2} \left( \frac{T_m}{\Delta T_{\text{homo}}} \right)^2 = 60k(T_m - \Delta T_{\text{homo}}) \quad (4-23)$$

From the highest undercooling degree found in literature for pure tin,  $\Delta T_{\text{homo}} = 190$  K according Perepezko [Perepezko\_1984] one gets the value of surface tension  $\gamma_{sl} = 0.074$  J·m<sup>-2</sup>. Note, however, that if we take  $\Delta T_{\text{homo}} \approx 104$  K (according to Turnbull [Turnbull\_1950]) one gets the value of surface tension  $\gamma_{sl} = 0.0545$  J·m<sup>-2</sup> a value which is about 50% higher than that

corresponding to  $\Delta T_{\text{homo}} = 190$  K. Note that this last  $\gamma_{\text{sl}}$  value practically coincides with the value obtained by Turnbull [Turnbull\_1950] comparing observed undercooling with nucleation rate considerations.

#### 4-4-2) Heterogeneous nucleation at the flat interface molten Sn /Cu<sub>6</sub>Sn<sub>5</sub>

Figure 4-33 represents schematically the nucleation of a spherical cap of tin on the Sn/Cu<sub>6</sub>Sn<sub>5</sub>( $\eta$ -phase) interface for two cases: contact angles  $\theta$  lower and higher than  $90^\circ$ .

The equilibrium contact angle  $\theta$  is given by Young equation  $\cos \theta = (\gamma_{\text{l}\eta} - \gamma_{\text{s}\eta})/\gamma_{\text{sl}}$ , where  $\gamma_{\text{l}\eta}$  and  $\gamma_{\text{s}\eta}$  are the liquid tin/ $\eta$  and solid tin/ $\eta$  interfacial tensions.

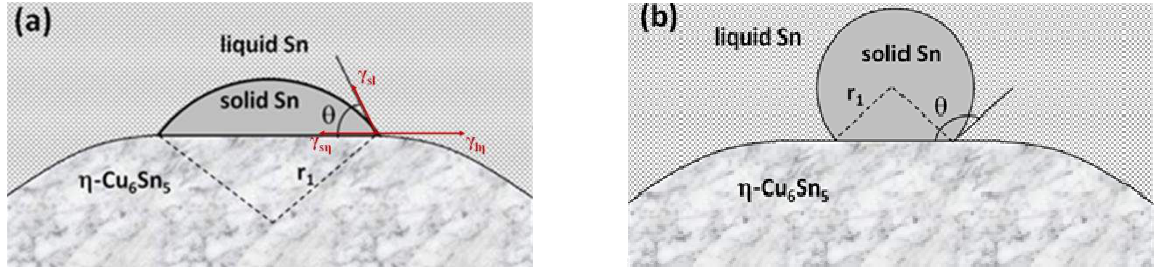


Figure 4-33. Nucleation of solid tin at the flat part of a Cu<sub>6</sub>Sn<sub>5</sub> scallop ( $\eta$  phase): contact angle  $\theta < 90^\circ$  (a) and  $\theta > 90^\circ$  (b).

Standard calculations lead to the following expression for the ratio of nucleation barriers for heterogeneous ( $\Delta G_{\text{planar}}^*$ ) and homogeneous ( $\Delta G_{\text{homo}}^*$ ) nucleation, taken at the same temperature (and, therefore, the same driving force):

$$\frac{\Delta G_{\text{planar}}^*}{\Delta G_{\text{homo}}^*} = \frac{2-3\cos\theta + \cos^3\theta}{4}. \quad (4-24)$$

Here we approximate the interfacial tension as temperature independent which can be considered as a good approximation given the fact that the surface energy of liquid tin changes only by less than 4% when a temperature change as high as 200 K occurs [Eustathopoulos\_1999].

Note that all equations are valid at  $\theta < \pi/2$  as well as at  $\theta > \pi/2$ .

Three limiting cases can be distinguished:

$$\text{a) } \theta \rightarrow 0 \Rightarrow \frac{\Delta G_{\text{planar}}^*}{\Delta G_{\text{homo}}^*} \rightarrow 0.$$

*2D-spreading of the solid phase* - solid tin wets the scallop ( $\gamma_{\text{sl}} + \gamma_{\text{s}\eta} < \gamma_{\text{l}\eta}$ ), making nucleation barrier tending to zero and thus making undercooling impossible.

$$\text{b) } \theta \rightarrow \frac{\pi}{2} \Rightarrow \frac{\Delta G_{\text{planar}}^*}{\Delta G_{\text{homo}}^*} \rightarrow \frac{1}{2}.$$

In this case, nucleation at the interface is favorable but barrier is still significant.

$$\text{c) } \theta \rightarrow \pi \Rightarrow \frac{\Delta G_{\text{planar}}^*}{\Delta G_{\text{homo}}^*} \rightarrow 1.$$

This limiting case seems "natural" since in this case the nuclei do not like surface of compound as a nucleation site, and only homogeneous nucleation becomes possible.

In general case one obtains:

$$\begin{aligned} \Delta G_{\text{planar}}^*(T_{\text{planar}}) &= \frac{2-3\cos\theta + \cos^3\theta}{4} \Delta G_{\text{homo}}^*(T_{\text{planar}}) = \\ &= \frac{2-3\cos\theta + \cos^3\theta}{4} \frac{16\pi}{3} \Omega_{\text{at}}^2 \frac{\gamma_{\text{sl}}^3}{q^2} \left( \frac{T_{\text{m}}}{\Delta T_{\text{planar}}} \right)^2 = 60k(T_{\text{m}} - \Delta T_{\text{planar}}) \end{aligned} \quad (4-25)$$

$\Delta T_{\text{planar}} = T_m - T_{\text{planar}}$  is the undercooling corresponding to the heterogeneous nucleation of tin in a planar surface of  $\text{Cu}_6\text{Sn}_5$  compound.

Combining equations (4-23) and (4-25) we obtain the equation with the only one unknown - the contact angle  $\theta$ :

$$\frac{2-3\cos\theta + \cos^3\theta}{4} = \left( \frac{\Delta T_{\text{planar}}}{\Delta T_{\text{homo}}} \right)^2 \left( \frac{T_m - \Delta T_{\text{planar}}}{T_m - \Delta T_{\text{homo}}} \right) \quad (4-26)$$

The application of Eq. (4-26) for pure Sn with  $T_m = 505$  K, and two different values of homogeneous undercooling ( $\Delta T_{\text{homo}} = 190$  K [Perepezko\_1984] and 104 K [Turnbull\_1950]) and heterogeneous undercooling ( $\Delta T_{\text{planar}} = 20$  K - this study and 40 K [Park\_YS\_2010]), leads to the calculated values of the contact angle  $\theta$  reported in Table 4-6. This table clearly indicates that the calculated value of the contact angle  $\theta$  strongly depends on the experimental values of undercooling required for homogeneous nucleation:  $\theta$  increases by about 45% or 30% when  $\Delta T_{\text{homo}}$  decreases or  $\Delta T_{\text{planar}}$  increases by a factor 2 respectively.

In the following we will choose the value of contact angle  $\theta \approx 32^\circ$ , calculated by using the highest undercooling value of  $\Delta T_{\text{homo}} = 190$  K found in literature [Perepezko\_1984] and the value of  $\Delta T_{\text{planar}} \approx 20$  K found in this study. Note however that in section 4-4-6 we will discuss the influence of the contact angle value on the calculated values of different parameters from calculations that will be performed in next sections.

$\Delta T_{\text{homo}}$ (K)	190		104	
$\Delta T_{\text{planar}}$ (K)	20	40	20	40
$\theta$ ( $^\circ$ )	32.3	46.5	41.9	61.8

Table 4-6. Calculated values of the contact angle  $\theta$  (see Figure 4-33) for two different values of homogeneous undercooling ( $\Delta T_{\text{homo}} = 190$  K [Perepezko\_1984] and 104 K [Turnbull\_1950]) and heterogeneous undercooling ( $\Delta T_{\text{planar}} = 20$  K - this study and 40 K [Park\_YS\_2010]).

#### 4-4-3) Nucleation of a spherical cap on a spherical particle

This case was firstly considered by Fletcher [Fletcher\_1958]. Also we performed the numerical calculations for estimation and comparison of nucleation barriers for different configurations.

The Gibbs energy of formation of a tin spherical cap of **radius**  $r_1$  on a  $\eta$ - $\text{Cu}_6\text{Sn}_5$  spherical particle of radius  $r > r_1$  (see Figure 4-34) can be given as:

$$\Delta G_{\text{cap}} = G_{\text{after}} - G_{\text{before}} = -\frac{\Delta g V_s}{\Omega_{\text{at}}} + \gamma_{\text{sl}} S_{\text{sl}} + (\gamma_{\text{sn}} - \gamma_{\text{sl}}) S_{\text{sn}}, \quad (4-27)$$

where  $V_s$  is the volume of the spherical cap,  $S_{\text{sl}}$  and  $S_{\text{sn}}$  are surface areas at the solid/liquid and solid/ $\eta$  interfaces respectively.

The geometrical factors in Eq. (4-27) can be calculated as:

$$S_{\text{sl}} = 2\pi r_1^2 (1 - \cos\alpha_1), \quad (4-28)$$

$$S_{\text{sn}} = 2\pi r^2 (1 - \cos\alpha),$$

$$V_s = \frac{\pi r_1^3}{3} (2 - 3\cos\alpha_1 + \cos^3\alpha_1) - \frac{\pi r^3}{3} (2 - 3\cos\alpha + \cos^3\alpha).$$

$$\text{where} \quad \cos\alpha = \frac{r - r_1 \cos\theta}{d}, \quad (4-29)$$

$$\cos\alpha_1 = -\frac{r_1 - r \cos\theta}{d},$$

and the distance  $d$  between the centers of the spherical cap and spherical particle is:

$$d = \sqrt{r^2 + r_1^2 - 2rr_1 \cos\theta}.$$

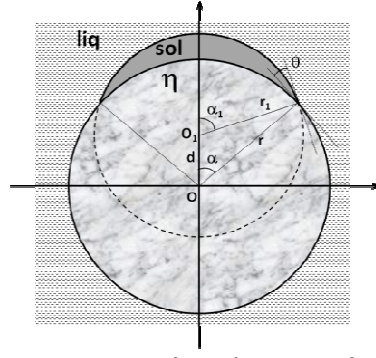


Figure 4-34. Schematic presentation of nucleation of a tin spherical cap (radius  $r_1$ ) on a spherical particle of  $\eta$ -Cu<sub>6</sub>Sn<sub>5</sub> phase (radius  $r$ ).

According to Fletcher [Fletcher\_1958] the expression of the critical embryo radius is given by:

$$r_1^{cr} = \frac{2\gamma_{sl}\Omega_{at}}{\Delta g} \quad (4-30)$$

The free energy of formation of the critical embryo is:

$$\Delta G_{cap}^* = \frac{8\pi}{3}\Omega_{at}^2 \frac{\gamma_{sl}^3}{\Delta g^2} f(\theta, r) = \frac{1}{2}\Delta G_{homo}^* f(\theta, r), \quad (4-31)$$

where  $f(m, x)$  is a geometrical factor. This factor is:

$$f(\theta, r) = 1 + \left(\frac{1-mx}{g}\right)^3 + x^3 \left\{ 2 - 3\left(\frac{x-m}{g}\right) + \left(\frac{x-m}{g}\right)^3 \right\} + 3mx^2 \left(\frac{x-m}{g} - 1\right),$$

where  $x = \frac{r}{r_1^{cr}}$ ,  $m = \cos \theta$  and  $g = (1 + x^2 - 2mx)^{\frac{1}{2}}$ .

When the particle radius  $r$  tends to infinity then  $\Delta G_{cap}^* \rightarrow \Delta G_{planar}^*$  with  $\Delta G_{cap}^* > \Delta G_{planar}^*$  (i.e., combining Eqs. (4-24) and (4-31), it is easy to check numerically that the ratio

$$\frac{\Delta G_{cap}^*}{\Delta G_{planar}^*} = \frac{\frac{1}{2}f(\theta, r)}{2-3\cos\theta+\cos^3\theta} \cdot 4 > 1, \text{ see Figure 4-37 in section 4-4-5). This means that nucleation}$$

at the positively curved interface of a solid particle is always more difficult than that at the planar interface. Therefore the undercooling for nucleation at a spherical particle should be larger than that at a planar interface.

Thus, nucleation of tin at spherical preexistent  $\eta$ -phase particles cannot be responsible for the significant decrease of the undercooling observed experimentally (1-7 K).

#### 4-4-4) Nucleation of a nanolayer on a spherical nanoparticle

This case is well described (see for example Ref. [Sear\_2008]), so we can briefly give the following equations.

The Gibbs energy of the layer formation (see Figure 4-35) can be derived as:

$$\Delta G_{layer} = -\frac{4}{3}\pi(r_1^3 - r^3)\Delta g + 4\pi r_1^2\gamma_{sl} - 4\pi r^2\gamma_{sl}\cos\theta \quad (4-32)$$

where  $r$  is the radius of the spherical nanoparticle and  $r_1 - r$  is the thickness of the nanolayer that forms a spherical shell all over the spherical particle.

Thereby, the critical radius is equal to:

$$r_1^{cr} = \frac{2\gamma_{sl}\Omega_{at}}{\Delta g} \quad (4-33)$$

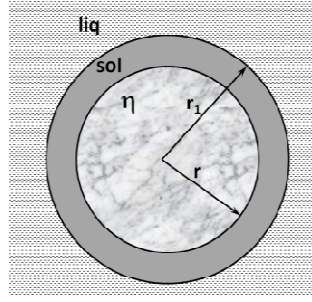


Figure 4-35. Schematic presentation of nucleation of a thin layer of tin over a  $\eta$ - $\text{Cu}_6\text{Sn}_5$  spherical particle (radius  $r$ ).

It is important to note that in this model the  $r_1$  value starts changing not from zero but from  $r_1 > 0$ . If the nanoparticle is large enough,  $r > r_1^{\text{cr}}$ , then the  $\Delta G_{\text{layer}}(r_1)$  curve (Eq. (4-32)) will start from overcritical radius and will be descending without barrier. By using Eqs. (4-21), the expression (4-32) can be represented in the form:

$$\Delta G(r_1) = \Delta G_{\text{homo}}(r_1) - \left( -\frac{4}{3} \frac{\pi r^3 \Delta g}{\Omega_{\text{at}}} + 4\pi r^2 \gamma_{\text{sl}} \cos \theta \right).$$

Therefore, the nucleation barrier in this case depends on the radius of the spherical nanoparticle  $r$  and can be represented as:

$$\Delta G^*(r) = \Delta G_{\text{homo}}^* - \left( -\frac{4}{3} \frac{\pi r^3 \Delta g}{\Omega_{\text{at}}} + 4\pi r^2 \gamma_{\text{sl}} \cos \theta \right) \quad (4-34)$$

One can see that the amount of decrease of the nucleation barrier due to the heterogeneity has itself the barrier like dependence on  $r$ . This dependence is non-monotonic and has a minimum (see Figure 4-37). It means that among all size distribution of nanoparticles only one specific size is optimal.

The optimal radius of the solid nanoparticle at which the nucleation barrier is minimal will be equal to:

$$r^{\text{opt}} = \frac{2\gamma_{\text{sl}} \Omega_{\text{at}} \cos \theta}{\Delta g} \quad (4-35)$$

$$\begin{aligned} \Delta G^*(r^{\text{opt}}) &= \Delta G_{\text{homo}}^* - \left\{ -\frac{4}{3} \frac{\pi \Delta g}{\Omega_{\text{at}}} \left( \frac{2\gamma_{\text{sl}} \cos \theta \Omega_{\text{at}}}{\Delta g} \right)^3 + 4\pi \left( \frac{2\gamma_{\text{sl}} \cos \theta \Omega_{\text{at}}}{\Delta g} \right)^2 \gamma_{\text{sl}} \cos \theta \right\} = \\ &= \Delta G_{\text{homo}}^* - \left( -\frac{32\pi}{3} \Omega_{\text{at}}^2 \frac{\gamma_{\text{sl}}^3}{\Delta g^2} \cos^3 \theta + 16\pi \Omega_{\text{at}}^2 \frac{\gamma_{\text{sl}}^3}{\Delta g^2} \cos^3 \theta \right) = \\ &= \Delta G_{\text{homo}}^* - \frac{16\pi}{3} \Omega_{\text{at}}^2 \frac{\gamma_{\text{sl}}^3}{\Delta g^2} \cos^3 \theta = \Delta G_{\text{homo}}^* (1 - \cos^3 \theta) \end{aligned}$$

$$\text{Thus : } \frac{\Delta G_{\text{layer}}^*(r_{\text{opt}})}{\Delta G_{\text{homo}}^*} = 1 - \cos^3 \theta \quad (4-36)$$

Knowing that:  $\Delta G_{\text{homo}}^* = 4\Delta G_{\text{planar}}^* / (2 - 3\cos \theta + \cos^3 \theta)$  (see Eq. (4-24)), we obtain for  $r = r_{\text{opt}}$ :

$$\frac{\Delta G_{\text{layer}}^*(r_{\text{opt}})}{\Delta G_{\text{planar}}^*} = \frac{4(1 - \cos^3 \theta)}{2 - 3\cos \theta + \cos^3 \theta} \quad (4-37)$$

Note that Eqs. (4-35) and (4-37) are valid only for  $r = r_{\text{opt}}$  that minimize the value of  $\Delta G_{\text{layer}}^*(r)$ .

One can easily check that  $4(1 - \cos^3 \theta) > 2 - 3\cos \theta + \cos^3 \theta$  and thus obtain:

$$\Delta G_{\text{layer}}^*(r) > \Delta G_{\text{layer}}^*(r_{\text{opt}}) > \Delta G_{\text{planar}}^* \quad (4-38)$$

This means that the heterogeneous nucleation of a spherical shell (over a spherical nanoparticle) is less favorable than the heterogeneous nucleation of a spherical cap on a flat surface of the same material. So, this mechanism should also be excluded as responsible of the observed decreasing of undercooling.

#### 4-4-5) Nucleation of a spherical cap on a spherical cavity

This case is described by the same equations as in section 4-4-3 with small changes (see Figure 4-36):

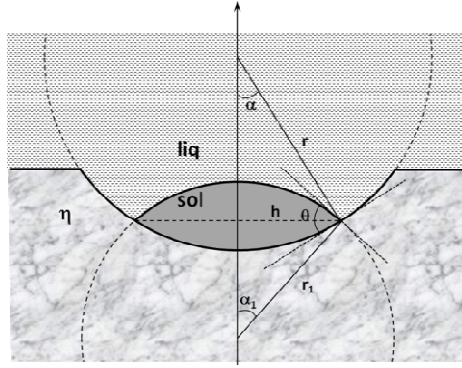


Figure 4-36. Schematic presentation of nucleation of a tin spherical cap (radius  $r_1$ ) on a spherical cavity of  $\eta\text{-Cu}_6\text{Sn}_5$  phase (radius  $r$ ).

$$\Delta G_{\text{cavity}} = G_{\text{after}} - G_{\text{before}} = -\frac{\Delta g V_S}{\Omega_{\text{at}}} + S_{\text{sl}} \gamma_{\text{sl}} - S_{\text{sn}} \gamma_{\text{sl}} \cos \theta \quad (4-39)$$

where  $V_S$  is the volume of the spherical cap,  $S_{\text{sl}}$  and  $S_{\text{sn}}$  are surface areas at the solid/liquid and solid/ $\eta$  interfaces respectively.

The geometrical factors in Eq. (4-37) can be calculated as:

$$S_{\text{sl}} = 2\pi r_1^2 (1 - \cos \alpha_1), \quad S_{\text{sn}} = 2\pi r^2 (1 - \cos \alpha), \quad (4-40)$$

$$V_S = \frac{\pi}{6} r (1 - \cos \alpha) (3h^2 + r^2 (1 - \cos \alpha)^2) + \frac{\pi}{6} r_1 (1 - \cos \alpha_1) (3h^2 + r_1^2 (1 - \cos \alpha_1)^2)$$

In full analogy with Eq. (4-30), the critical curvature radius of solid/liquid interface is

$$r_1^{\text{cr}} = \frac{2\gamma_{\text{sl}} \Omega_{\text{at}}}{\Delta g},$$

$$h^{\text{cr}} = \frac{r_1^{\text{cr}} \sin \theta}{\sqrt{\sin^2 \theta + (\cos \theta + r_1^{\text{cr}} / r)^2}}, \quad \sin \alpha_1^{\text{cr}} = \frac{\sin \theta}{\sqrt{\sin^2 \theta + (\cos \theta + r_1^{\text{cr}} / r)^2}}, \quad \alpha = \theta - \alpha_1 \quad (4-41)$$

The free energy formation of the critical embryo is:

$$\Delta G_{\text{cavity}}^* = \frac{1}{2} \Delta G_{\text{homo}}^* g(\theta, r) \quad (4-42)$$

with  $g(r, \theta)$  a function depending on  $\theta$  and  $r$ .

Using the same reasoning as in section 4-4-3 let us conclude that when the particle radius  $r$  tends to infinity then  $\Delta G_{\text{cavity}}^* \rightarrow \Delta G_{\text{planar}}^*$  with  $\Delta G_{\text{cavity}}^* < \Delta G_{\text{planar}}^*$  (i.e.,

$$\frac{\Delta G_{\text{cavity}}^*}{\Delta G_{\text{planar}}^*} = \frac{\frac{1}{2} g(\theta, r)}{2 - 3\cos \theta + \cos^3 \theta} \cdot 4 < 1 \text{ regardless the values of } \theta \text{ and } r). \text{ This means that the}$$

nucleation at the negatively curved interface of a solid particle is always easier than that at the planar interface. Therefore the undercooling for nucleation in the cavity should be smaller than that at a planar interface.

In order to compare  $\Delta G_{\text{cap}}^*$ ,  $\Delta G_{\text{layer}}^*$ ,  $\Delta G_{\text{cavity}}^*$  and  $\Delta G_{\text{planar}}^*$  for different values of the **radius  $r$  of the spherical catalyst particle**, we have performed numerical calculations for tin nucleation with the following parameters:

$T_m = 505$  K,  $q = 1.168 \cdot 10^{-20}$  J·at<sup>-1</sup>,  $\Omega_{\text{at}} = 2.7 \cdot 10^{-29}$  m<sup>3</sup>,  $\Delta T_{\text{planar}} = 20$  K ( $\Delta g = 4.633 \cdot 10^{-22}$  J·at<sup>-1</sup>) and  $\gamma_{\text{sl}} = 0.074$  J·m<sup>-2</sup> and  $\theta = 32^\circ$  corresponding to  $\Delta T_{\text{homo}} = 190$  K.

Figure 4-37 gives the calculated dependencies of the barrier Gibbs energy of formation of ( $\Delta G^*$ ) of the cap or shell at the interface with positive, infinite and negative curvature radii at the same bulk driving force (the same undercooling) versus absolute value of **radius  $r$**  of the spherical catalyst particle. As it can be seen from this figure, the nucleation of the cap is always more energetically favorable, thereby:

$$\Delta G_{\text{layer}}^* > \Delta G_{\text{cap}}^* > \Delta G_{\text{planar}}^* > \Delta G_{\text{cavity}}^* \quad (4-43)$$

Eq. (4-43) indicates that only nucleation at the cavity is more favorable than nucleation on the planar interface and thus it gives the smaller undercooling.

In order to estimate the radius of curvature of the cavity providing the low undercooling values obtained during the thermal cycles B (interrupted peaks - see Table 4-5), we solved numerically the Eq. (4-39):

$$\Delta G_{\text{cavity}}(\theta, r) = 60k(T_m - 5\text{K})$$

with a typical value of undercooling  $\Delta T = 5$  K in the case of regime B with the above physical values for tin: These calculations with  $\gamma_{\text{sl}} = 0.074$  J·m<sup>-2</sup> and  $\theta = 32^\circ$  gives a radius of curvature of the catalyst particles  **$r$  equal to 11.3 nm**.

Smaller radii should give smaller undercooling, so we can predict that the almost molten solder didn't contain any  $\eta$ -phase particle with cavities smaller than 11.3 nm radius if the undercooling is higher than 5 K.

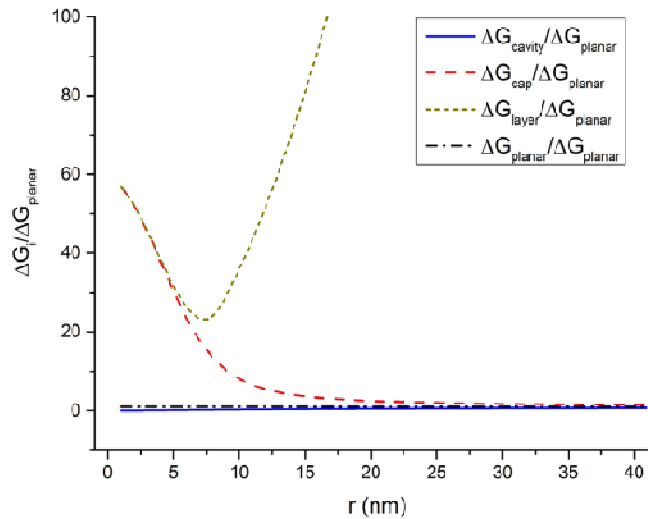


Figure 4-37. Calculated dependencies of the barrier Gibbs energy of formation of a cap or a shell at an interface with positive, infinite and negative curvature radii at the same bulk driving force (the same undercooling) versus absolute value of radius  $r$  of the spherical catalyst particle.

#### 4-4-6) Nucleation on the microgrooves

Two cases are possible (i) the case when the small solid particles of the  $\eta$ -phase have the microgrooves on their surface and (ii) the case of the nucleation on a step with various misorientation angles:

##### 4-4-6-1) The small solid particles of the $\eta$ -phase have microgrooves on their surface

As can be seen, from Figure 4-38, we consider nucleation of a **cylindrical nucleus** across the **grain boundary**. In this case, we can apply the theory developed in the framework of this thesis [Hodaj\_2013\_II] - see Appendix 3.

As it is shown in Appendix 3, the change in Gibbs free energy during the formation of a nucleus with different plum-like shape (depending on the values of  $\alpha$  and  $\beta$ ) is:

$$\Delta G_{gb} = -\Delta g n + (\tilde{\gamma} 4\pi r_0^2) n^{2/3}, \quad (4-44)$$

where

$$\tilde{\gamma} = \left(\frac{3}{2\pi}\right)^{1/3} \gamma_{sl} \left(\beta - \frac{\sin\beta}{\sin\alpha} \cos\theta\right)^{1/3}.$$

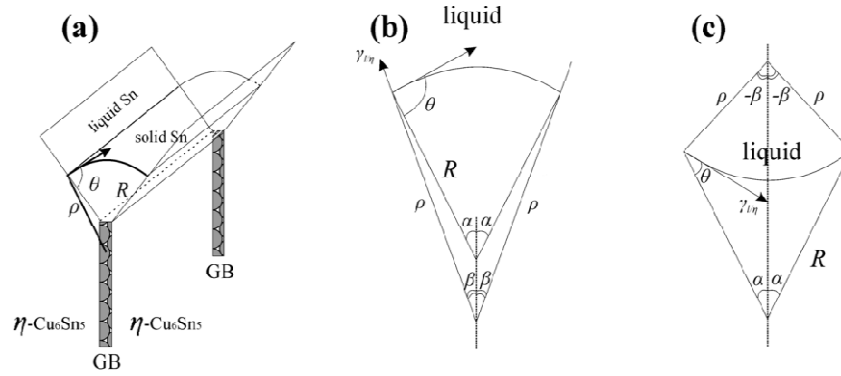


Figure 4-38. a) Geometry of nucleation at the triple joint solid/ $\eta$ -Cu<sub>6</sub>Sn<sub>5</sub> interface-solid/ $\eta$  interface-grain boundary; b) centre of curvature (O) at the solid side ( $\beta > 0$  and  $\theta > \pi/2 - \alpha$ ); c) centre of curvature at the liquid side ( $\beta < 0$  and  $\theta < \pi/2 - \alpha$ ).

The nucleation barrier can be deduced as:

$$\Delta G_{gb}^* = \frac{16\pi}{3} \frac{\Omega_{at}^2}{\Delta g^2} \tilde{\gamma}^3.$$

Comparison of  $\Delta G_{gb}^*$ ,  $\Delta G_{homo}^*$  and  $\Delta G_{planar}^*$  gives:

(i) If  $\beta \equiv \alpha + \theta - \pi/2 > 0$  ( $\theta > \pi/2 - \alpha$ ):

$$\frac{\Delta G_{gb}^*}{\Delta G_{homo}^*} = \left[ \frac{\tilde{\gamma}}{\tilde{\gamma}_{sl}} \right]^3 = \frac{3}{2\pi} \left( \beta - \frac{\sin\beta}{\sin\alpha} \cos\theta \right), \quad (4-45)$$

From Eqs. (4-24) and (4-45) one obtains:

$$\frac{\Delta G_{gb}^*}{\Delta G_{planar}^*} = \frac{\Delta G_{gb}^*}{\Delta G_{homo}^*} = \frac{3}{2\pi} \left( \beta - \frac{\sin\beta}{\sin\alpha} \cos\theta \right) \frac{\Delta G_{planar}^*}{\Delta G_{homo}^*} = \frac{6}{\pi} \frac{\beta - \frac{\sin\beta}{\sin\alpha} \cos\theta}{2-3\cos\theta + \cos^3\theta}, \quad (4-46)$$

with  $\cos\theta = \sin(\alpha - \beta)$ .

(ii) If  $\beta \equiv \alpha + \theta - \pi/2 \leq 0$  ( $\theta \leq \pi/2 - \alpha$ ):

$$\frac{\Delta G_{gb}^*}{\Delta G_{homo}^*} = 0 \quad \text{and} \quad \frac{\Delta G_{gb}^*}{\Delta G_{planar}^*} = 0,$$

where:  $\cos\theta = \frac{\gamma_{ln} - \gamma_{sn}}{\gamma_{ls}}$ ,  $\cos\alpha = \frac{\gamma_{gb}}{2\gamma_{ln}}$ .

So, in the heterogeneous nucleation of a solid phase at the rough substrate one may observe not one, but at least two spreading transitions:

a) If  $\frac{\gamma_{ln} - \gamma_{sn}}{\gamma_{sl}} \geq 1$ , then solid tin wets compound scallops and spreads over them,

so that solidification proceeds without any undercooling.

b) If  $\alpha < \frac{\pi}{2} - \theta$ , ( $\frac{\gamma_{ln} - \gamma_{sn}}{\gamma_{sl}} > \sin\alpha$ ), then one obtains a one-dimensional spreading

transition: solid tin wets the joint and spreads along it, so that, again, solidification proceeds without any undercooling.

Comparing cases 1, 2 and 3, we can predict that the joint of scallops helps solid tin to spread (at least in 1D).

We can identify 4 phase fields (see Figure 4-39):

(i)  $\frac{\gamma_{ln} - \gamma_{sn}}{\gamma_{sl}} \geq 1$  - two dimensional (2D) spreading, zero barrier.

(ii)  $1 > \frac{\gamma_{ln} - \gamma_{sn}}{\gamma_{sl}} \geq \sin\alpha$  ( $\theta \leq \pi/2 - \alpha$ ) - one-dimensional (1D) spreading, zero barrier.

(iii)  $\sin\alpha > \frac{\gamma_{ln} - \gamma_{sn}}{\gamma_{sl}} > -1$  ( $\pi/2 - \alpha < \theta < \pi$ ) - usual activated heterogeneous nucleation.

(iv)  $-1 > \frac{\gamma_{ln} - \gamma_{sn}}{\gamma_{sl}}$  ( $\theta = \pi$ ) - homogeneous nucleation.

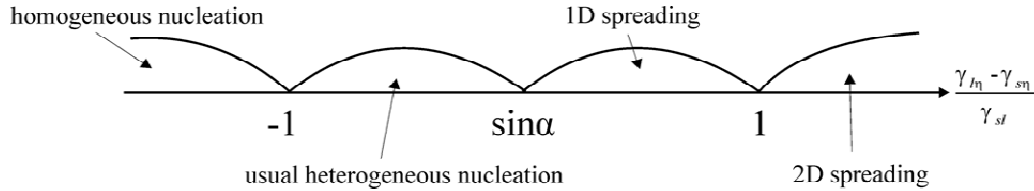


Figure 4-39. Phase fields (schematic presentation).

Varying the angle between scallops by choosing couples with different misorientation, one may try to observe the phase shape transition. Note that the linear size cannot be less than the atomic size,  $\rho_{min} = a$ .

Note also that the shape parameter will be limited, i.e. it will not go to infinity:

$$\varphi_{max} = \frac{n\Omega_{at}}{\rho_{min}^3\Psi} \approx \frac{n\Omega_{at}}{a^3\Psi(\beta \rightarrow 0)} \approx \frac{n\Omega_{at}}{a^3 \sin\alpha \cos\alpha} \approx \frac{n}{\sin\alpha \cos\alpha}$$

In this limiting transition it is important to take into account that  $\cos\theta = \sin(\alpha - \beta)$ , and then to develop a series in respect to the parameter  $\beta$ .

For  $n = 100$  atoms and values of  $\alpha = 30$  and  $45^\circ$ ,  $\varphi_{max}$  are about 230 and 200 respectively, i.e.  $l_{max}$  about 10 nm.

To summarize, considering the nucleation on the rough surfaces we found the theoretical possibility of a one-dimensional spreading transition along the grooves at the triple-junction of two solid-liquid rigid interfaces and a grain boundary.

#### 4-4-6-2) Nucleation on a step with various misorientation angles

Sholl and Fletcher [Sholl\_1970] also considered nucleation on a step with various misorientation angles, but they used an alternative assumption about the form of the nucleus: the part of a sphere cut by step planes (see Figure 4-40).

In the notation used in Ref. [Sholl\_1970], the contact angle was noted as  $\alpha$  (instead of  $\theta$  in this study), the misorientation was noted  $\eta$  and free energies of formation of critical nuclei on the flat surface  $\Delta G_F^*$  ( $= \Delta G_{\text{planar}}^*$  in our case) and on the step  $\Delta G_L^*$  ( $= \Delta G_{\text{step}}^*$  in our case) are given as:

$$\begin{aligned}\Delta G_{\text{planar}}^* &= \Delta G_F^* = (4\pi\gamma_{\text{sl}}^3\Omega_{\text{at}}^2 / 3\Delta g^2) K(\theta) \\ \Delta G_{\text{step}}^* &= \Delta G_L^* = (4\pi\gamma_{\text{sl}}^3\Omega_{\text{at}}^2 / 3\Delta g^2) F(\eta, \theta) \\ \frac{\Delta G_{\text{step}}^*}{\Delta G_{\text{planar}}^*} &= \frac{F(\eta, \theta)}{K(\theta)}\end{aligned}\quad (4-47)$$

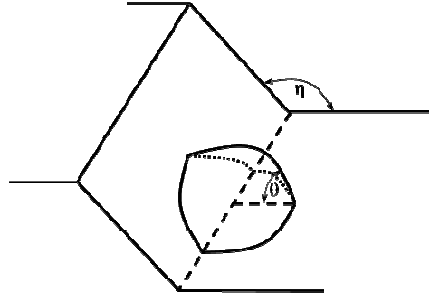


Figure 4-40. Formation of a nucleus with contact angle  $\theta$  on a step of angle  $\eta$ .

with geometrical factor as:

$$\begin{aligned}K(\theta) &= 2 - 3\cos\theta + \cos^3\theta, \\ F(\eta, \theta) &= \frac{1}{\pi} \left[ \cos\theta \sin^2\theta \sin\psi - \cos\theta (3 - \cos^2\theta)\psi + 4\sin^{-1} \left( \sin\frac{\psi}{2} \sin\frac{\eta}{2} \right) \right]\end{aligned}\quad (4-48)$$

where:  $\cos(\psi/2) = \text{ctg}\theta \text{ctg}(\eta/2)$ .

The authors give the dependence between geometrical factors proving that the nucleation is favorable on the step regardless of the misorientation angle  $\eta$  and wetting angle  $\theta$  ( $K(\theta) > F(\eta, \theta)$ , i.e.,  $\Delta G_{\text{step}}^* < \Delta G_{\text{planar}}^*$ ) - see Figure 4-41.

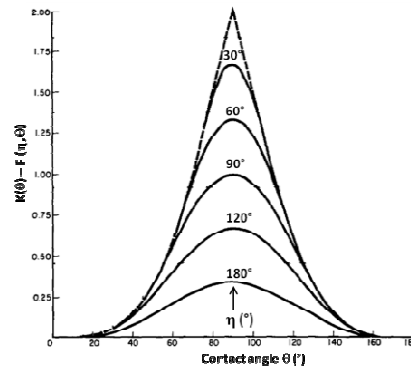


Figure 4-41. Difference between the geometrical factor on a flat surface,  $K(\theta)$ , and that on a step of angle  $\eta$ ,  $F(\eta, \theta)$ , as a function of contact angle  $\theta$  for representative values of step angle - according to Ref. [Johnson\_1975].

To answer the question about which nucleation regime is more energetically favorable (nucleation on the grain boundary - cylindrical shape embryo or nucleation on the step - spherical shape embryo), we performed simple numerical calculation. These calculations have been performed with the following data:  $T_m = 505$  K,  $q = 1.168 \cdot 10^{-20}$  J $\cdot$ at $^{-1}$ ,  $\Omega_{\text{at}} = 2.7 \cdot 10^{-29}$  m $^3$ ,  $\Delta T_{\text{gb}} = 5$  K ( $\Delta g = 1.156 \cdot 10^{-22}$  J at $^{-1}$ ) and  $\gamma_{\text{sl}} = 0.074$  J $\cdot$ m $^{-2}$  and  $\theta = 32^\circ$  corresponding to  $\Delta T_{\text{homo}} = 190$  K, where  $\Delta T_{\text{gb}}$  is the undercooling in the case of nucleation on the microgroove.

Figure 4-42 gives the dependence of the nucleation critical barrier on the misorientation angle ( $\eta_{GB} = 2\alpha$  in the case of the grain boundary nucleation or  $\eta$  in the case of step nucleation). As can be seen from Figure 4-42, the spherical shape of nucleus at the step (or inside the groove) provides lower nucleation barrier than the cut cylinder, regardless of the misorientation angle ( $\eta_{GB} = 2\alpha$  or  $\eta$ ). This conclusion is true regardless of the values of the contact angle  $\theta$ .

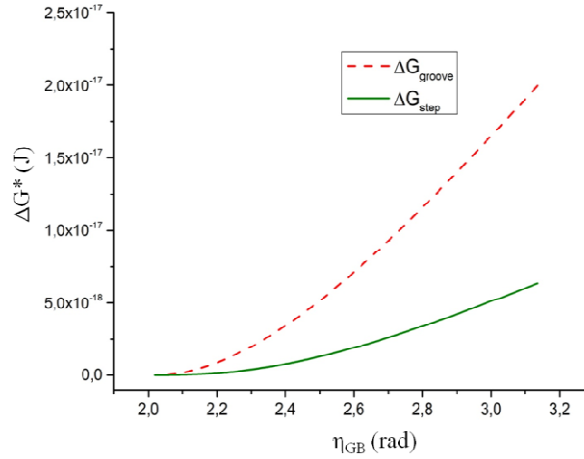


Figure 4-42. Dependence of the nucleation critical barrier on the misorientation angle ( $\eta_{GB} = 2\alpha$  or  $\eta$ ).

Nevertheless we made two independent evaluations for each case (sections 4-4-6-1 and 4-4-6-2):

1) Combining Eqs. (4-23) and (4-46) we obtain:

$$\frac{3}{2\pi} \left( \beta - \frac{\sin\beta}{\sin\alpha} \cos\theta \right) = \left( \frac{\Delta T_{gb}}{\Delta T_{homo}} \right)^2 \left( \frac{T_m - \Delta T_{gb}}{T_m - \Delta T_{homo}} \right) \quad (4-49)$$

Solution of Eq. (4-49) with  $\Delta T_{homo} = 190$  K,  $\Delta T_{gb} = 5$  K and  $\theta = 32^\circ$ , gives a global misorientation angle of the groove  $\eta_{GB} = 2\alpha = 122.6^\circ$ .

2) To estimate the misorientation angle  $\eta$  of the step we can solve Eq. (4-47) numerically with  $\Delta T_{gb} = 5$  K:

$$\Delta G_{step}(r, r_1, \theta) = 60k(T_m - 5 \text{ K}) \quad (4-50)$$

This gives us the misorientation angle equal to approximately  $\eta = 131.8^\circ$ . This value is higher than the "corresponding" global misorientation angle of the groove  $\eta_{GB} = 2\alpha = 122.6^\circ$ , see Figures 4-38 and 4-40.

Thus, we can predict that any remaining  $\text{Cu}_6\text{Sn}_5$  phase particle in the "almost molten" solder cannot contain any groove with angle  $\eta_{GB} = 2\alpha$  less than  $122.6^\circ$  if the undercooling is higher than 5 K.

Note however that the calculated values of curvature radii of cavities  $r_{cavity}$  (section 4-4-5), of misorientation angle of the groove  $\eta_{GB} = 2\alpha$  (section 4-4-6-1) and the misorientation angle of the step  $\eta$  (section 4-4-6-2), beyond which the heterogeneous nucleation for an undercooling value higher than  $\Delta T_B$ , depend on homogeneous undercooling  $\Delta T_{homo}$  and planar undercooling values  $\Delta T_{planar}$  ( $\Delta T_B$  designated here as the experimental undercooling value in the case of regime B - interrupted melting peak). Indeed, as it was mentioned in section 4-4-2, the calculated values of the solid-liquid interfacial energy  $\gamma_{sl}$  as well as those of the contact angle  $\theta$  depend on  $\Delta T_{homo}$  and  $\Delta T_{planar}$  values. In order to evaluate the variation of calculated values of  $r_{cavity}$ ,  $\eta_{GB}$  and  $\eta$  with  $\Delta T_{planar}$  and  $\Delta T_B$ , we have performed calculations of these parameters for two different values of  $\Delta T_{planar}$  and  $\Delta T_B$  and a fixed value of  $\Delta T_{homo} = 190$  K (the highest undercooling value of  $\Delta T_{homo}$  found in literature [Turnbull\_1950]. Table 4-7

summarizes the calculated values of  $r_{\text{cavity}}$ ,  $\eta_{\text{GB}} = 2\alpha$  and  $\eta$  as a function of  $\Delta T_{\text{planar}}$  and  $\Delta T_{\text{B}}$ . This table clearly shows that an increase in  $\Delta T_{\text{B}}$  by a factor higher than two leads to only a slight increase (lower than 20%) in  $r_{\text{cavity}}$ ,  $\eta_{\text{GB}}$  and  $\eta$ . On the contrary, if the value of  $\Delta T_{\text{planar}}$  increases by a factor of two, the calculated values of  $r_{\text{cavity}}$ ,  $\eta_{\text{GB}}$  and  $\eta$  decrease significantly. Note, however, that our experimental results show a very small variation of  $\Delta T_{\text{planar}}$  values (17 to 20 K, see Figure 4-30).

***Thereby, we can conclude that the sites of the favorable nucleation are cavities with curvature radii larger than about 10 nm or/and steps (grooves) on the surface of the solid particle with opening angle larger than about 120-130°.***

$\Delta T_{\text{planar}}$ (K)	<b>20</b>		40	
$\theta$ (°)	<b>32.3</b>		46.5	
$\Delta T_{\text{B}}$ (K)	2	<b>5</b>	2	5
cavity: $r_{\text{cavity}}$ (nm)	9.5	<b>11.3</b>	4.5	4.8
groove: $\eta_{\text{GB}} = 2\alpha$ (°)	108.2	<b>122.6</b>	84.8	93.0
step: $\eta$ (°)	122.8	<b>131.8</b>	92.4	98.8

Table 4-7. Calculated values of  $r_{\text{cavity}}$ ,  $\eta_{\text{GB}} = 2\alpha$  and  $\eta$  as a function of  $\Delta T_{\text{planar}}$  and  $\Delta T_{\text{B}}$ . The homogeneous undercooling value,  $\Delta T_{\text{homo}} = 190$  K, is taken from Ref. [Turnbull\_1950]. The retained values in this study are in bold.

#### 4-5) Conclusions

1. Specific DSC experiments of crystallization of Sn-0.7wt.%Cu alloy, under two different conditions - solder over  $\text{Cu}_6\text{Sn}_5$  phase and solder without any specially prepared interfaces, performed by using cyclic temperature change of the solder with total or with partial melting, lead to at least three categories of undercooling degrees (i) 1-7 K, (ii) 14-20 K and (iii) 45-60 K. The lower undercooling degrees (1-7 K) are reported for the first time in the case of Sn based solder alloys.

2. A practically full list of possible heterogeneous crystallization sites with simple geometrical forms has been considered. This includes nucleation at the curved interfaces with various signs of curvature, and also grooves and steps.

3. For each type of site and for each geometrical parameter the most probable supercooling can be found.

4. In the reflow processes (regime A) the full dissolution of any  $\text{Cu}_6\text{Sn}_5$  particles nanoparticles inside melt is reached, therefore heterogeneous nucleation is related only to solid impurities in the solder bulk or to the  $\text{Cu}_6\text{Sn}_5$  layer formed at Cu/liquid interface in the sandwich samples.

5. In the case of interrupted melting (regime B) there are some remaining  $\text{Cu}_6\text{Sn}_5$  particles in the melt. The sites of the favorable nucleation are, most probably, cavities with curvature radii larger than about ten nanometers or/and steps (grooves) on the surface of the solid particle with opening angle larger than about 120-130°.

### 5) Conclusions

By implementing a fast dipping experimental set-up (made in our laboratory), SEM-FEG and TEM techniques, we succeed to study *for the first time* the sequence of formation of intermetallic compounds on the interface between Cu and liquid Sn-Cu alloy at the very beginning of reaction (from 1 ms to 1 s) at 250°C. For a very short time between 1 ms to 40 ms the formation of the two intermetallic layers at the interface is revealed: a thin and homogenous layer of tiny grains (with size varying between 40 and 100 nm) and scalloped layer of free-standing or adjacent grains (with size varying between 50 and 500 nm). Grains

of both layer correspond perfectly to the basic  $\eta^*$ -Cu<sub>6</sub>Sn<sub>5</sub> structure. On the contrary, the Cu<sub>3</sub>Sn phase crystallites are not detected for such short reaction times. In its turn analysis of the interface between Cu plate dipped in liquid Sn-Cu alloy at 250°C for around 1 s revealed the formation of a thin layer of the  $\varepsilon$ -Cu<sub>3</sub>Sn phase (thickness  $\approx$  100 nm) and a scalloped layer of the Cu<sub>6</sub>Sn<sub>5</sub> phase (scallop height up to 500 nm). These experiments give the answer on one of the most interesting question in soldering: the initial nucleation and growth of the dominant  $\eta$ -Cu<sub>6</sub>Sn<sub>5</sub> phase is proved to happen first. It is also found what thickness (and at what time) this dominant phase should reach before formation of the other, initially suppressed,  $\varepsilon$ -Cu<sub>3</sub>Sn phase will happen.

We have also developed a theoretical approach on the suppression criteria of the second phase formation ( $\varepsilon$ -Cu<sub>3</sub>Sn) at Cu/Cu<sub>6</sub>Sn<sub>5</sub> interface in the Cu/Cu<sub>6</sub>Sn<sub>5</sub>/Sn system by assuming that Cu<sub>6</sub>Sn<sub>5</sub> is the first phase that grow at Cu/Sn interface in form of a continuous layer before the nucleation and growth of the second phase. This assumption is based on the experimental results obtained in section 2 of this Chapter. This theoretical model of the Cu<sub>3</sub>Sn suppression criterion at Cu/Sn interface matches well with the experimental findings presented in section 2. The theoretical criterion gives an estimate for the first formed  $\eta$ -Cu<sub>6</sub>Sn<sub>5</sub> phase thickness of about 0.6  $\mu$ m before the nucleation and growth of the second phase  $\varepsilon$ -Cu<sub>3</sub>Sn occurs, which is in agreement with the experimental results. Moreover, a theoretical modeling of even earlier stages of the  $\varepsilon$ -Cu<sub>3</sub>Sn phase nucleation is developed. In this second approach, the possibility of kinetic suppression of the lateral growth (from initially formed isolated nucleus) was discussed for the first time. The criterion of the lateral growth suppression was applied for Cu-Sn system on the basis of the available data of diffusivity in this system.

Finally, we performed specific DSC experiments of crystallization of eutectic Sn-Cu alloy in two different configurations: solder over Cu<sub>6</sub>Sn<sub>5</sub> phase and solder without any interfaces in order to study the heterogeneous nucleation of solid Sn during cooling of this alloy. By applying complete melting of the solder (reflow cycle) and partial melting thermal cycles we succeed to detect different categories of the undercooling degrees. The peculiar interest lays in detection, *for the first time*, of the low undercooling degrees in the range 1-7 K in the case of partial melting. Detailed analysis of different possible heterogeneous nucleation sites of Sn allowed us to conclude that: (i) In the case of the reflow process (complete melting of the solder), the Cu<sub>6</sub>Sn<sub>5</sub> particles are completely dissolved in the liquid bulk, therefore heterogeneous nucleation is related only to solid impurities in the solder bulk (or to Cu<sub>6</sub>Sn<sub>5</sub> layer formed at Cu/liquid interface in the case of solder joint). (ii) In its turn, when the melting of the solder is interrupted (partial melting), there are still some remaining Cu<sub>6</sub>Sn<sub>5</sub> nanoparticles in the melt providing the heterogeneous nucleation sites for Sn. A theoretical approach on heterogeneous nucleation in this last case (low undercooling values) shows that the sites of the favorable nucleation are, most probably, cavities with curvature radii larger than about ten nanometers or/and steps (grooves) on the surface of the solid particle with opening angle larger than about 120-130°.

## Chapter 5: Growth kinetics of intermetallic layers in the Cu /Sn system

### 1) Introduction

As already mentioned in Chapter 1, reaction between copper and tin-based solder (which is called soldering or reflow in case of liquid solder and solid-state aging in case of solid solder) had been known for a few thousands years but its exact mechanism is still under discussion. In previous chapter we already studied the first stage of  $\text{Cu}_6\text{Sn}_5$  phase formation at Cu/liquid Sn interface and discussed the conditions of successful nucleation and growth of  $\text{Cu}_3\text{Sn}$  intermetallic. In solid-state aging both intermediate phases ( $\text{Cu}_6\text{Sn}_5$  and  $\text{Cu}_3\text{Sn}$ ) growth rates are comparable. In reflow process the growth of  $\text{Cu}_6\text{Sn}_5$  is much faster. It means that the liquid state of solder creates some additional possibilities. According, for example, to Kim and Tu [Kim\_1996], Gusak and Tu [Gusak\_2002] and many others [Bader\_1995, Gagliano\_2003], these additional possibilities are related to full wetting of grain boundaries in  $\text{Cu}_6\text{Sn}_5$  phase by the liquid solder with formation of the liquid channels providing large flux of copper into molten solder with subsequent precipitation of additional  $\text{Cu}_6\text{Sn}_5$  on the interface of scallops with liquid solder. This interpretation was questioned by Görlich and Schmitz [Görlich\_2005], who argued that the grain boundaries may transform into kind of the prewetted boundaries but not into liquid channels. There is still a lot of controversy about the exponent of growth law. Thus, this traditional field still needs additional research and interpretation. We present several new ideas and results in this chapter.

The first idea is to compare the kinetics of  $\text{Cu}_6\text{Sn}_5$  phase growth for the normal couple Cu/Sn<sub>liquid</sub> and for the incremental couple  $\text{Cu}_3\text{Sn}/\text{Sn}_{\text{liquid}}$ . The change in the growth rate may give us a link with the mechanism of the IMC growth. We prepared the growth kinetic experiments at 250°C in two diffusion couples: classical couple of Cu and saturated Sn at 250°C, in which the formation of two IMC, namely  $\eta\text{-Cu}_6\text{Sn}_5$  and  $\varepsilon\text{-Cu}_3\text{Sn}$  proceeds and the incremental couple of as-prepared  $\text{Cu}_3\text{Sn}$  and saturated Sn at 250°C (*see section 2*).

The second key idea is to compare the reaction of copper with liquid and with solid solder at the same temperature. This task is realistic since tin is known for its high ability to supercooling. As it is shown in the previous chapter, nucleation of solid tin usually means overcoming of the rather high nucleation barriers. Therefore, it is possible to study the reaction of copper with solid tin and of copper with supercooled liquid tin at the same temperature. The differences between Cu/solid Sn and Cu/metastable liquid Sn interfacial reactions were studied at the same temperature of 222°C. The aim of this study is to clarify the role of the physical state of the solder on the morphology and on the growth kinetics of the reaction products (*see section 3*).

The third key idea is to treat the disappearance of liquid channel as the process starting from the nucleation of a solid island between the liquid channel walls. To predict the operating width of the liquid channels we have performed the model, which incorporates the heterogeneous nucleation of the  $\eta$ -phase nucleus overlapping the pre-existing liquid channel at its very bottom. Thus, we present the thermodynamic criterion for determination of the channel width in between two growing  $\eta$ -phase scallops (*see section 4*).

Therefore, in this Chapter the study of the growth kinetics of phases in Sn-Cu<sub>solder</sub>/Cu<sub>substrate</sub> system and competition of phases will be presented. The main purpose of the study is to reveal the factors that affect morphology of the reaction products and mechanisms of the growth of phases. The particular interest lays in proving the existence of the liquid channels between the growing scallops of the  $\eta\text{-Cu}_6\text{Sn}_5$  phase during reaction between Cu and tin-based solders at liquid state.

## 2) Phase growth competition in solid-liquid reactions between Cu or Cu<sub>3</sub>Sn compound and liquid Sn-based solder

### 2-1) Experimental procedure

The Cu<sub>3</sub>Sn compound was prepared from 99.99% Cu and 99.9% Sn base metals by melting in an alumina chamber furnace under vacuum. The metals were weighted to obtain the overall composition 62.0wt.%Cu with a total mass of about 2 g and then placed in an alumina crucible 10mm in diameter. The heat treatment cycle is described in Chapter 2 (section 5-3-3). The obtained pieces of the Cu<sub>3</sub>Sn compound were cross-sectioned, grounded, polished and ultrasonically cleaned with basic solutions. Cylindrical peaces 5-10 mm in diameter and 1-2 mm thick were thus obtained for reaction experiments.

Cu coupons (99.99% purity) with dimensions 10×6×1.5 mm<sup>3</sup> were grounded and fine polished from one side and ultrasonically cleaned. The Cu coupons and pieces of Cu<sub>3</sub>Sn were dipped firstly in a conventional liquid RMA flux and then in the liquid melt of pure tin at 250°C for 1 s. The thickness of tin layer over the Cu and Cu<sub>3</sub>Sn substrates varied from 20 to 200 μm. The obtained sandwich structures (Sn/substrate/Sn) were cut in small pieces of approximately 2×2 mm<sup>2</sup>. Each piece was then placed in a not reactive crucible, put in a heating chamber with precise temperature control and heated up to 250°C with a heating rate of 70°C·min<sup>-1</sup>. After isothermal holding at 250°C for the aimed reaction time, the samples were cooled down rapidly by high air flow resulting in an approximate cooling rate of 100°C·min<sup>-1</sup>. The reaction times were 10, 30, 120 and 480 min respectively.

The average thickness of the IMCs was calculated by measuring the total area of the IMCs and dividing it by the total length of the images. In fact, backscattered electron images are examined by an image analysis software (ImageJ) and the thickness of the interfacial layer is measured every 230 nm (about 4 measurements per micrometer). For each cross-section 3 images (about 200μm in length) were taken. In this way, the size distribution and the average value of the reaction layer thickness are obtained by a very large number of measurements.

### 2-2) Experimental results

Figure 5-1 gives SEM micrographs of the reaction product formed at the Cu/alloy interface and at the ε-Cu<sub>3</sub>Sn/alloy interface for the samples, which were aged at 250°C for 10, 30, 120 and 280 min. Figures 5-1a,c,e,g show that whatever the holding time at 250°C, the reaction product at the Cu/alloy interface consists of two IMC layers: a scallop-shaped compound η-Cu<sub>6</sub>Sn<sub>5</sub> on the solder side and a thin layer of ε-Cu<sub>3</sub>Sn compound on the Cu side. This observation is in agreement with the experimental results reported in previous studies, see for example Refs. [Tu\_2007, Gagliano\_2003].

Figures 5-1b,d,f,h show that whatever the holding time at 250°C, the reaction product at the ε-Cu<sub>3</sub>Sn/alloy interface consists of a single layer: a scallop-shaped compound η-Cu<sub>6</sub>Sn<sub>5</sub> presenting a very similar morphology as that of η layer formed at Cu/alloy interface. For comparison purpose, two typical micrographs of the cross section along more than 0.5 mm of the interface are given in Figure 5-2 for Cu/alloy and Cu<sub>3</sub>Sn/alloy samples after isothermal holding at 250°C for 2h.

For each sample, the average thickness  $e$  of each layer ( $e_{\eta}$  and  $e_{\epsilon}$  for Cu/tin couple and  $e'_{\eta}$  for ε-Cu<sub>3</sub>Sn/tin couple) were calculated using Image J software. The average values of  $e$  from samples used for each holding time are given in Table 5-1. This table shows that, for the Cu/alloy samples, the average thickness of the ε-Cu<sub>3</sub>Sn layer  $e_{\epsilon}$  is much lower than that of η-Cu<sub>6</sub>Sn<sub>5</sub> layer  $e_{\eta}$  regardless of the holding time at 250°C and  $e_{\epsilon}$  increases from about 0.5 μm to 4 μm when the holding time increases from 10 to 480 min. It shows also that the thickness of the η-Cu<sub>6</sub>Sn<sub>5</sub> layer formed at Cu/alloy interface ( $e_{\eta}$ ) is very close to that of η formed at ε-Cu<sub>3</sub>Sn/alloy interface.

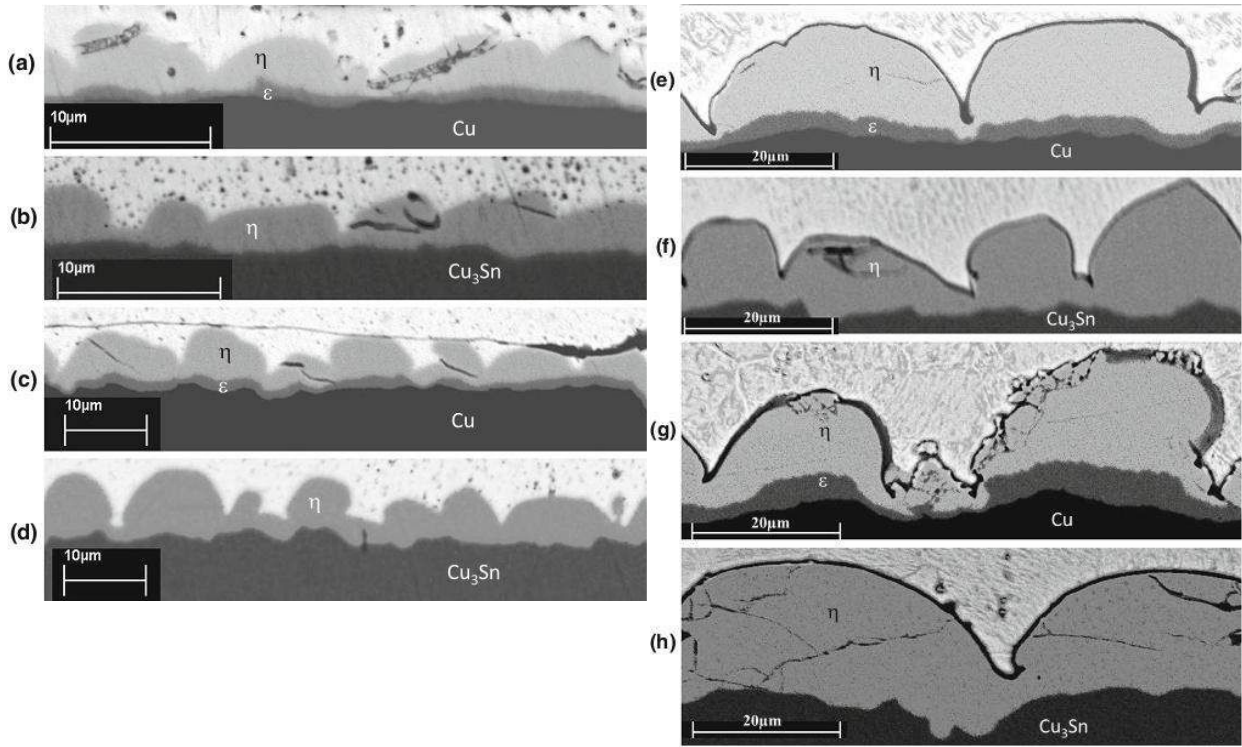


Figure 5-1. SEM micrograph of the Cu/Sn and  $\epsilon$ -Cu<sub>3</sub>Sn/Sn couple interfaces after 10 min (a, b), 30 min (c, d), 120 min (e, f) and 480 min (g, h) of reaction at 250°C.

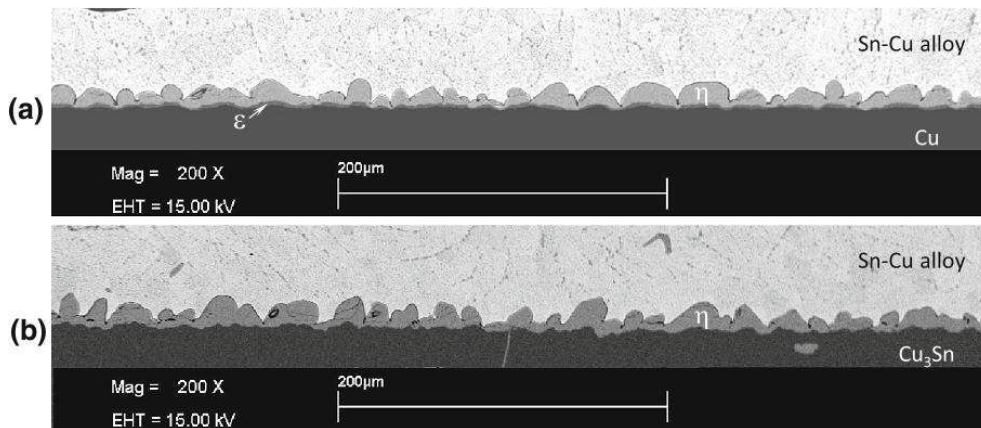


Figure 5-2. Typical SEM micrographs of the cross section of the Cu/Sn couple (a) and  $\epsilon$ -Cu<sub>3</sub>Sn/Sn (b) couple along more than 0.5 mm of the interface, after isothermal holding at 250°C for 2h.

In Figure 5-3, the average thickness of each layer ( $e_\eta$  and  $e_\epsilon$  for Cu/tin couple and  $e'_\eta$  for Cu<sub>3</sub>Sn/tin couple) are plotted against the square root and cubic root of time. The error bars in this Figure give the standard deviation from the average thickness of the interfacial layer calculated according to the procedure presented in section 2-1. These presentations are in relation to the fact that the mechanism of the phase growth in Cu/Sn system is still under discussion. Indeed, the most popular candidates for the power law of  $\eta$ -phase growth kinetics are 1/2 and 1/3. Therefore, we represented the data of growth kinetics by two different ways - (i) as dependence of average phase thickness on the *square root* of time (Figure 5-3a), and alternatively, (ii) as dependence on the *cubic root* of time (Figure 5-3b). Strictly speaking, more correctly would be to represent the results in the form:

$$(\Delta X)^2 = (\Delta X_0)^2 + (k_{1/2})^2 t \quad \text{or} \quad (\Delta X)^3 = (\Delta X_0)^3 + (k_{1/3})^3 t,$$

where  $\Delta X_0$  and  $\Delta X = e$  are the average thicknesses of a given layer  $i$  ( $i = \epsilon$  or  $\eta$ ) just after contact formation ( $t = 0$ ) and after a reaction time  $t$  respectively.  $k_{1/2}$  and  $k_{1/3}$  are the

growth constants of layer  $i$  depending on the operation mechanisms for the layer growth. Yet, at least for  $\eta$ -phase, the reached average thicknesses are much larger than initial ones. So, in representation we neglected the initial thickness just after contact formation.

Time, min	Cu/Sn couple		Cu <sub>3</sub> Sn/Sn couple
	$\epsilon$ -Cu <sub>3</sub> Sn thickness, $\mu\text{m}$	$\eta$ -Cu <sub>6</sub> Sn <sub>5</sub> thickness, $\mu\text{m}$	$\eta$ -Cu <sub>6</sub> Sn <sub>5</sub> thickness, $\mu\text{m}$
10	$0.50 \pm 0.27$	$3.31 \pm 0.29$	$3.12 \pm 0.13$
30	$0.91 \pm 0.09$	$3.52 \pm 0.74$	$5.27 \pm 0.32$
120	$2.07 \pm 0.65$	$7.58 \pm 0.14$	$10.46 \pm 0.86$
480	$3.97 \pm 0.77$	$12.75 \pm 1.00$	$13.81 \pm 1.11$

Table 5-1. Average values of the  $\epsilon$ -Cu<sub>3</sub>Sn and  $\eta$ -Cu<sub>6</sub>Sn<sub>5</sub> layers formed at the Cu/Sn interface and of  $\eta$ -Cu<sub>6</sub>Sn<sub>5</sub> layer formed at Cu<sub>3</sub>Sn/Sn interface after different isothermal holding at 250°C.

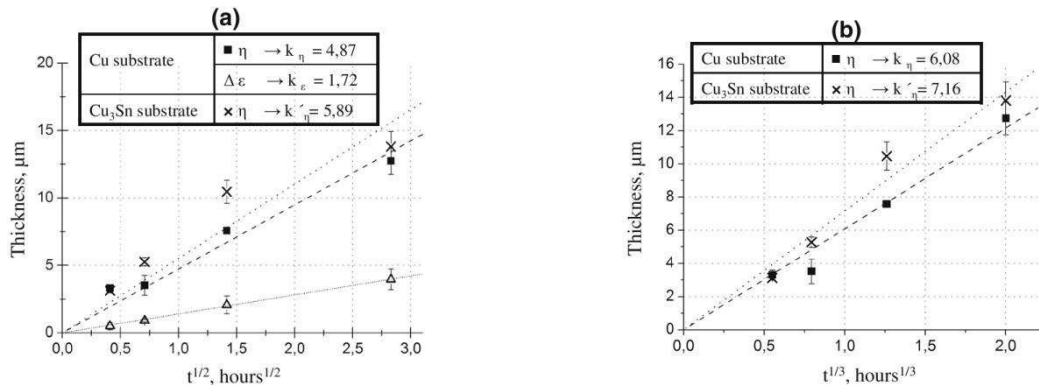


Figure 5-3. (a) Thickness ( $e$ ) of the  $\eta$ -phase and  $\epsilon$ -phase for the Cu/Sn diffusion couple and thickness of the  $\eta$ -phase for the Cu<sub>3</sub>Sn/Sn diffusion couple as a function of the square root of time. The straight lines represent the linear fit of the data for  $e = kt^{1/2}$ . (b) Thickness of the  $\eta$ -phase for the Cu/Sn and Cu<sub>3</sub>Sn/Sn diffusion couples as a function of the cube root of time. The straight lines represent the linear fit of the data for  $e = kt^{1/3}$ .

From Figure 5-3, we deduce the growth constants for  $\eta$ -Cu<sub>6</sub>Sn<sub>5</sub> phase layer:

(a) for the Cu/Sn couple:  $k_{1/2} = 4.87 \mu\text{m}\cdot\text{h}^{-1/2}$  and  $k_{1/3} = 6.08 \mu\text{m}\cdot\text{h}^{-1/3}$ ,

(b) for the  $\epsilon$ -Cu<sub>3</sub>Sn/Sn couple:  $k'_{1/2} = 5.89 \mu\text{m}\cdot\text{h}^{-1/2}$  and  $k'_{1/3} = 7.16 \mu\text{m}\cdot\text{h}^{-1/3}$ .

These values lead to a ratio between the experimental growth constants:

$$\frac{k'_{1/2}}{k_{1/2}} \approx 1.21 \quad \text{and} \quad \frac{k'_{1/3}}{k_{1/3}} \approx 1.18.$$

### 2-3) Theoretical analysis

In this section we will discuss and compare, from a theoretical point of view, the growth kinetics of  $\eta$ -Cu<sub>6</sub>Sn<sub>5</sub> layer in two configurations:

(a) Cu/ $\epsilon$ / $\eta$ /Sn (Cu/Sn couple) and (b)  $\epsilon$ / $\eta$ /Sn configuration (incremental couple).

We make the following assumptions concerning the growth mechanism of  $\eta$ -Cu<sub>6</sub>Sn<sub>5</sub> layer:

(i) growth kinetics limited by solid state diffusion - growth in parabolic regime and

(ii) growth kinetics limited by diffusion in liquid intergranular channels inside the  $\eta$ -Cu<sub>6</sub>Sn<sub>5</sub> layer.

### 2-3-1) Growth kinetics limited by solid state diffusion - parabolic regime

#### a) Cu/Sn couple: simultaneous growth of two phase layers ( $\epsilon$ and $\eta$ ) in parabolic regime

Let us start with reminding the well known equations for single-phase and two-phase growth of IMC continuous layers with narrow concentration ranges between two mutually almost insoluble (at the temperature of reaction) components [Gusak\_2010].

Let  $C$  be a mole fraction of copper (Cu):  $C_\eta = 6/11, C_\epsilon = 3/4$ . So far we assume that the so-called Wagner integrated diffusivities (products  $D_i\Delta C_i$  of average interdiffusion coefficient  $D_i$  and of concentration range  $\Delta C_i$ ) remain constant during reaction. This corresponds to bulk diffusion through them or to grain boundary diffusion with constant lateral grain size.

In such case the growth equations for two phase layers growing simultaneously in diffusion-controlled regime are determined by the flux balance equations at the moving boundaries Cu/ $\epsilon$ ,  $\epsilon/\eta$  and  $\eta/\text{Sn}$  (see Figure 5-4a) and by Fick's law inside each phase:

$$\frac{d\Delta X_\eta}{dt} = \frac{1}{C_\epsilon - C_\eta} \left( \frac{C_\epsilon}{C_\eta} \frac{D_\eta \Delta C_\eta}{\Delta X_\eta} - \frac{D_\epsilon \Delta C_\epsilon}{\Delta X_\epsilon} \right) \quad (5-1)$$

$$\frac{d\Delta X_\epsilon}{dt} = \frac{1}{C_\epsilon - C_\eta} \left( -\frac{D_\eta \Delta C_\eta}{\Delta X_\eta} + \frac{1 - C_\eta}{1 - C_\epsilon} \frac{D_\epsilon \Delta C_\epsilon}{\Delta X_\epsilon} \right) \quad (5-2)$$

If we consider the diffusion-controlled growth of both phases with constant effective diffusivities, one can assume from the very beginning that:

$$\Delta X_\eta = k_\eta \sqrt{t}, \quad \Delta X_\epsilon = k_\epsilon \sqrt{t}, \quad \Delta X_\epsilon / \Delta X_\eta = k_\epsilon / k_\eta \equiv r = \text{const} \quad (5-3)$$

Substituting it into initial equations, one gets:

$$\frac{k_\eta}{2} = \frac{1}{C_\epsilon - C_\eta} \left( \frac{C_\epsilon}{C_\eta} \frac{D_\eta \Delta C_\eta}{k_\eta} - \frac{D_\epsilon \Delta C_\epsilon}{k_\epsilon} \right), \quad \frac{k_\epsilon}{2} = \frac{1}{C_\epsilon - C_\eta} \left( -\frac{D_\eta \Delta C_\eta}{k_\eta} + \frac{1 - C_\eta}{1 - C_\epsilon} \frac{D_\epsilon \Delta C_\epsilon}{k_\epsilon} \right) \quad (5-4)$$

This set of two algebraic equations for the growth constants  $k_\epsilon$  and  $k_\eta$  has simple but clumsy solution. In our case, the Wagner diffusivity of  $\epsilon$ -phase is close to that of  $\eta$ -phase,  $D_\epsilon \Delta C_\epsilon / D_\eta \Delta C_\eta \approx 1$  [Kumar\_2011], which leads to  $k_\epsilon \approx 1.21$  and

$$k_\eta \approx 1.06 \sqrt{2D_\eta \Delta C_\eta} \quad (5-5)$$

#### b) Incremental $\epsilon/\text{Sn}$ couple: single $\eta$ layer growing parabolically between $\epsilon$ -phase and Sn

At first we formulate the general case when the marginal  $\epsilon$ -phase has concentration in between the homogeneity range and has higher copper content than needed for equilibrium with  $\eta$ -phase at the  $\epsilon/\eta$  phase boundary (see Figure 5-4b and Appendix 2). From calculation performed in Appendix 2, one can conclude that the smaller is the deviation of Cu concentration in the bulk  $\epsilon$ -phase from equilibrium with  $\eta$ -phase,  $C_{\epsilon/\eta}^{\text{eq}}$ , the faster will be the growth of  $\eta$ -phase. Thus, by assuming that  $C_{\epsilon/\eta}^{\text{eq}} = C_\epsilon = 3/4$ , we calculate the highest value of growth rate of  $\eta$ -phase growing between  $\epsilon$ -phase and liquid (see Figure 5-4b).

If we consider the diffusion-controlled growth of  $\eta$ -phase with constant effective diffusivities, one can assume from the very beginning that:

$$\Delta X'_\eta = k'_\eta \sqrt{t} \quad (5-6)$$

By writing the mass balance at  $\epsilon/\eta$  and  $\eta/\text{liquid Sn}$  interfaces (see Figure 5-4b),  $\Delta X'_\eta = X'_{\eta/\text{Sn}} - X'_{\epsilon/\eta}$ , one gets:

$$k'_\eta \equiv k'_{\eta/\text{Sn}} - k'_{\eta/\epsilon} = \sqrt{\frac{C_\epsilon}{C_\eta (C_\epsilon - C_\eta)}} 2D_\eta \Delta C_\eta \approx 2.6 \sqrt{2D_\eta \Delta C_\eta} \quad (5-7)$$

Comparison of Eq. (5-5) with Eq. (5-7) shows that the transition from Cu/Sn couple to incremental  $\epsilon$ -Cu<sub>3</sub>Sn/Sn couple will make the growth rate of  $\eta$ -phase faster ( $k'_{1/2} > k_{1/2}$ ), by a factor  $2.6/1.06 = 2.45$  if Wagner integrated diffusivities are equal in both  $\epsilon$  and  $\eta$  phases. Note that this case corresponds to the Cu/Sn system for which  $D_{\epsilon}\Delta C_{\epsilon} \sim D_{\eta}\Delta C_{\eta}$  [Kumar\_2011].

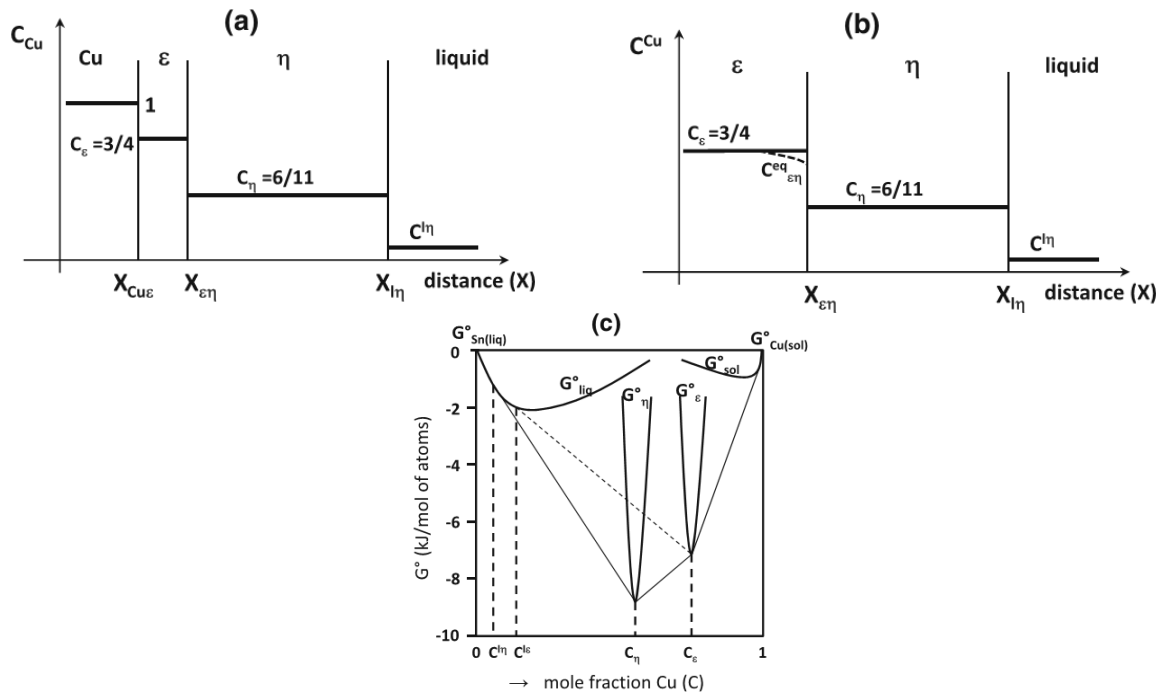


Figure 5-4. (a) Schematic presentation of variation of Cu concentration through the solid Cu/liquid Sn and (b) through the  $Cu_3Sn$ /liquid system. (c) Schematic presentation of variation of the Gibbs free-energy formation of (Sn,Cu) liquid phase, (Cu,Sn) solid phase and  $\eta$ -Cu<sub>6</sub>Sn<sub>5</sub> and  $\epsilon$ -Cu<sub>3</sub>Sn compounds at  $T = 523$  K indicating the stable equilibria (—) and the metastable liquid/ $\epsilon$  equilibrium (---). Reference states: stable states at 523 K (pure liquid Sn and pure solid Cu) [Hodaj\_2014, Shim\_1996, Dinsdale\_1991].

2-3-2) Reaction of Cu with liquid Sn occurs by Cu penetration through the liquid intergranular channels of  $\eta$ -phase

**a) Cu/Sn couple: simultaneous growth of two phase layers ( $\epsilon$  and  $\eta$ ).**

In some studies, it is shown that the much faster growth kinetics of the  $\eta$ -Cu<sub>6</sub>Sn<sub>5</sub> compared to that of  $\epsilon$ -Cu<sub>3</sub>Sn phase, is due to the fact that during the reaction between molten solder and copper, the growth of Cu<sub>6</sub>Sn<sub>5</sub> scallops takes place at the solder/metal interface by rapid liquid state diffusion through nanometric liquid channels between Cu<sub>6</sub>Sn<sub>5</sub> scallops, leading thus to a rapid growth rate of this phase [Kim\_1996].

In order to evaluate the evolution of the average scallop size (see Figure 5-5a) we use a simplified version of FDR model developed in Ref. [Gusak\_2002]. We assume that:

- i) All scallops have the same size  $a = H = R$  (see Figure 5-5b), where  $a$  and  $H$  are the average values of the base radius and height of a  $\eta$ -scallop respectively ( $a = h = R$  in the case of a semispherical-form);
- ii) The liquid is homogeneous in concentration and already saturated by copper for  $X > R$  and a constant concentration gradient exists in the liquid phase (channels) from the top of the liquid/ $\eta$  interface ( $X = X^{\eta}$ ), where the copper concentration corresponds to the liquid/ $\eta$  equilibrium concentration ( $C^{\eta}$ ) to the  $\epsilon$ / $\eta$  interface at the bottom of the channels ( $X = X^{\epsilon\eta}$ ), where the copper concentration in the liquid channels corresponds to the liquid/ $\epsilon$  metastable equilibrium ( $C^{\epsilon}$ ) - see Figures 5-4c and Figure 5-5c.

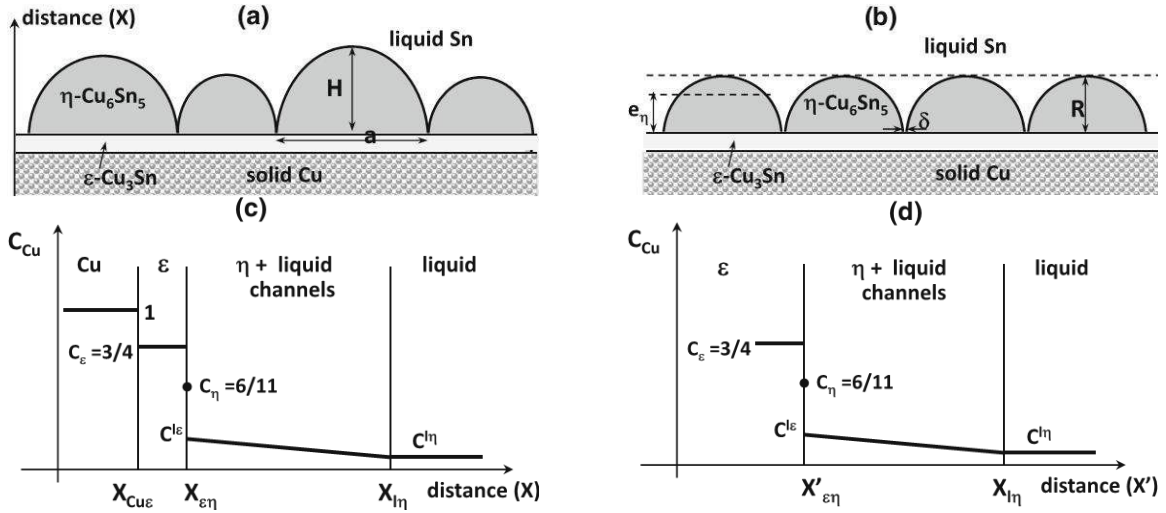


Figure 5-5. Model system: (a) Schematic morphology of  $\eta$ - $\text{Cu}_6\text{Sn}_5$  phase formed at the solid Cu/liquid Sn interface. (b) Simplified schematic morphology of  $\eta$ - $\text{Cu}_6\text{Sn}_5$  phase formed at the solid Cu/liquid Sn interface ( $a = H = R$ ). (c) Schematic presentation of variation of Cu concentration through the solid Cu/liquid Sn and (d) through the  $\text{Cu}_3\text{Sn}$ /liquid system considering that liquid channels exist inside the  $\eta$ - $\text{Cu}_6\text{Sn}_5$  layer.

For the fluxes of Cu atoms (number of atoms per unit area per unit time) through both intermetallic phases (evidently, through  $\varepsilon$ -phase layer and liquid channels) we can use the following expressions [Gusak\_2002]:

$$\Omega J^{(\varepsilon)} = \frac{\tilde{D}^{(\varepsilon)} \Delta C_{\varepsilon}^{\text{eq}}}{\Delta X_{\varepsilon}} \quad (5-8)$$

$$\Omega J^{(\eta)} = D_{\text{Cu}}^{\text{melt}} \frac{C^{l/\varepsilon} - C^{l/\eta}}{R} \frac{S^{\text{free}}}{S^{\text{total}}} = \frac{\delta}{R^2} D_{\text{Cu}}^{\text{melt}} (C^{l/\varepsilon} - C^{l/\eta}), \quad (5-9)$$

where  $\Omega$  is an atomic volume,  $\tilde{D}^{(\varepsilon)} \Delta C_{\varepsilon}^{\text{eq}}$  is the integrated diffusion coefficient in  $\varepsilon$ -phase,  $D_{\text{Cu}}^{\text{melt}}$  is the diffusion coefficient of Cu in liquid Sn-Cu solution,  $C^{l/\varepsilon}$  and  $C^{l/\eta}$  are the equilibrium concentration of Cu at the liquid/ $\varepsilon$ -phase and liquid/ $\eta$  phase interface correspondingly (see Figure 5-4c). According to the constraint that the interface between the scallops and Cu is occupied completely by scallops except the thin channels, we have:  $N\pi R^2 \approx S^{\text{total}} = \text{constant}$ , where  $N$  is the number of scallops. The free surface (the cross-sectional area of channels at the bottom) for the supply of Cu from the substrate is:  $S^{\text{free}} = 2\pi R N (\delta/2) = (\delta R) S^{\text{total}}$  where  $\delta$  is the channel width. Note that the number of liquid channels per unit area of reaction interface (proportional to  $S^{\text{free}}/S^{\text{total}} = \delta R$ ) is higher for a scallop-form  $\eta$ -phase compared to a semispherical-form  $\eta$ -phase. The error on  $\delta R$  value can be estimated to be given by the  $a/H$  ratio (about 20-30%).

Then the basic kinetic equations for simultaneous growth of both phases are:

$$\begin{aligned} (1 - C_{\varepsilon}) \frac{dX^{\text{Cu}/\varepsilon}}{dt} &= - \frac{\tilde{D}^{(\varepsilon)} \Delta C_{\varepsilon}^{\text{eq}}}{\Delta X_{\varepsilon}} \\ (C_{\varepsilon} - C_{\eta}) \frac{dX^{\varepsilon/\eta}}{dt} &= - \frac{\delta D_{\text{Cu}}^{\text{melt}}}{H^2} (C^{l/\varepsilon} - C^{l/\eta}) + \frac{\tilde{D}^{(\varepsilon)} \Delta C_{\varepsilon}^{\text{eq}}}{\Delta X_{\varepsilon}} \\ (C_{\eta} - 0) \frac{dX^{\eta/\text{Sn}}}{dt} &= \frac{\delta D_{\text{Cu}}^{\text{melt}}}{H^2} (C^{l/\varepsilon} - C^{l/\eta}) \end{aligned} \quad (5-10\text{a,b,c})$$

The growth rate of each layer can be found as the difference in the velocities of two interfaces, for example for  $\varepsilon$ -phase layer:  $\frac{d\Delta X_{\varepsilon}}{dt} = \frac{dX^{\varepsilon/\eta}}{dt} - \frac{dX^{\text{Cu}/\varepsilon}}{dt}$ .

Equations for phase thicknesses are then:

$$\frac{d\Delta X_\varepsilon}{dt} = \left( \frac{1}{C_\varepsilon - C_\eta} + \frac{1}{1 - C_\varepsilon} \right) \frac{\tilde{D}^{(\varepsilon)} \Delta c_\varepsilon^{\text{eq}}}{\Delta X_\varepsilon} - \frac{\delta D_{\text{Cu}}^{\text{melt}}}{(C_\varepsilon - C_\eta) H^2} (C^{1/\varepsilon} - C^{1/\eta}) \quad (5-11a)$$

$$\frac{dH}{dt} = \left( \frac{1}{C_\eta} + \frac{1}{C_\varepsilon - C_\eta} \right) \frac{\delta D_{\text{Cu}}^{\text{melt}}}{H^2} (C^{1/\varepsilon} - C^{1/\eta}) - \frac{1}{C_\varepsilon - C_\eta} \frac{\tilde{D}^{(\varepsilon)} \Delta c_\varepsilon^{\text{eq}}}{\Delta X_\varepsilon} \quad (5-11b)$$

From experiment we know that during soldering  $\varepsilon$ -phase grows slowly. Let us use a steady-state approximation for the  $\varepsilon$ -phase:

$$\begin{aligned} & \left( \frac{1}{C_\varepsilon - C_\eta} + \frac{1}{1 - C_\varepsilon} \right) \frac{\tilde{D}^{(\varepsilon)} \Delta c_\varepsilon^{\text{eq}}}{\Delta X_\varepsilon} - \frac{\delta D_{\text{Cu}}^{\text{melt}}}{(C_\varepsilon - C_\eta) H^2} (C^{1/\varepsilon} - C^{1/\eta}) \approx 0 \Rightarrow \\ & \Rightarrow \frac{\tilde{D}^{(\varepsilon)} \Delta c_\varepsilon^{\text{eq}}}{\Delta X_\varepsilon} \approx \frac{1 - C_\varepsilon}{1 - C_\eta} \frac{\delta D_{\text{Cu}}^{\text{melt}}}{H^2} (C^{1/\varepsilon} - C^{1/\eta}) \end{aligned} \quad (5-12)$$

Then, substituting Eq. (5-12) into Eq. (5-11b), one obtains:

$$\frac{dH}{dt} \approx \frac{1}{C_\eta (1 - C_\eta)} \frac{\delta D_{\text{Cu}}^{\text{melt}}}{H^2} (C^{1/\varepsilon} - C^{1/\eta})$$

Simple integration gives:

$$\begin{aligned} H^{\text{at Cu substrate}} &= \left( \frac{3 \delta D_{\text{Cu}}^{\text{melt}}}{C_\eta (1 - C_\eta)} (C^{1/\varepsilon} - C^{1/\eta}) t \right)^{1/3} \\ H^{\text{at Cu substrate}} &= \left( \frac{3 \delta D_{\text{Cu}}^{\text{melt}}}{C_\eta (1 - C_\eta)} (C^{1/\varepsilon} - C^{1/\eta}) \right)^{1/3} t^{1/3} = (k_{1/3})_{\text{calc}} t^{1/3} \end{aligned} \quad (5-13)$$

Where  $(k_{1/3})_{\text{calc}}$  is the calculated growth constant of the  $\eta$ -phase in the case of Cu/Sn couple by Cu penetration through the liquid intergranular channels of  $\eta$ -phase.

### b) Incremental $\varepsilon$ /Sn couple: single $\eta$ layer growing between $\varepsilon$ -phase and Sn by copper penetration through the liquid intergranular channels of $\eta$ -phase

If  $\varepsilon$ -phase becomes marginal (as was realized in our experiment) and, as above, there is no flux inside this phase, then one obtains for incremental couple  $\varepsilon$ -Cu<sub>3</sub>Sn/liquid Sn saturated with Cu (see Figure 5-5d). Only one phase is growing ( $\eta$ -phase) in the form of scallops. Once more by making the approximations used in Eq. (5-9) the basic kinetic equations for growth of  $\eta$ -phase at  $\varepsilon$ /liquid interface become:

$$\begin{aligned} (C_\varepsilon - C_\eta) \frac{dX^{\varepsilon/\eta}}{dt} &= - \frac{\delta D_{\text{Cu}}^{\text{melt}}}{H^2} (C^{1/\varepsilon} - C^{1/\eta}) \\ (C_\eta - 0) \frac{dX^{\eta/\text{Sn}}}{dt} &= \frac{\delta D_{\text{Cu}}^{\text{melt}}}{H^2} (C^{1/\varepsilon} - C^{1/\eta}) \end{aligned} \quad (5-14)$$

Then, Eqs. (5-14) for  $H = X^{\eta/\text{Sn}} - X^{\varepsilon/\eta}$  lead to:

$$\frac{dH}{dt} = \left( \frac{1}{C_\eta} + \frac{1}{C_\varepsilon - C_\eta} \right) \frac{\delta D_{\text{Cu}}^{\text{melt}}}{H^2} (C^{1/\varepsilon} - C^{1/\eta}) \quad (5-15)$$

Simple integration of Eq. (5-15) gives:

$$H^{\text{incremental}} = \left( \frac{C_\varepsilon}{C_\eta (C_\varepsilon - C_\eta)} 3 \delta D_{\text{Cu}}^{\text{melt}} (C^{1/\varepsilon} - C^{1/\eta}) \right)^{1/3} t^{1/3} = (k'_{1/3})_{\text{calc}} t^{1/3} \quad (5-16)$$

where  $(k'_{1/3})_{\text{calc}}$  is the calculated growth constant of the  $\eta$ -phase in the case of incremental  $\varepsilon/\text{Sn}$  couple by Cu penetration through the liquid intergranular channels of  $\eta$ -phase.

Thus the ratio between the average values of  $H = R$  (but also between the average thicknesses of the  $\eta$ -layer) obtained for both cases can be calculated from Eqs. (5-13) and (5-16):

$$\frac{H^{\text{incremental}}}{H^{\text{at Cu substrate}}} = \frac{(k'_{1/3})_{\text{calc}}}{(k_{1/3})_{\text{calc}}} = \left( \frac{(1-C_\eta)C_\varepsilon}{(C_\varepsilon-C_\eta)} \right)^{1/3} \approx 1.19 \quad (5-17)$$

#### 2-4) Comparison of theory and experiment

We can see that the experimental value of the ratio of cubic root dependencies for full Cu/Sn and incremental  $\varepsilon/\text{Cu}_3\text{Sn}$  couples  $(k'_{1/3}/k_{1/3})_{\text{exp}} \approx 1.18$  practically coincides with our theoretical prediction:  $(k'_{1/3}/k_{1/3})_{\text{calc}} \approx 1.19$ , see Eq. (5-17). This is much better than if one tries to represent the data as square root dependencies. Indeed, in this last case we have  $(k'_{1/2}/k_{1/2})_{\text{calc}} \approx 2.45$ , value much higher than the experimental one  $(k'_{1/2}/k_{1/2})_{\text{exp}} \approx 1.21$  (see Figure 5-3).

Moreover, Eq. (5-16) gives the possibility to estimate the product of copper diffusivity in channel and channel width:

$$\delta D_{\text{Cu}}^{\text{melt}} = \frac{(k'_{1/3})_{\text{calc}}^3}{3} \frac{C_\eta (C_\varepsilon - C_\eta)}{C_\varepsilon (C_\varepsilon^{1/\varepsilon} - C_\eta^{1/\eta})} \quad (5-18)$$

where  $C_\eta = 6/11$  and  $C_\varepsilon = 3/4$  are the copper concentrations in  $\eta\text{-Cu}_6\text{Sn}_5$  and  $\varepsilon\text{-Cu}_3\text{Sn}$  respectively. The difference of copper concentrations  $C_\varepsilon^{1/\varepsilon} - C_\eta^{1/\eta} \approx 8 \times 10^{-3}$  in liquid tin between equilibrium with  $\varepsilon\text{-Cu}_3\text{Sn}$  and with  $\eta\text{-Cu}_6\text{Sn}_5$  phases is obtained from thermodynamic data [Hodaj\_2014, Dinsdale\_1991, Shim\_1996]. With these data Eq. (5-18) becomes:

$$\delta D_{\text{Cu}}^{\text{melt}} \approx 5.7 \cdot (k'_{1/3})_{\text{calc}}^3 \quad (5-19)$$

We recall that the experimental variation with time of the average thickness of the  $\eta\text{-Cu}_6\text{Sn}_5$  phase ( $e_\eta$ ) is given in section 2-2 (see Figure 5-3b) by:

$$e_\eta = (k'_{1/3})_{\text{exp}} t^{1/3} \quad (5-20)$$

whereas the calculated variation with time of the average height of scallops (see Figure 5-5) is evaluated in section 2-3-2 by:

$$H^{\text{incremental}} = R = (k'_{1/3})_{\text{calc}}^3 t^{1/3} \quad (5-21)$$

Combining Eqs. (5-20) and (5-21) and the evaluation of the ratio  $e_\eta/R = \pi/4$  (see Figure 5-5b), one obtains:

$$(k'_{1/3})_{\text{calc}} = \frac{4}{\pi} (k'_{1/3})_{\text{exp}} \quad (5-22)$$

Eqs. (5-19) and (5-22) lead to:

$$\delta D_{\text{Cu}}^{\text{melt}} \approx 7.3 \cdot (k'_{1/3})_{\text{exp}}^3 \quad (5-23)$$

Taking the data on kinetics for  $\varepsilon$ -liquid solder interaction from section 2-2, Figure 5-3b:  $(k'_{1/3})_{\text{exp}} \approx 7.2 \mu\text{m} \cdot \text{h}^{-1/3} \approx 4.7 \times 10^{-7} \text{m} \cdot \text{s}^{-1/3}$ , one can estimate the product  $\delta D_{\text{Cu}}^{\text{melt}}$  from Eq. (5-23) as approximately  $8 \times 10^{-19} \text{m}^3 \cdot \text{s}^{-1}$ .

Knowing the estimate for diffusivity in liquid solder as approximately  $10^{-9} \text{m}^2 \cdot \text{s}^{-1}$ , one can estimate the channel width as about 1 nm, which is not far from the estimate of Jong-ook Suh et al in [Suh\_2008] for tin-lead solder (about 2.5 nm).

## 2-5) Conclusions

For the first time the reaction with liquid tin-based solder was studied by direct interaction between specially prepared  $\epsilon$ -Cu<sub>3</sub>Sn phase and liquid tin saturated with copper at 250°C. The reaction product formed at the  $\epsilon$ -Cu<sub>3</sub>Sn/liquid Sn-Cu alloy interface consists of the single  $\eta$ -Cu<sub>6</sub>Sn<sub>5</sub> phase with a scallop morphology similar to the classical morphology of the  $\eta$ -Cu<sub>6</sub>Sn<sub>5</sub> phase formed at Cu/liquid Sn interface.

Comparison of growth kinetics of the  $\eta$ -Cu<sub>6</sub>Sn<sub>5</sub> phase in Cu/ $\epsilon$ / $\eta$ /liquid Sn-Cu and  $\epsilon$ / $\eta$ /liquid Sn-Cu systems shows that in the second case (incremental couple) the average thickness of the  $\eta$  layer is about only 20% greater. This relatively small difference in the growth kinetics of  $\eta$ -Cu<sub>6</sub>Sn<sub>5</sub> phase between the two couples can be explained if the  $\eta$ -Cu<sub>6</sub>Sn<sub>5</sub> phase growth occurs by liquid state diffusion via the liquid channels between scallops of  $\eta$ -phase and thus supports the FDR model. The average width of liquid channel in the  $\eta$ -Cu<sub>6</sub>Sn<sub>5</sub> phase is estimated to be about 1 nm.

## 3) Differences between Cu/solid Sn and Cu/metastable liquid Sn interfacial reactions at identical temperature: role of the liquid state on the kinetics of interfacial reactions and the morphology of the reaction product

### 3-1) Introduction

The principal aim of this section is to study the differences between Cu/solid Sn and Cu/metastable liquid Sn interfacial reactions at identical temperature and to determine the role of the liquid state in the kinetics of the interfacial reactions as well as in the morphology of the reaction product. For this purpose, we have performed specific DSC experiments of interfacial reactivity between metastable liquid Sn-0.7wt.%Cu alloy and Cu substrate as well as between solid Sn-0.7wt.%Cu alloy (*noted below by Sn-Cu alloy*) and a Cu substrate at rigorously the same temperature of 222°C. Afterwards, we compare and analyze these experimental results and perform a theoretical analysis of the growth kinetics of the  $\eta$ -Cu<sub>6</sub>Sn<sub>5</sub> phase in both configurations.

### 3-2) Experimental procedure

In order to reveal the influence of the physical state of the solder on the growth kinetics and morphology of the intermetallic phases we have performed experiments with pure Cu and Sn-Cu alloy at 222°C in two configurations:

- (i) Solid state aging of the couple Cu/solid Sn-Cu alloy
- (ii) Interfacial reaction between Cu and metastable liquid Sn-Cu solder.

In order to monitor and control the physical state of the Sn-Cu solder as well as to set the accurate precise reaction temperature, these experiments have been carried out using a 2920 TA Instruments Differential Scanning Calorimetry apparatus.

The initial Cu/Sn-Cu alloy couples were prepared by dipping Cu foils for 1 s into a bath of Sn-0.7wt.%Cu alloy at 250°C as described in previous section (see Chapter 2 for experimental details).

Cu sheet had a thickness of 0.5 mm. It was successively cut, ground and fine polished from one side with a 0.25  $\mu$ m particle size diamond suspension and ultrasonically cleaned. Afterwards, the Cu coupons were dipped into conventional liquid RMA flux and then into a bath of Sn-Cu liquid alloy at 250°C for 1 s. After the dipping process, the thickness of the Sn-Cu alloy layer over the Cu coupon was about 200  $\mu$ m. The obtained sandwich structures (Sn-Cu alloy/ Cu substrate / Sn-Cu alloy) were ground from the unpolished side until the Sn-Cu alloy layer was completely removed from this side and then cut in small pieces of approximately 2×2 mm<sup>2</sup>. In the following, this structure is called "sandwich structure".

The dipping conditions (flux, temperature, time) were determined in order to obtain good wetting and thus an intimate contact between the solder and the copper substrate. This

important point is verified after dipping experiments as well as after the "reflow" experiments by scanning electron microscopy (SEM) examination of the copper/solder interface - see section 3-3.

The "reflow" experiments consist in heating the "sandwich structure" up to 235°C and cooling down at a cooling rate of 3 K·min<sup>-1</sup>. Figure 5-6a gives a typical DSC curve observed during a simple reflow process showing that the solidification of the Sn-Cu alloy occurs at about 209°C, i.e. the undercooling is about 18 K (the melting temperature of the alloy being 227°C - see below).

The samples were placed in the DSC and two thermal cycles (regimes) were applied:

(i) **Regime I** for the solid state aging, when the samples were heated up to 222°C and annealed at this temperature for the aging times varying from 1 h to 32 h (see the temperature-time profile in Figure 5-6b).

(i) **Regime II** for the liquid state aging (study of the interfacial reaction between Cu and metastable liquid alloy at 222°C). For these experiments, the samples were firstly reflowed by heating up to 235°C in order to melt the Sn-Cu alloy and afterwards cooled down to 222°C (with cooling rate 3 K·min<sup>-1</sup>) in order to achieve the metastable supercooling of the solder. Then samples were maintained at this temperature for different aging times varying from 1 h to 32 h. All details concerning the DSC curves observed during these experiments are given in two typical graphics shown in Figure 5-6c (temperature - time curve) and Figure 5-6d (heat flow - temperature curve). After each experiment, the solidification peak was clearly detected with the same heat release as in the case of a simple reflow process. If the solidification peak was not observed during cooling, the experiment was considered as not valid because, in this case, the solidification has occurred during the isothermal hold at 222°C.

The onset temperature of the heating curve (between points B and C in Figure 5-6d) indicates that the average melting temperature of the Sn-Cu alloy is 227°C ± 1°C which is very close to the melting temperature of the binary Cu-Sn eutectic alloy given in the literature [Saunders\_1990]. After the reflow process (from C to D) the sample was cooled down to 222°C (point E) and maintained at this temperature for a time corresponding to the liquid state aging (from E to E'). Afterwards, during the cooling of the sample an exothermic peak is observed at about 210°C (point G). The heat release corresponding to this peak is the same as that obtained during solidification after a classical reflow process. The presence of this peak demonstrates that alloy was in a metastable liquid state during aging at 222°C. Note that in all experiments performed in this study by using cycle II, the solidification temperature of Sn-Cu alloy was between 205 and 212°C, i.e.; the undercooling is about 15-22 K. These undercooling values are similar to those observed during a simple reflow process (see Chapter 4, section 3-4).

After isothermal holding at 222°C for the desired reaction time, the samples were cooled down to the room temperature. Afterwards, the samples were mounted in the resin, cross-sectioned, polished and ultrasonically cleaned. Thereafter, optical microscope and Leo - S440 scanning-electron microscope (SEM) in backscatter mode at 15 kV were employed to examine the cross-section of the samples.

The average thickness of the intermetallic compounds (IMCs) was calculated by measuring the total area of the IMCs and dividing it by the total length using backscattered electron images and ImageJ analysis software. The interfacial layer is measured every 230 nm (about 4 measurements per micrometer). For each cross-section, 3 images (about 200 μm in length) were taken. In this way, the size distribution and the average value of the reaction layer thickness was obtained from a very large number of measurements.

### 3-3) Results and discussion

#### 3-3-1) Comparison of the growth kinetics between Cu/metastable liquid alloy and Cu/solid alloy at identical temperature, role of the driving force of Cu<sub>6</sub>Sn<sub>5</sub> formation

Figure 5-7 presents the SEM micrographs of the Cu substrate/Sn-Cu alloy interfaces after the dipping experiments, i.e., after 1 s of contact between liquid alloy at 250°C and Cu

substrate (Figure 5-7a) and after a reflow process (Figure 5-7b) according to the thermal cycle given in Figure 5-6a - maximal temperature equal to 235°C. It is clearly seen that, in both cases, the interfacial reaction between copper substrate and the solder alloy has led to the formation of a scallop-like interfacial layer about 0.5 μm and 4 μm thick respectively. The formation of IMC between liquid Sn-Cu alloys and Cu substrate has been widely studied in the literature (see for example [Tu\_2007, Laurila\_2005]) and it is well established that the reaction layer is composed of the Cu<sub>3</sub>Sn compound on the copper side and of the Cu<sub>6</sub>Sn<sub>5</sub> compound on the solder side.

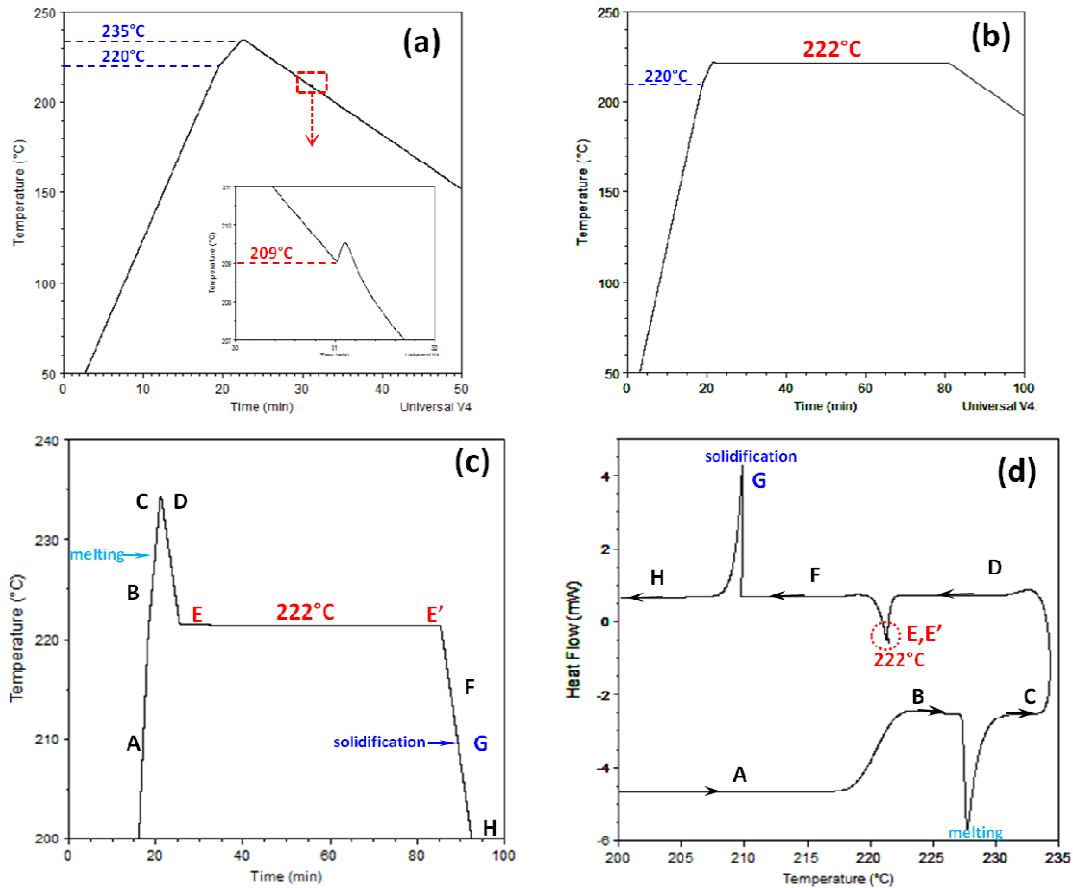


Figure 5-6. (a) Typical DSC curves from thermal aging of Cu/Sn-Cu alloy samples. (a) Simple reflow process. (b) Solid state annealing at 222°C of a pre-reflowed sample. (c and d) Reflow process followed by an isothermal aging at 222°C (temperature-time (c) and heat flow-time (d) curves).

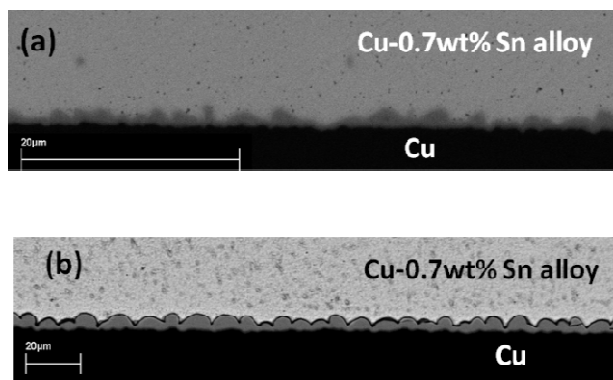


Figure 5-7. SEM micrographs of the Cu substrate/solder alloy interfaces after the dipping experiments, i.e., after 1 s of contact between liquid alloy and Cu substrate (a) and after a reflow process (b).

Figure 5-8 gives SEM micrographs of the reaction product formed at the Cu/metastable liquid Sn-Cu alloy interface and Cu/solid Sn-Cu alloy interface for the samples aged at 222°C for 1 h, 8 h, 16 h and 32 h by using thermal cycles corresponding to regime I and regime II respectively.

Figure 5-8(a-d) show that whatever the holding time at 222°C for Cu/*metastable liquid alloy* system, the reaction product at the Cu/Sn-Cu alloy interface consists of two IMCs layers: a scallop-shaped compound  $\eta$ -Cu<sub>6</sub>Sn<sub>5</sub> on the solder side and a thin layer of  $\epsilon$ -Cu<sub>3</sub>Sn compound on the Cu side. This observation is in agreement with the experimental results reported in previous studies (see for example [Tu\_2007, Laurila\_2005]).

Figure 5-8(a-d) show also that whatever the holding time at 222°C for Cu/*solid Sn-Cu alloy* system, the reaction product consists of two intermetallic layers  $\eta$ -Cu<sub>6</sub>Sn<sub>5</sub> on the solder side and a thin layer of  $\epsilon$ -Cu<sub>3</sub>Sn on the Cu side but, contrary to the previous case, the  $\eta$ -Cu<sub>6</sub>Sn<sub>5</sub> layer appears as a uniform planar layer that is comparable to that of the  $\epsilon$ -Cu<sub>3</sub>Sn layer.

For each sample, the average thickness  $e$  of each layer ( $e_\eta$  and  $e_\epsilon$  for Cu/liquid alloy couple and  $e'_\eta$  and  $e'_\epsilon$  for Cu/solid alloy couple) was calculated (see section 3-2).

The initial average thicknesses of the  $\eta$  and  $\epsilon$  layers at the beginning of the isothermal aging at 222°C depend on the thermal history of the sample, i.e. regime I or regime II.

In the case of regime I, the initial thicknesses of  $\eta$  and  $\epsilon$  layers are considered those obtained after the dipping process (i.e.  $e_\epsilon = 0.10 \mu\text{m}$  and  $e_\eta = 0.40 \mu\text{m}$  - see Figure 5-7a). In the case when the regime II is applied, the initial thicknesses are evaluated by the values of the thicknesses obtained after a reflow process (i.e.  $e_\epsilon = 0.74 \mu\text{m}$  and  $e_\eta = 3.53 \mu\text{m}$  - see Figure 5-7b).

The average values of  $e$  for samples used for each holding time are given in Table 5-2. This Table shows that, for the Cu/liquid alloy samples, the average thickness of the  $\epsilon$ -Cu<sub>3</sub>Sn layer is much lower than that of the  $\eta$ -Cu<sub>6</sub>Sn<sub>5</sub> layer ( $e_\epsilon \ll e_\eta$ ) regardless of the holding time at 222°C and  $e_\epsilon$  increases from about 1  $\mu\text{m}$  to 4  $\mu\text{m}$  when the holding time increases from 1 to 32 h. It shows also that in the case of Cu/solid Sn-Cu alloy samples the thickness of the  $\epsilon$ -Cu<sub>3</sub>Sn layer is close to that of the  $\eta$ -Cu<sub>6</sub>Sn<sub>5</sub> layer ( $e'_\epsilon \sim e'_\eta$ ) but also close to that of the  $\epsilon$ -Cu<sub>3</sub>Sn layer formed at Cu/liquid Sn-Cu alloy interface ( $e'_\epsilon \sim e_\epsilon$ ).

In Figure 5-9, the average thickness of each layer ( $e_\eta$  and  $e_\epsilon$  for Cu/liquid Sn-Cu alloy couple and  $e'_\eta$  and  $e'_\epsilon$  for Cu/solid Sn-Cu alloy couple) is plotted versus time as well as versus square root and cube root of time. The error bars in this figure give the standard deviation from the average thickness of the interfacial layer calculated according to the procedure presented in section 3-2. The growth kinetics are plotted in two different ways - (i) as dependence of the average phase thickness on the square root of time (Figures 5-9b,c), and alternatively, (ii) as dependence on the cube root of time (Figure 5-9d). These plots show that the power law of the  $\eta$ -phase growth kinetics is in the range between 1/2 and 1/3. The variation of the thickness of reaction layers are thus given by the following equations:

$$e_i^2 = e_{0,i}^2 + (k_i)^2 t \quad \text{for layer } i \text{ (} i = \eta \text{ or } \epsilon \text{) in regimes I or II} \quad (5-24a)$$

$$e_\eta^3 = e_{0,\eta}^3 + (k_\eta^*)^3 t \quad \text{only for } \eta \text{ layer in regime II} \quad (5-24b)$$

where  $e_0$  and  $e$  are the average thicknesses of a given layer  $i$  ( $i = \epsilon$  or  $\eta$ ) just at the beginning of isothermal holding at 222°C ( $t = 0$ ) and after a certain reaction time  $t$  respectively.  $k$  and  $k^*$  are the growth kinetic constants of layer  $i$  depending on the operation mechanisms for the layer growth.

From Figure 5-9, the growth kinetic constants for  $\eta$ -Cu<sub>6</sub>Sn<sub>5</sub> and  $\epsilon$ -Cu<sub>3</sub>Sn layers are:

**a) For the Cu/liquid alloy couple:**

$$\begin{aligned} k_\eta &= 0.302 \pm 0.009 \mu\text{m} \cdot \text{min}^{-1/2} \text{ (adj. } R^2 = 99.6\%), \\ k_\epsilon &= 0.0783 \pm 0.0079 \text{ (adj. } R^2 = 93.1\%) \mu\text{m} \cdot \text{min}^{-1/2} \quad \text{and} \\ k_\eta^* &= 1.371 \pm 0.071 \mu\text{m} \cdot \text{min}^{-1/3} \text{ (adj. } R^2 = 97.7\%) \end{aligned} \quad (5-25)$$

These values are in agreement with those obtained by Liang et al. [Liang\_2006] for the Cu/liquid Sn-3.5wt.%Ag alloy and Cu/liquid Sn-3.5wt.%Ag-0.7wt.%Cu alloy couples at 225°C as well as with those obtained by extrapolation at 222°C of experimental results reported by Gagliano et al [Gagliano\_2003] for the Cu/liquid Sn couple for temperatures between 250 and 325°C.

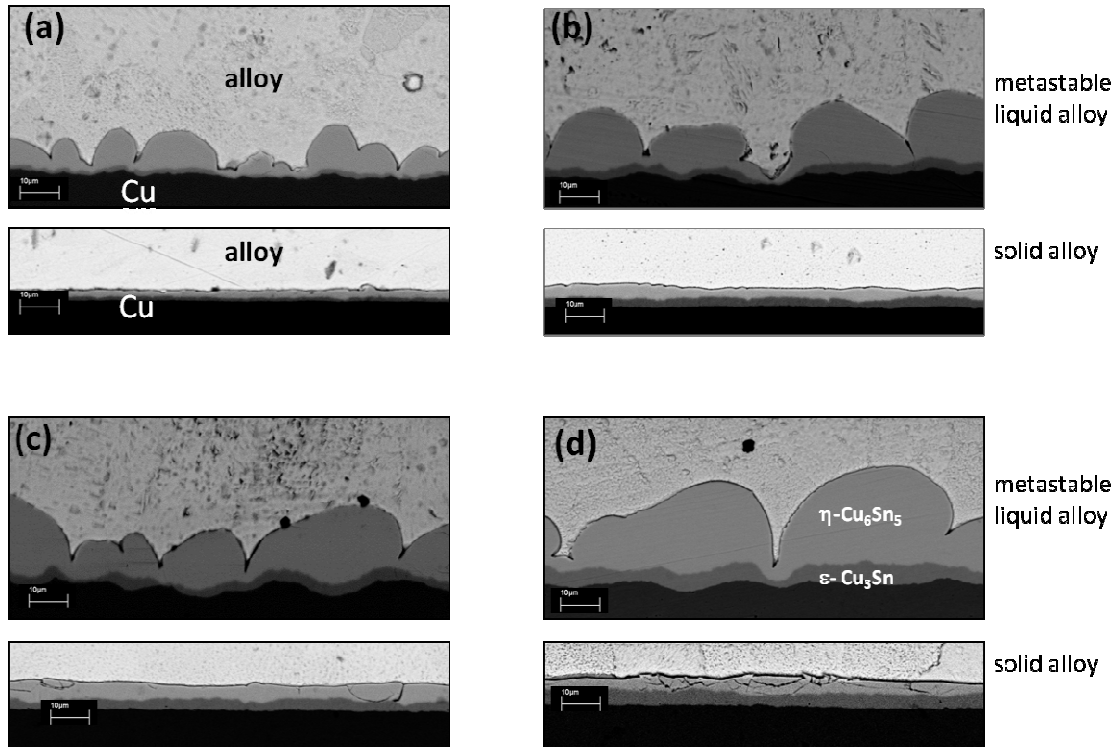


Figure 5-8. SEM micrographs of the reaction product formed at the Cu/metastable liquid alloy interface and Cu/solid alloy interface for samples aged at 222°C for 1h (a), 8h (b), 16h (c) and 32h (d) by using thermal cycles corresponding to regime I (metastable liquid Sn-Cu alloy) and regime II (solid Sn-Cu alloy), respectively.

Time (h)	Regime I (solid solder at 222°C)		Regime II (metastable liquid solder at 222°C)	
	$e'_{\epsilon\text{-Cu}_3\text{Sn}}$ (μm)	$e'_{\eta\text{-Cu}_6\text{Sn}_5}$ (μm)	$e_{\epsilon\text{-Cu}_3\text{Sn}}$ (μm)	$e_{\eta\text{-Cu}_6\text{Sn}_5}$ (μm)
0*	0.10 ± 0.03	0.40 ± 0.12	0.74 ± 0.04	3.53 ± 0.30
1	0.80 ± 0.02	1.87 ± 0.39	1.04 ± 0.04	6.42 ± 0.54
4	-	-	1.47 ± 0.25	7.74 ± 0.67
8	2.04 ± 0.16	3.23 ± 0.42	2.11 ± 0.16	10.51 ± 0.88
16	2.92 ± 0.11	3.90 ± 0.40	2.90 ± 0.15	13.51 ± 0.72
32	3.94 ± 0.10	4.42 ± 0.19	4.06 ± 0.30	16.58 ± 0.39

\*  $t = 0$  corresponds to dipping process ( $t \approx 1$  s - see text).

Table 5-2. Average values of thicknesses ( $e$ ) of intermetallic layers  $\epsilon$ -Cu<sub>3</sub>Sn and  $\eta$ -Cu<sub>6</sub>Sn<sub>5</sub> formed at Cu/Sn-Cu alloy interface after the thermal cycles I and II (see Figure 5-7 and Figure 5-8).

**b) For the Cu/solid alloy couple:**

$$k'_{\eta} = 0.0785 \pm 0.0084 \mu\text{m} \cdot \text{min}^{-1/2} \text{ (adj. } R^2 = 96.9\%) \text{ and}$$

$$k'_{\epsilon} = 0.0885 \pm 0.0008 \mu\text{m} \cdot \text{min}^{-1/2} \text{ (adj. } R^2 = 99.9\%) \quad (5-26)$$

These values are in agreement within 20% with those obtained by Onishi et al. [Onishi\_1975] and Paul et al. [Paul\_2004] for the Cu/solid Sn couples at 220°C and 215°C respectively.

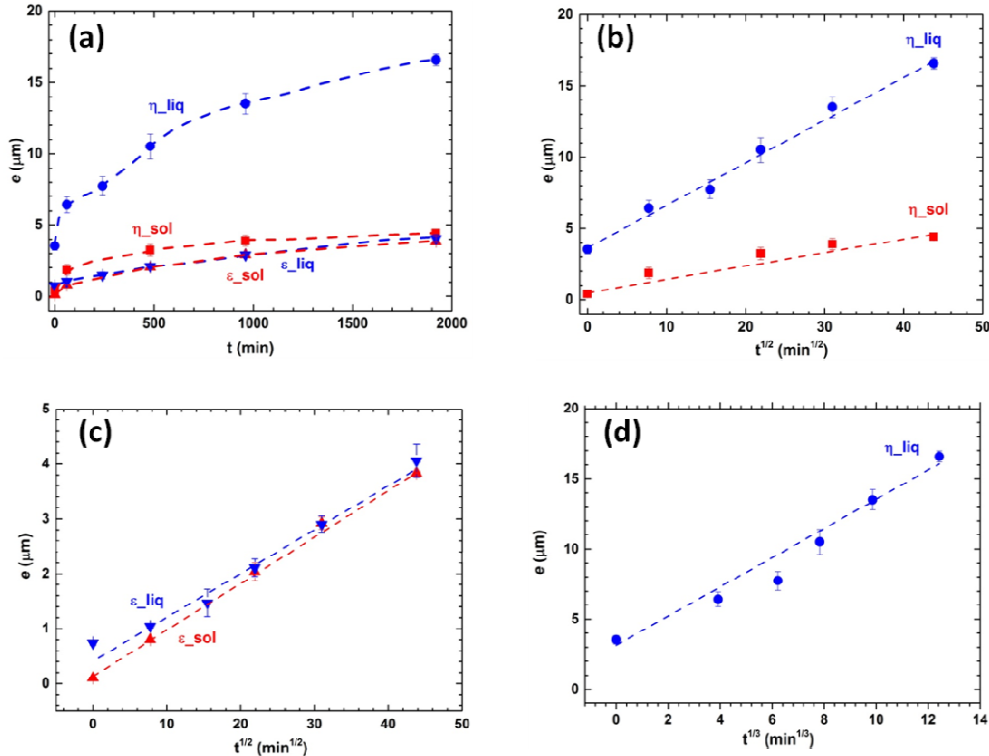


Figure 5-9. Average thickness of  $\epsilon\text{-Cu}_3\text{Sn}$  and  $\eta\text{-Cu}_6\text{Sn}_5$  layers formed at Cu/metastable Sn-Cu liquid alloy and Cu/Sn-Cu solid alloy interfaces versus reaction time (a), the square root (b, c) and the cube root (d) of reaction time at 222°C.

Note that in the case of Cu/liquid alloy couple, it is not easy to determine in a clear and certain way from Figure 5-9b and Figure 5-9d which of the growth laws given by Eqs. (5-24a) or (5-24b) corresponds better to the growth kinetics of the  $\eta\text{-Cu}_6\text{Sn}_5$  layer. However, it seems that the curve corresponding to the parabolic growth law ( $e^2 = e_0^2 + k^2t$ ) fits better the experimental results (Figure 5-9b). Thus in the following, for all case, the parabolic growth law was chosen.

From Eqs. (5-25) and (5-26):

$$\frac{k_{\eta}}{k_{\epsilon}} \approx 3.9 \quad \frac{k'_{\eta}}{k'_{\epsilon}} \approx 0.9 \quad (5-27a)$$

$$\frac{k_{\eta}}{k'_{\eta}} \approx 3.8 \quad \frac{k_{\epsilon}}{k'_{\epsilon}} \approx 0.9 \quad (5-27b)$$

Although Cu/liquid alloy and Cu/solid alloy experiments were performed with rigorously the same alloy composition and temperature, two significant differences can be seen from Figures 5-8 and 5-9:

(i) The morphology of the  $\eta\text{-Cu}_6\text{Sn}_5$  layer: scallop-shaped for liquid state and uniform thickness for the solid Sn-Cu alloy.

(ii) The growth kinetics of  $\eta\text{-Cu}_6\text{Sn}_5$  layer in the Cu/liquid Sn-Cu alloy system is much faster than that in Cu/solid Sn-Cu alloy system: after 32 hours of reaction, the average thickness of the  $\eta\text{-Cu}_6\text{Sn}_5$  layer in the first case is about four times higher than that obtained in the second case.

The large difference in growth kinetics and morphology of the  $\eta\text{-Cu}_6\text{Sn}_5$  phase layer, when Cu/metastable liquid Sn-Cu alloy system is replaced with Cu/solid Sn-Cu alloy system, points out the existence of a peculiar growth mechanism. Indeed, if we assume that the

growth kinetics of the reaction layers is limited in both cases by bulk solid diffusion, a possible explanation of this difference based on the thermodynamic factors is not valid here since, as it will be shown below, the driving force for  $\eta$  phase formation is almost the same in both cases.

Figure 5-10a presents a schematic copper concentration profile through the Cu/solid Sn and Cu/liquid Sn diffusion couples showing the formation of a continuous layer of  $\text{Cu}_3\text{Sn}$  and  $\text{Cu}_6\text{Sn}_5$  intermetallics. Figure 5-10b gives a schematic presentation of the variation with the copper molar fraction ( $c$ ) of the Gibbs free energy of formation ( $G$ ) of the (Sn,Cu) liquid phase, (Cu,Sn) solid phase and  $\eta$ - $\text{Cu}_6\text{Sn}_5$  and  $\epsilon$ - $\text{Cu}_3\text{Sn}$  compounds at  $T = 222^\circ\text{C}$  indicating the stable and metastable equilibria. It shows in particular the equilibria at the  $\eta$ - $\text{Cu}_6\text{Sn}_5$ /liquid Sn-Cu alloy and  $\eta$ - $\text{Cu}_6\text{Sn}_5$ /solid Sn-Cu alloy interfaces as well as the chemical potentials of Cu and Sn in the liquid ( $\mu_{\text{Cu-liq}}$ ) and solid ( $\mu_{\text{Cu-sol}}$ ) alloys corresponding to these equilibria. In Figure 5-10c the variations of chemical potential of copper ( $\mu_{\text{Cu}}$ ) through the interfacial systems show that, for both diffusion couples,  $\mu_{\text{Cu}}$  is identical through Cu substrate and  $\epsilon$ - $\text{Cu}_3\text{Sn}$  layer and is different through  $\eta$ - $\text{Cu}_6\text{Sn}_5$  layer and the solder alloy.

From Figure 5-10b, the driving forces of formation of  $\eta$ - $\text{Cu}_6\text{Sn}_5$ , by reaction between  $\epsilon$ - $\text{Cu}_3\text{Sn}$  and either solid or metastable liquid Sn-Cu alloy, are given by the segments AC and BC respectively. In order to evaluate these driving forces, we used CALPHAD data to build the concentration dependence of the Gibbs free energy of formation  $G(c)$  (in  $\text{J}\cdot\text{mole}^{-1}$ ) in the form of  $G$ -HSER [Dinsdale\_1991].

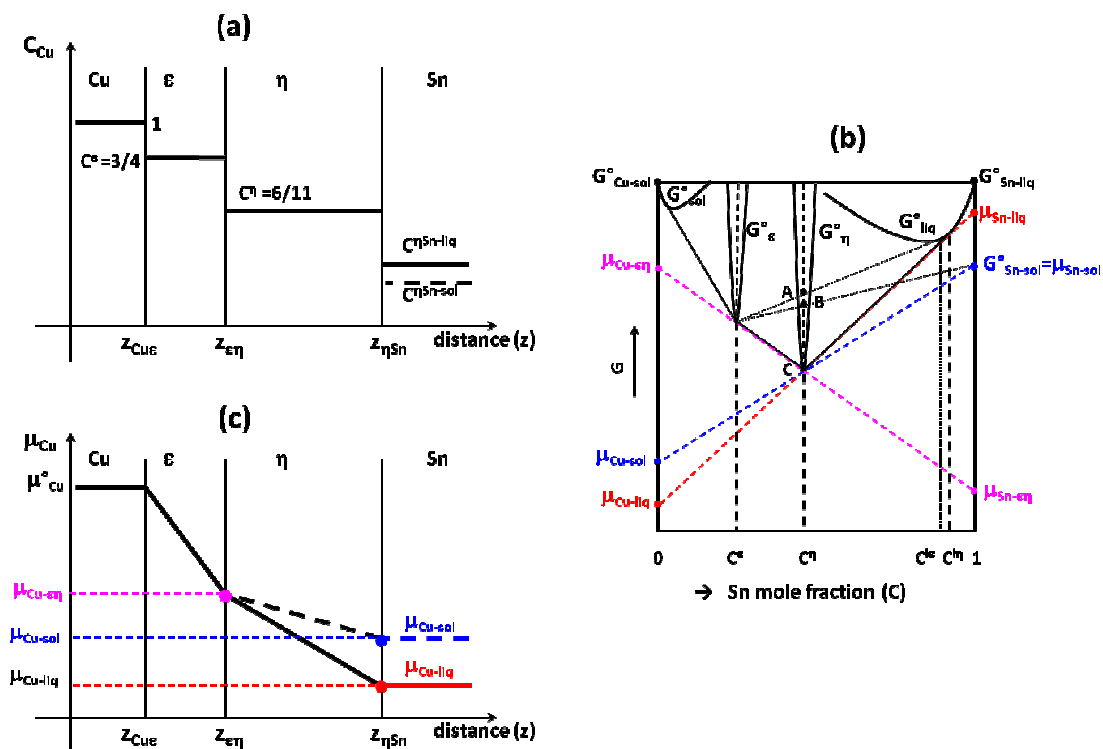


Figure 5-10. (a) Schematic presentation of variation of Cu concentration through the Cu/solid Sn-Cu alloy and Cu/liquid Sn-Cu alloy diffusion couples showing the formation of continuous layer of  $\epsilon$ - $\text{Cu}_3\text{Sn}$  and  $\eta$ - $\text{Cu}_6\text{Sn}_5$  intermetallics. (b) Schematic presentation of variation of the Gibbs free energy formation of (Sn,Cu) liquid phase, (Cu,Sn) solid phase and  $\eta$ - $\text{Cu}_6\text{Sn}_5$  and  $\epsilon$ - $\text{Cu}_3\text{Sn}$  compounds at  $T = 222^\circ\text{C}$  indicating the stable and metastable equilibria as well as the chemical potentials of Cu and Sn corresponding to these equilibria. (c) Schematic variations of chemical potential of Cu through Cu/solid Sn-Cu alloy and Cu/liquid Sn-Cu alloy interfacial systems.

Figure 5-11 gives the calculated variation of the Gibbs free energy of formation ( $G$ ) of (Sn,Cu) liquid phase and (Cu,Sn) solid phase as a function of molar fraction of Cu as well as

the Gibbs free energy of formation  $\varepsilon$ -Cu<sub>3</sub>Sn and  $\eta$ -Cu<sub>6</sub>Sn<sub>5</sub> compounds and pure solid and liquid Sn and Cu. All data used for obtaining the  $G(c)$  curves is given in Appendix 2. From these curves, we evaluate the driving forces of formation of  $\eta$ -Cu<sub>6</sub>Sn<sub>5</sub> phase from  $\varepsilon$ -Cu<sub>3</sub>Sn phase and either solid or metastable liquid Sn-Cu alloy that are about 405 and 411 J/mol of atoms respectively (segment AB in Figure 5-11a).

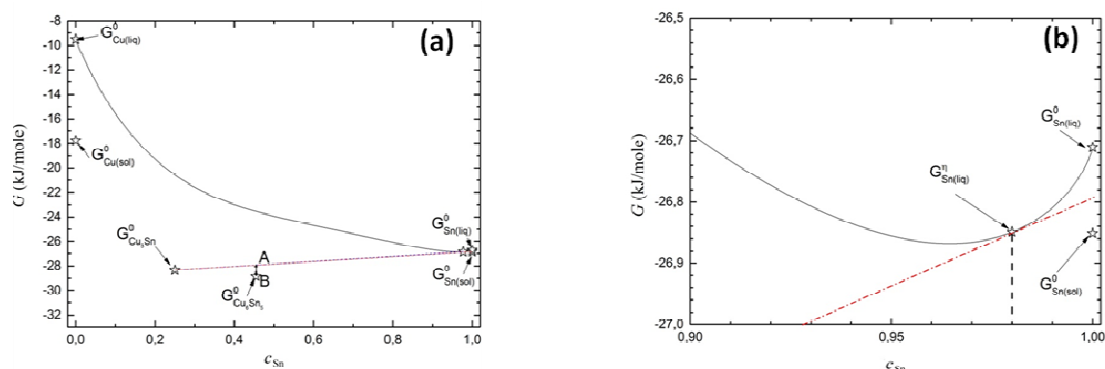


Figure 5-11. Calculated variation of the Gibbs free energy of formation of (Sn,Cu) liquid phase as a function molar fraction of Sn ( $c_{Sn}$ ) as well as the Gibbs free energy of formation of  $\varepsilon$ -Cu<sub>3</sub>Sn and  $\eta$ -Cu<sub>6</sub>Sn<sub>5</sub> compounds and pure solid and liquid Cu and Sn [Park\_2012, Dinsdale\_1991, Song\_2004].

**Thus, these calculations clearly indicate that the difference in the driving force of formation of  $\eta$ -Cu<sub>6</sub>Sn<sub>5</sub> phase between the two cases is lower than 2%.**

If it is assumed that the growth of  $\eta$ -Cu<sub>6</sub>Sn<sub>5</sub> and  $\varepsilon$ -Cu<sub>3</sub>Sn intermetallic layers is limited by solid state diffusion then this small increase in the driving force of formation of  $\eta$ -Cu<sub>6</sub>Sn<sub>5</sub> phase (< 2%) is far from being sufficient to lead to the large difference in the growth rate of the  $\eta$ -Cu<sub>6</sub>Sn<sub>5</sub> layer observed experimentally when one diffusion couple is replaced by the other ( $k_{\eta}/k'_{\eta} = 3.8$ , see Eq. (5-27b)). Indeed, as it is shown in Appendix 4, if the growth kinetics of both phases was limited by bulk solid state diffusion, an increase in the driving force by more than 700% is necessary in order to lead to the observed difference.

**Thus, these experiments provide unambiguous proof of the influence of the structural state of solder on the reaction rate. At the same temperature, in the case of the solder in the liquid state the reaction rate is much higher than in the case of solid solder. There are two interrelated reasons for this:**

(i) **Formation of liquid channels at least between some of Cu<sub>6</sub>Sn<sub>5</sub> scallops and diffusion of copper through these channels coupled with a much faster diffusion of copper in the liquid than in the solid state (according to Refs. [Gusak\_2002, Chen\_1999, Suh\_2008]).** In these studies, it is shown that the much faster growth kinetics of the  $\eta$ -Cu<sub>6</sub>Sn<sub>5</sub> compared to that of  $\varepsilon$ -Cu<sub>3</sub>Sn phase, is due to the fact that during the reaction between molten solder and copper, the growth of Cu<sub>6</sub>Sn<sub>5</sub> scallops takes place by a rapid liquid state diffusion through nanometric liquid channels formed at least between some Cu<sub>6</sub>Sn<sub>5</sub> scallops, leading thus to a rapid growth rate of this phase.

(ii) **Diffusion of copper through the grain boundaries of  $\eta$ -Cu<sub>6</sub>Sn<sub>5</sub> phase coupled with a much faster diffusion of copper in the liquid than in the solid solder (according to Ref. [Görlich\_2005]).** Indeed, as it was discussed by Görlich et al. [Görlich\_2005], the very fast diffusion of copper through the reaction layer in the Cu/liquid Sn-based alloys can also be explained by the very fast diffusion of copper through the grain boundaries of  $\eta$ -Cu<sub>6</sub>Sn<sub>5</sub> phase but this requires a grain boundary diffusion coefficient  $D_{GB}$  of about  $5 \cdot 10^{-10} \text{ m}^2 \text{ s}^{-1}$  close to the values for the bulk melts.

While the very high value of  $D_{GB}$  at 250°C could not be excluded [Görlich\_2005], to the best of our knowledge no experimental value of grain boundary diffusion coefficient of copper in the  $\eta$ -Cu<sub>6</sub>Sn<sub>5</sub> phase are reported in literature. Note also that there has not been any

experimental proof of existence of liquid channels through the  $\eta$ -Cu<sub>6</sub>Sn<sub>5</sub> layer formed between the Cu substrate and liquid Sn-based alloys in the literature.

In order to further understand the role of the liquid solder on the reaction kinetics, two supplementary specific experiments were made using Cu/Sn-Cu samples that have already undergone a **solid state** isothermal aging for 16h at 222°C after a reflow process (called sample\*). The DSC thermal cycle for this sample\* given in Figure 5-12 shows all details concerning melting, solidification peak of the solder at about 210°C (E) during cooling down to 200°C followed by heating up to 222°C and isothermal aging at 222°C (KK'). The presence of the solidification peak (E) demonstrates that the solder has been in solid state during isothermal aging at 222°C.

a) *The first experiment* consists in reflowing the sample\* at 235°C and cooling it down to the room temperature (see Figure 5-6a for the temperature-time curve). The total time during which Sn-Cu alloy is maintained in the liquid state during this reflow process is evaluated to be about 10 min.

b) *In the second experiment* the sample\* was firstly reflowed and afterwards it was maintained for 16h at 222°C in such a way that the Sn-Cu alloy remained in the metastable liquid state at this temperature. The DSC thermal cycle for this sample is similar to that given in Figure 5-6c.

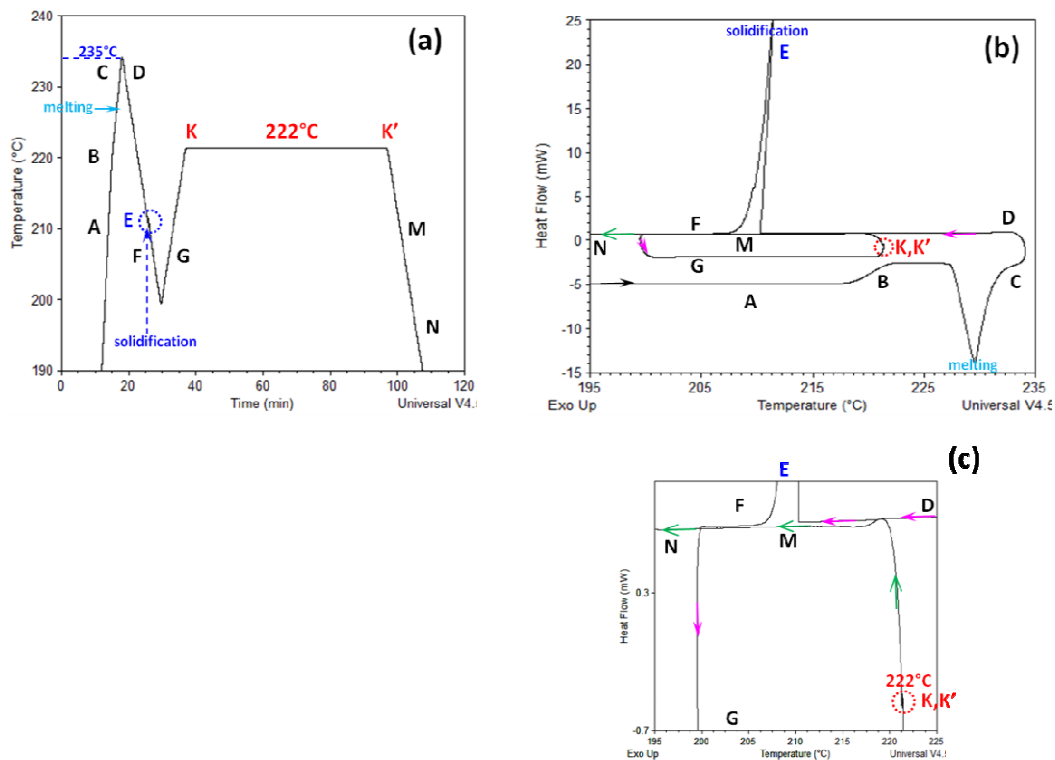


Figure 5-12. Temperature-time (a) and heat flow-temperature (b, c) DSC curves of a Cu/Sn-Cu alloy sample that undergoes a reflow process at 235°C followed by a liquid state isothermal aging for 16h at 222°C (KK') and cooling (solidification peak (E) at about 210°C).

Figure 5-13 gives SEM micrographs of Cu/Sn-Cu alloy interfacial system for sample\* after one reflow (Figure 5-13c) and after a **liquid state** isothermal aging for 16h at 222°C (Figure 5-13d). For comparison purposes, SEM micrographs of the reflowed sample (Figure 5-13a) and sample\* (Figure 5-13b - **solid state** aging for 16h at 222°C) are also reported.

Comparison of Figure 5-13a and Figure 5-13b shows that, during solid state aging of the reflowed sample, the Cu<sub>6</sub>Sn<sub>5</sub> layer transforms from scallop shape to planar type which is due to the reduction in the interfacial energy.

Comparison of Figure 5-13b and 13c clearly shows that the contact between the liquid alloy and the planar  $\text{Cu}_6\text{Sn}_5$  layer during a reflow process leads to a major disruption of the  $\text{Cu}_6\text{Sn}_5$ /alloy interface: from a planar to an irregular interface forming a scallop-structure. This is due to the very good wetting of the  $\text{Cu}_6\text{Sn}_5$  phase by the liquid tin which quickly penetrates deep into grain boundaries in  $\text{Cu}_6\text{Sn}_5$ , leading to intergranular grooves. Indeed a careful examination of the microstructure of the reactive layers of sample\* (Figure 5-13b) by SEM secondary electron images, performed by using a Ga ions focused beam, shows that the grain size of the planar  $\text{Cu}_6\text{Sn}_5$  phase is about 5-10  $\mu\text{m}$  (see Figure 5-14). The fact that this value is similar to the size of  $\text{Cu}_6\text{Sn}_5$  scallops in Figure 5-13c strongly suggests that the grain boundaries of  $\text{Cu}_6\text{Sn}_5$  phase are penetrated by the liquid alloy during the reflow of the sample\*.

Note finally that, a liquid state aging of sample\* for 16h at 222°C leads to a significant increase in the thickness of the  $\eta$ - $\text{Cu}_6\text{Sn}_5$  layer and a significant decrease of the  $\varepsilon$ - $\text{Cu}_3\text{Sn}$  layer (see Table 5-3 that summarizes the thicknesses of  $\varepsilon$  and  $\eta$  layers after different thermal treatments for specific experiments). The fact that during liquid state aging the thickness of  $\varepsilon$ - $\text{Cu}_3\text{Sn}$  layer decreases while that of  $\eta$ - $\text{Cu}_6\text{Sn}_5$  layer increases suggests that the Wagner's integrated coefficient of  $\eta$ - $\text{Cu}_6\text{Sn}_5$  phase ( $D_\eta\Delta c_\eta$ ) is much higher than that of  $\varepsilon$ - $\text{Cu}_3\text{Sn}$  phase:  $D_\eta\Delta c_\eta \gg D_\varepsilon\Delta c_\varepsilon$ .  $D_i$  and  $\Delta c_i$  ( $i = \eta$  or  $\varepsilon$ ) are the diffusion coefficient and the variation of the concentration of the diffusion species through the layer  $i$  respectively. Indeed, as it is clearly demonstrated in Ref. [Philibert\_1994], if  $D_1\Delta c_1/e_1 \gg D_2\Delta c_2/e_2$  then the phase 2 regresses as it is consumed by the phase 1. This result indicates that a change in the state of the solder phase from solid to liquid (at the same temperature) leads to a large change in the ratio of diffusion coefficients in  $\eta$ - $\text{Cu}_6\text{Sn}_5$  and  $\varepsilon$ - $\text{Cu}_3\text{Sn}$  layer.

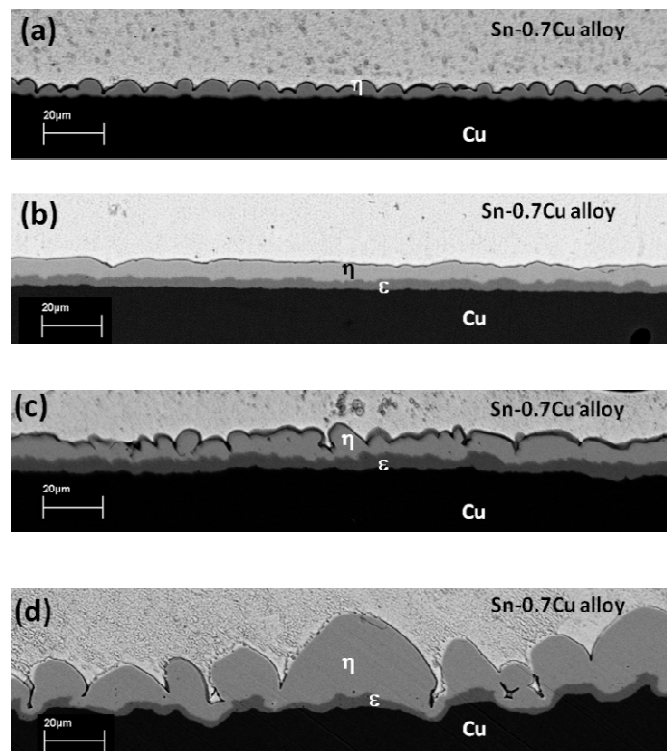


Figure 5-13. SEM micrographs of a Cu/Sn-Cu alloy after a reflow (a), after a reflow followed by a **solid state** isothermal aging for 16 h at 222°C (called sample\*) (b). SEM micrographs of sample\* after one reflow (c) and after one reflow followed by a **liquid state** isothermal aging for 16h at 222°C (c).

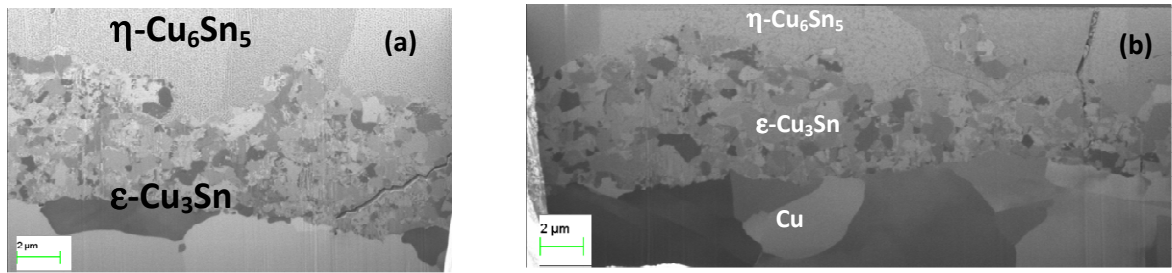


Figure 5-14. Two SEM secondary electron images (performed with a focused Ga ions beam) of the Cu/Sn interface of the sample\* (see Figure 5-13b) showing the formation of a granular  $\text{Cu}_3\text{Sn}$  layer (average grain size around  $1 \mu\text{m}$ ) and a part of  $\text{Cu}_6\text{Sn}_5$  layer with a grain size of about  $5\text{-}10 \mu\text{m}$ .

Thermal treatment	$e_{\varepsilon\text{-Cu}_3\text{Sn}} (\mu\text{m})$	$e_{\eta\text{-Cu}_6\text{Sn}_5} (\mu\text{m})$
1 reflow	$0.74 \pm 0.30$	$3.53 \pm 0.30$
sample* = 1 reflow + 16h at $222^\circ\text{C}$ solid state	$2.98 \pm 0.08$	$5.65 \pm 0.23$
sample* + 1 reflow	$4.49 \pm 0.25$	$6.46 \pm 0.60$
sample* + 16h at $222^\circ\text{C}$ liquid state	$2.57 \pm 0.15$	$16.47 \pm 0.70$

Table 5-3. Average values of thicknesses ( $e$ ) of intermetallic layers  $\varepsilon\text{-Cu}_3\text{Sn}$  and  $\eta\text{-Cu}_6\text{Sn}_5$  formed at Cu/Sn-Cu alloy interface after different thermal cycles (see text).

### 3-3-2) Modelling of growth kinetics of $\eta\text{-Cu}_6\text{Sn}_5$ layer at Cu/liquid Sn-based alloy interface

It is very interesting to note that most of the tips of V-grooves detected by SEM characterization are located at a distance ( $h$ ) of about  $3\text{-}5 \mu\text{m}$  from the  $\varepsilon\text{-Cu}_3\text{Sn}$  layer and this distance remains practically constant regardless the reaction time (see Figures 5-8 and 5-13). Note also that scallop size increases in both parallel and perpendicular directions to the Cu/alloy interface which is in agreement with numerous studies reported in literature. In our case diffusion through the Cu/ $\text{Cu}_3\text{Sn}$  interface is not a growth rate controlling process [Gusak\_2002].

In order to evaluate the time evolution of the average scallop size we use a simplified model based on the model proposed by [Gusak\_2002] (FDR model) and modified by [Liashenko\_2014]. We will describe the growth kinetics of  $\text{Cu}_6\text{Sn}_5$  layer between Cu and the Sn-Cu liquid alloy by assuming that it is controlled by the diffusion of copper through nanometric liquid channels formed between  $\text{Cu}_6\text{Sn}_5$  scallops (according to Refs. [Gusak\_2002, Chen\_1999, Suh\_2008]) and then we will deduce the minimal thickness of the liquid channels. Note however that not necessarily all the grain boundaries of  $\eta\text{-Cu}_6\text{Sn}_5$  layer are penetrated in the same way. Moreover, the triple lines can be penetrated much more than the grain boundaries as it was recently demonstrated by Dolgoplov et al [Dolgoplov\_2007] who investigated aluminium grain boundary wetting by liquid tin. They showed that the penetration depth of liquid tin along the triple junctions is much higher than along the grain boundaries of aluminum.

In the following, we propose two scenarios concerning the geometrical configuration of the liquid channels as schematically shown in Figure 5-15:

(a) **All the grain boundaries of  $\eta\text{-Cu}_6\text{Sn}_5$  layer are penetrated in the same way** (Figure 5-15b). As a first approximation, we assume that liquid channels with average **width  $\delta$**  exist between the mono-sized hemispherical scallops (with **radius  $R$** ) of growing  $\eta\text{-Cu}_6\text{Sn}_5$  phase and that all scallops have the same size  **$a = R = H$**  (see Figure 5-15a). The nanometric channels that link the tips of the grooves with the thin granular  $\varepsilon\text{-Cu}_3\text{Sn}$  layer have an average **length  $h$** .

(b) *Only the triple line junctions are penetrated in the same way*, the liquid channels are considered as cylindrical with an average radius equal to  $r$  (the grain boundaries are not penetrated - see Figure 5-15c).

The initial area of Cu/solder alloy interface is noted by  $S^{\text{tot}}$ . The cross-sectional area of channels for the supply of Cu from the substrate to the liquid/ $\eta$  interface is designated by  $S^{\text{chan-a}}$  in case (a) and  $S^{\text{chan-b}}$  in case (b).

We assume that in both cases, a constant concentration gradient exists in the liquid channels from the tip of the channels ( $z = 0$ , where the copper concentration corresponds to the liquid/ $\varepsilon$  metastable equilibrium ( $c^{\text{le}}$ )) to the tip of the groove ( $z = h$ ) where the copper concentration is very close to the liquid/ $\eta$  equilibrium concentration ( $c^{\text{ln}}$ ), i.e.  $c(z = h) \approx c^{\text{ln}}$ . Indeed, the steady state condition for the metastable  $\varepsilon$ /liquid interface leads to the condition:

$$\frac{\Delta c^{\text{chan}}}{h} S^{\text{chan}} = \frac{\Delta c^{\text{bulk}}}{e_{\eta}} S^{\text{tot}} \quad (5-28)$$

Thus, 
$$\frac{\Delta c^{\text{bulk}}}{\Delta c^{\text{chan}}} = \frac{e_{\eta}}{h} \frac{S^{\text{chan}}}{S^{\text{tot}}} \ll 1 \quad (5-29)$$

The inequality (5-29) is satisfied as long as  $S^{\text{chan}} \ll S^{\text{tot}}$  that is true for nanometric channels.  $\Delta c^{\text{chan}}/h$  and  $\Delta c^{\text{bulk}}/e_{\eta}$  are the copper concentration gradients through the liquid channels and from the top of the channels ( $z = h$ ) to the liquid/ $\eta$  interface ( $z \sim e$ ) respectively.

Thus, the condition (5-29)  $\Delta c^{\text{bulk}} = c(z = e) - c(z = h) = c^{\text{ln}} - c(z = h) \ll \Delta c^{\text{chan}} = c(z = h) - c(z = 0) = c(z = h) - c^{\text{le}}$  clearly indicates that  $c(z = e) = c^{\text{ln}} \approx c(z = h)$ .

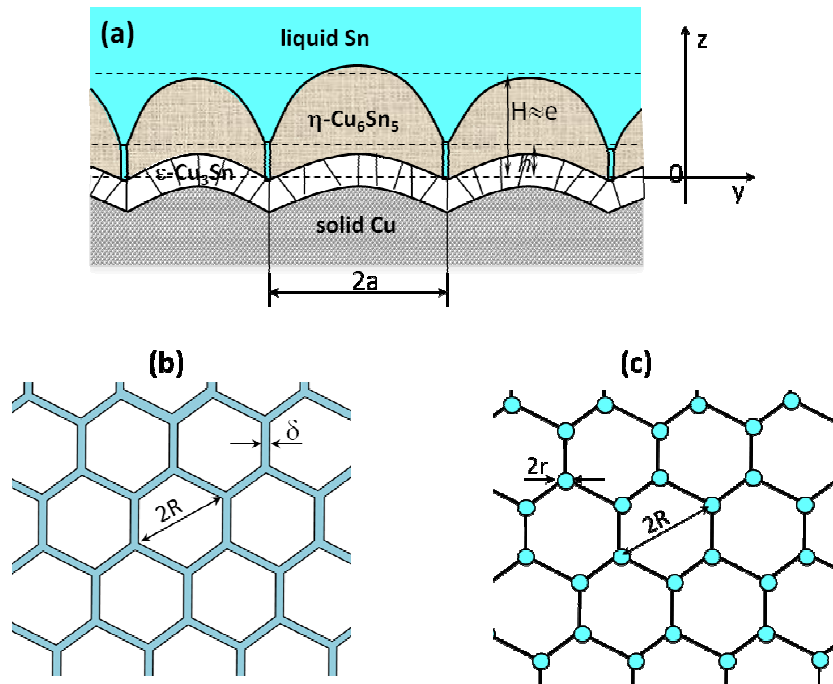


Figure 5-15. Model system: (a) Simplified schematic morphology of  $\eta\text{-Cu}_6\text{Sn}_5$  phase formed at the solid Cu/liquid Sn interface ( $a = H = R$ ). (b) Schematic presentation of formation of liquid channels with average width  $\delta$  between the mono-sized hemispherical scallops of  $\eta\text{-Cu}_6\text{Sn}_5$  phase penetrated in the same way. (c) Schematic presentation of formation of cylindrical liquid channels formed at the  $\eta\text{-Cu}_6\text{Sn}_5$  triple line junctions penetrated in the same way.

The fluxes of Cu atoms (in moles of atoms per unit time) through the  $\varepsilon$ -phase layer ( $J^{\varepsilon}$ ), through the liquid channels ( $J^{\text{chan}}$ ) and the flux  $J^{\eta}$  - from the top of the channels ( $\varepsilon$ /liquid interface,  $z = h$ ) to the liquid/ $\eta$  interface ( $z = e$ ) leading to the growth of  $\eta$  layer are given by the following expressions:

$$J^\varepsilon = \frac{\tilde{D}^\varepsilon \Delta c_\varepsilon}{e_\varepsilon V_\varepsilon} S^{\text{tot}} \quad (5-30)$$

$$J^{\text{ch}} = D_{\text{Cu}}^{\text{liq}} \frac{c^{\text{le}} - c^{\text{ln}}}{h V_{\text{Sn}}} S^{\text{chan}} \quad (5-31)$$

$$J^\eta = \frac{de_\eta}{dt} \frac{c^\eta}{V_\eta} S^{\text{tot}} \quad (5-32)$$

$V_\varepsilon$ ,  $V_{\text{Sn}}$  and  $V_\eta$  are the molar volume of the  $\varepsilon$ -Cu<sub>3</sub>Sn, liquid Sn and  $\eta$ -Cu<sub>6</sub>Sn<sub>5</sub> phase respectively (in m<sup>3</sup> per mol of atoms),  $\tilde{D}^\varepsilon \Delta c_\varepsilon$  is the integrated diffusion coefficient in the  $\varepsilon$  phase,  $D_{\text{Cu}}^{\text{liq}}$  is the diffusion coefficient of Cu in liquid Sn-Cu alloy,  $c^{\text{le}}$  and  $c^{\text{ln}}$  are the equilibrium concentration of Cu at the liquid/ $\varepsilon$  and liquid/ $\eta$  interface respectively (see Figure 5-10) and  $c_\eta = 6/11$  is the copper concentrations in  $\eta$ -Cu<sub>6</sub>Sn<sub>5</sub> and  $de_\eta/dt$  is the growth rate of  $\eta$ -Cu<sub>6</sub>Sn<sub>5</sub> layer.

Note that from experiment we know that during soldering  $\varepsilon$ -phase grows slowly thus let us use a steady-state approximation for the  $\varepsilon$ -phase that, in this case, can be given by:

$$J^\eta \approx J^{\text{chan}} \quad (5-33)$$

From Eqs. (5-31), (5-32) and (5-33), one obtains:

$$\frac{de_\eta}{dt} \frac{c^\eta}{V_\eta} S^{\text{tot}} = D_{\text{Cu}}^{\text{liq}} \frac{c^{\text{le}} - c^{\text{ln}}}{h V_{\text{Sn}}} S^{\text{chan}} \quad (5-34)$$

$$\text{i.e.,} \quad \frac{de_\eta}{dt} = \frac{D_{\text{Cu}}^{\text{liq}} (c^{\text{le}} - c^{\text{ln}})}{h} \frac{V_\eta}{c^\eta} \frac{S^{\text{chan}}}{V_{\text{Sn}} S^{\text{tot}}} \quad (5-35)$$

Application of Eq. (5-35) with  $c_\eta = 6/11$  and  $V_{\text{Sn}} = 1.7 \times 10^{-5}$  and  $V_\eta = 1.1 \times 10^{-5}$  mole of atoms per m<sup>3</sup> [Song\_2004] gives:

$$\frac{de_\eta}{dt} \approx \frac{6}{5} \frac{D_{\text{Cu}}^{\text{liq}} (c^{\text{le}} - c^{\text{ln}})}{h} \frac{S^{\text{chan}}}{S^{\text{tot}}} \quad (5-36)$$

In the following, we will evaluate the  $S^{\text{chan}}/S^{\text{tot}}$  ratio in cases (a) and (b) and deduce the corresponding  $\eta$ -Cu<sub>6</sub>Sn<sub>5</sub> layer growth law.

***a) All the grain boundaries of  $\eta$ -Cu<sub>6</sub>Sn<sub>5</sub> layer are penetrated in the same way (Figure 5-15b)***

Given the fact that the interface between the scallops and Cu is occupied completely by scallops except the thin channels, we have:  $N\pi R^2 \approx S^{\text{tot}} = \text{constant}$ , where  $N$  is the number of scallops and  $S^{\text{tot}}$  the initial area of Cu/solder alloy interface. The total cross-sectional area of channels in this case is then:

$$S^{\text{chan-a}} = 2\pi R N \frac{\delta}{2} = \frac{\delta}{R} S^{\text{tot}} = \frac{2}{3} \frac{\delta}{e_\eta} S^{\text{tot}} \quad (5-37)$$

where  $\delta$  is the channel width and  $e_\eta$  the average thickness of the  $\eta$  layer. The ratio  $R/e_\eta \approx 3/2$  is evaluated by considering that the total volume of the  $\eta$  layer  $V_\eta = S^{\text{tot}} e_\eta$  can also be approximated by  $V_\eta \approx N 2\pi R^3/3 \approx 2 S^{\text{tot}} R/3$ .

Note that the number of the liquid channels per unit area of reaction interface (proportional to  $S^{\text{chan}}/S^{\text{tot}} = \delta R$ ) is higher for a scallop-form  $\eta$ -phase compared to a semispherical-form  $\eta$ -phase. The error on  $\delta R$  value can be estimated to be given by the  $a/H$  ratio (about 20-30%) where  $a$  and  $H$  are the average values of base radius and height of a  $\eta$ -scallop respectively ( $a = H = R$  in the case of a semispherical-form).

Eqs. (5-36) and (5-37) lead to:

$$\frac{de_{\eta}}{dt} = \frac{4}{5} \frac{D_{\text{Cu}}^{\text{liq}} (c^{\text{le}} - c^{\text{ln}})}{h} \frac{\delta}{e_{\eta}} \quad (5-38)$$

Simple integration of Eq. (5-38) gives:

$$e_{\eta}^2 - e_{0,\eta}^2 = \frac{8}{5} D_{\text{Cu}}^{\text{liq}} (c^{\text{le}} - c^{\text{ln}}) \frac{\delta}{h} t = k_{\eta}^2 t \quad (5-39)$$

$e_{0,\eta}$  corresponds to the average thickness of the  $\eta$  layer at  $t = 0$ .  $k_{\eta}^2$  is the growth constant of the  $\eta$ -phase in  $\text{m}^2 \cdot \text{s}^{-1}$  that can be determined experimentally. From Eq. (5-39) we obtain:

$$\frac{\delta}{h} = \frac{5}{8} \frac{k_{\eta}^2}{D_{\text{Cu}}^{\text{liq}} (c^{\text{le}} - c^{\text{ln}})} \quad (5-40)$$

It is very interesting to note that, for a given liquid Sn-based alloy, Eq. (5-40) clearly indicates that the ratio  $\delta h$  depends only on temperature, as it is the case for  $D_{\text{Cu}}^{\text{liq}}$ ,  $k_{\eta}$ ,  $c^{\text{le}}$  and  $c^{\text{ln}}$ , thus  $\delta h = f_1(T)$ .

**b) Only all the triple line junctions are penetrated in the same way (Figure 5-15c)**

From Figure 5-15c, it is easy to evaluate the total number of the triple junctions penetrated by the liquid alloy  $N^{\text{TJ}} \approx 2N$ . The total cross-sectional area of channels in this case is then:

$$S^{\text{chan-b}} = \pi r^2 N^{\text{TJ}} \approx 2\pi r^2 N = 2 \frac{r^2}{R^2} S^{\text{tot}} = \frac{8}{9} \frac{r^2}{e_{\eta}^2} S^{\text{tot}} \quad (5-41)$$

where  $r$  is the average radius of cylindrical liquid channels.

Eqs. (5-36) and (5-41) lead to:

$$\frac{de_{\eta}}{dt} \approx \frac{16}{15} \frac{D_{\text{Cu}}^{\text{liq}} (c^{\text{le}} - c^{\text{ln}})}{h} \frac{r^2}{e_{\eta}^2} \quad (5-42)$$

Simple integration of Eq. (5-42) gives:

$$e_{\eta}^3 - e_{0,\eta}^3 = \frac{16 D_{\text{Cu}}^{\text{liq}} (c^{\text{le}} - c^{\text{ln}})}{5} \frac{r^2}{h} t = k_{\eta}^{*3} t \quad (5-43)$$

$k_{\eta}^{*3}$  is a growth constant of the  $\eta$ -phase in  $\text{m}^3 \cdot \text{s}^{-1}$  that can be determined experimentally. From Eq. (5-43) we obtain:

$$\frac{r^2}{h} = \frac{5}{16} \frac{k_{\eta}^{*3}}{D_{\text{Cu}}^{\text{liq}} (c^{\text{le}} - c^{\text{ln}})} \quad (5-44)$$

Note that, as in the previous case, for a given liquid Sn-based alloy, Eq. (5-44) clearly indicates that the ratio  $r^2/h$  depends only on temperature,  $r^2/h = f_2(T)$ .

### 3-3-3) Application

We will use Eqs. (5-40) and (5-44) to estimate the thickness of liquid channels  $\delta$  in case (a) - Figure 5-15b and the average radius  $r$  of cylindrical liquid channels in case (b) - Figure 5-15c. These applications will be performed for  $T = 222^{\circ}\text{C}$  but also for  $T = 250^{\circ}\text{C}$  by using experimental data of  $k_{\eta}^2$  and  $k_{\eta}^{*3}$  at  $250^{\circ}\text{C}$  that we have recently published in Ref. [Liashenko\_2014].

The difference of copper concentrations in the liquid alloy in equilibrium with  $\epsilon\text{-Cu}_3\text{Sn}$  and that with  $\eta\text{-Cu}_6\text{Sn}_5$  phase ( $c^{\text{le}} - c^{\text{ln}}$ ) is obtained from thermodynamic data [Dinsdale\_1991, Song\_2004, Hodaj\_2013] (detailed calculations are given in Appendix 2). All experimental and calculated data are summarized in Table 5-4 which also gives the calculated values of the diffusion coefficient of copper in liquid tin [Ma\_1960].

From Eqs. (5-40) and (5-44) and experimental and calculated data reported in Table 5-4, one can calculate the values of ratios  $\delta h$  and  $r^2/h$  that are also reported in Table 5-4.

$T(^{\circ}\text{C})$	$222^{\circ}\text{C}$	$250^{\circ}\text{C}$
$c^{\text{le}}$	0.0230	0.0315
$c^{\text{ln}}$	0.0200	0.0228
$c^{\text{le}} - c^{\text{ln}}$	$3.0 \times 10^{-3}$	$8.7 \times 10^{-3}$
$D_{\text{Cu}}^{\text{liq}}$ ( $\text{m}^2 \text{s}^{-1}$ ) [Ma_1960]	$2.4 \times 10^{-9}$	$3.5 \times 10^{-9}$
$k_{\eta}^2$ ( $\text{m}^2 \text{s}^{-1}$ )	$1.52 \times 10^{-15}$	$6.59 \times 10^{-15}$ [Liashenko_2014]
$k_{\eta}^{*3}$ ( $\text{m}^3 \text{s}^{-1}$ )	$4.30 \times 10^{-20}$	$6.24 \times 10^{-20}$ [Liashenko_2014]
$\delta h$	$1.30 \times 10^{-4}$	$1.35 \times 10^{-4}$
$r^2/h$ (m)	$1.87 \times 10^{-9}$	$0.64 \times 10^{-9}$

Table 5-4. Calculated and experimental values of different thermodynamic and kinetic parameters (see text).

By assuming that the length of the liquid channels ( $h$ ) in both cases (a) and (b) is about  $5 \mu\text{m}$ , one can estimate the average width ( $\delta$ ) of channels in case (a) and the average radius ( $r$ ) of cylindrical channels in case (2):

- at  $T = 222^{\circ}\text{C}$ :  $\delta \approx 0.7 \text{ nm}$ ,  $r \approx 100 \text{ nm}$
- at  $T = 250^{\circ}\text{C}$ :  $\delta \approx 0.8 \text{ nm}$ ,  $r \approx 60 \text{ nm}$

Note that the values of the average width  $\delta$  of the liquid channels in case (a), about  $1 \text{ nm}$ , are not far from the estimate of Jong-ook Suh et al in [Suh\_2008] for tin-lead solder (about  $2.5 \text{ nm}$ ). Note however that the calculated value of  $\delta$  is underestimated because the **nanometric liquid channels are not necessary formed between all  $\text{Cu}_6\text{Sn}_5$  scallops** as it is assumed in our model, i.e. the real surface of liquid channels  $S^{\text{chan}}$  is lower than that assumed in the model.

Note finally that the estimated values of the average radius ( $r$ ) of cylindrical channels in case (b) (some tens of nanometers) are sufficiently high to be detected by the Transmission Electron Microscopy (TEM), the major difficulty being to obtain the lamella in such a way that it contains the triple line junction formed by the boundaries of  $\eta\text{-Cu}_6\text{Sn}_5$  scallops.

### 3-4) Conclusions

In this work, **interfacial reactions between Cu substrate and metastable liquid Sn-0.7wt.%Cu alloy at  $222^{\circ}\text{C}$  are studied for the first time**. The reaction times were as long as 32 hours. This is achieved by performing specific DSC experiments in order to monitor and control the physical state of the alloy as well as to set the accurate reaction temperature.

Similar experiments were performed to study the reaction kinetics between Cu substrate and solid Sn-0.7wt.%Cu alloy at  $222^{\circ}\text{C}$  in order to compare the growth kinetics of the reaction product with that obtained for the solid Cu/metastable liquid Sn-0.7wt.%Cu alloy couple at rigorously the same temperature.

It is shown that a change in the state of the solder phase from solid to liquid leads to large differences in the growth kinetics as well as in the morphology of the  $\eta\text{-Cu}_6\text{Sn}_5$  reaction layer, despite the fact that experiments are performed at the same temperature.

Thermodynamic calculations show that the driving force of the reaction cannot be at the origin of these significant changes and thus, **our experiments provide unambiguous proof of the influence of the structural state of solder on the reaction rate**.

A theoretical analysis of the growth kinetics of  $\eta\text{-Cu}_6\text{Sn}_5$  phase at Cu substrate/liquid Sn-Cu alloy is performed by using a simplified and modified model based on existed models, in particular the FDR model. The large difference in the growth kinetics of the  $\eta\text{-Cu}_6\text{Sn}_5$  phase between the two couples (Cu/solid and Cu/metastable liquid alloy) can be explained if the growth occurs by the liquid state diffusion via the liquid channels of nanometric width

formed between grain boundaries of  $\eta$ -Cu<sub>6</sub>Sn<sub>5</sub> phase and/or by cylindrical channels of radius of some tens of nanometers formed at the triple line junctions by  $\eta$ -Cu<sub>6</sub>Sn<sub>5</sub> scallops.

#### 4) Theoretical prediction of the liquid channel width in Cu/liquid solder reactions

Formation of the scallop-like  $\eta$ -phase Cu<sub>6</sub>Sn<sub>5</sub> during reaction of copper substrate with liquid tin-based solder (with a little higher than eutectic one) proceeds much (by several orders of magnitude) faster than the same phase growth in reaction with solid solder under temperature just a little lower than eutectic one. It cannot be related to the temperature dependence of diffusion in intermetallic compound. Instead, it is related to the easy-diffusion paths emerging between neighboring scallops, which let copper intensively diffuse into the melt and there to react with tin at the scallop/liquid interfaces. To the best of our knowledge, there are 3 ways of interpreting the easy-diffusion paths in the mentioned system:

1. According to [Tu\_2007,Tu\_2011,Gusak\_2002, Suh\_2008, Liashenko\_2014], paths are just liquid channels formed due to full wetting of inter-scallop boundaries by liquid solder, so that grain-boundary tension between two neighboring grains of compound is larger than two interface tensions between scallop and liquid solder:

$$\gamma_{\eta\eta} > 2\gamma_{\eta/l}. \quad (5-45)$$

*In this case the liquid channels are formed towards the very bottom of scallops – towards the copper substrate (at first) and later towards the layer of  $\varepsilon$ -phase Cu<sub>3</sub>Sn.*

2. According to [Görlich\_2005], wetting of grain-boundaries by the liquid solder is not full:  $\gamma_{\eta\eta} < 2\gamma_{\eta/l}$ . In this case the easy paths are the grooved grain boundaries between scallops.

3. There is also a compromise possibility [Suh\_2008]: scallops growing at the base of the same copper grain, have close orientations, so that grain boundaries between them have low tension, condition (2) is satisfied; on the other hand the scallops growing at different (neighboring) grains, have large misorientations, grain-boundaries between them have high tension, they are wetted by liquid solder, condition (1) is satisfied.

Cases (1) and (3) mean the existence of the liquid channels. As shown in [Gusak\_2002], the growth and coarsening kinetics of soldering reaction is determined, first of all, by the width of these channels. To measure this width (may be, a few nanometers) directly, in situ, under condition of molten solder, seems to be not possible. After freezing the morphology changes (no full wetting anymore).

Thus, it is of major importance to make some reasonable theoretical predictions for the width of channels. Obviously, it cannot be too big, since there is a driving force of reaction which will lead to filling the existing gap by the  $\eta$ -phase growing grains. On the other hand, it cannot be zero because then two compound/liquid interfaces will convert into one grain-boundary between two solid grains, then the energy will increase due to condition (5-45).

Let us consider the channel of some width  $\delta$  dividing the two parallel walls of  $\eta$ -compound grains, based on the substrate of  $\varepsilon$ -phase (see Figure 5-16). In this configuration the bottom of the channel presents the contact of liquid tin-based solution and  $\varepsilon$ -phase, so that in usual free contact one might expect emergence of  $\eta$ -phase. Yet, in our case it should mean simultaneously the change of surface energy. It means that we actually have the nucleation problem – competition of bulk and surface terms. The only peculiarity is that the nucleus now is the island of  $\eta$ -phase containing grain-boundary instead of two preexisting  $\eta$ -phase/liquid interfaces.

Nucleation can be “homogeneous” (“kissing” of grains somewhere at arbitrary point contact of two walls - disk of  $\eta$ -phase) and “heterogeneous” - emerging of  $\eta$ -phase island (semi-cylindrical or rectangular “sheet” of  $\eta$ -phase) at the base of  $\varepsilon$ -phase bottom. The second possibility seems to be more probable due to presence of copper necessary to form “sheet” of  $\eta$ -phase from the tin-based liquid.

For simplicity consider semi-disc of radius  $R$  and thickness  $\delta$  at the bottom of the channel. Semi-disc consists of two semi-discs of some thicknesses  $\delta_1, \delta_2, \delta_1 + \delta_2 = \delta$ , being the “continuations” of the two neighboring grains. Exact position of grain-boundary (and related ratio  $\delta_1/\delta_2$  does not influence the energy and therefore is not important).

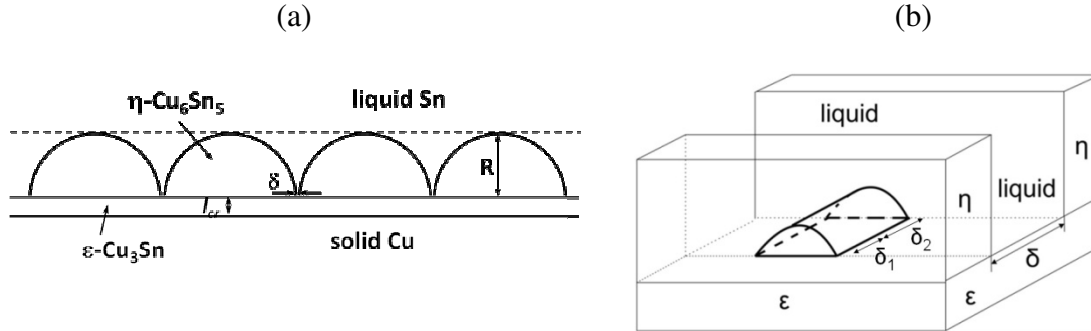


Figure 5-16. Schematic presentation of the solid Cu/liquid Sn interfacial system showing the formation of a thin, homogeneous in thickness,  $\varepsilon\text{-Cu}_3\text{Sn}$  layer and a scalloped-form layer of  $\eta\text{-Cu}_6\text{Sn}_5$  phase (a). Schematic formation of the emerging of semi-cylindrical  $\eta$ -phase island between two parallel  $\eta$ -phase scallop walls above the  $\varepsilon$ -phase.

The change of Gibbs free energy due to formation of semi-disc is equal to

$$\Delta G(R, \delta) = \left( -\frac{\Delta g_{\varepsilon+\text{solder} \rightarrow \eta}}{\Omega} \right) \cdot \delta \cdot \frac{1}{2} \pi R^2 + (\gamma_{\eta/\eta} - 2\gamma_{\eta/\text{liquid}}) \cdot \frac{1}{2} \pi R^2 + \gamma_{\eta/\text{liquid}} \cdot \pi R \cdot \delta + (\gamma_{\eta/\varepsilon} - \gamma_{\varepsilon/\text{liquid}}) \cdot 2R \cdot \delta \quad (5-46)$$

The first term is a “bulk” one. The second term corresponds to change from two solid/liquid interfaces to one grain-boundary. The third term corresponds to the side semicircle. The last, fourth term, corresponds to change of bottom rectangular side interface from liquid/epsilon to eta/epsilon.

As usual in nucleation problems, let us unite terms with squared radius and with linear radius:

$$\Delta G(R, \delta) = \left( \gamma_{\eta/\eta} - 2\gamma_{\eta/\text{liquid}} - \frac{\Delta g_{\varepsilon+\text{solder} \rightarrow \eta}}{\Omega} \delta \right) \cdot \frac{1}{2} \pi R^2 + \left( \frac{\pi}{2} \gamma_{\eta/\text{liquid}} + \gamma_{\eta/\varepsilon} - \gamma_{\varepsilon/\text{liquid}} \right) \cdot \delta \cdot 2R \quad (5-47)$$

One can easily see that the  $R$ -dependence of Gibbs free energy:

$$(1) \text{ can have typical barrier type at } \delta > \frac{\gamma_{\eta/\eta} - 2\gamma_{\eta/\text{liquid}}}{\Delta g_{\varepsilon+\text{solder} \rightarrow \eta}} \Omega$$

or

$$(2) \text{ can be monotonically increasing at } \delta < \frac{\gamma_{\eta/\eta} - 2\gamma_{\eta/\text{liquid}}}{\Delta g_{\varepsilon+\text{solder} \rightarrow \eta}} \Omega.$$

Thus, there exists some “critical” channel width, *under which* further filling of the liquid channel by eta-phase is *impossible*.

$$\delta^* = \frac{\gamma_{\eta/\eta} - 2\gamma_{\eta/\text{liquid}}}{\Delta g_{\varepsilon+\text{solder} \rightarrow \eta}} \Omega \quad (5-48)$$

If  $\delta > \delta^*$  then nucleation is not even needed, and channel will proceed becoming narrower by normal movement of walls till the width reaches the mentioned critical value.

Thus, our simple model *predicts* the operating width of the liquid channels.

## 5) Conclusions

The main contributions of this study in the traditional problem of phase growth kinetics in Cu-Sn interaction can be formulated as follows:

(i) The growth kinetic of  $\eta$ -Cu<sub>6</sub>Sn<sub>5</sub> formed at bulk Cu<sub>3</sub>Sn/liquid Sn interface was studied by direct interaction between specially prepared  $\epsilon$ -Cu<sub>3</sub>Sn specimens and liquid tin saturated with copper at 250°C. Direct comparison of Cu<sub>6</sub>Sn<sub>5</sub> growth kinetics in standard Cu/liquid Sn and in incremental Cu<sub>3</sub>Sn/liquid Sn couple gave us a link with the mechanism of the  $\eta$ -Cu<sub>6</sub>Sn<sub>5</sub> phase growth at solid Cu/liquid Sn interface. The obtained results are also consistent with the FDR model.

(ii) Interfacial reactions between Cu substrate and metastable liquid Sn-0.7wt.%Cu alloy at 222°C are studied for the first time for reaction times as long as 32 hours. This is achieved by performing specific DSC experiments in order to monitor and control the physical state of the alloy as well as to set the accurate reaction temperature. Direct comparison (for the first time) of Cu/liquid solder and Cu/solid solder reaction kinetics and morphology at the *same* temperature lead to the conclusion that the large difference in the growth kinetics between the two couples can be explained if the growth occurs by the liquid state diffusion via the liquid channels of nanometric width formed between grain boundaries of  $\eta$ -Cu<sub>6</sub>Sn<sub>5</sub> phase and/or by cylindrical channels of radius of some tens of nanometers formed at the triple line junctions by  $\eta$ -Cu<sub>6</sub>Sn<sub>5</sub> scallops.

A theoretical evaluation (for the first time) of the liquid channel width is performed for the first time. Evaluation is consistent with FDR model.

## General conclusions

In order to keep the trend of complexity growth of the integrated-circuit technology some new approaches should emerge. *One of them is the transition from two-dimensional paradigm to three-dimensional one in **packaging** of the integrated circuits. One of the principal limitations in the packaging is the ability to join different parts of the integrated circuit.* The main process used for this is **soldering**, meaning the joining of metallic parts by use of a filler metallic alloy or pure metal (solder alloy) placed between the parts to be joined. A good adhesion should be attained not only between the liquid alloy and the solid parts but also between the solidified alloy and the solid parts after cooling at room temperature. There are numerous phenomena that intervene in the soldering process such as: wetting of the solid parts by the liquid alloy and solid/liquid interfacial interactions (dissolution, diffusion, nucleation and growth of interfacial products) when the solder is in the liquid state (*reflow process*) as well as undercooling, nucleation and solidification of the bulk solder alloy during cooling of the whole system to room temperature.

Thus, the fundamental study of such phenomena in the most used solid Cu/liquid Sn system in joining technologies in electronic industry becomes crucial nowadays especially with the significant decrease of the size of a solder bump in the micrometer scale.

The main scope of this thesis was to answer some of the fundamental questions in relation with the phenomena of wetting, nucleation and growth of intermetallic phases at reactive interface that intervene in the **soldering** process very often used in electronic packaging and assembly.

***The main conclusions of this study on (i) wetting, (ii) nucleation and (iii) growth kinetics in soldering process can be summarized as following:***

### ***(i) Wetting of Cu, Ag and their intermetallics with Sn***

The wettability of the metallic substrates such as Cu, Ag and their main intermetallics with Sn ( $\text{Cu}_3\text{Sn}$ ,  $\text{Cu}_6\text{Sn}_5$  and  $\text{Ag}_3\text{Sn}$ ) by liquid Sn, Sn-Cu solders and Pb was studied by implementing the *dispensed drop technique in the high-vacuum furnace and using of a rapid camera* for recording the spreading process.

Preliminary wetting experiments of liquid Sn on Cu substrate followed by a CDD camera allow to study the influence of the annealing of the Cu substrate under high vacuum at  $800^\circ\text{C}$  on its wetting behavior. For wetting experiments performed at  $250\text{-}400^\circ\text{C}$ , the annealing has practically no influence on the first and final measured contact angles. On the contrary, for temperatures  $500\text{-}600^\circ\text{C}$ , it leads to a significant increase in the spreading kinetics.

In order to distinguish the non-reactive spreading of liquid Sn-Cu alloys on the non reacted Cu substrate and a possible reactive spreading with formation of intermetallics, some wetting experiments were followed by the high speed camera. It allowed us to reveal that, in temperature range  $300\text{-}600^\circ\text{C}$ , the first stage of wetting of Cu substrate by liquid Sn or Sn-Cu liquid alloy is very rapid (in less than 10 ms), the spreading rate being about  $0.25\text{ m}\cdot\text{s}^{-1}$ . During this stage, corresponding to a non reactive spreading process, the spreading kinetics of Sn or Sn-Cu alloy droplet is practically temperature independent and similar to that of the non-reactive liquid Pb over Cu substrate at  $400^\circ\text{C}$ . It allows us to conclude that the equilibrium contact angle of liquid Sn on a non-reacted and clean surface is lower than  $30^\circ$ .

Wetting experiments of  $\text{Cu}_3\text{Sn}$  and  $\text{Cu}_6\text{Sn}_5$  intermetallics, performed for the first time, leads to a better understanding of reactive wetting in Cu/liquid Sn system. It was found that the non-reactive contact angles of liquid Sn on a  $\text{Cu}_3\text{Sn}$  surface, attained in less than 10 ms, decrease from  $23$  to  $10^\circ$  when the experimental temperature increases from  $300$  to  $500^\circ\text{C}$ , which should be mainly due to the oxidation extent of the substrate surface. During wetting experiments of bulk and scalloped  $\text{Cu}_6\text{Sn}_5$  compound at  $390^\circ\text{C}$ , low contact angle of about  $20^\circ$  is attained in less than 10 ms. These results allow to conclude that the non-reactive

equilibrium contact angles of liquid Sn on Cu<sub>3</sub>Sn and Cu<sub>6</sub>Sn<sub>5</sub> could be lower than that on Cu. Moreover, a rapid infiltration of liquid Sn into the Cu<sub>6</sub>Sn<sub>5</sub> bulk substrate proceeding through the wetted grain-boundaries and/or its open porosities is in agreement with the very good wetting of this compound by liquid Sn.

From experimental results of wetting of Cu and Cu<sub>6</sub>Sn<sub>5</sub> substrates it can be concluded that wetting of Cu proceeds in two stages: (i) a rapid *non-reactive stage* during which the contact angle decreases down to 30° in less than 10 ms and (ii) a slow *reactive stage* during which the contact angle decreases from 30 to 23° in about 3 s at 400°C.

Results of wetting experiments of Ag and Ag<sub>3</sub>Sn substrates by liquid Sn allow us to propose a mechanism of the spreading kinetics in two stages: (a) a *very rapid non reactive wetting*, the contact angle decreasing down to the equilibrium contact angle on the non reacted Ag substrate ( $\theta_{Ag} \approx 20^\circ$ ) in less than 10 ms (spreading rate higher than 0.1 m/s) and (b) a *slow reactive wetting stage* (spreading rate lower than 10<sup>-3</sup> m/s) from  $\theta_{Ag}$  to the equilibrium contact angle of liquid Sn on the reaction product layer, i.e., on Ag<sub>3</sub>Sn ( $\theta_{Ag_3Sn} \approx 10^\circ$ ).

**(ii) Nucleation (a) at Cu/liquid Sn reactive interfaces and (b) inside the solder bulk**

***a) Nucleation at Cu/liquid Sn reactive interfaces***

By implementing a fast dipping experimental set-up (made in our laboratory), SEM-FEG and TEM techniques, we succeed to study *for the first time* the sequence of formation of intermetallic compounds at the interface between Cu and liquid Sn-Cu alloy at the very beginning of reaction (from 1 ms to 1 s ) at 250°C. For very short periods of time (1 to 40 ms), two intermetallic layers are formed at the interface: a thin and homogenous layer (40-100 nm thick) and a scalloped layer (50-500 nm thick). Both layers correspond perfectly to the basic  $\eta^*$ -Cu<sub>6</sub>Sn<sub>5</sub> structure. No  $\epsilon$ -Cu<sub>3</sub>Sn phase crystallites are detected for such short reaction times. For reaction time about 1 s two reaction layers are detected at the interface: a thin layer of  $\epsilon$ -Cu<sub>3</sub>Sn phase ( $\approx 100$  nm thick) and a scalloped layer of Cu<sub>6</sub>Sn<sub>5</sub> phase (height up to 500 nm). These experiments give, for the first time, the answer on one of the most opened and interesting question in soldering: the first phase that appears at Cu/Sn interface is the Cu<sub>6</sub>Sn<sub>5</sub> phase and Cu<sub>3</sub>Sn phase does not appear at the interface as long as the thickness of the Cu<sub>6</sub>Sn<sub>5</sub> phase is at least lower than about 500 nm.

In the same field of interest, we have developed a theoretical approach on the suppression criteria of the second phase formation ( $\epsilon$ -Cu<sub>3</sub>Sn) at the reactive Cu/Sn interface by assuming that Cu<sub>6</sub>Sn<sub>5</sub> is the first phase that grows at the interface in form of a continuous layer. This model leads to the critical thickness of the first Cu<sub>6</sub>Sn<sub>5</sub> layer under which, the nucleation and growth of the second phase (Cu<sub>3</sub>Sn) is forbidden. The evaluated critical thickness of Cu<sub>6</sub>Sn<sub>5</sub> layer given by this model is in agreement with the experimental results obtained in this study. Moreover, a theoretical modeling of even earlier stages of the isolated nucleus of  $\epsilon$ -Cu<sub>3</sub>Sn phase nucleation is developed where the possibility of kinetic suppression of the lateral growth was discussed for the first time. The criterion of the lateral growth suppression was applied for Cu-Sn system on the basis of the available data of diffusivity in this system.

***b) Nucleation inside the solder bulk***

Crystallization of eutectic Sn-Cu alloy was studied by performing specific DSC experiments in two different configurations: solder over Cu<sub>6</sub>Sn<sub>5</sub> phase and solder without any interfaces in order to study the heterogeneous nucleation of solid Sn during cooling of this alloy. By applying thermal cycles of complete melting and partial melting of the solder, different categories of the undercooling degrees are obtained. In particular, low undercooling degrees (1-7 K) are detected *for the first time* in the case of partial melting. A theoretical approach on heterogeneous nucleation in this last case shows that the sites of the favorable nucleation are, most probably, cavities with curvature radii larger than about ten nanometers or/and steps (grooves) on the surface of the solid particle with opening angle larger than about 120-130°. This study allows to conclude about the heterogeneous nucleation sites of solid Sn:

(i) In the case of complete melting of the solder (reflow process), the  $\text{Cu}_6\text{Sn}_5$  particles are completely dissolved in the liquid bulk and nucleation is related only to solid impurities in the solder bulk (or to  $\text{Cu}_6\text{Sn}_5$  layer formed at Cu/liquid interface in the case of solder joints). (ii) In the case of partial melting, there are still some remaining  $\text{Cu}_6\text{Sn}_5$  nanoparticles in the melt providing the heterogeneous nucleation sites for Sn.

### **(iii) Growth kinetics of reaction layers at Cu/liquid Sn interface**

The growth mechanisms of the  $\eta\text{-Cu}_6\text{Sn}_5$  phase formed by reaction between Cu and liquid Sn, for which still a lot of controversy exists in literature, were studied experimentally and theoretically.

- The growth kinetic of  $\eta\text{-Cu}_6\text{Sn}_5$  formed at bulk  $\text{Cu}_3\text{Sn}$ /liquid Sn interface was studied by direct interaction between specially prepared  $\varepsilon\text{-Cu}_3\text{Sn}$  specimens and liquid tin saturated with copper at  $250^\circ\text{C}$ . Direct comparison of  $\text{Cu}_6\text{Sn}_5$  growth kinetics in standard Cu/liquid Sn and in incremental  $\text{Cu}_3\text{Sn}$ /liquid Sn couple gave a link with the operating mechanism of the  $\eta\text{-Cu}_6\text{Sn}_5$  phase growth at solid Cu/liquid Sn interface. The obtained results are also consistent with the FDR model.

- In order to eliminate the differences in the driving force of diffusion between Cu/solid couples and Cu/liquid couples we performed, for the first time, specific experiments of interfacial reactions between Cu substrate and metastable liquid Sn-0.7wt.%Cu alloy at  $222^\circ\text{C}$  for reaction times as long as 32 hours. This is achieved by performing specific DSC experiments in order to monitor and control the physical state of the alloy as well as to set the accurate reaction temperature. Direct comparison of Cu/liquid solder and Cu/solid solder reaction kinetics and morphology at the *same* temperature leads to the conclusion that the large difference in the growth kinetics between the two couples can be explained if the growth occurs by the liquid state diffusion via the liquid channels of nanometric width formed between grain boundaries of  $\eta\text{-Cu}_6\text{Sn}_5$  phase and/or by cylindrical channels of radius of some tens of nanometers formed at the triple line junctions by  $\eta\text{-Cu}_6\text{Sn}_5$  scallops. A theoretical evaluation (for the first time) of the liquid channel width is performed for the first time. Evaluation is consistent with FDR model.

***Future fundamental research*** on the wetting of Cu and Cu-Sn intermetallics by liquid solder alloys and on the initial stages of reaction at Cu/liquid solder interface can be for example:

- In situ high temperature x-ray diffraction of reactive products formed during reactive wetting experiments performed by the dispensed drop technique, as a function of time (and temperature) associated with the wetting kinetics. The problem of surface oxidation should be resolved by using in situ cleaning of the substrate surface in a specific chamber that communicates with the wetting experimental chamber.

- In situ high temperature x-ray diffraction characterization of reactive phases formed at Cu/liquid solder interface during rapid dipping experiments.

- TEM experiments for detecting liquid channels in the  $\eta$ -phase.

- Determine the role of different alloying elements in liquid Sn and/or in solid Cu on the morphology and growth kinetic of reaction product.

## Appendix 1 Phase diagram of the binary Ag-Sn system.

Figure A1-1 gives the phase diagram of the binary Ag-Sn system.

This phase diagram presents two intermetallic compounds, the non stoichiometric  $\zeta$  and the stoichiometric  $\text{Ag}_3\text{Sn}$  compound. In the temperature range below  $300^\circ\text{C}$ , the Sn-Ag binary system has the following eutectic transformation at  $221^\circ\text{C}$  for the composition Sn-3.5%Ag:  $\text{Liq} \rightarrow \text{Ag}_3\text{Sn} + \text{Sn}$ .

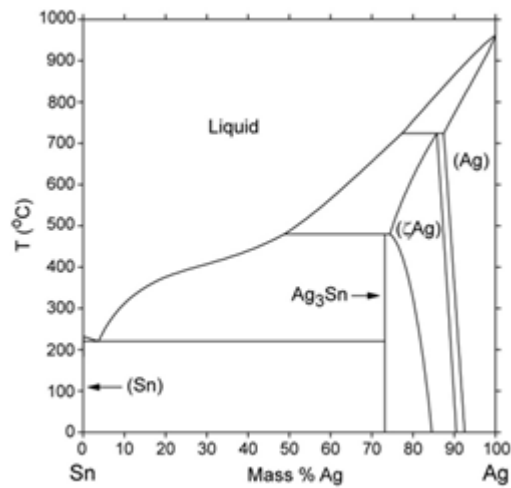


Figure A1-1 Phase diagram of the binary Ag-Sn system [1].

[1] <http://www.metallurgy.nist.gov>

## Appendix 2: Determination of the Gibbs free energy of formation of different phases in Cu-Sn system by using CALPHAD approach

To find the equilibrium concentration of Cu at the liquid/ $\epsilon$  phase and liquid/ $\eta$  phase interface we used CALPHAD data to build the Gibbs energy concentration dependence ( $G_1(c)$  in  $\text{J}\cdot\text{mol}^{-1}$ ) on the Figure 4-22 and Figure 5-11 in the form of  $G$ - $H$ SER [1].

$$G_1(c_{\text{Sn}}) = c_{\text{Sn}}G_1^{\text{Sn}} + (1-c_{\text{Sn}})G_1^{\text{Cu}} + RT(c_{\text{Sn}}\ln(c_{\text{Sn}}) + (1-c_{\text{Sn}})\ln(1-c_{\text{Sn}})) + c_{\text{Sn}}(1-c_{\text{Sn}})(Lf_0 + (2c_{\text{Sn}}-1)Lf_1 + (2c_{\text{Sn}}-1)^2Lf_2) \quad (\text{A2-1})$$

$G_1^{\text{Sn}}, G_1^{\text{Cu}}$  are the Gibbs free energy for the pure liquid Sn and pure liquid Cu, given by the following expressions:

$$G_1^{\text{Sn}} = 9496.31 - 9.809114 T - 8.2590486 T \ln(T) - 0.01681442 9T^2 + 2.623131.1 0^{-6}T^3 - 1081244/T \quad (\text{A2-2})$$

$$G_1^{\text{Cu}} = 5194.277 + 120.973331T - 24.112392T \ln(T) - 2.65684.10^{-3}T^2 + 0.129223.10^{-6}T^3 + 52478/T - 5.849.10^{-21}T^7 \quad (\text{A2-3})$$

Energetic components are taken from the thermodynamic assessment of Shim et al [2]:

$$\begin{aligned} Lf_0 &= -9002.8 - 5.8381T \\ Lf_1 &= -20100.4 + 3.6366T \\ Lf_2 &= -10528.4 \end{aligned} \quad (\text{A2-4})$$

Reference states are FCC\_A1 (Cu) and BCT\_A5 (Sn) at 295.15K.

We take the relations for Gibbs potentials of the stoichiometric phases as [2]:

$$G^{\eta} = -6869.5 - 0.1589 T + 0.545 G_s^{\text{Cu}} + 0.455 G_s^{\text{Sn}} \quad (\text{A2-5})$$

$$G^{\epsilon} = -8194.2 - 0.2043T + 0.75 G_s^{\text{Cu}} + 0.25 G_s^{\text{Sn}} \quad (\text{A2-6})$$

where the relations for the Gibbs free energy of the solid Sn and Cu are given as:

$$G_s^{\text{Cu}} = 7770.458 + 130.485235 T - 24.112392 T \ln(T) - 0.00265684 T^2 + 1.29223 \cdot 10^{-7} T^3 - 52478/T \quad (\text{A2-7})$$

$$G_s^{\text{Sn}} = 2524.724 + 4.005269T - 8.2590486 T \ln(T) - 0.01681442 9T^2 + 2.623131 \cdot 10^{-6} T^3 - 1081244/T - 1.2307 \cdot 10^{25} T^9 \quad (\text{A2-8})$$

Application of Eqs. (A1-5) to (A1-8) gives:

$$\text{(i) at } T = 495 \text{ K: } G^{\eta} = -28847.4 \text{ J}\cdot\text{mol}^{-1} \text{ and } G^{\epsilon} = -28831.8 \text{ J}\cdot\text{mol}^{-1}, \\ c^{\eta} = 0.020 \text{ and } c^{\epsilon} = 0.023.$$

$$\text{(ii) at } T = 523 \text{ K: } G^{\eta} = -30413 \text{ J}\cdot\text{mol}^{-1} \text{ and } G^{\epsilon} = -29784.2 \text{ J}\cdot\text{mol}^{-1}, \\ c^{\eta} = 0.023 \text{ and } c^{\epsilon} = 0.032.$$

[1]: Dinsdale, A. (1991). SGTE data for pure elements. Calphad, 15(4), 317-425.

[2]: Shim, J. H., Oh, C. S., Lee, B. J., & Lee, D. N. (1996). Thermodynamic assessment of the Cu-Sn system. Zeitschrift für Metallkunde, 87(3), 205-212.

### Appendix 3: Nucleation of a solid at the triple joint formed between two solid/ $\eta$ interfaces and a $\eta/\eta$ grain boundary

Let consider the nucleation of a solid cylindrical nucleus of Sn (from liquid Sn) at the triple joint formed between two solid/ $\eta$  interfaces and a  $\eta/\eta$  grain boundary. We take the nucleus as a “slice” of solid tin in the form of a “curved prism” with two flat lateral faces and one cylindrical surface (length  $l$ , radius of curvature  $r$  - see Figure A3-1). The shape ratio ( $\varphi = l/\rho$ ) should be optimized at each volume (number of atoms in the nucleus).

According to elementary geometry (Figure A3-1):

$$\begin{cases} \varepsilon = \frac{\pi}{2} - \theta, \Rightarrow \beta = \theta + \alpha - \frac{\pi}{2}, \\ \beta + \varepsilon = \alpha \end{cases}, \quad (\text{A3-1})$$

where, additionally to equilibrium conditions for angle  $\theta$ , one more equilibrium condition exists *before* solidification at the joint:

$$2\gamma_{l\eta} \cos\alpha = \gamma_{gb}. \quad (\text{A3-2})$$

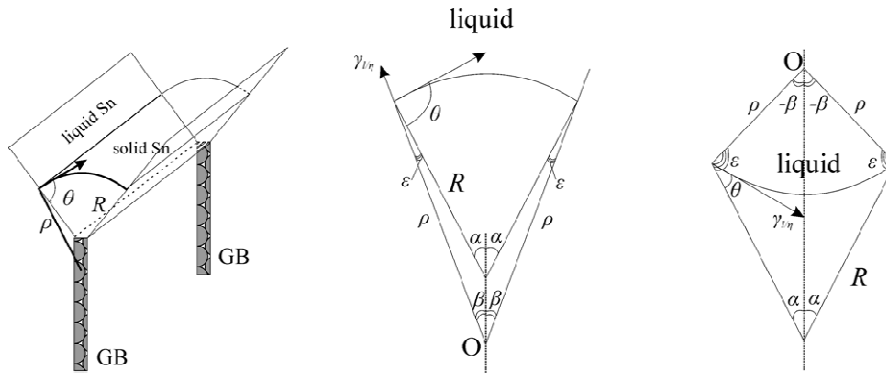


Figure A3-1. a) Geometry of nucleation at the triple joint solid/ $\eta$  interface-solid/ $\eta$  interface-grain boundary; b) centre of curvature ( $O$ ) at the solid side ( $\beta > 0$  and  $\theta > \pi/2 - \alpha$ ); c) centre of curvature at the liquid side ( $\beta < 0$  and  $\theta < \pi/2 - \alpha$ ).

There is still some doubt on whether or not full wetting of grain boundaries occurs between grains of the compound by liquid tin. In the case of full wetting ( $2\gamma_{l\eta} < \gamma_{gb}$ , [1]) one has liquid channels between scallops going all the way to the substrate or to the  $\text{Cu}_3\text{Sn}$  thin layer. In the case of partial wetting [2], a compromise was suggested by Jong-ook-Suh *et al.* [3], namely full wetting between scallops growing at the base of neighbouring Cu grains, and partial wetting between scallops based on the same Cu grain and therefore having a small misorientation.

Here we consider possible nucleation of solid tin at the triple joint with partial wetting,  $\frac{\gamma_{gb}}{2\gamma_{l\eta}} < 1$ . The total surface energy, which should be optimized, is given by

$$W^{\text{surf}}(n, \varphi) = 2\gamma_{ls} S^{\text{base}} + \gamma_{ls} S^{\text{top}} + 2(\gamma_{s\eta} - \gamma_{l\eta}) S^{\text{side}} = 2\gamma_{ls} \left( S^{\text{base}} + \frac{S^{\text{top}}}{2} - S^{\text{side}} \cos\theta \right) \quad (\text{A3-3})$$

Elementary geometrical considerations, for example for the case  $\beta > 0$ , imply

$$S^{\text{base}} = \frac{1}{2} R^2 2\beta - 2 \cdot \frac{1}{2} R\rho \sin\varepsilon = R^2 \beta - R\rho \cos\theta, \quad (\text{A3-4})$$

$$\frac{R}{\sin(\pi - \alpha)} = \frac{\rho}{\sin\beta} \Rightarrow R = \rho \frac{\sin\alpha}{\sin\beta}, \text{ so that}$$

$$S^{\text{base}} = \rho^2 \frac{\sin\alpha}{\sin\beta} \left( \beta \frac{\sin\alpha}{\sin\beta} - \cos\theta \right). \quad (\text{A3-5})$$

One can easily check by direct derivation that, in case of  $\beta < 0$  ( $\theta + \alpha < \frac{\pi}{2}$ ), the expression for  $S^{base}$  remains formally the same and positive (the first term becomes negative and the second term positive). Note that in this case the centre of curvature appears over the top.

$$S^{top} = (R \cdot 2\beta) \cdot l = (\varphi\rho) \left( \rho \frac{\sin\alpha}{\sin\beta} \right) \cdot 2\beta = \varphi\rho^2 2\beta \frac{\sin\alpha}{\sin\beta},$$

$$S^{side} = \rho l = \varphi\rho^2.$$

Thus, we can consider the surface energy as a function of linear size parameter  $\rho$  and of shape parameter  $\varphi = l/\rho$ .

$$W^{surf}(\rho, \varphi) = 2\gamma_{ls}\rho^2 \left\{ \frac{\sin\alpha}{\sin\beta} \left( \beta \frac{\sin\alpha}{\sin\beta} - \cos\theta \right) + \varphi\beta \frac{\sin\alpha}{\sin\beta} - \varphi\cos\theta \right\}$$

$$\text{By introducing the notation } \psi = \frac{\sin\alpha}{\sin\beta} \left( \beta \frac{\sin\alpha}{\sin\beta} - \cos\theta \right), \quad (\text{A3-6})$$

the expression for  $W^{surf}$  becomes

$$W^{surf}(\rho, \varphi) = 2\gamma_{ls}\rho^2\psi \left( 1 + \frac{\sin\beta}{\sin\alpha}\varphi \right)$$

The parameters ( $\rho$ ,  $\varphi$  and  $\psi$ ) are linked by the constraint of volume (the number of atoms multiplied by the atomic volume):  $n\Omega_{at} = S^{base}l = \varphi\rho \cdot \rho^2 \frac{\sin\alpha}{\sin\beta} \left( \beta \frac{\sin\alpha}{\sin\beta} - \cos\theta \right) = \varphi\rho^3\psi$ ,

leading to  $\varphi = \frac{n\Omega_{at}}{\rho^3\psi}$ , so that

$$W^{surf}(n, \rho(\varphi)) = 2\gamma_{ls}\rho^2\psi \left( 1 + \frac{\sin\beta}{\sin\alpha} \frac{n\Omega_{at}}{\rho^3\psi} \right) = 2\gamma_{ls}\psi \left( \rho^2 + \frac{\sin\beta}{\sin\alpha} \frac{n\Omega_{at}}{\psi} \frac{1}{\rho} \right) \quad (\text{A3-7})$$

The minimization of  $W^{surf}(n, \varphi)$  over  $\varphi$  (or  $\rho$ ) at fixed  $n$  leads to

$$\rho_{opt} = n^{1/3} \Omega_{at}^{1/3} \left( \frac{1}{2\psi} \frac{\sin\beta}{\sin\alpha} \right)^{1/3}, \quad \varphi_{opt} = \frac{n\Omega_{at}}{\rho_{opt}^3\psi} = 2 \frac{\sin\alpha}{\sin\beta}.$$

Clearly the expression for  $\varphi_{opt}$  applies only for  $\beta = \alpha + \theta - \frac{\pi}{2} > 0$  (or  $\theta > \pi/2 - \alpha$ ). When  $\beta$  tends to zero, the optimal shape parameter tends to infinity. When  $\beta$  becomes negative, expression (A3-7) for the surface energy as a function of the inverse of  $\rho$  becomes monotonic (see Figure A3-2).

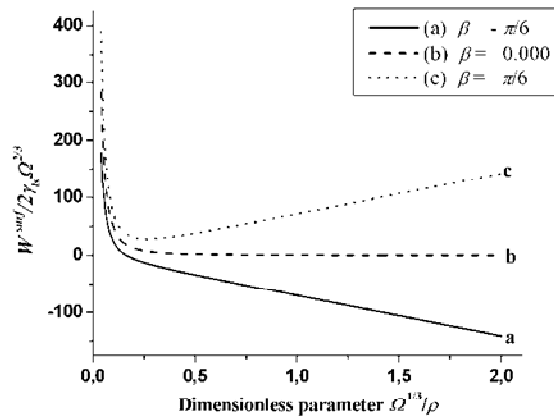


Figure A3-2. Minimization of the surface energy over dimensionless parameter  $\Omega^{1/3}/\rho$  for  $\alpha = \pi/4$ ,  $n = 100$  and  $\beta = -\pi/6$  (a);  $\beta = 10^{-4}$  (b);  $\beta = \pi/6$  (c).

Thus, with negative and zero values of  $\beta$ , nuclei of solid Sn will tend to spread almost as a line along the junction scallop 1 - scallop 2 grain boundary. Of course, in this case one can introduce at least one more factor - the line tension of the junction, which will make the infinite line impossible and of course the curvature radius  $\rho$  cannot be less than the atomic size - see below.

Inserting the values of  $\varphi_{\text{opt}}$  and  $\rho_{\text{opt}}$  in Eq. (A2-7), the expression for  $W^{\text{surf}}$  becomes

$$W^{\text{surf}}(n_{\text{opt}}, \varphi_{\text{opt}}) = 2\gamma_{\text{ls}}\psi \left( \frac{n^{2/3}\Omega_{\text{at}}^{2/3}\sin\beta}{2\sin\alpha \cdot \psi} \right)^{2/3} \left( 1 + \frac{\sin\beta}{\sin\alpha} \cdot \frac{2\sin\alpha}{\sin\beta} \right) = \left( \frac{3}{2\pi} \right)^{1/3} \gamma_{\text{ls}} n^{2/3} \Omega_{\text{at}}^{2/3} \psi^{1/3} \left( \frac{\sin\beta}{\sin\alpha} \right)^{2/3},$$

with  $\psi$  given by Eq.(A3-6) and by introducing the notation  $\tilde{\gamma} = \left( \frac{3}{2\pi} \right)^{1/3} \gamma_{\text{ls}} \left( \beta - \frac{\sin\beta}{\sin\alpha} \cos\theta \right)^{1/3}$ , an expression for  $W^{\text{surf}}$  as a function of the number of atoms,  $n$ , in the nuclei is obtained:

$$W_{\text{optimized}}^{\text{surf}} = \tilde{\gamma} 4\pi r_0^2 n^{2/3}.$$

[1]: Gusak, A. M., & Tu, K. N. (2002). Kinetic theory of flux-driven ripening. *Physical Review B*, 66(11), 115403.

[2]: Görlich, J., Schmitz, G., & Tu, K. N. (2005). On the mechanism of the binary Cu/Sn solder reaction. *Applied Physics Letters*, 86(5), 053106.

[3]: Suh, J. O., Tu, K. N., & Tamura, N. (2007). Preferred orientation relationship between Cu<sub>6</sub>Sn<sub>5</sub> scallop-type grains and Cu substrate in reactions between molten Sn-based solders and Cu. *Journal of Applied Physics*, 102(6), 63511-63511.

#### Appendix 4: Evaluation of the increase in the driving force of diffusion in the solid Cu/liquid Sn-Cu couple, necessary to lead to a given increase in the growth kinetics of $\eta$ -Cu<sub>6</sub>Sn<sub>5</sub> phase

If we consider that growth of compound  $i$  layers ( $i = \eta$ -Cu<sub>6</sub>Sn<sub>5</sub> or  $\varepsilon$ -Cu<sub>3</sub>Sn) at Cu/Sn interface is limited by the solid state diffusion - growth in parabolic regime ( $e_i^2 = e_{0i}^2 + k_i^2 t$ ), then the ratio between the kinetic growth constants  $k_i$  of these layers can be calculated. All calculations details are given in Ref. [1] where it is assumed that the so-called Wagner integrated diffusivities (products  $D_i \Delta c_i$  of average interdiffusion coefficient  $D_i$  and of concentration range  $\Delta c_i$ ) remains constant during reaction. The ratio between the growth kinetic constants for  $\eta$  ( $k_\eta$ ) and  $\varepsilon$  layers ( $k_\varepsilon$ ),  $r = k_\eta/k_\varepsilon$ , is then given by [1]:

$$\frac{k_\eta}{k_\varepsilon} = r = \frac{\beta c^\varepsilon / c^\eta - r}{-\beta + r(1 - c^\eta) / (1 - c^\varepsilon)} \quad (\text{A4-1})$$

$$\text{where} \quad \beta = \frac{D_\eta \Delta c_\eta}{D_\varepsilon \Delta c_\varepsilon} \quad (\text{A4-2})$$

$c^\eta = 6/11$  and  $c^\varepsilon = 3/4$  are the mole fractions of copper in the  $\eta$ -Cu<sub>6</sub>Sn<sub>5</sub> and  $\varepsilon$ -Cu<sub>3</sub>Sn phases respectively. With the values of  $c^\eta$  and  $c^\varepsilon$  given above, Eq. (A4-1) becomes:

$$r = \frac{11(11\beta - r)}{8(20r - \beta)} \quad (\text{A4-3})$$

$$\text{or:} \quad \beta = \frac{8r(20r + 1)}{11(8r + 11)} \quad (\text{A4-4})$$

In order to evaluate the variation in the copper flux through the  $\eta$ -Cu<sub>6</sub>Sn<sub>5</sub> and  $\varepsilon$ -Cu<sub>3</sub>Sn phase layers with the driving force of copper diffusion, the diffusion flux of copper in the compound  $i$ ,  $J_i$  ( $i = \eta$ -Cu<sub>6</sub>Sn<sub>5</sub> or  $\varepsilon$ -Cu<sub>3</sub>Sn) is most conveniently expressed in terms of the chemical potential gradient  $\mu_i$  [2]:

$$J_i = -\frac{D_i}{V_i^m} \frac{\partial c_i}{\partial z} = -\frac{D_i^*}{RTV_i^m} \frac{\partial \mu_i}{\partial z} = -\frac{A_i}{V_i^m} \frac{\partial \mu_i}{\partial z} \quad (\text{A4-5})$$

where  $V_i^m$  is the molar volume of phase  $i$  ( $\text{m}^3$  per mol of atoms),  $D_i^*$  is the self-diffusion coefficient of copper in the considered phase,  $A_i = D_i^*/RT$  is a constant at fixed temperature and  $c_i$  is the molar fraction of copper in the phase  $i$  (it is nearly constant across the layer because of the narrow range of homogeneity).

Assuming a steady state profile for the copper chemical potential across the  $\eta$ -Cu<sub>6</sub>Sn<sub>5</sub> and  $\varepsilon$ -Cu<sub>3</sub>Sn phase layer, in first approximation, it can be deduced from Eq. (A4-5) that:

$$D_i \Delta c_i \approx A_i \Delta \mu_i \quad (\text{A4-6})$$

where  $\Delta c_i$  and  $\Delta \mu_i$  are the variations of the molar fraction and chemical potential of copper through the phase  $i$  respectively.

From Eqs. (A4-2) and (A4-6), the expression of  $\beta$  becomes:

$$\beta = \frac{A_\eta \Delta \mu_\eta}{A_\varepsilon \Delta \mu_\varepsilon} = B \Delta \mu_\eta \quad (\text{A4-7})$$

where  $B = A_\eta / (A_\varepsilon \Delta \mu_\varepsilon)$  is practically constant. Indeed, as it is shown in Figure 5-10c, for a given temperature, the variation of the chemical potential of Cu through the  $\varepsilon$ -Cu<sub>3</sub>Sn layer in the Cu/ $\varepsilon$ -Cu<sub>3</sub>Sn/ $\eta$ -Cu<sub>6</sub>Sn<sub>5</sub>/Sn system ( $\Delta \mu_\varepsilon$ ) remains constant whatever the state of Sn (liquid or solid).

From Eq. (A4-4) we can evaluate the variation of parameter  $\beta$  with the ratio  $r = k_\eta/k_\varepsilon$  when the Cu/metastable liquid alloy couple is replaced by the Cu/solid alloy couple. Let note  $r = r_{\text{liq}} = k_\eta/k_\varepsilon$  and  $r' = r_{\text{sol}} = k'_\eta/k'_\varepsilon$  the values of  $r$  corresponding to the Cu/metastable liquid

alloy the Cu/solid alloy couple respectively. From experimental results at 222°C we have (see Eq. (5-27a)):

$$r = 3.9 \text{ and } r' = 0.9 \quad (\text{A4-8})$$

Replacing these values of  $r$  and  $r'$  in Eq. (A2-4), gives:

$$\beta = 5.31 \text{ and } \beta' = 0.68 \quad (\text{A4-9})$$

Thus, if the growth kinetics of both  $\text{Cu}_6\text{Sn}_5$  and  $\varepsilon\text{-Cu}_3\text{Sn}$  layers is limited by solid state diffusion then the calculated value of the ratio between  $\Delta\mu_\eta$  (variation of chemical potential of copper through the  $\text{Cu}_6\text{Sn}_5$  layer in the case of Cu/metastable liquid alloy couple) and  $\Delta\mu'_\eta$  (in the case of Cu/solid alloy couple) will be given by:

$$R_{\text{calc}} = (\beta/\beta')_{\text{calc}} = (\Delta\mu_\eta / \Delta\mu'_\eta)_{\text{calc}} = 7.81 \quad (\text{A4-10})$$

Note however that the value of  $R_{\text{calc}}$  is much higher than that of  $R_{\text{Calphad}} = \Delta\mu_\eta/\Delta\mu_\varepsilon$  obtained using the CALPHAD approach for the Cu/metastable liquid Sn-Cu alloy and Cu/solid Sn-Cu alloy systems at 222°C (see Figure 5-10b):

$$R_{\text{Calphad}} = (\Delta\mu_\eta / \Delta\mu'_\eta)_{\text{Calphad}} = (\Delta\mu_\eta^{\text{liq}} / \Delta\mu_\eta^{\text{sol}})_{\text{Calphad}} = \frac{-30583.6+26776.8}{-30510.8+26851.3} = 1.04 \quad (\text{A4-11})$$

***From Eqs. (A4-10) and (A4-11) we can definitively conclude that, when the Cu/solid alloy couple is replaced by the Cu/metastable liquid alloy couple at 222°C, the increase in the driving force of copper (or tin) diffusion will be only 4%.*** This increase in the driving force of diffusion is far from being sufficient in order to lead to the large difference in the ratio  $r = k_\eta/k_\varepsilon$  observed experimentally when the solid alloy is replaced by the liquid alloy. Indeed, if the growth kinetics of both phases was limited by bulk solid state diffusion, an increase in the driving force by more than 700% (see Eq. (A4-10)) is necessary for being in agreement with experimental results.

[1]: Liashenko, O., Gusak, A. M., & Hodaj, F. (2014). Phase growth competition in solid/liquid reactions between copper or  $\text{Cu}_3\text{Sn}$  compound and liquid tin-based solder. *Journal of Materials Science: Materials in Electronics*, 25(10), 4664-4672.

[2]: Van Loo, F. J. J. (1990). Multiphase diffusion in binary and ternary solid-state systems. *Progress in Solid State Chemistry*, 20(1), 47-99.

## References

1. [Amkor\_2011]: [<http://www.amkor.com/go/packaging>]
2. [Amkor\_2012]: [<http://www.amkor.com/go/packaging/copper-wire-bonding>]
3. [Amore\_2008]: Amore, S., Ricci, E., Borzone, G., & Novakovic, R. (2008). Wetting behaviour of lead-free Sn-based alloys on Cu and Ni substrates. *Materials Science and Engineering: A*, 495(1), 108-112.
4. [Arenas\_2004]: Arenas, M. F., & Acoff, V. L. (2004). Contact angle measurements of Sn-Ag and Sn-Cu lead-free solders on copper substrates. *Journal of electronic materials*, 33(12), 1452-1458.
5. [Arfaei\_2012]: Arfaei, B., Kim, N., & Cotts, E. J. (2012). Dependence of Sn grain morphology of Sn-Ag-Cu solder on solidification temperature. *Journal of electronic materials*, 41(2), 362-374.
6. [Bader\_1995]: Bader, S., Gust, W., & Hieber, H. (1995). Rapid formation of intermetallic compounds interdiffusion in the Cu-Sn and Ni-Sn systems. *Acta metallurgica et materialia*, 43(1), 329-337.
7. [Barmak\_1990]: Barmak, K., Coffey, K. R., Rudman, D. A., & Foner, S. (1990). Phase formation sequence for the reaction of multilayer thin films of Nb/Al. *Journal of applied physics*, 67(12), 7313-7322.
8. [Belyakov\_2014]: Belyakov, S. A., & Gourlay, C. M. (2014). Heterogeneous nucleation of  $\beta$ Sn on NiSn<sub>4</sub>, PdSn<sub>4</sub> and PtSn<sub>4</sub>. *Acta Materialia*, 71, 56-68.
9. [Bertheau\_2014]: Thesis manuscript of J. Bertheau " Etude et caractérisation d'interconnexions intermétalliques à partir de plots de cuivre et d'alliages Sn-Ag-Cu pour l'empilement tridimensionnel de composants actifs ", Grenoble University, 2014.
10. [Bertheau\_2014\_II]: Bertheau, J., Hodaj, F., Hotellier, N., & Charbonnier, J. (2014). Effect of intermetallic compound thickness on shear strength of 25  $\mu$ m diameter Cu-pillars. *Intermetallics*, 51, 37-47.
11. [Biance\_2004]: Biance, A. L., Clanet, C., & Quéré, D. (2004). First steps in the spreading of a liquid droplet. *Physical Review E*, 69(1), 016301.
12. [Boettinger\_1992]: Boettinger, W. J., Handwerker, C. A., & Smith, L. C. (1992). On the wetting of the intermetallics Cu<sub>6</sub>Sn<sub>5</sub> and Cu<sub>3</sub>Sn by Pb-Sn alloys. *The Metal Science of Joining*, edited by MJ Cieslak, JH Perepezko, S. Kang, and ME Glicksman (The Minerals, Metals and Materials Society, Warrendale, PA, 1992), 183-189.
13. [Cassie\_1948]: Cassie, A. B. D. (1948). Contact angles. *Discussions of the Faraday Society*, 3, 11-16.
14. [Chan\_1998]: Chan, Y. C., So, A. C., & Lai, J. K. L. (1998). Growth kinetic studies of Cu-Sn intermetallic compound and its effect on shear strength of LCCC SMT solder joints. *Materials Science and Engineering: B*, 55(1), 5-13.
15. [Chang\_2003]: Chang, H. Y., Chen, S. W., Wong, D. S. H., & Hsu, H. F. (2003). Determination of reactive wetting properties of Sn, Sn-Cu, Sn-Ag, and Sn-Pb alloys using a wetting balance technique. *Journal of materials research*, 18(06), 1420-1428.
16. [Chakrabarti\_1984]: Chakrabarti, D. J., & Laughlin, D. E. (1984). The Cu- Pb (Copper-Lead) system. *Bulletin of Alloy Phase Diagrams*, 5(5), 503-510.
17. [Chen\_1999]: Chen, S. W., & Yen, Y. W. (1999). Interfacial reactions in Ag-Sn/Cu couples. *Journal of Electronic Materials*, 28(11), 1203-1208.
18. [Chen\_2011]: Chen, D., Ho, C. E., & Kuo, J. C. (2011). Current stressing-induced growth of Cu<sub>3</sub>Sn in Cu/Sn/Cu solder joints. *Materials Letters*, 65(9), 1276-1279.
19. [Chiu\_2014]: Chiu, W. L., Liu, C. M., Haung, Y. S., & Chen, C. (2014). Formation of nearly void-free Cu<sub>3</sub>Sn intermetallic joints using nanotwinned Cu metallization. *Applied Physics Letters*, 104(17), 171902.
20. [Chopra\_1982]: Chopra, R., Ohring, M., & Oswald, R. S. (1982). Low temperature compound formation in CuSn thin film couples. *Thin Solid Films*, 94(4), 279-288.

21. [Coffey\_1989]: Coffey, K. R., Clevenger, L. A., Barnak, K., Rudman, D. A., & Thompson, C. V. (1989). Experimental evidence for nucleation during thin-film reactions. *Applied Physics Letters*, 55(9), 852-854.
22. [Dezellus\_2000]: Dezellus, O. (2000). Contribution à l'étude des mécanismes de mouillage réactif (Doctoral dissertation, Institut National Polytechnique de Grenoble-INPG).
23. [Dezellus\_2002]: Dezellus, O., Hodaj, F., & Eustathopoulos, N. (2003). Progress in modelling of chemical-reaction limited wetting. *Journal of the European Ceramic Society*, 23(15), 2797-2803.
24. [Dezellus\_2003]: Dezellus, O., Hodaj, F., & Eustathopoulos, N. (2003). Progress in modelling of chemical-reaction limited wetting. *Journal of the European Ceramic Society*, 23(15), 2797-2803.
25. [Dinsdale\_1991]: Dinsdale, A. (1991). SGTE data for pure elements. *Calphad*, 15(4), 317-425.
26. [Dolgopopolov\_2007]: Dolgopopolov, N. A., Petelin, A. L., Rakov, S. V., & Simanov, A. V. (2007). Penetration of liquid tin along grain boundaries and triple grain-boundary junctions of aluminum. *Russian Journal of Non-Ferrous Metals*, 48(2), 126-130.
27. [Drevet\_1996]: Drevet, B., Landry, K., Vikner, P., & Eustathopoulos, N. (1996). Influence of substrate orientation on wetting kinetics in reactive metal/ceramic systems. *Scripta materialia*, 35(11), 1265-1270.
28. [Dupré\_1869]: Dupré, A., & Dupré, P. (1869). *Théorie mécanique de la chaleur*. Gauthier-Villars.
29. [Emeric\_2006]: Emeric, E. (1998). Etude des réactions à l'état solide dans des multicouches Al/Co: application à la formation de films minces quasicristallins (Doctoral dissertation).
30. [Espie\_1994]: Espie, L., Drevet, B., & Eustathopoulos, N. (1994). Experimental study of the influence of interfacial energies and reactivity on wetting in metal/oxide systems. *Metallurgical and materials transactions A*, 25(3), 599-605.
31. [Eustathopoulos\_1999]: Eustathopoulos, N., Nicholas, M. G., & Drevet, B. (Eds.). (1999). *Wettability at high temperatures (Vol. 3)*. Elsevier.
32. [Eustathopoulos\_2005]: Eustathopoulos, N. (2005). Progress in understanding and modeling reactive wetting of metals on ceramics. *Current Opinion in Solid State and Materials Science*, 9(4), 152-160.
33. [Fletcher\_1958]: Fletcher, N. (1958). Size effect in heterogeneous nucleation. *The Journal of chemical physics*, 29(3), 572-576.
34. [Furtauer\_2013]: Furtauer, S., Li, D., Cupid, D., & Flandorfer, H. (2013). The Cu–Sn phase diagram, Part I: new experimental results. *Intermetallics*, 34, 142-147.
35. [Gagliano\_2002]: Gagliano, R. A., Ghosh, G., & Fine, M. E. (2002). Nucleation kinetics of Cu<sub>6</sub>Sn<sub>5</sub> by reaction of molten tin with a copper substrate. *Journal of electronic materials*, 31(11), 1195-1202.
36. [Gagliano\_2003]: Gagliano, R. A., & Fine, M. E. (2003). Thickening kinetics of interfacial Cu<sub>6</sub>Sn<sub>5</sub> and Cu<sub>3</sub>Sn layers during reaction of liquid tin with solid copper. *Journal of electronic materials*, 32(12), 1441-1447.
37. [Geguzin\_1979]: Geguzin, Y., *Fiz. Met. Metalloved.* 47 (1979) p. 821.
38. [de Gennes\_1985]: De Gennes, P. G. (1985). Wetting: statics and dynamics. *Reviews of modern physics*, 57(3), 827.
39. [Görlich\_2005]: Görlich, J., Schmitz, G., & Tu, K. N. (2005). On the mechanism of the binary Cu/Sn solder reaction. *Applied Physics Letters*, 86(5), 053106.
40. [Gong\_2008]: Gong, J., Liu, C., Conway, P. P., & Silberschmidt, V. V. (2008). Evolution of CuSn intermetallics between molten SnAgCu solder and Cu substrate. *Acta Materialia*, 56(16), 4291-4297.
41. [Gong\_2009]: Gong, J., Liu, C., Conway, P. P., & Silberschmidt, V. V. (2009). Initial formation of CuSn intermetallic compounds between molten SnAgCu solder and Cu substrate. *Scripta Materialia*, 60(5), 333-335.

42. [Gösele\_1982]: Gösele, U., & Tu, K. N. (1982). Growth kinetics of planar binary diffusion couples: "Thin-film case" versus "bulk cases". *Journal of Applied Physics*, 53(4), 3252-3260.
43. [Gusak\_1982]: Gusak, A. M., & Gurov, K. P. (1982). The Kinetics of Phase Formation in the Diffusion Zone During Interdiffusion. *General Theory. Fiz. Met. Metalloved.*, 53(5), 842-847.
44. [Gusak\_2002]: Gusak, A. M., & Tu, K. N. (2002). Kinetic theory of flux-driven ripening. *Physical Review B*, 66(11), 115403.
45. [Gusak\_2010]: Gusak, A. M., Zaporozhets, T. V., Lyashenko, Y. O., Kornienko, S. V., Pasichnyy, M. O., & Shirinyan, A. S. (2010). Diffusion-controlled solid state reactions: in alloys, thin-films, and nanosystems. *John Wiley & Sons*.
46. [Halimi\_1987]: Halimi, R., Chpilevski, E. M., & Gorbachevski, D. A. (1987). Cinétique de formation de composés intermétalliques dans les couches minces de Cu/Sn. *Thin solid films*, 148(1), 109-119.
47. [d'Heurle\_1986]: d'Heurle, F. M., & Gas, P. (1986). Kinetics of formation of silicides: A review. *Journal of materials research*, 1(01), 205-221.
48. [Hitchcock\_1981]: Hitchcock, S. J., Carroll, N. T., & Nicholas, M. G. (1981). Some effects of substrate roughness on wettability. *Journal of Materials Science*, 16(3), 714-732.
49. [Hodaj\_2013]: Hodaj, F., Petit, L., Baggetto, L., Boisier, O., & Verneyre, L. (2013). Undercooling of Sn–Ag–Cu alloys: solder balls and solder joints solidification. *International Journal of Materials Research*, 104(9), 874-878.
50. [Hodaj\_2013\_II]: Hodaj, F., Gusak, A. M., & Liashenko, O. (2013). Possibility of a shape phase transition for solidification of tin at scallop-like surfaces of Cu<sub>6</sub>Sn<sub>5</sub>. *Philosophical Magazine Letters*, 93(3), 166-173.
51. [Horsthemke\_1981]: Horsthemke, A., & Schröder, J. J. (1985). The wettability of industrial surfaces: contact angle measurements and thermodynamic analysis. *Chemical Engineering and Processing: Process Intensification*, 19(5), 277-285.
52. [Hsiao\_2012]: Hsiao, H. Y., Liu, C. M., Lin, H. W., Liu, T. C., Lu, C. L., Huang, Y. S., ... & Tu, K. N. (2012). Unidirectional growth of microbumps on (111)-oriented and nanotwinned copper. *Science*, 336(6084), 1007-1010.
53. [Huang\_2004]: Huang, Z., Conway, P. P., Liu, C., & Thomson, R. C. (2004). The effect of microstructural and geometrical features on the reliability of ultrafine flip chip microsolder joints. *Journal of electronic materials*, 33(10), 1227-1235.
54. [Huang\_2009]: Huang, Y. C., Wu, K. S., & Chen, S. W. (2009, October). Size and substrate effects upon undercooling of Pb-free solders. In *Microsystems, Packaging, Assembly and Circuits Technology Conference, 2009. IMPACT 2009. 4th International* (pp. 662-665). IEEE.
55. [Huang\_2014]: Huang, M. L., & Yang, F. (2014). Size effect model on kinetics of interfacial reaction between Sn-xAg-yCu solders and Cu substrate. *Scientific reports*, 4.
56. [Jeong\_2004]: Jeong, S. W., Kim, J. H., & Lee, H. M. (2004). Effect of cooling rate on growth of the intermetallic compound and fracture mode of near-eutectic Sn-Ag-Cu/Cu pad: Before and after aging. *Journal of electronic materials*, 33(12), 1530-1544.
57. [Johnson\_1975]: Johnson, W. C., White, C. L., Marth, P. E., Ruf, P. K., Tuominen, S. M., Wade, K. D., ... & Aaronson, H. I. (1975). Influence of crystallography on aspects of solid-solid nucleation theory. *Metallurgical Transactions A*, 6(4), 911-919.
58. [Kang\_2005]: Kang, S. K., Lauro, P., Shih, D. Y., Henderson, D. W., & Puttlitz, K. J. (2005). Microstructure and mechanical properties of lead-free solders and solder joints used in microelectronic applications. *IBM Journal of Research and Development*, 49(4.5), 607-620.
59. [Kang\_2007]: Kang, S. K., Cho, M. G., Lauro, P., & Shih, D. Y. (2007). Study of the undercooling of Pb-free, flip-chip solder bumps and in situ observation of solidification process. *Journal of materials research*, 22(03), 557-560.

60. [Keller\_2011]: Keller, J., Baither, D., Wilke, U., & Schmitz, G. (2011). Mechanical properties of Pb-free SnAg solder joints. *Acta Materialia*, 59(7), 2731-2741.
61. [Key Chung\_2010]: Chung, C. K., Duh, J. G., & Kao, C. R. (2010). Direct evidence for a Cu-enriched region at the boundary between Cu<sub>6</sub>Sn<sub>5</sub> and Cu<sub>3</sub>Sn during Cu/Sn reaction. *Scripta Materialia*, 63(2), 258-260.
62. [Key Chung\_2013]: Chung, C. K., Chen, Y. J., Yang, T. L., & Kao, C. R. (2013). Reactions of Sn-4.0 Ag-0.5 Cu on Cu and Electroless Ni Substrate in Premelting Soldering Process. *Journal of electronic materials*, 42(6), 1254-1259.
63. [Kim\_1996]: Kim, H. K., & Tu, K. N. (1996). Kinetic analysis of the soldering reaction between eutectic SnPb alloy and Cu accompanied by ripening. *Physical Review B*, 53(23), 16027.
64. [Kim\_2002]: Kim, K. S., Huh, S. H., & Sukanuma, K. (2002). Effects of cooling speed on microstructure and tensile properties of Sn–Ag–Cu alloys. *Materials Science and Engineering: A*, 333(1), 106-114.
65. [Kim\_2009]: Kim, T., Lee, J., Kim, Y., Kim, J. M., & Yuan, Z. (2009). Investigation of the Dynamic Reactive Wetting of Sn-Ag-Cu Solder Alloys on Ni (P)/Au Coated Cu Substrates. *Materials transactions*, 50(11), 2695-2698.
66. [Klinger\_1998]: Klinger, L., Brechet, Y., & Purdy, G. (1998). On the kinetics of interface-diffusion-controlled peritectoid reactions. *Acta materialia*, 46(8), 2617-2621.
67. [Kritsalis\_1994]: Kritsalis, P., Drevet, B., Valignat, N., & Eustathopoulos, N. (1994). Wetting transitions in reactive metal/oxide systems. *Scripta metallurgica et materialia*, 30(9), 1127-1132.
68. [Kubaschewski\_2013]: Kubaschewski, O., Alcock, C. B., & Spencer, P. J. *Materials thermochemistry*. (Pergamon Press, Oxford, 1993).
69. [Kumar\_2011]: Kumar, S., Handwerker, C. A., & Dayananda, M. A. (2011). Intrinsic and interdiffusion in Cu-Sn system. *Journal of phase equilibria and diffusion*, 32(4), 309-319.
70. [Lapie\_2007]: Labie, R., Ruythooren, W., & Van Humbeeck, J. (2007). Solid state diffusion in Cu–Sn and Ni–Sn diffusion couples with flip-chip scale dimensions. *Intermetallics*, 15(3), 396-403.
71. [Landry\_1997]: Landry, K., Rado, C., Voitovich, R., & Eustathopoulos, N. (1997). Mechanisms of reactive wetting: the question of triple line configuration. *Acta materialia*, 45(7), 3079-3085.
72. [Larsson\_1995]: Larsson, A. K., Stenberg, L., & Lidin, S. (1995). Crystal structure modulations in η-Cu<sub>5</sub>Sn<sub>4</sub>. *Zeitschrift für Kristallographie*, 210(11), 832-837.
73. [Laurila\_2005]: Laurila, T., Vuorinen, V., & Kivilahti, J. K. (2005). Interfacial reactions between lead-free solders and common base materials. *Materials Science and Engineering: R: Reports*, 49(1), 1-60.
74. [Lee\_2002]: Lee, T. Y., Choi, W. J., Tu, K. N., Jang, J. W., Kuo, S. M., Lin, J. K., ... & Kivilahti, J. K. (2002). Morphology, kinetics, and thermodynamics of solid-state aging of eutectic SnPb and Pb-free solders (Sn–3.5 Ag, Sn–3.8 Ag–0.7 Cu and Sn–0.7 Cu) on Cu. *Journal of Materials Research*, 17(02), 291-301.
75. [Li\_2012]: Li, X., Zu, F., Gao, W., Cui, X., Wang, L., & Ding, G. (2012). Effects of the melt state on the microstructure of a Sn–3.5% Ag solder at different cooling rates. *Applied Surface Science*, 258(15), 5677-5682.
76. [Liang\_2006]: Liang, J., Dariavach, N., Callahan, P., & Shangguan, D. (2006). Metallurgy and kinetics of liquid-solid interfacial reaction during lead-free soldering. *Materials transactions*, 47(2), 317-325.
77. [Liao\_2004]: Liao, C. N., & Wei, C. T. (2004). Effect of intermetallic compound formation on electrical properties of Cu/Sn interface during thermal treatment. *Journal of electronic materials*, 33(10), 1137-1143.
78. [Liashenko\_2014]: Liashenko, O., Gusak, A. M., & Hodaj, F. (2014). Phase growth competition in solid/liquid reactions between copper or Cu<sub>3</sub>Sn compound and liquid tin-based solder. *Journal of Materials Science: Materials in Electronics*, 25(10), 4664-4672.

79. [Lin\_2012]: Lin, K. L., Lin, Y. W., & Yu, C. H. (2012). The interphases formed during the very early stage liquid solder/metal substrate interaction of the soldering process. *JOM*, 64(10), 1184-1189.
80. [Lucadamo\_2001]: Lucadamo, G., Barmak, K., Carpenter, D. T., & Rickman, J. M. (2001). Microstructure evolution during solid state reactions of Nb/Al multilayers. *Acta materialia*, 49(14), 2813-2826.
81. [Lucenko\_2003]: Lucenko, G., & Gusak, A. (2003). A model of the growth of intermediate phase islands in multilayers. *Microelectronic engineering*, 70(2), 529-532.
82. [Ma\_1960]: Ma, C. H., & Swalin, R. A. (1960). A study of solute diffusion in liquid tin. *Acta metallurgica*, 8(6), 388-395.
83. [Matsumoto\_2005]: Matsumoto, T., & Nogi, K. (2008). Wetting in soldering and microelectronics. *Annu. Rev. Mater. Res.*, 38, 251-273.
84. [Maveety\_2004]: Maveety, J. G., Liu, P., Vijayen, J., Hua, F., & Sanchez, E. A. (2004). Effect of cooling rate on microstructure and shear strength of pure Sn, Sn-0.7 Cu, Sn-3.5 Ag, and Sn-37Pb solders. *Journal of electronic materials*, 33(11), 1355-1362.
85. [Mehrer\_1990]: Mehrer, H. (2007). *Diffusion in solids: fundamentals, methods, materials, diffusion-controlled processes* (Vol. 155). Springer Science & Business Media.
86. [Mei\_2005]: Mei, Z., Ahmad, M., Hu, M., & Ramakrishna, G. (2005, June). Kirkendall voids at Cu/solder interface and their effects on solder joint reliability. In *Electronic Components and Technology Conference, 2005. Proceedings. 55th* (pp. 415-420). IEEE.
87. [Mortensen\_1997]: Mortensen, A., Drevet, B., & Eustathopoulos, N. (1997). Kinetics of diffusion-limited spreading of sessile drops in reactive wetting. *Scripta Materialia*, 36(6), 645-651.
88. [Nogita\_2005]: Nogita, K., Read, J., Nishimura, T., Sweatman, K., Suenaga, S., & Dahle, A. K. (2005). Microstructure control in Sn-0.7 mass% Cu alloys. *Materials transactions*, 46(11), 2419-2425.
89. [Onishi\_1975]: Onishi, M., & Fujibuchi, H. (1975). Reaction-diffusion in the Cu-Sn system. *Transactions of the Japan Institute of Metals*, 16(9), 539-547.
90. [Pan\_2008]: Pan, C. C., Yu, C. H., & Lin, K. L. (2008). The amorphous origin and the nucleation of intermetallic compounds formed at the interface during the soldering of Sn-3.0 Ag-0.5 Cu on a Cu substrate. *Applied Physics Letters*, 93(6), 1912.
91. [Pan\_2011]: Pan, C. C., & Lin, K. L. (2011). The interfacial amorphous double layer and the homogeneous nucleation in reflow of a Sn-Zn solder on Cu substrate. *Journal of Applied Physics*, 109(10), 103513.
92. [Panchenko\_2014]: Panchenko, I., Croes, K., De Wolf, I., De Messemaeker, J., Beyne, E., & Wolter, K. J. (2014). Degradation of Cu 6 Sn 5 intermetallic compound by pore formation in solid-liquid interdiffusion Cu/Sn microbump interconnects. *Microelectronic Engineering*, 117, 26-34.
93. [Park\_2010]: Park, M. S., & Arroyave, R. (2010). Formation and growth of intermetallic compound Cu<sub>6</sub>Sn<sub>5</sub> at early stages in lead-free soldering. *Journal of electronic materials*, 39(12), 2574-2582.
94. [Park\_2012]: Park, M. S., & Arróyave, R. (2012). Concurrent nucleation, formation and growth of two intermetallic compounds (Cu 6 Sn 5 and Cu 3 Sn) during the early stages of lead-free soldering. *Acta Materialia*, 60(3), 923-934.
95. [Paul\_2004]: Paul, A., Kodentsov, A. A., & van Loo, F. J. (2004). Intermetallic growth and Kirkendall effect manifestations in Cu/Sn and Au/Sn diffusion couples: Dedicated to Prof. Dr. Helmut Mehrer on the occasion of his 65th birthday. *Zeitschrift für Metallkunde*, 95(10), 913-920.
96. [Park\_YS\_2010]: Park, Y. S., Kwon, Y. M., Moon, J. T., Lee, Y. W., Lee, J. H., & Paik, K. W. (2010, June). Effects of fine size lead-free solder ball on the interfacial reactions and joint reliability. In *Electronic Components and Technology Conference (ECTC), 2010 Proceedings 60th* (pp. 1436-1441). IEEE.

97. [Pasichnyy\_2005]: Pasichnyy, M., & Gusak, A. (2005, April). Modeling of Phase Competition and Diffusion Zone Morphology Evolution at Initial Stages of Reaction Diffusion. In *Defect and Diffusion Forum* (Vol. 237, pp. 1193-1198).
98. [Pasichnyy\_2008]: Pasichnyy, M., & Gusak, A. (2008, May). Model of Lateral Growth Stage during Reactive Phase Formation. In *Defect and Diffusion Forum* (Vol. 277, pp. 47-52).
99. [Paul\_2011]: Paul, A., Ghosh, C., & Boettinger, W. J. (2011). Diffusion parameters and growth mechanism of phases in the Cu-Sn system. *Metallurgical and Materials Transactions A*, 42(4), 952-963.
100. [Pearson's database\_2014]: [http://www.asminternational.org/materials-resources/online-databases/-/journal\\_content/56/10192/6382084/DATABASE](http://www.asminternational.org/materials-resources/online-databases/-/journal_content/56/10192/6382084/DATABASE).
101. [Perepezko\_1984]: Perepezko, J. H. (1984). Nucleation in undercooled liquids. *Materials Science and Engineering*, 65(1), 125-135.
102. [Philibert\_1994]: Philibert, J. (1994, May). Reactive interdiffusion. In *Materials Science Forum* (Vol. 155, pp. 15-30).
103. [Protsenko\_2001]: Protsenko, P., Terlain, A., Traskine, V., & Eustathopoulos, N. (2001). The role of intermetallics in wetting in metallic systems. *Scripta Materialia*, 45(12), 1439-1445.
104. [Rönkä\_2008]: Rönkä, K. J., Van Loo, F. J. J., & Kivilahti, J. I. P. R. (1998). A diffusion-kinetic model for predicting solder/conductor interactions in high density interconnections. *Metallurgical and Materials Transactions A*, 29(12), 2951-2956.
105. [Saiz\_2007]: Saiz, E., Tomsia, A. P., Rauch, N., Scheu, C., Rühle, M., Benhassine, M., & Lopez-Esteban, S. (2007). Nonreactive spreading at high temperature: Molten metals and oxides on molybdenum. *Physical Review E*, 76(4), 041602.
106. [Saiz\_2010]: Saiz, E., Benhassine, M., De Coninck, J., & Tomsia, A. P. (2010). Early stages of dissolutive spreading. *Scripta Materialia*, 62(12), 934-938.
107. [Salleh\_2014]: Salleh, M. M., McDonald, S. D., Yasuda, H., Sugiyama, A., & Nogita, K. (2015). Rapid Cu<sub>6</sub>Sn<sub>5</sub> growth at liquid Sn/solid Cu interfaces. *Scripta Materialia*, 100, 17-20.
108. [Saunders\_1997]: Saunders, N., & Miodownik, A. P. (1990). The Cu-Sn (copper-tin) system. *Bulletin of Alloy Phase Diagrams*, 11(3), 278-287.
109. [Satyanarayan\_2011]: Satyanarayan, S., & Prabhu, K. N. (2011). Reactive wetting, evolution of interfacial and bulk IMCs and their effect on mechanical properties of eutectic Sn-Cu solder alloy. *Advances in Colloid and Interface Science*, 166(1-2), 87-118.
110. [Sear\_2008]: Sear, R. P. (2008). Nucleation of a liquid on aerosol nanoparticles. *EPL (Europhysics Letters)*, 83(6), 66002.
111. [Shang\_2009]: Shang, P. J., Liu, Z. Q., Pang, X. Y., Li, D. X., & Shang, J. K. (2009). Growth mechanisms of Cu<sub>3</sub>Sn on polycrystalline and single crystalline Cu substrates. *Acta Materialia*, 57(16), 4697-4706.
112. [Shen\_2010]: Shen, P., Yin, Z., Yang, J., Sun, J., Jiang, Z., & Jiang, Q. (2010). Wetting of Cu substrates with micrometer and nanometer grains by molten Sn-3.5 Ag-0.7 Cu alloy. *Surface and Interface Analysis*, 42(12-13), 1681-1684.
113. [Shim\_1996]: Shim, J. H., Oh, C. S., Lee, B. J., & Lee, D. N. (1996). Thermodynamic assessment of the Cu-Sn system. *Zeitschrift für Metallkunde*, 87(3), 205-212.
114. [Sholl\_1970]: Sholl, C. A., & Fletcher, N. H. (1970). Decoration criteria for surface steps. *Acta Metallurgica*, 18(10), 1083-1086.
115. [Shuttleworth\_1948]: Shuttleworth, R., & Bailey, G. L. J. (1948). The spreading of a liquid over a rough solid. *Discussions of the Faraday Society*, 3, 16-22.
116. [Sobczak\_2007]: Sobczak, N., Kudyba, A., Nowak, R., Radziwill, W., & Pietrzak, K. (2007). Factors affecting wettability and bond strength of solder joint couples. *Pure and Applied Chemistry*, 79(10), 1755-1769.
117. [Song\_2004]: Song, J. Y., Yu, J., & Lee, T. Y. (2004). Effects of reactive diffusion on stress evolution in Cu-Sn films. *Scripta materialia*, 51(2), 167-170.

118. [Song\_2006]: Song, F., & Lee, S. R. (2006, May). Investigation of IMC thickness effect on the lead-free solder ball attachment strength: comparison between ball shear test and cold bump pull test results. In *Electronic Components and Technology Conference, 2006. Proceedings. 56th* (pp. 8-pp). IEEE.
119. [Su\_1997]: Su, L. H., Yen, Y. W., Lin, C. C., & Chen, S. W. (1997). Interfacial reactions in molten Sn/Cu and molten In/Cu couples. *Metallurgical and Materials Transactions B*, 28(5), 927-934.
120. [Suh\_2007]: Suh, J. O., Tu, K. N., & Tamura, N. (2007). Preferred orientation relationship between Cu<sub>6</sub>Sn<sub>5</sub> scallop-type grains and Cu substrate in reactions between molten Sn-based solders and Cu. *Journal of Applied Physics*, 102(6), 63511-63511.
121. [Suh\_2007\_II]: Suh, J. O., Tu, K. N., & Tamura, N. (2007). Dramatic morphological change of scallop-type Cu<sub>6</sub>Sn<sub>5</sub> formed on (001) single crystal copper in reaction between molten SnPb solder and Cu. *Applied Physics Letters*, 91(5), 51907-51907.
122. [Suh\_2008]: Suh, J. O., Tu, K. N., Lutsenko, G. V., & Gusak, A. M. (2008). Size distribution and morphology of Cu<sub>6</sub>Sn<sub>5</sub> scallops in wetting reaction between molten solder and copper. *Acta Materialia*, 56(5), 1075-1083.
123. [Tang\_2010]: Tang, W. M., He, A. Q., Qi, L. I. U., & Ivey, D. G. (2010). Solid state interfacial reactions in electrodeposited Cu/Sn couples. *Transactions of Nonferrous Metals Society of China*, 20(1), 90-96.
124. [Tanner\_1979]: Tanner, L. H. (1979). The spreading of silicone oil drops on horizontal surfaces. *Journal of Physics D: Applied Physics*, 12(9), 1473.
125. [Tian\_2011]: Tian, T., Xu, F., Han, J. K., Choi, D., Cheng, Y., Helfen, L., ... & Tu, K. N. (2011). Rapid diagnosis of electromigration induced failure time of Pb-free flip chip solder joints by high resolution synchrotron radiation laminography. *Applied Physics Letters*, 99(8), 082114.
126. [Tsao\_2011]: Tsao, L. C. (2011). An investigation of microstructure and mechanical properties of novel Sn<sub>3</sub>. 5Ag<sub>0</sub>. 5Cu-XTiO<sub>2</sub> composite solders as functions of alloy composition and cooling rate. *Materials Science and Engineering: A*, 529, 41-48.
127. [Tu\_1973]: Tu, K. N. (1973). Interdiffusion and reaction in bimetallic Cu-Sn thin films. *Acta Metallurgica*, 21(4), 347-354.
128. [Tu\_1982]: Tu, K. N., & Thompson, R. D. (1982). Kinetics of interfacial reaction in bimetallic Cu-Sn thin films. *Acta Metallurgica*, 30(5), 947-952.
129. [Tu\_1996]: Tu, K. N. (1996). Cu/Sn interfacial reactions: thin-film case versus bulk case. *Materials Chemistry and Physics*, 46(2), 217-223.
130. [Tu\_2003]: Tu, K. N. (2003). Recent advances on electromigration in very-large-scale-integration of interconnects. *Journal of applied physics*, 94(9), 5451-5473.
131. [Tu\_2007]: Tu, K. N. (2007). *Solder joint technology* (pp. 211-288). New York: Springer.
132. [Tu\_2013]: Tu, K. N., Hsiao, H. Y., & Chen, C. (2013). Transition from flip chip solder joint to 3D IC microbump: Its effect on microstructure anisotropy. *Microelectronics Reliability*, 53(1), 2-6.
133. [Tung\_2014]: Tung, B. T., Watanabe, N., Kato, F., Kikuchi, K., & Aoyagi, M. (2014, May). Flip-chip bonding alignment accuracy enhancement using self-aligned interconnection elements to realize low-temperature construction of ultrafine-pitch copper bump interconnections. In *Electronic Components and Technology Conference (ECTC), 2014 IEEE 64th* (pp. 62-67). IEEE.
134. [Turnbull\_1950]: Turnbull, D. (1950). Formation of crystal nuclei in liquid metals. *Journal of Applied Physics*, 21(10), 1022-1028.
135. [Vianco\_2004]: Vianco, P. T., Rejent, J. A., & Hlava, P. F. (2004). Solid-state intermetallic compound layer growth between copper and 95.5 Sn-3.9 Ag-0.6 Cu solder. *Journal of electronic materials*, 33(9), 991-1004.

136. [Vuorinen\_2007]: Vuorinen, V., Laurila, T., Mattila, T., Heikinheimo, E., & Kivilahti, J. K. (2007). Solid-state reactions between Cu (Ni) alloys and Sn. *Journal of Electronic Materials*, 36(10), 1355-1362.
137. [Wagner\_1969]: Wagner, C. (1969). The evaluation of data obtained with diffusion couples of binary single-phase and multiphase systems. *Acta Metallurgica*, 17(2), 99-107.
138. [Wang\_2006]: Wang, H., Gao, F., Ma, X., & Qian, Y. (2006). Reactive wetting of solders on Cu and Cu<sub>6</sub>Sn<sub>5</sub>/Cu<sub>3</sub>Sn/Cu substrates using wetting balance. *Scripta materialia*, 55(9), 823-826.
139. [Warren\_1998]: Warren, J. A., Boettinger, W. J., & Roosen, A. R. (1998). Modeling reactive wetting. *Acta Materialia*, 46(9), 3247-3264.
140. [Wei\_2012]: Wei, G., & Wang, L. (2012, August). Effects of cooling rate on microstructure and microhardness of lead-free Sn-3.0 Ag-0.5 Cu solder. In *Electronic Packaging Technology and High Density Packaging (ICEPT-HDP), 2012 13th International Conference on* (pp. 453-456). IEEE.
141. [Wenzel\_1936]: Wenzel, R. N. (1936). Resistance of solid surfaces to wetting by water. *Industrial & Engineering Chemistry*, 28(8), 988-994.
142. [Xu\_2006]: Xu, L., & Pang, J. H. (2006, June). Effect of intermetallic and Kirkendall voids growth on board level drop reliability for SnAgCu lead-free BGA solder joint. In *Electronic Components and Technology Conference, 2006. Proceedings. 56th* (pp. 8-pp). IEEE.
143. [Yang\_1994]: Yang, W., Messler, R. W., & Felton, L. E. (1994). Microstructure evolution of eutectic Sn-Ag solder joints. *Journal of Electronic Materials*, 23(8), 765-772.
144. [Yang\_2012]: Yang, M., Li, M., & Wang, C. (2012). Interfacial reactions of eutectic Sn<sub>3.5</sub>Ag and pure tin solders with Cu substrates during liquid-state soldering. *Intermetallics*, 25, 86-94.
145. [Yin\_2011]: Yin, L., & Borgesen, P. (2011). On the root cause of Kirkendall voiding in Cu<sub>3</sub>Sn. *Journal of Materials Research*, 26(03), 455-466.
146. [Young\_1805]: Young, T. (1805). An essay on the cohesion of fluids. *Philosophical Transactions of the Royal Society of London*, 65-87.
147. [Yu\_2006]: Yu, C. H., & Lin, K. L. (2006). The atomic-scale studies of the behavior of the crystal dissolution in a molten metal. *Chemical physics letters*, 418(4), 433-436.
148. [Yu\_2009]: Yu, A., Lau, J. H., Ho, S. W., Kumar, A., Hnin, W. Y., Yu, D. Q., ... & Kwong, D. L. (2009, May). Study of 15µm pitch solder microbumps for 3D IC integration. In *Electronic Components and Technology Conference, 2009. ECTC 2009. 59th* (pp. 6-10). IEEE.
149. [Yu\_2013]: Yu, C., Chen, J. S., Wang, K. Y., Chen, J. Q., & Lu, H. (2013). Suppression effect of Cu and Ag on Cu<sub>3</sub>Sn layer in solder joints. *Journal of Materials Science: Materials in Electronics*, 24(11), 4630-4635.
150. [Yu\_2014]: Yu, C., Yang, Y., Chen, J., Xu, J., Chen, J., & Lu, H. (2014). Effect of deposit thickness during electroplating on Kirkendall voiding at Sn/Cu joints. *Materials Letters*, 128, 9-11.
151. [Zang\_2011]: Zang, L., Yuan, Z., Xu, H., & Xu, B. (2011). Wetting process and interfacial characteristic of Sn-3.0 Ag-0.5 Cu on different substrates at temperatures ranging from 503K to 673K. *Applied Surface Science*, 257(11), 4877-4884.
152. [Zang\_2012]: Zang, L., Yuan, Z., Cao, Z., Matsuura, H., & Tsukihashi, F. (2012). Reactive Wetting Processes and Triple-Line Configuration of Sn-3.5 Ag on Cu Substrates at Elevated Temperatures. *Journal of electronic materials*, 41(8), 2051-2056.
153. [Zeng\_2005]: Zeng, K., Stierman, R., Chiu, T. C., Edwards, D., Ano, K., & Tu, K. N. (2005). Kirkendall void formation in eutectic SnPb solder joints on bare Cu and its effect on joint reliability. *Journal of applied physics*, 97(2), 4508.
154. [Zhao\_2009]: Zhao, H., Wang, H. Q., Sekulic, D. P., & Qian, Y. Y. (2009). Spreading Kinetics of Liquid Solders over an Intermetallic Solid Surface. Part 2: Lead-Free Solders. *Journal of electronic materials*, 38(9), 1846-1854.

155. [Zhao\_2009\_II]: Zhao, H., Nalagatla, D. R., & Sekulic, D. P. (2009). Wetting kinetics of eutectic lead and lead-free solders: spreading over the Cu Surface. *Journal of electronic materials*, 38(2), 284-291.
156. [Zhou\_2012]: Zhou, B., Bieler, T. R., Wu, G., Zaefferer, S., Lee, T. K., & Liu, K. C. (2012). In Situ Synchrotron Characterization of Melting, Dissolution, and Resolidification in Lead-Free Solders. *Journal of electronic materials*, 41(2), 262-272.
157. [Zou\_2008]: Zou, H. F., Yang, H. J., & Zhang, Z. F. (2008). Morphologies, orientation relationships and evolution of Cu<sub>6</sub>Sn<sub>5</sub> grains formed between molten Sn and Cu single crystals. *Acta Materialia*, 56(11), 2649-2662.





UNIVERSITÉ  
GRENOBLE  
ALPES

## THÈSE

Pour obtenir le grade de

**DOCTEUR DE L'UNIVERSITÉ GRENOBLE  
ALPES**

**préparée dans le cadre d'une cotutelle entre  
l'Université Grenoble Alpes et l'Université de  
Cherkasy**

Spécialité : **Matériaux, Mécanique, Génie Civil, Electrochimie**

Arrêté ministériel : le 6 janvier 2005 - 7 août 2006

Présentée par

**Oleksii LIASHENKO**

Thèse dirigée par **Fiqiri HODAJ** et  
codirigée par **Andriy GUSAK**

préparée au sein des **Laboratoires SIMaP et SSM**

dans l'École Doctorale **I-MEP2**

# **Mouillage, germination et croissance lors du brasage en électronique**

Thèse soutenue publiquement le **23 Octobre 2015**,  
devant le jury composé de :

**Mme. Marie-Laurence GIORGI**

Professeur à l'Ecole Centrale de Paris, Rapporteur

**M. Dominique MANGELINCK**

Directeur de Recherches IM2NP, Université d'Aix-Marseille, Rapporteur

**M. Alain HAZOTTE**

Professeur à l'Université de Lorraine, Président

**M. Andriy GUSAK**

Professeur à l'Université de Cherkasy, Co-directeur

**M. Fiqiri HODAJ**

Professeur à Grenoble INP, Directeur

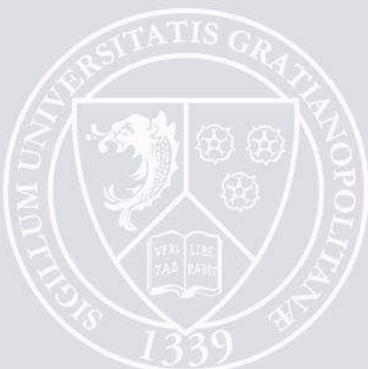




## Table des matières

<b>1) Introduction générale.....</b>	<b>2</b>
<b>2) Etude bibliographique.....</b>	<b>4</b>
2.1) Brasage en microélectronique.....	4
2.2) Le système Cu-Sn dans la technologie de brasage.....	4
2.3) Mouillage de Cu et des intermétalliques $\text{Cu}_6\text{Sn}_5$ et $\text{Cu}_3\text{Sn}$ par les alliages liquides base Sn.....	5
2.4) Réactions interfaciales entre Cu et les alliages liquides base Sn.....	5
2.5) Germination hétérogène pendant la cristallisation de Sn liquide ou des alliages liquides Sn-Ag-Cu: solidification des billes de brasure et des joints de brasure.....	6
<b>3) Méthodes expérimentales et matériaux.....</b>	<b>7</b>
3.1) Méthode de la goutte posée: principe.....	7
3.2) Méthode de la goutte déposée.....	7
3.3) Installation expérimentale d'immersion rapide d'un solide dans un bain liquide.....	8
3.4) Elaboration des intermétalliques $\eta\text{-Cu}_6\text{Sn}_5$ , $\epsilon\text{-Cu}_3\text{Sn}$ et $\text{Ag}_3\text{Sn}$ .....	8
<b>4) Mouillage du Cu, Ag et des intermétalliques des systèmes Cu-Sn et Ag-Sn par Sn ou les alliages Sn-Cu liquides.....</b>	<b>10</b>
4.1) Mouillage du Cu par Sn liquide ou par les alliages Sn-Cu liquides.....	10
4.2) Mouillage de $\text{Cu}_6\text{Sn}_5$ par un alliage Sn-7.8wt.%Cu "pré-saturé" à 390°C.....	12
4.3) Mouillage de Ag et $\text{Ag}_3\text{Sn}$ par Sn liquide.....	13
<b>5) Etude du phénomène de germination lors du brasage en électronique.....</b>	<b>15</b>
5.1) Etude expérimentale des étapes initiales de formation des produits de réaction à l'interface Cu/Sn liquide.....	15
5.2) Modélisation de germination et croissance de $\text{Cu}_3\text{Sn}$ à l'interface Cu/ $\text{Cu}_6\text{Sn}_5$ du système Cu/ $\text{Cu}_6\text{Sn}_5$ /Sn liquide.....	16
5.3) Critères de suppression cinétique de croissance latérale des phases intermédiaires, application à $\text{Cu}_3\text{Sn}$ .....	17
5.4) Spectre de modes de germination dans la cristallisation des brasures Sn-Cu: résultats expérimentaux et modélisation théorique.....	18
<b>6) Cinétique de croissance des intermétalliques dans le système Cu/Sn.....</b>	<b>23</b>
6.1) Compétition de croissance de couches interfaciales : systèmes Cu/Sn liquide et $\text{Cu}_3\text{Sn}$ /Sn liquide.....	23
6.2) Différences entre les réactions interfaciales dans les couples Cu/Sn solide et Cu/Sn liquide métastable à la même température: Rôle de l'état physique de Sn.....	23
<b>7) Conclusions générales.....</b>	<b>29</b>
<b>8) Bibliographie.....</b>	<b>31</b>

## 1) Introduction générale

Il est difficile d'imaginer une sphère de la vie qui n'a pas été influencée ou au moins légèrement touchée par la microélectronique. Etant l'une des perles du progrès scientifique depuis le siècle dernier, sa capacité en tant que science ouvre des frontières pour les nouvelles technologies et stimule la recherche globale. Dans une période qui a duré plusieurs décennies, mais qui est relativement court à l'âge de notre civilisation, la microélectronique est devenue une révélation qui a rendu notre vie quotidienne plus confortable et efficace.

Le niveau de développement de la microélectronique nous amène à la loi Moore. Cette loi a prouvé sa vérité dans la dernière moitié du 20<sup>e</sup> siècle: le nombre de composants dans les circuits intégrés a doublé tous les deux ans. La science dans le monde et dans l'industrie a réussi à augmenter le nombre de transistors par puce d'un facteur  $5 \times 10^5$  avec une diminution de la taille d'une puce d'un facteur 700 (14 nm actuellement). La tendance à la miniaturisation est toujours actuelle, mais évidemment sa limite se situe quelque part dans l'échelle atomique. Cette limitation naturelle devrait être contournée par un progrès technologique dans le but de maintenir la tendance définie par la loi de Moore. Tandis que le coût d'un transistor a diminué de façon significative au cours des dernières décennies, le prix général de l'ensemble du processus de fabrication augmente de façon exponentielle. Cette seconde loi (appelée loi de Rock ou la deuxième loi de Moore) ne pourrait pas limiter le développement scientifique générale, mais elle peut retarder l'application des approches existantes pour remplir les conditions de la loi de Moore.

Par conséquent, des nouvelles approches devraient émerger pour maintenir la tendance de croissance de la complexité de la technologie des circuits intégrés. *La transition de paradigme de deux dimensions à trois dimensions dans un assemblage des circuits intégrés est l'une des ces approches, qui devrait fournir quelques nouvelles générations de circuits intégrés. L'une des limitations principales de l'assemblage (packaging) est la capacité à assembler les différentes parties du circuit intégré.* Le processus utilisé pour réaliser ces opérations est le **brassage**. Il signifie l'assemblage de pièces métalliques à l'aide d'un alliage métallique placé entre les pièces à assembler. Le système est chauffé à température supérieure au point de fusion de l'alliage d'apport et inférieure aux points de fusion des deux pièces à assembler. Une bonne adhérence doit être atteinte non seulement entre l'alliage liquide et les éléments solides, mais aussi entre l'alliage solidifié et les parties solides après refroidissement à la température ambiante.

Il existe de nombreux phénomènes qui interviennent dans le processus de brassage, tels que: le *mouillage* des parties solides par l'alliage liquide et les *interactions interfaciales* solide/liquide (dissolution, diffusion, *germination et croissance* des produits interfaciaux) quand la brasure est à l'état liquide (par le processus de *refusion - reflow* en anglais), ainsi que la *surfusion*, la *germination* et la *solidification* de l'alliage pendant le refroidissement du système à la température ambiante.

Le brassage est la technique la plus utilisée dans l'industrie microélectronique pour assembler l'*UBM* (Under Bump Metallization en anglais), à savoir les films minces de Cu sur les circuits imprimés, etc. Le système Cu-Sn est le plus utilisé dans la technologie de brassage en électronique et les brasures à base de Sn, souvent utilisées sous la forme d'une bille de brasure, sont utilisées dans presque toutes les techniques d'assemblage. La taille des billes de brasure modernes utilisées dans la technologie d'assemblage est inférieure à 100  $\mu\text{m}$  et diminue avec la tendance à la miniaturisation.

La taille des billes de brasure utilisées au cours de ce processus détermine la capacité à miniaturiser l'assemblage des puces. Les diverses difficultés technologiques apparaissent avec cette miniaturisation. L'une d'entre elles est l'anisotropie des propriétés du joint en raison du développement de très petit nombre de grains formés à l'interface entre le substrat métallique et la brasure ou dans de brasure. Il devient alors indispensable de contrôler les interactions interfaciales entre la brasure et le substrat, mais aussi la microstructure des substrats et de la brasure métallique avant et après la brasure, pour limiter les problèmes de fiabilité pendant le fonctionnement du dispositif en service.

Lorsque la taille d'une bille de brasure diminue de manière significative (par exemple vers quelques micromètres), les interactions interfaciales devraient être contrôlées à l'échelle nanométrique afin de contrôler la microstructure interfaciale. De plus, pendant le refroidissement du système jusqu'à la température ambiante, de très hauts degrés de surfusion peuvent être atteints dans ces systèmes micrométriques. Cet effet conduit à l'apparition d'équilibre métastable et/ou de phases métastables qui peuvent profondément influencer la microstructure et les propriétés mécaniques du joint. Ainsi, l'étude fondamentale de ces phénomènes dans le système Cu solide/Sn liquide, le plus utilisé dans les technologies d'assemblage en électronique, devient essentielle actuellement.

Les défis scientifiques en micro- et nano-électronique concernant le processus de **brassage** en électronique (**soldering** en anglais) définissent le cadre de cette thèse. Notre but est de répondre à certaines des questions scientifiques clés dans le domaine de brassage, qui sont importantes pour la résolution des problèmes qui apparaissent avec la miniaturisation des circuits intégrés.

Tout d'abord, dans la **section 2** nous décrivons la problématique de la technologie de brassage moderne. Cette section comprend une étude bibliographique de la technologie de brasage, de la fiabilité, de la mouillabilité de substrats métalliques par des brasures liquides et de la réaction entre eux (dissolution, germination au niveau des interfaces et cinétique de croissance des couches interfaciales), ainsi que le phénomène de germination dans la brasure elle-même qui intervient au cours du refroidissement.

La **section 3** résume les méthodes expérimentales et les matériaux utilisés dans cette étude. En particulier, elle donne une description détaillée de l'élaboration des phases intermétalliques utilisées pour les expériences de mouillage ainsi que la description d'un équipement spécifique utilisé pour l'étude de l'étape initiale de l'interaction entre la brasure liquide et le substrat Cu.

Comme notre but est d'étudier les premières étapes de l'interaction entre les substrats métalliques et les alliages liquides (tels que la germination et la croissance), la connaissance des paramètres de base de ce processus est cruciale. L'angle de contact des brasures liquides sur le substrat en cuivre, qui en principe permet d'évaluer les énergies interfaciales, est l'un de ces paramètres. A cet effet, dans la **section 4**, on étudie en particulier la mouillabilité du Cu par les brasures liquides à base de Sn. Dans des systèmes réactifs Cu/ alliage base Sn liquide (souvent des alliages Sn-Ag-Cu appelés SAC), deux couches d'intermétalliques sont formées à l'interface,  $\text{Cu}_3\text{Sn}$  côté Cu et  $\text{Cu}_6\text{Sn}_5$  côté brasure. De plus, pour l'étude du mouillage réactif, mais aussi pour les phénomènes de germination au niveau des interfaces réactives, il est très utile de connaître les propriétés de mouillage de ces intermétalliques. En outre, comme au cours du refroidissement de brasures Sn-Ag-Cu, la phase  $\text{Ag}_3\text{Sn}$  peut germer la première à l'intérieur de la brasure, les propriétés de mouillage de cette phase par la brasure liquide sont très utiles pour l'étude de la germination dans les brasures liquides surfondues. Pour ces raisons, dans la section 4, nous avons étudié aussi le mouillage de  $\text{Cu}_3\text{Sn}$ ,  $\text{Cu}_6\text{Sn}_5$  et  $\text{Ag}_3\text{Sn}$  intermétalliques par Sn liquide.

Dans la **section 5**, la question de la germination à l'interface Cu solide/ alliage liquide pendant le processus de brassage ainsi que celle de germination à l'intérieur de la brasure pendant le refroidissement du système à température ambiante sont traitées à la fois expérimentalement et théoriquement:

- Afin de répondre à la question importante de la séquence de formation des phases à l'interface réactive Cu/Sn liquide nous avons réalisé des expériences spécifiques d'immersion très rapide de Cu dans Sn liquide (temps de réaction de 1 ms à 1 s). En outre, nous avons développé une approche théorique sur les critères de suppression de formation de la deuxième phase ( $\text{Cu}_3\text{Sn}$  dans ce cas) à l'interface  $\text{Cu}_6\text{Sn}_5/\text{Sn}$  du système Cu/ $\text{Cu}_6\text{Sn}_5/\text{Sn}$ .

- La germination de Sn dans le alliage Sn-Cu liquide surfondu est étudiée par calorimétrie différentielle à balayage (DSC) en utilisant des cycles thermiques avec fusion totale ou fusion partielle de la brasure et ceci dans deux configurations (a) brasure en contact avec la phase  $\text{Cu}_6\text{Sn}_5$  et (b) brasure toute seule. Par ailleurs, dans cette section, une approche théorique de germination hétérogène est proposée afin de déterminer les sites favorables de germination hétérogène en comparant les surfusions expérimentales avec celles calculées.

La morphologie et l'épaisseur des couches intermétalliques formées à l'interface Cu solide/Sn liquide jouent un rôle essentiel sur les caractéristiques physiques des interfaces ainsi que sur les caractéristiques mécaniques du joint. Dans la littérature, il y a encore beaucoup de controverse concernant l'exposant de la loi de croissance de la couche de  $\text{Cu}_6\text{Sn}_5$  et surtout concernant les mécanismes régissant la croissance et la morphologie de cette couche. Afin d'approfondir nos connaissances dans ce domaine, nous avons effectué deux types d'expériences spécifiques sur le système Cu/Sn qui sont présentés dans la **section 6**:

- Nous comparons la cinétique de la croissance de la phase  $\text{Cu}_6\text{Sn}_5$  pour le couple standard Cu/Sn liquide et pour le couple incrémental  $\text{Cu}_3\text{Sn}/\text{Sn}$  liquide. Le changement dans le taux de croissance peut nous donner un lien avec le mécanisme de la croissance des intermétalliques.

- Nous comparons, pour la première fois, la cinétique de croissance de la phase  $\text{Cu}_6\text{Sn}_5$  entre le cuivre et la brasure liquide métastable avec celle entre le cuivre et la brasure solide stable à la même température. Ceci est réalisé en effectuant des expériences spécifiques par calorimétrie différentielle à balayage (DSC) afin de contrôler l'état physique de l'alliage et de régler la température de façon précise. Nous déterminons ainsi les facteurs qui affectent la morphologie des produits de réaction et les mécanismes de croissance des phases et une modélisation de la cinétique de croissance est proposée.

Enfin, dans cette section, une évaluation théorique de la largeur des canaux liquide à l'intérieur de la phase  $\text{Cu}_6\text{Sn}_5$ , responsable de diffusion rapide dans cette phase, dans le système Cu/ $\text{Cu}_3\text{Sn}/\text{Cu}_6\text{Sn}_5/\text{Sn}$ , est effectuée.

Une synthèse des conclusions principales de cette étude sera donnée à la **section 7** de ce manuscrit ainsi qu'un certain nombre des perspectives en ce qui concerne certaines des questions fondamentales sur le sujet du processus de brassage, qui ne sont pas encore élucidées.

## 2) Etude bibliographique

### 2.1) Brasage en microélectronique

Le brasage est une technique clé pour réaliser l'assemblage des parties métalliques séparées avec l'utilisation d'un alliage métallique ou d'un métal d'apport placé entre les pièces à assembler. Connue depuis des milliers d'années, cette technique est principalement utilisée dans l'industrie microélectronique pour l'assemblage de UBM, à savoir les films minces de cuivre sur les circuits imprimés, fils de cuivre, etc. Le système Cu-Sn est le plus rencontré dans la technologie de brasage en électronique et les brasures à base de Sn sont utilisées dans presque toutes les techniques d'assemblage. Les brasures (alliages de brasure) sont essentiellement des alliages à base d'étain souvent utilisés sous la forme d'une bille de brasure. La taille des billes de brasure modernes utilisées dans la technologie d'assemblage est inférieure à 100  $\mu\text{m}$  et diminue avec la tendance de miniaturisation.

La réaction de brasage classique qui se développe au cours du processus de reflow (refusion) comprend le mouillage réactif du substrat de cuivre et la croissance de composés intermétalliques (IMC) à l'interface substrat solide/brasure liquide [Tu\_2007]. L'opération de reflow (voir Figure 1) comprend un cycle de chauffage et de refroidissement, au cours duquel la température dépasse celle de fusion de la brasure par quelques dizaines de degrés et le temps de passage à l'état liquide est de quelques minutes (typiquement 2-3 minutes).

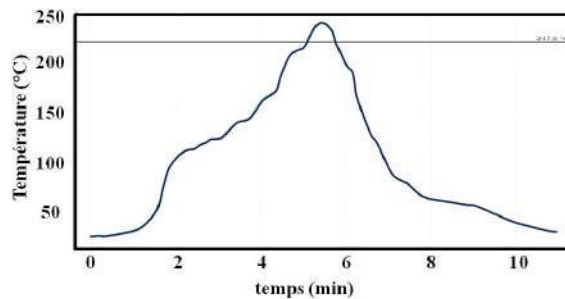


Figure 1. Profil températures-temps d'une refusion (reflow) typique [Bertheau\_2014].

La tendance permanente à la miniaturisation conduit à de nouveaux défis et les problèmes de fiabilité sont les problèmes les plus essentiels. La diminution significative de la dimension de brasure (ou du joint de brasure) obéit à la tendance suivante [Tu\_2013]: (i) la technologie flip-chip moderne (voir Figure 2) utilise des billes de brasure de diamètre d'environ 100  $\mu\text{m}$ ; (ii) le passage aux circuits 3D (trois dimensionnels) intégrés réduit la taille à 20  $\mu\text{m}$ ; (iii) la prévision est que le diamètre du joint brasé peut être réduit à 1  $\mu\text{m}$ .

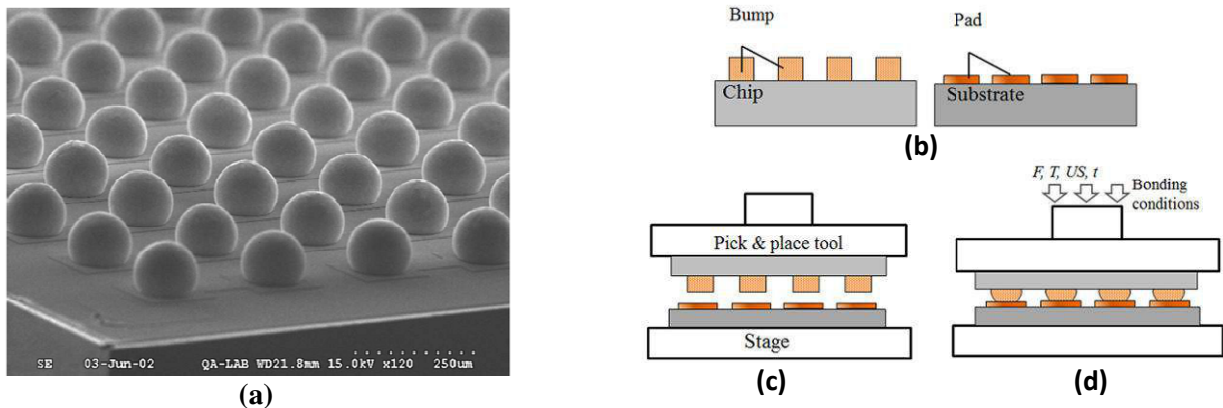


Figure 2. a) Ball Grid Array (BGA) de billes de brasure sur une surface de la puce [Tu\_2007]. Schéma de la méthode flip chip (puce retournée) d'assemblage de puces [Tung\_2014] pour assembler la puce contenant des solder bumps sur un substrat avec des piliers de cuivre (b) avec un alignement "pick and place tool" (c) et refusion (reflow) (d).

### 2.2) Le système Cu-Sn dans la technologie de brasage

Il y a deux intermétalliques (IMC) communs dans la brasure,  $\text{Cu}_6\text{Sn}_5$  et  $\text{Cu}_3\text{Sn}$ , qui croissent rapidement et forment des couches continues à l'interface Cu/brasure base Sn. Le taux de germination des IMC, la séquence et le

lieu de germination sont des sujets de grand intérêt scientifique. Les températures de fonctionnement des dispositifs microélectroniques étant significativement inférieures à celle de fusion de la brasure, la croissance rapide des IMC au cours du reflow (refusion) joue un rôle essentiel dans l'établissement de l'adhésion entre le substrat et la brasure.

### **2.3) Mouillage de Cu et des intermétalliques $\text{Cu}_6\text{Sn}_5$ et $\text{Cu}_3\text{Sn}$ par les alliages liquides base Sn**

La mouillabilité des solides utilisés à l'industrie micro-électronique est d'un intérêt essentiel car elle affecte fortement la géométrie et la fiabilité mécanique du joint de brasure ainsi que la réactivité initiale à l'interface entre le substrat d'origine et de brasure. En général, on distingue le mouillage non réactif et le mouillage réactif [Eustathopoulos\_1999]. Dans le cas du brassage en électronique on rencontre très souvent le mouillage réactif car les brasures usuelles à base Sn sont très réactives avec Cu, ce qui signifie que le mouillage est suivi par la formation rapide de composés intermétalliques à l'interface [Tu\_2007] (souvent les deux processus mouillage et réactivité se déroulent simultanément - c'est le mouillage réactif). Le processus de mouillage est régi par un ensemble de conditions, y compris l'état de surface, la viscosité de la brasure, l'atmosphère ambiante, la réactivité et l'oxydation de la surface du substrat et/ou de la brasure. Nous étudierons plus particulièrement le mouillage du Cu pur et des intermétalliques  $\text{Cu}_6\text{Sn}_5$  et  $\text{Cu}_3\text{Sn}$  par des alliages de brasures liquides (base Sn).

Toutes les études rapportées dans la littérature sur le mouillage des substrats métalliques par les alliages liquides à base Sn montrent que très peu d'expériences de mouillage sont effectuées avec la méthode de la goutte déposée. La plupart des expériences de mouillage dans ces systèmes sont effectuées en utilisant la méthode classique de la goutte posée où la fusion et l'homogénéisation de l'alliage métallique interfèrent avec le processus d'étalement et de diffusion. En plus ces expériences ne sont pas effectuées dans des conditions isothermes. De plus, la combinaison de la méthode de la goutte déposée avec un contrôle de l'atmosphère n'est indiquée que par un nombre très limité d'études. La majorité des études rapportent des angles de contact finaux, mesurés pour Sn liquide ou pour des alliages à base de Sn liquides sur des substrats de Cu, dans la gamme de 26 à 43°. Il convient de noter que l'addition d'Ag, Cu ou Bi dans la brasure conduit à diminuer de l'angle de contact vers 13°. Notez cependant que, en général, ces angles de contact finaux sont obtenus après l'interaction de la brasure liquide avec Cu solide pendant au moins quelques minutes et leur signification physique n'a pas été précisée.

Seulement très peu d'études ont porté leur intérêt sur le mouillage des phases intermétalliques  $\text{Cu}_6\text{Sn}_5$  et  $\text{Cu}_3\text{Sn}$  par des brasures liquides à base de Sn. Jusqu'à présent ces études comprennent la mise en œuvre de la seule technique de la goutte posée avec l'utilisation de flux. Ainsi, il est difficile de conclure si l'angle de contact de l'étain liquide sur les phases intermétalliques (IMC) est inférieur ou supérieur à l'angle de contact sur le substrat de Cu non réagi. Néanmoins, le fort effet de l'oxydation de surface a été détecté pour le mouillage des phases IMC.

Des études récentes sur les étapes initiales d'étalement non réactif (jusqu'à 10 ms) dans les systèmes métalliques (gouttelettes d'Ag, Cu et Au liquide sur substrat Mo) est une sorte de guide pour la détection de l'étape d'étalement non réactif dans les systèmes Cu/Sn liquide et Ag/Sn liquides. La détection de cette étape (et des angles de contact correspondants) serait essentielle pour la détermination de l'angle de contact d'équilibre de Sn liquide sur les substrats de Cu et Ag avant la formation d'un produit de réaction à l'interface liquide/solide.

### **2.4) Réactions interfaciales Cu et les alliages liquides base Sn**

La croissance des phases intermétalliques entre le cuivre solide et les brasures à base d'étain liquides, pendant les dernières étapes de la réaction, est bien étudiée expérimentalement. Le modèle FDR [Gusak\_2002] peut être utilisé pour la description de la croissance lors du processus de refusion (reflow) lorsque le temps de réaction avec la brasure liquide ne dépasse pas quelques minutes. Néanmoins, des résultats récents montrent que les modèles de cinétique de croissance devraient être revus pour l'étape initiale de la réaction (temps de réaction  $t < 10$  s), ainsi que pendant les dernières étapes de la réaction ( $t > 30$  min). La séquence de germination des IMCs à l'interface Cu/Sn est encore en discussion et devrait être revue. De même le critère de suppression de la croissance de la phase  $\varepsilon$ - $\text{Cu}_3\text{Sn}$  (si ce critère existe) doit être défini.

Au cours de réaction à l'état solide, la cinétique de croissance des IMCs obéit à une loi parabolique. Le processus de croissance peut être bien décrit par les modèles existants de croissance de phase au cours de réactions à l'état solide. Cependant, l'ambiguïté des résultats expérimentaux dans la compétition de la croissance au cours des dernières étapes du recuit à l'état solide (lorsque la phase dominante n'est pas clairement identifiée) doit être étudiée en détails. Un effort particulier devrait être fait pour révéler les facteurs conduisant au développement des porosités à l'interface.

## **2.5) Germination hétérogène pendant la cristallisation de Sn liquide ou des alliages liquides Sn-Ag-Cu: solidification des billes de brasure et des joints de brasure**

Le fait que le substrat de cuivre et aussi les autres substrats métalliques (Ni, Ag, ... voir par exemple les réf. [Chang\_2003, Wang\_2006, Sobczak\_2007, Matsumoto\_2008, Kim\_2009]) sont très bien mouillés par les alliages de brasure liquides (mouillage réactif), peut conduire à une conclusion préliminaire que la germination au cours du refroidissement d'une brasure liquide devient plus facile par une germination hétérogène sur le substrat métallique (en fait, sur la couche de réaction intermétallique formée à interface substrat/brasure).

Cependant, le degré de surfusion pendant le brasage des alliages à base de Sn (ou Sn pur) sur Ag ou Cu est encore élevé ( $> 15$  K). Ceci a conduit récemment Belyakov et Gourlay [Belyakov\_2014] à la conclusion que les composés intermétalliques rencontrés dans le brasage,  $\text{Ag}_3\text{Sn}$  et  $\text{Cu}_6\text{Sn}_5$  sont inefficaces à catalyser la germination de Sn. Ces auteurs [Belyakov\_2014] ont montré que cristaux d'autres composés intermétalliques  $\text{NiSn}_4$ ,  $\text{PdSn}_4$  et  $\text{PtSn}_4$  sont des sites de germination hétérogène pour Sn, ce qui réduit la surfusion de germination de Sn de 35 K à 3-4 K seulement.

Malgré le fait que plusieurs travaux ont récemment été consacrés à la germination de l'étain dans le volume de la brasure, le rôle des différents sites potentiels de germination hétérogènes d'étain à l'intérieur de la bille de brasure n'a pas encore été élucidé. En outre, il n'y a pas d'études spécifiques traitant la comparaison des degrés de surfusion obtenus après une fusion partielle de la brasure et après une refusion (reflow) dans les configurations: (i) billes de brasure et (ii) joint de brasure préparés par refusion (reflow) d'alliage de brasure sur le substrat de cuivre.

### 3) Méthodes expérimentales et matériaux

#### 3.1) Méthode de la goutte posée : principe

La méthode de la goutte posée consiste à suivre la variation de la forme d'une goutte de métal ou d'alliage placée sur un substrat plan et horizontal, lorsqu'on se trouve à une température supérieure à la température de fusion du métal ou de l'alliage considéré. La masse des gouttes utilisées est faible (de 20 à 100 mg), on peut alors considérer que la déformation de la goutte sous l'effet de la gravité est faible, et que la forme de la goutte est une calotte sphérique. On mesure les paramètres caractéristiques suivants (Figure 3): le rayon de base  $R$  et la hauteur  $h$  de la goutte et les angles de contact à gauche ( $\theta_g$ ) et à droite ( $\theta_d$ ). A partir de ces mesures, on déduit la valeur moyenne de l'angle de contact:

$$\theta = (\theta_l + \theta_r)/2 \quad (1)$$

On peut calculer  $\theta$  à partir des dimensions linéaires de la goutte supposée être une calotte sphérique:

$$\theta = 2 \arctan (h/R)(\theta_l + \theta_r)/2 \quad (2)$$

Dans l'approximation d'une sphère tronquée, on calcule le volume de la goutte par la relation suivante :

$$V = \pi r^3 (2 - 3 \cos \theta + \cos^3 \theta) / (3 \sin^3 \theta) \quad (3)$$

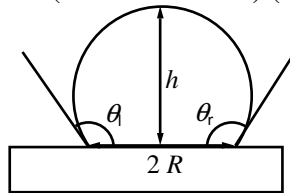


Figure 3. Paramètres caractéristiques de la goutte posée.

#### 3.2) Méthode de la goutte déposée

La version classique de la méthode de la goutte posée présente quelques désavantages, car la fusion et l'homogénéisation de l'alliage métallique interfèrent avec le processus d'étalement. Pour cette raison, nous mettons en œuvre la version modifiée de cette technique: la méthode de la goutte déposée qui permet la séparation des processus de fusion et d'étalement d'un alliage sur un substrat. A cette fin, une configuration spéciale est mise en œuvre (voir Figure 4). Le substrat est placé sur une "table tournante", alors que l'alliage est fondu dans un creuset céramique situé au-dessus du substrat. Le creuset communique dans sa partie inférieure avec un capillaire en alumine de diamètre intérieur 0.6 mm et de longueur d'environ 5 mm. Quand l'alliage est complètement fondu, une gouttelette de liquide est extrudée par le capillaire, puis l'ensemble (creuset + capillaire + goutte) est déplacé vers le substrat. Quand la partie inférieure de la goutte touche le substrat, un étalement spontané de la goutte se produit sur le substrat.

L'ensemble du processus de dépôt est enregistré par une caméra rapide (jusqu'à 5000 images/s). Ceci permet de visualiser toute les étapes du dépôt et de l'étalement de la goutte (voir Figure 4): (i) extraction de la goutte du capillaire (Figure 4a), (ii) transfert de la goutte sur le substrat (Figure 4b), (iii) mouillage du substrat et formation d'un pont liquide avec le capillaire (Figure 4c) et (iv) détachement et étalement de la goutte (Figure 4d).

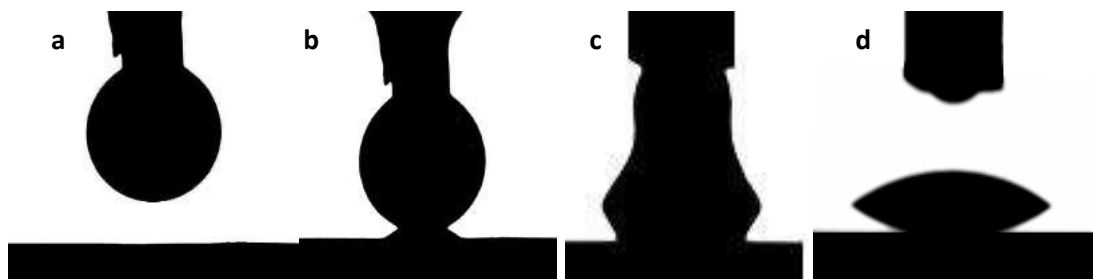


Figure 4. Différentes étapes du dépôt de gouttelettes par la technique de la goutte déposée: a) extrusion de la goutte; b) transfert de la goutte; c) étalement avec formation de pont liquide; d) détachement de la goutte.

### 3.3) Installation expérimentale d'immersion rapide d'un solide dans un bain liquide

Pour étudier les premières étapes de la réaction métal solide-alliage liquide, nous avons conçu et construit une installation spécifique afin de réaliser des expériences d'immersion rapide (voir Figure 5) qui consistent à immerger un substrat dans un bain liquide pendant un temps donné.

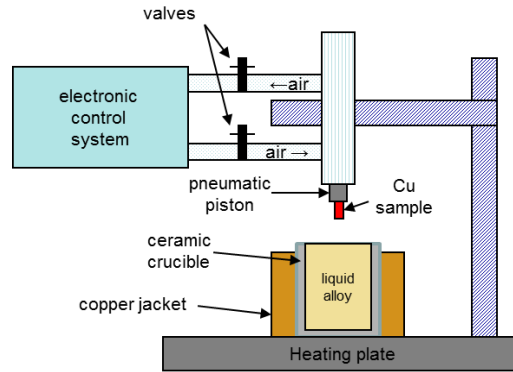


Figure 5. Installation expérimentale d'immersion rapide

Le creuset en céramique contenant l'alliage est placé sur une plaque chauffante capable de chauffer jusqu'à 350°C. Le creuset est entouré d'une feuille en Cu d'épaisseur 1 cm afin d'assurer une bonne homogénéité thermique dans le creuset. Un piston pneumatique a été utilisé pour immerger le substrat de Cu dans le bain liquide pendant une durée bien déterminée. Un système spécial de commande électronique a été conçu et construit au cours de la thèse afin de commander le commutateur d'écoulement de l'air sous haute pression afin de déplacer le piston pneumatique. La pression du flux d'air entrant et sortant peut être également réglé manuellement par deux vannes. Cela permet de contrôler la vitesse d'immersion de l'échantillon qui est mesurée par une caméra CCD

La Figure 6 présente les détails concernant l'étalonnage de la vitesse d'immersion de l'échantillon qui est déterminée en utilisant une caméra CCD conventionnelle (25 images/s). Chaque expérience d'immersion est répétée 5 fois afin de mesurer la durée moyenne de l'immersion. Le cycle total d'un mouvement aller-retour du piston a lieu en 130-170 ms (voir Figure 6) et donc la vitesse d'immersion varie de 0.3 à 0.4 m/s. La profondeur maximale d'immersion de la feuille de Cu étant de 6 mm, le temps maximal de contact entre Cu et l'alliage liquide est d'environ 30-40 ms dans la zone du Cu qui touche la première le bain liquide et d'environ 1 ms dans la zone qui touche à peine le bain liquide.

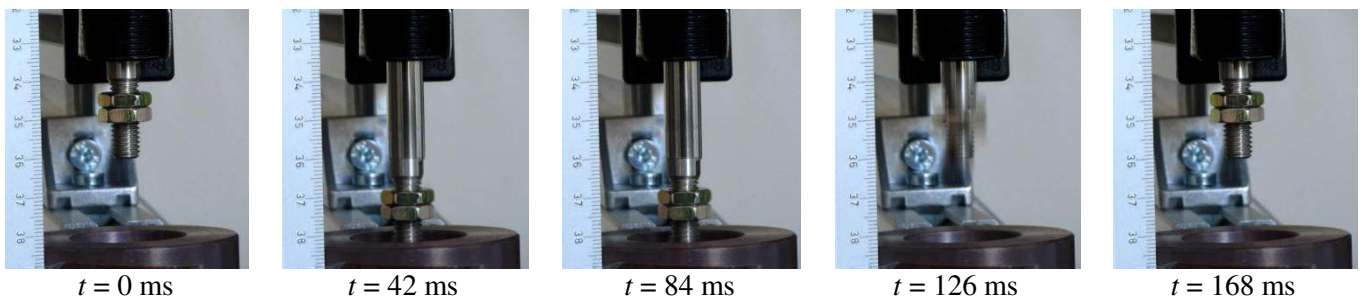


Figure 6. Contrôle de la vitesse d'immersion. Le piston effectue son cycle de mouvement avec une période de 130-170 ms. La vitesse d'immersion est 0.3-0.4 m/s

### 3.4) Elaboration des intermétalliques $\eta$ -Cu<sub>6</sub>Sn<sub>5</sub>, $\epsilon$ -Cu<sub>3</sub>Sn et Ag<sub>3</sub>Sn

Trois intermétalliques (IMC) ont été préparés au laboratoire pour les études de mouillabilité et de réactivité:  $\eta$ -Cu<sub>6</sub>Sn<sub>5</sub> (40.0wt.% Cu),  $\epsilon$ -Cu<sub>3</sub>Sn (62.0wt% Cu) et Ag<sub>3</sub>Sn (3.7wt.% Ag). Un autre type de "substrat" d'IMC a été aussi utilisé dans cette étude: la phase Cu<sub>6</sub>Sn<sub>5</sub> en forme de "scallop" (aspérité) formée par réaction entre Cu solide et Sn liquide et "relevée" par attaque chimique sélective de Sn. Nous donnons ci-dessous quelques détails de la préparation des intermétalliques Cu<sub>6</sub>Sn<sub>5</sub> et Cu<sub>3</sub>Sn.

La Figure 7a présente les micrographies MEB des sections de l'échantillon Cu<sub>6</sub>Sn<sub>5</sub>. On voit que la majeure partie de l'échantillon contient un grand nombre de pores micrométriques, ainsi que quelques petites inclusions de taille maximale d'environ 100  $\mu$ m. Ces inclusions n'ont pas été détectées par analyse XRD ce qui peut dû à leur faible quantité. Il s'agirait probablement des inclusions de Cu ou de Cu<sub>3</sub>Sn.

L'échantillon  $\text{Cu}_6\text{Sn}_5$  en forme "scallop" a été préparé par réaction entre Cu et Sn liquide à  $350^\circ\text{C}$  pendant 2 heures dans un four alumine sous vide secondaire  $1.6 \times 10^{-4}$  Pa. La configuration du système à la fin de la réaction est  $\text{Cu}/\text{Cu}_3\text{Sn}/\text{Cu}_6\text{Sn}_5/\text{Sn}$ . Ensuite, tout l'étain situé sur la phase  $\text{Cu}_6\text{Sn}_5$  a été dissous par attaque chimique avec une solution acide ( $\text{HCl}$  10%,  $\text{C}_2\text{H}_5\text{OH}$  90%) chauffée jusqu'à  $70^\circ\text{C}$ . La Figure 7b montre les micrographies MEB de la surface de  $\text{Cu}_6\text{Sn}_5$  après l'attaque chimique relevant ainsi la forme des grains (du type "scallop"). Comme on peut le voir sur cette figure, la taille moyenne de grain de  $\text{Cu}_6\text{Sn}_5$  varie de 5 à  $25 \mu\text{m}$ .

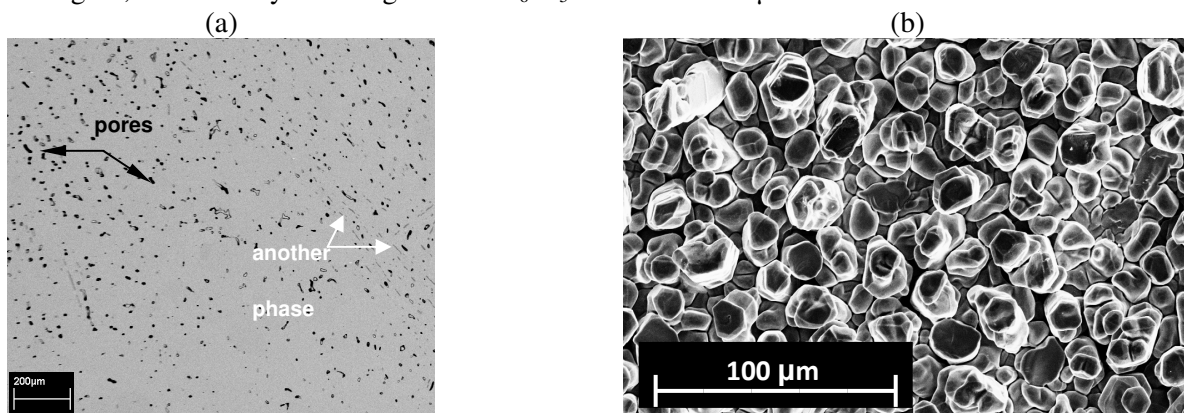


Figure 7. Images ESB-SEM de  $\text{Cu}_6\text{Sn}_5$  élaboré en forme "massif" (a) et aspérité "scallop" (b)

La phase  $\epsilon\text{-Cu}_3\text{Sn}$  a été préparée dans le four alumine à partir de morceaux de Cu et de Sn (38wt.%) pur placés dans un creuset en alumine. Le cycle d'élaboration comprend un chauffage sous vide ( $1.6 \times 10^{-4}$  Pa), avec une vitesse de chauffe  $v = 5^\circ\text{C}/\text{min}$  jusqu'à  $200^\circ\text{C}$  suivi de  $v = 2^\circ\text{C}/\text{min}$  jusqu'à  $600^\circ\text{C}$ . Après, l'argon a été introduit dans la chambre et l'ensemble du système a été chauffé jusqu'à  $800^\circ\text{C}$  avec  $v = 20^\circ\text{C}/\text{min}$  et maintenu à cette température pendant 30 min. Ensuite, le système a été refroidi avec  $v = 10^\circ\text{C}/\text{min}$  jusqu'à  $750^\circ\text{C}$  et avec  $v = 1^\circ\text{C}/\text{min}$  jusqu'à  $630^\circ\text{C}$ . Un maintien isotherme de 4h à  $630^\circ\text{C}$  a été effectué afin de "stabiliser" la phase  $\text{Cu}_3\text{Sn}$ , ensuite le four a été refroidi naturellement à la température ambiante avec  $v = 2^\circ\text{C}/\text{min}$ .

#### 4) Mouillage du Cu, Ag et des intermétalliques des systèmes Cu-Sn et Ag-Sn par Sn ou les alliages Sn-Cu liquides

##### 4.1) Mouillage du Cu par Sn liquide ou par les alliages Sn-Cu liquides

La Figure 8 présente la variation avec le temps de l'angle de contact  $\theta$  et le diamètre de base  $d$  de la goutte lors du mouillage de l'alliage liquide Sn-7.8wt.%Cu déposé sur Cu à 390°C (après 2 heures de préchauffage du Cu à cette température). Comme on peut le voir sur cette figure, l'étalement de la goutte est très rapide : l'angle de contact diminue de 120 à environ 30° pendant les premières millisecondes d'étalement.

La Figure 9 relie quelques points expérimentaux particuliers avec des images en temps réel prises lors de l'expérience de mouillage. On peut constater que jusqu'à environ  $(6-7) \times 10^{-3}$  s un pont liquide existe entre la goutte et le capillaire. Après un certain temps ce pont est détruit et la goutte s'étale rapidement jusqu'à environ 20° et ensuite elle oscille. Les oscillations ne sont pas amorties jusqu'à environ 0.1 s et elles sont reliées à la variation à la fois de  $\theta$  et de  $d$  (voir Figure 8). L'amplitude maximale des oscillations de  $d$  est d'environ 1.5% de sa valeur finale (mesurée à 0.1 s :  $d_f = 3.15$  mm) tandis que celle des oscillations de  $\theta$  est d'environ 30% de sa valeur finale ( $\theta_f = 27^\circ$ ). La fréquence de ces oscillations est d'environ  $150 \text{ s}^{-1}$ .

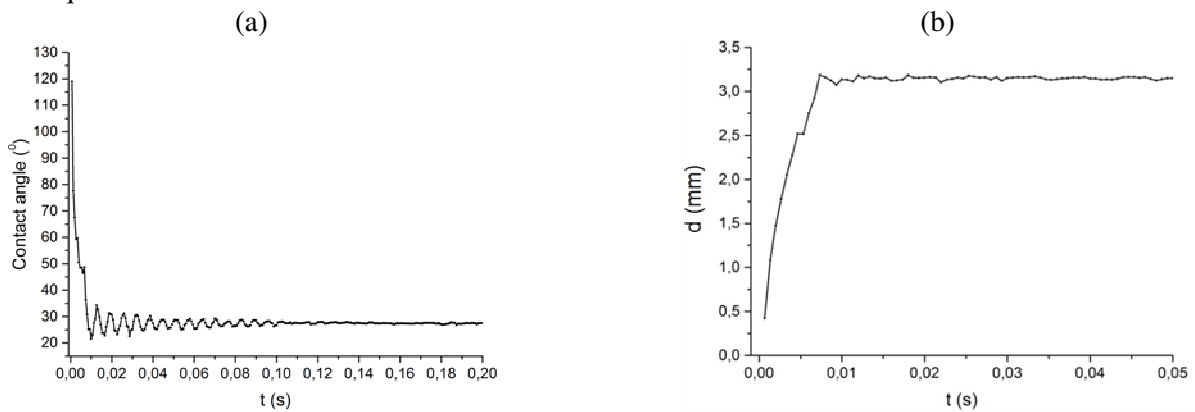
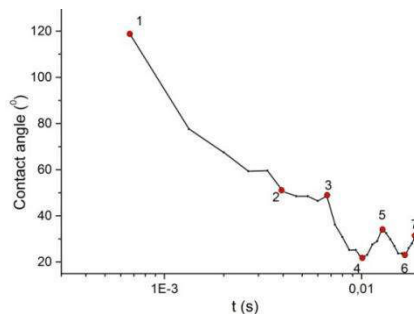


Figure 8. Variation de l'angle de contact  $\theta$  (a) et du diamètre base de la goutte  $d$  (b) avec le temps. Système Cu/alliage Sn-7.8wt.%Cu à 390°C.



Point	1	2	3	4	5	6	7
t(ms)	0.7	3.9	6.6	10.0	12.7	16.6	18.7

Figure 9. Oscillations de la gouttelette d'alliage Sn-7.8wt.%Cu déposée sur un substrat de Cu à 390°C.

Etant donné que dans le cas des gouttes de Sn sur Cu, l'étape très rapide d'étalement se produit en environ 10 ms quelle que soit la température de 300 à 600°C, on a rapporté sur la même Figure 10 la cinétique d'étalement de Sn sur Cu à différentes températures  $T$  mais aussi celle de Pb liquide à 400°C. Cette Figure montre que, lors de la première étape de mouillage la cinétique d'étalement est presque indépendante de  $T$ . En outre la cinétique d'étalement du Sn dans cette étape est très similaire à celle du Pb (étalement non réactif du Pb sur Cu). Noter par ailleurs que la dépendance presque linéaire de la variation du diamètre de base  $d$  de la goutte avec la racine carrée du temps ( $d \sim t^{1/2}$ ) est en bon accord avec les travaux de Saiz et al. [Saiz\_2010] qui ont étudié l'étalement non réactif des métaux liquides sur des substrats métalliques.

Les expériences de mouillage des substrats de Cu préchauffés à 800°C par Sn liquide entre 300 à 600°C montrent donc que la première étape d'étalement, lorsque  $\theta$  diminue jusqu'à environ 30° en moins de 10 ms, peut être attribuée à l'étalement non réactif de Sn liquide sur la surface de Cu. Compte tenu du fait que ces expériences de mouillage sont effectuées avec des surfaces de Cu pouvant contenir des nanoparticules d'oxyde, on peut conclure que l'angle d'équilibre de Sn liquide sur une surface de Cu propre et non réagi est inférieur à 30°. L'étape d'étalement non réactif peut être suivie par une étape d'étalement réactif qui peut correspondre à la dissolution du substrat dans le liquide et/ou à la formation de couches réactives de  $\text{Cu}_3\text{Sn}$  et  $\text{Cu}_6\text{Sn}_5$  à l'interface Cu/Sn. Le rôle probable de ces couches sur le processus de mouillage sera étudié dans les sections suivantes.

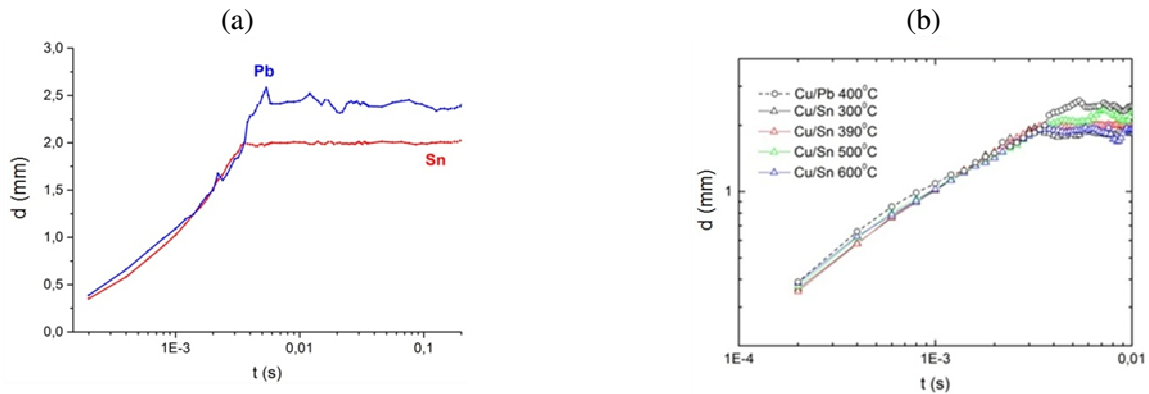


Figure 10. (a) Comparaison des cinétiques d'étalement (variation de diamètre de base de la goutte  $d$  en fonction du temps) de Sn et Pb liquide déposés sur Cu à 390 et 400°C respectivement. (b) Comparaison des cinétiques d'étalement des gouttelettes de Sn sur Cu à différentes températures (300 à 600°C). Substrats de Cu préchauffé initialement à 800°C pendant 2 h

#### Caractérisation de quelques échantillons Cu/Sn sélectionnés

Dans cette section, on présentera la caractérisation de certains échantillons Cu/Sn sélectionnés après une expérience de mouillage à 250°C. Noter cependant que l'objectif de cette section n'est pas nécessairement de présenter une relation entre la cinétique d'étalement et les microstructures interfaciales observées. En effet, ces microstructures obtenues après le refroidissement des échantillons à la température ambiante, ne correspondent pas nécessairement à l'état du système à la température d'expérience.

Les gouttelettes déposées ont été inspectées par MEB : vue de dessus et sections transversales. La Figure 11 montre une vue du dessus de la gouttelette de Sn déposée à 250°C sur Cu sous un vide de  $2 \times 10^{-5}$  Pa. La goutte solidifiée a une forme pratiquement circulaire (voir Figure 11a) et la formation d'un halo d'intermétallique autour de la goutte est détectée (voir Figure 11b). L'analyse EDX a révélé l'existence des couches des phases  $\epsilon\text{-Cu}_3\text{Sn}$  et  $\eta\text{-Cu}_6\text{Sn}_5$  de même largeur (d'environ 10  $\mu\text{m}$ ) en avant de l'étain solidifié. L'analyse de la section transversale de la même gouttelette (voir la Figure 11c) montre la formation d'une couche continue et fine près du substrat de Cu qui correspond à la phase  $\epsilon\text{-Cu}_3\text{Sn}$  et d'une couche épaisse côté Sn, contenant des aspérités ("scalops"), qui est identifiée comme la phase  $\eta\text{-Cu}_6\text{Sn}_5$ . L'interface  $\epsilon\text{-Cu}_3\text{Sn}/\text{Cu}$  est relativement plane et la majeure partie de la goutte solidifiée est exempte de larges précipités de  $\text{Cu}_6\text{Sn}_5$ . Cela est dû à la température expérimentale faible ainsi que à la limite de solubilité faible de Cu dans le Sn liquide à 250°C (environ 5%at. [Saunders\_1997]).

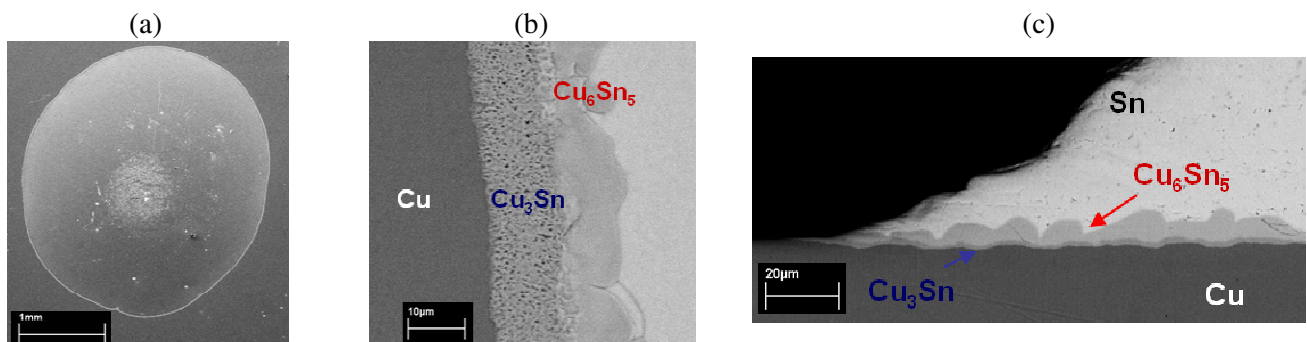


Figure 11. Micrographies MEB de la gouttelette de Sn déposée sur Cu par la technique de la goutte déposée à 250°C sous un vide de  $2 \times 10^{-5}$  Pa. Vue générale du dessus de la gouttelette (a) vue de dessus près de la triple ligne (b) et vue transversale (c).

#### 4.2) Mouillage de $\text{Cu}_6\text{Sn}_5$ par un alliage Sn-7.8wt.%Cu "pré-saturé" à 390°C

La Figure 12 donne la variation avec le temps de l'angle de contact  $\theta$  et du diamètre de base  $d$  d'une gouttelette d'alliage Sn-7.8wt.% Cu déposée sur un substrat de  $\text{Cu}_6\text{Sn}_5$  à 390°C après 4 h de recuit à cette température. Cette figure montre que l'angle de contact instantané décroît très rapidement jusqu'à environ 20° en moins de 10 ms et ensuite il oscille autour de cette valeur. La même remarque concerne le diamètre de base de la goutte. Sur la base de trois expériences différentes, on déduit que l'angle d'équilibre de l'alliage liquide sur  $\text{Cu}_6\text{Sn}_5$  est d'environ 20°. Cette valeur est inférieure à celle obtenue sur la surface de Cu à la même température.

La Figure 13 présente les détails des oscillations de  $\theta$  (cercles rouges, ligne rouge) et  $d$  (triangles bleus, lignes bleues) au cours de l'étalement de la goutte. Ces oscillations disparaissent pratiquement après environ 1 s (voir Figure 12). Nous avons suivi l'évolution de  $\theta$  avec le temps jusqu'à environ 10 s d'étalement et observé une diminution significative de la hauteur de la goutte ( $h$ ) sans aucun changement notable de son diamètre de base. Ensuite, après environ 16 minutes de contact avec  $\text{Cu}_6\text{Sn}_5$  à 390°C,  $h$  diminue de 0.2 à environ 0.05 mm.

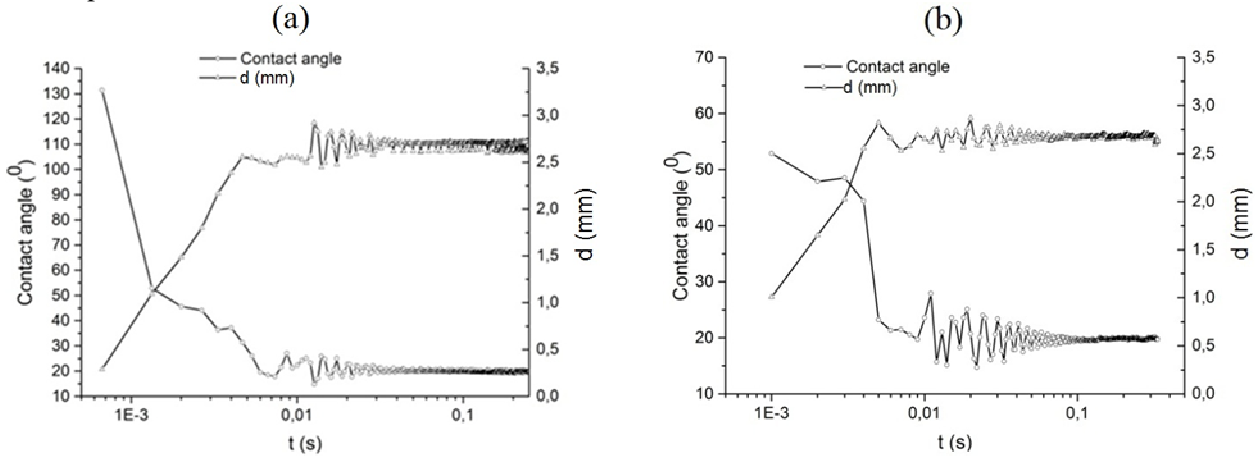


Figure 12. Variation avec le temps de l'angle de contact  $\theta$  et du diamètre de base  $d$  d'une gouttelette de l'alliage Sn-7.8wt.%Cu déposée sur un substrat de  $\text{Cu}_6\text{Sn}_5$  à 390°C après 4 heures de recuit à cette température.

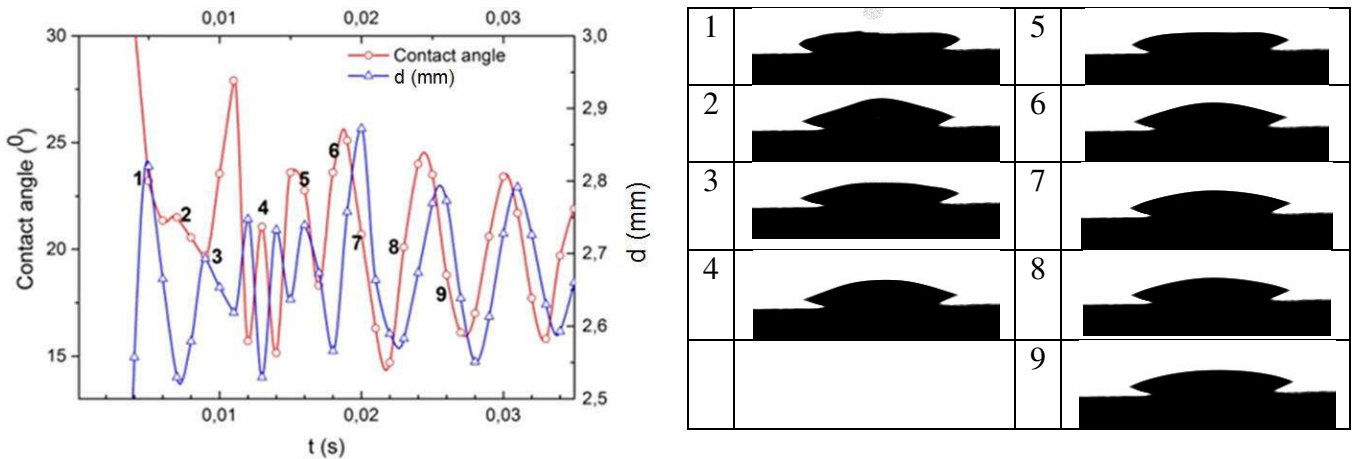


Figure 13. Oscillations de la goutte de l'alliage Sn7.8wt.%Cu déposée sur  $\text{Cu}_6\text{Sn}_5$  à 390°C.

Une analyse MEB détaillée des échantillons a révélé que l'alliage liquide est infiltré dans le substrat (voir Figure 14). Cette figure montre que les "voies d'infiltration" sont les joints de grains du substrat  $\text{Cu}_6\text{Sn}_5$ . L'investigation MEB d'une gouttelette (voir Figure 14) montre qu'il n'y a pas d'étain solidifié situé au-dessus du substrat de  $\text{Cu}_6\text{Sn}_5$ . Seuls des petits précipités de Sn sont observés partout à l'intérieur du substrat  $\text{Cu}_6\text{Sn}_5$  (et non seulement dans les régions au-dessous de la gouttelette) - voir la Figure 14b. L'infiltration complète de la goutte a duré environ 30 minutes.

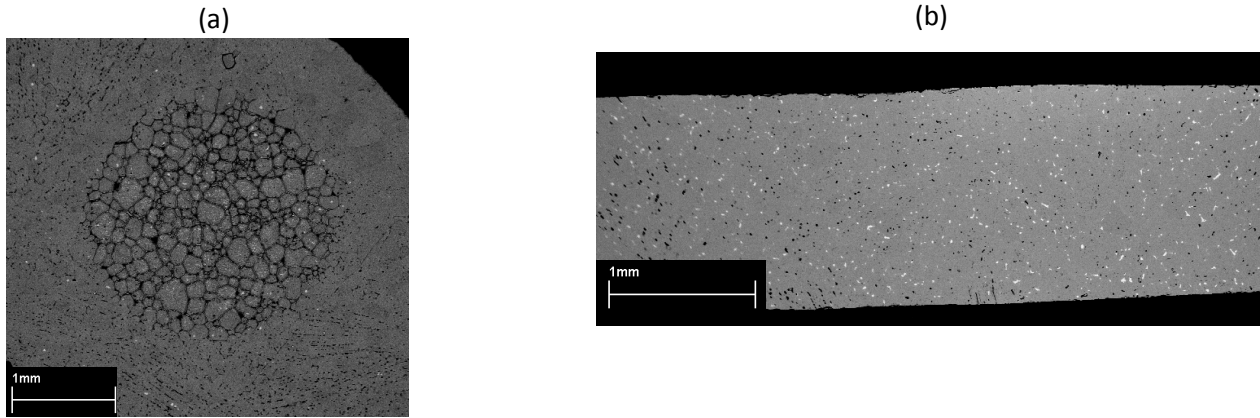


Figure 14. a) Vue de dessus du système goutte de Sn-7.8wt%Cu déposée sur le substrat de  $Cu_6Sn_5$ . Le phénomène d'infiltration est détecté avec le mouillage des joints de grains; b) L'alliage liquide Sn7.8wt%Cu est infiltré totalement dans le substrat et des particules de Sn sont détectées dans  $Cu_6Sn_5$ .

### 4.3) Mouillage de Ag et $Ag_3Sn$ par Sn liquide

La Figures 15a montre que l'étalement de Sn liquide sur un substrat d'Ag à  $400^\circ C$  est très rapide et l'angle de contact diminue jusqu'à environ  $20^\circ$  en moins de 10 ms. Ensuite, la goutte oscille autour de l'angle de contact final ( $\approx 20^\circ$ ) et ces oscillations disparaissent pratiquement après environ 1 s. Comme dans les sections précédentes, nous pouvons conclure ici que l'angle de contact d'équilibre de Sn liquide sur Ag est d'environ  $20^\circ$  à  $40^\circ$ . Cependant, l'angle de contact continue à diminuer, même après 10 ms, mais avec une vitesse d'étalement beaucoup plus faible que celle pour des temps inférieur à 10 ms. L'angle de contact diminue de  $20^\circ$  à  $10^\circ$  après environ 1 s. La vitesse d'étalement moyenne pour  $t < 10$  ms est  $V_1 = (dR/dt) \approx 0.14$  m/s alors que pour  $10$  ms  $< t < 2$  s elle est de plusieurs ordres de grandeur plus faible:  $V_2 = (dR/dt) \approx 3.5 \times 10^{-4}$  m/s, ici  $R = d/2$  représente le rayon de la base de goutte.

La Figures 15b montre que l'étalement de Sn liquide sur  $Ag_3Sn$  à  $400^\circ C$  est très rapide et l'angle de contact diminue jusqu'à environ  $10^\circ$  en moins de 10 ms et ensuite il reste pratiquement constant.

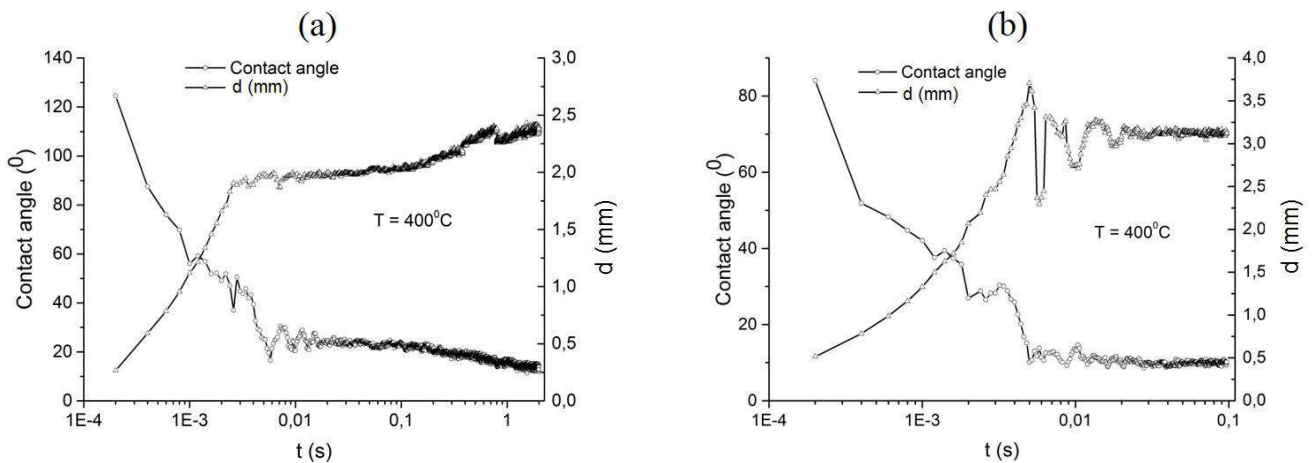


Figure 15. Variation avec le temps de l'angle de contact  $\theta$  et du diamètre de base  $d$  des gouttelettes de Sn déposées sur un substrat de Ag (a) et un substrat de  $Ag_3Sn$  (b) à  $400^\circ C$ .

La Figure 16a, qui présente une image MEB de l'échantillon Ag/Sn (expérience de mouillage à  $400^\circ C$ ), montre qu'une couche réactionnelle continue, identifiée en tant que phase  $Ag_3Sn$ , est formée à l'interface. On voit clairement qu'à la ligne triple, la gouttelette de Sn est située au-dessus de la couche de réaction  $Ag_3Sn$ . De plus, la dissolution du substrat Ag est très prononcée à  $400^\circ C$ . Cette dissolution est mise en évidence par une grande quantité de précipités d' $Ag_3Sn$  dans la goutte formés lors de la solidification, mais aussi par la forme non plane de l'interface liquide/solide.

La Figure 16b présente une image MEB de l'échantillon Ag/ $Ag_3Sn$  (expérience de mouillage à  $400^\circ C$ ). Elle montre qu'il n'y a pas de formation de couche réactionnelle à l'interface et qu'il y a une dissolution du substrat conduisant à la formation de précipités d' $Ag_3Sn$  dans la goutte lors de la solidification.

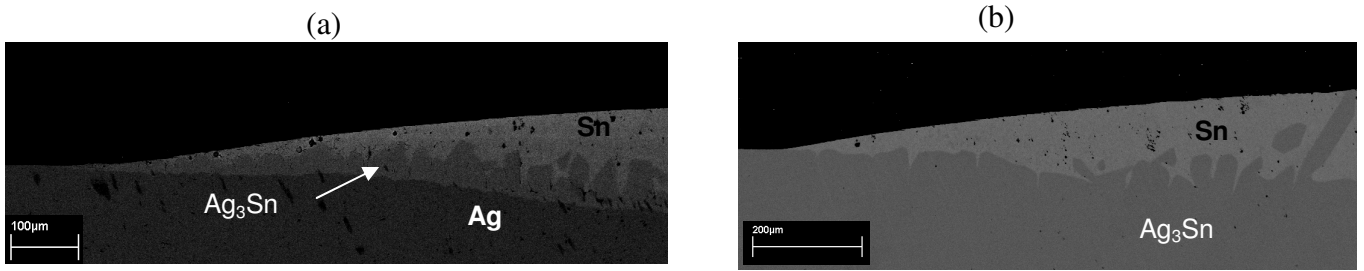


Figure 16. Images MEB des interfaces Sn/Ag (a) et Sn/Ag<sub>3</sub>Sn (b) à 400°C.

Ces résultats nous permettent de proposer le scénario suivant pour le mouillage d'Ag par Sn liquide à 400°C (Figure 17):

L'angle de contact d'équilibre de Sn liquide sur un substrat non réagi d'Ag ( $\theta_{Ag} \approx 20^\circ$ ) est supérieur à son angle de contact d'équilibre sur le substrat Ag<sub>3</sub>Sn ( $\theta_{Ag_3Sn} \approx 10^\circ$ ). Ainsi, quand une gouttelette de Sn liquide est mise en contact avec Ag, elle s'étale avec un angle de contact instantané qui diminue de  $180^\circ$  à l'angle de contact d'équilibre sur le substrat d'Ag non réagi ( $\theta_{Ag} \approx 20^\circ$ ), atteint en moins de 10 ms (étalement non réactif). Ensuite, la réaction interfaciale entre Sn liquide et Ag conduit à la formation, à l'interface, d'une couche continue du composé Ag<sub>3</sub>Sn. Ainsi, après un certain temps, le Sn liquide se trouve sur la couche d'Ag<sub>3</sub>Sn avec un angle de contact  $\theta_{Ag}$  qui est supérieur à son angle d'équilibre sur Ag<sub>3</sub>Sn ( $\theta_{Ag_3Sn}$ ). Par conséquent, le Sn liquide continuera à réagir avec Ag en avant de la ligne triple (LT) liquide-solide-vapeur pour former Ag<sub>3</sub>Sn ce qui conduit à la croissance latérale du composé Ag<sub>3</sub>Sn. Ce couplage entre mouillabilité et réactivité à la ligne triple conduit à l'étalement du liquide jusqu'à ce que l'angle de contact instantané devienne égal à l'angle de contact d'équilibre de Sn liquide sur le produit de réaction Ag<sub>3</sub>Sn (mouillage réactif, voir par exemple [Eustathopoulos\_1999]). Ainsi, la gouttelette Sn liquide s'étale par mouillage réactif de  $\theta_{Ag} \approx 20^\circ$  à  $\theta_{Ag_3Sn} \approx 10^\circ$ .

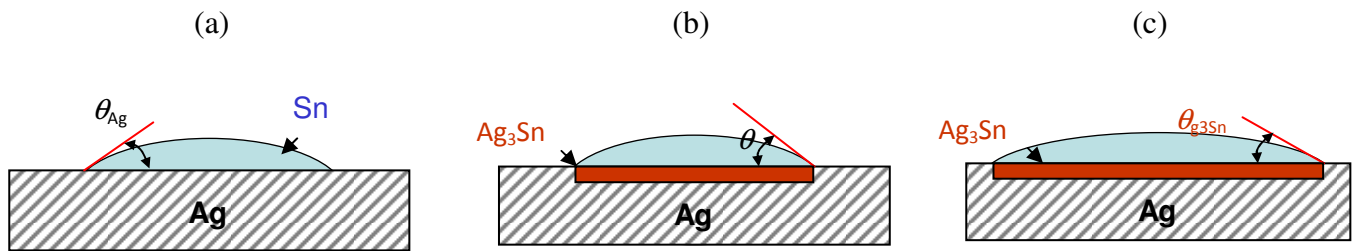


Figure 17. Représentation schématique du mouillage réactif d'un substrat d'Ag par Sn liquide avec la formation, à l'interface, d'une couche réactive d'Ag<sub>3</sub>Sn qui est mieux mouillée que le substrat initial Ag non réagi.

## 5) Etude de la germination aux interfaces Cu/alliage de brasure et dans le volume de la brasure

### 5.1) Etude expérimentale de formation initiale du produit de réaction à l'interface Cu/Sn liquide

Dans cette section, nous présentons une étude expérimentale de la réaction interfaciale entre le Cu solide et un alliage Sn-0.7wt%Cu liquide pendant des durées de contact très courte (de 1 ms à 1 s) à 250°C. Cette étude est réalisée par la mise en œuvre d'un dispositif expérimental d'immersion rapide (conçu et construit dans notre laboratoire) couplée avec des caractérisations MEB-FEG et TEM afin de révéler la séquence de formation des composés intermétalliques à l'interface Cu/Sn liquide ainsi que l'évolution de la morphologie et de l'épaisseur moyenne des produits de réaction lors des premiers instants de la réaction. Ainsi, le but de cette section est de d'apporter une réponse plus précise à la question importante (et ouverte) de la séquence de formation des phases réactives à l'interface Cu/Sn liquide.

Les expériences ont été réalisées principalement dans l'équipement d'immersion rapide décrit dans le paragraphe (voir Figure 5). Une feuille de Cu (10×2×(0.1-0.5) mm) est plongée dans un bain liquide de l'alliage Sn-0.7wt.%Cu à 250°C (désigné **Substrat 1**, voir Figure 18). La profondeur maximale d'immersion est de 6 mm, le temps maximal de contact entre Cu/liquide est d'environ 40 ms dans la zone qui touche la première le bain liquide et d'environ 1 ms dans la zone qui touche à peine le bain liquide.

Dans le cas de l'immersion manuelle, la feuille de Cu de mêmes dimensions que le substrat 1 est immergée sur une profondeur d'environ 2 mm. Après l'immersion, l'interface Cu/Sn a été analysée dans une zone située à une distance de 1.5 mm de la pointe de l'échantillon, ce qui correspond à une durée de réaction d'environ 1 s (noté **Substrat 2**). Le temps d'immersion a été évalué à l'aide un chronomètre.

Le Tableau 1 donne la liste des échantillons analysés dont le temps d'immersion  $t$  varie de ~ 1 ms à 1 s. Les échantillons désignés par les lettres A à F ont été extraits du *même substrat de Cu* immergé dans Sn liquide en utilisant l'équipement d'immersion rapide (*Substrat 1*) tandis que l'échantillon désigné par la lettre Z a été extrait du substrat de Cu plongé manuellement dans Sn liquide (*Substrat 2*).

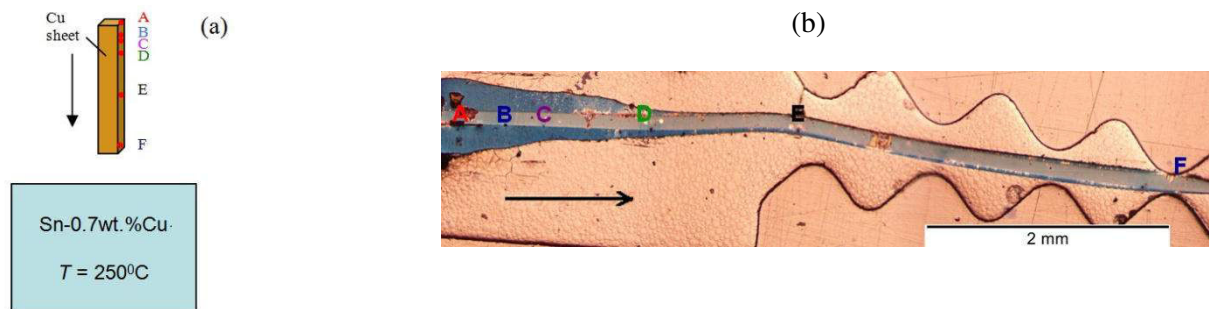


Figure 18. a) Présentation schématique des zones (points) analysés sur le substrat 1. b) Image optique du substrat 1 indiquant l'emplacement des échantillons désignés par les lettre A à F. La direction de l'immersion est indiquée par une flèche.

Echantillon	A	B	C	D	E	F	Z
Intervalle $t$ (ms)	0-1	1-1.5	2-2.5	10-13	15-19	30-38	~1000

Tableau 1. Liste des échantillons caractérisés (A à Z) qui ont subi les expériences d'immersion et les temps de réaction correspondant entre Cu solide et l'alliage Sn-Cu liquide à 250°C.

La réaction entre le Cu solide et alliage Sn-0.7wt.%Cu liquide a été étudiée après des temps de réaction très courts de 1 ms à 1 s par MEB-FEG avec la mise en œuvre de la préparation des échantillons par FIB. Les Figures 19a-e montrent que le produit de réaction consiste d'une seule couche réactionnelle pour les temps de réaction de 1 ms à 40 ms. Sa morphologie se modifie au cours du temps, d'une couche plane d'épaisseur 40 nm (Figure 19a) à une couche réactionnelle en forme d'*aspérités* (scallops) avec une épaisseur moyenne de 1  $\mu$ m. Lorsque le temps de réaction augmente à 1 s, deux couches sont détectées à l'interface (voir Figure 19f). Afin d'identifier la nature des différentes phases contenues dans le produit de réaction nous avons effectué des caractérisations TEM de certains échantillons.

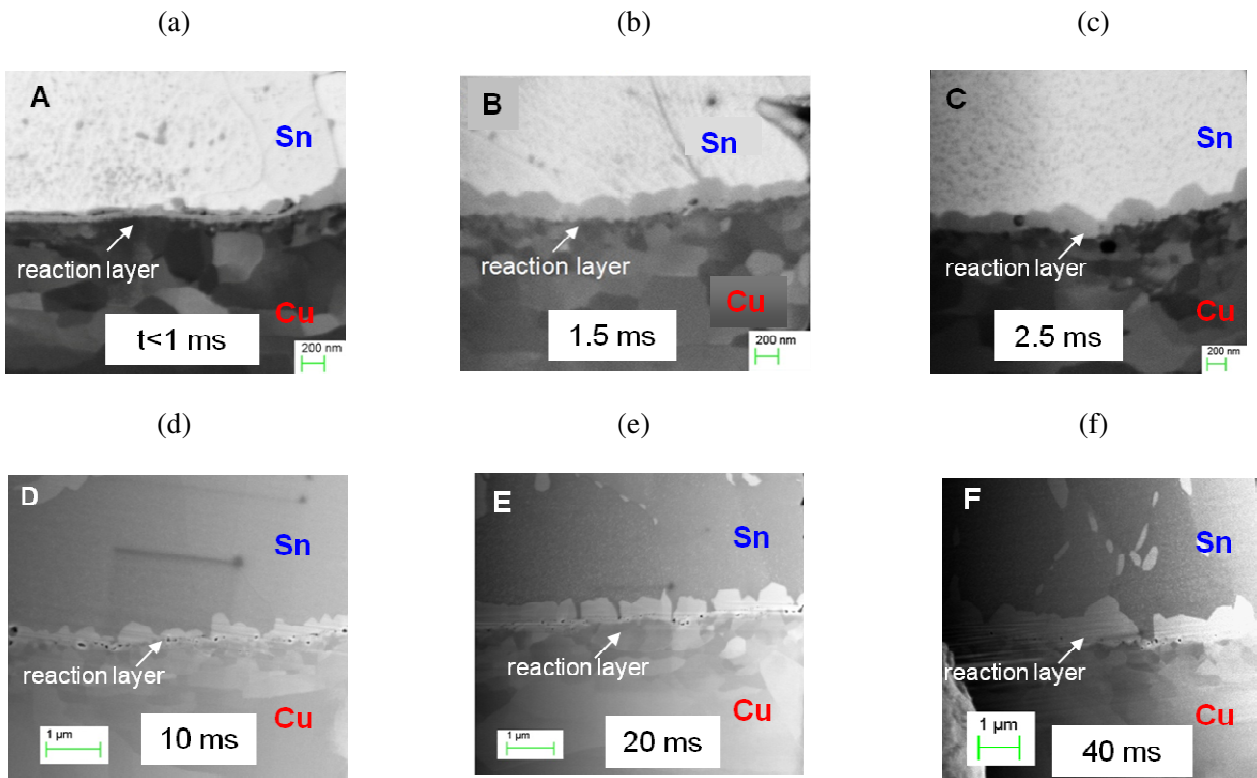


Figure 19. Micrographies MEB-FEG en mode ESB de l'interface Cu/Sn-Cu après interaction à 250°C: a) Ech. A - temps de réaction  $t$  inférieur à 1 ms; b) Ech. B,  $t < 1.5$  ms; c) Ech. D,  $t < 13$  ms; d) Ech. E,  $t < 19$  ms; e) Ech. F,  $t < 38$  ms; f) Ech. Z,  $t < 1$  s.

L'étude de TEM a été réalisée sur trois échantillons A, B et E issus du substrat 1 et sur le l'échantillon Z issu du substrat 2 (voir Figure 20). L'analyse de TEM des échantillons A, B et E (temps de réaction variant de 1 à 19 ms) a démontré, *pour la première fois*, que le produit de réaction à l'interface Cu/alliage liquide est composé de deux couches:

- (i) une couche sous forme de précipités (*free-standing scallops*), de dimensions variant de 50 à 500 nm, avec une structure cristalline correspondant à la structure de base de la phase  $\eta$ -Cu<sub>6</sub>Sn<sub>5</sub>;
- (ii) une couche mince, continue et homogène composée de grains minuscules (de dimension 40 à 100 nm) ayant la même structure que la première couche (phase  $\eta$ ).

L'analyse de l'échantillon Z (temps de réaction d'environ 1 s) a révélé une microstructure très similaire à celle obtenue lors des opérations de refusion (reflow) classique (voir paragraphe 6): une couche mince et homogène composés de grains de la phase  $\epsilon$ -Cu<sub>3</sub>Sn coté Cu et une couche plus épaisse de la phase  $\eta$ -Cu<sub>6</sub>Sn<sub>5</sub> contenant des aspérités (*scallops*) coté Sn.

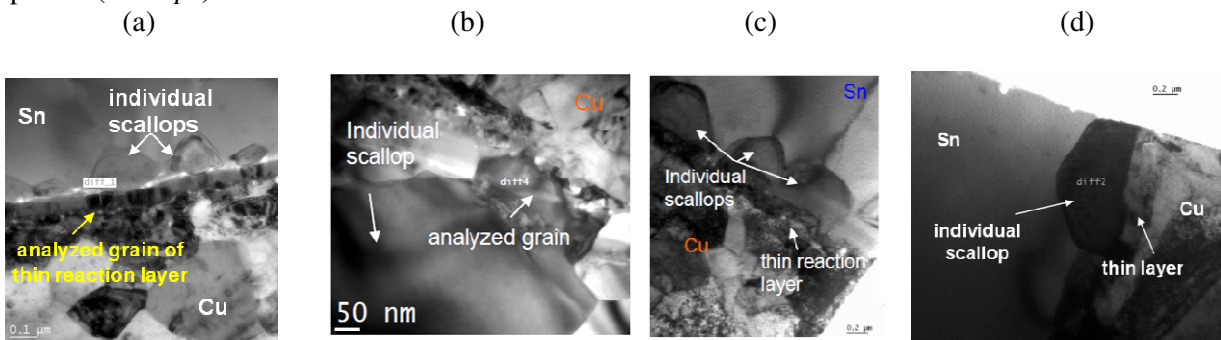


Figure 20. Images de TEM des différentes zones de réaction entre Cu et l'alliage Sn-Cu liquide à 250°C montrant l'évolution des produits de réaction à l'interface en fonction du temps de réaction  $t$ . (a) et (b) Ech. B,  $t < 1,5$  ms, c) Ech. E,  $t < 19$  ms et d) Ech. Z,  $t < 1$  s.

## 5.2) Modélisation de la germination et la croissance de $\text{Cu}_3\text{Sn}$ à l'interface $\text{Cu}/\text{Cu}_6\text{Sn}_5$ du système $\text{Cu}/\text{Cu}_6\text{Sn}_5/\text{Sn}$ liquide

Nous faisons l'hypothèse que des canaux liquides d'épaisseur moyenne  $\delta$  existent entre les grains hémisphériques (rayon  $R$ ) de la phase  $\eta\text{-Cu}_6\text{Sn}_5$  croissante (voir paragraphe 6), comme montré sur la Figure 21a. Nous admettons aussi que la couche de la phase  $\varepsilon\text{-Cu}_3\text{Sn}$  d'une épaisseur constante minimale  $l_{cr}$  se forme par germination et croissance latérale et tente de croître entre la phase  $\eta$  et  $\text{Cu}$ . Il est évident que physiquement l'épaisseur de la couche de la phase  $\varepsilon$  ne peut pas être plus petite que, par exemple, 1 nm (épaisseur critique de germination). Nous souhaitons estimer la taille critique de la phase  $\eta$  ( $R = R^*$ ) au-dessus de laquelle la phase  $\varepsilon$  commence à croître. Une analyse détaillée de ce problème conduit à la valeur de  $R^*$  :

$$R > R^* = \sqrt{\frac{(c^{1/\varepsilon} - c^{1/\eta})(1 - c^\varepsilon)}{1 - c^\eta} \frac{D_{\text{Cu}}^{\text{melt}}}{\tilde{D}^{(\varepsilon)} \Delta c_c^{\text{eq}}} \delta \cdot l_{cr}^\varepsilon}. \quad (4)$$

Après l'application numérique de l'équation (4), avec les paramètres physico-chimique du système  $\text{Cu-Sn}$ , on trace la courbe  $R^*(\delta)$  - voir Figure 21-b. Selon Jong-ook Suh et al. [Suh\_2008] la largeur des canaux liquide a été estimée d'environ 2.5 nm, ce qui donne  $R^* \approx 0.6 \mu\text{m}$ .

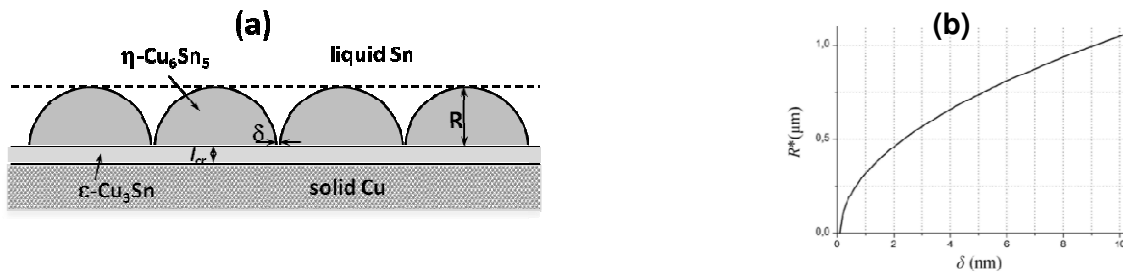


Figure 21. a) Morphologie schématique de la phase  $\eta\text{-Cu}_6\text{Sn}_5$  formée à l'interface  $\text{Cu}/\text{Sn}$  liquide; b) Variation de l'épaisseur critique ( $R^*$ ) de la phase  $\eta$  en fonction de la largeur des canaux liquides ( $\delta$ ) à l'intérieur cette phase.

Ces évaluations prédisent que la couche de la phase  $\varepsilon\text{-Cu}_3\text{Sn}$  peut croître à condition que l'épaisseur moyenne ( $R$ ) de la phase  $\eta\text{-Cu}_6\text{Sn}_5$  soit supérieure à environ  $0.5 \mu\text{m}$ . Ce résultat est en accord avec les résultats expérimentaux obtenus dans la section 5.1. En effet, la formation de la phase  $\varepsilon\text{-Cu}_3\text{Sn}$  a été détectée expérimentalement seulement après un certain temps d'incubation inférieur à 1s quand l'épaisseur de la phase  $\eta\text{-Cu}_6\text{Sn}_5$  atteint  $0.5 \mu\text{m}$  (voir la section 5-1 pour l'échantillon Z).

Pour plus de détails sur ce paragraphe voir la référence [Hodaj\_2013].

## 5.3) Critères de suppression cinétique de croissance latérale des phases intermédiaires, application à $\text{Cu}_3\text{Sn}$

Considérons un système binaire A/B contenant les phases intermédiaires 1 et 2. On suppose que la première phase qui se forme à l'interface est la phase 1. Dans ce paragraphe on examine la cinétique de croissance de la phase 2 sous forme d'îlots tout au long de l'interface 1/B (voir Figure 22). Les hypothèses principales du modèle sont les suivantes:

- 1) La diffusion dans le volume de la phase 2 est négligeable.
- 2) La diffusion des constituants se produit tout au long des interfaces mobiles de l'îlot: les atomes B se déplacent tout au long de l'interface 1/2 et les atomes A se déplacent tout au long d'interface 2/B. Pour des raisons de simplicité, les coefficients de diffusion des atomes A et B tout au long des interfaces concernées seront considérés comme identiques et égaux  $D_{\text{int}}$ .
- 3) La diffusion tout au long de l'interface conduit à une sursaturation locale  $\Delta c(l)$  tout au long de la limite de phase; l'excès de composant B à l'interface 1/2 et l'excès du composant A à l'interface 2/B conduisent à la croissance de la phase 2 et par conséquent au mouvement de deux interfaces selon la direction normale.
- 4) La vitesse de déplacement de l'interface  $U$  est considérée comme proportionnelle à la sursaturation locale sur cette interface:

$$U = k\Delta c \quad (5)$$

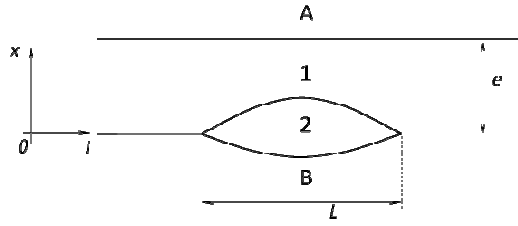


Figure 22. Représentation schématique du système interfacial A/B montrant la formation d'une couche continue du premier composé 1 (d'épaisseur  $\Delta x_1$ ) qui se forme le premier à l'interface et la formation d'un îlot de la phase 2 à l'interface B/I, sous forme de lentille cylindrique.

Sur la base de ces hypothèses, nous établissons l'expression de croissance de la phase 2 : Les îlots de la phase 2 (de largeur  $L$ ) ne peuvent croître que si l'épaisseur de la phase 1 ( $\Delta x_1 = e$ ) est supérieure à une valeur critique donnée par l'équation suivante :

$$L < \sqrt{\frac{4\Delta x_1 \delta D_{\text{int}} \Delta c_2}{D_1 \Delta c_1}}, \quad (6)$$

où  $\Delta c_1$  et  $\Delta c_2$  sont les variations de concentration à travers les phases 1 et 2,  $D_1$  est le coefficient de diffusion dans la phase 1 et  $\delta D_{\text{int}}$  le produit épaisseur du joint de grain x coefficient de diffusion interfacial.

Nous avons appliquée cette approche au système binaire Cu/Sn liquide à  $T = 250^\circ\text{C}$  (phase 1 =  $\text{Cu}_6\text{Sn}_5$  et phase 2 =  $\text{Cu}_3\text{Sn}$ ). Le tableau 2 montre que pour des valeurs élevées de  $\delta D_{\text{int}}$  la germination de la phase  $\epsilon\text{-Cu}_3\text{Sn}$  n'est pas supprimée par la croissance de la phase "vampire"  $\eta\text{-Cu}_6\text{Sn}_5$  tandis que pour des faibles valeurs de  $\delta D_{\text{int}}$  la germination de la phase  $\epsilon$  peut être supprimée par la croissance de la phase  $\eta$ .

$\delta D_{\text{int}}$ ( $\text{m}^2\text{s}^{-1}$ )	$10^{-21}$	$10^{-22}$	$10^{-23}$	$10^{-24}$	$10^{-25}$
$L_\epsilon$ (in nm) for $e_\eta = 1\mu\text{m}$	200	60	20	6	2
$e_\eta$ (in $\mu\text{m}$ ) for $L_\epsilon = 1\text{nm}$	0.025	0.25	2.5	25	250

Tableau 2. Valeurs correspondantes de l'épaisseur de la phase  $\epsilon\text{-Cu}_3\text{Sn}$  ( $L_\epsilon$ ) et de l'épaisseur critique la phase  $\eta\text{-Cu}_6\text{Sn}_5$  ( $e_\eta$ ) déduites de l'équation (6) pour différentes valeurs du paramètre  $\delta D_{\text{int}}$ .

Pour plus de détails sur ce paragraphe voir la référence [Gusak\_2015].

#### 5.4) Spectre de modes de germination lors de la cristallisation de brasures Sn-Cu: résultats expérimentaux et modélisation théorique

Dans cette section, nous analysons expérimentalement et théoriquement différentes possibilités de cristallisation de l'alliage Sn-0.7wt.%Cu et en particulier nous rapportons, pour la première fois, des degrés de surfusion faibles (1-7 K) pour cet alliage. La surfusion de cet alliage est mesurée par des expériences de cycles thermiques effectuées au DSC. Deux conditions différentes sont utilisées pour l'alliage de brasure Sn-0.7wt.%Cu:

(i) Alliage en contact direct avec la phase  $\text{Cu}_6\text{Sn}_5$ , préparé en plongeant pendant 1s une feuille de Cu dans un bain d'alliage liquide Sn-0.7wt.%Cu à  $250^\circ\text{C}$  conduisant à la formation d'une interface alliage/ $\text{Cu}_6\text{Sn}_5$  servant de sites de germination hétérogène de Sn (appelé *échantillon sandwich*).

(ii) Alliage Sn-0.7wt.% Cu sans aucune interface spécialement préparée (appelé *pièce d'alliage*).

Deux cycles thermiques (régimes) ont été appliqués pour chaque type d'échantillon :

(a) Chauffage avec à une vitesse de chauffe  $v = 10 \text{ K}\cdot\text{min}^{-1}$  jusqu'à  $235^\circ\text{C}$  suivi d'un maintien isotherme de 5 minutes, puis refroidissement jusqu'à la température ambiante avec  $v = 1 \text{ K}\cdot\text{min}^{-1}$ . (*régime A* - appelé reflow ou reflow, voir Figure 23).

(b) Chauffage jusqu'à  $200^\circ\text{C}$  avec  $v = 10 \text{ K}\cdot\text{min}^{-1}$  et ensuite avec  $v = 2 \text{ K}\cdot\text{min}^{-1}$  suivi d'un arrêt instantané du chauffage dès qu'on atteint le pic de fusion et enfin refroidissement avec  $v = 10 \text{ K}\cdot\text{min}^{-1}$  (*régime B* - appelé fusion partielle ou pic interrompu, voir la Figure 23).

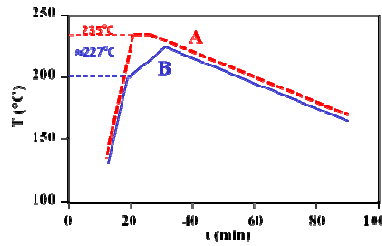


Figure 23. Profils de chauffage et de refroidissement lors des expériences de DSC.

Les Figures 24a et 24b montrent les courbes de chauffage et de refroidissement de dix pièces de l'alliage Sn-0.7wt.% Cu lorsque les cycles thermiques A et B sont appliqués respectivement.

Les Figures 25a et 25b montrent les courbes de chauffage et de refroidissement d'un échantillon type sandwich Cu/Sn-0.7wt%Cu lorsque les cycles thermiques A et B sont respectivement répétés 10 fois.

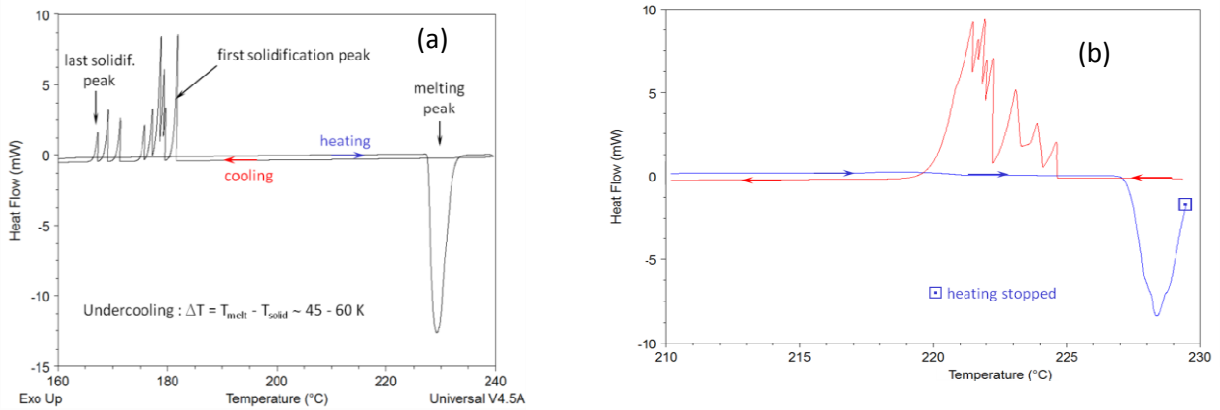


Figure 24. a) Courbes DSC de 10 pièces d'alliage Sn-0.7wt.%Cu montrant les pics de fusion et de solidification a) lorsque le cycle thermique A est appliqué et b) lorsque le cycle thermique B est appliqué.

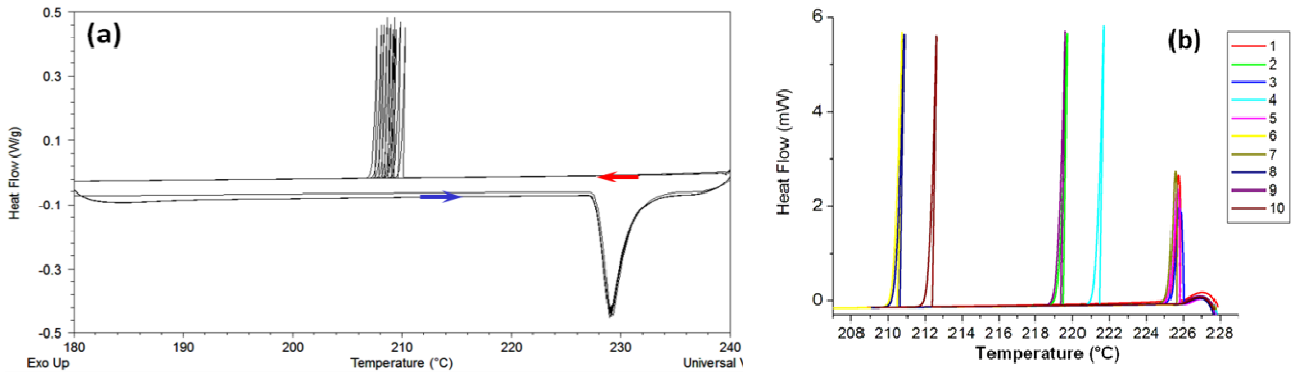


Figure 25. a) Courbes DSC d'échantillon sandwich Sn-0.7wt.%Cu/Cu montrant les pics de fusion et de solidification a) lorsque le régime A est appliqué 10 fois et b) lorsque le régime B est appliqué 10 fois.

Le Tableau 3 résume tous les résultats de DSC concernant les valeurs de surfusion obtenues pour les deux configurations (pièces d'alliage seuls ou configuration sandwich) quand les cycles thermiques A et B sont appliqués. Selon ce tableau, on peut classer les degrés de surfusion d'alliage Sn-0.7wt.%Cu dans trois catégories:

(a) faible (1-7 K); (b) intermédiaire (14-20 K) et (c) haute degrés de surfusion ( $\Delta T = 45-60$  K).

Configuration	Cycle thermique A (refusion)		Cycle thermique B (interrompu)	
	Sn-Cu	Cu/Sn-Cu	Sn-Cu	Cu/Sn-Cu
Surfusion (K)	5-60	7-20	2-7	1-7 (7 times); 14-17 (3 times)

Tableau 3. Valeurs expérimentales de surfusion, obtenues pour les deux configurations (pièces d'alliage seuls et configuration sandwich), lorsque les cycles thermiques A et B sont appliqués.

La réduction significative de la surfusion de l'alliage liquide après le cycle thermique A, de 45-60 K (cas de pièces d'alliage) à 17-20 K (cas d'échantillons sandwich) est probablement due à la présence de  $\text{Cu}_6\text{Sn}_5$  à l'interface brasure liquide/cuivre qui favorise la germination hétérogène grâce à un très bon mouillage de Sn sur  $\text{Cu}_6\text{Sn}_5$ . Cette réduction significative de la surfusion suggère fortement que le maintien de l'alliage Sn-0.7wt.%Cu pendant 5 minutes à 235°C conduit à la dissolution complète des précipités de  $\text{Cu}_6\text{Sn}_5$  au sein de cet alliage.

Afin d'expliquer l'obtention de différentes valeurs de surfusion nous relierons chaque degré de surfusion au type de site de germination hétérogène correspondant. Pour cela, nous faisons une liste (la plus complète possible) des sites possibles de germination afin de trouver des interrelations entre les caractéristiques géométriques de ces sites (courbure, angles) et les valeurs les plus probables de surfusion. Un critère empirique pratique de germination consiste à prendre comme barrière énergétique de germination  $\Delta G^* = 60kT$  [Johnson\_1975].

Afin d'obtenir l'auto-cohérence du système, nous déterminons tous les paramètres nécessaires seulement à partir des expériences de surfusion. A savoir, nous évaluons la tension interfaciale liquide/solide  $\gamma_{sl}$  à partir des valeurs de surfusion expérimentales obtenues dans la littérature lors de la germination homogène de l'étain. Ensuite nous appliquons le même critère  $\Delta G^* = 60kT$  pour la germination hétérogène sur une interface plane liquide/ $\eta$ - $\text{Cu}_6\text{Sn}_5$  et nous évaluons l'angle de contact  $\theta$ . Ensuite, connaissant les valeurs de  $\gamma_{sl}$  et  $\theta$  nous procédons à des modes de germination les plus complexes. En particulier, nous considérons :

(a) la germination d'une calotte sphérique sur une cavité sphérique et (b) la germination d'une calotte sphérique ou d'une calotte cylindrique sur un microsillon (groove ou step).

### a) Germination d'une calotte sphérique sur une cavité sphérique

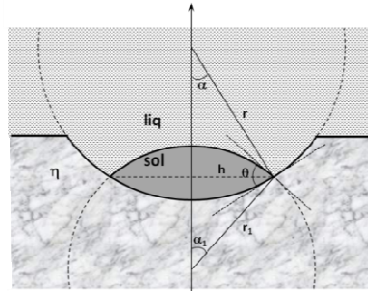


Figure 26. Représentation schématique de la germination d'une calotte sphérique d'étain (rayon  $r_1$ ) sur une cavité sphérique de la phase  $\eta$ - $\text{Cu}_6\text{Sn}_5$  (rayon  $r$ ).

Les calculs standard de germination conduisent à l'expression suivante du rapport des barrières de germination hétérogène ( $\Delta G_{\text{planar}}^*$ ) et homogène ( $\Delta G_{\text{homo}}^*$ ), pour la même température et, par conséquent, pour la même force motrice:

$$\frac{\Delta G_{\text{planar}}^*}{\Delta G_{\text{homo}}^*} = \frac{2-3\cos\theta + \cos^3\theta}{4} \quad (7)$$

L'énergie de Gibbs de formation d'une calotte sphérique (voir figure 26) est exprimée comme suit:

$$\Delta G_{\text{cavity}} = G_{\text{after}} - G_{\text{before}} = -\frac{\Delta g V_S}{\Omega_{\text{at}}} + S_{sl} \gamma_{sl} - S_{s\eta} \gamma_{sl} \cos\theta \quad (8)$$

où  $V_S$  est le volume de la calotte sphérique,  $S_{sl}$  et  $S_{s\eta}$  sont les aires des interfaces solide/liquide et solid/ $\eta$  respectivement.

Après un certains nombre de calculs, on obtient la barrière énergétique de germination de la calotte:

$$\Delta G_{\text{cavity}}^* = \frac{1}{2} \Delta G_{\text{homo}}^* g(\theta, r) \quad (9)$$

avec  $g(r, \theta)$  une fonction dépendante de  $\theta$  et de  $r$ .

Lorsque le rayon du cavité  $r$  tend vers l'infini alors  $\Delta G_{\text{cavity}}^* \rightarrow \Delta G_{\text{planar}}^*$  avec  $\Delta G_{\text{cavity}}^* < \Delta G_{\text{planar}}^*$  :

$$\text{i.e.,} \quad \frac{\Delta G_{\text{cavity}}^*}{\Delta G_{\text{planar}}^*} = \frac{\frac{1}{2} g(\theta, r)}{2-3\cos\theta + \cos^3\theta} \cdot 4 < 1 \quad (10)$$

Cela signifie que la germination sur une interface type cavité de courbure négative est toujours plus facile que celle sur une interface plane. Par conséquent, la surfusion correspondante à la germination hétérogène dans une cavité doit être inférieure à celle sur une interface plane.

Afin d'estimer le rayon de courbure de la cavité conduisant aux faibles valeurs de surfusion obtenues pendant les cycles thermiques B (voir le tableau 3), nous avons résolu numériquement l'équation (10) avec une valeur typique de surfusion  $\Delta T_{cavity} = 5K$ :

$$\Delta G_{cavity}(\theta, r) = 60k(T_m - 5K) \quad (11)$$

Les valeurs de différents paramètres utilisés pour Sn sont : température de fusion  $T_m = 505 K$ , chaleur de fusion  $q = 1.168 \cdot 10^{-20} J \cdot at^{-1}$ , volume atomique  $\Omega_{at} = 2.7 \cdot 10^{-29} m^3$ ,  $\Delta T_{planar} = 20K$  ( $\Delta g = 4.633 \cdot 10^{-22} J \cdot at^{-1}$ ),  $\Delta T_{homo} = 190K$  et  $\gamma_{sl} = 0.074 J \cdot m^{-2}$  et  $\theta = 32^\circ$ .

Avec une valeur typique de surfusion  $\Delta T_{cavity} = 5K$ , dans le cas du régime B, les calculs donnent un rayon de courbure des particules de catalyseur  $r = 11.3 nm$ . Donc, plus le rayon des cavités diminue plus la surfusion  $\Delta T$  devient faible. Nous pouvons donc conclure que, si on obtient des surfusions  $\Delta T > 5K$  la brasure presque fondue ne contient pas de particules de la phase  $\eta-Cu_6Sn_5$  avec des cavités de rayon inférieur à environ 1 nm.

### b) Germination sur un microsillon (step, groove)

Nous considérons deux cas: (i) germe sous forme de calotte sphérique et (ii) de calotte cylindrique.

#### b.1) Germe sous forme de calotte cylindrique

La géométrie de cette configuration est donnée sur la Figure 27. La variation de l'énergie libre de Gibbs pendant la formation du germe est donnée par l'expression :

$$\Delta G_{gb} = -\Delta gn + (\tilde{\gamma} 4\pi r_0^2) n^{2/3}, \quad (12)$$

où  $\tilde{\gamma} = \left(\frac{3}{2\pi}\right)^{1/3} \gamma_{sl} \left(\beta - \frac{\sin\beta}{\sin\alpha} \cos\theta\right)^{1/3}$ ,  $n$  = nombre d'atomes/germe et l'angle  $\beta$  est tel que  $\cos\theta = \sin(\alpha + \beta)$ .

Après un certains nombres de calculs, on obtient une relation entre la surfusion dans le cas de germination hétérogène d'une calotte cylindrique sur un microsillon (noté  $\Delta T_{gb}$ ) et la surfusion dans le cas de la germination homogène ( $\Delta T_{homo}$ ) :

$$\frac{3}{2\pi} \left(\beta - \frac{\sin\beta}{\sin\alpha} \cos\theta\right) = \left(\frac{\Delta T_{gb}}{\Delta T_{homo}}\right)^2 \left(\frac{T_m - \Delta T_{gb}}{T_m - \Delta T_{homo}}\right) \quad (13)$$

La solution de l'équation (13) avec  $\Delta T_{homo} = 190K$ ,  $\Delta T_{gb} = 5K$  et  $\theta = 32^\circ$ , donne  $\alpha = 122.6^\circ$ .

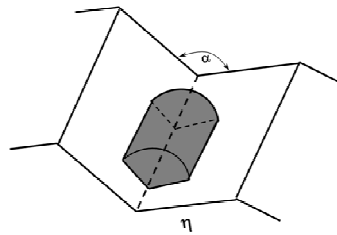


Figure 27. Germe sous forme de calotte cylindrique formé sur un microsillon (step) d'angle  $\alpha$ .

#### b.2) Germe sous forme de calotte sphérique

Ce problème a été déjà traité par Sholl et Fletcher [Sholl\_1970] (voir Figure 28). Ici, la barrière énergétique de germination est notée  $\Delta G_{step}^*$ . Le même type de calculs que ci-dessus, donnent:

$$\begin{aligned} \Delta G_{planar}^* &= \Delta G_F^* = (4\pi\gamma_{sl}^3\Omega_{at}^2 / 3\Delta g^2)K(\theta) \\ \Delta G_{step}^* &= \Delta G_L^* = (4\pi\gamma_{sl}^3\Omega_{at}^2 / 3\Delta g^2)F(\eta, \theta) \end{aligned} \quad (14)$$

$$\frac{\Delta G_{\text{step}}^*}{\Delta G_{\text{planar}}^*} = \frac{F(\eta, \theta)}{K(\theta)} \quad (15)$$

Les facteurs géométriques  $F(\eta, \theta)$  et  $K(\theta)$  sont explicités dans la référence [Sholl\_1970].

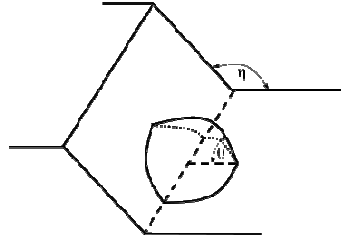


Figure 28. Germe sous forme de calotte sphérique formé sur un microsillon (step) d'angle  $\eta$ .

Afin d'estimer la valeur de l'angle  $\eta$ , nous résolvons numériquement l'équation (15) avec  $\Delta T_{\text{step}} = 5\text{K}$ :

$$\Delta G_{\text{step}}^* = 60k_{\text{B}}(T_{\text{m}} - 5\text{K}) \quad (16)$$

Cela conduit à une valeur de l'angle de désorientation  $\eta$  égale à environ  $\eta = 131.8^\circ$ .

***Ainsi, on peut conclure que les sites de germination favorable sont des cavités avec des rayons de courbure supérieurs à environ 10 nm et/ou des microsillons (steps, grooves) sur la surface des particules solides de la phase  $\eta\text{-Cu}_6\text{Sn}_5$  avec un angle d'ouverture inférieur à environ 120 à 130°.***

Pour plus de détails sur ce paragraphe voir la référence [Liashenko\_2015].

## 6) Cinétique de croissance des couches interfaciales dans le système Cu/Sn

Dans ce domaine traditionnel de croissance aux interfaces réactives solide/liquide, il y a encore besoin de recherche et d'interprétation supplémentaires afin de comprendre les mécanismes opérationnels. Nous présentons dans cette section plusieurs idées nouvelles ainsi que les résultats obtenus.

La première idée est de comparer la cinétique de croissance de la phase  $\text{Cu}_6\text{Sn}_5$  dans un couple normal de diffusion Cu/Sn liquide avec celle dans le couple incrémental  $\text{Cu}_3\text{Sn}/\text{Sn}$  liquide. Le changement dans le taux de croissance peut donner un lien avec le mécanisme de croissance de la phase  $\text{Cu}_6\text{Sn}_5$  (voir section 6.1).

La deuxième idée clé est de comparer la réaction du cuivre avec un alliage eutectique Sn-Cu liquide et avec le même alliage Sn-Cu solide à la même température. Le but de cette étude est de clarifier le rôle de l'état physique de la brasure sur la morphologie et sur la cinétique de croissance de la phase  $\text{Cu}_6\text{Sn}_5$  (voir section 6.2).

### 6.1) Compétition de croissance de couches interfaciales : systèmes Cu/Sn liquide et $\text{Cu}_3\text{Sn}/\text{Sn}$ liquide

#### Résultats expérimentaux:

La figure 29 donne les micrographies MEB du produit de réaction formé aux interfaces Cu/Sn et  $\varepsilon\text{-Cu}_3\text{Sn}/\text{Sn}$  après un maintien à  $250^\circ\text{C}$  pendant 10, 30, 120 et 480 min. Les Figures 29a,c,e,g montrent que quel que soit le temps de maintien à  $250^\circ\text{C}$ , le produit de réaction à l'interface Cu/Sn est constitué de deux couches: une couche en forme de "scallops",  $\eta\text{-Cu}_6\text{Sn}_5$  côté liquide et une couche mince du composé  $\varepsilon\text{-Cu}_3\text{Sn}$  côté Cu. Ceci est en accord avec les résultats expérimentaux rapportés dans les études antérieures, voir par exemple [Tu\_2007, Gagliano\_2003]. Les Figures 29b,d,f,h montrent que quel que soit le temps de maintien à  $250^\circ\text{C}$ , le produit de réaction à l'interface  $\varepsilon\text{-Cu}_3\text{Sn}/\text{liquide}$  est constitué d'une seule couche du composé  $\eta\text{-Cu}_6\text{Sn}_5$  présentant une morphologie en forme de "scallops" très similaire à celle de la couche de  $\eta\text{-Cu}_6\text{Sn}_5$  formée à l'interface Cu/liquide.

Dans la Figure 30, les épaisseurs moyennes de chaque couche ( $e_\eta$  et  $e_\varepsilon$  pour le couple Cu/Sn et  $e'_\eta$  pour le couple  $\text{Cu}_3\text{Sn}/\text{Sn}$ ) sont reportées en fonction de la racine carrée et racine cubique de temps. Ces présentations sont en relation avec le fait que le mécanisme de croissance de phase dans le système Cu/Sn est encore en discussion. En effet, dans la littérature, on trouve des lois de croissance en  $t^{1/2}$  et  $t^{1/3}$ . Par conséquent, nous avons représenté les données de cinétique de croissance de deux manières différentes : (i) épaisseur en fonction de la de la racine carrée du temps de réaction (Figure 30a) et (ii) en fonction de la racine cubique du temps (Figure 30b).

$$e^2 = (k_{1/2})^2 t \quad \text{et} \quad e^3 = (k_{1/3})^3 t \quad (17)$$

A partir de la Figure 30, on déduit les constantes cinétiques de croissance de la phase  $\eta\text{-Cu}_6\text{Sn}_6$  :

(a) pour le couple Cu/Sn :  $k_{1/2} = 4.87 \mu\text{m}\cdot\text{h}^{-1/2}$  et  $k_{1/3} = 6.08 \mu\text{m}\cdot\text{h}^{-1/3}$ ,

(b) pour le couple  $\varepsilon\text{-Cu}_3\text{Sn}/\text{Sn}$  :  $k'_{1/2} = 5.89 \mu\text{m}\cdot\text{h}^{-1/2}$  et  $k'_{1/3} = 7.16 \mu\text{m}\cdot\text{h}^{-1/3}$ .

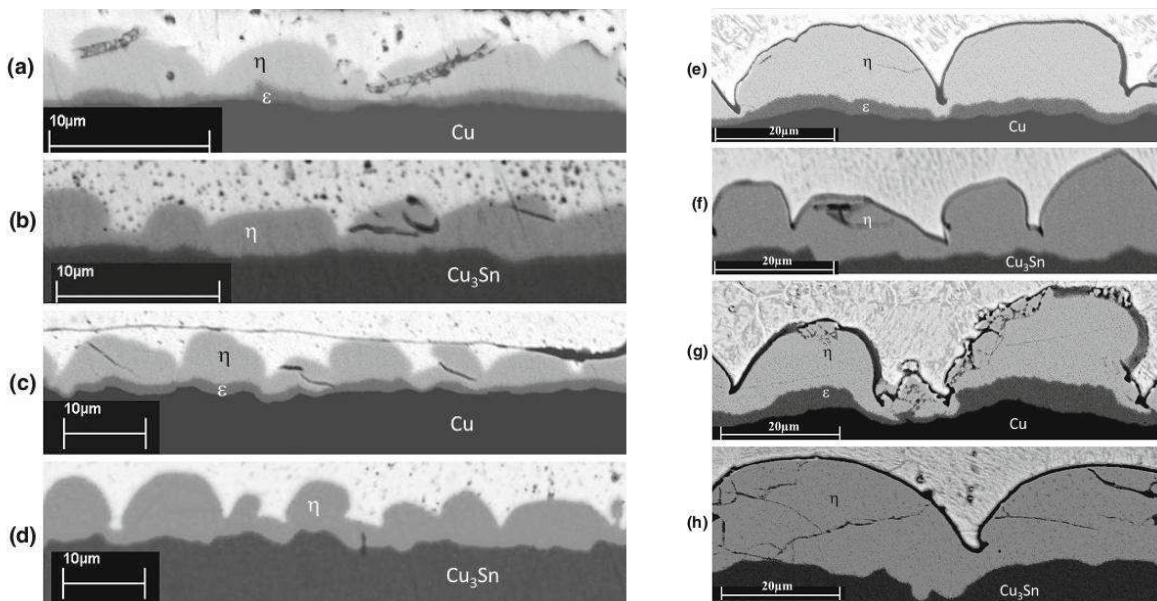


Figure 29. Micrographies MEB des interfaces Cu/Sn et  $\varepsilon\text{-Cu}_3\text{Sn}/\text{Sn}$  après 10 min (a, b), 30 min (c, d), 120 min (e, f) et 480 min (g, h) de réaction à  $250^\circ\text{C}$ .

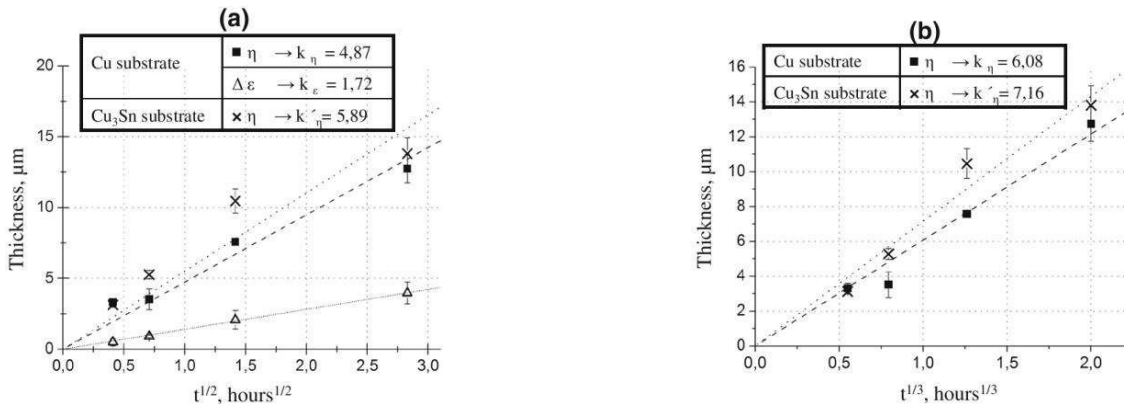


Figure 30. (a) Epaisseur ( $e$ ) des phases  $\eta$ -Cu<sub>6</sub>Sn<sub>5</sub> et  $\varepsilon$ -Cu<sub>3</sub>Sn pour le couple Cu/Sn et épaisseur de la phase  $\eta$  pour le couple Cu<sub>3</sub>Sn/Sn en fonction de la racine carrée du temps. (b) Epaisseur de la phase  $\eta$  pour les couples Cu/Sn et Cu<sub>3</sub>Sn/Sn en fonction de la racine cubique du temps. Les lignes droites représentent les ajustements linéaires des données pour  $e = kt^{1/2}$  et  $e = kt^{1/3}$  respectivement

### Analyse théorique

#### a) Croissance par diffusion en phase solide

Si l'on suppose que la cinétique de croissance est limitée par la diffusion en phase solide, on obtient la loi classique de croissance parabolique :

##### a-1) Couple Cu/Sn : croissance simultanée des phases $\eta$ et $\varepsilon$

En considérant les bilans de masse aux interfaces réactives, on obtient:

$$k_{\varepsilon} \approx 1.21 \text{ et } k_{\eta} \approx 1.06\sqrt{2D_{\eta}\Delta C_{\eta}}.$$

$D_{\eta}$  et  $\Delta C_{\eta}$  sont le coefficient de diffusion et la variation de concentration de Cu dans la phase  $\eta$ .

##### a-2) Couple incrémental $\varepsilon$ -Cu<sub>3</sub>Sn/Sn : une seule phase formée (phase $\eta$ )

En considérant les bilans de masse aux interfaces réactives, on obtient:

$$k'_{\eta} \equiv k'_{\eta/\text{Sn}} - k'_{\eta/\varepsilon} = \sqrt{\frac{C_{\varepsilon}}{C_{\eta}(C_{\varepsilon} - C_{\eta})} 2D_{\eta}\Delta C_{\eta}} \approx 2.6\sqrt{2D_{\eta}\Delta C_{\eta}} \quad (18)$$

#### b) Croissance par diffusion en phase liquide à travers des canaux liquide dans la phase $\eta$

Dans certaines études on montre que, la cinétique de croissance de la phase  $\eta$ -Cu<sub>6</sub>Sn<sub>5</sub> est plus rapide que celle de la phase  $\varepsilon$ -Cu<sub>3</sub>Sn car la croissance de  $\eta$ -Cu<sub>6</sub>Sn<sub>5</sub> a lieu par diffusion à l'état liquide au travers des canaux liquides nanométrique dans la phase  $\eta$  qui conduit à une vitesse de croissance rapide de cette phase [Kim\_1996]. Afin d'évaluer la largeur moyenne de ces canaux (notée  $\delta$ ), nous appliquons une version simplifiée du modèle FDR développé par Gusak et al. [Gusak\_2002].

##### b-1) Couple Cu/Sn liquide

La relation finale de l'évolution temporelle de la hauteur moyenne des "scallop" de  $\eta$ -Cu<sub>6</sub>Sn<sub>5</sub> est donné par :

$$H^{\text{at Cu substrate}} = \left( \frac{3\delta D_{\text{Cu}}^{\text{melt}}}{C_{\eta}(1 - C_{\eta})} (C^{l/\varepsilon} - C^{l/\eta}) \right)^{1/3} t^{1/3} = (k_{1/3})_{\text{calc}} t^{1/3} \quad (19a)$$

$(k_{1/3})_{\text{calc}}$  est la constante cinétique de croissance de la phase  $\eta$  dans le cas où le Cu diffuse dans les canaux liquides nanométriques aux joints de grains de cette phase.  $C_{\eta}$  est la concentration de la phase  $\eta$ .  $C^{l/\varepsilon}$  et  $C^{l/\eta}$  sont les concentrations d'équilibre aux interfaces liquide/ $\varepsilon$  et liquide/ $\eta$  respectivement.

##### b-2) Couple Cu<sub>3</sub>Sn/Sn liquide

Dans ce cas de croissance de la seule phase  $\eta$ , on peut montrer que la hauteur moyenne des "scallop" de la phase  $\eta$ -Cu<sub>6</sub>Sn<sub>5</sub> est donné par l'expression:

$$H^{\text{incremental}} = \left( \frac{C_{\varepsilon}}{C_{\eta}(C_{\varepsilon} - C_{\eta})} 3\delta D_{\text{Cu}}^{\text{melt}} (C^{l/\varepsilon} - C^{l/\eta}) \right)^{1/3} t^{1/3} = (k'_{1/3})_{\text{calc}} t^{1/3} \quad (19b)$$

Ainsi, à partir des Eqs. (19a) et (19b), le rapport entre les valeurs moyennes de H (mais aussi entre les épaisseurs moyennes de la phase  $\eta$ ) dans les deux configurations b-1 et b-2, devient:

$$\frac{H^{incremental}}{H^{at\ Cu\ substrate}} = \frac{(k'_{1/3})_{calc}}{(k_{1/3})_{calc}} = \left( \frac{(1-C_\eta)C_\varepsilon}{(C_\varepsilon - C_\eta)} \right)^{1/3} \approx 1.19 \quad (20)$$

### Comparaison entre théorie et expérience

La valeur expérimentale du rapport des constantes cinétiques dans le cas de la loi cubique de croissance,  $(k'_{1/3}/k_{1/3})_{exp} \approx 1.18$ , est pratiquement la même que celle obtenue par les prédictions théoriques  $(k'_{1/3}/k_{1/3})_{calc} \approx 1.19$ . En plus, l'Equation (19b) permet d'estimer le produit du coefficient de diffusion du cuivre  $D_{Cu}^{melt}$  avec la largeur des canaux liquides ( $\delta$ ) dans la phase  $\eta$  :

$$\delta D_{Cu}^{melt} = \frac{(k'_{1/3})_{calc}^3}{3} \frac{C_\eta (C_\varepsilon - C_\eta)}{C_\varepsilon (C_\varepsilon^{1/\varepsilon} - C_\eta^{1/\eta})} \quad (21)$$

Avec les données expérimentales pour le couple for  $\varepsilon$ -Cu<sub>3</sub>Sn/Sn liquide:  $(k'_{1/3})_{exp} \approx 7.2 \mu\text{m}\cdot\text{h}^{-1/3} \approx 4.7 \times 10^{-7} \text{m}\cdot\text{s}^{-1/3}$ , à partir de l'Equation (21), on peut estimer le produit  $\delta D_{Cu}^{melt} \approx 8 \times 10^{-19} \text{m}^3\cdot\text{s}^{-1}$ . Connaissant le coefficient de diffusion du cuivre dans l'étain liquide  $D_{Cu}^{melt} \approx 10^{-9} \text{m}^2\cdot\text{s}^{-1}$ , on peut estimer la largeur des canaux liquides d'environ 1 nm, valeur proche de celle estimée par Jong-ook Suh et al [Suh\_2008] pour les alliages base Sn ( $\approx 2.5$  nm).

### 6.2) Différences entre les réactions interfaciales dans les couples Cu/Sn solide et Cu/Sn liquide métastable à la même température: Rôle de l'état physique de Sn

L'objectif principal de cette section est d'étudier les différences entre les réactions interfaciales Cu/Sn solide et Cu/Sn liquide métastable à la même température afin de déterminer le rôle de l'état liquide sur la cinétique de croissance des produits de réaction ainsi que sur leur morphologie. Dans ce but, nous avons réalisé des expériences spécifiques de DSC afin d'étudier la réactivité interfaciale d'une part entre un substrat de Cu et l'alliage eutectique Sn-0.7wt.% Cu liquide métastable et d'autre part entre Cu et l'alliage solide Sn-0.7wt.%Cu à la même température de 222°C. (La température de fusion de cet alliage est de 227°C). Ensuite, nous comparons et analysons les résultats expérimentaux afin d'effectuer une analyse théorique de la cinétique de croissance de la phase de  $\eta$ -Cu<sub>6</sub>Sn<sub>5</sub> dans les deux configurations.

#### Résultats expérimentaux

Les échantillons utilisés sont des couples Cu/alliage Sn-0.7Cu réalisés par immersion rapide (< 1s de contact) de feuilles de Cu dans un bain d'alliage Sn-0.7Cu liquide à 250°C.

Deux cycles thermiques (régimes) ont été appliqués aux échantillons dans un DSC:

(i) Régime I, réactivité à l'état solide - les échantillons ont été chauffés jusqu'à 222°C et recuit à cette température pendant des temps de maintien variant de 1 h à 32 h.

(ii) Régime II, réactivité à l'état liquide (étude de la réaction interfaciale entre Cu et l'alliage liquide métastable à 222°C). Les échantillons ont été tout d'abord fondus à 235°C et ensuite refroidi jusqu'à 222°C dans un état métastable et maintenus à 222°C pendant un temps donné variant de 1 h à 32 h (voir Figure 31).

La Figure 32 donne des micrographies MEB du produit de réaction formé aux interfaces Cu/alliage liquide métastable et Cu/alliage solide pour les échantillons maintenus à 222°C pendant 1 h, 8 h, 16 h et 32h en utilisant des cycles thermiques correspondant aux régimes I et II respectivement. Cette Figure montre que quelque soit le temps de maintien à 222°C, le produit de réaction à l'interface Cu/liquide métastable se compose de deux couches: d'une couche épaisse du composé  $\eta$ -Cu<sub>6</sub>Sn<sub>5</sub> sous forme de "scallops" côté alliage et d'une couche fine et continue du composé  $\varepsilon$ -Cu<sub>3</sub>Sn côté Cu.

Dans la figure 33, l'épaisseur moyenne de chaque couche ( $e_\eta$  et  $e_\varepsilon$ ) pour le couple Cu/alliage liquide et  $e'_\eta$  et  $e'_\varepsilon$  pour le couple Cu/alliage solide est tracée en fonction du temps ainsi qu'en fonction de la racine carrée et la racine cubique de temps. Ces courbes montrent la valeur de l'exposant n ( $e_i \sim k_i t^n$ ) se trouve entre 1/2 et 1/3. La variation de l'épaisseur des couches de réaction est alors représentée par les équations suivantes:

$$\begin{aligned} e_i^2 &= e_{0,i}^2 + (k_i)^2 t && \text{pour la couche } i \text{ (} i = \eta \text{ ou } \varepsilon \text{) dans le régimes I et II} \\ e_\eta^3 &= e_{0,\eta}^3 + (k_\eta^*)^3 t && \text{seulement pour la couche } \eta \text{ dans le régime II} \end{aligned} \quad (22)$$

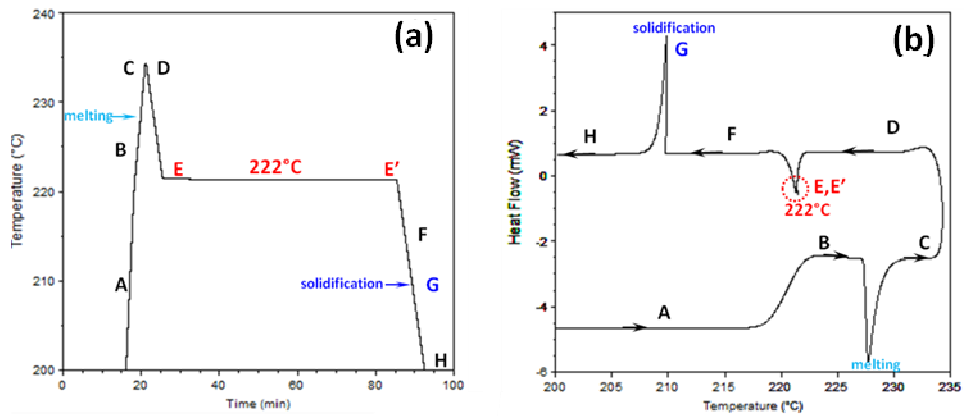


Figure 31. Courbes DSC obtenus pendant le cycle thermique II : maintien isotherme à 222°C de l'alliage liquide métastable Sn-0.7wt%Cu. (a) Courbe température-temps, (b) courbe flux de chaleur-température.

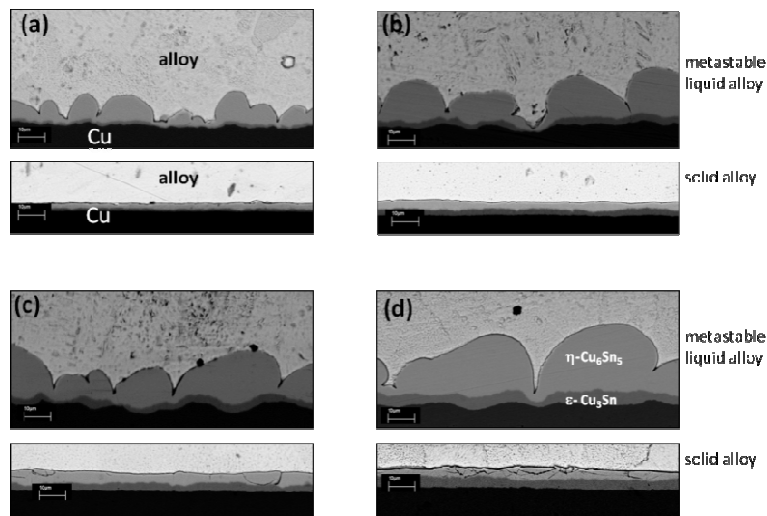


Figure 32. Micrographies MEB du produit de réaction formé aux interfaces Cu/alliage Sn-0.7wt%Cu après un maintien isotherme à 222°C pendant 1 h (a), 8h (b), 16 h (c) et 32h (d). Cycles thermiques utilisés : régime I pour l'alliage solide et régime II pour l'alliage liquide..

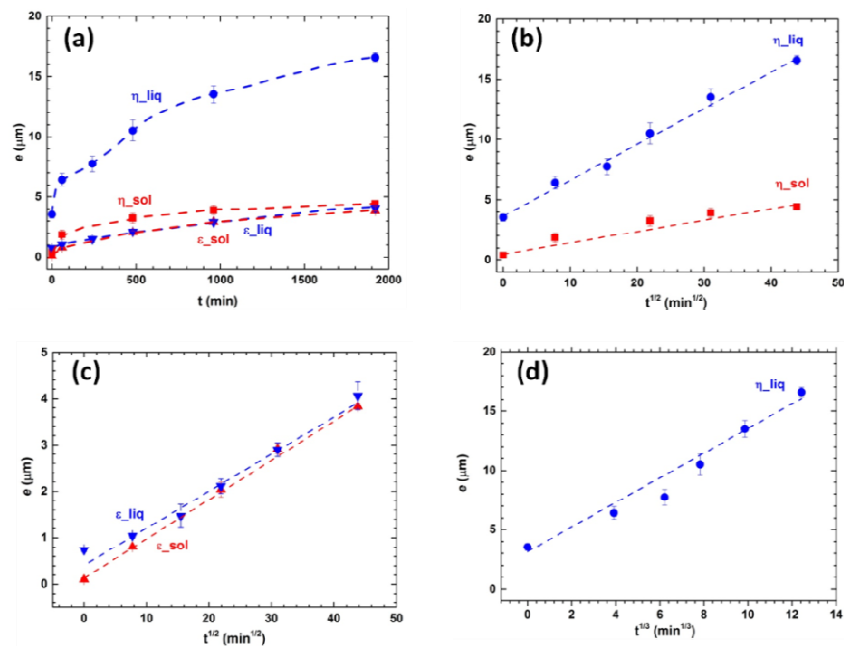


Figure 33. Épaisseur moyenne des couches des phases  $\epsilon$ -Cu<sub>3</sub>Sn et  $\eta$ -Cu<sub>6</sub>Sn<sub>5</sub> formées aux interfaces Cu/alliage Sn-Cu liquide métastable et Cu/alliage Sn-Cu solide en fonction du temps de réaction (a), de la racine carrée (b, c) et de la racine cubique (d) du temps de réaction à 222°C.

A partir de la Figure 33, on peut déduire les constants cinétique de croissance des couches  $\eta$  et  $\varepsilon$ :

**a) Pour le couple Cu/alliage liquide métastable:**

$$\begin{aligned} k_{\eta} &= 0.302 \pm 0.009 \mu\text{m} \cdot \text{min}^{-1/2} \text{ (adj. } R^2 = 99.6\%) , \\ k_{\varepsilon} &= 0.0783 \pm 0.0079 \text{ (adj. } R^2 = 93.1\%) \mu\text{m} \cdot \text{min}^{-1/2} \\ k_{\eta}^* &= 1.371 \pm 0.071 \mu\text{m} \cdot \text{min}^{-1/3} \text{ (adj. } R^2 = 97.7\%) \end{aligned} \quad (23)$$

Ces valeurs sont en accord avec celles obtenues par Liang et al. [Liang\_2006] pour les couples Cu/alliage Sn-3.5wt.%Ag liquide et Cu/alliage Sn-3.5wt.%Ag-0.7wt.%Cu liquide à 225°C, ainsi qu'avec celles obtenues par extrapolation à 222°C à partir des résultats expérimentaux rapportés par Gagliano et al [Gagliano\_2003] pour le couple Cu/Sn liquide pour des températures comprises entre 250 et 325°C.

**b) Pour le couple Cu/alliage solide:**

$$\begin{aligned} k'_{\eta} &= 0.0785 \pm 0.0084 \mu\text{m} \cdot \text{min}^{-1/2} \text{ (adj. } R^2 = 96.9\%) \\ k'_{\varepsilon} &= 0.0885 \pm 0.0008 \mu\text{m} \cdot \text{min}^{-1/2} \text{ (adj. } R^2 = 99.9\%) \end{aligned} \quad (24)$$

Ces valeurs sont en accord, à 20% près, avec celles obtenues par Onishi et al. [Onishi\_1975] et Paul et al. [Paul\_2004] pour les couples Cu/Sn solides à 220°C et 215°C respectivement. Noter que dans le cas du couple Cu/liquide, il est pas facile de déterminer d'une manière claire et certaine laquelle des lois de croissance donnée par Eqs. (24) correspond au mieux à la cinétique de croissance de la couche  $\eta$ -Cu<sub>6</sub>Sn<sub>6</sub>. Cependant, il semble que la loi de croissance parabolique correspond mieux aux résultats expérimentaux (Figure 33b). Ainsi, dans ce qui suit, la loi de croissance parabolique a été choisie. A partir des équations (23) et (24) on obtient:

$$\frac{k_{\eta}}{k_{\varepsilon}} \approx 3.9 \quad \frac{k'_{\eta}}{k'_{\varepsilon}} \approx 0.9 \quad (25a)$$

$$\frac{k_{\eta}}{k'_{\eta}} \approx 3.8 \quad \frac{k_{\varepsilon}}{k'_{\varepsilon}} \approx 0.9 \quad (25b)$$

Bien que les expériences Cu/alliage liquide et Cu/alliage solide ont été effectuées à la même température et avec un alliage de même composition, deux différences importantes peuvent être constatées à partir des Figures 32 et 33:

(i) La morphologie de la couche  $\eta$ -Cu<sub>6</sub>Sn<sub>5</sub>: épaisseur non uniforme et morphologie du type "scallops" pour l'alliage liquide et épaisseur uniforme pour l'alliage solide.

(ii) La cinétique de croissance de la couche  $\eta$ -Cu<sub>6</sub>Sn<sub>5</sub> dans le couple Cu/liquide est beaucoup plus rapide que dans le couple Cu/solide: après 32 heures de réaction, l'épaisseur moyenne de la couche de  $\eta$ -Cu<sub>6</sub>Sn<sub>5</sub> dans le premier cas est environ quatre fois supérieure à celle obtenue dans le second cas.

La grande différence dans la cinétique de croissance et la morphologie de la couche de la phase  $\eta$ -Cu<sub>6</sub>Sn<sub>5</sub>, quand le couple Cu/alliage liquide métastable est remplacé par le couple Cu/alliage souligne l'existence d'un mécanisme de croissance particulier. En effet, si l'on suppose que la cinétique de croissance des couches de réaction est limitée dans les deux cas par la diffusion en phase solide, une explication possible de cette différence sur la base des facteurs thermodynamiques n'est pas valable ici car la force motrice de formation de la phase  $\eta$  est pratiquement la même dans les deux cas.

### **Modélisation de la croissance de la phase $\eta$ -Cu<sub>6</sub>Sn<sub>5</sub> à l'interface Cu/alliage liquide**

Il est très intéressant de noter que la plupart des bouts des sillons dans la phase  $\eta$ -Cu<sub>6</sub>Sn<sub>5</sub>, détectées par SEM, sont situés à une distance ( $h$ ) d'environ 3 à 5  $\mu\text{m}$  à partir de la couche de  $\varepsilon$ -Cu<sub>3</sub>Sn et cette distance reste pratiquement constante quelle que soit le temps de réaction (voir Figure 32). Dans ce qui suit nous proposons deux scénarios concernant la configuration géométrique des canaux liquides dans la couche de la phase  $\eta$ -Cu<sub>6</sub>Sn<sub>5</sub>, comme indiqué schématiquement sur la Figure 34:

**(a) Tous les joint de grains de  $\eta$ -Cu<sub>6</sub>Sn<sub>5</sub> sont pénétrés de la même façon** (Figure 34b).

En première approximation, on suppose que des canaux liquides, de largeur moyenne  $\delta$ , existent entre les scallops hémisphériques (de rayon  $R$ ) de phase  $\eta$ -Cu<sub>6</sub>Sn<sub>5</sub> et que tous les scallops ont la même taille  $a = R = H$  (voir Figure 34a). Les canaux nanométriques qui relient les extrémités des sillons avec la couche de granulaire fine de  $\varepsilon$ -Cu<sub>3</sub>Sn ont une **longueur moyenne  $h$** .

**(b) Seulement les jonctions triples (lignes triples) sont pénétrées de la même façon**, les canaux liquides sont considérés cylindriques avec un rayon moyen noté  $r$ .

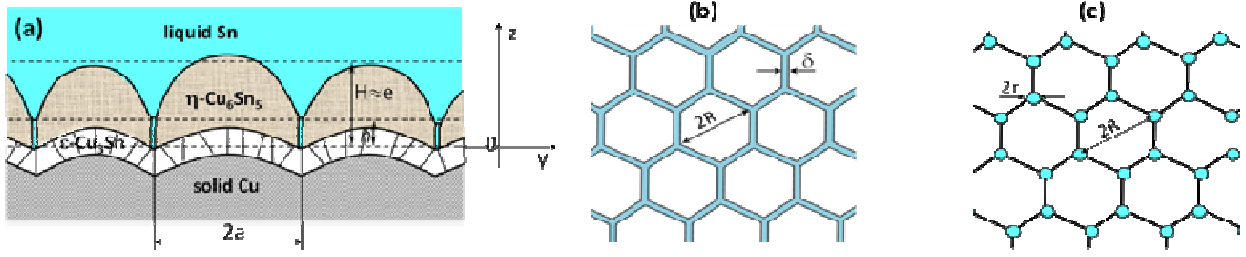


Figure 34. Système modèle: (a) Morphologie schématique de la phase  $\eta\text{-Cu}_6\text{Sn}_5$  formée à l'interface Cu/Sn liquide ( $a = R = H$ ). (b) Représentation schématique de formation de canaux liquides (b) de largeur  $\delta$  entre les scallops hémisphériques de  $\eta\text{-Cu}_6\text{Sn}_5$  et (c) cylindriques de rayon  $r$  formés au niveau des lignes triples.

Après quelques calculs on obtient les résultats suivants selon le cas:

**a) Tous les joints de grains de  $\eta\text{-Cu}_6\text{Sn}_5$  sont pénétrés de la même façon** (Figure 34b) :

$$\frac{\delta}{h} = \frac{5}{8} \frac{k_{\eta}^2}{D_{\text{Cu}}^{\text{liq}}(c^{\text{le}} - c^{\text{ln}})} \quad (26)$$

Il est très intéressant de noter que, pour un alliage Sn-liquide donné, l'Eq. (26) indique clairement que le rapport  $\delta h$  ne dépend que de la température, comme cela est le cas pour  $D_{\text{Cu}}^{\text{liq}}$ ,  $k_{\eta}$ ,  $c^{\text{le}}$  et  $c^{\text{ln}}$ , donc  $\delta h = f_1(T)$ .

**b) Seulement les jonctions triples (lignes triples) sont pénétrées de la même façon** (Figure 34c) :

$$\frac{r^2}{h} = \frac{5}{16} \frac{k_{\eta}^{*3}}{D_{\text{Cu}}^{\text{liq}}(c^{\text{le}} - c^{\text{ln}})} \quad (27)$$

On remarque que, comme dans le cas précédent, pour un alliage liquide donné, l'Eq. (27) indique clairement que le rapport  $r^2/h$  ne dépend que de la température,  $r^2/h = f_2(T)$ .

Nous utilisons les Eqs. (26) et (27) pour estimer l'épaisseur des canaux liquides  $\delta$  dans le cas (a) et le rayon  $r$  des canaux liquides cylindriques dans le cas (b). Ces applications sont effectuées pour  $T = 222^\circ\text{C}$ , mais aussi pour  $T = 250^\circ\text{C}$  en utilisant des données expérimentales de  $k_{\eta}^2$  et  $k_{\eta}^{*3}$  à  $250^\circ\text{C}$  récemment publié [Liashenko\_2014].

La différence de concentrations en cuivre dans l'alliage liquide en équilibre avec  $\varepsilon\text{-Cu}_3\text{Sn}$  et avec  $\eta\text{-Cu}_6\text{Sn}_5$  ( $c^{\text{le}} - c^{\text{ln}}$ ) est obtenue à partir de données thermodynamiques [Dinsdale\_1991, Song\_2004, Hodaj\_2013]. A partir des Eqs. (26) et (27) et des données expérimentales et calculées, on peut calculer les valeurs des rapports  $\delta h$  et  $r^2/h$ . En supposant que la longueur des canaux liquides ( $h$ ) est d'environ  $5 \mu\text{m}$ , on peut estimer la largeur moyenne ( $\delta$ ) de canaux dans le cas (a) et le rayon moyen ( $r$ ) des canaux cylindriques dans le cas (b):

- à  $T = 222^\circ\text{C}$ :  $\delta \approx 0.7 \text{ nm}$ ,  $r \approx 100 \text{ nm}$
- à  $T = 250^\circ\text{C}$ :  $\delta \approx 0.8 \text{ nm}$ ,  $r \approx 60 \text{ nm}$

Noter qu'ici, la valeur calculée de  $\delta$  est sous-estimée car les canaux liquides nanométriques ne sont pas nécessaires formés entre tous les grains (scallop) de  $\text{Cu}_6\text{Sn}_5$  comme il est supposé dans notre modèle.

Notons enfin que les valeurs estimées du rayon moyen ( $r$ ) des canaux cylindriques dans le cas (b) (quelques dizaines de nm) sont suffisamment élevées pour être détecté par TEM, la principale difficulté étant d'obtenir des lamelles de telle sorte qu'elles contiennent la ligne de jonction triple formée par les grains de la phase  $\eta \text{ Cu}_6\text{Sn}_5$ .

## 7) Conclusions générales

Il existe de nombreux phénomènes qui interviennent dans le processus de brasage, tels que: le mouillage des parties solides par l'alliage liquide et les interactions interfaciales solide/liquide (dissolution, diffusion, germination et croissance des produits d'interface) lorsque la brasure est à l'état liquide, ainsi que la surfusion, la germination et la solidification de l'alliage de brasage pendant le refroidissement du système à la température ambiante.

L'étude fondamentale de ces phénomènes dans le système Cu/alliages liquides base Sn, qui est le système le plus utilisé lors du brasage en électronique, devient crucial, en particulier avec la diminution significative des dimensions des joints de brasure à l'échelle du micromètre.

L'objectif principal des travaux de cette thèse était de répondre à certaines des questions fondamentales en relation avec les phénomènes de mouillage, de germination et de croissance de phases intermétalliques aux interfaces réactives qui interviennent dans le processus de brasage lors de l'assemblage en électronique.

***Les principales conclusions de cette étude sur (i) le mouillage, (ii) la germination et (iii) la cinétique de croissance dans les processus de brasage peuvent être résumées comme suit:***

### ***(i) Mouillage de Cu, Ag et de leurs intermétalliques avec Sn:***

La mouillabilité des substrats métalliques Cu et Ag et de leurs principaux intermétalliques avec Sn ( $\text{Cu}_3\text{Sn}$ ,  $\text{Cu}_6\text{Sn}_5$  et  $\text{Ag}_3\text{Sn}$ ) par Sn, l'alliage Sn-Cu et Pb liquide a été étudiée en utilisant la technique de la goutte déposée dans un four sous vide secondaire et suivie d'une caméra rapide pour l'enregistrement du processus d'étalement.

Cette étude a permis de démontrer que, dans la gamme de température 300-600°C, la première étape d'étalement sur Cu est très rapide (étalement non réactif en moins de 10 ms), la vitesse d'étalement étant d'environ 0.25 m/s et que la deuxième étape (étalement réactif) est beaucoup plus lente. Au cours de la première étape, la cinétique d'étalement est pratiquement indépendante de la température et similaire à celle du plomb liquide à 400°C (étalement non réactif). Cela nous permet de conclure que l'angle de contact d'équilibre de Sn liquide sur une surface non-réagi et propre de Cu est inférieur à 30°.

Les expériences de mouillage des intermétalliques  $\text{Cu}_3\text{Sn}$  et  $\text{Cu}_6\text{Sn}_5$ , réalisées pour la première fois, ont permis une meilleure compréhension du phénomène de mouillage réactif dans le système Cu/Sn liquide. Les angles de contact non réactifs de Sn liquide sur une surface de  $\text{Cu}_3\text{Sn}$ , atteint en moins de 10 ms, diminuent de 23 à 10° lorsque la température augmente de 300 à 500°C, ce qui devrait être principalement due au degré d'oxydation de la surface du Cu. Au cours des expériences de mouillage du composé  $\text{Cu}_6\text{Sn}_5$  à 390°C, de faibles angles de contacts d'environ 20° ont été atteints en moins de 10 ms. En outre, une infiltration rapide de Sn liquide dans le substrat de  $\text{Cu}_6\text{Sn}_5$  à travers les joints de grains mouillés et/ou les porosités ouvertes est en accord avec le très bon mouillage de ce composé par Sn liquide. Ces résultats permettent de conclure que, le mouillage du Cu a lieu en deux étapes: une étape très rapide d'étalement non réactif et une étape lente d'étalement réactif.

Les résultats des expériences de mouillage de Ag et  $\text{Ag}_3\text{Sn}$  par le Sn liquide nous ont permis de proposer un mécanisme de la cinétique d'étalement en deux étapes: (a) un mouillage très rapide non réactif, l'angle de contact diminuant jusqu'à l'angle d'équilibre sur Ag non réagi ( $\theta_{\text{Ag}} \approx 20^\circ$ ) en moins de 10 ms (vitesse d'étalement supérieure à 0.1 m/s) et (b) une étape de mouillage réactif lente de  $\theta_{\text{Ag}}$  à l'angle d'équilibre de Sn liquide sur la couche de produit de réaction,  $\text{Ag}_3\text{Sn}$  ( $\theta_{\text{Ag}_3\text{Sn}} \approx 10^\circ$ ).

### ***(ii) Germination (a) à l'interface réactive Cu/ Sn liquide et (b) dans l'alliage de brasure***

#### ***a) Germination à l'interface réactive Cu/Sn liquide***

En mettant en œuvre un dispositif expérimental d'immersion rapide réalisé dans notre laboratoire, les techniques de SEM-FEG et de TEM, nous avons réussi à étudier, pour la première fois, la séquence de formation des composés intermétalliques à l'interface Cu/alliage Sn-Cu liquide à 250°C, pour des temps d'interaction entre 1 ms et 1 s. Pour les de temps d'interaction très court (1 à 40 ms), deux couches intermétalliques sont formées à l'interface: une couche mince et homogène (40-100 nm d'épaisseur) et une couche d'épaisseur non homogène (50-500 nm). Les deux couches correspondent parfaitement à la structure de  $\eta\text{-Cu}_6\text{Sn}_5$ . Aucune cristallite de la phase  $\varepsilon\text{-Cu}_3\text{Sn}$  n'est détectée pour de telles durées de réaction. Pour un temps de réaction d'environ 1 s deux couches de réaction sont détectées à l'interface: une couche fine de la phase  $\varepsilon\text{-Cu}_3\text{Sn}$  (épaisseur  $\approx 100$  nm) et une couche de la phase  $\text{Cu}_6\text{Sn}_5$  (hauteur maximale de 500 nm). Ces expériences donnent, pour la première fois, la réponse à l'une des questions les plus ouverts et intéressante concernant le brasage en électronique: la première phase qui se forme à l'interface Cu/Sn est la phase  $\text{Cu}_6\text{Sn}_5$  et la phase  $\text{Cu}_3\text{Sn}$  ne croit pas à l'interface tant que l'épaisseur de la phase  $\text{Cu}_6\text{Sn}_5$  est inférieure à environ 500nm.

Dans le même domaine d'intérêt scientifique, nous avons développé une approche théorique sur les critères de suppression de la deuxième phase ( $\varepsilon\text{-Cu}_3\text{Sn}$ ) formée à l'interface réactive Cu/Sn liquide en supposant que  $\text{Cu}_6\text{Sn}_5$

est la première phase qui se forme sous forme d'une couche continue. Ce modèle conduit à l'épaisseur critique de la première couche de  $\text{Cu}_6\text{Sn}_5$  au-dessous de laquelle, la germination et la croissance de la seconde phase ( $\text{Cu}_3\text{Sn}$ ) est supprimée. L'épaisseur critique de la couche de  $\text{Cu}_6\text{Sn}_5$  évaluée par ce modèle est en accord avec les résultats expérimentaux obtenus dans cette étude. En outre, une modélisation théorique d'étapes antérieures de formation d'embryons isolés de la phase  $\varepsilon\text{-Cu}_3\text{Sn}$  est développée avec succès dans le cas d'une suppression de la cinétique de croissance latérale de cette phase.

#### *(b) Germination dans l'alliage de brasure*

La cristallisation de l'alliage eutectique Sn-Cu a été étudiée par des expériences spécifiques de DSC dans deux configurations différentes: alliage de brasure en contact avec la phase  $\text{Cu}_6\text{Sn}_5$  (joint de brasure) et alliage de brasure seul. En appliquant des cycles thermiques de fusion complète et partielle de la brasure, on obtient différentes catégories de degrés de surfusion. En particulier, des degrés de faible surfusion ( $\Delta T = 1-7$  K) sont détectés pour la première fois dans le cas de la fusion partielle. Une approche théorique de la germination hétérogène dans ce dernier cas montre que les sites de germination favorables sont, probablement, des cavités des particules  $\text{Cu}_6\text{Sn}_5$  non dissoutes avec des rayons de courbure d'environ 10nm et/ou des marches (steps) sur la surface de ces particules avec un angle d'ouverture d'environ 120 à 130°. Cette étude a permis de conclure sur les sites hétérogènes de germination de Sn solide: (i) Dans le cas de fusion complète de l'alliage (refusion), les particules  $\text{Cu}_6\text{Sn}_5$  sont complètement dissoutes dans la brasure liquide et la germination a lieu uniquement sur des impuretés solides (ou sur la couche de  $\text{Cu}_6\text{Sn}_5$  formée à l'interface Cu/alliage dans le cas de joints de brasure), (ii) Dans le cas d'une fusion partielle, les nanoparticules de  $\text{Cu}_6\text{Sn}_5$  non dissoutes dans la brasure liquide, servent de sites de germination hétérogènes de Sn solide.

#### *(iii) Cinétique de croissance des couches interfaciales à l'interface Cu/Sn liquide*

Les mécanismes de croissance de la phase de  $\eta\text{-Cu}_6\text{Sn}_5$ , formée par réaction entre Cu et Sn liquide, pour lesquels il existe encore beaucoup de controverse dans la littérature, ont été étudiés expérimentalement et théoriquement.

- La cinétique de croissance de la phase  $\eta\text{-Cu}_6\text{Sn}_5$  formée à l'interface  $\text{Cu}_3\text{Sn}/\text{Sn}$  liquide a été étudiée par une interaction directe entre des spécimens de  $\varepsilon\text{-Cu}_3\text{Sn}$  préparés spécialement pour cette étude et Sn liquide saturé en Cu à 250°C. La comparaison de la cinétique de croissance de l'intermétallique  $\text{Cu}_6\text{Sn}$  dans le couple standard Cu/Sn liquide et dans le couple incrémental  $\text{Cu}_3\text{Sn}/\text{Sn}$  liquide a contribué à la compréhension des mécanismes de croissance de la phase  $\eta\text{-Cu}_6\text{Sn}_5$ . Les résultats obtenus sont également compatibles avec le modèle FDR.

- Afin d'éliminer toute différence de force motrice de diffusion entre les couples Cu/Sn solides et Cu/Sn liquide nous avons effectué, pour la première fois, des expériences spécifiques de réactions d'interface entre Cu et le liquide métastable Sn-0.7wt%Cu à 222°C pour des temps de réaction aussi long que 32 heures. Ceci est réalisé en effectuant des expériences spécifiques de DSC afin de contrôler l'état physique de l'alliage ainsi que de régler la température de façon précise. La comparaison directe des cinétiques de croissance des couches réactionnelles et de leur morphologie aux interfaces Cu/brasure liquide et Cu/brasure solide, à la même température, conduit à la conclusion suivante: La très grande différence dans la cinétique de croissance entre les deux couples peut être expliquée si la croissance se produit par diffusion à l'état liquide par l'intermédiaire de canaux liquides de largeur nanométrique formés entre les joints de grains de la phase  $\eta\text{-Cu}_6\text{Sn}_5$  et/ou par des canaux cylindriques de rayon de quelques dizaines de nanomètres formées aux jonctions triples des grains de  $\eta\text{-Cu}_6\text{Sn}_5$ . Une évaluation théorique de la largeur de ces canaux liquides est effectuée pour la première fois et elle est cohérente avec le modèle FDR.

## 8) Bibliographie

1. [Belyakov\_2014]: Belyakov, S. A., & Gourlay, C. M. (2014). Heterogeneous nucleation of  $\beta$ Sn on NiSn 4, PdSn 4 and PtSn 4. *Acta Materialia*, 71, 56-68.
2. [Bertheau\_2014]: Thesis manuscript of J. Bertheau " Etude et caractérisation d'interconnexions intermétalliques à partir de plots de cuivre et d'alliages Sn-Ag-Cu pour l'empilement tridimensionnel de composants actifs ", Grenoble University, 2014.
3. [Chang\_2003]: Chang, H. Y., Chen, S. W., Wong, D. S. H., & Hsu, H. F. (2003). Determination of reactive wetting properties of Sn, Sn-Cu, Sn-Ag, and Sn-Pb alloys using a wetting balance technique. *Journal of materials research*, 18(06), 1420-1428.
4. [Dinsdale\_1991]: Dinsdale, A. (1991). SGTE data for pure elements. *Calphad*, 15(4), 317-425.
5. [Eustathopoulos\_1999]: Eustathopoulos, N., Nicholas, M. G., & Drevet, B. (Eds.). (1999). *Wettability at high temperatures* (Vol. 3). Elsevier.
6. [Gagliano\_2003]: Gagliano, R. A., & Fine, M. E. (2003). Thickening kinetics of interfacial Cu<sub>6</sub>Sn<sub>5</sub> and Cu<sub>3</sub>Sn layers during reaction of liquid tin with solid copper. *Journal of electronic materials*, 32(12), 1441-1447.
7. [Gusak\_2002]: Gusak, A. M., & Tu, K. N. (2002). Kinetic theory of flux-driven ripening. *Physical Review B*, 66(11), 115403.
8. [Gusak\_2015]: Gusak, A., Hodaj, F., & Liashenko, O. (2015). Criteria of kinetic suppression of lateral growth of intermediate phases. *Philosophical Magazine Letters*, 95(2), 110-121.
9. [Hodaj\_2013]: Hodaj, F., Gusak, A. M., & Liashenko, O. (2013). Possibility of a shape phase transition for solidification of tin at scallop-like surfaces of Cu<sub>6</sub>Sn<sub>5</sub>. *Philosophical Magazine Letters*, 93(3), 166-173.
10. [Johnson\_1975]: Johnson, W. C., White, C. L., Marth, P. E., Ruf, P. K., Tuominen, S. M., Wade, K. D., ... & Aaronson, H. I. (1975). Influence of crystallography on aspects of solid-solid nucleation theory. *Metallurgical Transactions A*, 6(4), 911-919.
11. [Kim\_1996]: Kim, H. K., & Tu, K. N. (1996). Kinetic analysis of the soldering reaction between eutectic SnPb alloy and Cu accompanied by ripening. *Physical Review B*, 53(23), 16027.
12. [Kim\_2009]: Kim, T., Lee, J., Kim, Y., Kim, J. M., & Yuan, Z. (2009). Investigation of the Dynamic Reactive Wetting of Sn-Ag-Cu Solder Alloys on Ni (P)/Au Coated Cu Substrates. *Materials transactions*, 50(11), 2695-2698.
13. [Liang\_2006]: Liang, J., Dariavach, N., Callahan, P., & Shanguan, D. (2006). Metallurgy and kinetics of liquid-solid interfacial reaction during lead-free soldering. *Materials transactions*, 47(2), 317-325.
14. [Liashenko\_2014]: Liashenko, O., Gusak, A. M., & Hodaj, F. (2014). Phase growth competition in solid/liquid reactions between copper or Cu<sub>3</sub>Sn compound and liquid tin-based solder. *Journal of Materials Science: Materials in Electronics*, 25(10), 4664-4672.
15. [Liashenko\_2015]: Liashenko, O. Y., & Hodaj, F. (2015). Differences in the interfacial reaction between Cu substrate and metastable supercooled liquid Sn-Cu solder or solid Sn-Cu solder at 222° C: Experimental results versus theoretical model calculations. *Acta Materialia*, 99, 106-118.
16. [Matsumoto\_2005]: Matsumoto, T., & Nogi, K. (2008). Wetting in soldering and microelectronics. *Annu. Rev. Mater. Res.*, 38, 251-273.
17. [Onishi\_1975]: Onishi, M., & Fujibuchi, H. (1975). Reaction-diffusion in the Cu-Sn system. *Transactions of the Japan Institute of Metals*, 16(9), 539-547.
18. [Paul\_2004]: Paul, A., Kodentsov, A. A., & van Loo, F. J. (2004). Intermetallic growth and Kirkendall effect manifestations in Cu/Sn and Au/Sn diffusion couples: Dedicated to Prof. Dr. Helmut Mehrer on the occasion of his 65th birthday. *Zeitschrift für Metallkunde*, 95(10), 913-920.
19. [Saiz\_2010]: Saiz, E., Benhassine, M., De Coninck, J., & Tomsia, A. P. (2010). Early stages of dissolutive spreading. *Scripta Materialia*, 62(12), 934-938.
20. [Saunders\_1997]: Saunders, N., & Miodownik, A. P. (1990). The Cu-Sn (copper-tin) system. *Bulletin of Alloy Phase Diagrams*, 11(3), 278-287.
21. [Sholl\_1970]: Sholl, C. A., & Fletcher, N. H. (1970). Decoration criteria for surface steps. *Acta Metallurgica*, 18(10), 1083-1086.
22. [Sobczak\_2007]: Sobczak, N., Kudyba, A., Nowak, R., Radziwill, W., & Pietrzak, K. (2007). Factors affecting wettability and bond strength of solder joint couples. *Pure and Applied Chemistry*, 79(10), 1755-1769.
23. [Song\_2004]: Song, J. Y., Yu, J., & Lee, T. Y. (2004). Effects of reactive diffusion on stress evolution in Cu-Sn films. *Scripta materialia*, 51(2), 167-170.
24. [Suh\_2008]: Suh, J. O., Tu, K. N., Lutsenko, G. V., & Gusak, A. M. (2008). Size distribution and morphology of Cu<sub>6</sub>Sn<sub>5</sub> scallops in wetting reaction between molten solder and copper. *Acta Materialia*, 56(5), 1075-1083.

- 25.[Tu\_2007]: Tu, K. N. (2007). Solder joint technology (pp. 211-288). New York: Springer.
- 26.[Tu\_2013]: Tu, K. N., Hsiao, H. Y., & Chen, C. (2013). Transition from flip chip solder joint to 3D IC microbump: Its effect on microstructure anisotropy. *Microelectronics Reliability*, 53(1), 2-6.
- 27.[Tung\_2014]: Tung, B. T., Watanabe, N., Kato, F., Kikuchi, K., & Aoyagi, M. (2014, May). Flip-chip bonding alignment accuracy enhancement using self-aligned interconnection elements to realize low-temperature construction of ultrafine-pitch copper bump interconnections. In *Electronic Components and Technology Conference (ECTC), 2014 IEEE 64th* (pp. 62-67). IEEE.
28. [Wang\_2006]: Wang, H., Gao, F., Ma, X., & Qian, Y. (2006). Reactive wetting of solders on Cu and Cu<sub>6</sub>Sn<sub>5</sub>/Cu<sub>3</sub>Sn/Cu substrates using wetting balance. *Scripta materialia*, 55(9), 823-826.